Geochemical and petrographic insights from speleothems: Records of Holocene Eastern Mediterranean climate.

Emily Nicole Peckover

A thesis submitted for the degree of

Doctor of Philosophy

School of Environmental Sciences

University of East Anglia

May 2017

Abstract

In this thesis, new Holocene palaeoclimate information from speleothems is presented from three regions (central Peloponnese Greece, south west Turkey and the eastern forelands of the Zagros Mountains, Iran) where the spatial distribution of Holocene climate records is low. This study uses a multi-proxy approach with particular emphasis on petrography and stable isotope analysis.

Holocene growth of stalagmite KTR-2 (11,900 yr BP to 6700 yr BP) from Limnon Cave in the central Peloponnese is broadly coincident with the formation of Sapropel 1. The early Holocene was generally wetter than at present. A record of the 8.2 kyr event was obtained from KTR-2 using high resolution trace element ICP-MS and micromilled stable isotope samples. Arid conditions are implied by $\delta^{18}O$ and trace elements, with aridity probably beginning ~9000 yr BP. $\delta^{13}C$ data suggests precipitation may have been strongly seasonal during the 8.2 kyr event.

Distinct grey coloured layers in HY-8, a stalagmite from Sirtlanini Cave, SW Turkey, represent fire events occurring above the cave; there is however, no suggestion that the fires occurred during periods of relatively enhanced aridity. The palaeoclimate record spans ~5600 yr BP to the present day, but does not indicate any significant long term reduction in precipitation. The HY-8 $\delta^{18}O$ record suggests the 4.2 kyr anomaly was a two-step aridity event occurring between 4290 and 3850 yr BP. A distinct pluvial event from 4890-4290 yr BP is also recorded by $\delta^{18}O$, as is evidence for the Little Ice Age (630-280 yr BP).

The Holocene section of stalagmite KT-3, from the eastern forelands of the Zagros Mountains in Iran, grew from 9400 yr BP to present. The early Holocene until ~7000 yr BP was wetter than the present day. Multiple proxies show falling precipitation amounts from ~7000 yr BP, plateauing from ~3000 yr BP to present. There is very little short term fluctuation in $\delta^{18}O$ but the overall trend has a profile similar to the decline of solar insolation in the Holocene, which appears to be responsible for the long term reduction in winter precipitation. In KT-3, the correlation between Ba/Ca and $\delta^{13}C$ fluctuations might be a more sensitive indicator of moisture. A significant positive $\delta^{13}C$ excursion could be recording the 8.2 kyr event.

Additionally, this thesis presents a specific petrographic study from two different, but discontinuously grown, Turkish stalagmites. These stalagmites grew very differently and within different epochs. Petrography has been used to interpret and relate fabrics to their environment of formation and identified micro-dissolution as a prominent feature of growth. A link between these micro-dissolution events and stratigraphically inverted U-series dates is proposed.

Acknowledgements

Firstly, my biggest thanks must go to my supervisors Julian Andrews and Peter Rowe, not least for allowing me to undertake this research in the first place, for always be available for any questions, guidance and discussion I have needed but ultimately letting me develop this research independently. To Julian for the support needed in these last few months of writing and to Peter for all the help when I was just starting out.

This thesis would not have been possible without the analytical expertise and help of Alina Marca and Graham Chilvers at UEA and Steve Noble and Diana Sahy at NIGL. Thank you to Alina for guiding me through 3 years of working in SIL. A further thanks to Steve and Diana for accommodating me at NIGL throughout the stages of U-series analysis and also for not laughing my out of the door when I explained the basis for Chapter 4!

A huge thank you has to go to my best office mate Ruth Kirk, who has let me moan and complain about anything and everything and still managed to be massively supportive. Thank you for being such a great friend in work and out! To Osgur McDermott-Long, the best annoying office mate you could ask for, sticking it out to the bitter end. We might end up in Karma after this. And to all the other PhDs I have encountered on the way with a special mention for Richard Jones.

Finally a massive thank you to my constant champion Benjamin Gale who can be credited for me applying for this PhD in the first place. Thank you for always trying to understand, keeping a 100% success rate at lifting my mood and still wanting to marry me at the end of it!

Table of Contents

List of Figures

List of Tables

Chapter 1: Introduction

1.1 Rationale

Over geological time natural (pre-anthropogenic influenced) climatic variability is known to have been forced by a number of drivers. These range from long term orbital fluctuations such as precessional and eccentricity controlled glacial/interglacial cycles and solar radiation changes, to shorter, internally forced fluctuations, such El Niño (Frappier et al., 2002) or the North Atlantic Oscillation (Proctor et al., 2000). It is these changes occurring on shorter timescales of years to decades that arguably will be most keenly felt on human timescales. Palaeoclimate records provide the key time-integrated information on the forcing and response to change in climate systems; they provide the key context for understanding when climate change can be considered 'unusual'.

The Holocene is recognised as an interglacial with onset occurring at 11,700 yr before AD 2000 (Walker et al., 2009) at the end of the Younger Dryas stadial. Climatic conditions in the European Holocene are generally considered as 'warm and wet' and are often described as 'stable' particularly when compared to the previous glacial period. Aside from the glacial termination, orbitally controlled climate change through the Holocene is controlled largely by precession, directing the Northern Hemisphere away from the sun in the summer which has gradually reduced summer solar insolation and the contrast in climate between seasons (Imbrie et al., 1992).

However, at least six significant rapid climate changes (Mayewski et al., 2004) have occurred during the Holocene, some of which have been linked to major societal upheaval in the Eastern Mediterranean region. The internal forcing and spatial distribution of the effects of these climate events are not completely understood. The 8.2 kyr event is a well-documented, widespread northern hemispheric event (Alley et al., 1997 among many), with effects felt by civilisations in the Eastern Mediterranean (Berger and Guilaine 2009). There is evidence for a dry event at 5.2 kyr in Italy and Israel (Zanchetta et al., 2014) but the 4.2 kyr event is most widely discussed for its potential impact on the collapse of the Akkadian Empire (Weiss et al., 1993; Cullen et al., 2000; Clarke et al., 2016; Weiss 2016). A 400 year period of drought starting at 3.2 kyr is thought to be the cause of the Late Bronze Age Collapse, which appears in some Mediterranean and Middle

Eastern archaeology (Weiss 1982; Kaniewski et al., 2010; Drake 2012). Finally, some regional records suggest evidence for the smaller magnitude, shorter events of the Medieval Warm Period ~1000-1300 AD (e.g. Crowley and Lowery 2000; Yavuz et al., 2007; Mann et al., 2009; Dean et al., 2013) and the Little Ice Age ~ 1350-1850 AD (for example Kuniholm 1990; Grove 2001; Touchan et al., 2007; Yavuz et al., 2007; Kaniewski et al., 2011).

The Eastern Mediterranean and Middle East regions sit within a transitional belt between temperate mid-latitudes and arid tropical zones, such that the controls on the region's climate are complex and changeable over the course of a year. The importance of climate in these regions is two-fold. Historically, the Eastern Mediterranean and the Middle East were key locations for the development of settlements, agriculture and urbanisation of modern humans. Today, the Mediterranean in particular, is densely populated and is consistently projected by climate models to become both drier and warmer across all seasons (Christensen et al., 2007; Christensen et al., 2013). There is already evidence of long term drying trends (>900 years) in parts of the Mediterranean and Middle East (Cook et al., 2016). Due to the dynamic nature and the high spatial variability of the region's climate, the Intergovernmental Panel on Climate Change (IPCC) highlighted the importance of increasing the number of palaeoclimate records from the Mediterranean and Middle East to reduce the uncertainty when predicting future climate change (Christensen et al., 2013).

Even though published research on the climate of the Eastern Mediterranean and Middle East is extensive, there is still need for targeted palaeoclimatic records from these regions. Spatial resolution of speleothem records in Eastern Mediterranean and Middle Eastern countries, particularly those studied here, is still low compared to the western Mediterranean. Additionally, more localised controls such as topography and proximity to moisture sources have a large impact on local climate, making spatial variability quite high. This variability and the presence, magnitude and timing of long term trends within the Holocene climate are still much debated, such that new information helps build a more accurate picture.

1.2   Research Aims

The overarching aim of this thesis is to increase the knowledge of Eastern Mediterranean and Middle East Holocene climatology during part of the Holocene Epoch (last 11,500 years), using multiple speleothem climate proxies. Speleothem records in this study have been targeted specifically from regions where the resolution of Holocene climate data is low.

Specific targets to achieve this include:

- Exploring Holocene climate based on the records of individual stalagmite chronologies by creating a west to east transect of caves from central southern Greece (Limnon Cave) to north west Iran (Katalakhor Cave), including south west Turkey (Sirtlanini Cave).
- Adopting a multi proxy approach including stable isotopes, petrography, trace elements and Raman spectroscopy.
- Specifically aiming towards more extensive use of speleothem petrography, particularly as a tool for locating appropriate locations for U-series samples and additionally expanding discussion on the environment of formation of fabric types. A further stalagmite from Dim Cave in SW Turkey was studied in conjunction with Sirtlanini Cave to better achieve this.
- Placing newly created stalagmite records within the context of previous climatic records from the Holocene in the region.

In light of these aims the thesis is structured as follows. First a literature review of modern climate controls (Chapter 2) and the underpinning context for understanding speleothem proxies (Chapter 3). Following this, Chapter 4 is dedicated to petrography, using two Turkish stalagmites which grew discontinuously and showed stratigraphic inconsistences in U-series dating. The subsequent chapters (Chapters 5-7) discuss the palaeoclimate records from each region within the west-east transect, although Sirtlanini Cave in Turkey is discussed first (Chapter 5) for better continuity with Chapter 4 as aspects essential to the record are presented in this preceding chapter.

1.3   Study sites

Throughout the area discussed in this thesis the large scale climatic controls are believed to be broadly similar, with relatively localised effects forced by topography and proximity to different moisture sources (see Chapter 2 for a full overview). This means that the cave sites within the study transect are all linked by similar Mediterranean-type climate with wet winters and warm, dry summers. While this research focuses on the Holocene, a Pleistocene aged stalagmite from SW Turkey (Dim-1) was also included. The approach here was not to establish a climate record as this was already attempted by Wickens (2013). Rather, stalagmite Dim-1 was studied principally because it helped inform discussion on the use of petrography to help refine an age model. However, the petrography also proved useful to refine understanding of the stalagmites environment of formation.
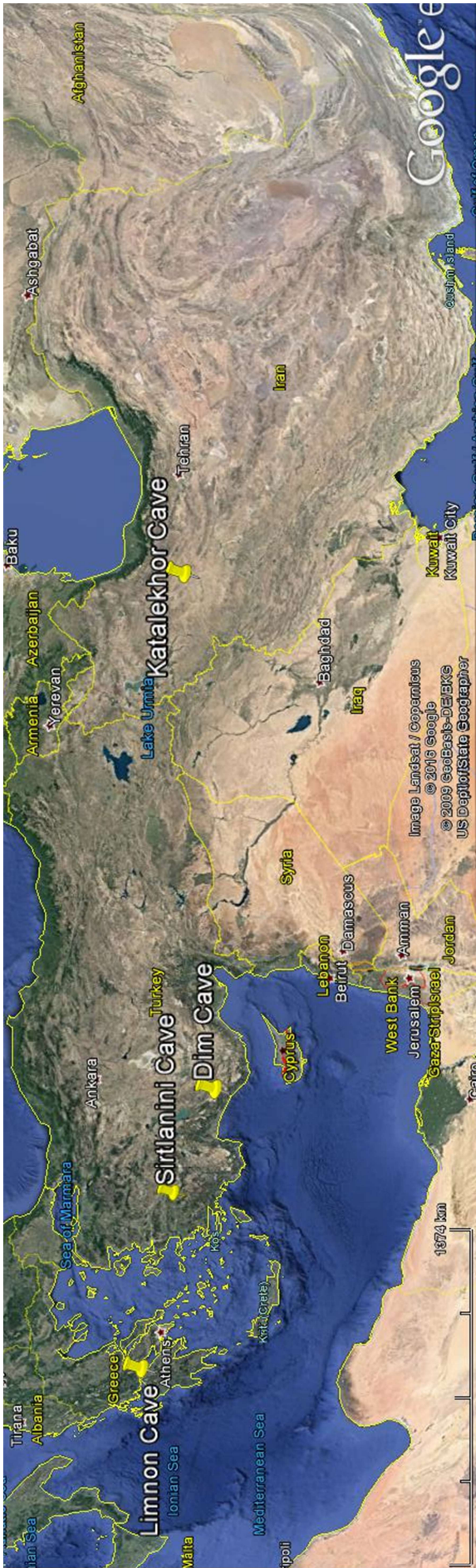
Figure 1.1: Study area of Greece, Turkey and Iran with cave sites marked. Limnon Cave, Sirtlanini Cave and Katalekhor Cave are considered in the Holocene palaeoclimate transect, while Dim Cave is discussed in Chapter 4 as part of a petrographic study.

Greece lies on the western fringes of the Eastern Mediterranean region and is bordered by three seas, the Ionian to the west, Mediterranean to the south and Aegean to the east. Greece is highly mountainous, the Pindus Mountains forming a central spine of roughly N-S orientation. The second principal range forms the Peloponnese Peninsula which is separated from central Greece by the Gulf of Corinth.

Turkey is also fringed by separate water bodies: the entire northern border of the country abuts the Black Sea, the Mediterranean Sea fringes non-landlocked borders to the south and becomes the Aegean Sea in the west. The key topographic features are the two mountain ranges the Pontic to the north and the Taurus to the south. These ranges converge in the east and are separated by a high plateau which occupies much of central Turkey - the Central Anatolian Plateau. Iran is fringed to the south by the Persian Gulf and Gulf of Oman, and has a partial northern limit formed by the Caspian Sea. Iran has two major mountain chains, the Zagros running down the western border into the south, and the Alborz forming a rim around the Caspian Sea coastline.

1.4.1 Considerations when using stalagmites forming in seasonal climates

Growth of stalagmites forming in semi-arid or seasonal growth environments, as observed in all four cave sites within this study, is dependent on sufficient water infiltration and storage within the karst (Fleitmann et al., 2008a). As a result, calcite precipitation rates may vary by season and stalagmite growth can be strongly biased towards the winter when precipitation and recharge is highest (Frisia et al., 2003). During particularly dry periods, depositional hiatuses might occur. This seasonal precipitation of $CaCO_3$ will lead to a seasonal bias in geochemical proxies, particularly $\delta^{18}O$ (McDermott 2004; McDermott et al., 2006). During the dry, warm summer months, evaporative enrichment of surface water, and its oxygen isotopic composition is likely to take place before entry to the epikarst and the cave (Lachniet, 2009); this will enrich $\delta^{18}O$ values relative to the source precipitation (Bar-Matthews et al., 1996).

1.4 Advantages of using speleothems as climate proxies

The term speleothem refers to any secondary cave deposit, but principally stalagmites, stalactites and flowstones. These formations can be made of any of the 250 recorded cave minerals (Hill and Forti 1997), but only calcium carbonates and gypsum form commonly (Hill and Forti 1997). Stalagmites are by far the most frequently used for palaeoclimate reconstruction due to their regular structure and more predictable growth (McDermott, 2004). Speleothems can grow in a range of cave environments and usually they are preserved as the originally deposited $CaCO_3$ (McDermott 2004), being not particularly susceptible to later alteration (Fairchild et al., 2006a).

As terrestrial climate proxies, speleothems are important archives for comparison against deep-sea and ice-core records (Lauritzen and Lundberg 1999) especially as they produce lengthy, often unbroken records that form relatively rapidly in comparison to other records, and can be absolutely dated back to 500,000 years (Bourdon et al., 2003). The cave environment largely protects growing speleothems from external physical erosion, allowing growth for long periods of time. Speleothems are considered more reliable than other terrestrial proxies, such as lacustrine records, which are more susceptible to diagenetic alteration and are usually less reliably dated (McDermott 2004).

Speleothem science has a long history but its growing importance in recent years is underscored by the numbers of publications that have appeared since the late 1990s (Fairchild et al., 2006a; Fleitmann et al., 2008b). The primary reason for this increase has been the development of high precision U-series dating using thermal ionisation mass spectrometry (TIMS) (Edwards et al., 1986) and later inductively coupled plasma mass spectrometry (ICP-MS) (Shen et al., 2012). This development has allowed the use of smaller sample sizes, even with younger Holocene stalagmites, that can have ppb abundances of uranium and thorium. Progress in dating speleothems has also coincided with advances in other analytical techniques, such as mass spectroscopy, allowing investigation of climatic signals at much higher resolution than was previously possible (Fleitmann et al., 2008b). A particularly welcome outcome of these advances is the ability to capture records at near annual or annual resolution (e.g. Fleitmann et al., 2004; Treble et al., 2005; Tan et al., 2006; Baker et al., 2015) and increasingly at a seasonal scale (e.g. Johnson et al., 2006; Mattey et al., 2008a; Boch et al., 2011; Orland et al., 2012).

Speleothem growth is typically very sensitive to external climate forcing and can record a range of palaeoclimate/environmental conditions in both carbon and oxygen isotopes, petrography, trace elements and organic content. The fact that many speleothems are known to deposit carbonate

at close to isotopic equilibrium with their parent dripwaters (Tremaine et al., 2011), is essential to disentangle climatic signals from other signals influenced by, for example, the karst system.

Long term growth of speleothems has proved invaluable for the understanding of Quaternary palaeoclimate on glacial/interglacial timescales, particularly in semi-arid regions (e.g. Bar-Matthews et al., 1999; Frumkin et al., 2000; Bar-Matthews et al., 2003; Fleitmann et al., 2007) where other information is sparse. Speleothem records help to understand lower latitude response to events recorded in Greenland ice sheets (including Cheng et al., 2006; Cheng et al., 2009a; Drysdale 2009; Fleitmann et al., 2009) and help confirm and tighten the ice core timescales. Speleothems have added to the understanding of atmospheric teleconnections between the North Atlantic and the Asian Monsoon operating over glacial timescales (Cheng et al., 2006; Cheng et al., 2009a). On shorter Holocene timescales speleothems have allowed further understanding on the movement of the ITCZ (Fleitmann et al., 2007; Fensterer et al., 2013), the pattern of El Nino (Asmerom et al., 2007) and monsoonal changes (Fleitmann et al., 2003, 2007). More significantly for this study, advances in analytical techniques coupled with the variable growth of stalagmites, has allowed detailed scrutiny of changes in monsoonal summer precipitation over 100s of years (Denniston et al., 2000), investigation of smaller scale, less far reaching climate patterns such as the North Atlantic Oscillation (Proctor et al., 2000; Wassenburg et al., 2013) and short lived climate changes such as the 8.2 kyr event (prominently Cheng et al., 2009b), 5.2 kyr event (Zanchetta et al., 2014) and 4.2 kyr event (e.g. Bar-Matthews and Ayalon 2011).

A further advantage is that cave calcite can be linked to precipitation amounts from instrumental records (e.g. Fleitmann et al., 2004; Mattey et al., 2008b). In the most ideal study long term cave monitoring should be utilised in conjunction with stalagmite collection. Cave monitoring allows an in depth understanding into current environmental conditions within the specific cave for example temperature, humidity, drip rate and evaporation potential and how parameters may change over the course of seasons-years. Cave monitoring is also useful because stable isotopes have complex controlling factors particularly at high resolution (Fairchild et al., 2006a) and these processes may or may not be controlled by climate.

To date there is still not a comparatively large number of papers published concerning modern calcite precipitation and the monitored cave environment (i.e. Bar-Matthews et al., 1996; Genty and Deflandre 1998; Frisia et al., 2000; Mattey et al., 2008b; Tremaine et al., 2011; Riechelmann et al., 2013; Borsato et al., 2015) and the range of parameters monitored varies. Additionally fossil speleothem records that have been accompanied by cave monitoring (examples include Frisia et al., 2002; Boch et al., 2011) are even more limited. Of particular interest to the content of this

thesis is that only one of those monitoring programmes is based in the Eastern Mediterranean/Near East regions (Bar-Matthews et al., 1996). There is additionally very little laboratory research on laboratory grown calcite under cave conditions and the controls on signal preserved in geochemical proxies (e.g. Day and Henderson, 2011 and references therein, Day and Henderson, 2013 and references therein). Few research groups have the resources to achieve a large scale monitoring programme (Fleitmann et al., 2008), including this study, and is a recognised limitation of the work.

Chapter 2. Modern Climatology of the Eastern Mediterranean and Iran.

2.1   Modern Climate

The geographical position of the Eastern Mediterranean and Iran is within the climatic transitional belt between temperate mid latitude westerlies and arid tropical zones (Spanos et al., 2003) at the margin of the low pressure system to the north and the descending limb of the tropical southern Hadley cell (Lionello et al., 2006) (Figure 2.1). The transition between these two pressure systems migrate, to about 60°N in the summer (Karaca et al., 2000). This increases the influence of the closer climate system with the temperate westerlies having more influence in the winter. As a result, the climate of the Eastern Mediterranean is strongly seasonal with typically warm and dry summers, mild wet winters and distinct influences operating at different times of the year. These influences are both external and internal to the Mediterranean Basin itself creating a complex climatology.
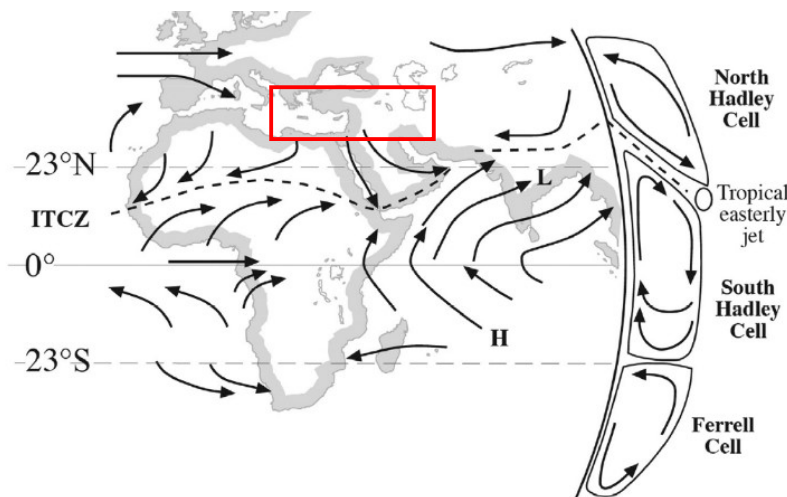
Figure 2.1: Atmospheric circulation during the summer in the Northern Hemisphere. H indicates areas of high pressure and L areas of low pressure. The study region of this thesis is highlighted in the red box. After Rohling et al. (2015).

2.1.1 Large scale climate controls

2.1.1.1 North Atlantic Oscillation

The North Atlantic Oscillation (NAO) is the meridional oscillation of atmospheric pressure at sea level between the subpolar Icelandic Low and the subtropical Azores High (van Loon and Rogers 1978). The climatic effects which arise from changes in the NAO are often referred to as a see-saw (originally van Loon and Rogers 1978) as temperatures in the north (Greenland) show the opposite response to temperature in the south (Europe), i.e. when temperatures are higher than average in Greenland, they will be lower than average in Europe (van Loon and Rodgers 1978). Additionally, the strength of the anomalies at each pole of the system creates a pressure gradient over the North Atlantic; this directly controls the speed and direction of mid-latitude westerlies (Lamb and Peppler 1987). The NAO Index is in a positive state during periods when the difference in sea level pressure in winter months between the Azores and Iceland is higher than average and vice versa for negative NAO states (Rogers 1984).

During positive NAO phases the area of maximum atmospheric moisture transport extends much further north and east, reducing precipitation to the Mediterranean as a whole (Hurrell 1995). Additionally less moisture is delivered to Iran in winters during positive NAO phases (Hurrell 1995). A positive NAO also leads to warmer winters in Europe and the Mediterranean (Hurrell 1995). There is a link in the occurrence of extreme cold events in the Eastern Mediterranean and the rest of Europe in more recent years suggesting that these are controlled by very negative NAO phases (Maheras et al., 1999).

The NAO is also thought to control a smaller, Mediterranean Basin wide, pressure oscillation from west to east, known as the Mediterranean Oscillation (MO) (Conte et al., 1989). This occurs because precipitation variability across the Mediterranean creates regimes that are not consistent with other large scale circulation dynamics (Dünkeloh and Jacobeit 2003). The MO has similar characteristics to the NAO, it is apparent at the surface and at 500 hPa, and predominantly effects winter and spring climate (Maheras et al., 1999). Changes in the MO can be statistically correlated to changes in the NAO (Maheras et al., 1999). It has been observed that a negative NAO phase is associated with wet conditions in the western Mediterranean and drier conditions in the east (Maheras et al., 1999; Dünkeloh and Jacobeit 2003).
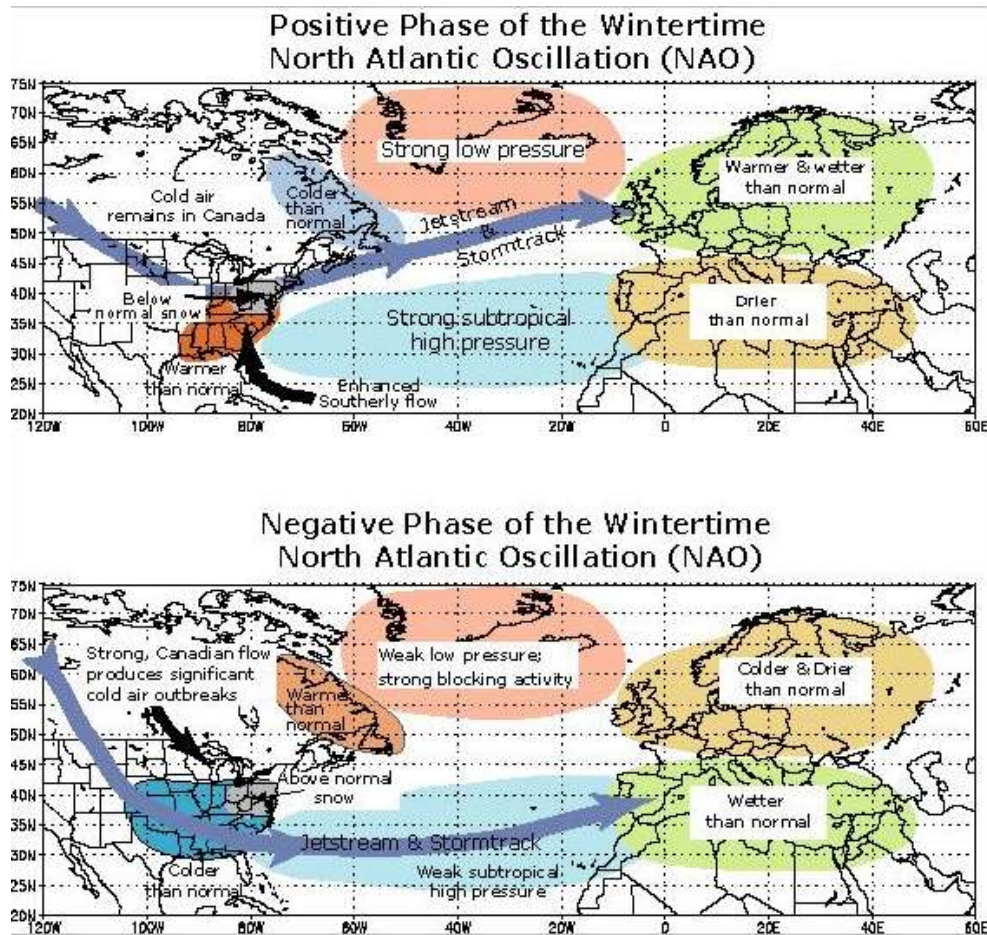
Figure 2.2: Positive and negative phases of the NAO and effects across the Northern Hemisphere.

Image credit National Oceanic and Atmospheric Administration www.noaa.gov.

2.1.1.2 North Sea-Caspian Pattern

The North Sea-Caspian Pattern (NCP) is an upper (500hPa) level atmospheric teleconnection affecting the Eastern Mediterranean region (Kutiel and Benaroch 2002) and Iran (Ghasemi and Khalili 2008). The magnitude of the NCP Index indicates if the NCP is in a positive phase (high magnitude) or negative phase (low magnitude) (Kutiel and Benaroch 2002). The NCP affects atmospheric circulation between two poles located in the North Sea close to Britain and around Turkey: the Black Sea and Caspian Sea and the Balkans (Kutiel and Benaroch 2002; Tatli 2007). During positive NCP phases, north-eastern atmospheric circulation between the Caspian and North Sea is increased, while during negative NCP south-westerly circulation is increased (Kutiel

and Benaroch 2002; Brunetti and Kutiel 2011). The effect of the NCP is less pronounced, and therefore less important, during the summer months (Kutiel and Benaroch 2002).

There are clear indications that the NCP has an effect on temperature throughout the year in the Eastern Mediterranean and Middle East (Kutiel et al., 2002; Tatli 2007; Ghasemi and Khalili 2008; Brunetti and Kutiel 2011) and a possible effect on rainfall in Turkey and Greece (Kutiel et al., 2002). In both Greece and Turkey mean temperatures across the year were higher during negative NCP phases; the biggest differences are observed in winter months and the effect stronger in Turkey (Kutiel et al., 2002) as the largest temperature anomalies are observed in the Black Sea (Brunetti and Kutiel 2011). In Iran the same result is observed as winter surface air temperatures are increased during negative NCP phases (Ghasemi and Khalili 2008). The NCP possibly creates a precipitation gradient in Greece from north-south, with northern Greece receiving more rainfall during negative NCP and Crete during positive NCP (Kutiel et al., 2002). Similarly, in Turkey a weak SW-NE precipitation gradient is observed, with negative NCP phases delivering more rainfall to the SW and positive NCP causing increased rainfall in the NE (Kutiel et al., 2002).

2.1.1.3 *Eastern Atlantic Western Russia Pressure Pattern*

The formation of the Eastern Atlantic Western Russia pressure pattern (EAWR) in the Mediterranean is similar to the NCP; involving the circulation of upper atmospheric air flows at 700 and 850 hPa (Barnston and Livezey, 1987; Krichak and Alpert 2005) creating differing pressure anomalies over western and south-western Russia and NW Europe (Krichak and Alpert 2005). Positive EAWR intervals cause negative (cyclonic) pressure anomalies over Russia and positive pressure anomalies (anticyclonic) over Europe (Krichak and Alpert 2005). This means that drier than normal conditions over much of the Mediterranean are coincident with positive EAWR phases and vice versa (Kirchak and Alpert 2005). As the NCP, the EAWR effect is present during winter (Kirchak and Alpert 2005). The EAWR seems to have a stronger effect on airflow direction of atmospheric circulation derived from the Eastern Mediterranean than systems entering from the west (Kirchak and Alpert 2005). Positive EAWR intervals primarily occur at the same time as positive NAO and their formation may be linked to intensification of the NAO (Kirchak and Alpert 2005). The influence of the EAWR has possibly been identified in a Turkish speleothem record over the last 500 years (Jex et al., 2011).

2.1.1.4 Siberian High Pressure System

In winter the development of the Siberian High in eastern Eurasia (40–65°N, 80–120°E, Panagiotopoulos et al., 2005) creates complex and spatially variable effects, but can be observed in Turkey and Greece and as far west as Britain and Spain (D'Arrigo et al., 2005). Generally, the Siberian High is associated with colder winter temperatures across Europe into SE Asia, although no significant correlations to colder temperatures are seen within Mediterranean temperature changes (Panagiatopoulous et al., 2005). Significant negative correlations have been observed between the Siberian High and Mediterranean sea level pressure (Panagiatopoulous et al., 2005, D'Arrigo et al., 2004) suggesting that during intensified Siberian High anomalies the sea level pressure in the Mediterranean is lower, which might induce more rainfall events in the region. On the other hand a possible link exists between a strengthened Siberian High and enhanced cyclogenesis in the Mediterranean (Panagiatopoulous et al., 2005), suggesting that either mode of the Siberian High can produce wetter conditions in the Mediterranean. The possible link between stronger Siberian High periods and a strengthened jet stream positioned in the eastern Mediterranean Sea (Panagiatopolous et al., 2005) south of Greece and Turkey, might create drier and colder conditions in the Eastern Mediterranean compared to the rest of the Basin. The Siberian High creates a high pressure anomaly over Iran during the winter (Kehl 2009) but does not usually block depressions from the west.

2.1.1.5 Basin cyclogenesis

As well as low pressure systems tracking across the Mediterranean from the Atlantic in winter, the development of cyclones within the Mediterranean Sea itself has a strong effect on the climatology of Turkey and Greece. These cyclones, secondary lows to those from the west, form along areas which have both temperature and dew point gradients (baroclinicity) or when upper atmospheric troughs interact with mountain ranges (Alpert et al., 2006; Flocas et al., 2010). Local basin cyclogenesis also brings wetter winter weather to the Eastern Mediterranean (Alpert et al., 1990; Spanos et al., 2003; Alpert et al., 2006). Cyclones generally move along preferred tracks (Alpert et al., 1990) and depressions are enhanced when the subtropical and polar jet streams interact (Zhou et al., 2008). Turkey is typically affected by cyclones forming in the centres at the Gulf of Genoa, the Aegean and off Cyprus (Alpert et al., 1990; Türkeş, 1998; Karaca et al., 2000; Spanos et al., 2003; Zhou et al., 2008; Flocas et al., 2010). Northern parts of Turkey are also affected by cyclogenesis from the Black Sea (Spanos et al., 2003; Fleitmann et al., 2009). Basin cyclones which effect Greece originate in the Adriatic and the Gulf of Genoa (Alpert et al., 1990; Brzović, 1999; Spanos et al., 2003; Zhou et al., 2008).
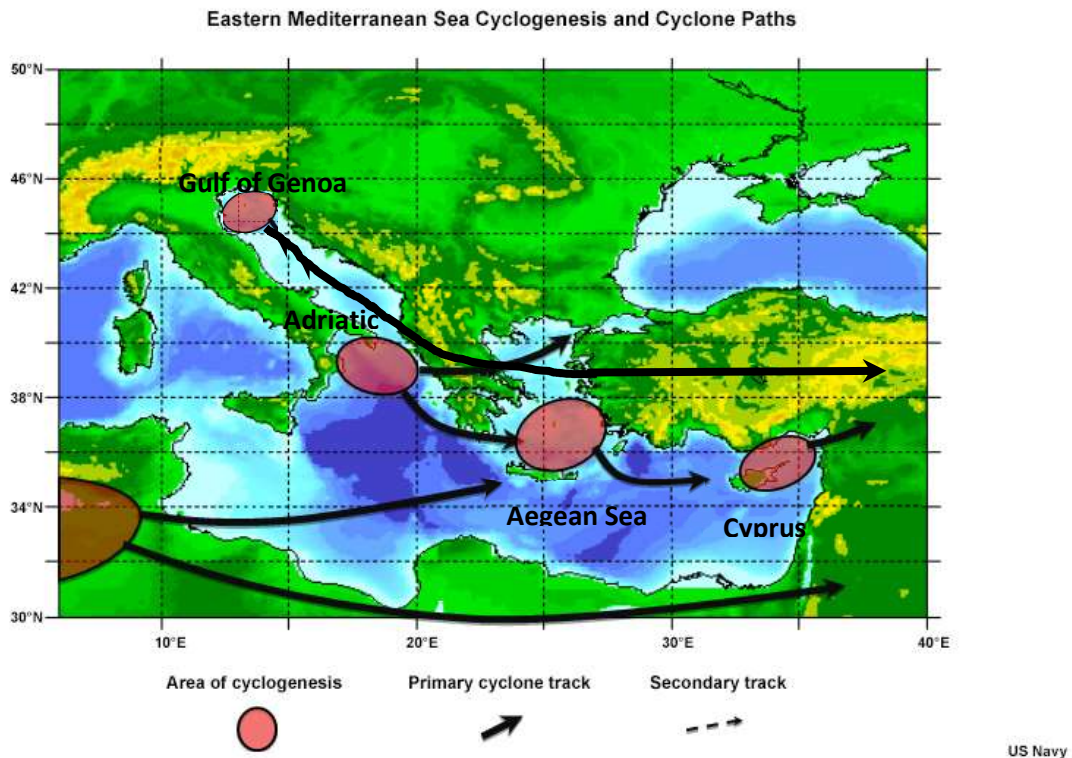
Figure 2.3: Areas of cyclogenesis and subsequent cyclone tracks adapted from www.meted.ucar.edu, credit US Navy.

2.1.1.6   Monsoonal Influence

In summer, the Hadley cell moves north reducing the influence of the Atlantic on the Eastern Mediterranean and Iran (Lionello et al., 2006) and allowing other factors to control summer climate. In summer, strong adiabatic subsidence of air is observed in the Eastern Mediterranean (and Iran) which is controlled by the intensity of the Asian Monsoon rather than the northward movement of the Hadley Cell (Rodwell and Hoskins 1996). Heating associated with the Monsoon creates upper level Rossby waves which propagate between the adiabatic ascent of air north of the Bay of Bengal (Rodwell and Hoskins 1996) and subsequent descent of air centred over the Eastern Mediterranean (except the Black Sea), Red Sea and Northeast Africa (Rodwell and Hoskins 1996, (Raicich et al., 2003; Ziv etal., 2004; Tyrlis et al., 2013).

The response to this pressure system is complex. Descent is forced here because the Rossby waves meet the advection of colder air masses from the north (Rodwell and Hoskins 1996). Additionally, local large orographic effects (such as the Taurus Mountains and Zagros Mountains) interact with the Rossby waves, enhancing mid and low level flow, thus leading to higher air subsidence over the Eastern Mediterranean and Iran (Tyrlis et al., 2013). However, at lower atmospheric levels the expansion of the heat low caused by the Asian Monsoon (via the Persian Trough) creates long term northerly winds (Etesians) due to the west-east pressure gradient between Anatolia and the Balkans (Figure 2.4) (Biten and Sa' Aroni, 1992).
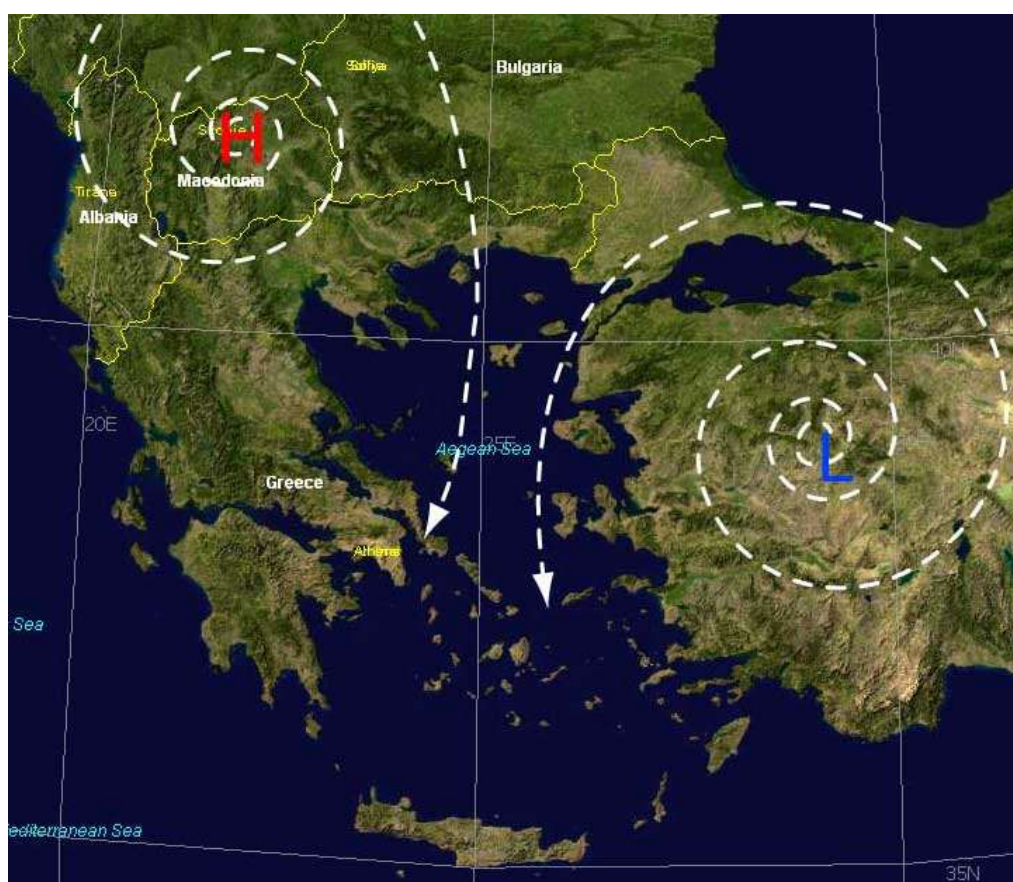
Figure 2.4: Development of the Etesian winds via the low level temperature/pressure difference created by the expansion of the low temperature Asian Monsoon into the Eastern Mediterranean via the Persian Trough (Bitan and Saaroni 1992) and relatively higher pressure systems occurring over the Balkans. Image credit Piotr Flatau www.commons.wikimedia.org*.*

The effect of the teleconnection between the Asian Monsoon and Eastern Mediterranean causes dry weather with low frequency rainfall in the summer (Spanos et al., 2003). While large scale subsidence may be expected to create periods of convective rainfall, it is rare due to the effect of the Etesians (Ziv et al., 2004, Tyrlis et al., 2013). This is because the winds reduce the amount of warming and thus cloud formation and rainfall (Ziv et al., 2004, Tyrlis et al., 2013) and instead create a more stable temperature regime (Ziv et al., 2004) (Figure 2.5)
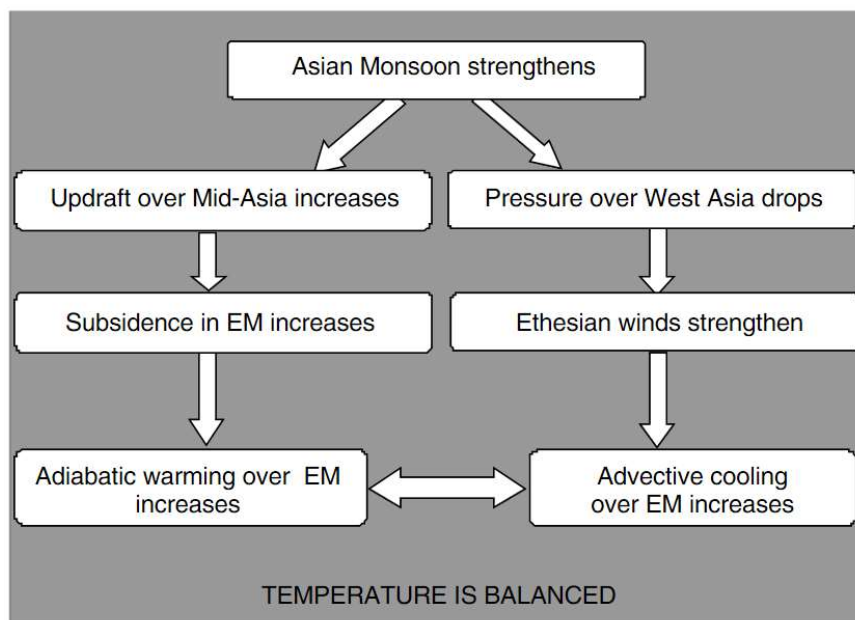
Figure 2.5: Creation of prolonged dry conditions during summers in the Eastern Mediterranean and Iran but stable temperatures due to the upper and lower atmospheric teleconnections associated with the Asian Monsoon (after Ziv et al., 2004).

2.1.2 Regional Climate

2.1.2.1 Greece

As with Turkey, Greek climate is generally described as typically Mediterranean; however, the presence of inland mountain ranges such as the Peloponnese and Pindus create a distinctive continental climate in these areas, where rainfall is less seasonal and winters are colder (Dotsika

et al., 2010). A N-S temperature gradient exists with the south exhibiting more subtropical temperatures than the north (Dotiska et al., 2010). Precipitation in the winter is sourced from Atlantic frontal depressions or Mediterranean Basin cyclogenesis (Xoplaki et al., 2000), although some cyclones originating in North Africa can also affect Greece (Alpert et al., 1990). Rainfall over Greece is decreasing overall but is most significant in the western mountain ranges, the north and the east (Xoplaki et al., 2000). There is evidence that a reduction in winter cyclone activity in the region of Greece accounts for reduced winter rainfall (Xoplaki et al., 2000; Maheras et al., 2004).

Frontal depressions approach Greece across the Ionian Sea reaching the west of the country first (Flocas and Giles, 1991) (Figure 2.6); as a result, rainfall is much higher in the west than the east (Flocus and Giles 1991; Xoplaki et al., 2000.). As unstable maritime air is forced over the continent the orographic effect of the north west and central mountain ranges forces more rainout from depressional fronts in these regions (Xoplaki et al., 2000, Argiriou & Lykoudis 2006) (Figure 2.6). In the summer, the heating and elevation of the mountain ranges in Greece create localised convective thunderstorms, further adding to rainfall totals compared to the rest of the country (Xoplaki et al., 2000; Kambezidis et al., 2010).

Limnon Cave is located within the montane central Peloponnese. Its high elevation and westerly position receives more rainfall than caves studied in Turkey and Iran. Seasonality of rainfall also less pronounced in the region relative to Turkey and Iran.
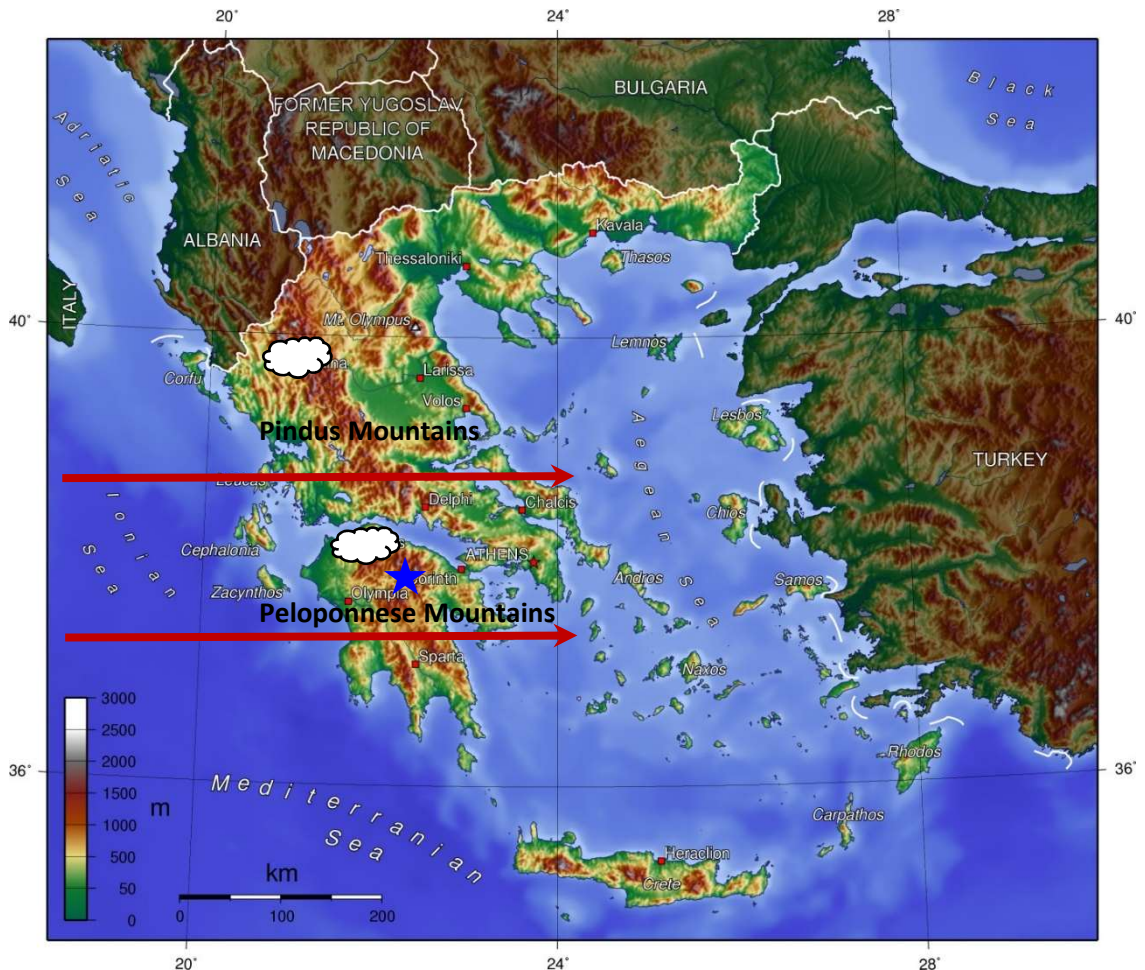
Figure 2.6: Depressional tracks over Greece (red arrows) and the interaction with mountain ranges (labelled). As unstable frontal depressions reach the topographically higher points the orographic effect forces the release of precipitation. Blue star shows location of Limnon Cave.

Topographic image credit Captain Blood www.commons.wikimedia.org.

2.1.2.2   Turkey

Turkish climate is typically Mediterranean, with warm dry summers and cool, wet winters (e.g. Kadioğlu 2000; Sariş et al., 2010; Unal et al., 2010). As explained previously in winter the dominance of the polar front and Westerlies brings cold air masses to Turkey (Türkeş and Erlat, 2003; Unal et al., 2010). The Siberian anticyclone also influences winter climate, but this continental airmass is typically dry unless it becomes saturated with water over the Black Sea

(Sariş et al., 2010). Localised cyclogenesis also provides a large proportion of Turkish winter rainfall (see Section 2.1.1.5). The northward movement of the polar front and the influence of the Monsoon and high pressure systems from the south ensure Turkey is dry in summer (Lionello et al., 2006). Generally, the proportion of winter precipitation over Turkey is thought to be decreasing and the proportion of spring, summer and autumn precipitation is increasing (Türkeş et al., 2009). However the IPCC projections predict increasing aridity for Turkey (Christensen et al., 2007) and the Mann-Kendall test indicates overall annual precipitation is on a decreasing trend (Unal et al., 2010).

Regional climate, particularly rainfall, is locally influenced by proximity to the coast and position in relation to the Anatolian Plateau, particularly in the east where mountains are most numerous and elevation is higher (Kadioğlu, 2000; Sariş et al., 2010). Precipitation is enhanced on the windward slopes of mountains and at coasts compared to the interior (Kadioğlu 2000, Sariş et al., 2010). The amount and seasonality of precipitation in Turkey is predominatly controlled by the general atomospheric circulation (Kadioğlu 2000, Sariş et al., 2010). Maxiumum values of rainfall in spring, summer and autumn can be linked to continentality causing localised thunderstorms (Kadioğlu 2000). Generally, the Turkish interior sees low levels of mainly concective rainfall while the coastal regions are dominated by frontal depressions and the effects of orography (Sariş et al., 2010).

Türkeş (1996) identified 7 precipitation regimes in Turkey based on the seasonal percentage of annual rainfall (Figure 2.7). This was subsequently refined to include longer term wet/dry cyclicity defining 4 distinct regimes (Türkeş 1998):

- The Mediterranean Coast- clear seasonal pattern and peak winter rainfall
- the Black Sea Coast- where rainfall is relatively uniform
- the Continental Interior- peak spring rainfall
- Northeast Anatolia- peak spring-summer rainfall.
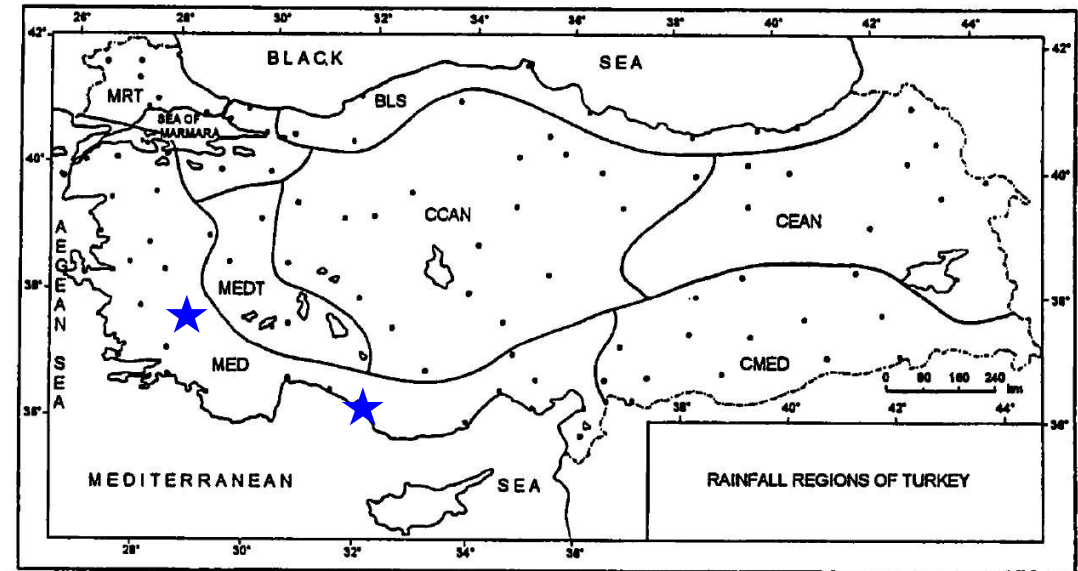
Figure 2.7: Rainfall regions of Turkey after Türkeş 1996. MED: Mediterranean, MEDT: Mediterranean to Central Anatolia Transition, CCAN: Continental Central Anatolia, CEAN: Continental Eastern Anatolia, CMED: Continental Mediterranean, MRT: Mediterranean to Black Sea transition and BLS: Black Sea. Blue stars show the locations of Sirtlanini and Dim Caves.

Based on both classifications by Türkeş (1996, 1998) rainfall in the region of both Sirtlanini Cave and Dim Cave should be part of the Mediterranean Coast regime, which shows typical strongly seasonal Mediterranean precipitation occurrence. Later work by Sariş et al., (2010) refined precipitation zones of Turkey based on the magnitude of precipitation events and the timing of precipitation throughout the year. This identified 6 rainfall regimes with clear coastal, inland and transistional patterns (Figure 2.8). Rainfall regimes of Sariş et al., (2010) show a close match to Türkeş (1996). Under the Sariş et al., (2010) classification Sirtlanini and Dim Caves differ slightly in their precipitation regimes. Sirtlanini occurs in a transistional zone with rains starting in autumn, through to spring and peaking in December (Sariş et al., 2010). The magnitude of rainfall in the region of Sirtlanini is the same classification as Thrace, which is strongly dominated by westerly derived depressions (Sariş et al., 2010). Dim Cave occurs in a coastal regime and shows a much higher rainfall classification than Sirtlanini (Sariş et al., 2010). Additionally, the onset of rainfall around Dim Cave is more rapid than Sirtlanini with gradual drying towards the summer months. Higher influence of convective rainfall in the region of Dim Cave likely causes higher spring precipitation amounts than at Sirtlanini (Türkeş 1998, Sariş et al., 2010).
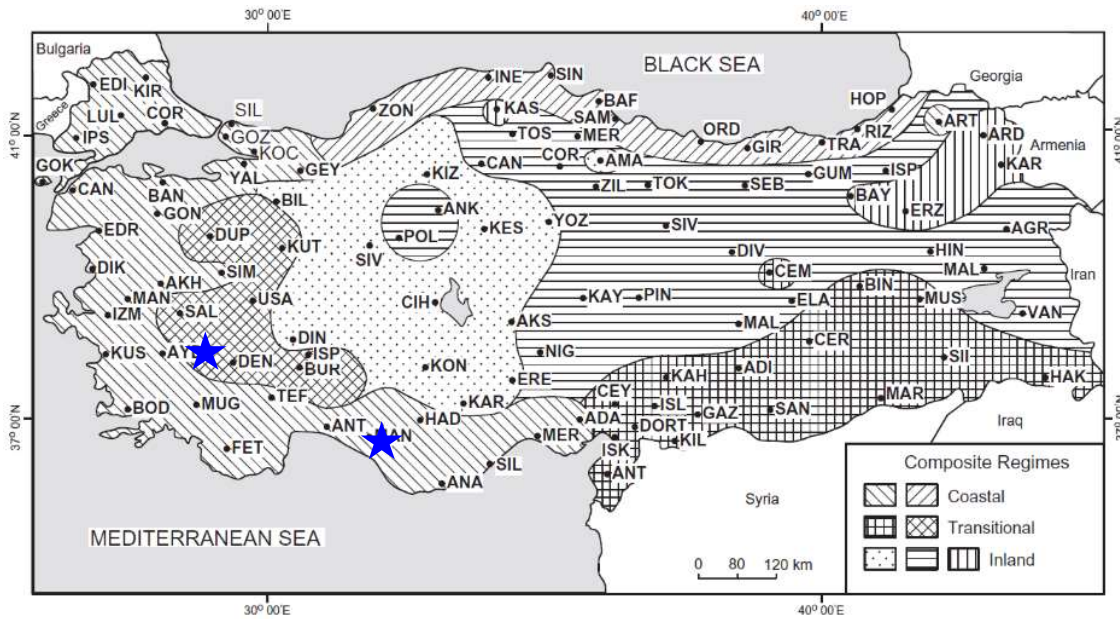
Figure 2.8: Rainfall regimes of Turkey after Sariş et al., (2010). Blue stars show the locations of Sirtlanini and Dim Caves.

2.1.2.4   Iran

Despite its position well to the east of the Mediterranean Sea, the climate of Iran is still strongly of the Mediterranean type (Evans et al., 2004) and also has enhanced winter precipitation (Dinpashoh et al., 2004) as seen in Greece and Turkey. 75% of Iran is arid or semi-arid due to the combination of predominantly NW-NE wind directions transporting mostly dry air masses and the effect of solar radiation (Kehl 2009). Winter rainfall is derived from westerlies; however, winter troughs developed by westerlies in the Eastern Mediterranean do not extend into Iran. Thus the Mediterranean influence on the climate of Iran is mainly though development of cyclones and anticyclones (Alijani 2002). Where troughs develop closer to Iran, particularly over Syria and the Caspian, they have a strong effect on Iranian climate (Alijani 2002). The Syrian trough effects western Iran and the Caspian trough affects central and eastern Iran (Alijani 2002). Changes in specific flow patterns greatly affect precipitation and temperature. Development of a deep Caspian trough, via the intrusion of northerly cold air, modulates precipitation while a NW air flow reduces both precipitation and temperature; and a SW flow increases precipitation and temperatures (Alijani 2002). The Siberian High creates a larger high pressure anomaly over Iran in the winter than the Eastern Mediterranean but this is usually not strong enough to block

depressions (Kehl 2009). However, the intensity of cyclones is dependent on the strength of the Siberian High (Kehl 2009). In summer over southern central Iran a significant thermal low develops and creates dry northerly winds across the country due to the relatively high pressure over Europe (Kehl 2009). The Zagros and Alborz mountain ranges prevent rainfall from the Caspian and Mediterranean depressions reaching the interior of the country (Alijani 2008, Kehl 2009, Modarres and Sarhadi 2011) (Figure 2.10). The interaction of the mountain ranges causes orographic convection and subsequent higher rainfall amounts in the Caspian region, the northern Alborz and the NW Zagros Mountains (Kehl 2009). Additionally this creates a very dry continental interior covering a large part of the Iranian landmass (Modarres and Sarhadi 2011) (Figure 2.9).
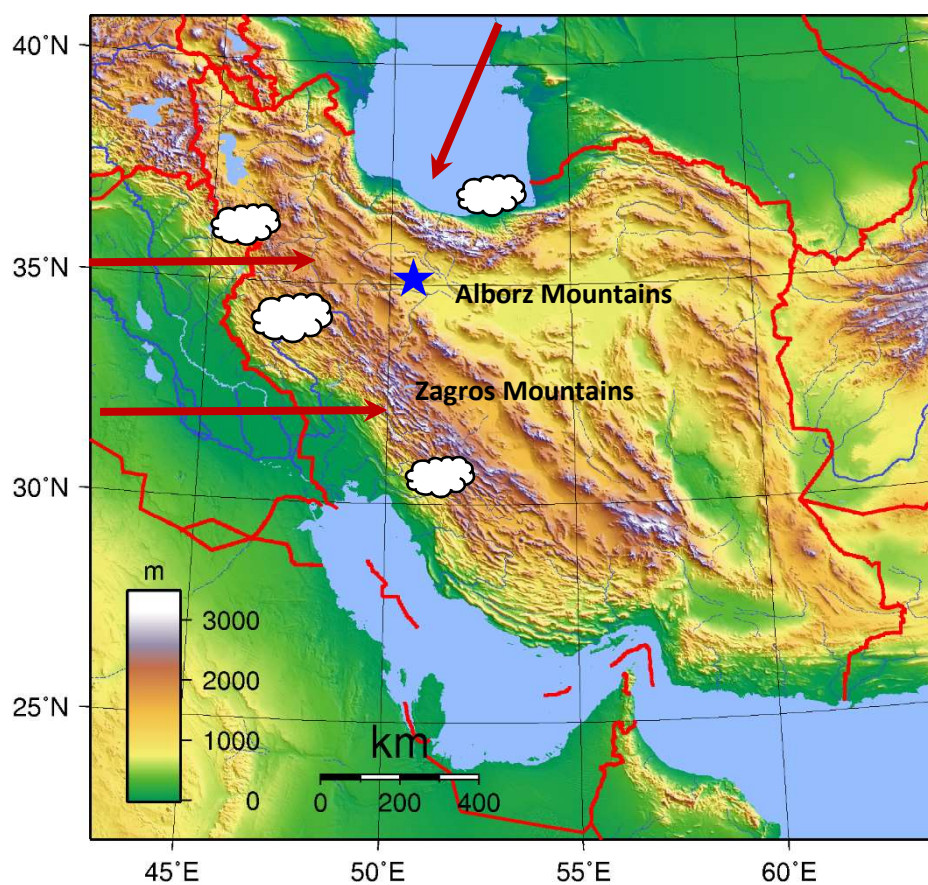
Figure 2.9: overleaf. Depressional tracks over Iran (red arrows) and the interaction with mountain ranges (labelled). As unstable frontal depressions reach the topographically higher points the orographic effect forces the release of precipitation. Depressions originate from the west and also the Caspian Sea. Rainfall is concentrated over the western Zagros and the northern Alborz leaving a very dry continental interior. Blue star shows the location of Katalekhor Cave.

Topographic image credit Sadalmelik www.commons.wikimedia.org
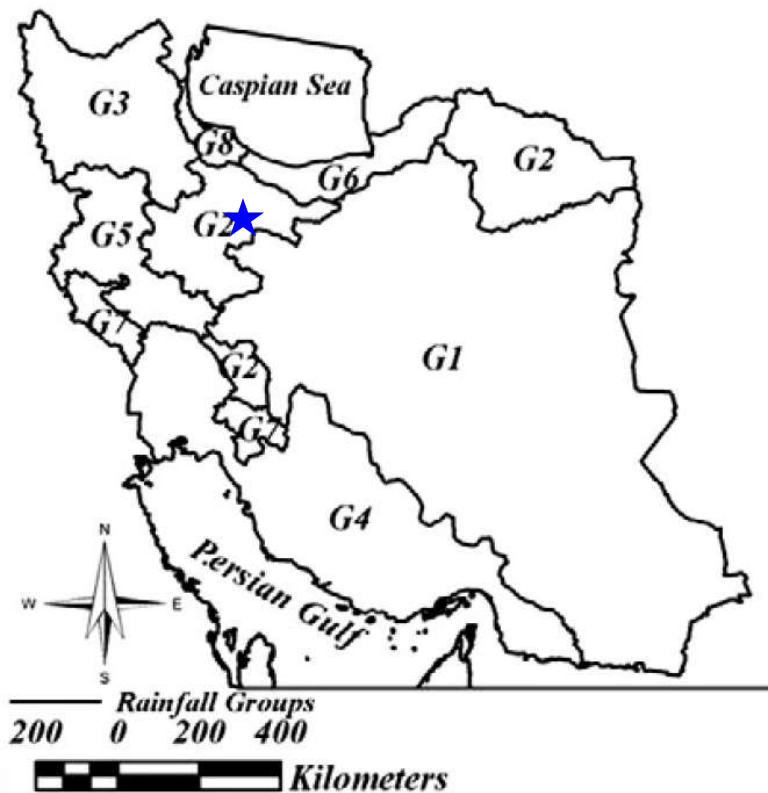
Figure 2.10: Climate regions of Iran after Modarres and Sarhadi (2011). G1: arid and semi-arid central interior Iran. G2: highland areas of the arid and semi-arid interior Iran. G3: NW colder regions. G4: lowland Zagros and Persian Gulf regime. G5: western Zagros with slightly lower precipitation. G6: Caspian Sea regime. G7: western Zagros with slightly higher precipitation. G8: Caspian Sea regime, differs from G6 as a W-E decreasing precipitation gradient is observed. Blue star shows the location of Katalekhor Cave.

Katalekhor Cave is situated on the eastern forelands of the Zagros Mountains. The orographic effect of the Zagros Mountains intensifies precipitation events on the western slopes and reduces precipitation on the eastern slope (Alijani 2008); the cave region is therefore in the drier zone. The Zagros Mountains also affect the spatial distribution of rainfall in colder seasons when rainfall is restricted to the western slopes; by contrast in the summer it is more evenly spread (Alijani 2008). Precipitation is mostly received from systems originating from North Atlantic depressions or cyclogenesis in the Mediterranean (Stevens et al., 2001; Mordarres and Sarhadi 2011). Katalekhor Cave is located in region G2 (Modarres and Sarhadi 2011) of a semi-arid to arid interior highland region receiving rainfall from the Mediterranean (Figure 2.10).

Chapter 3: Speleothems and Climate Proxies

3.1 Speleothem Formation

A speleothem is a secondary mineral deposit formed during physio-chemical reactions of primary cave minerals (Hill and Forti 1997). The term is morphology dependent, therefore composition can be any cave mineral; however, in karstic limestone/dolomite caves the most common composition is calcium carbonate (Hill and Forti 1997). Palaeoclimate studies commonly focus on 3 speleothem types- stalagmites, stalactites and flowstones (Fairchild et al., 2006a). However, most research is undertaken using stalagmites as they often display relatively simple, layered growth (Fairchild et al., 2006a) whereas coeval growth layers in stalactites are difficult to sample (Baker et al., 1999; Lauritzen and Lundberg 1999).

Precipitation of speleothems occurs when groundwaters entering a cave are supersaturated with respect to $CaCO_3$, a function of carbonate dissolution in the soil and epikarst (via equations 1 and 2, Figure 3.1). Dissolution is principally controlled by the creation of slightly acidic (carbonic acid) percolating meteoric water as a result of high pCO_2 in the soil due to decomposition of organic matter and biological respiration (Fairchild and Baker 2012). Degassing of drip waters as they enter the cave, facilitates precipitation of $CaCO_3$ on the cave roof or floor. Degassing is favoured because the partial pressure of CO_2 in the soil water is much higher than in the cave (Lauritzen and Lundberg 1999, Fairchild et al., 2006a see reaction 3 in Figure 3.1). Evaporation of drip waters may also precipitate $CaCO_3$ when the solubility product of $CaCO_3$ is exceeded by increasing Ca^{2+} ion concentration (Schwarcz 2007). Stalagmites are built up by successive growth layering of $CaCO_3$ precipitate. This process may not be continuous, depending on the chemical or physical properties of drip water which can lead to undersaturation of calcite, dissolution of the stalagmite top and hiatuses in growth.

Dissolution

Precipitation

Soil Zone

Karstic Zone

Cave (Speleothem)

$$H_2O + CO_2 \longrightarrow H_2CO_3$$

$$CaCO_3 + H_2CO_3 \longrightarrow Ca^{2+} + 2HCO_3^-$$

$$Ca^{2+} + 2HCO_3^- \longrightarrow CaCO_3 + H_2O + CO_2$$
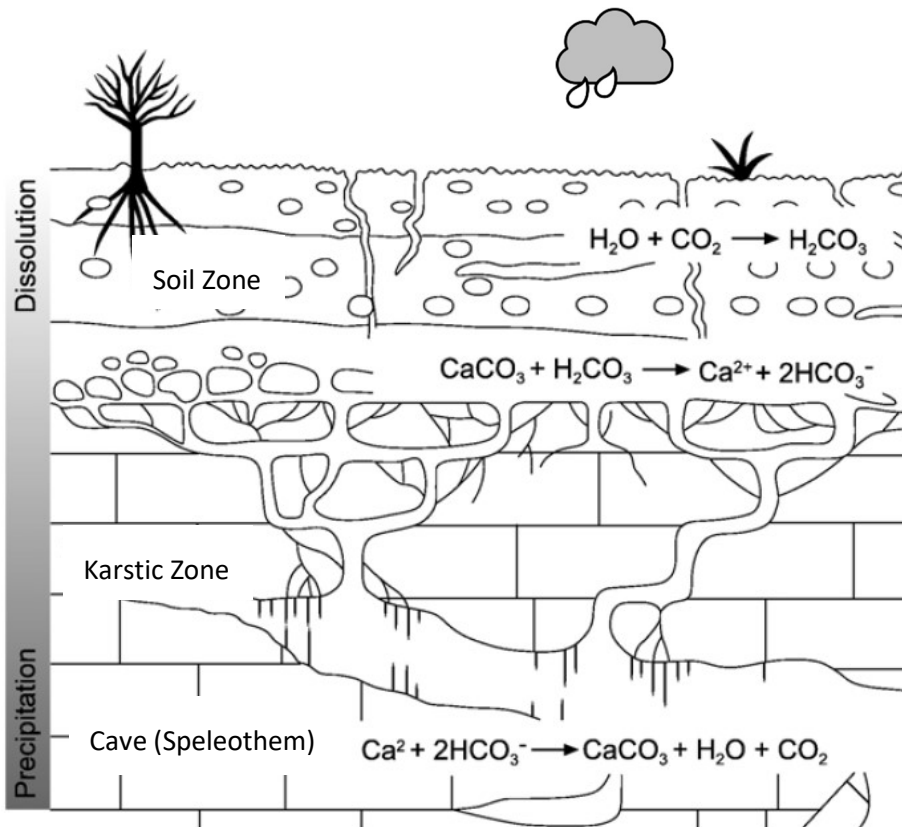
Figure 3.1: Interaction of meteoric water and groundwater in the soil zone, karstic zone and cave shown via equations after Fairchild et al., 2006a. In the soil zone decomposition of organic matter creates CO_2 which causes slight acidification in percolating waters. This slightly acidic water comes into contact with limestone or dolomite rocks above a cave system in the karstic zone, leading to the dissolution and soluble uptake of $CaCO_3$ in the water. Speleothems are precipitated in the cave as a function of degassing of drip waters as they enter the cave.

3.2 Factors controlling growth and growth rate

The initial controls on growth of speleothems are dependent on processes occurring in the karst host rock which most simply supplies dissolved $CaCO_3$ to the cave itself. These controls are:

- The kinetics of dissolution at the solid/liquid phase boundary between the karst water and host rock
- the conversion of groundwaters to carbonic acid by uptake of CO_2 increasing dissolution of the bedrock limestone
- Mass transport of important dissolved species (i.e. Ca^{2+}, HCO_3^{2-}) by the water flow (Buhmann and Dreybrodt 1985)

These factors modulate the basic primary control on speleothem growth, the amount and availability of Ca^{2+} ions in dripwaters entering the cave (Dreybrodt 1981; Baker et al., 1998). Theoretical but simplified conditions within the cave itself, which then determine if and what the rate deposition of $CaCO_3$ in speleothems are:

- the degassing of CO_2 from dripwaters to the cave atmosphere
- diffusion of Ca^{2+} ions to crystal surfaces
- surface controlled precipitation of $CaCO_3$
- production of CO_2 at the crystal surface due to the deposition of $CaCO_3$ (Dreybrodt 1980)

In practice the conditions are made much more complicated by the fact that each single condition is controlled by multiple factors which are often inherently linked. Growing numbers of studies using annual laminations demonstrate that an annual growth rate is climatically sensitive (Fairchild et al., 2006a and references therein) but controls are not necessarily exclusively climatic (e.g. Frisia et al., 2000). Typical growth rates for speleothems in temperate climates are 10-100 μm/yr and 300-500 μm/yr in sub-tropical caves (Fairchild et al., 2006a). Growth, growth rates and the factors that control them also control growth fabrics, stable isotope compositions and trace element contents: therefore a basic understanding is essential for further palaeoclimatic interpretation.

For simplicity it is often assumed that stalagmite growth is more or less constant; however, it is likely that at least seasonal biases in growth rate occur (Fairchild et al., 2006a). This is particularly true in semi-arid or Mediterranean climatic zones where precipitation and therefore drip rate are seasonally biased towards the colder months (e.g. Bar-Matthews et al., 1997; Bar-Matthews et al., 2003; Verheyden et al., 2008; Jex et al., 2011; Rowe et al., 2012).

3.2.1 CaCO$_3$ supersaturation

In most caves, pCO$_2$ gradients are the primary driver for CaCO$_3$ supersaturation but in situations where pCO$_2$ in the cave matches atmospheric levels the concentration of Ca^{2+} in the drip water will be the main driver of supersaturation and growth (Baker et al., 1998; Genty, et al., 2001a; Baldini, 2010). Additionally, supersaturation can be controlled by drip rate (see Section 3.2.4). Generally higher rates of supersaturation will cause faster growth (Frisia et al., 2000) but will also affect fabric types (McDermott et al., 1999; Frisia et al., 2000; Frisia and Borsato, 2010).

3.2.2 Cave pCO$_2$ and ventilation

Degassing of CO$_2$ is a key driver of calcite precipitation in caves and relies on the exchange of air at the growth site between the cave and dripwater. Degassing will occur where there is a CO$_2$ concentration difference between cave air and drip water which ultimately derives its CO$_2$ from the soil (McDermott 2004; Fairchild et al., 2006a), leading to the precipitation of CaCO$_3$ during the process. Degassing can occur anywhere in the karst system prior to reaching the speleothem and the effects of this are discussed in Section 3.6.2.2.

Ventilation has a strong control on growth, as better ventilated cave systems have lower pCO$_2$ which will increase speleothem growth rates (Fairchild et al., 2006c). Seasonal changes in air circulation in caves are a common control on growth and growth rate (e.g. Spötl et al., 2005; Baldini et al., 2008; Baldini 2010). Changes in ventilation controlled by climate may be predictable. In winter, the cave environment is usually flushed with relatively CO$_2$ poor air, enhancing degassing and CaCO$_3$ saturation (Spötl et al., 2005). In the summer a lower gradient in pCO$_2$ between the soil and cave atmosphere will lower the growth rate of CaCO$_3$ providing all other controls are unchanged (Frisia et al., 2000). A lower gradient may also be created by aridity, which decreases soil productivity and pCO$_2$ (Genty et al., 2001a). Furthermore changes in ventilation cause changes in crystal growth fabrics and lamination (Frisia et al., 2000; Mattey et al., 2010; Boch et al., 2011) which will grow at different rates and have different amounts of porosity. The role of degassing is more important in conjunction with feeding drip waters which have very low flow, as degassing is more prolonged allowing saturation to rise (McDermott et al., 1999; Frisia et al., 2000). However, enhanced degassing can also be achieved by mechanisms that are not climate driven. For example speleothems located close to cave entrances are likely to be subject to enhanced air flow increasing supersaturation and growth rate (Frisia and Borsato 2010), thus care must be taken when sampling to avoid these types of speleothem.

3.2.3 Temperature

The classic karst model implies that seasonal enrichment in soil CO_2 and water hardness is controlled by higher temperatures, effects that are transferred to the cave environment altering cave air composition and speleothem growth rates (Spötl et al., 2005). In practice, however, it has proved difficult to find evidence of this process (Spötl et al., 2005). Conversely, there is a statistically significant relationship between seasonal temperature and soil-derived pCO_2 in drip water (Spötl et al., 2005). Evidence from measured cave pCO_2 in different climate regimes imply soil temperature is a major control on growth (Baldini 2010), as maximum soil pCO_2 can be observed at the highest temperatures (Genty et al., 2001a, Spötl et al., 2005). Genty et al. (2001a) note strong correlation between drip rate and mean annual temperature for sites which have substantial soil cover. Warmer temperatures increase soil CO_2 production and these findings are corroborated at sites with poor soil cover, where the relationship is not seen (Genty et al., 2001a). Ultimately, these effects are limited by moisture availability (Baldini 2010). These processes do not actively alter the cave air composition but the pCO_2 gradient between the water and the cave air is enhanced increasing speleothem growth.

Additionally climatically controlled ventilation changes are driven by pressure gradients forced by temperature changes outside the cave (Spötl et al., 2005, Mattey et al., 2010, Boch et al., 2011). This will ultimately affect growth and growth rate by either increasing or decreasing degassing of cave drip waters.

Temperature changes (likely linked to aridity) can force change in the mineralogy of speleothems as aragonite precipitation is favoured by increased temperature (Railsback et al., 1994; Frisia et al., 2002; Lachniet et al., 2012), this is driven by changes in for example the relative concentration of Mg (see Section 3.6.2.5).

3.2.4 Drip rate and karst flow

A wide range of drip rates allow stalagmite formation (Frisia et al., 2000; Fairchild et al., 2006b) and as speleothems are able to form in semi-arid settings (Fairchild et al., 2006a) water availability may not be the main factor influencing growth and growth rate. Conditions where drip rate will be a more influential control on stalagmite growth include when Ca^{2+} ions are delivered slowly to the drip tip (Fairchild and McMillian 2007). Additionally intra annual growth rates are

more strongly controlled by drip rate when drip rate is slow, or slow but seasonally variable (Genty et al 2001a). Flow rate and therefore drip rate can vary with seasonal change in infiltration (Genty and Deflandre 1998) which can be related to precipitation. Fairchild et al., (2006b) noted that sporadic recharge events matched increases in drip volume but often drip water response was not linearly related to precipitation amount. This is due to the complex nature of the pathways, water storage and mixing in the epikarst.

Generally, stalagmite growth rates correlate strongly with mean annual temperature and drip water calcium carbonate amount but not drip rate (Genty et al., 2001a); thus the significance of changing drip rate may lie in the effect it has on other growth controls. For example, higher drip rates may indicate higher flow, less water-rock interaction and lower calcite supersaturation, which may slow growth (Frisia et al., 2000). Summer increases in Ca^{2+} may be caused by an increase in saturation due to water being stored in the epikarst longer, an indirect result of low flow rate (Baker et al., 1998).

3.3   Morphology and Petrography

3.3.1 Morphology

Early work on speleothems considered the relationship between morphology and formation and Allison (1923) made the first attempt at classifying stalagmite shape based on parameters such as drip rate and evaporation. The link between morphology and climate change was recognised by Franck (1965). However as mathematical/physio-chemical considerations became vogue in the 70s and 80s (for example Curl 1972, 1973; Gams 1981) stalagmite morphology was largely forgotten as a research topic (Baldini 2010) being used mostly as a guide for field sampling. At the fundamental level, stalagmite shape and diameter is controlled by flow rate: diameter decreases with lower flows/increased drip interval and diameter increases with drip fall height (Gams 1981; Kaufmann 2003) but is also affected by temperature and $CaCO_3$ concentration (Kaufmann 2003). If all these parameters remain unchanged the diameter of the stalagmite will remain constant over the course of growth (Kaufmann 2003).

Most palaeoclimate studies using stalagmites aim to use 'candle stick' morphologies which assume the stalagmites grew straight upward. A theoretical equilibrium shape is achieved under constant growth conditions when the whole surface is growing by the same vertical distance in a

given timeframe (Romanov et al., 2008). In reality, stalagmites often contain periods of differing width and sometimes kinks from changes in growth axis, all of which can be indicative of changing drip conditions.

3.3.2 Petrography

The use of petrography is not new in speleothem studies but it is vital in the assessment of speleothem suitability for palaeoclimate research. From the 1970s onward there has been debate and disagreement regarding the interpretation of crystal fabrics and their linkage to environmental conditions, competitive growth and diagenesis, especially the significance of mineralogical change from calcite to aragonite *or vice versa* (see in particular Folk and Assereto 1976 and Kendall and Broughton 1978 and intervening discussions: Kendall and Broughton 1977; Folk 1977).

The assessment of diagenetic alteration is perhaps the most common application for speleothem petrographical studies. Discussions on aragonite to calcite diagenesis (for example Frisia et al., 2002; Spötl et al., 2002; Ortega et al., 2005; Perrin et al., 2014) are numerous and studies of calcite-calcite neomorphism (Frisia et al., 1996; Frisia et al., 2000; Frisia and Borsato 2010) have also become common. Further uses of petrography include the environmental interpretation of growth conditions of different $CaCO_3$ fabrics (notably Railsback et al., 1994; McDermott et al., 1999; Frisia et al., 2000; Turgeon and Lundberg, 2001; Railsback et al. 2002; Frisia and Borsato, 2010; Frisia 2015), formation and petrographic significance of annual lamination (for example Mattey et al., 2010; Boch et al., 2011) and its use in chronology (Baker et al., 2008), and evaluating microstructures in response to drip water supply (Railsback et al., 2011, 2013, 2014). Speleothem petrography has also been used to inform studies on the mechanisms of $CaCO_3$ growth (including White 2012 and references therein; Riechelmann et al., 2014).

3.3.2.1 Polymorphs
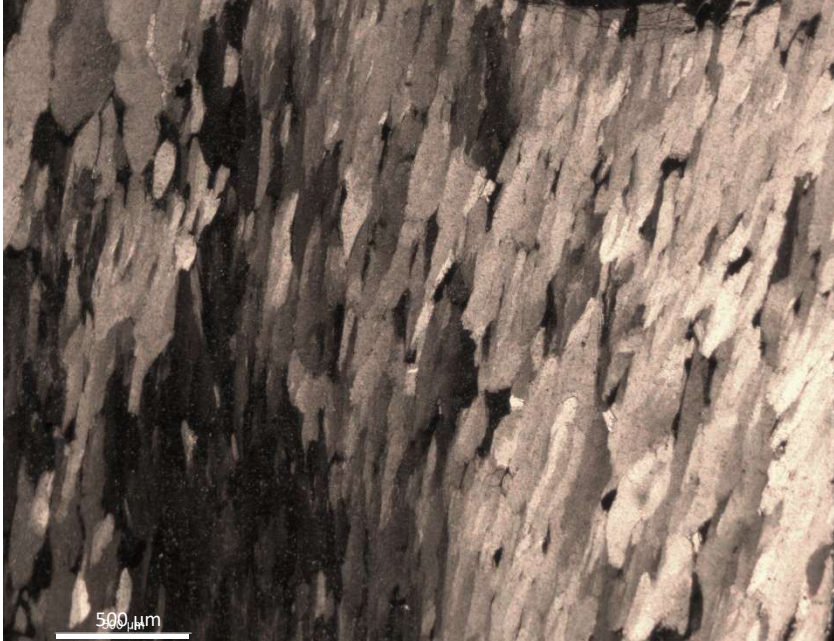
In simplest terms speleothems are comprised of crystals of calcium carbonate, which are themselves formed of groups of smaller bodies called crystallites (Kendall and Broughton 1978). As the smallest unit, crystallites control overall growth and shape of a crystal. Crystallite terminations on the speleothem surface become dominant as they do not disturb the flow of water from the feeding drip (Kendall and Broughton 1978).
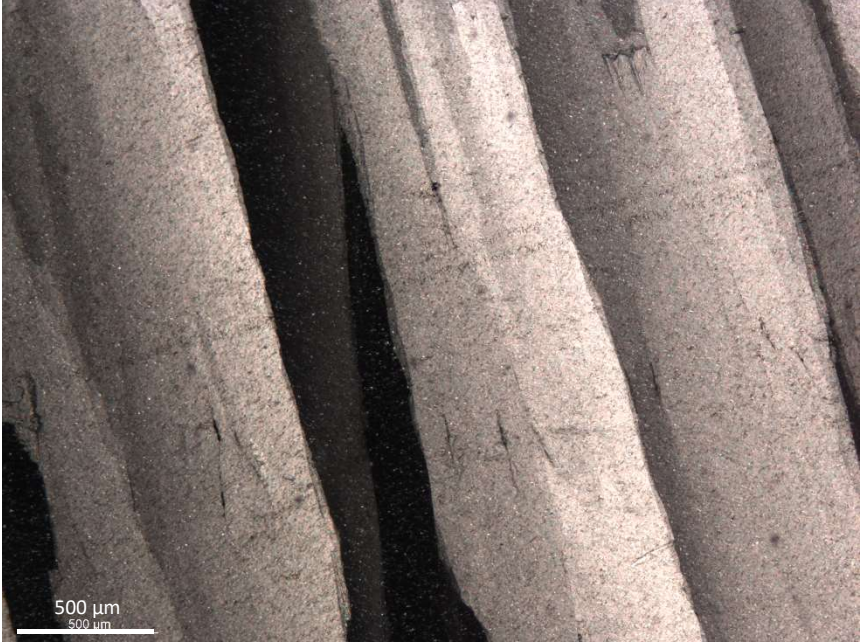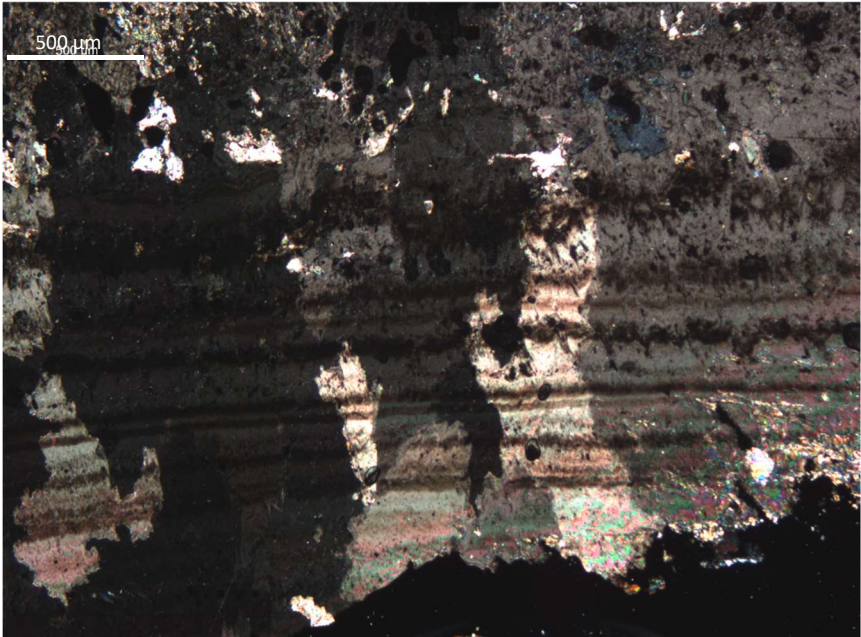
In carbonate speleothems both $CaCO_3$ polymorphs, calcite and aragonite, may precipitate based on individual drip conditions-although calcite is more common. There are a number of suggested controls on the precipitation of each polymorph. Aragonite is reported to form in more restricted conditions than calcite, such as high Mg situations (Frisia et al., 2002) which may occur from enhanced water residence time or dissolution of rocks containing high Mg-calcite or dolomite (McDermott et al., 2004) and during very dry periods (Railsback et al., 1994; Frisia et al., 2002; McDermott 2004; Lachniet et al., 2012)

Co-existence of aragonite and calcite in individual speleothems is well known (e.g. Railsback et al., 1994, 2002; Spötl et al., 2002; McMillan et al., 2005; Perrin et al., 2014); usually the polymorphs form at different times (as layers) when the environmental conditions described above change (for example Railsback et al., 1994; McMillian et al., 2005; this volume Chapter 4). It is also possible to precipitate both aragonite and calcite concurrently in the same layer when there are laterally varying degrees of evaporation across the growth surface (Railsback et al., 1994; this volume Chapter 4). This said, aragonite preservation is not always favoured, being a more soluble mineral than calcite (Frisia et al., 2002). This results in stabilization or neomorphism, where aragonite is partially or wholly replaced by 'secondary calcite'. Thus some speleothems exhibit both primary calcite and secondary calcite that replaced former aragonite (including Spötl et al., 2002; McMillian et al., 2005; Perrin et al., 2014). Such calcitization of aragonite will disturb geochemical proxies such as stable isotopes and trace elements including elements like U that control U-series dates (Railsback et al., 2002; Lachniet et al., 2012)

3.3.2.2   Fabrics and fabric interpretations

A crystal fabric describes the spatial orientation of crystallites and the relationships between them (Frisia et al., 2000). Individual crystals in the same fabric will grow in a similar way and therefore have the same morphological characteristics such as orientation and crystal shape. Interpretation of crystal fabrics is thus used to inform on growth parameters and interpret likely environmental conditions (McDermott et al., 1999; Frisia et al., 2000). The following tables (3.1 and 3.2) outline typical fabric attributes observed in the stalagmites used in this study.

Type/Subtype	Fabric Characteristics
Columnar	Crystals align perpendicular to growing surface. Crystal boundaries can be straight or serrated. All subtypes are formed from the regular stacking of crystallites which remain in optical continuity. Differentiation between sub-types is based on length/width ratios. Can display visible lamination which may be defined by alternating open and compact calcite. Columnar calcites form via the regular stacking of crystallites whereby the more consistent the stacking the straighter the boundaries and more uniform the extinction.
Short	Length/width ratio <6:1

Proper	Length/width ratio ~6:1 extinction is uniform and crystals are clearly elongated along the c-axis.
Elongate	Length/width ratio greatly exceeds 6:1, clear elongation along the c-axis. Extinction maybe uniform or sweeping.
Open	Characteristics as seen in columnar proper but with pores between crystals.
Microcrystalline	Length/width ratio <6/1. High concentration of crystal defects compared to the other columnar calcites. Crystallites are not as uniformly stacked and do not grow in full optical continuity leading to crystals with irregular boundaries and patchy extinction.

Equant	As described by Alan C Kendall pers. comm. (2014). Squat in shape so the difference between the length and width is smaller than columnar types but still displays preferred elongation. Differs from mosaic fabric by defining clear growth directions and preferred elongation.
Dendritic	Clearly branching rods of crystals which show multiple directions of growth often cross cutting in a scaffold like arrangement. Branching is caused by the uneven stacking of crystallites creating a series of microsteps/kinks. Extinction is zoned to particular branching domains. Lamination and banding is uncommon but maybe defined by alternating open and compact forms.
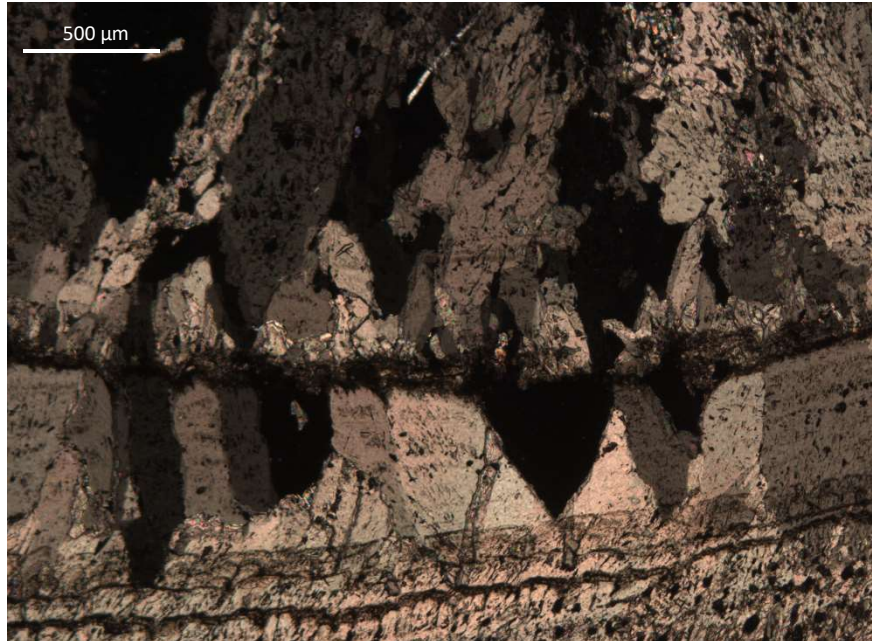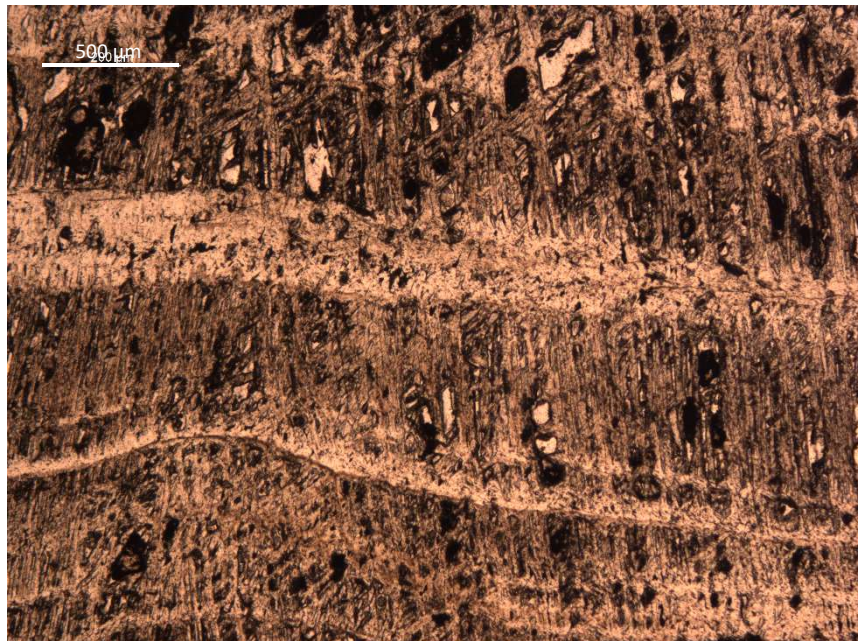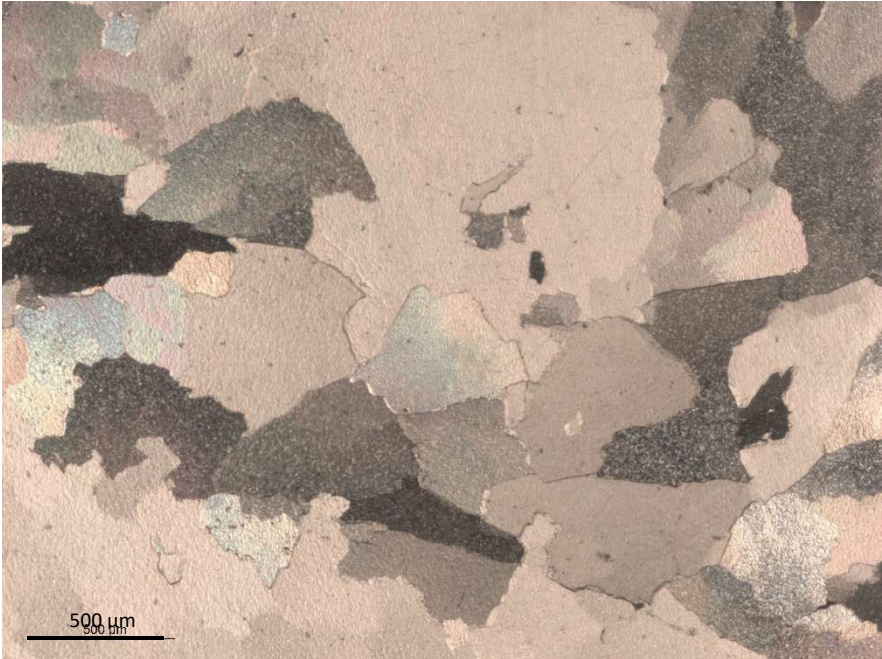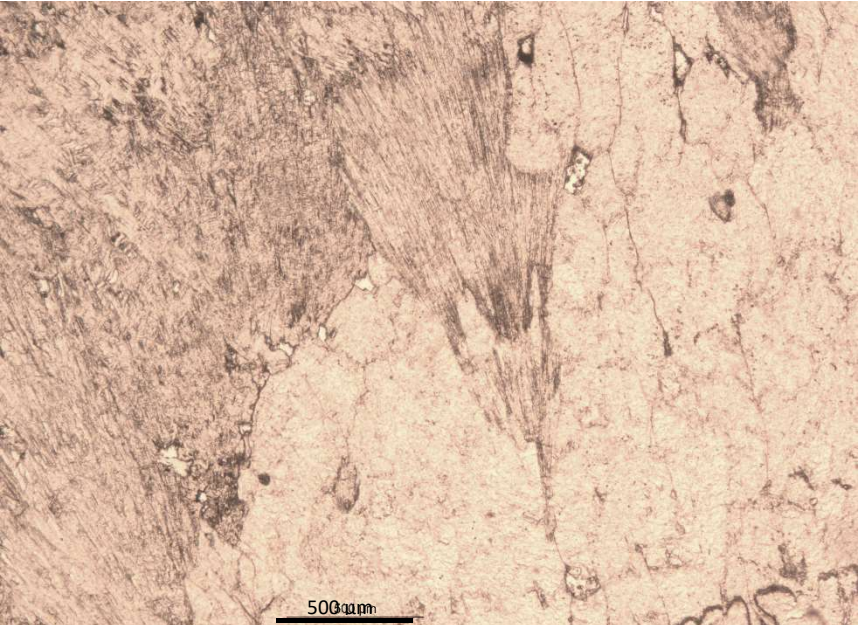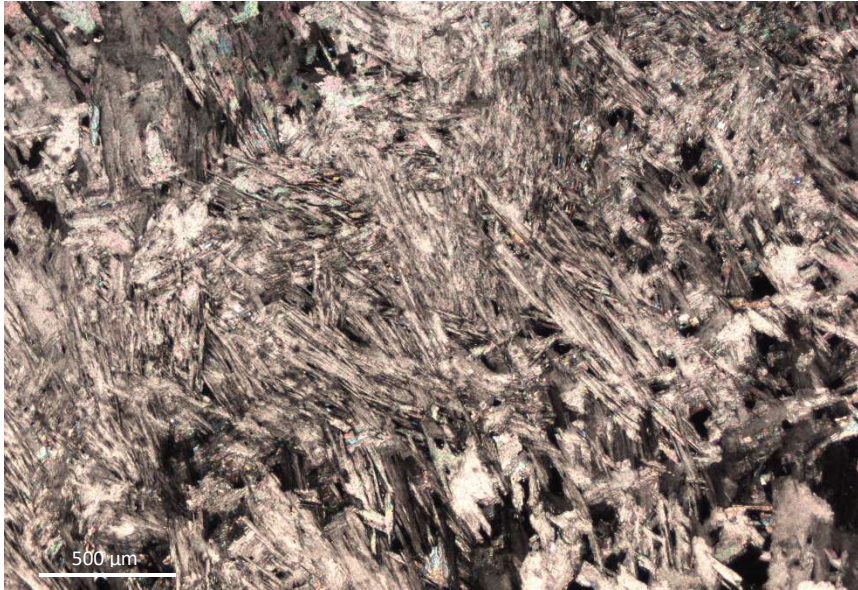
Open	Most common form displays irregular primary porosity between branches.
Compact	No observable porosity between branches.
Mosaic	Euhedral to sub-euhedral crystals without preferred elongation. 500 µm

Table 3.1: Last 4 pages. Characteristics of common calcite fabrics as described in Frisia et al., 2000, Frisia and Borsato 2010 and by personal communication from Alan C Kendall 2014. Fabrics noted are displayed by stalagmites used in this study. Photomicrographs are examples from stalagmites used in this study.

Table 3.2: Next page. Characteristics of common aragonite fabrics as described in Frisia et al., 2000, Frisia and Borsato 2010. Fabrics noted are displayed by stalagmites used in this study. Photomicrographs are examples from stalagmites used in this study.

Type/Subtype	Fabric Characteristics
Rays	Appears in fan like splays. Can form from high Mg-calcite but is distinguished from columnar by crystals radiating out from a central point. Length to width ratio exceeds 6:1 and elongation is along the c-axis. Extinction is uniform to patchy. Lamination is not present but banding maybe defined by compact vs porous sections of crystals.
Acicular (Needles)	Can be regular and elongated along the c-axis or disordered where length to width ratio greatly exceeds 6:1 but doesn't show clear growth orientations. Extinction is likely to sweep across a number of crystals. Again lamination is not present but banding maybe defined by compact vs porous sections of crystals.

Type/Subtype	Assumed growth conditions
Columnar	Generally form in quasi equilibrium conditions. Drip rate is consistent but varies between subtypes. Drip rate is usually the controlling factor between different columnar calcite types.
Short	Low and constant degree of $CaCO_3$ supersaturation with low organic content.
Proper	Low and constant degree of $CaCO_3$ supersaturation with low organic content.
Elongate	Drip rate maybe higher to form elongate columnar than other columnar sub types. $CaCO_3$ supersaturation (and optical continuity) are persistent over longer periods to account for increased length. Low organic content. May form under higher Mg/Ca ratios than the other columnar subtypes.
Open	Changes between open and compact typically denote a change in drip rate, open columnar requires more variable drip rates and $CaCO_3$ supersaturation to form.
Microcrystalline	Higher concentration of defects indicates either a higher growth rate or the presence of impurities such as organic detritus. The transition between other columnar calcites and microcrystalline appears to be related to drip rate. Drip rates have a larger range and are typically faster but remain constant when forming this type. May also define other columnar fabrics which have been split due to increased drip rates (Alan C Kendall pers. comm. 2014).
Equant	As described by Alan C Kendall pers. comm. (2014). Where more water is present for a longer period as growth is less restricted. This includes conditions where the film of water covering the stalagmite top is thicker or where water has pooled.
Dendritic	Forms under conditions of predominantly high but variable $CaCO_3$ supersaturation which maybe controlled by fluctuating drip rates or by strong but variable degassing effects (and evaporation).
Open	Open and compact form due to slightly differing $CaCO_3$ supersaturation.
Compact	Open and compact form due to slightly differing $CaCO_3$ supersaturation.
Mosaic	Forms by the replacement of aragonite or other calcite fabrics. Mosaic is the most common diagenetic fabric. Lack of elongation and preferred orientation suggest no dominant growth direction.

Table 3.3: Overleaf. Interpretations of the environment of formation of calcite fabrics listed in
Table 3.1. Interpretations are derived from Frisia et al., 2000; Frisia and Borsato 2010 and by
personal communication from Alan C Kendall (2014).

Type/Subtype	Assumed growth conditions
Rays	Stable but low drip rate but dry drip periods can occur. Mg/Ca ratios are high to cause inhibition of calcite growth and can show covariance with drip rate. Feeding drip water has high alkalinity.
Needles	Where growth direction is disordered faster precipitation due to higher supersaturation is implied. As aragonite is likely to form in drier conditions than calcite (see above) this is likely to be controlled by degassing.

Table 3.4: Interpretation of the environment of formation of aragonite fabrics listed in
Table 3.2 Interpretations are derived from Frisia et al., 2000; Frisia and Borsato 2010.

3.3.2.3 Hiatuses

Hiatuses represent periods of cessation of stalagmite growth, most commonly related to a lack of drip water. Hiatuses in the micromorphology may be denoted by an E type surface (Railsback et al., 2013) or corrosion lines (Martín-García et al., 2011). Both these expressions are formed by erosion of the stalagmite which may occur during periods of $CaCO_3$ undersaturation in dripwater either before or after growth stops and display corrosion of underlying crystals (Martín-García et al., 2011; Railsback et al., 2013). These surfaces may also be coated by inorganic or organic detritus and clays deposited if dripwater resumption is fast (Railsback et al., 2013).

Moreover, if drip rate had been reducing over a period prior to growth cessation, stalagmite diameter may show a gradual reduction approaching the hiatus. The culmination of reducing drip

water might be represented in the micromorphology by L-type layers (Railsback et al., 2013), i.e. stacking of layers with progressively reduced lateral extent with the hiatus itself marked by the final thinnest layer. Renewed growth subsequently drapes over and encases earlier growth (Railsback et al., 2013). It should be noted, however, that the bounding type L surface may not necessarily represent a hiatus or a hiatus of a dateable length and may just be a period of slower growth (Railsback et al., 2011). Changes in the growth axis may also accompany hiatuses.

3.3.2.4 Lamination and layers

Lamination in stalagmites can be defined by a number of morphological characteristics, typically responding to cyclic or rhythmic responses to local environmental changes which may themselves be driven by external forcing such as annual or seasonal changes (including Baker et al., 1993; Genty and Quinif, 1996; Borsato et al., 2007; Mattey et al., 2008a, 2010; Boch et al., 2011). Lamination is often defined by changes in crystal morphology, fabric and porosity (Kendall and Broughton 1978; Frisia et al., 2000; Fairchild et al., 2006), usually alternating porous and compact fabric types (Genty and Quinif 1996; Frisia et al., 2000; Mattey et al., 2010; Boch et al., 2011). Fluctuating levels of humic and fulvic acids are also common in lamination (Baker et al., 1993; Shopov et al., 1994; Huang et al., 2001; van Beynen et al., 2001). Changing rates of infiltration between seasons may also create single organic-rich layers on top of annual lamination (Borsato et al., 2007). These types of lamination are particularly useful for chronological studies as each lamination or couplet can be interpreted temporally. Lamination counting can thus increase the accuracy of U-series age models by providing a high resolution and absolute timescale, if lamina can be proven to have formed annually (e.g. Tan et al., 2006; Baker et al., 2008; Domínguez-Villar et al., 2012).

Singular climatic events can be recorded in speleothems by changes to layering or lamination. Layers of detrital minerals may indicate higher infiltration events (Railsback et al., 2011) and the presence of aragonitic layers in calcite stalagmites can be related to dry events (Railsback et al., 1994; Denniston et al., 2000; McMillan et al., 2005; Gázquez et al., 2012). Black soot rich laminations in Polish stalagmites have been interpreted as markers for human occupation of caves (Gradziński et al., 2003, 2007).

3.3.2.5 Diagenesis

In Section 3.3.2.1 the metastability of aragonite and its potential to be altered to 'secondary calcite' is discussed. Processes of diagenesis can be most confidently identified in situations where former mineral, texture and chemical composition of the primary phase is retained. Examples include relict needles or bundles of aragonite or diagenetic calcite pseudomorphing an aragonitic fabric (e.g. Frisia et al., 2002; Spötl et al., 2002; Perrin et al., 2014). Aragonite to diagenetic aragonite alteration is unusual but has been inferred from a gradual textural change from acicular ray aragonite to larger ray crystals (Perrin et al., 2014).

Diagenetic alteration, through dissolution-reprecipitation reactions, to a new fabric, is often inferred by the presence of mosaic fabrics (Section 3.3.2.2; Frisia et al., 2000) although even this is open to some doubt as mosaics could form as primary fabrics (Alan C Kendall pers. comm. 2014). Calcite to diagenetic calcite neomorphism is particularly problematic as such alteration may not leave any petrographic evidence (Frisia 1996). Columnar calcite, for example can be formed diagenetically (Perrin et al., 2014) but is unlikely to look any different from its primary counterpart. Domains in a stalagmite with comparatively larger crystals, or large euhedral crystals with lower porosity have been considered evidence for recrystallization (Railsback et al., 2002; Muñoz-García et al., 2012) as original fabrics are better interconnected by porosity (Muñoz-García et al., 2012).

In the absence of petrographic indicators diagenesis may be implied by the presence of dissolutional or erosional layers (e.g. Railsback et al., 2011; Perrin et al., 2014) or by unusual geochemistry, such as abnormally low U values (Railsback et al., 2002) or abnormally high Sr contents in calcite (Frisia 1996).

The evidence for diagenesis in a given stalagmite is thus likely to be cryptic and requires careful consideration as part of any speleothem study.

3.4   U-Series Dating

A major advantage of speleothems as terrestrial climate recorders is that their mineralogy in theory allows dating to high precision over the last 500 ka via U-series methodologies (Bourdon et al., 2003). Naturally three radioactive decay chains occur but dating in speleothems is achieved using the third step in the ^{238}U decay chain, the decay of ^{234}U to ^{230}Th.
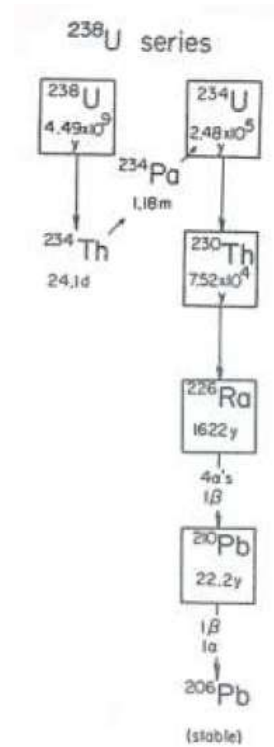
Figure 3.2: Partial decay scheme and half-lives of the ^{238}U isotope including the decay of ^{234}U to ^{230}Th used in speleothem dating. Adapted from Schwarcz 1978.

3.4.1   General principles

Radioactivity in karstic rocks overlying caves is likely to have reached secular equilibrium for nuclides in the ^{238}U and ^{235}U decay series (Richards and Dorale 2003), whereby the activity ratio of the parent is equal to that of the daughter (Bourdon et al., 2003) and each decay of a parent atom results in a decay of a daughter atom (Ivanovich and Harmon 1986). This is due to the fact the parent U isotopes have much longer half-lives than any intermediate daughter isotopes (Bourdon et al., 2003). Removal of nuclides by percolating waters which will eventually precipitate speleothems disturbs this equilibrium, thus secondary deposits (including speleothems) when first

emplaced will be in disequilibrium. In a closed system time can be quantified by the decay constants of radioactive isotopes as they return to secular equilibrium (Schwarcz 1978; Richards and Dorale 2003). These decay constants are used to create a ^{230}Th/^{234}U activity ratio which in turn is used to determine age (these are related through the Equation 3.1). This is known as disequilibrium dating (Schwarcz 1978) and under optimal conditions will occur when ^{234}U and U^{238} are deposited in complete absence of ^{230}Th (Schwarcz 1978).

$$\frac{^{230}Th}{^{234}U} = \frac{^{238}U}{^{234}U}\left(1 - e^{-\lambda_{230}t}\right) + \frac{\lambda 230}{\lambda 230 - \lambda 234} \times \left(1 - \frac{^{238}U}{^{234}U}\right)\left(1 - e^{-\lambda 230 - \lambda 234)t}\right)$$

Equation 3.1: ^{230}Th/^{234}U ratio showing the relationship between decay constants of species of U and Th.

In addition to obtaining a ^{230}Th/^{234}U activity ratio a ^{234}U/^{238}U activity ratio is also required to gain an age from a sample. As a visual aid activity ratios are plotted on an isochron plot with curved isochrones (lines of constant age), where the slope gives the age of the sample (Ivanovich 1982; Ludwig 2003). An example of an isochron plot with ages for a closed system with no ^{230}Th initially present is shown in Figure 3.3.
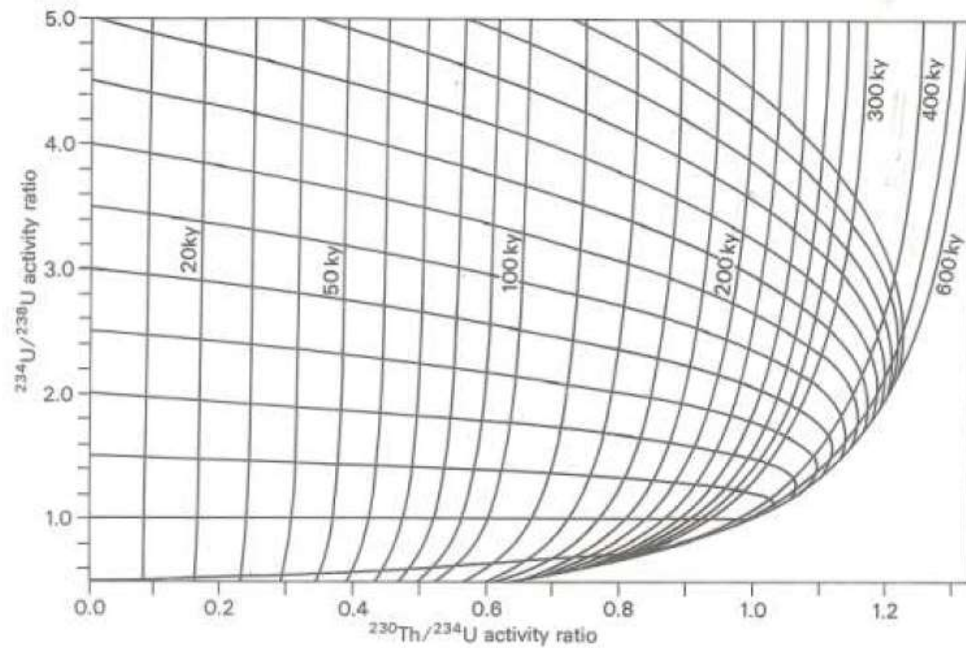
Figure 3.3: Isochron (lines of constant age) plot of ages for a closed system with no ^{230}Th initially present based on the activity ratios of $^{230}Th/^{234}U$ and $^{234}U/^{238}U$ (Ivanovich 1982).

3.4.2 Assumptions for speleothems

This method is applicable to speleothems due to differing solubility behaviours of U and Th in the surface and near surface hydrosphere, U is highly soluble and is readily mobilized as the uranyl ion (6+) (Gascoyne 1982; Bourdon et al., 2003; Richards and Dorale 2003). In the 4+ oxidation state Th is insoluble but readily hydrolysed (Gascoyne 1982; Richards and Dorale 2003). U therefore is able to form numerous mineral complexes, in particular carbonates, phosphates, sulphates and silicates (Gascoyne 1982). Most Th is transported on the surface of insoluble resistate minerals, such as iron hydroxides, and on the surfaces of clay minerals (Gascoyne 1982; Richards and Dorale 2003). Both elements however can be strongly affiliated with organic matter such as humic and fulvic acids (Gascoyne 1982; Richards and Dorale 2003), a regular feature of speleothem chemistry. It is assumed the affinity of U to mineral complexes greatly outweighs transportation via organic materials (Gascoyne 1982).

3.4.3 Potential problems

The method is most applicable to CaCO$_3$ which is considered 'clean'-i.e. an absence of inorganic or organic detritus. However the environment of formation of speleothems means this is sometimes not the case and thus unknown quantities of [230]Th may be incorporated not related to radioactive decay in CaCO$_3$ (Schwarcz and Latham 1989). 'Initial' [230]Th is commonly corrected by measuring the content of [232]Th and a using reasonable value for continental detritus (Bourdon et al., 2003) or local isochron value (Ludwig 2003; Hellstrom 2006).

Assuming detrital Th is accurately corrected for, stalagmite ages produced by U-series dating will be correct providing the system remains closed: no radioactive components have been added or removed (Schwarcz 1978). The U-series method will be interrupted if the stalagmite is "opened" during which it is subjected to conditions which are considerably different to original precipitation conditions (Borsato et al., 2003). These commonly lead to speleothem diagenesis or removal of material. Post depositional recrystallisation of carbonate can be observed petrographically in speleothems, particularly the neomorphism of aragonite to calcite (see Section 3.3.2.5) and will alter radioactive ratios during the process of recrystallisation. A recrystallized speleothem could exhibit a large range in U concentrations (>1 ppm) due to U loss (Railsback et al., 2002). Erroneous dates are also associated with significant (a few centuries) growth hiatuses and these can often be linked to phases of CaCO$_3$ dissolution (e.g. Railsback et al., 2011).

It is suggested the use of petrography is essential for screening speleothems for diagenesis to check suitability for U-series dating (Frisia et al., 2000, Railsback et al., 2002, Borsato et al., 2003) and additionally individual dating locations in speleothems which have not undergone diagenesis but form under changing drip conditions (this volume Chapter 4). These issues are partially addressed in Chapter 4 of this thesis.

3.5 Stable Isotopes

The use of stable isotopes in spelean $CaCO_3$ to infer environmental conditions of growth and climate is widespread, encompassing worldwide locations and climate regimes.

3.5.1 Fractionation and isotopic equilibrium

Fractionation is the process of exchanging isotopes between two molecular species, which occurs during both chemical and physical processes and forces a physical or chemical transformation (Urey 1947). Fractionation is a thermodynamic reaction and thus the species will react at different rates creating unequal distributions of concentrations on either side of the reaction (Urey 1947).

Fractionation occurs in two forms: equilibrium fractionation and kinetic fractionation. During equilibrium fractionation the ratios of different isotopes in all compounds are constant at a given temperature. Equilibrium fractionation is desired in spelean calcite because when it is deposited at, or close to, isotopic equilibrium with cave water, $\delta^{18}O$ can be assumed to reflect the $\delta^{18}O$ in the dripwater and cave temperature at the time of deposition (McDermott et al., 2006; Schwarcz 2007). Equilibrium fractionation is most likely approximated if stalagmite deposition occurs via slow CO_2 outgassing (Hendy 1971).

$$Ca^{2+} + 2HCO_3^- \leftrightharpoons CaCO_3 + CO_2 + H_2O$$

Equation 3.1: reaction for precipitating or dissolving calcite in drip water

Kinetic fractionation occurs during incomplete or unidirectional reactions, this causes disequilibrium reactions where the light isotope is preferentially used or removed from the reaction first. In the cave environment more rapid degassing or evaporation will likely promote disequilibrium effects: evaporation for example allows selective removal of light isotopes in the gas phase, leading to progressive enrichment in heavy isotopes in the water and the precipitating stalagmite calcite (Hendy 1971). Evaporation is minimised in caves in cool temperate regions, as cave atmospheres are typified by high relative humidity (McDermott, 2004; McDermott et al., 2006). Evaporation, however, is likely to be more prominent in the stable isotope composition of semi-arid environments as more evaporation occurs in the epikarst in these settings (Bar-

Matthews et al., 1996). Additionally kinetic enrichment has been observed to occur during degassing (Hendy 1971; Mickler et al., 2004).

Based on $\delta^{18}O$ values, many calcite stalagmites are deposited in 'quasi-equilibrium' relatively low supersaturation, constant drip rate and relatively humidity ~100% (McDermott et al., 2006; (Fairchild et al., 2006); but an enrichment relative to Kim and O'Neil (1997) predicted inorganic fractionation factor occurs frequently (McDermott et al., 2006; Tremaine et al., 2011). In recent years studies on modern cave $CaCO_3$ precipitation suggest isotopic disequilibrium occurs frequently (for example (Mickler et al., 2004; Genty, 2008; Tremaine et al., 2011; Riechelmann et al., 2013b). Thus small amplitude variations in $\delta^{18}O$ over short timescales might reflect kinetically driven fractionation events rather than a climate driven signal (McDermott et al., 2006). If such an effect is commonplace it may be prudent to factor in kinetic fractionation as part of the enrichment signal for all stalagmite $\delta^{18}O$ records. The importance of using stalagmites deposited in isotopic equilibrium has lessened in recent years as better understanding of the processes that cause isotopic variation have been driving speleothem studies. Furthermore it is much less likely that the conditions of formations of semi-arid speleothems will form 'quasi-equilibrium' conditions.

3.5.2 Signals in Oxygen Isotopes

Under equilibrium conditions oxygen isotopes in speleothems reflect the isotopic composition of the meteoric water that forms cave drip waters and the in-cave temperature at which the calcite or aragonite forms (Hendy 1971; McDermott et al., 2006; Lachniet 2009). However, in most cases $\delta^{18}O$ variations in the meteoric water cycle are much larger (Lachniet 2009) than those caused by temperature changes in the cave. Thus $\delta^{18}O$ in drip waters of most caves will reflect $\delta^{18}O$ of precipitation (controls on which are discussed below) and importantly, for studies of caves in semi-arid (or Mediterranean) climates, evaporative processes which take place in the soil, karst and cave (McDermott et al., 1999).

3.5.2.1 Paleo-temperature

When carbonate has been deposited in isotopic equilibrium a palaeo-temperature can be defined from the $\delta^{18}O$ of the $CaCO_3$ due to the temperature dependent oxygen isotopic fractionation between calcite and water. This has been determined empirically, initially by Epstein (1953) who produced the palaeotemperature equation:

$$\mathbf{T\ (°C) = 16.5 - 4.3\ (\delta^{18}O\ calcite - \delta^{18}O\ water) + 0.14\ (\delta^{18}O\ calcite - \delta^{18}O\ water)}$$

Equation 3.2 Temperature calculation using $\delta^{18}O$ (Epstein et al., 1953)

There have been several revisions of the fractionation factor since this early work and the one most commonly used for speleothems is that of Kim and O'Neil (1997) (Equation 3.3).

$$1000\ \ln(\alpha CaCO_3\text{-}H_2O) = 2.76(10^6 T^{-2}) - 3.96$$

Equation 3.3: Kim and O'Neil (1997)

However, it has been pointed out by McDermott et al. (2006) that, in a plot of 100lnα vs. 1000/T(K), most speleothem data lie above the equilibrium line, suggesting that few speleothems are precipitated in true isotopic equilibrium. Tremaine et al. (2011) reviewed all the published speleothem data and showed that they lie along a line defined by Equation 3.4.

$$1000\ \ln \alpha = 16.1\ (10^3\ T^{-1}) - 24.6$$

Equation 3.4: Tremaine et al. (2011)

Just above, and almost parallel to, that of Kim and O'Neil (1997). It may therefore be the case that the empirical, laboratory derived, temperature fractionation factors do not fully reflect the

conditions under which speleogenesis occurs and that in most cases speleothems are formed under conditions that closely approach isotopic equilibrium (or quasi-equilibrium). In sites where $\delta^{18}O$ of precipitation is controlled by temperature, a positive correlation can be observed between the site's mean annual temperature and the mean $\delta^{18}O$ of precipitation (Dansgaard, 1964) in spelean $CaCO_3$.

Additionally to temperature dependent fractionation of $\delta^{18}O$, in poorly ventilated caves air temperatures remain fairly constant throughout the year as seasonal temperature changes outside have little effect. Cave air temperature is thus close to the mean annual air temperature outside the cave (McDermott 2004, McDermott et al., 2006). In the absence of other controls it would be expected that a rise in air temperature would result in a shift to enriched $\delta^{18}O$, but only if effects of evaporation are minimal (McDermott et al., 1999). Palaeo-temperature calculations are further hindered by unclear controls on the temperature dependence of $\delta^{18}O$ in the cave atmosphere which are both variable and site specific (McDermott 2004).

3.5.2.2 Changes in isotopes of meteoric precipitation

Fractionation processes which govern the $\delta^{18}O$ values of $CaCO_3$ are also responsible for changing $\delta^{18}O$ defined by Rayleigh distillation, related to phase changes at different points in the hydrological cycle, for example when moisture enters the vapour phase after evaporation of ocean water (Dansgaard 1964). Ice volume changes (particularly at interglacial/glacial timescales) alter ocean $\delta^{18}O$ values (Lauritzen and Lundberg 1999). However large scale ice sheet collapse during the Holocene is estimated to only have decreased oceanic $\delta^{18}O$ in the regions of ice caps by 0.3 ‰ during the early Holocene (Stuiver et al., 1995) and so its effect in the timescales of this study are negligible.

The first control on isotopes of precipitation is the $\delta^{18}O$ value of seawater (Dansgaard 1964) local values of which are connected to salinity (controlled by evaporation), freshwater run off, precipitation, sea ice contribution and ocean and atmospheric circulation (Lachniet 2009). The main driver of $\delta^{18}O$ values of precipitation from seawater is the amount of evaporation as fractionation causes the $\delta^{18}O$ of the evaporating vapour to be isotopically lighter than its associated water body (Lachneit 2009). As vapour condenses into the liquid phase, the water droplets are isotopically enriched due to the preferential incorporation of ^{18}O into the liquid phase (Dansgaard 1964). This condensation requires a drop in temperature which may be provided by frontal cooling or orographic lifting (Lachneit 2009). As an air mass moves away from its source the process of Rayleigh distillation causes progressive 'rainout' of heavier oxygen

isotopes, leaving the source vapour isotopically depleted. Thus through time and with further distance from the source precipitation will become gradually isotopically lighter; with the isotopically heaviest rain falling closest to the source.

The $\delta^{18}O$ composition of precipitation becomes increasingly positive as temperature increases. (Dansgaard 1964). This is known as the temperature effect and is caused by the temperature dependence of fractionation as outlined in Section 3.5.2.1. Possibly its key influence is on seasonal precipitation $\delta^{18}O$ records due to the differences in temperature across the year (Lachniet 2009). Temperature also has a control on the altitude effect whereby the decrease in mean annual temperature with increasing elevation causes $\delta^{18}O$ to decline (Lachniet 2009). However temperature changes can also have an effect on rainfall amount as well as directly on $\delta^{18}O$ values; land and sea surface temperature increases have been linked to a reduction in rainfall in semi-arid speleothems (Bar-Matthews et al., 2003).

The amount effect is most apparent in regions where mean annual temperature exceeds 15°C (usually tropical locations) (Dansgaard 1964) and has been noted in semi-arid locations (e.g. Bar-Matthews et al., 2003). It is possible to observe a negative relationship with the $\delta^{18}O$ of precipitation decreasing as rainfall amount increases (Dansgaard 1964) as heavier isotopes are preferentially rained out. This means the heaviest $\delta^{18}O$ from the water vapour occurs closest to the source. However some overprinting of this signal can occur due to the evaporation of raindrops during drier periods relatively enriching $\delta^{18}O$ values (Dansgaard 1964).

The continental effect is also caused by the preferential rainout of heavier isotopes because as air masses travel over continents they progressively lose their moisture and cool (Dansgaard 1964) the effect is decreasing $\delta^{18}O$ of precipitation with distance over land away from the sea.

The original moisture source is a key parameter on $\delta^{18}O$ of precipitation because all moisture sources have differing isotopic signals, with ocean $\delta^{18}O$ composition ~0 ‰ at present. This is particularly evident in sources with a strong glacial/interglacial difference in $\delta^{18}O$ composition such as the Mediterranean Sea (4-5 ‰ heavier during glacials), which can be traced in speleothem samples (Bar-Matthews et al., 1996). Therefore, changes in moisture sources may modify the amount of rainout (and $\delta^{18}O$ prior to reaching the cave by moving to warmer or cooler paths (McDermott et al., 1999)). Observed changes in $\delta^{18}O$ of speleothems have previously been linked to moisture source changes at regional atmospheric levels such as the monsoons (including Burns et al., 2002; Fleitmann et al., 2003, 2007).

3.5.2.3 Soil, karst and in cave processes

Overall climatic signals from precipitation are likely to be modified in the soil, karst and cave system, before being 'locked in' to the precipitating speleothem. (Hendy 1971, Bar-Matthews et al., 1996). Soil waters commonly reflect the $\delta^{18}O$ of precipitation but values can be increased by evaporative processes (Lachniet 2009). In locations where soil recharge events are associated with intense rainfall or storms with low $\delta^{18}O$ compositions the enrichment in isotopes within the soil by evaporation may be reduced (Dansgaard 1964; Gat 1996). Vegetation itself doesn't have a direct effect on $\delta^{18}O$ except in its role in evapo-transpiration processes (Lachniet 2009).

High frequency climatic signals maybe reduced by increased residence time in the karst which increases the likelihood of mixing differently aged and sourced waters (Fairchild et al., 2006a). Slow drips are possibly associated with large storage times and are more likely to represent annual $\delta^{18}O$ variations (McDermott et al., 2006). Fast drips are expected to show high frequency variation (possibly seasonal) $\delta^{18}O$ if they also represent minimal storage in the epikarst (McDermott et al., 2006; McDonald et al., 2007). Processes in the karst, even with fast drips, may cause a delay in drip response to rainfall events (Mattey et al., 2008b). Thus palaeoclimate signals might under some circumstances be drip rate dependent (Baldini et al., 2006).

As soon as drip water enters the cave air CO_2 exchange begins. However the overall effect on isotopes is minimised at sites with high drip rates as full CO_2 exchange requires about 3000 seconds (Dreybrodt and Scholz 2011), although some oxygen isotope fractionation will occur before the process is complete. Rapid CO_2 outgassing and other kinetic effects such as evaporation enrich $\delta^{18}O$ signals and add high frequency 'noise' (Hendy 1971). Dripwater $\delta^{18}O$ in semi-arid climates is more fractionated relative to its source meteoric water due to evaporative processes in the soil and karst (Bar-Matthews et al., 1996). Speleothems from semi-arid climates are thus likely to record a combination of heavier $\delta^{18}O$ isotopes from in-cave and karst fractionation processes as well as the meteoric signal (Bar-Matthews et al., 1996; Fairchild et al., 2006a). In regions where the amount effect is dominant, during periods of low drip and slow infiltration evaporation can produce the same results as would be expected from the amount effect (Fleitmann et al., 2004) by further relative enrichment of $\delta^{18}O$ in dripwaters feeding speleothems. Evaporation may also occur in caves with low relative humidity or air circulation (Lachniet 2009). Kinetic fractionation occurs during rapid degassing which may be related to increased ventilation (Frisia et al., 2000; Spötl et al., 2005) or highly supersaturated dripwaters (Mickler et al., 2004).

3.5.2.4 Orbital and solar insolation controls

In speleothems with longer growth periods it may be possible to detect changes in oxygen isotopes controlled by climate/precipitation changes linked with fluctuations in Milankovitch cycles. These observations are particularly clear in Chinese stalagmites (Fairchild et al., 2006a). However during the Holocene solar insolation is more common large scale forcing of speleothem $\delta^{18}O$ (e.g. Neff et al., 2001; Fleitmann et al., 2003; Frisia et al., 2003; Muñoz et al., 2015).

3.5.3 Signals in Carbon Isotopes

Unlike oxygen isotopes carbon isotope records are largely not temperature dependent and more closely represent the sources and mixing processes during the formation of dissolved inorganic carbonate in drip waters (Schwarcz 2007). Largely $\delta^{13}C$ will be controlled by bedrock weathering and/or input from soil CO_2 (McDermott 2004) although atmospheric CO_2 can also be a significant factor (Richards and Dorale 2003). Generally carbon isotopic ratios display the balance between the heavier bedrock signal (dissolved inorganic carbon) and lighter soil biogenic carbon (dissolved organic carbon (McDermott et al., 2006).

3.5.3.1 Bedrock vs soil CO_2 signals

The importance of bedrock signals is determined by whether the system is geochemically open or closed (Fairchild et al., 2006a; Dreybrodt and Scholz 2011). Natural karstic systems are usually, at least partially open, but as the system becomes more closed DIC $\delta^{13}C$ will approach that of the dissolving bedrock: a truly closed system would represent bedrock $\delta^{13}C$ as it is isolated from the soil reservoir (McDermott 2004). Additionally under these conditions the $\delta^{13}C$ in the speleothem will be slightly affected by the partial pressure of CO_2 in the cave atmosphere (Dreybrodt and Scholz 2011) as faster rates of degassing create enrichment in $\delta^{13}C$ (McDermott et al., 1999). Minimal soil and vegetation above the cave will increase the $\delta^{13}C$ values by introducing a larger signal from the dissolved bedrock when water infiltration rates are low during arid periods (Bar-Matthews et al., 2003). On the other hand an increase in soil and vegetation above the cave will decrease $\delta^{13}C$ by adding more isotopically light biogenic carbon to the system (Baldini et al., 2005). Higher $\delta^{13}C$ may also be achieved by incomplete equilibrium with soil during faster infiltration events and may be associated with wet periods (Bar-Matthews et al., 2003;

McDermott 2004). Speleothem $\delta^{13}C$ records are thus often a combination of both bedrock and soil CO_2 (Bar-Matthews et al., 1996) where the signal will be dominated by the larger source.

Human activity may also leave a tracer on bedrock vs soil CO_2 $\delta^{13}C$ activity as deforestation and reduced soil thickness could lead to an increase in seepage water which is likely to cause a markedly different signal in the $\delta^{13}C$ record of the stalagmite (Fairchild et al., 2006c)

3.5.3.2   C4 vs C3 plants

[14]C activity in modern speleothems and feeding waters shows organically sourced carbon accounts for 80-95% of the activity (Genty et al., 2001b). The dominance of this organic derivation is thus controlled by the isotopic composition of the soil organic matter. In semi-arid environments $\delta^{13}C$ signals in speleothems can be controlled by shifts between C4 and C3 type vegetation (Bar-Matthews et al., 1997) because the differing metabolic pathways of photosynthesis are represented by quite different $\delta^{13}C$ compositions. C4 vegetation (dryland grasses) utilise a much higher $\delta^{13}C$ than C3 vegetation as enzymes which preferentially use ^{12}C are used less in the C4 pathway (Slack and Hatch 1967). This leads to ranges in speleothem of -6 ‰ to $+2$ ‰ for C4 and -14 ‰ to -6 ‰ for C3 (McDermott 2004). The ranges in speleothems are offset from the isotopic values utilised during plant photosynthesis due to the input of the DIC component creating an equilibration between plant sourced CO_2 and DIC (Emrich et al., 1970). This explains why soil CO_2 is consistently less negative than $\delta^{13}C$ of source plant material (Frumkin et al., 2000). Vegetation signals are particularly apparent in open karst systems as continuous equilibrium can be reached between the relatively infinite soil CO_2 reservoir and infiltrating waters (McDermott 2004). These conditions will dominate any $\delta^{13}C$ contribution from the isotopically heavier bedrock reservoir (McDermott 2004; Dreybrodt and Scholz 2011).

3.5.3.3   Atmospheric CO_2 signals

Full equilibrium between infiltrating water and the soil or karst may not be achieved under conditions where soil-water residence times are comparatively short (such as during high infiltration events). Under these conditions DIC $\delta^{13}C$ may partly record an atmospheric CO_2 signal (McDermott 2004), which fluctuated between -6.6 ‰ and -6.3 ‰ over the course of the Holocene (Indermühle et al., 1999). This may also occur during periods where the soil CO_2 contribution is dominated by atmospheric CO_2, for example in winter when soil biology is least active (Dreybrodt and Scholz 2011). An atmospheric CO_2 signal imprinted on soil CO_2 values is

likely to cause a mixed but higher δ^{13}C value than expected for soil CO_2 values (Dreybrodt and Scholz 2011). However, it is noted that the impact of changing atmospheric δ^{13}C is likely to be negligible in comparison to the significant contribution of bedrock and soil δ^{13}C (Fairchild et al., 2006a).

3.5.3.4 Degassing and evaporation signals

Degassing is the most common process in caves that can imprint a signal on speleothem δ^{13}C values (Baker et al., 1997). As degassing imparts a disequilibrium effect that allows the lighter atom to escape preferentially to the gas phase (Section 3.5.1) it creates heavier calcite speleothem δ^{13}C values (McDermott et al., 1999). This process can affect DIC δ^{13}C before reaching the precipitating stalagmite, if precipitation (so called 'prior calcite precipitation') occurs during degassing into air pockets in the epikarst (Fairchild et al., 2000). The issue of prior calcite precipitation is discussed further in Section 3.6.2.2. In the cave environment, changes in seasonal ventilation will influence degassing more strongly during some periods than others (Frisia et al., 200; Boch et al., 2011; Tremaine et al., 2011). It is more likely that variation will be larger in δ^{13}C in semi-arid caves as warmer temperatures enhance degassing resulting in an imprint of enriched δ^{13}C on top of the fluctuating soil CO_2/bedrock signal (Bar-Matthews et al., 1996). Speleothems which grow in regions of the cave with enhanced airflows such as near the cave entrance are particularly subjected to greater degassing and enriched δ^{13}C (Frisia et al., 2000; Spötl et al., 2005).

Speleothems with dendritic fabrics often have heavier δ^{13}C values than those with other fabrics (McDermott et al., 1999). As dendritic fabrics are thought to represent rapid growth during periods of high supersaturation with respect to calcite (and often low drip rate) it may well be that degassing is the forcing variable for both observations (Frisia et al., 2000). There is a suggestion that high drip rates may not be subjected to degassing signals (Dreybrodt and Scholz 2011) and clear differences in δ^{13}C values between fast drips and all other drip types are noted in Bar-Matthews et al. (1996).

Evaporation in the cave will produce heavier δ^{13}C signals (although evaporation is not limited to the cave, the same result will occur in the soil and karst) which can be associated with dry periods (McDermott 2004).

3.6 Trace Elements

Trace element studies in speleothems were first undertaken with a view to palaeotemperature reconstruction, particularly the idea that Mg incorporation in calcite is temperature dependent (Gascoyne 1982). It was later shown that this temperature dependency signal is usually dwarfed by other effects (discussed below) reflecting the various pathways of supply of Mg and modification of its concentration before incorporation in calcite (e.g. Fairchild et al., 2000; Borsato et al., 2007; Fairchild and Treble 2009; Hartland et al., 2012; Rutlidge et al., 2014).

This noted, trace element information in stalagmites can be helpful in identifying a number of processes related to both climatic and other environmental drivers, particularly when combined with stable isotopes and petrographic data.

3.6.1 Origins and incorporation of trace elements in speleothems

Mg, Sr and, to a certain extent Ba, are differentiated from other trace elements which might be present in speleothems because they are directly incorporated into $CaCO_3$ crystal lattices by substituting for Ca (Fairchild and Treble 2009). The largest source of Mg and Sr is the limestone bedrock above the cave (Fairchild and Treble 2009) but Mg and Sr can also be sourced from salts, which can build up in arid zone soils where evaporation of soil moisture exceeds infiltration (McDonald et al., 2007). Transport of Mg and Sr to the speleothem growth surface relies on chemical mobilisation (i.e. ease of dissolution) from soil and bedrock (Fairchild and Treble 2009). Thus differences in host rocks, e.g. dolostone vs limestone, could be reflected in Mg and Sr concentrations. A mixed dolomite calcite karst system will alter the ratios of Sr and Mg in speleothems. Calcite signals will be observed first as dolomite weathers much slower and is characterised by the higher concentrations of Mg than the latter (Fairchild et al., 2000). Negative correlations between Mg/Ca and Sr/Ca may reflect changes in dissolution of the host rock, where dolomite is depleted in Sr relative to calcite (Roberts et al., 1998). In these systems an increase in residence time will increase dolomite dissolution (Fairchild et al., 2000). Salts and other easily leached compounds might account for cases where karst waters are enriched in these elements relative to the bedrock composition (Fairchild et al., 2000).

There is widespread evidence of trace metals binding with organic colloids (Hartland et al., 2012). Borsato et al., (2007) in particular noted the association of heavy trace metals Y, Zn, Cu and Pb with organic rich, highly fluorescent laminations in Ernesto Cave, Italy. Later work by Hartland et

al., (2012) expanded the inventory to include Ni, Ti, Mn, Al and Fe. These elements are assumed to be adsorbed to $CaCO_3$ crystal growth surfaces. Most metals may preferentially associate with particulate transport (>100 nm) over fine colloidal fractions; a notable exception is Al which is preferentially bound to small, dissolved fractions less than 1 nm in size (Hartland et al., 2012). Transport of organically associated trace elements therefore relies on hydrological changes to infiltration rate and volume of soil waters (Fairchild and Treble 2009).

All commonly used trace elements in speleothem studies have multiple sources and thus multiple transport pathways. Mg, Sr and Ba can all be associated with detritus, and this issue is particularly acute when dissolved concentrations are low: while Ba, for example is often in low total concentration and while it can be incorporated in the growing crystal lattice (Fairchild et al., 2000; Hori et al., 2013) it has also been shown to associate with organics in speleothems (Borsato et al., 2007; Rutlidge et al., 2014). Silicates and clay rich soils strongly bind Ba which may make concentrations higher in speleothems from semi-arid areas (Rutlidge et al., 2014). However it may be possible to prove that Ba is sourced from bedrock where it shows a positive covariance with Mg and Sr (McDonald et al., 2007). P is typically sourced from soil fractions and may have either organic or inorganic derivation (Borsato et al., 2007).

3.6.2 Factors controlling trace element compositions in speleothems

3.6.2.1 Distribution coefficients

Equilibrium trace element concentrations in a mineral (or solution) are controlled by their relative concentration (in mineral or solution) which is describe by the partition coefficient (Equation 3.5).

$$(Tr/Ca_{CaCO_3}) = K_{Tr} (Tr/Ca)_{solution}$$

Equation 3.5 partition coefficients of trace elements and Ca in solution (Morse and Bender 1990)

As the coefficients of Mg and Sr are both much less than one the effect is that they will be less readily removed from the bedrock or karst water than Ca (Fairchild and Treble 2009). This means in the first instance, dripwaters entering the cave will be enriched in the trace elements relative to

the bedrock and particularly in caves where prior calcite precipitation is common. Mg/Ca and Sr/Ca ratios will therefore also be higher in the speleothem than the bedrock (see below) (Fairchild and Treble 2009).

3.6.2.2 Prior Calcite Precipitation

Arguably the strongest control on Mg/Ca and Sr/Ca ratios over timescales longer than a year is the effect of prior calcite precipitation (PCP) in various areas of the epikarst and cave before it reaches the growing stalagmite tip (Fairchild et al., 2000). This process increases the ratio of Mg and Sr relative to Ca because the large difference in partition coefficients (Fairchild and Treble 2009) causes Ca to be preferentially removed in the 'prior precipitate' (Fairchild et al., 2000).

The extent of PCP is considered to be controlled mainly by water availability (Fairchild et al., 2000; Tremaine and Froelich 2013) related to relatively dry conditions where water-epikarst contact times are longer, increasing the concentration of ions and the chance of degassing into air pockets in the karst (Fairchild et al., 2000). Conversely PCP is reduced during high discharge or recharge conditions in the aquifer as the amount of ventilated pore space is reduced (Spötl et al., 2005; McDonald et al., 2007). The same process will occur in the cave during drier conditions as drip rates are reduced and degassing enhanced (McDonald et al., 2007; Tremaine and Froelich 2013). Variations in Mg/Ca and Sr/Ca driven by PCP have the potential to record palaeohydrological change, but only prevails in sites where precipitation is greater than evaporation (Fairchild et al., 2000; McDonald et al., 2007; Tremaine and Froelich 2013; Rutlidge et al., 2014). Additionally it may only be possible to relate variations specifically to water residence times at sites where Mg and Sr have a single bedrock source (Tremaine and Froelich 2013).

In some cases PCP is predominantly driven by variation in degassing. In this case the difference between pCO_2 between the soil and cave environment could be the controlling factor or dynamic ventilation of the cave air where soil pCO_2 is more consistent (Spötl et al., 2005). During low pCO_2 periods higher Mg/Ca and Sr/Ca ratios can be linked to more enriched $\delta^{13}C$, as rates of degassing are higher (see Section 3.5.3.4). This control is observed in New St Michael's Cave, Gibraltar where cave air pCO_2 varies seasonally. Highest Mg/Ca ratios are observed in the summer months but in this case is controlled by low pCO_2 driven by chimney ventilation between the cave and atmosphere due to the lower temperature and density differentials in the summer (Mattey et al., 2010). However speleothems located in sections of the cave with better ventilation (such as the entrance) may have higher pCO_2 variation and enhanced degassing not related to climate (Frisia et al., 2000).

3.6.2.3 Source changes, residence time and mixing

Studies of multiple speleothem samples from single caves show that the karst is not uniform in trace element concentration (for example McDonald et al., 2007), at any given site there may be a reservoir of a particular element increasing the concentration in one speleothem over another. Trace element levels, for example, will be lower in waters dissolving more ancient speleothems or secondary calcite precipitated in fractures than those dissolving bedrock (McDonald et al., 2007).

The length of residence time is a key driver of trace element compositions. The longer the residence time the longer the karst water has to equilibrate with trace elements in the host rock and achieve maximum saturation (Fairchild et al., 2000; Fairchild and Treble 2009). Additionally the longer the residence time the more substantial the mixing of water from different sources is likely to be (Spötl et al., 2005). High Mg/Ca therefore can imply significant mixing or longer residence times (Verheyden et al., 2000; Spötl et al., 2005).

Despite the importance of the length of residence time in the karst, it is unlikely that flow times through any given location are changing dramatically, so hydrological routing (changing the source of trace elements) and mixing are likely to be more important (Fairchild and Treble 2009). Source changes are likely to be a primary driver of trace element changes which are not obviously attributed to climate controls, other trace element or stable isotope patterns.

3.6.2.4 Infiltration (precipitation) amount

Organically transported trace elements can be linked to rainfall amount as they are washed out of the soil during precipitation events (Hartland et al., 2012). Collodial transport of some or most of the Al, P, Cu, Zn, Y, Mn, Fe and Pb in soils is enhanced during periods of higher infiltration (Borsato et al., 2007; Hartland et al., 2012). High fluxes of natural organic matter and associated trace metals may occur during rapid, short lived increases in drip water rate occurring after peak infiltration events (Hartland et al., 2012), from extreme rainfall events or related to seasonal differences in water infiltration (Borsato et al., 2007). Metals associated with course (>100 nm) colloidal fractions, including Fe, Mn and Zn are not found in fractionated drip waters during normal dripping conditions suggesting they are filtered in the karst region (Hartland et al., 2012). The association of P with nutrient uptake in plants, suggests increases in P could be related to vegetation die back, thus marking higher infiltration events which could be related to seasonality of vegetation (Huang et al., 2001).

In addition to increasing Mg/Ca and Sr/Ca via PCP (Section 3.6.2.2) dry conditions can increase these ratios against calcite by the production of easily leached trace element salts due to the effect of evaporation of water in the soil (McDonald et al., 2007; Fairchild and Treble 2009; Rutlidge et al., 2014). Furthermore under drier conditions Mg and Sr may be selectively leached from the soil, as well as from the bedrock, as residence time in the soil is higher (Fairchild et al., 2000; Huang et al., 2001). Conversely, under high flow conditions, lower Mg/Ca in dripwater may be exhibiting dilution effects (Fairchild and Treble, 2009). Large rainfall events can change flow rate from seepage flow to shaft flow (Fairchild and Treble, 2009) limiting the uptake of trace elements via dissolution in the karst. There is a number of studies that have linked variations in Mg/Ca to records of rainfall (Fairchild and Treble 2009).

3.6.2.5 Crystal morphology and defects

Mg/Ca ratios are thought by some to control a variety of calcite fabric types (Frisia et al., 2000). Mg concentration is particularly important in controlling the precipitation of aragonite which occurs when the Mg/Ca ratio exceeds 1:1 (Frisia et al., 2002). High Sr levels are also associated with aragonite precipitation, as the aragonite lattice can accept more Sr than calcite (McMillian et al., 2005).

There is evidence for a relationship between certain trace elements and defect sites in $CaCO_3$ crystals. Sr in particular, is incorporated in larger quantities at higher growth rates which could be linked to defects arising during growth (Fairchild and Treble 2009). Higher Sr concentrations may therefore be found in fabrics exhibiting higher growth rates, as more defects are created during faster growth (Kendall and Broughton 1978; Frisia et al., 2000). Borsato et al. (2007) observed small peaks superimposed on longer trends in P which may be related to growth defects. Opposing relationships between Sr and P when observed together in organic rich laminae might suggest Sr is outcompeted for defect spaces when colloidally transported particles are present in higher volumes (Huang et al., 2001; Borsato et al., 2007).

Chapter 4. Sirtlanini and Dim Caves, Turkey: Petrography and Micro-dissolution related to Environments of Formation and Dating Anomalies.

This chapter consists of two parts. Firstly it examines the petrography and geochemical composition of two stalagmites from southwest Turkey, one of Holocene and one of Last Interglacial age. The first part utilises the extensive thin section coverage of both stalagmites to help inform on the environment of formation. The dating of these has proved very difficult, with multiple samples not falling in stratigraphic order. The second part of this chapter considers petrographic observations and the U-series data together, and in some detail, in an attempt to understand the factors that might be contributing to the discordant age patterns.

4.1 Introduction

4.1.1 Cave Settings

Sirtlanini Cave (37°37' 36.7" N, 28°41' 20.5" E) is located close to the village of Çamarası (~40 km south west of Denizli in south west Turkey (Figure 4.1). The cave entrance is 830 m.a.s.l. with a tubular entrance ~3 m long and ~1 m in height. The cave is on two different levels, with the second chamber ~3 m below the entrance chamber (Mason 2009). The limestone is probably of Mid Miocene age, part of the sedimentary cover of the Central Menderes Massif (Gokten et al., 2001). Epikarst thickness is roughly 25 m and a thin reddish soil above the cave supports sclerophyllous scrub (Mason 2009). In July 2006 cave temperature was 17.2 °C and humidity 100% (Mason 2009).

In contrast to Sirtlanini, Dim Cave (36°32' 25.0' N, 32°06' 32.8' E) has a coastal location 11 km north of Alanya and 145 km east from Antalya (Figure 4.1). The cave formed in limestone on the slopes of Cebel Reis mountain (Kunt et al., 2008), part of the Middle Taurus Mountains. Dim Cave developed along a major NW-SE fault zone. (www.dimcave.com.tr). The cave entrance is 232 m a.s.l and the cave itself is 360 m long, 10-15 m high and wide with a small lake at the far end (Kunt et al., 2008). Vegetation above the cave is Mediterranean evergreen shrub with a very thin soil (<20 cm) (Ünal-İmer et al., 2015). A relatively constant temperature of 18-19 °C and humidity of approximately 90 % is recorded by the owners, the MAGTUR Co. This is confirmed by data

collected in March 2009 when air temperature ranged from 18.1 to 18.6 °C and humidity from 96 to 99% (Wickens 2013).

Figure 4.1: Location of Sirtlanini and Dim Caves in relation to closest towns (Denizli and Alanya respectively) and IAEA weather stations. Insets show Google Earth images for topographic reference. Looking west towards Aydin for Sirtlanini (top) and east from the edge of Alanya for Dim (bottom).
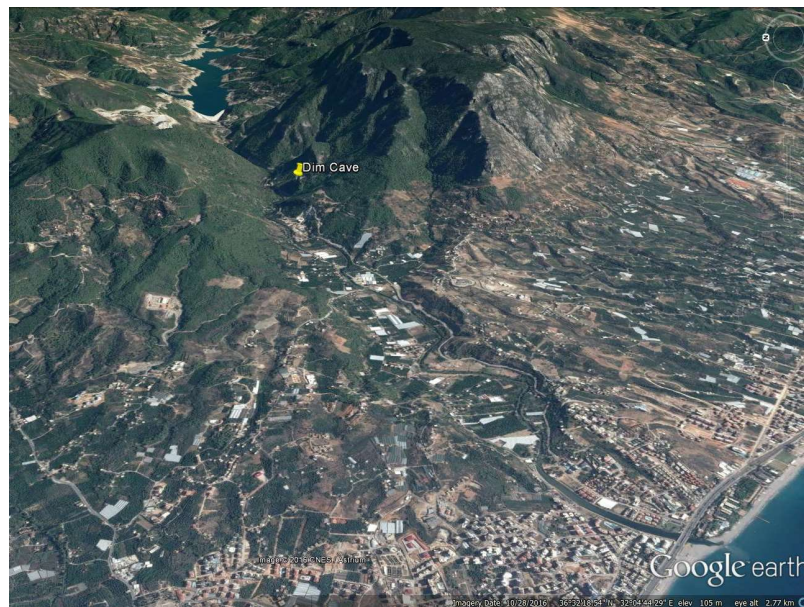
4.1.2 HY-8

Stalagmite HY-8 was active when collected from Sirtlanini Cave in July 2006 and is a typical candlestick stalagmite of 502 mm total length (Figure 4.2). HY-8 was collected from the second chamber 40-45 m from the cave entrance (Mason 2009). Only very occasional drips were present in the entirety of the cave at the time of collection (Mason 2009). Growth was probably initiated during the late Pleistocene but the majority of growth occurred during the Holocene (Section 4.2.6).
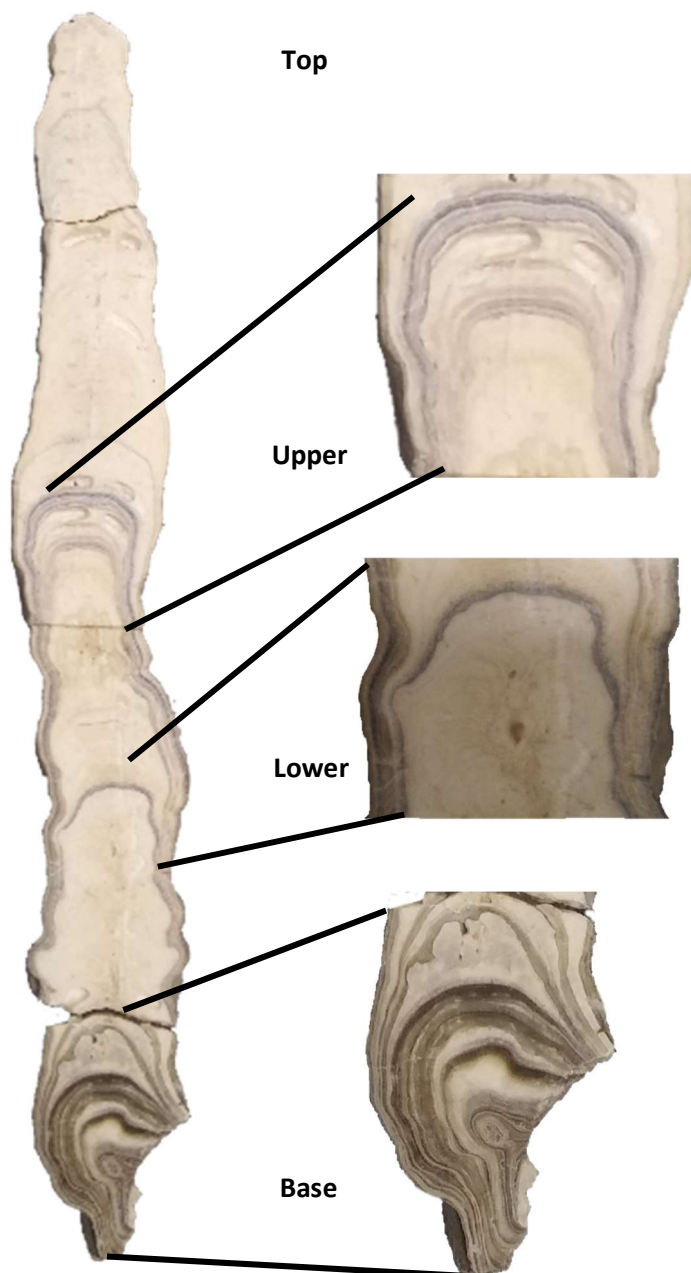
Figure 4.2: Full profile of stalagmite HY-8, with key features of the macromorphology (grey layers) highlighted.

4.1.3 Dim-1

Dim-1 is fossil stalagmite totalling 568 mm of length but with the top missing (Figure 4.3). It was toppled when collected with a small actively growing stalagmite on the outside (Wickens 2013). Dripping was observed in the cave at collection but not above Dim-1 (Wickens 2013). Dim-1 is believed to be of early last interglacial age (Section 4.2.6). A hiatus is observed at 480 mm.

Figure 4.3: Full profile of stalagmite Dim-1, with key features of the macromorphology highlighted. This includes the hiatus at 480 mm (green dashed lines). The mixed calcite/aragonite layer is highlighted between the hiatus and the black dashed line. 'Wing' morphology is highlighted in the box. Aragonite layer preserved at the flank and possible to trace across the stalagmite is highlighted in the blue circle.

4.1.4 Local Climates

Turkey has 7 precipitation regimes designated by Türkeş (1996); both caves are situated in the region of Mediterranean climate (Türkeş 1996, Figure 2.7 Chapter 2). Winters are mild and wet, with hot arid summers. Precipitation and air temperature data for the nearest weather stations are presented separately for each cave.

4.1.4.1 HY-8

The closest weather stations to Sirtlanini are Muğla (1935-2014) and Nazilli (1961-1990) (Climate Explorer). Both records are nearly complete during their timeframes, with Nazilli located 55 km from the cave.

There is much similarity in the distribution of rainfall at both locations and both show a strong seasonal pattern. At both stations, over 50% of rainfall falls in winter (Table 5.1) with December the wettest month. Less than 5 % of rainfall occurs in summer which translates into < 40 mm at Muğla and < 30 mm at Nazilli. Sharp changes in rainfall amount are noted between seasons, particularly between November and December. Rainfall at Muğla is higher than at Nazilli, probably caused by its closer proximity to the coast. Rainfall is, however, better distributed between seasons at Nazilli (Table 5.1), particularly in spring which has 3.5% more rainfall compared to Muğla.

	Muğla Precipitation (%)	Nazilli Precipitation (%)
Winter	58.7	51.9
Spring	19.5	22.9
Summer	3.0	4.5
Autumn	18.8	20.7

Table 4.1: Percentage of precipitation contribution by season for Muğla weather station for the period 1935-2014 in column 1 and for Nazilli weather station for the period 1961-1990 (column 2).
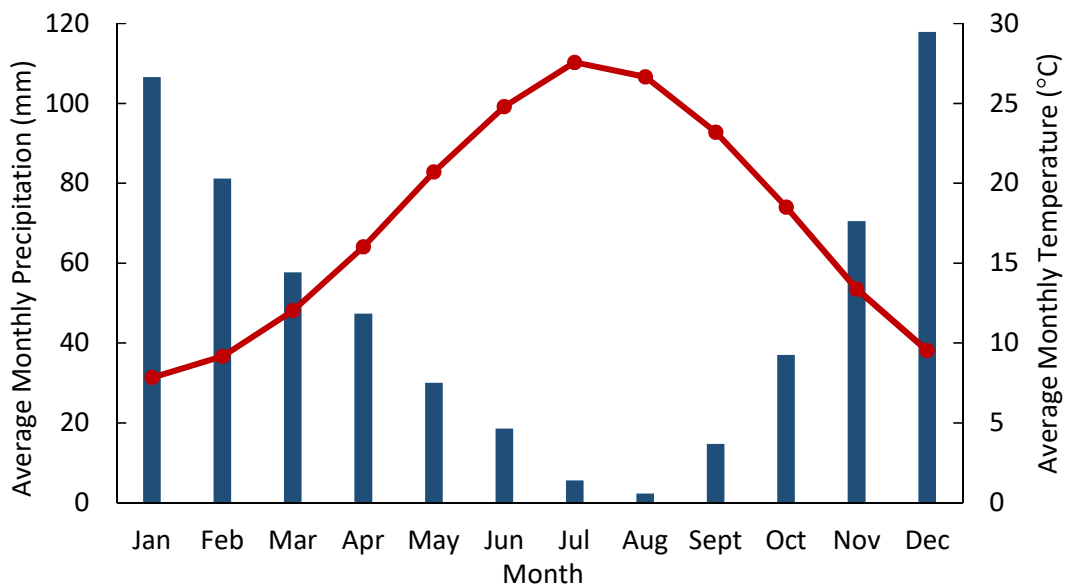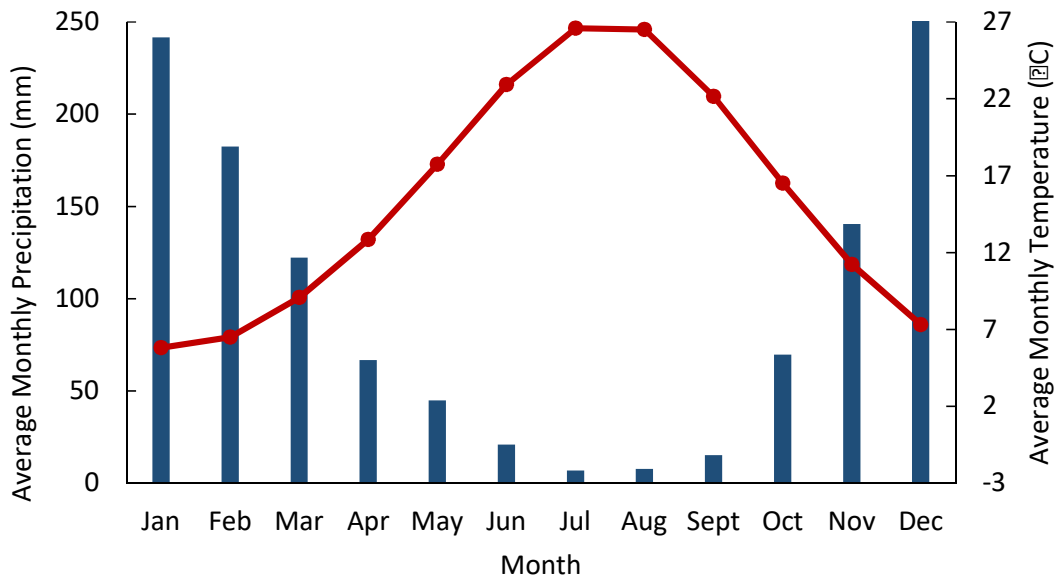
Figure 4.4: Monthly precipitation averages (blue bars) and temperature averages (red line) for Muğla (above) and Nazilli (below) for the periods 1935-2014 and 1961-1990 respectively. Clear seasonality is observed in precipitation with most rainfall occurring in winter months. Temperatures peak in July and August and on average do not fall below 6°C.

Mean winter temperatures do not fall below 6°C at either location, but Sirtlanini Cave is situated at higher altitude (>200 m above Muğla, >600 m above Nazilli) suggesting that snow may fall at altitude around the cave. With high summer temperatures ~27°C and very low precipitation in July and August in particular, longer interval drip rates and more evaporation in the soil and epikarst is likely during these months. There is a strong bias towards winter precipitation with minor input in spring and autumn; thus speleothem growth rates (and isotopic compositions) will mostly be determined by winter rainfall.

In the region of Sirtlanini Cave itself, average annual precipitation values is estimated to be ~700 mm per (Türkeş 1996), similar to the mean annual total at Nazilli (627 mm) but significantly lower than Muğla (1196 mm). There is good agreement that most rainfall occurs in winter, ~300 mm and the least in summer <100 mm (Kadioğlu 2000). However, more rain falls in spring (~200 mm) than in autumn (~100 mm) (Kadioğlu 2000). Sariş et al. (2010) classified the area as a 'transitional regime' where precipitation peaks in December but the rainy period starts in autumn and continues into spring.

4.1.4.2 Dim-1

The closest weather stations to Dim-1 are Hadim (1961-1990) and Alanya (1961-1992) (Climate Explorer), and both datasets are near complete. As with the stations closest to HY-8, precipitation is strongly seasonal. Most precipitation occurs in winter, ~50% at both stations and lowest in the summer (Table 4.2 and Figure 4.5). Maximum average rainfall is much higher at Alanya (227 mm) than Hadim (132 mm) as it is much closer to the coast. November is wetter in Alanya than Hadim but the percentage of precipitation that fall in the summer in Hadim is 6.5 % compared to 1.5 % in Alanya.

	Hadim Precipitation (%)	Alanya Precipitation (%)
Winter	49.7	56.3
Spring	24.3	18.6
Summer	6.5	1.5
Autumn	19.4	23.6

Table 4.2: Percentage precipitation contribution by season for Hadim (column 1) during the period 1961-1990 and Alanya (column 2) from 1961-1992.
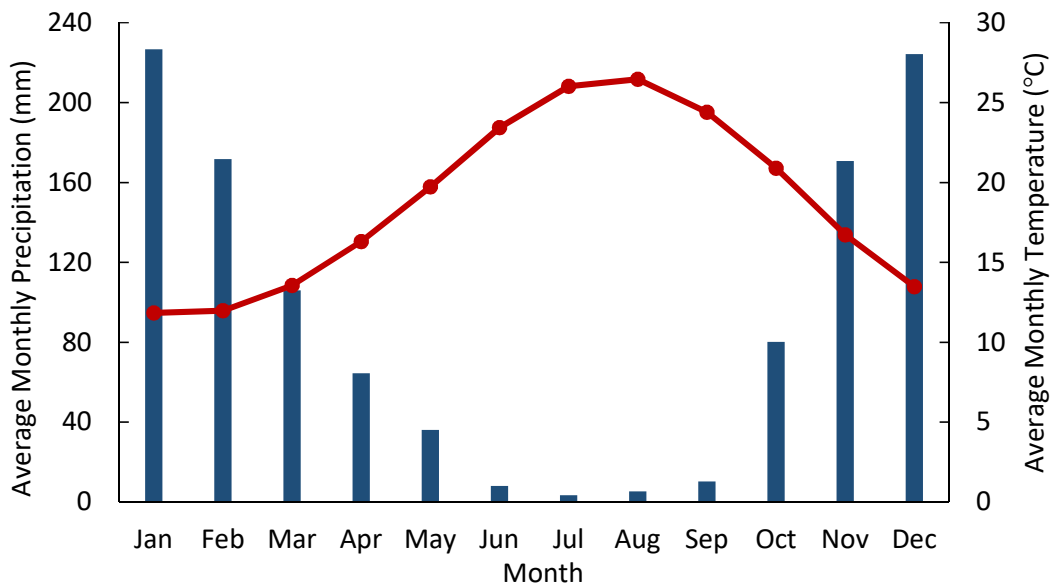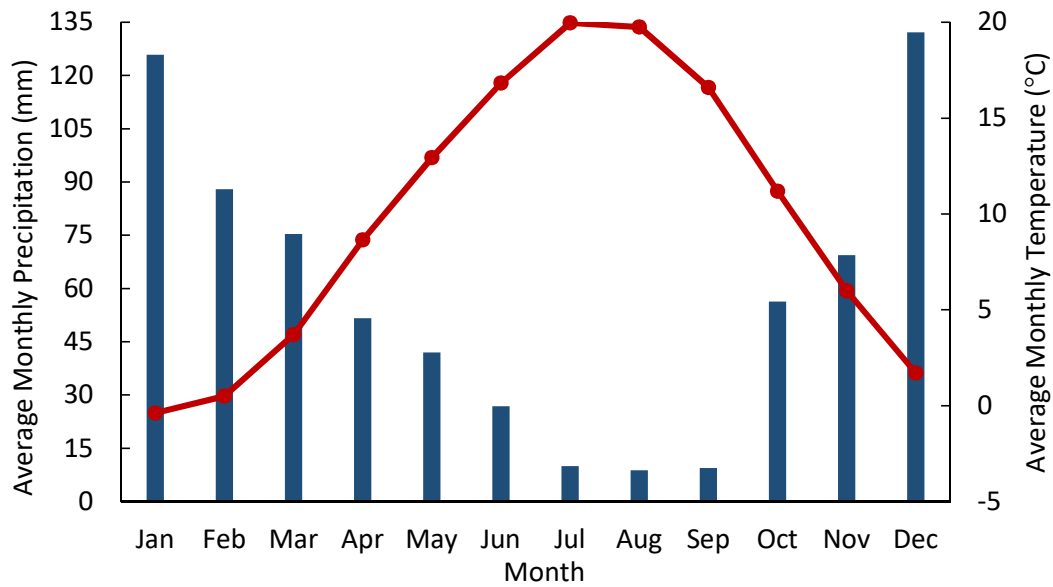
Figure 4.5: Monthly precipitation averages (blue bars) and temperature averages (red line) for Hadim (above) and Alanya (below) for the periods 1961-1990 and 1961-1992 respectively. Clear seasonality is observed in precipitation with most rainfall occurring in winter months. Temperatures peak in July and August but average temperatures are over 5 ℃ lower in Hadim than Alanya.

Temperatures are different between these records it being cooler throughout the year in Hadim compared to Alanya (Figure 4.5). At Alanya, coldest temperatures are well above freezing, such that snowfall is very uncommon at sea level; it is noted it may occur at cave elevation. Mean summer temperatures at Hadim peak at 20 °C, compared to 26 °C in Alanya, which is closer to the cave. This suggests that despite low summer rainfall at both sites, Alanya will experience relatively more evaporation, combined with drip rate reductions or pauses during the summer, reducing the likelihood of growth during these months. Overall mean precipitation is higher at Alanya which is favourable for speleothem growth; however, most growth will occur in winter, with some autumn and spring representation as well.

Türkeş et al. (1996) suggest that mean average rainfall is around 1000 mm in the region of Dim Cave, consistent with the Alanya station. Principal component analysis by Kadioğlu et al. (2000) shows that the percentages of rainfall by season in the region of Dim Cave are ~20 % in spring, ~5 % in summer, ~15 % in autumn and 55 % in winter. All these findings are consistent with the Alanya data; the station is classified as a regime with a rapid onset of winter rainfall to a high magnitude December peak and gradual drying to the summer months (Sariş et al., 2010).

4.2   Results

4.2.1   HY-8 Morphology

HY-8 is a cream calcitic stalagmite with distinctive macromorphological features (Figure 4.2). The most striking of these are sets of marked black (between 0 and 69 mm) and grey/blue layers, hereafter referred to as 'grey layers'. A singular 1mm thick grey layer occurs at 163 mm to 164 mm and much thinner dispersed layers are visible between 260 mm and 287 mm. Individual layer thickness in this upper grey layer set is 19 μm to 129 μm but the amalgamation of layers are <0.2 mm to 5 mm thick in hand specimen. HY-8 is subject to frequent changes in growth axis (predominantly 19 mm, 165 mm, 239 mm, 405 mm and 453 mm). Changes in growth axis consistently precede a thinning of the stalagmite diameter. Thinning of the diameter also occurs at 263 mm without an associated change in growth axis. Subsequent precipitation following a reduction in diameter fully encases the flanks of previous stalagmite growth. This keeps overall stalagmite thickness fairly uniform (average 55 mm). Lamination is prevalent through the majority of the stalagmite and is particularly well developed in the region 287-403 mm. Macro-vugs are notably in the central axis throughout the stalagmite length.

4.2.2   HY-8 Petrography

The primary fabric of HY-8 is dendritic with clear deviations to microcrystalline calcite (Frisia et al., 2000) during deposition of grey layers. This is with the exception of the layer at 163-164 mm which comprises equant/euhedral calcite (Railsback et al., 1994; Alan C Kendall pers. comm. 2015). Porosity is dependent on fabric with open dendritic being the most porous, porosity of the stalagmite as a whole is therefore generally high. Micro-vuggy porosity is a common feature of the central axis. Most of HY-8 is inclusion poor. The top of the stalagmite is not corroded which is consistent with the stalagmite actively forming when collected.

Dendritic fabric occurs mostly in its open form (Frisia et al., 2000) which is highly porous. However, lamination is defined by alternating open and compact dendritic calcite (Figure 4.6) which differs from open dendritic by its lack of porosity (Frisia and Borsato 2010). A proportion of the fabric in both open and compact forms displays a single dominant branching direction, most often aligned to growth direction (Figure 4.6). A lack of two growth directions is contradictory to the identifying features of dendritic outlined in Frisia (2015). However in many areas of mainly single branching crystallites it is possible to observe minor lateral cross branching (Figure 4.6 A

and B). It is possible that as the dominant branch is strongly controlled by the predominant growth direction, it masks secondary branching causing it to appear absent. The open fabric also displays a high level of non-linear porosity and both open and compact fabrics display lateral extinction boundaries consistent with dendritic fabric (Frisia and Borsato 2010). These observations have led to assignment of the fabric as dendritic.

The thickness of laminations is highly variable (0.9 μm -1.4 mm) and open dendritic laminae are commonly thicker. Thickness can vary laterally and discontinuous sub laminations are present. Laminations are thinner around vugs of all sizes located down the central axis (Figure 4.6 D)
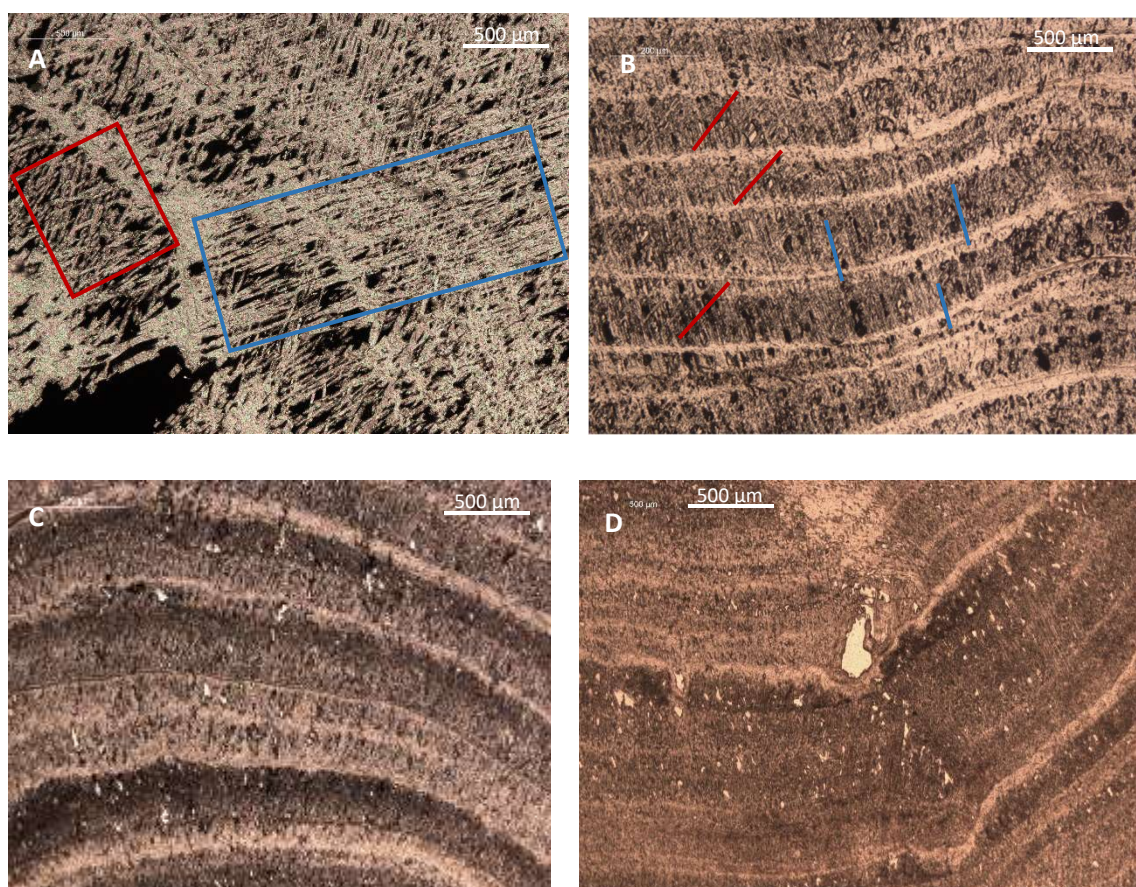
Figure 4.6: Dendritic fabrics in HY-8. A. Largely open dendrites. Cross branching is clearly observed (red box) while the section in the blue box shows a singular dominant branching direction. B. Laminated dendrites mostly showing one dominant branch in line with growth direction (examples highlighted blue). Minor cross branching examples are highlighted in red. C. Typical lamination in HY-8 showing the variation in width of laminations and discontinuous nature of some laminations widths laterally. D. Lamination compressed underneath a micro vug.

Deviations away from dendritic fabrics occur during deposition of grey layers. In these instances two fabrics are observed. The most common is a microcrystalline fabric which is easily identified by patchy extinction zones (Frisia et al., 2000). The microcrystalline fabric is much less porous than open dendritic calcite (Figure 4.7 A and B). Extinction zones of the microcrystalline calcite suggest crystals are variable in length, often ranging from 157 µm to 900 µm. Microcrystalline calcite is present in all grey layer locations aside from the 1 mm thick layer at 163-164 mm. Crystal sizes range from 160-430 µm. Some crystal terminations are clearly pointed (Figure 4.7 C and D) and elongation in the direction of growth is clearly visible in most crystals.
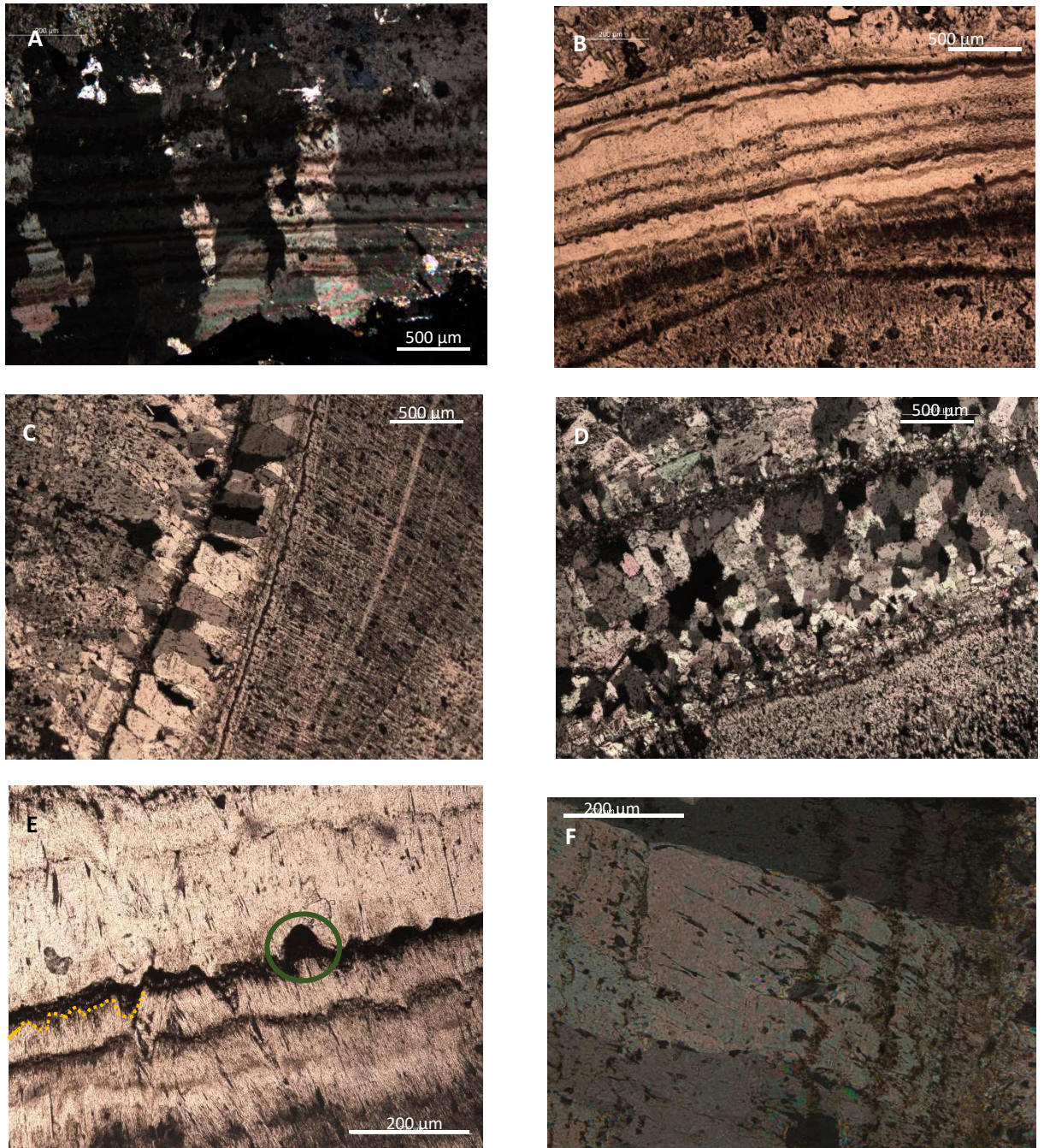
Figure 4.7: Microcrystalline fabrics and sub horizontal surfaces. A and B. Microcrystalline calcite showing characteristic irregular patchy extinction and very low porosity. B. Also displays distinct sub horizontal detritus rich surfaces which occur frequently within the microcrystalline fabric. C and D. Equant/euhedral calcite of various sizes and mostly showing elongation towards growth direction. E. Detritus rich surface highlighting corrosion to underlying calcite crystals and a detritus filled pit (green circle). F. Thorn inclusions in the base section of the stalagmite. The presence of these inclusions gives grey layers in the base a darker blacker colour.

The distinct blue-grey layering observed between 260 and 287 mm appears to be the result of stacks of organic and detritus (clay) rich, sub horizontal, layers forming parallel to growth within the microcrystalline calcite (see below). It is sometimes possible to observe a corroded texture on underlying crystal terminations and occasionally detritus filled pits (Figure 4.7 E). These horizons occur below and above the equant/euhedral calcite grey layer at 163 mm to 164 mm. The layers in the basal section of HY-8 also display these detrital-rich layers but some of the darker (black) colouration is caused by an increase in thorn inclusion density in microcrystalline calcite (Figure 4.7 F). Similar layers have formed at the top of some compact dendritic laminations but are not ubiquitously associated with them. These layers are typically not as distinct, they are thinner (~10 µm) and can be discontinuous. A light brown colour in thin section suggests the presence of detritus (Figure 4.7).

4.2.3 Composition of grey layers in HY-8

The clear colour and fabric distinctions of grey layers in HY-8 were scrutinised for observable geochemical signals. Two filtered residues were created from a chip of the base of HY-8 which was dissolved in 10% hydrochloric acid (HCL) and filtered via an in-line syringe with polycarbonate Millipore filters of 1 µm and 0.4 µm pore sizes. Additionally, sections of both sets of grey layers at 163-164 mm and 260-266 mm were analysed intact.

4.2.3.1   SEM and optical microscopy

EDX spectra from SEM analysis revealed the chemistry of the amorphous matrix (which formed most of the residue) predominantly contained aluminium silicates with varying amounts of K, Mg, Fe and Na (Figure 4.8). Silicon was also identified in some samples. Two grass cuticle epidermal-like (Jensen et al., 2007) structures were observed by SEM of the 1 µm filter but did not give a clear carbon signal in EDX (Figure 4.9). Unstructured, but often rounded brown and black particles were readily observed via optical microscopy in the filtered residue as well as large concentrations of scattered black particles and agglomerations (Figure 4.10)
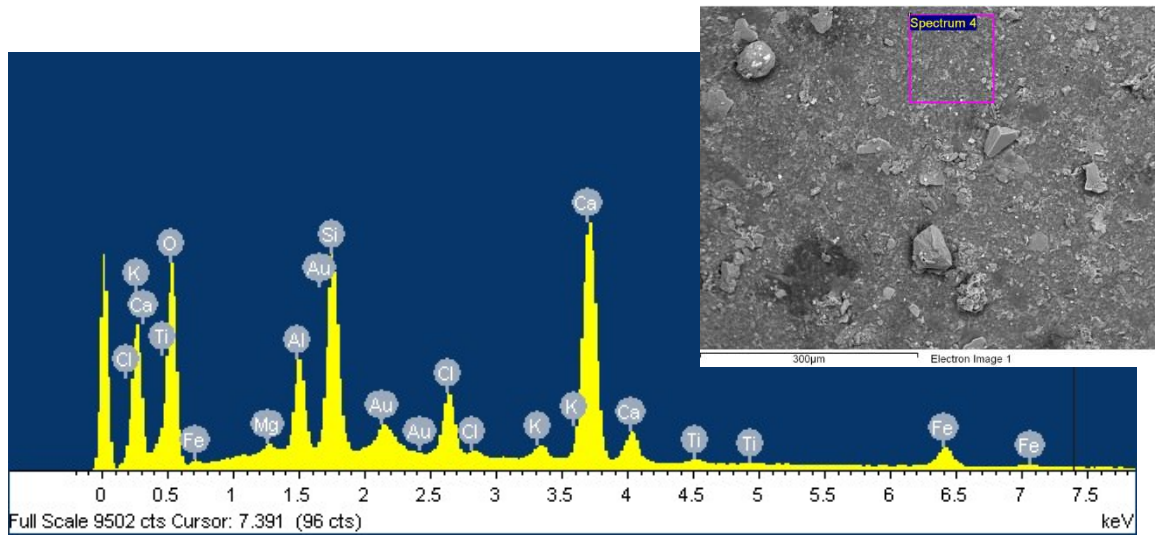
Figure 4.8: EDX spectra representative of the 'matrix' of a filtered residue, using the 0.4 µm millipore filter.

Figure 4.9: Fragment from the 1 µm fraction filtered residue. Fragment appears to have a texture similar to plant cuticle cells (Jensen et al., 2007). It was not possible to obtain a clear chemical signal of its composition.
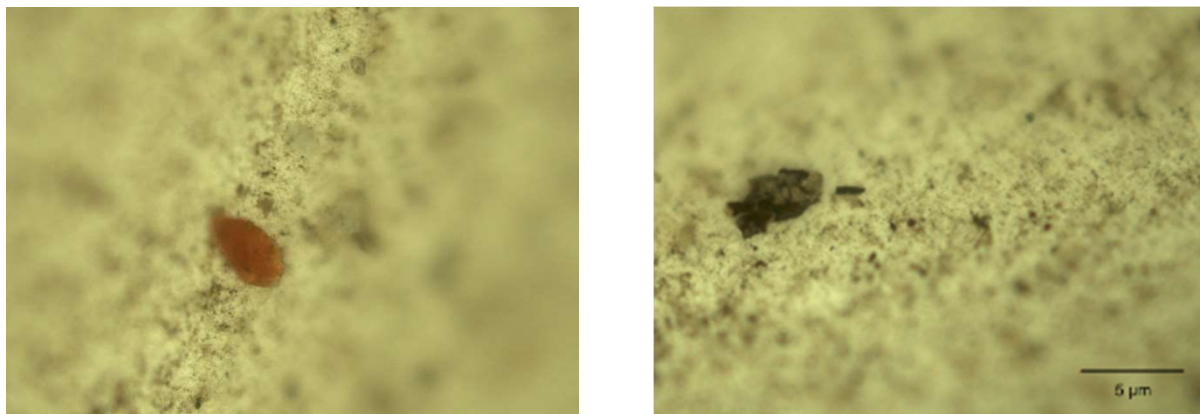
Figure 4.10: Representative particles seen in the 1 μm filter residue, using transmitted light to observe true colour.

4.2.3.2 Raman Spectroscopy

Two sections of HY-8 grey layers (163-164 mm and 275-287 mm) and a filtered residue from basal grey layers were analysed via Raman spectroscopy (John Brindle pers. comm. 2014, 2015, Methods Appendix). Microscopically visible black particles were present in all samples. Their composition consistently contained peaks in the spectra at ~1343 cm^{-1} and ~1589 cm^{-1} with a less intense 'saddle' connecting the two. The spectra in Figure 4.11 contains both a black particle and some calcite matrix as the spot size of the laser slightly exceeded the particle size. It therefore has an extra peak not visible in other spectra at 1085 cm^{-1} as well as a group of peaks at shorter wavelengths. Figure 4.12 shows a curve corrected spectra for a filter residue which suggests while only 3 peaks are clearly visible, a more discrete peak is also observed at 1726 cm^{-1} and at ~1200 cm^{-1} slightly overlapping the ~1343 cm^{-1} peak.
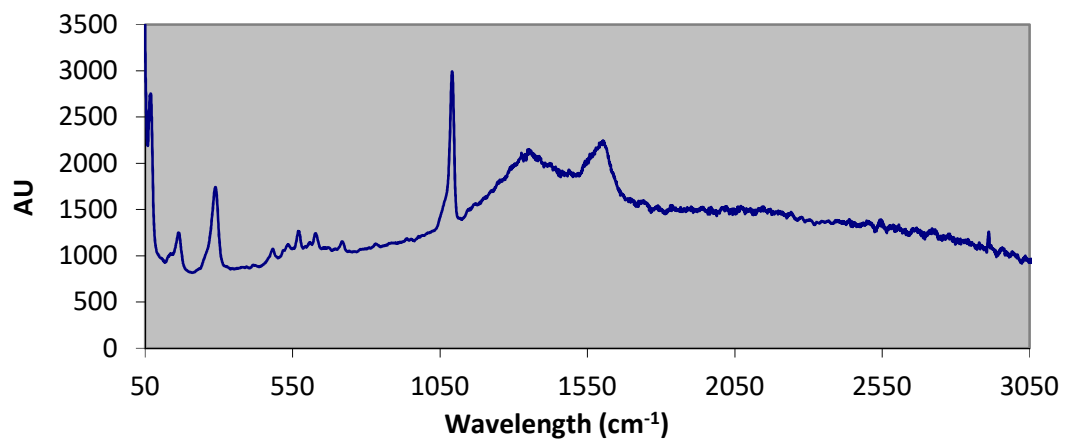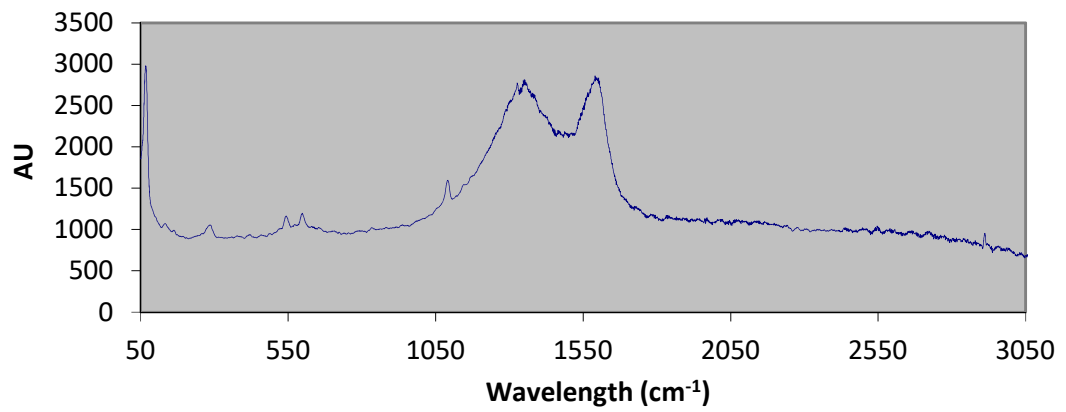
Figure 4.11: Raman spectroscopy spectra for 2 black particles identified within the grey layers of HY-8. Signals clearly match in both spectra although the intensity is higher in spectra 1. This is likely due to the particle being slightly smaller than the spot size of the laser and so some calcite matrix was also analysed.
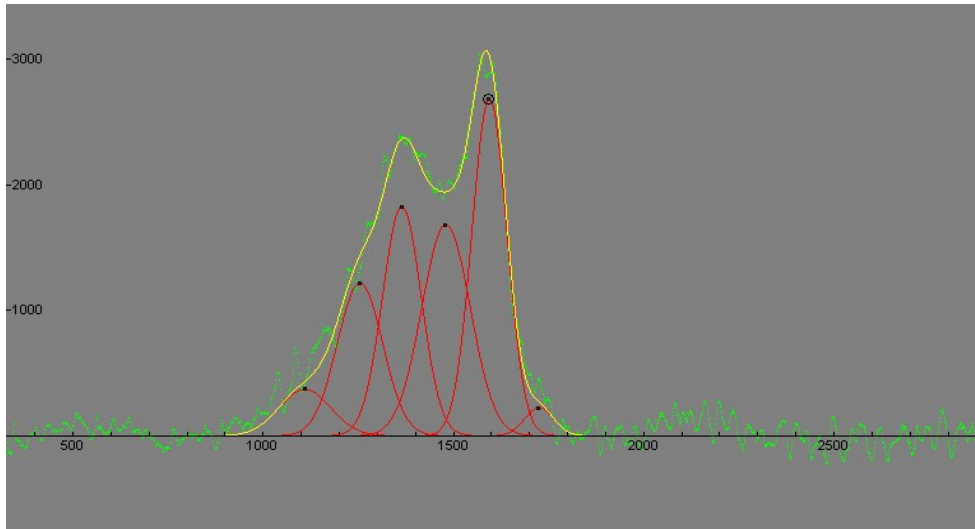
Figure 4.12: The main peaks from spectra 1 with curve correction applied (John Brindle pers. comm. 2014). Without the correction it is only possible to observe 3 peaks but when applied the correction highlights 2 further discrete peaks.

4.2.3.4   Trace Elements

Elements analysed were selected to help identify organic matter and soil components as outlined in Borsato et al. (2007) and Hartland et al. (2012). Measurements via continuous laser ablation traces were used rather than quantitative spot measurements as identifying peaks in concentrations associated with grey layers was sufficient. Transects were run through the width of grey layers between 260 mm and 266 mm. Two continuous transects of 5 mm and 7 mm (to cover calcite not related to grey layer deposition) were analysed, the full method is provided in the Methods Appendix.

The 7 mm track shows peaks in all trace elements analysed in the area of 5200 μm to 5250 μm (Figure 4.13). Peaks are very clear for Al, Fe (both >3000 ppm) and Zn (>800 ppm) compared to background. A small peak was also observed for Mn (>100 ppm). Minor peaks in Al and Fe also occur in the regions around 4300 μm and 5500-5750 μm. All increases in concentration occur within the limits of the darkest and widest grey layer of the analysed section ~4 mm to 5.5 mm.

Of the 5 mm track there is no observable signal in Mn as the record is too noisy. There is also significant noise in the Zn record, but broad peaks in concentration are visible all of which correspond to distinctly elevated concentrations in Al and Fe except for 3027 µm to 3036 µmA broad peak in Zn between 3609 µm and 3926 µm corresponds to large peaks in Al and Fe at 3711 µm (1854 ppm and 1257 ppm respectively). A final broad peak in Zn (4168-4403 µm) corresponds with a major peak in both Al and Fe at 4272 µm.
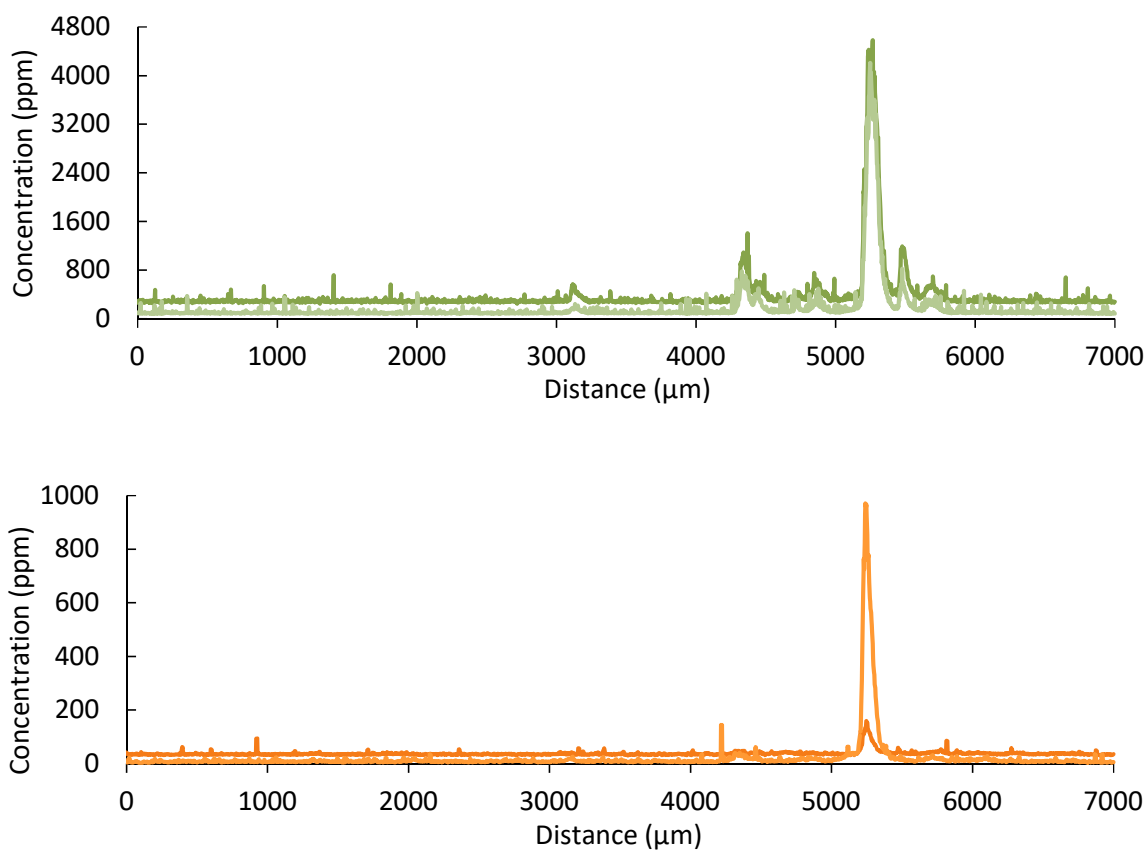
Figure 4.13: Changes in concentration over the 7 mm transect in Fe and Al (top, Al dark green, Fe light green) and Mn and Zn (bottom, Mn light orange, Zn dark). Large peaks are clearly visible at very similar times for all trace elements.
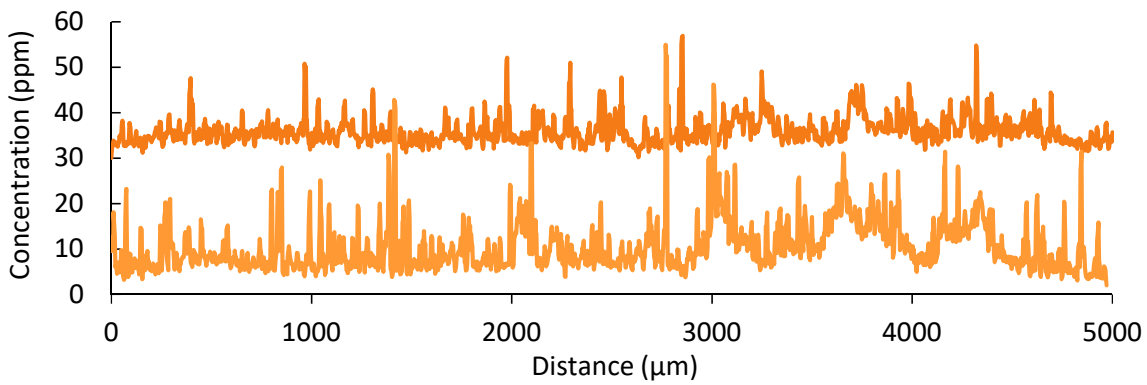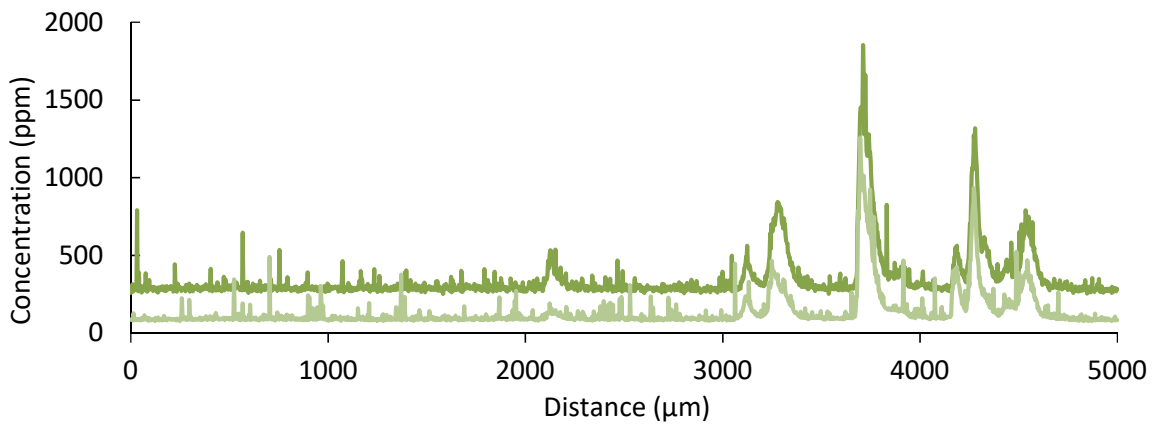
Figure 4.14: Changes in concentration over the 5 mm transect in Fe and Al (top, Al dark green, Fe light green) and Mn and Zn (bottom, Mn dark orange, Zn light orange). Peaks are difficult to decipher in Mn but broad peaks identifiable in Zn concentrations can be correlated to clearer narrow peak in Fe and Al.

4.2.4 Dim-1 Morphology

Dim-1 is a typical candlestick stalagmite with fairly linear growth, although two changes in growth axis are observed at 105 mm and at ca 480 mm. The latter is a clear hiatus with a prominent boundary and thinning in stalagmite diameter immediately above. Dim-1 is primarily composed of grey and cream calcites but the position of these calcites is irregular within the speleothem, with gradational but apparently inter-fingering transitions from grey in the central axis to cream outer portions. In a few areas the cream calcite is present across the whole stalagmite width (notably 362-365 mm and 433-447 mm); a relationship similar to the 'wings' exhibited in the JeG-stm-1 stalagmite from Jeita Cave, Lebanon (Verheyden et al., 2008) (Figure 4.2). Pink aragonite occurs in clear short layers on the flanks of the speleothem (Figure 4.2) at 306 mm, 425 mm, 448 mm, 454 mm, 465 mm, 532 mm and 559 mm as well as encasing the entire stalagmite. The terminal relationship of the encasing aragonite is not observed due to the broken top. A prominent layer ~13 mm thick at ca. 467 mm immediately prior to the hiatus appears to be composed of predominantly aragonite based on colour, fabric appearance and autoradiation (Wickens 2013). Using slabs progressively further from the central axis, it was possible to observe an apparent difference in the location of the aragonite associated with the layer preceding the hiatus. In slabs away from the central axis more aragonite is present and the layer is less clearly defined.

4.2.5 Dim-1 Petrography

Calcite within Dim-1 is formed of 3 types of columnar fabric elongate, short and 'proper' (Frisia and Borsato 2010) with aragonite showing multiple fabrics where present. Transitions between calcite and aragonite are complex and can be sharp or gradual. The whole stalagmite is inclusion-poor aside from periodic linear horizons parallel to growth direction. Porosity tends to be low in aragonite (<2%), high in cream calcites (~65%) and moderate in grey calcites (~30%). Some porosity may be secondary in nature particularly in grey calcites as it is largely restricted to crystal terminations.

Grey columnar crystals are typically >1 mm long elongate columnar calcite (Frisia and Borsato 2010); shorter crystals could be termed 'proper' columnar (Frisia and Borsato 2010) where they are not long enough to be elongate (Figure 4.15 A and B). Cream calcite crystals are much shorter (<700 μm), more typical of short columnar and columnar proper (Frisia and Borsato 2010). The defining difference in colour is due to the higher porosity of the cream calcite. Additional

differences include that pores in cream columnar fabrics are not necessarily restricted to crystal terminations and have more rounded boundaries and terminations (Figure 4.15). Despite the appearance in hand specimen boundaries between the two calcite fabrics are gradual on both sides. However, it is possible to observe potentially truncated inclusion horizons around 373 mm (Figure 4.15 C and D).
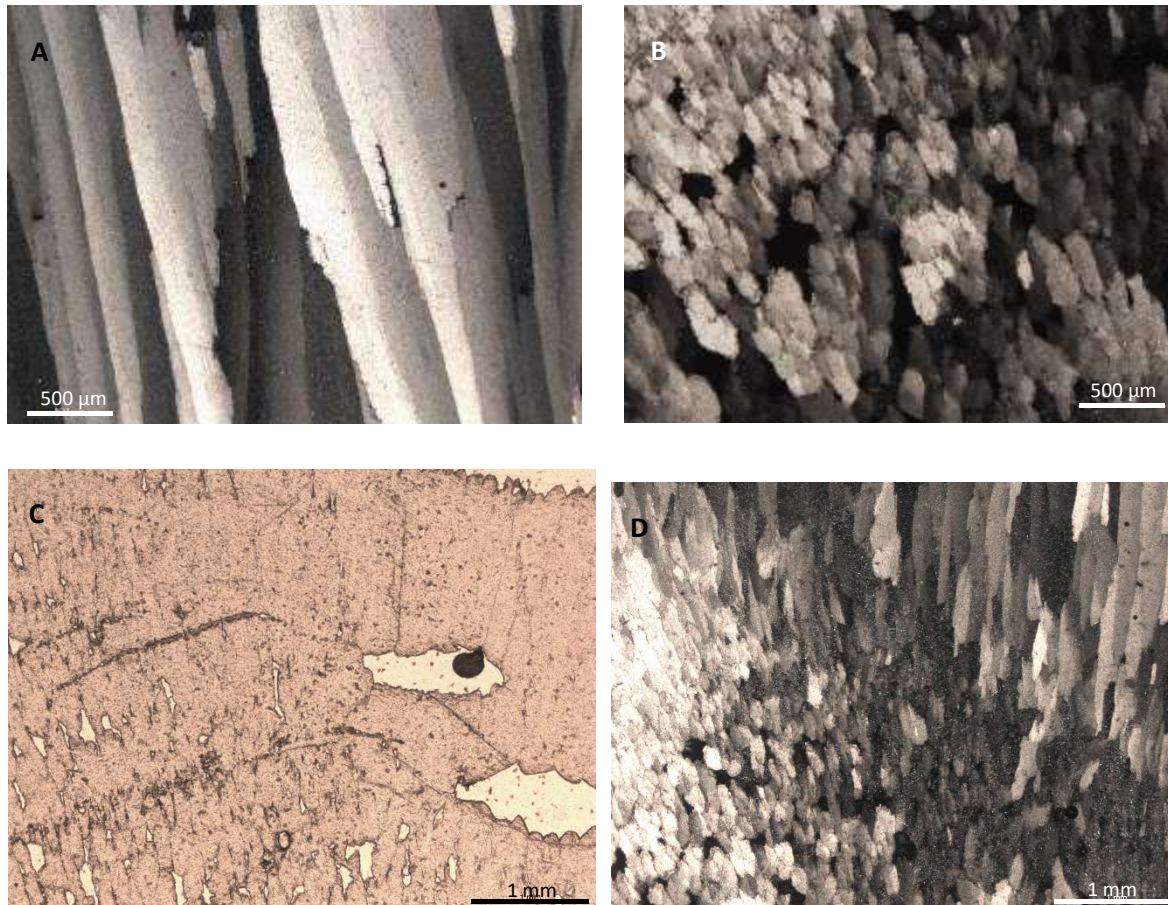
Figure 4.15: Calcite fabrics and boundaries. A. Typical low porosity grey elongated columnar calcite. B. Typical shorter higher porosity cream short columnar calcite. C and D The boundary between light and dark calcites ~373 mm. C shows in ppl truncated inclusion horizons suggestive of a sharp boundary but in xpl individual crystals suggest the boundary is more gradual.

Dim-1 also contains a variety of aragonitic fabrics: ray, disordered needle and spherulitic fabrics (Figure 4.16). Rays can be well developed growing parallel to the direction of growth or may show no preferred growth. The distinct aragonite layers visible in hand specimen are typically only a few mm in length and pass laterally into sub-horizontal (occasionally undulose) inclusion rich linear surfaces parallel to growth in the central axis (Figure 4.17 A and B). Inclusions are typically spherical with sizes ranging from <1 μm to 15 μm. In a few places the inclusion horizons are associated with 400-600 μm wide patches of calcite with anomalous or feathered extinction (Figure 4.17 H). At 304 mm, in an isolated case crystals are visibly offset (Figure 4.17 L). Occasionally these linear inclusion horizons laterally transform into dark, thick linear surfaces (mean 70 μm) defining calcite terminations of underlying crystals (Figure 4.17 C and D). It is not clear if the colouration is caused by detritus or a further increase in concentration of inclusions Inclusion horizons can occur elsewhere in the stalagmite without any associated aragonite but are discrete and at times discontinuous.
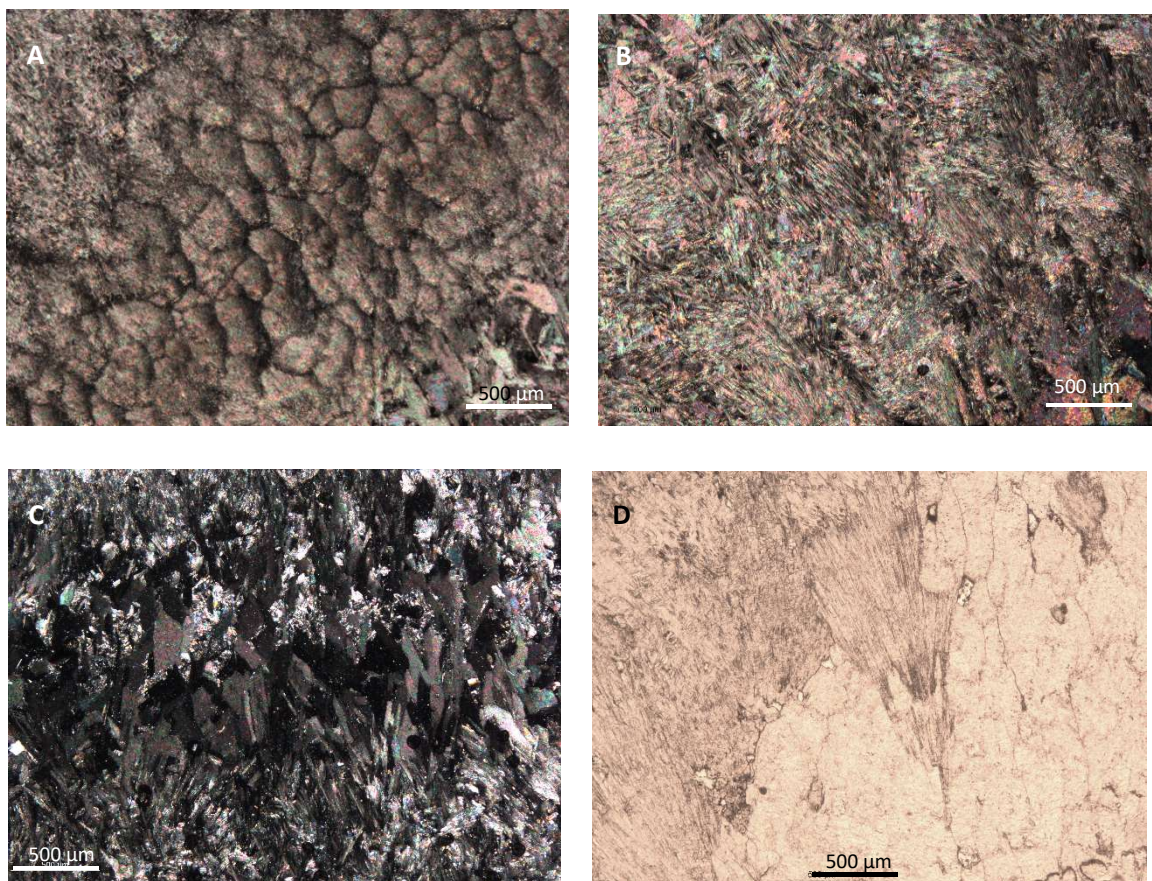
Figure 4.16: Aragonite fabrics in Dim-1. A. Spherulitic aragonite. B. Disordered aragonite needles. C. Coalesced aragonite needles. D. Ray aragonite.
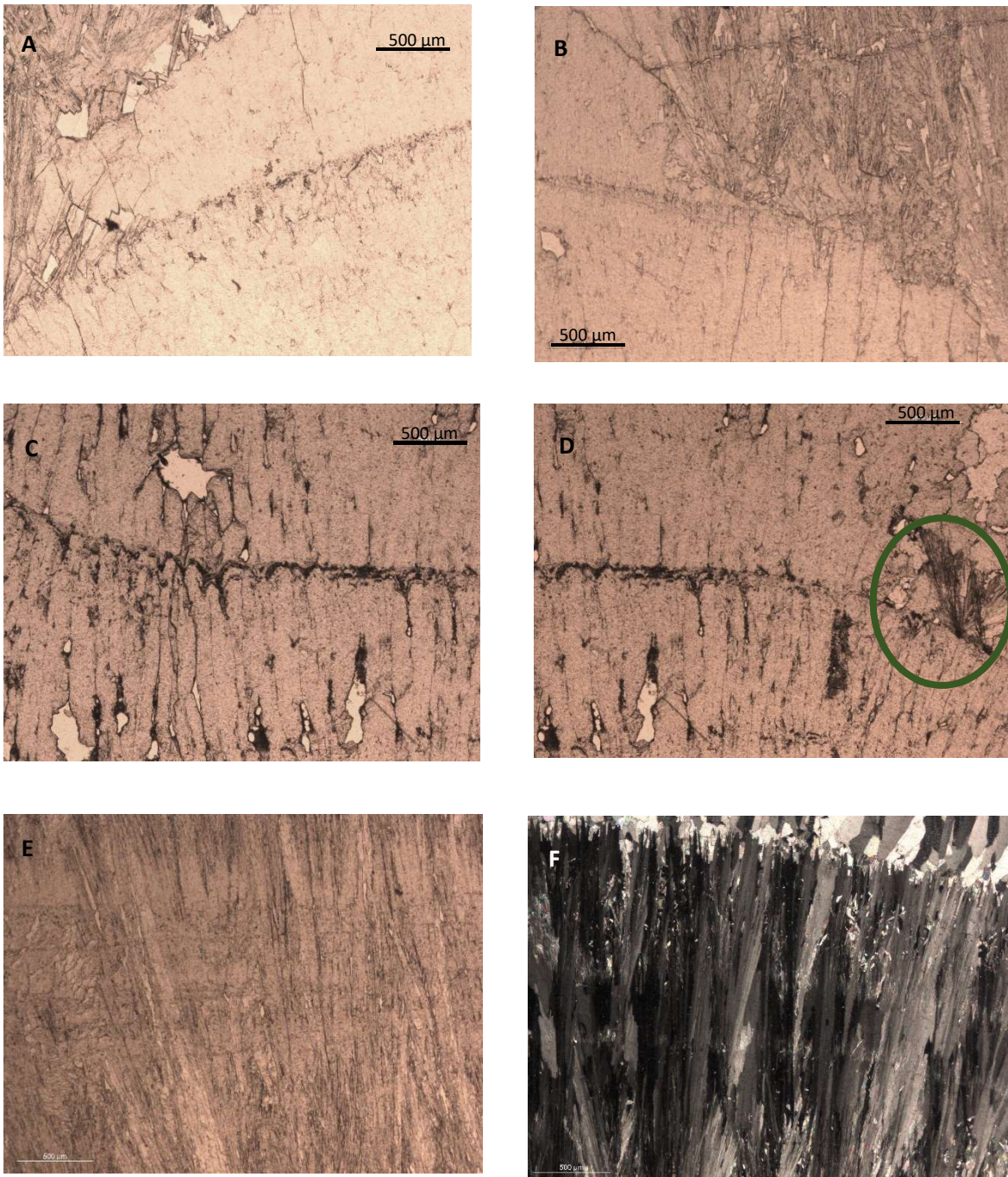
Figure 4.17: Sub horizontal surfaces in Dim-1. A. Sub horizontal inclusion surface projects directly from the edge boundary of aragonite at the lower boundary of the main layer preceding the hiatus. B. The same inclusion surface from the other side of the stalagmite. C. Thick sub horizontal surface (further extension laterally of D) with etching calcite of terminations below. D. A thicker sub horizontal surface extending from preserved aragonite rays (green circle). E-F. Stacked inclusion surfaces (ppl) with isolated aragonite needles associated (xpl).
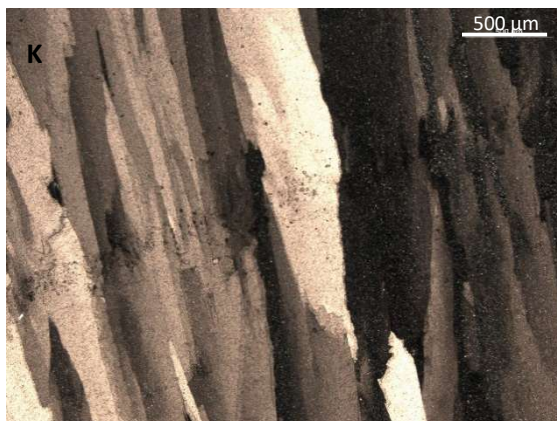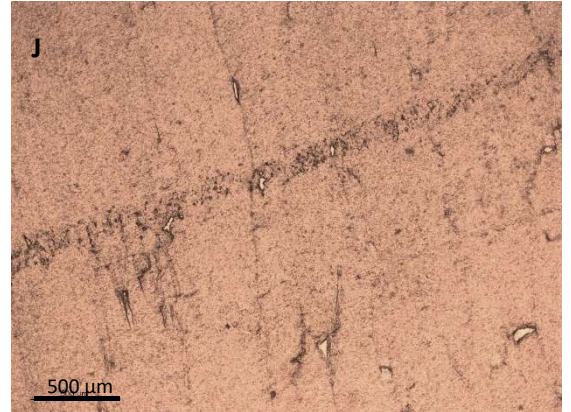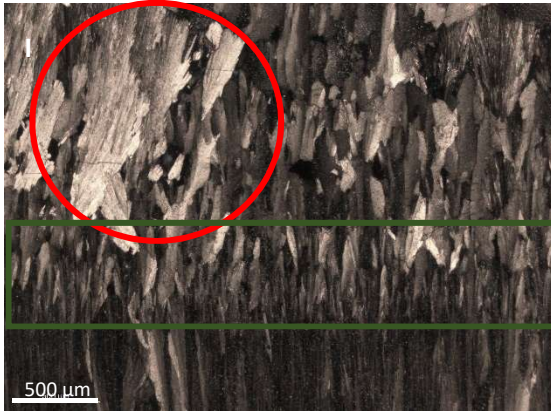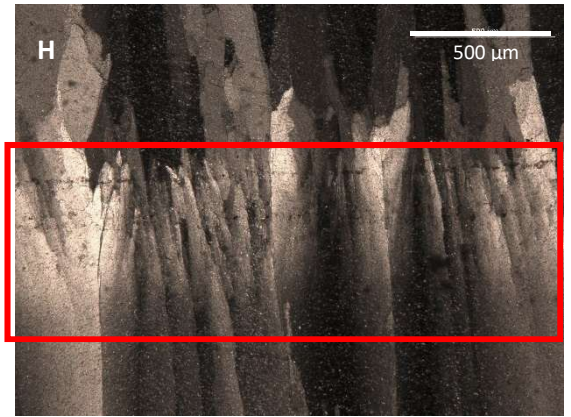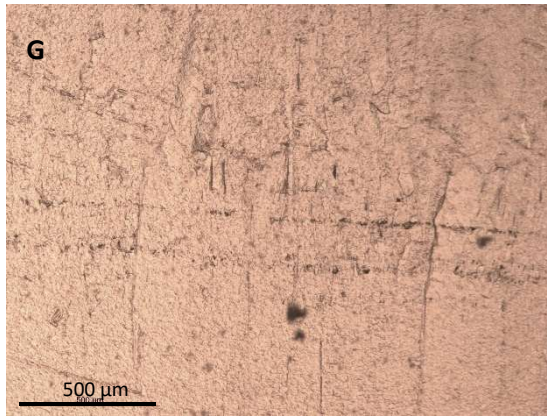
Figure 4.17 continued: G-H. Stacked inclusion surfaces show a zone of alteration in extinction associated with them (highlighted red) (G ppl and H xpl). I. Edge of preserved aragonite rays (red circle) from former aragonite layer associated with a small band of feathered extinction (highlighted green) and a change in calcite form. J-K. Inclusion surface which is visible in the macromorphology but does not show alteration in extinction. L. Inclusion surface showing offset of calcite crystals above in xpl.

At ~300 mm at the lower boundary of the main aragonitic layer below the hiatus, a thick linear surface directly extends from preserved aragonite parallel to growth. The lower boundary of the ~13 mm thick layer is complex (Figure 4.3) showing thinning calcite in the central axis with aragonite encasing the top and flanks. The overlying transition is sharp with aragonite rays growing directly from columnar crystal terminations (Figure 4.18 A). At the flanks the boundary is straight but apparently gradual (Figure 4.18 B-D). Despite the colour the layer below the hiatus is not formed entirely of aragonite but of alternating aragonite and calcite (Figure 4.18 E-F). The relationship between the fabrics is complex as there are no sharp boundaries and the thickness of each layer varies laterally. Calcite, as seen at the lower boundary, is only present in the central axis and grades into aragonite at the flanks (Figure 4.18 G-J). Aragonite shows ray fabrics in one layer but is less structured in others. Multiple linear inclusion horizons, parallel to growth cut both fabrics where calcite is present and are often associated with isolated, single aragonite needles (Figure 4.18 G and H). The upper boundary preceding the abrupt offset in the growth axis and reduction in growth diameter at 480 mm (Figure 4.3) is a sharp but undulose aragonite-calcite transition (Figure 4.18 K).

Petrography confirms the inference from the macromorphology that more aragonite is present closer to the flanks in Dim-1. Aragonite was deposited up to 0.5 mm lower on the flank than the bottom boundary layer in the central axis. Aragonite fabrics are spherulitic and ray bundles (Figure 4.19 A and B). The upper boundary is highly irregular (Figure 4.19 C and D). Isolated calcite crystals can be surrounded by aragonite and isolated aragonite rays can be surrounded by calcite (Figure 4.19 E and F).
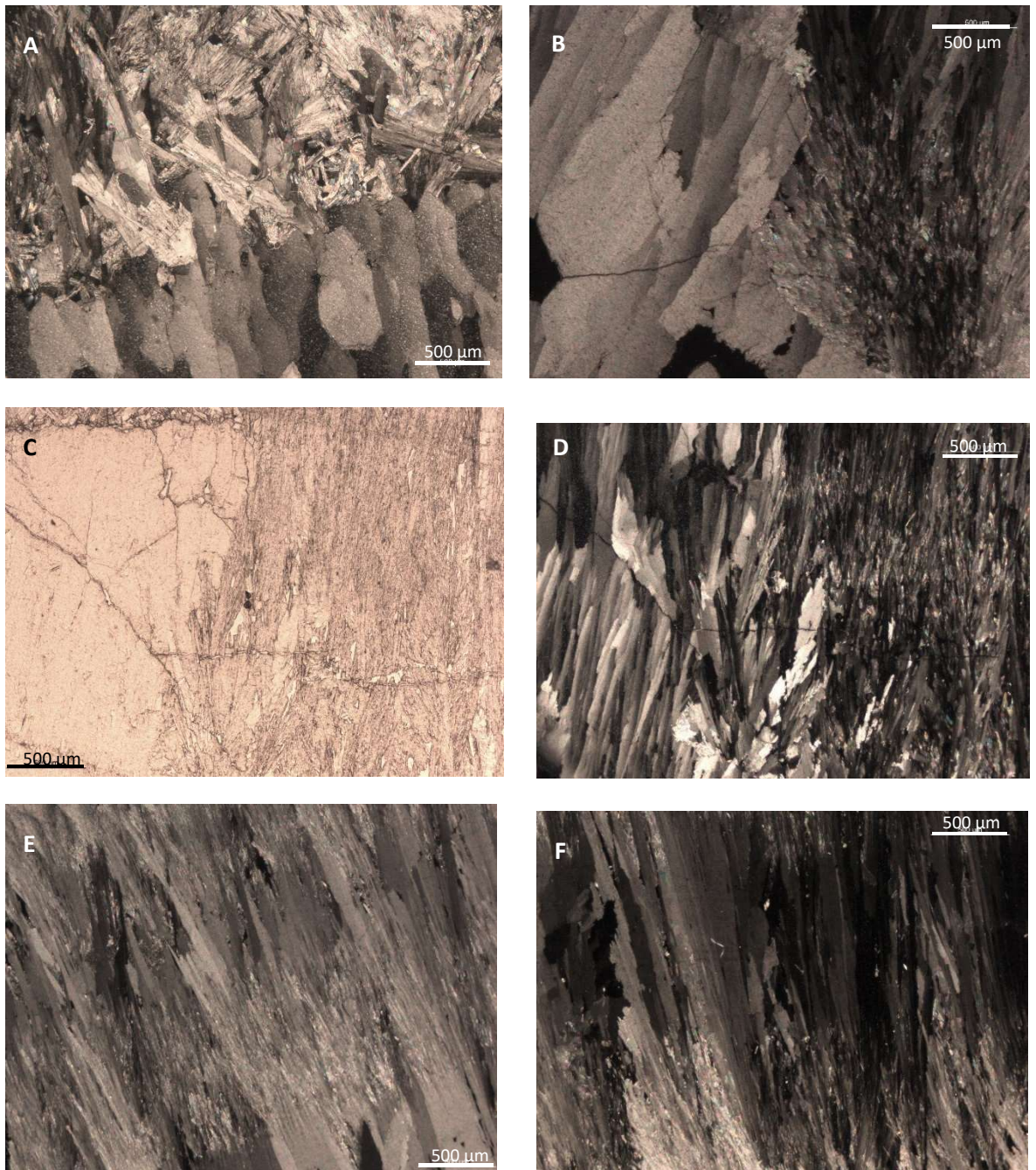
Figure 4.18: Petrography of the main layer before the hiatus ca 300-480 mm. A. Lower boundary shows aragonite rays growing directly off calcite terminations in the central axis. B-D. Lateral relationships of the lower boundary. B. Vertical calcite crystals with sharp but not eroded boundary to laterally growing aragonite needles. C. Apparent sharp lateral boundary between calcite (lighter) and aragonite (darker) in ppl but no dissolution. D. Same boundary as C but in xpl. Shows that boundary is more gradual. E-F. Layers of aragonite needles and columnar calcite in the layer preceding the hiatus.
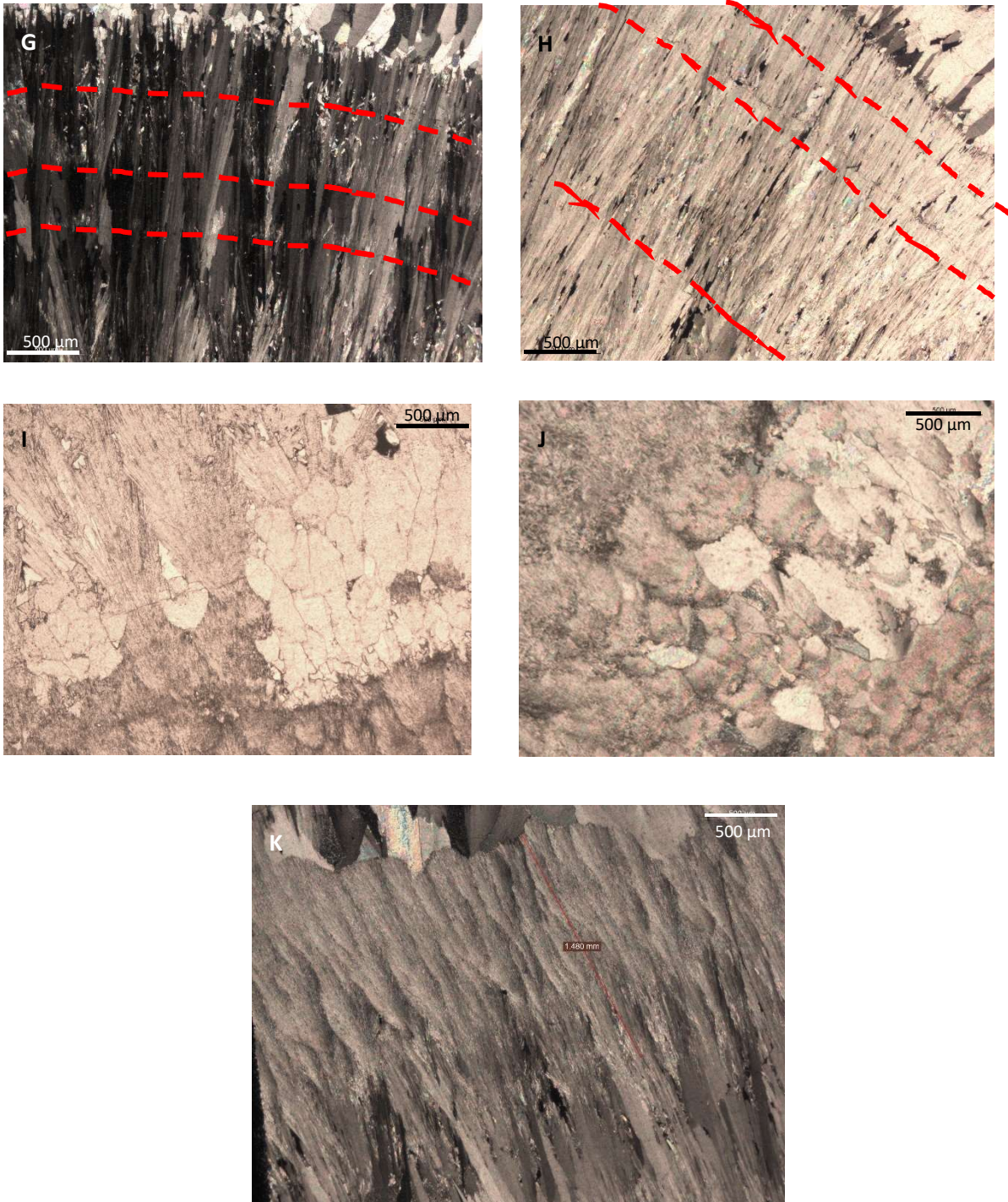
Figure 4.18 continued: G. Calcite and partial aragonite with horizontal surfaces highlighted by aragonite needles in the central axis. H. the same depth but further laterally in the stalagmite, section is now entirely composed of aragonite needles, boundary is gradual. Horizontal surfaces are still present (highlighted on G and H in red). I and J. Other lateral transitions between aragonite and calcite show clearly individual calcite crystals and aragonite spherulites. K. Undulose sharp boundary between aragonite and calcite at the upper boundary and hiatus surface.
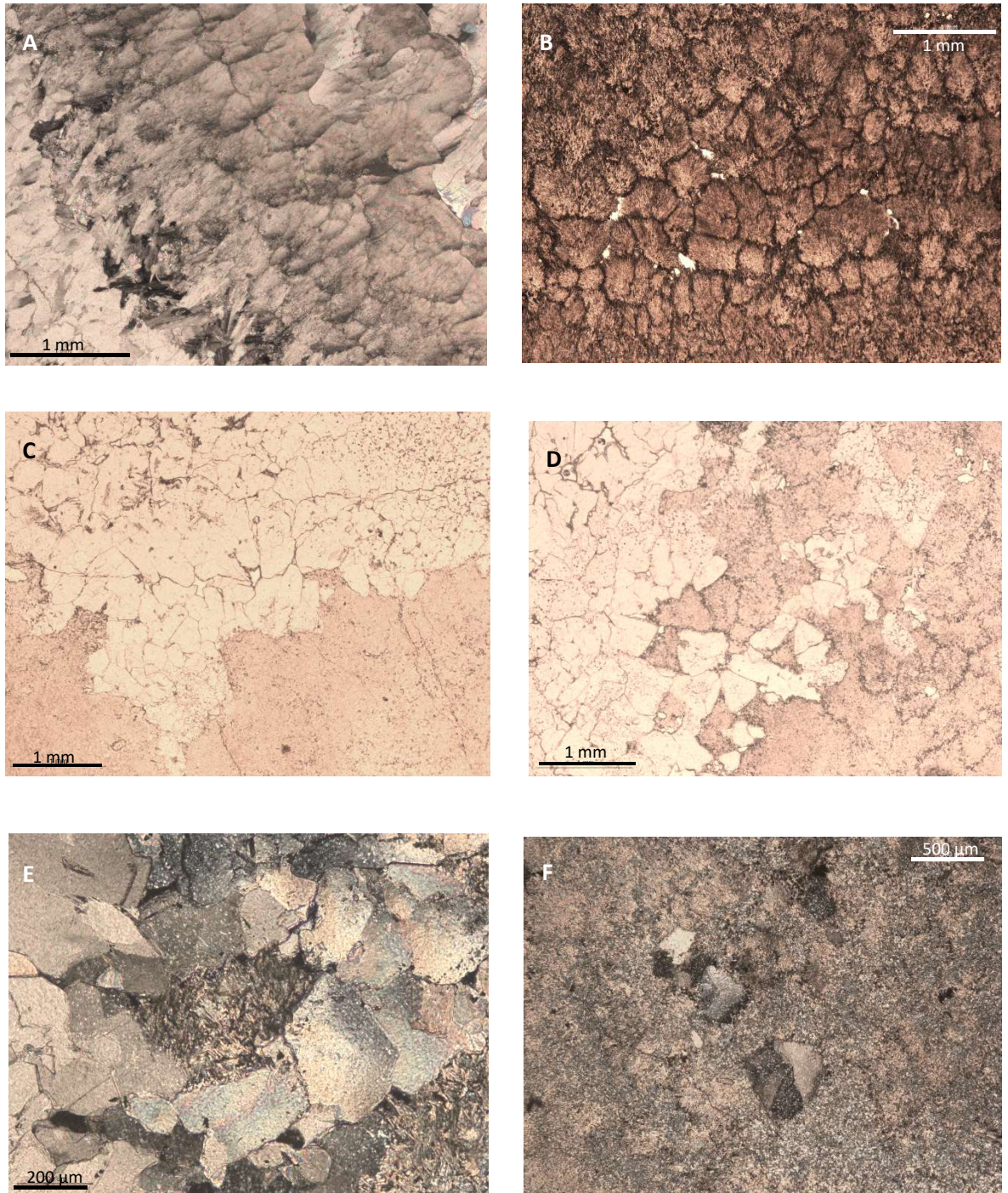
Figure 4.19: Fabrics and relationships within the flank of Dim-1. A ray and spherulitic aragonite. B Aragonite spherulites. C and D. Relationships between aragonite and overlying calcite at the boundary equivalent to the hiatus in the central axis. E. Isolated aragonite ray bundle surrounded by calcite a few mm above the boundary. F. Isolated calcite crystals surrounded by aragonite just below the boundary.

4.2.6 U Series

Twenty-four U-series dates were obtained from HY-8 (Figure 4.20) and 25 from Dim-1 (Figure 4.21). Samples from both stalagmites were run at the NERC Isotope Geosciences Laboratory via the methods listed in the Methods Appendix. Results are displayed in Tables 4.3 and 4.4. Both stalagmites have ages which are stratigraphically discordant, making it difficult to construct robust age models.

In HY-8, a number of samples display ^{230}Th/^{238}U ratios higher than is compatible with their stratigraphic position, including HY8 19, HY8 161, HY8 349 and HY8 389. ^{230}Th concentration within some of these samples display a similar trend to ^{230}Th/^{238}U, showing higher than expected values. ^{238}U depletion is possible in samples HY8 399 and HY8 419. Organic matter and detritus have a strong presence in HY-8 (Section 4.3.2.1), with samples drilled in or near grey layers showing higher ^{232}Th. There is, however, no obvious relationship between abnormal dates and unusual ^{232}Th concentrations. ^{238}U is considerably lower in samples below 264 mm (increase is >0.12 ppm). Given the range in dates, growth of HY-8 could have been initiated in the Late Pleistocene, but the majority of growth took place in the mid to late Holocene. The dating discrepancies for HY-8 are discussed in Section 4.3.3.

HY8 484 **627 ± 12**

Top

HY8 419 **969 ± 19**

HY8 399 **904 ± 12**

HY8 389 **2307 ± 21**

HY8 364 **1124 ± 23**

HY8 349 **3563 ± 83**

Upper

HY8 293 **1296 ± 37**

HY8 264 **2964 ± 39**

HY8 250 **3810 ± 46**

HY8 213 **3937 ± 55**

HY8 174 **4665 ± 60**
HY8 161 **6383 ± 75**

HY8 147 **4328 ± 85**

Lower

HY8 120 **4958 ± 57**

HY8 110 **4765 ± 51**
HY8 105 **4352 ± 64**

HY8 52 **6398 ± 602**

HY8 40 **8188 ± 385**

Base

HY8 27 **5820 ± 139**
HY8 19 **23,821 ± 2724**
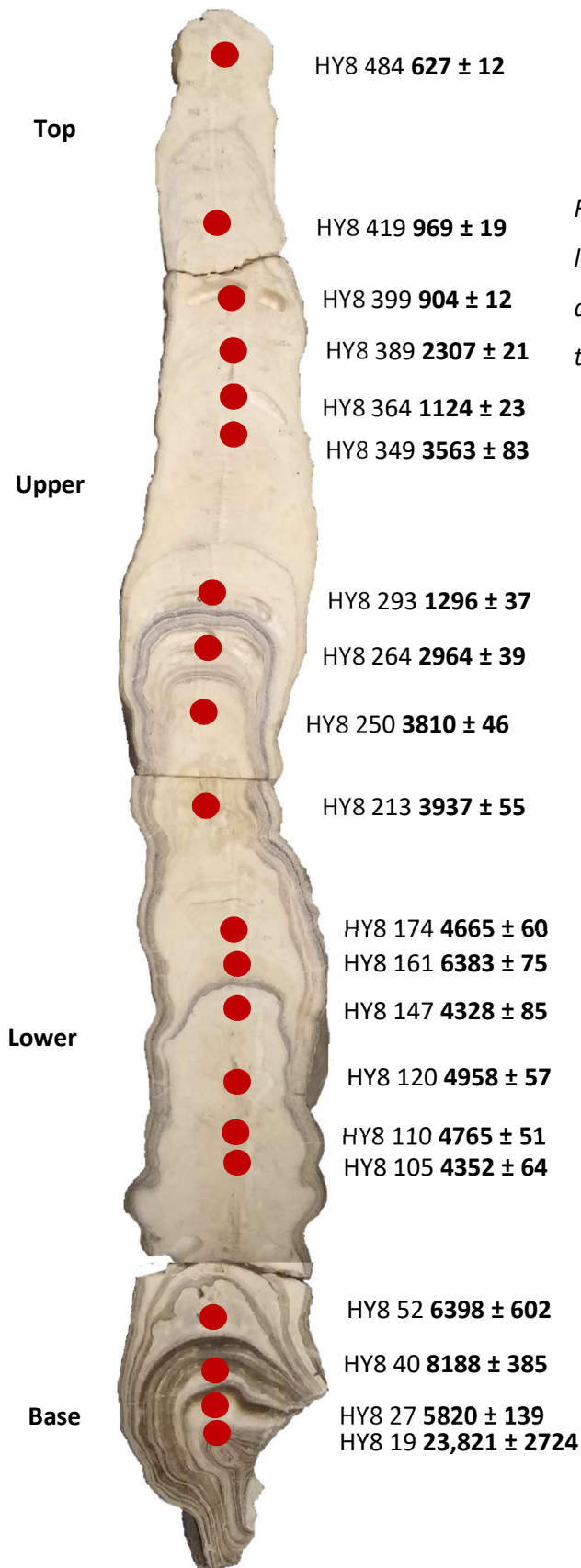
Figure 4.20: HY-8 full age profile. Sample locations are highlighted by red circles and reveal stratigraphic incoherency in the ages obtained.

20 mm

93

Sample Name	Height above base (mm)	^{238}U (ppm)	^{230}Th (ppb x10^6)	^{232}Th (ppb)	$^{234}U/^{238}U$	$^{230}Th/^{238}U$	$^{230}Th/^{232}Th$	Initial $^{234}U/^{238}U$	Date uncorr (yr BP)	Date corr (yr BP)
HY8 484	484	0.21124	27.5	0.08567	1.017 ± 0.002	0.0064 ± 0.0001	48.9	1.017 ± 0.002	706 ± 9	627 ± 12
HY8 419	419	0.1758	31.9	0.107624	1.020 ± 0.002	0.0096 ± 0.0002	48.48	1.020 ± 0.002	1055 ± 13	969 ± 19
HY8 399	399	0.2606	47.4	0.112398	1.017 ± 0.002	0.0090 ± 0.0001	64.2	1.017 ± 0.002	980 ± 8	904 ± 12
HY8 389	389	0.2459	71.5	0.183713	1.017 ± 0.002	0.0219 ± 0.0002	89.98	1.017 ± 0.002	2395 ± 14	2307 ± 21
HY8 364	364	0.26023	47.8	0.25446	1.018 ± 0.001	0.0110 ± 0.0002	35.19	1.018 ± 0.001	1219 ± 10	1124 ± 23
HY8 349	349	0.18659	107.9	0.13078	1.020 ± 0.002	0.0334 ± 0.0008	145.24	1.020 ± 0.002	3662 ± 82	3563 ± 83
HY8 293	293	0.40554	86.1	0.685933	1.020 ± 0.001	0.0126 ± 0.0004	23.55	1.020 ± 0.001	1409 ± 11	1296 ± 37
HY8 264	264	0.20908	97.6	0.3567	1.034 ± 0.001	0.0283 ± 0.0004	51.32	1.034 ± 0.001	3077 ± 18	2964 ± 39
HY8 250	250	0.08103	47.9	0.130506	1.031 ± 0.002	0.0360 ± 0.0004	68.77	1.031 ± 0.002	3921 ± 32	3810 ± 46
HY8 213	213	0.07593	49.4	0.146663	1.024 ± 0.002	0.0369 ± 0.0005	58.75	1.024 ± 0.002	4075 ± 38	3937 ± 55
HY8 174	174	0.06525	46.7	0.143617	1.026 ± 0.002	0.0436 ± 0.0005	61.04	1.027 ± 0.002	4795 ± 39	4665 ± 60
HY8 161	161	0.05612	54.1	0.129179	1.023 ± 0.003	0.0588 ± 0.0007	78.47	1.024 ± 0.003	6515 ± 59	6383 ± 75
HY8 147	147	0.06164	45.1	0.210231	1.027 ± 0.003	0.0405 ± 0.0008	36.86	1.027 ± 0.002	4510 ± 46	4328 ± 85
HY8 120	120	0.08837	67.1	0.172652	1.028 ± 0.003	0.0463 ± 0.0005	72.84	1.028 ± 0.003	5078 ± 40	4958 ± 57
HY8 110	110	0.07795	57.1	0.154776	1.029 ± 0.002	0.0446 ± 0.0005	69.14	1.029 ± 0.002	4889 ± 30	4765 ± 51
HY8 105	105	0.07422	55.3	0.134098	1.029 ± 0.003	0.0409 ± 0.0006	69.42	1.030 ± 0.002	4487 ± 51	4352 ± 64
HY8 52	52	0.08006	86.7	2.322513	1.029 ± 0.005	0.0593 ± 0.0060	7.00	1.030 ± 0.005	7307 ± 56	6398 ± 602
HY8 40	40	0.08191	149.9	0.658053	1.027 ± 0.003	0.0748 ± 0.0030	29.04	1.027 ± 0.003	8522 ± 348	8188 ± 385
HY8 27	27	0.07264	65.7	0.463435	1.029 ± 0.002	0.0540 ± 0.0010	26.57	1.029 ± 0.002	6070 ± 45	5820 ± 139
HY8 19	19	0.06153	330.7	6.595001	1.029 ± 0.015	0.2027 ± 0.0220	6.4	1.032 ± 0.017	27172 ± 1273	23821 ± 2724

Table 4.3: U-series results for HY-8. All errors are 2 s.d. and age corrections assume detrital component has bulk earth composition (see Methods Appendix). Samples drilled in or near grey layers are highlighted in blue.

94

In Dim-1, $^{234}U/^{238}U$ ratios generally reduce upward through stalagmite but not linearly; the changes may be influenced by rainfall amount (Rowe et al., in prep). $^{230}Th/^{238}U$ also shows an overall decline upward, but a number of samples (e.g. Dim 29-10, Dim 41-8, Dim 29-9 and Dim 41-6) may have been be subject to isotopic disturbance. Calcite samples show an upward increasing trend in ^{238}U concentration after 460 mm, but no trend is observed in aragonite samples. Obvious concentration anomalies occur in Dim 29-9, which is highly enriched relative to the rest of the samples, and Dim 37-5 with a ^{230}Th concentration much larger than expected for the accompanying ^{238}U concentration (despite $^{230}Th/^{238}U$ not appearing to be anomalous). Aragonite ^{238}U and ^{230}Th concentrations are highly variable but show no trend. . The Dim-1 samples typically have high $^{230}Th/^{232}Th$ values, particularly in aragonitic samples, suggesting low detrital content. The dating discrepancies for Dim-1 are discussed in Section 4.3.4.

Dim 52-4 **128,477 ± 689** located on flank within flank slab traced to aragonitic layer starred (*)

Dim 29-10 **117,454 ± 588**

Dim 52-3 **127,816 ± 688**

Dim 41-8 **117,201 ± 597**

Dim 52-2 **128.759 ± 687**

*

Dim 37-5 **129,199 ± 682**

Dim 29-9 **136,092 ± 809**

Dim 52-1

Dim 41-6 **119,698 ± 610**

127,825 ± 741

Dim 29-7 **120,695 ± 1,025**

Dim 41-5 **122,704 ± 659**

Dim 52-5 **128,198 ± 688** located in flank slab within the layer preceding the hiatus

Dim 41-4 **126,377 ± 729**

Dim 37-3 **130,422 ± 831**

Dim 33-6 **125,439 ± 729**

Dim 41-2 **120,606 ± 642**

Dim 102-2 **128,986 ± 663**

Dim 102-1 **128,072 ± 670**

Figure 4.21: Dim-1 full age profile. Sample locations are highlighted by red circles and reveal stratigraphic incoherency in the ages obtained.

Dim 41-1 **126,234 ± 672**

Dim 33-4 **128,590 ± 696**

Dim 37-1 **129,439 ± 791**

Dim 37-4 **130,650 ± 682**

Dim 33-5 **119,973 ± 681**

Dim 29-6 **132,642 ± 1,363**

Dim 37-2 **131,412 ± 829**

20 mm

96

Sample Name	Calcite/aragonite	Height above base (mm)	U (ppm)	^{230}Th (ppb)	^{232}Th (ppb)	^{234}U/^{238}U	^{230}Th/^{238}U	^{230}Th/^{232}Th	Initial ^{234}U/^{238}U	Date uncorr (yr BP)	Date corr (yr BP)
Dim 52-3	aragonite	above top	1.06214	0.016113	0.925185	1.304 ± 0.001	0.9348 ± 0.003	3266.01	1.437 ± 0.002	127,896 ± 688	127,816 ± 688
Dim 29-10	calcite	568	0.42987	0.006244	0.307244	1.310 ± 0.002	0.8951 ± 0.002	3811.04	1.432 ± 0.002	117,531 ± 588	117,454 ± 588
Dim 52-2	aragonite	566	3.28267	0.050254	0.681092	1.310 ± 0.001	0.9434 ± 0.003	13836.81	1.446 ± 0.002	128,825 ± 687	128,759 ± 687
Dim 41-8	calcite	564	0.42148	0.006146	0.419371	1.316 ± 0.001	0.8985 ± 0.002	2748.2	1.440 ± 0.002	117,284 ± 597	117,201 ± 597
Dim 52-4	aragonite	558	4.66183	0.071474	0.27876	1.313 ± 0.001	0.9448 ± 0.003	48083.07	1.450 ± 0.002	128,540 ± 689	128,477 ± 689
Dim 52-1	aragonite and calcite	502	6.35514	0.036466	3.963273	1.311 ± 0.001	0.9400 ± 0.003	4586.83	1.446 ± 0.002	127,899 ± 741	127,825 ± 741
Dim 37-5	calcite	493	0.38356	0.015527	0.748919	1.302 ± 0.001	0.9384 ± 0.002	1462.55	1.435 ± 0.002	129,302 ± 682	129,199 ± 682
Dim 29-9	calcite	485	0.77148	0.011598	0.344729	1.255 ± 0.001	0.9264 ± 0.003	6309.09	1.375 ± 0.002	136,164 ± 809	136,092 ± 809
Dim 41-6	aragonite and calcite	478	2.49831	0.037400	0.179411	1.333 ± 0.002	0.9225 ± 0.002	39093.34	1.467 ± 0.002	119,761 ± 610	119,698 ± 610
Dim 52-5	calcite	478	4.13826	0.063494	0.988054	1.316 ± 0.002	0.9455 ± 0.003	12051.13	1.453 ± 0.002	128,265 ± 688	128,198 ± 688
Dim 29-7	Aragonite possible calcite	472	1.86208	0.027913	0.373691	1.329 ± 0.002	0.9238 ± 0.004	14007.72	1.462 ± 0.002	127,61 ± 1,025	126,95 ± 1,025
Dim 41-5	calcite	463	0.24933	0.003733	0.116442	1.316 ± 0.002	0.9227 ± 0.002	6012.2	1.447 ± 0.002	122,776 ± 659	122,704 ± 659
Dim 41-4	calcite	425	0.17145	0.002630	0.190489	1.325 ± 0.002	0.9453 ± 0.003	2589.26	1.464 ± 0.003	126,462 ± 729	126,377 ± 729
Dim 37-3	calcite	357	0.16546	0.002743	0.988579	1.400 ± 0.002	1.0216 ± 0.003	520.3	1.575 ± 0.002	130,597 ± 831	130,422 ± 831
Dim 33-6	calcite	354	0.16965	0.002761	0.264717	1.402 ± 0.002	1.0029 ± 0.003	1955.92	1.573 ± 0.002	125,531 ± 729	125,439 ± 729
Dim 41-2	calcite	304	0.14732	0.002437	0.136232	1.453 ± 0.002	1.0193 ± 0.003	3354.34	1.636 ± 0.002	120,685 ± 642	120,606 ± 642
Dim 102-2	calcite	257	0.15059	0.002783	0.565238	1.551 ± 0.002	1.1388 ± 0.003	923.19	1.793 ± 0.002	129,114 ± 663	128,986 ± 663
Dim 102-1	calcite	215	0.15168	0.002659	0.63902	1.484 ± 0.002	1.0805 ± 0.003	780.43	1.695 ± 0.002	128,212 ± 670	128,072 ± 670
Dim 41-1	calcite	166	0.16619	0.003236	0.170181	1.645 ± 0.002	1.1998 ± 0.003	3565.56	1.921 ± 0.003	126,312 ± 672	126,234 ± 672
Dim 33-4	calcite	132	0.15807	0.003214	0.449677	1.695 ± 0.002	1.2531 ± 0.004	1340.24	1.999 ± 0.003	128,695 ± 696	128,590 ± 696
Dim 37-1	calcite	120	0.18522	0.003769	0.204169	1.690 ± 0.002	1.2540 ± 0.004	3461.77	1.995 ± 0.003	129,518 ± 791	129,439 ± 791
Dim 37-4	calcite	92	0.12588	0.002678	0.176088	1.752 ± 0.002	1.3112 ± 0.004	2852.26	2.088 ± 0.003	130,732 ± 682	130,650 ± 682
Dim 33-5	calcite	85	0.14412	0.002851	0.439439	1.716 ± 0.002	1.2191 ± 0.004	1216.55	2.005 ± 0.003	120,081 ± 681	119,973 ± 681
Dim 29-6	calcite	17	0.10387	0.002071	0.379638	1.638 ± 0.002	1.2289 ± 0.007	1023.01	1.928 ± 0.004	132,761 ± 1,363	132,642 ± 1,363
Dim 37-2	calcite	5	0.100832	0.002031	0.266214	1.662 ± 0.002	1.2413 ± 0.004	1430.59	1.959 ± 0.003	131,515 ± 829	131,412 ± 829

Table 4.4: Overleaf. U-series results for Dim-1. All errors are 2 s.d. and age corrections assume detrital component has bulk earth composition (see Methods Appendix).

4.3   Discussion

4.3.1   Linear detritus rich layers and inclusion horizons: Expressions of micro-dissolution

Petrography revealed the occurrence of regular linear layers or surfaces in both stalagmites which represent unusual events during the course of growth. This section discusses the evidence and reasoning behind the interpretation that these surfaces are formed by periods of micro-scale dissolution. Similar layers/surfaces have been described in the literature by Railsback et al. (2011, 2013) as erosion surfaces and also by Martín-García et al. (2011) as corrosion lines. The term dissolution is preferred here, mainly because of its more common usage in speleothem studies and because 'erosion' is a generic term. The prefix micro is adopted because even when a thin line is observed in hand specimen, the detail of the surface can only be observed in thin section.

4.3.1.1   HY-8

Linear growth interruption surfaces in HY-8 have two distinct but related forms. Type 1 surfaces are up to 50 µm thick, with black or dark brown colour, associated with grey layer fabrics. They are often positioned above etched underlying calcite crystals, or detritus-filled pits. These surfaces are morphologically similar to the Type E (erosion) surfaces of Railsback et al. (2011, 2013) and corrosion lines of Martín-García et al. (2011). Type 2 linear surfaces are seen in compact dendritic calcite and are lighter brown in colour. Type 2 surfaces do not show obvious etching of underlying calcite crystal terminations.

Corroded terminations of calcite crystals underlying both Type 1 surfaces is a clear indicator of dissolution. Pits are likely to have resulted from enlargement of pores by localised dissolution exploiting crystallographic weaknesses in the underlying calcite. Linear surfaces occurring above compact dendritic calcite, in direct association with vuggy porosity in the central axis, almost certainly represent drip pits which are firm evidence of dissolution. The association between some growth interruption surfaces and drip pits suggests that surfaces not directly associated

with drip pits can also be interpreted as dissolution surfaces, albeit with a little less confidence. Formation of Type 2 surfaces in compact dendritic fabrics probably occurred when drip waters were less aggressive, promoting dissolution/reprecipitation reactions, rather than wholesale corrosion; the result was a more compact reprecipitation fabric.

4.3.1.2 Dim-1

In Dim-1, multiple linear surfaces are typically dark in colour and as in HY-8, show evidence of etching and corrosion of underlying calcite crystal terminations, interpreted to be directly linked to dissolution. There is, however, a less clear resemblance to the Type E surfaces (Railsback et al., 2011, 2013) and corrosion lines (Martín-García et al., 2011) mentioned previously.

In Dim-1 most linear surface features are defined by inclusion horizons. Importantly Dim-1 is, aside from these sub-horizontal inclusion horizons, an inclusion poor stalagmite. Thus these surfaces are likely to be an expression of growth disturbance, because under normal growth conditions crystallite coalescence was near perfect (Kendall and Broughton, 1978; Bodnar, 2003). Growth disturbance with linear inclusion horizons associated with aragonite needles is clear evidence of dissolution of earlier-formed aragonite. It is likely that inclusion horizons that display altered extinction patterns can also be attributed to dissolution; fragmentation of otherwise large extinction zones, and in some cases feathered extinction, indicates crystal splitting by increased drip water which promotes partial dissolution along existing lines of crystallographic weakness (Alan C Kendall pers. comm. 2015). These types of inclusion horizons are always contained within calcite crystals adjacent to preserved aragonite layers on the flanks. While some inclusion horizons show no associated aragonite needles or altered extinction, the association of inclusion horizons and dissolution elsewhere makes it possible to invoke the same interpretation for these surfaces. Furthermore at 304 mm a surface showing underlying calcite corrosion and extending directly from preserved aragonite at the flank, grades into an inclusion horizon without calcite extinction. Occasional undulose inclusion-rich surfaces may be caused by inclusions defining crystallite edges.

4.3.2 Petrographic (and geochemical) interpretations of environments of formation

4.3.2.1 HY-8

Specific changes in growth parameters are defined by changes in, and the relationships between, fabrics in HY-8. The majority of HY-8 has dendritic fabric which forms under conditions of high supersaturation (Frisia et al., 2000). As discussed in Chapter 3 (Section 3.2.1), supersaturation of $CaCO_3$ in cave water may be related to drip rates, or kinetic effects such as prolonged degassing or evaporation. Kinetic effects can also be related to drip rate (particularly during long drip intervals), but dendritic calcite can also be a feature of predominantly dry conditions (McDermott et al., 1999). In these situations dendritic calcite forms from fluctuating discharges, which under extreme conditions, may alternate between rapid discharge and no drip (Frisia et al., 2000). As HY-8 was collected from a chamber which displays high humidity, and is situated below the entrance chamber, it is probable that the formation of the dendritic fabric is directly related to drip rate rather than changing air flows which can create rapid degassing conditions required to precipitate dendritic fabric (Frisia et al., 2000). In HY-8, it is most likely that dendritic fabrics formed from predominantly low discharges causing outgassing to occur over long periods. Some variation in drip discharge may be recorded by alternating compact and open dendritic lamination, the compact lamination defining slightly increased drip water supply.

The predominance of drip water controlling dendritic formation in HY-8 is best evidenced by the relationship between dendritic calcite and other fabric types, which occur during deposition of grey layers. The formation of both microcrystalline and equant/euhedral fabrics require higher drip rates than dendritic calcite. Equant fabrics in particular are usually found where pooling or a constant, comparatively thick water film is present, providing less restriction on growth (Alan C Kendall 2015 pers. comm.). Euhedral calcite precipitated in a speleothem from Botswana is interpreted to have formed under a thick water layer (Railsback et al., 1994). Drip rates which form microcrystalline calcite are typically variable but constant (Frisia and Borsato 2010). In particular, the formation of microcrystalline calcite is readily attributed to the presence of soil detritus and colloidal particles, which actively inhibit growth; characterised by the patchy appearance of extinction zones in crystals (Frisia et al., 2000). Increased soil material within stalagmites implies higher infiltration events (Borsato et al., 2007; Hartland et al., 2012). Furthermore both equant/euhedral and microcrystalline calcites are associated with micro-dissolution surfaces showing frequent increases in drip water, particularly those causing obvious corrosion.

Strongly coloured brown or black layering is infrequently noted in stalagmites but has a number of potential causes. These include the presence of clay (Railsback et al., 2011), Mn-Fe rich outer crusts (Gázquez et al., 2011), higher levels of organic material (e.g. van Beynen et al., 2001; Gázquez et al., 2012) and charcoal and other combustion products from fires within the cave (markers of early human activity) (Gradziński et al., 2003, 2007). In HY-8 the presence of soil-derived inorganic and organic detritus in the grey layers is shown by combined trace elements, Raman spectroscopy and SEM analysis, in both equant/euhedral and microcrystalline fabrics. EDX data confirmed grey layers contained clays (aluminium silicates) of various compositions.

While SEM and optical microscopy suggested the likely presence of organic materials, including possible grass cuticle cells, the presence of carbon was not confirmed by EDX. The identification of soot in HY-8 was also inferred, but not proven, by Mason (2009). Positive identification of carbon and of soot was, however, established in the present research by Raman spectroscopy. The identification of carbon is from the presence of the 'G' peak (graphite) at around 1580 cm^{-1} which represents well-structured carbon lattices (Sadezky et al., 2005). Soot particles, are essentially highly disordered graphite structures (Sadezky et al., 2005) primarily due to the large amount of edges from the agglomeration of nanoparticles (Santamaria et al., 2013). This is identified in Raman spectra by the presence of 'defect' (D) peaks, with increasing disorder implied with increasing number of bands. The most intense of these is the D1 peak which is the second clear peak on all spectra at ~1343 cm^{-1}. The lower intensity peak joining the G and D1 band together denotes the D3 peak which is commonly attributed to the amorphous carbon fraction of soot (Sadezky et al., 2005). The small peak recognised at 1726 cm^{-1}, may represent translational vibrational modes in C=C or C=O groups, the latter is plausible in combustion products (Brindle pers. comm. 2014) such as soot.

Organic materials may also be inferred by a suite of resistive/heavy trace elements which bind with organic colloids including Zn, Mn, Al and Fe as described by Borsato et al., (2007) and Hartland et al., (2012). Large peaks in concentrations of Zn, Fe, Al and Mn within HY-8 correlate directly with the darkest colouration of the grey layers. With the exception of Al, the trace metals analysed in this study are hypothesised to preferentially associate with the transport of larger organic colloids over 100 nm than finer ones (Hartland et al., 2012). This interpretation implies that the deposition of higher concentrations of these trace metals in grey layers occurs under conditions of particularly high infiltration.

Observations from petrography and geochemistry of HY-8 suggests dynamic growth interrupted by numerous short periods of dissolution and longer periods of fabric changes related to increasing drip rates. Normal growth in HY-8 is represented by dendritic calcite which appears to

be controlled by high supersaturation with respect to CaCO$_3$ due to low drip discharge in predominantly dry conditions. Within the normal growth phases, compact dendritic calcite represents increased drip discharge and slower growth via reducing degassing and supersaturation. Compact lamina which are topped by a micro-dissolution surface may have been formed during dissolution events, with calcite reprecipitating in a more compact form. The conditions needed to create micro-dissolution may be related to growth pauses, coinciding with particularly dry periods. The dissolution surface would thus be an expression of the resumption of dripping if initially fast enough to be undersaturated with respect to calcite (cf. Railsback et al., 1994). Short (few month) hiatuses in growth are not uncommon in the formation of dendritic calcite (Frisia et al., 2000; Frisia and Borsato 2010). Alternating open and compact lamination which does not have associated micro-dissolution therefore represent fluctuating but constant growth. Sections of coupled open and compact dendritic lamination records periods of variability in discharge, which may be seasonal or annual (Chapter 5 Section 5.3.3).

The deposition of grey layers represents marked changes from the normal mode of growth during periods of increased drip water supply. Formation of both microcrystalline and equant/euhedral fabrics requires higher discharge than the normally precipitated dendritic calcite, although some microcrystalline fabrics can form in variable discharge conditions (Frisia et al., 2000). Similarly to Railsback et al. (1994) equant/euhedral calcite probably formed under a thicker film of water. There is no evidence within the cave that the soot (and possibly charcoal) present in HY-8 grey layers originated from fires in the cave. The stalagmite was collected from a lower chamber of the cave and the entrance height is no bigger than a crawl space (Mason 2009). It seems unlikely fires would be set in a cave with such low ventilation. Furthermore, soot is located in layers which also contain clays and increased concentrations of trace elements commonly associated with organic material which must have originated at the surface. Of particular note is the observation of trace metals associated with larger colloidal transport. This association suggests the drip water precipitating the grey layers must have had a high volume and rapid flow to flush larger particles through an epikarst system that normally filters them out (Fairchild et al., 2006a). Rapid infiltration events leave little time for waters to dissolve CaCO$_3$ causing undersaturation of drip waters with respect to calcite and stalagmite erosion. This is expressed in HY-8 as micro-dissolution surfaces within the grey layers and is the same process suggested for Type E surfaces described by Railsback et al., (2013) which are very similar in appearance. Therefore the highest infiltration events are likely to be represented by micro-dissolution surfaces in the grey layers. The deposition of grey layers might be caused by increased rainfall or possibly increased infiltration due to fires stripping the vegetation. Stable isotope evidence and palaeoclimatic implications are explored in Chapter 5.

4.3.2.2 Dim-1

The co-existence of aragonite with calcite in stalagmites is contentious and in many situations calcite is deemed to have at least partially replaced aragonite (e.g. Frisia et al., 2002; Spötl et al., 2002; Lachniet et al., 2012; Perrin et al., 2014). However, examples of co-precipitation of both polymorphs in the same stalagmite do exist (e.g. Railsback et al., 1994; Spötl et al., 2002; McMillan et al., 2005). This issue requires careful evaluation. Previous research into the Dim-1 stalagmite concluded that calcite in the stalagmite was diagenetic (Wickens 2013) but this has been re-evaluated using detailed petrography and more comprehensive thin section coverage. The primary evidence for the recrystallization of aragonite to calcite in Dim-1 was based on the irregular appearance of the top aragonite boundary closer to the flanks, which suggested corrosion (Wickens 2013) (Figure 4.22). In the central axis, a mostly aragonite layer formed with clearly delineated boundaries. Therefore the presence of more aragonite at the flanks than the central axis was interpreted as the result of the recrystallization process being more effective at the main drip site than the flanks (Wickens 2013). In this study extensive petrographic observation has shown that the relationship between aragonite and calcite is complex. It is possible to identify three distinct boundaries between aragonite and calcite. None show the recrystallization of aragonite to calcite.

Figure 4.22: Location of aragonite in the central axis (left) vs location closer to the flank (photo from Wickens 2013). Clearly at the flanks aragonite is more prevalent than in the central axis. The boundary is very irregular in the flank compared to the central axis (boundaries highlighted by black dashed lines). The relationship of aragonite in the flank was used in Wickens 2013 as evidence for the replacement of a primary aragonite stalagmite to calcite, with the process more effective at the main drip site.

In Dim-1 the first boundary type is defined by layers where aragonite is present on the flank but in the central axis its former position is marked by a micro-dissolution surface (see Section 4.2.5) (Figure 4.23). Some of these micro-dissolution surfaces display isolated aragonite needles in direct association with them. Relict aragonite needles within calcite crystals are traditionally interpreted as markers for diagenesis (Frisia and Borsato 2010). However, in these areas, the interpretation is that aragonite which had precipitated has been dissolved and calcite has reformed in its former position as passive precipitation, rather than an in situ recrystallization. These dissolution events may have been of short duration removing a small amount of $CaCO_3$. Assuming the true thickness is preserved at the flanks it is estimated the minimum thickness removed could be 2-5 mm, but layers are almost always thicker in the central axis.
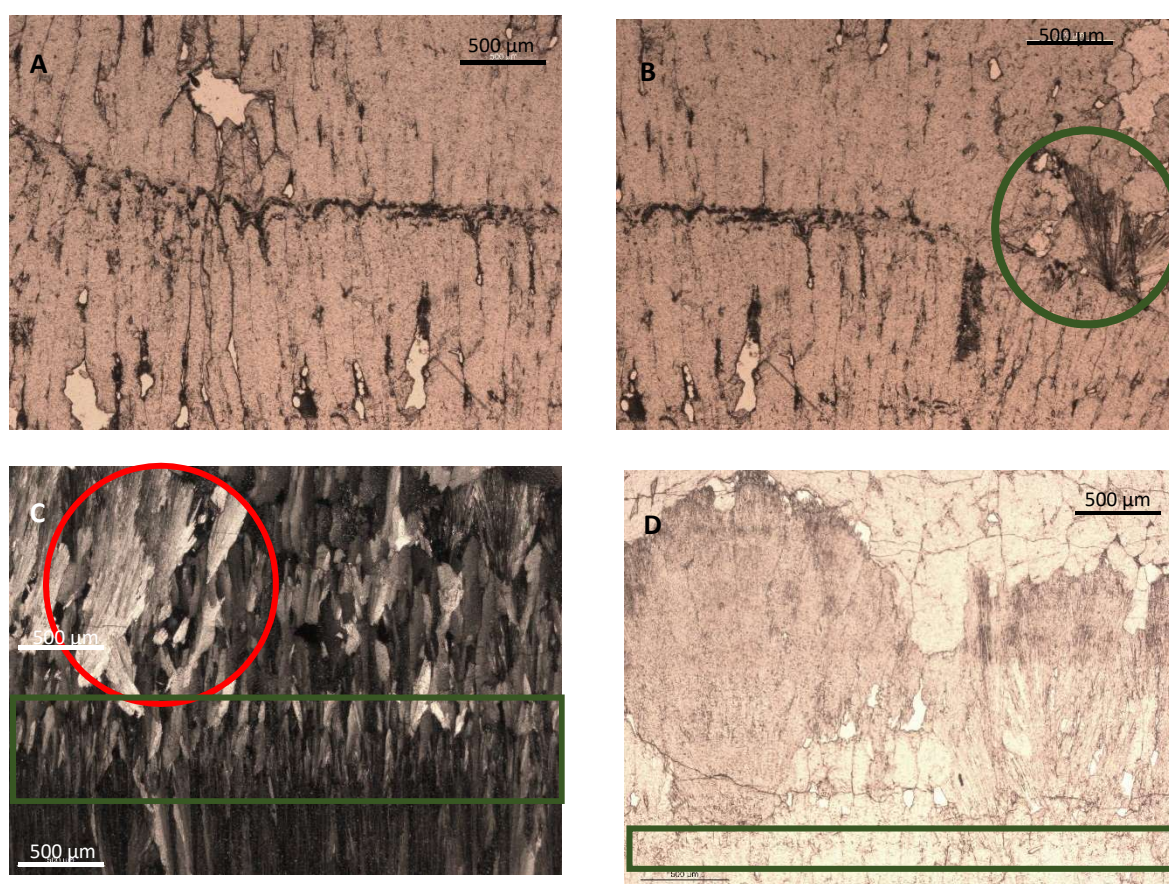
Figure 4.23: Calcite aragonite boundary type 1, micro-dissolution surfaces associated with the former position of dissolved aragonite layers with some aragonite preservation at the flanks: A. Thick sub horizontal surface (further extension laterally of B) with etching of calcite terminations below. B. A thicker sub horizontal surface extending from preserved aragonite rays (green circle). C. The green box highlights a sub horizontal inclusion horizon and altered calcite extinction marking a micro-dissolution event with preserved aragonite rays in the red circle. D. A large section of preserved aragonite rays from close to the top of Dim-1, the green box highlights the inclusion horizon from the associated micro-dissolution event.

The second boundary type is defined in the layer preceding the main hiatus (460-480 mm). In this section calcite transitions laterally into aragonite without evidence of dissolution or the clear, typically irregular boundaries which occur between aragonite and replacive calcite (Rader and Grimaldi 1961) (Figure 4.24). Boundaries between aragonite spherulites and adjacent columnar calcite are smoothly curved suggesting concurrent competitive growth (Alan C Kendall pers. comm. 2015) (Figure 4.24 C and D). This is evidence that in Dim-1 calcite and aragonite are were to grow at the same time along the same growing surface from the same drip water.
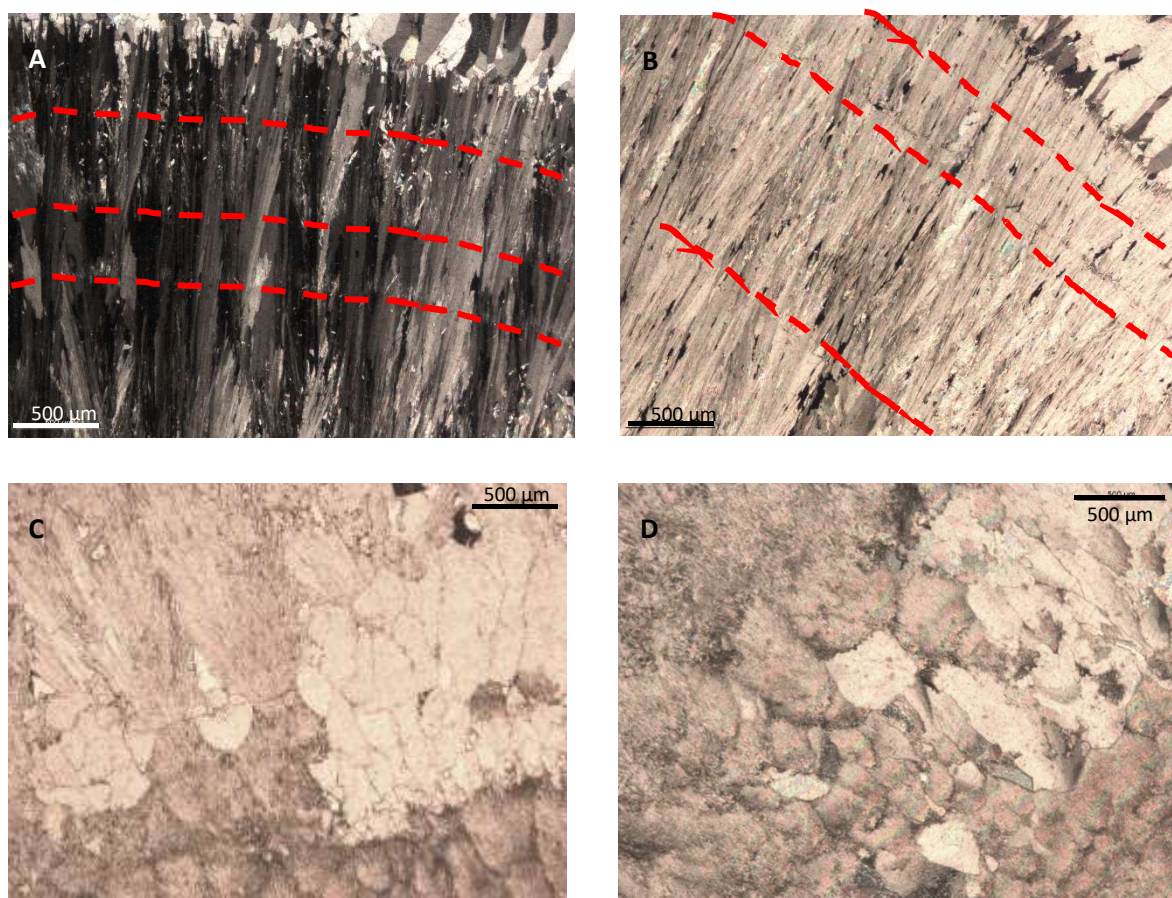
Figure 4.24: Boundary type 2, Lateral gradual transitions between primary calcite and aragonite. A and B. Calcite deposition in the central axis gradually transitions into aragonite deposition at the flanks of the main layer. Precipitation must have occurred at the same time as later dissolution surfaces (red) are present in both fabrics. C and D. Curved competitive boundaries between aragonite spherulites and primary calcite indicates that both fabrics grew concurrently.

The third boundary type is specifically related to the interaction between aragonite and the calcite above the irregular boundary in the flank (Figure 4.25). Again there is no clear evidence of dissolution in this area. Aragonite mostly forms spherulites, and where these are in contact with short columnar calcites they retain their rounded shapes, which would not be expected if replacement was occurring and suggest some concurrent competitive growth (Figure 4.25 A). Furthermore there is evidence of pore spaces between aragonite and calcite containing terminations of aragonite needles and of intact aragonite terminations within overlying calcite crystals (Figure 4.25 B and C). This is further evidence that drip water is able to precipitate both $CaCO_3$ polymorphs and, at this time, was not aggressive enough to dissolve the aragonite below. Finally it is possible to observe 'islands' of calcite surrounded completely by aragonite (Figure 4.25 E) which cannot be explained as aragonite replacing calcite, proving conclusively that at the flanks calcite was not recrystallizing aragonite.
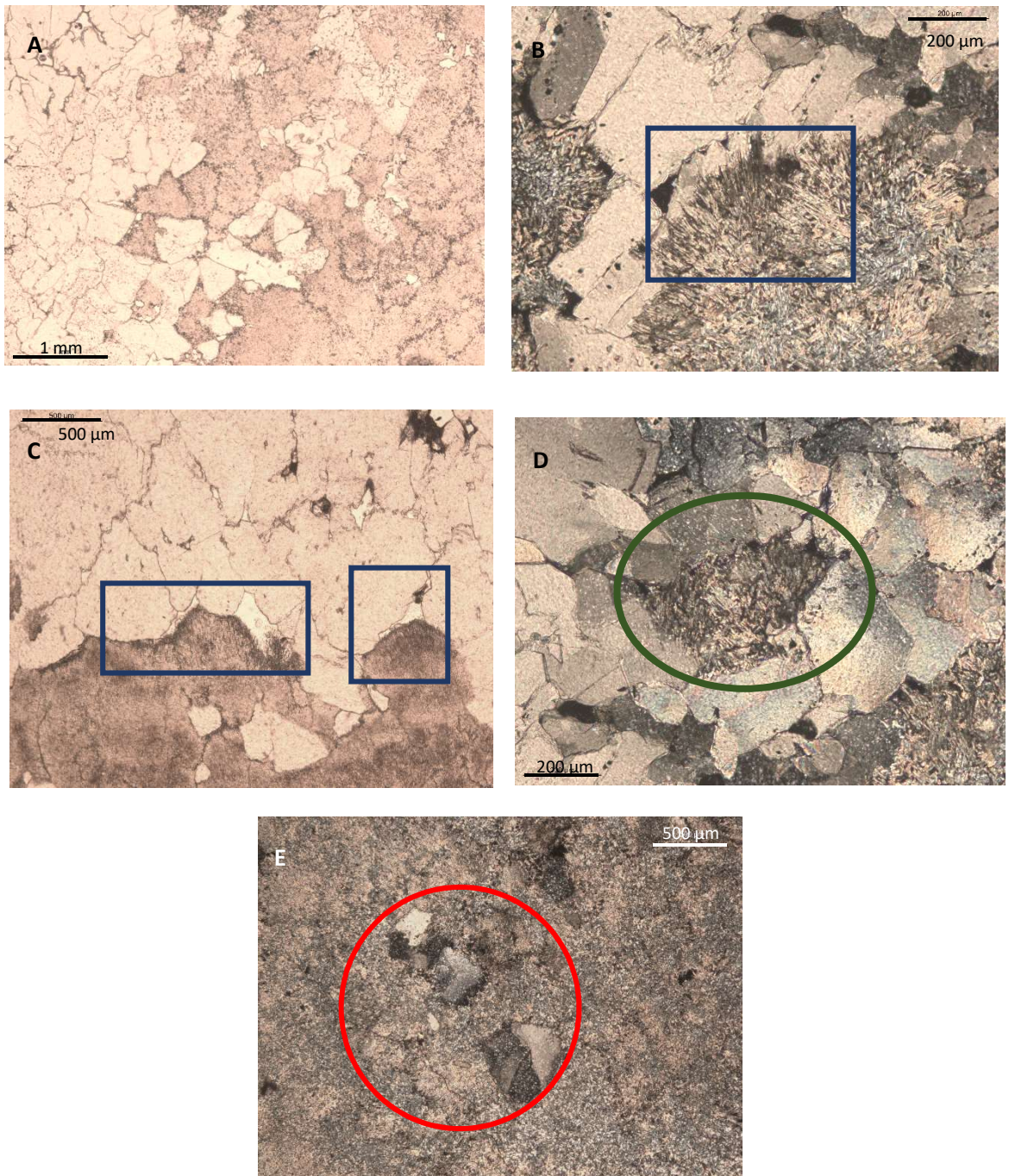
Figure 4.25: Boundary type 3, primary calcite and aragonite relationships in the flank. A Relationships between aragonite and overlying calcite at the boundary equivalent to the hiatus in the central axis. There is no clear evidence for dissolution and the growth of calcite is 'patchy' but aragonite spherulites retain rounded boundaries. B Intact aragonite terminations within calcite Blue box). C. Open pore spaces between calcite and aragonite, containing aragonite terminations (blue boxes). D Isolated aragonite ray bundle surrounded by calcite (green circle). E. Isolated calcite crystals surrounded by aragonite (red circle).

Studies have suggested that mixed aragonite and calcite speleothems precipitate due to changes in Mg/Ca ratios (e.g. (Railsback et al., 1994; Frisia et al., 2002; Spötl et al., 2002; McMillan et al., 2005; Wassenburg et al., 2012; Riechelmann et al., 2014). Recent work in Spain using drip waters which precipitate both aragonite and calcite at present found that changes in drip water Mg/Ca ratios were the only clear prominent control on which polymorph was precipitated as a speleothem (Rossi and Lozano 2016). The minimum drip water Mg/Ca ratios which precipitate aragonite over calcite is not known but is likely to be around 1.1 (Frisia et al., 2002, Rossi and Lozano 2016) but has been recorded as low as ~0.5 (Riechelmann et al., 2014). Factors in the karst that control Mg/Ca ratio are water residence time (Musgrove and Banner 2004) and PCP (Fairchild et al., 2000), an increase in both factors creates higher Mg/Ca ratios which would favour aragonite precipitation. Mixed-calcite aragonite speleothems have been used as indicators of periods of increased aridity (Railsback et al., 1994; Spötl et al., 2002; McMillan et al., 2005; Wassenburg et al., 2012; Riechelmann et al., 2014; Rossi and Lozano 2016) as both PCP and water residence time can be controlled by effective precipitation and evaporation (McDonald et al., 2007; Fairchild and Treble, 2009).

Petrographic findings show that most Dim-1 precipitated calcite with distinct periods of aragonite layers forming at certain periods. Tracing these layers via micro-dissolution surfaces into the central axis define a thinner stalagmite diameter and therefore reduced drip supply (Kaufmann 2003). This is corroborated by aridity indicators ($\delta^{18}O$ and $^{86}Sr/^{87}Sr$) within the mostly aragonite layer preceding the hiatus (Wickens 2013, Rowe et al., in prep) and shows that in Dim-1 the presence or former presence of aragonite can be related to aridity. It is likely these dissolution-precipitation phases occurred in a time period well below the resolution of dating, on a scale of years to decades (Rowe et al., in prep) and thus do not represent major hiatuses. Additionally annual alternating layers of aragonite in the Drotsky's Cave stalagmite were sometimes partially dissolved by increased drip water prior to the deposition of calcite (Railsback et al., 1994).

Most of the layer preceding the hiatus is comprised of aragonite and combined with $\delta^{18}O$ and $^{86}Sr/^{87}Sr$ (Wickens 2013, Rowe et al., in prep) gives evidence that it was a relatively more arid event than the rest of the deposition of Dim-1. However calcite layers within the layer identify discrete higher infiltration events not recorded by geochemistry. Calcite is only precipitated in the central axis of these layers. Laterally, competitive growth boundaries to aragonite imply that during these times drip water composition above the Dim-1 stalagmite was very close to the calcite inhibition threshold. Aragonite precipitating away from the drip site on a small scale at the central axis but also more prominently in the flanks of Dim-1 suggests that Mg/Ca ratios increase past the threshold in these locations. Increasing Mg/Ca as a by-product of the precipitation of calcite (Fairchild et al., 2000) could cause this switch, but as aragonite is only present at the flanks,

it is likely this threshold is reached by the increased evaporation of the film of water in flank locations compared to the central axis. This is also observed in the Drotksy's Cave stalagmite, Botswana with evaporation given as the cause (Railsback et al., 1994).

4.3.3 HY-8: Factors contributing to discordant age patterns

This section aims to relate samples with micro-dissolution surfaces to discrepancies in U-series results in HY-8. The aim is to create a coherent age model, while also attempting to identify patterns of response in the U-series data.

4.3.3.1 Samples containing micro-dissolution

Petrographic observations show that 42 % of the areas sampled for U-series in HY-8 contained multiple micro-dissolution surfaces (Table 4.5). Other samples which also yielded uncertain ages may similarly be related to other evidence for micro-dissolution, framing the possibility that micro scale dissolution disrupts the U-series system enough to create disparities in dating. Obvious and large reversals in ages accompanied by micro-dissolution features are highlighted by red boxes in Table 4.5 and are discussed in the following section. In HY-8 problematic dates are associated with all fabrics except equant/euhedral calcite which was not sampled.

Sample Name	Height above base (mm)	Date corr (yr BP)	Micro-dissolution
HY8 484	484	627 ± 12	
HY8 419	419	969 ± 19	Micro-dissolution. Detritus rich surfaces associated with lamination and with micro vugs which are quite common in this area.
HY8 399	399	904 ± 12	Stratigraphically coherent age but micro-dissolution present. Singular micro-vug 0.6 mm in width with some brown sub horizontal surfaces associated.
HY8 389	389	2307 ± 21	Micro-dissolution. Brown organic rich sub horizontal surfaces.
HY8 364	364	1124 ± 23	
HY8 349	349	3563 ± 83	Micro-dissolution. Brown organic rich sub horizontal surfaces, very occasionally showing corrosion associated with lamination.
HY8 293	293	1296 ± 37	
HY8 264	264	2964 ± 39	
HY8 250	250	3810 ± 46	
HY8 213	213	3937 ± 55	Stratigraphically coherent date but micro-dissolution present. Occasional sub horizontal organic rich surfaces associated with micro vug, <0.5 mm in width. Surfaces extend <1 mm from vug.
HY8 174	174	4665 ± 60	
HY8 161	161	6383 ± 75	Micro-dissolution. Brown sub horizontal organic rich surfaces, some defining lamination, some associated with micro vugs in the drip zone.
HY8 147	147	4328 ± 85	
HY8 120	120	4958 ± 57	Possible micro-dissolution, brown sub horizontal organic rich surfaces topping lamination and micro vugs on opposite side of slab. May be laterally pervasive.
HY8 110	110	4765 ± 51	
HY8 105	105	4352 ± 64	
HY8 52	52	6398 ± 602	Micro-dissolution associated with grey layers. Sub horizontal detritus surfaces with some micro-vugs.
HY8 40	40	8188 ± 385	Micro-dissolution associated with grey layers. Clear sub horizontal detrital defined surfaces
HY8 27	27	5820 ± 139	Dissolution associated with corrosion surface in hand specimen, sample does not directly sample the surface itself but diameter is reduced by overlying corrosion.
HY8 19	19	23821 ± 2724	Micro-dissolution associated with grey layers, organics present.

Table 4.5: HY-8 U-series results with observations for micro-dissolution including appearance. Samples highlighted in red boxes show samples which can be identified as stratigraphically incoherent.

4.3.3.2   Samples with known age discrepancies

In HY-8 samples HY8 161, HY8 349, and HY8 389 are all too old by ~1000-2000 years to fit coherently into an age model that includes all other dated samples (Figure 4.28). These samples are not associated with grey layers but all contain high levels of organics (Table 4.5).

HY8 349 shows evidence of corrosion below micro-dissolution surfaces and HY8 161 contains a number of micro-vugs with associated micro-dissolution surfaces. In all three samples evidence for micro-dissolution is abundant, such that dating sample trenches must have incorporated multiple short dissolution surfaces. U-series data for HY8 161 shows elevated ^{230}Th/^{238}U; ~ 0.1 higher than surrounding dates (Figure 4.26). ^{238}U concentration is slightly reduced but more obvious is the 1 ppb increase in ^{230}Th (Figure 4.27). This seems to imply that Th has been introduced during the dissolution event. The small reduction in ^{238}U could be interpreted as evidence that U had been removed during the event, but it seems unlikely that such opposing processes could occur together.

HY8 349 has a ^{230}Th/^{238}U ratio higher than samples above and below, while ^{234}U/^{238}U is very slightly increased although not significantly (Figure 4.27). The ^{238}U concentration in HY8 349 is lower than neighbouring samples (0.187 ppm vs 0.26 ppm in HY8 364) but ^{230}Th concentration is much elevated when compared to HY8 364 (0.000108 ppm vs 48 ppm) (Figure 4.27). It seems possible that Th has been added during the dissolution event, and as with HY8 161 there is a possibility that U could have been removed at the same time. The ^{232}Th concentration is similar to many other samples in the speleothem and ^{230}Th/^{232}Th ratio is by far the highest observed.

HY8 389 has a ^{234}U/^{238}U comparable to samples above and below, but a clear peak is present in the ^{230}Th/^{238}U ratios (>0.01) (Figure 4.26). ^{238}U has a similar concentration relative to other samples but ^{230}Th is clearly higher than adjacent samples (Figure 4.27). The concentrations suggest that Th could have been added into this sample. The ^{230}Th/^{232}Th ratio is high (Table 4.3) implying detrital contamination is unlikely to be a factor.

All the known anomalous dates in HY-8 give U-series ages too old by a fairly consistently by ~1000-2000 years and are associated with higher ^{230}Th concentrations implying that Th has been added relative to surrounding samples. There is a presence of organic detritus associated with these dissolution events, corroborated by results from Raman spectroscopy and trace elements.
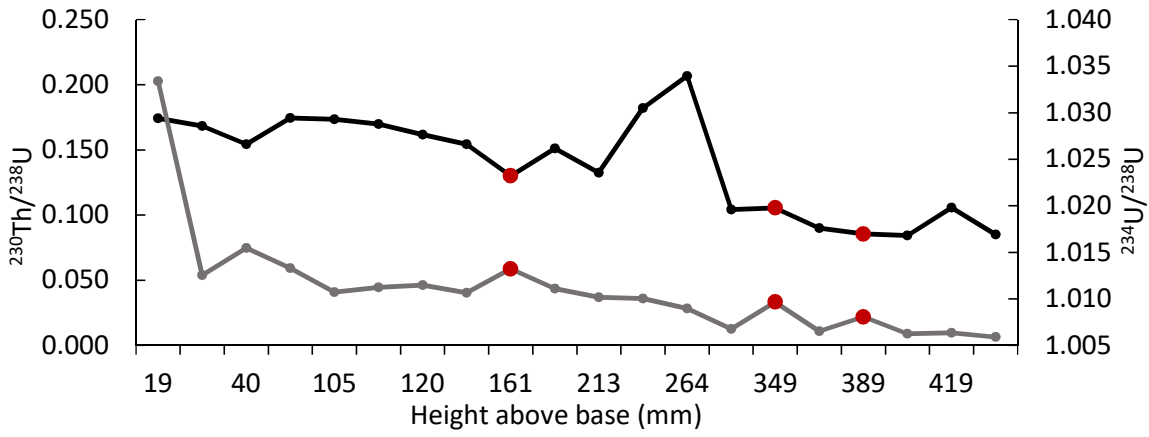
Figure 4.26: $^{234}U/^{238}U$ (black series) and $^{230}Th/^{238}U$ (grey series) relationship and variation against sample depth in HY-8. Samples discussed in this section are highlighted in red.
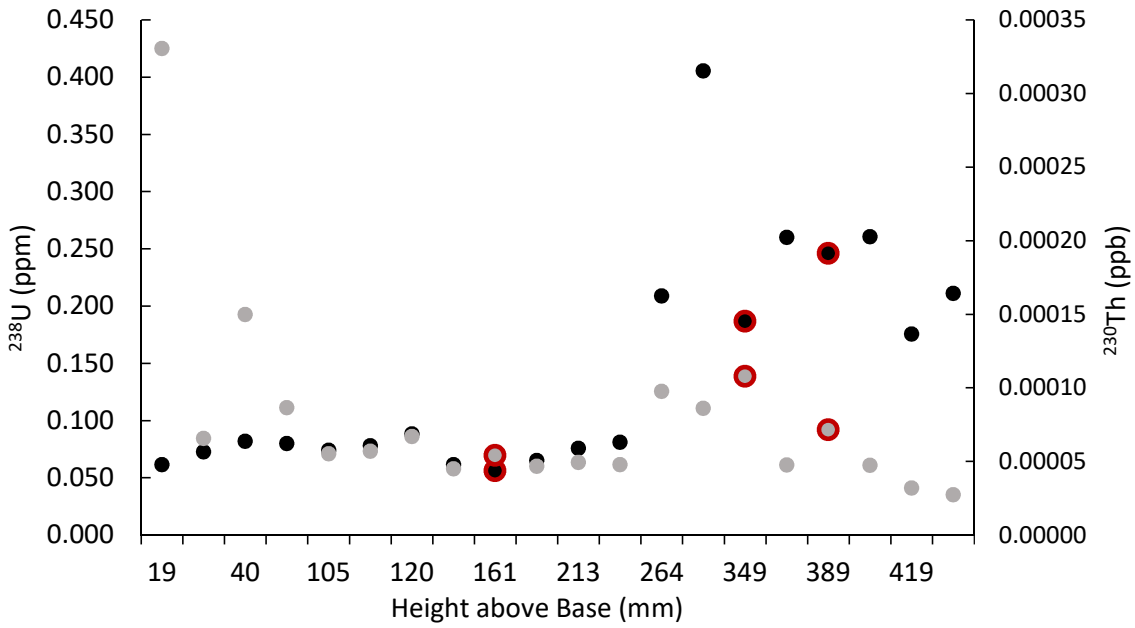
Figure 4.27: Changes in concentrations of ^{238}U (black) and ^{230}Th (grey) by sample depth in HY-8. Samples discussed in this section are highlighted in red.

HY8 399 **904 ± 12**

HY8 389 **2307 ± 21**

HY8 364 **1124 ± 23**

HY8 349 **3563 ± 83**

HY8 293 **1296 ± 37**

HY8 264 **2964 ± 39**

HY8 250 **3810 ± 46**

HY8 213 **3937 ± 55**

HY8 174 **4665 ± 60**

HY8 161 **6383 ± 75**

HY8 147 **4328 ± 85**

HY8 120 **4958 ± 57**

HY8 110 **4765 ± 51**

HY8 105 **4352 ± 64**

20 mm
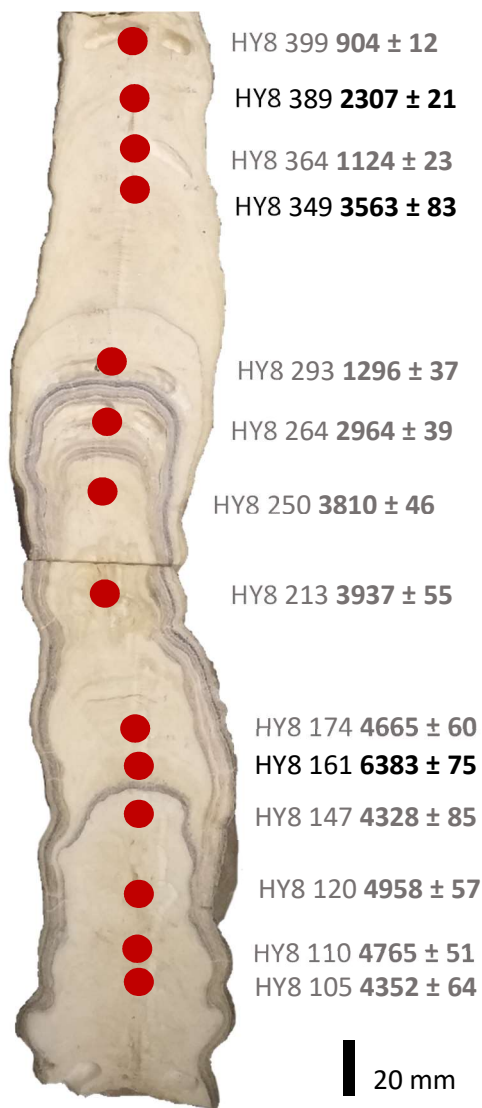
Figure 4.28: Samples discussed in this section highlighted in black compared to neighbouring dates (grey) indicating the older ages of these samples in comparison to adjacent samples.

4.3.3.3   Samples containing microdissolution and organic detritus.

The discussion of known age discrepancies and the link to micro-dissolution showed a clear trend between micro-dissolution, an increase in organics (Section 4.3.2.1) and an increase in ^{230}Th producing an older age in HY-8. This next section will therefore cover the rest of the dates in HY-8 which contain micro-dissolution and evidence of organic detritus from thin section and in some cases higher ^{232}Th, which are listed in Table 4.6.

Sample Name	Height above base (mm)	Date corr (yr BP)	Micro-dissolution
HY8 419	419	969 ± 19	Micro-dissolution. Detritus rich sub horizontal surfaces associated with lamination and with micro vugs which are quite common down the central axis.
HY8 399	399	904 ± 12	Stratigraphically coherent age but micro-dissolution present. Singular micro-vug 0.6 mm in width with some brown sub horizontal surfaces associated.
HY8 213	213	3937 ± 55	Stratigraphically coherent date but micro-dissolution present. Occasional sub horizontal organic rich surfaces associated with micro vug, <0.5 mm in width. Surfaces extend <1 mm from vug.
HY8 120	120	4958 ± 57	Possible micro-dissolution, brown sub horizontal organic rich surfaces associated with lamination and micro vugs on opposite side of slab. May be laterally pervasive.
HY8 52	52	6398 ± 602	Micro-dissolution associated with grey layers. Sub horizontal detritus surfaces with some micro-vugs.
HY8 40	40	8188 ± 385	Micro-dissolution associated with grey layers. Clear sub horizontal detrital defined surfaces
HY8 27	27	5820 ± 139	Dissolution associated with corrosion surface seen in hand specimen, sample does not directly sample the surface but diameter is reduced by overlying corrosion.
HY8 19	19	23821 ± 2724	Micro-dissolution associated with grey layers, organics present.

Table 4.6: HY-8 samples containing organic detritus and micro-dissolution surfaces.

Samples drilled directly from grey layers in the Base of HY-8 all contain micro-dissolution surfaces and the largest concentration of organics. Ages produced from HY8 19, HY8 40 and HY8 52 do show stratigraphic coherence (Table 4.6) but it is possible to observe discrepancies in U-series data similar to samples in Section 4.3.2.2 and thus ages could be discounted. HY8 19 yields a significantly older date of 23,820 yr BP (Table 4.7) which is much older than the rest of HY-8. Therefore initiation of the growth of HY-8 appears to be much earlier than the main portion of growth. The $^{234}U/^{238}U$ ratio of HY8 19 is not dissimilar to samples stratigraphically higher in the stalagmite (Figure 4.29). Additionally ^{238}U concentration is fairly consistent if slightly lower than HY8 27 and HY8 40 (Figure 4.30). The $^{230}Th/^{232}Th$ ratio of HY8 19 is 6.4 and ^{232}Th concentrations are also highest of the rest of the HY-8 samples indicating high detrital content. The date has been corrected for detrital Th and was put through the extra cleaning step to attempt to oxidise organic material (see Methods Appendix) but ^{230}Th concentration is around 4 times higher than any other sample (Figure 4.30). Although we cannot say if this date is incorrect it does potentially point to a link between micro-dissolution and the addition of Th during the event. Typically the addition of ^{230}Th without associated ^{238}U would produce a date older than is correct.

HY8 40 shows a higher $^{230}Th/^{238}U$ in comparison to stratigraphically higher dates (Figure 4.29). ^{238}U values do not indicate a loss of U contributed to the higher $^{230}Th/^{238}U$ but ^{230}Th concentration is clearly increased relative to the rest of the dates, showing the second highest value (Figure 4.30). As this date contains micro-dissolution, similarly to HY8 19, it is possible to link micro-dissolution events in HY-8 to elevated Th levels. Although the date fits stratigraphically, on this basis, it is probably too old.

The final sample located within grey layers is HY8 52. The same patterns are seen in this sample $^{234}U/^{238}U$ has similar values to stratigraphically higher samples, accompanied by similar ^{238}U concentrations implying that U has not been lost. $^{230}Th/^{238}U$ is lower than HY8 40 but still elevated by 0.02 relative to samples which come after (Figure 4.29). ^{230}Th concentrations are not as significantly increased as in HY8 19 and 40 but it is possible to infer that Th had been added during the micro-dissolution event.

Samples HY8 27, HY8 120 and HY8 419 are not located within grey layers thus the amount of organic detritus is vastly reduced but where micro-dissolution surfaces are present, organic material is still visible associated with the surface itself. The response to micro-dissolution in these samples is not consistent with the observations made in samples with significant organic content suggesting that the amount of organic material may be a significant control on the addition of Th into the system during dissolution events. For instance HY8 419 has a concentration of ^{238}U that is reduced by 0.176 ppm relative to samples below and 0.035 ppm relative to HY8 484

above; whilst ^{230}Th concentration is similar to HY8 484 (Figure 4.30). This suggests that the cause of this possibly older date is the removal of U during the micro-dissolution event. This nuclide movement is not obvious in the ratios, the ^{234}U/^{238}U ratio higher than surrounding dates (although overlaps at 2 s.d) and the ^{230}Th/^{238}U is similar (Figure 4.29).

The date of 5820 yr BP for HY8 27 is probably too young, although stratigraphically it would be compatible with the dates from 105 mm and above if the samples at 40 mm and 52 mm (8188 yr BP and 6398 yr BP respectively) were demonstrated to be invalid. As with other samples in the Base section HY8 27 has a ^{234}U/^{238}U and ^{230}Th/^{238}U ratio similar to stratigraphically higher samples. There are no anomalous values in nuclide concentrations either (Figure 4.30). Given the proximity in age in these samples this is to be expected. The shape of the stalagmite in the region of the HY8 27 sample trench is highly irregular, showing a 'wavy' pattern and reduced width (Figure 4.31). Thin section observations confirm that this distinctive appearance is caused by a region of corrosion underneath an interval of grey layer deposition.

Comparable observations to HY8 27 of U-series ratios are made for HY8 120 which has an apparent age ~400 years older than the preceding sample below. However the concentrations of both nuclides are elevated compared to surrounding samples (Figure 4.30). HY8 120 is drilled on the opposite side of the slab to a 6 mm vug with associated dissolution. The assumption is that dissolution associated with this vug is pervasive enough to also occur in the region of the HY8 120 sample trench. All three samples (HY8 27, HY8 120 and HY8 419) show evidence of micro-dissolution but produced dates which appear too old (HY8 120 and HY8 419) and too young (HY8 27).

However, HY8 213 and HY8 399 appear to suggest that the density of micro-dissolution surfaces is an important factor in the amount of nuclide mobility. Both samples contain micro-dissolution surfaces but they are infrequent, discontinuous and very localised in extent (often <1 mm), much less than observed in the rest of the affected dates. Neither sample appears to display anomalies in U-series ratios or nuclide concentrations and calculated ages (HY8 213: 3937 yr BP, HY8 399: 904 yr BP) are stratigraphically coherent. These observations might advocate a limit on the amount of dissolution which can occur within stalagmites that doesn't upset relative ratios of nuclides and therefore cause inconsistencies in dating.
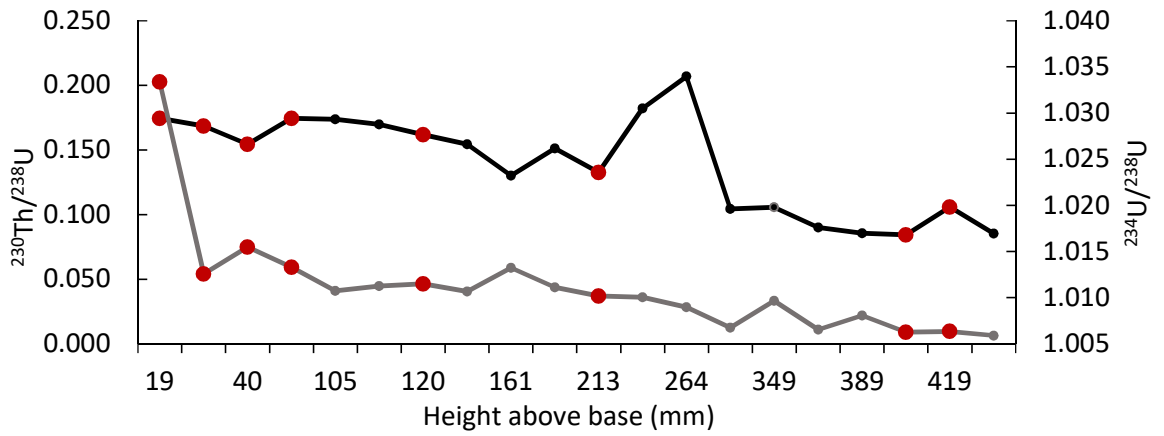
Figure 4.29: $^{234}U/^{238}U$ (black) and $^{230}Th/^{238}U$ (grey) relationship and variation against sample depth in HY-8. Samples discussed in this section are highlighted in red.

Figure 4.30: Changes in concentrations of ^{238}U (black) and ^{230}Th (grey) by sample depth in HY-8. Samples discussed in this section are highlighted in red. The ^{238}U value for HY8 120 is located beneath the ^{230}Th value.

117

HY8 484 **627 ± 12**

HY8 419 **969 ± 19**

HY8 399 **904 ± 12**

HY8 389 **2307 ± 21**

HY8 364 **1124 ± 23**

HY8 349 **3563 ± 83**

HY8 293 **1296 ± 37**

HY8 264 **2964 ± 39**

HY8 250 **3810 ± 46**

HY8 213 **3937 ± 55**

HY8 174 **4665 ± 60**

HY8 161 **6383 ± 75**

HY8 147 **4328 ± 85**

HY8 120 **4958 ± 57**

HY8 110 **4765 ± 51**

HY8 105 **4352 ± 64**

HY8 52 **6398 ± 602**

HY8 40 **8188 ± 385**

HY8 27 **5820 ± 139**

HY8 19 **23,821 ± 2724**

20 mm

Figure 4.31: Samples discussed in this section highlighted in black compared to neighbouring dates (grey) indicating the stratigraphic incoherence between the samples discussed and adjacent ones. Inset shows the morphology and sampling trenches for the samples in the Base which were drilled on the opposite side to the one show in the main figure.

4.3.3.4   Other Samples with dating inconsistences

Samples HY8 105, HY8 110, HY8 147 and HY8 174 do not plot in stratigraphic order, but inversions are only on the scale of a few hundred years (Table 4.7). Only very minor isotope migration would be necessary to cause the observed discordance, reflected in the lack of an obvious geochemical signal. The lack of any petrographic feature makes identification of such small scale effects impossible. All ^{234}U/^{238}U ratios indistinguishable within error. Samples which are stratigraphically coherent with each other (i.e. HY8 147 can only fit consistently with HY8 105 below), do apparently show similar changes in nuclide concentrations. Both HY8 105 and 147 have relatively lower ^{230}Th and ^{238}U concentrations and HY8 110 and 174 relatively higher ^{230}Th and ^{238}U concentrations. Either set of samples could fit reasonably within the age model.

Sample Name	Height above base (mm)	Date corr (yr BP)
HY8 174	174	4665 ± 60
HY8 147	147	4328 ± 85
HY8 110	110	4765 ± 51
HY8 105	105	4352 ± 64

Table 4.7: HY-8 samples between 105 and 174 mm without micro-dissolution but still showing inconsistences in dating.
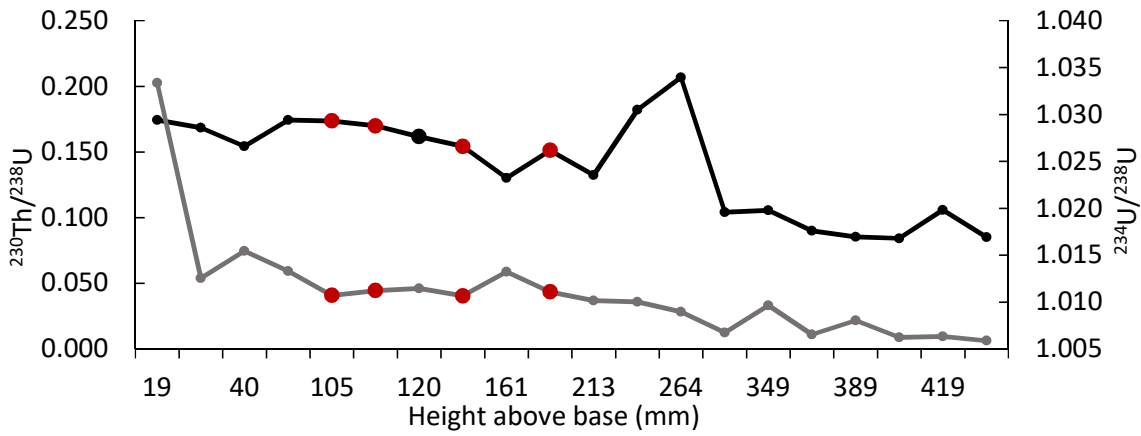
Figure 4.32: $^{234}U/^{238}U$ (black series) and $^{230}Th/^{238}U$ (grey series) relationship and variation against sample depth in HY-8. Samples discussed in this section are highlighted in red.
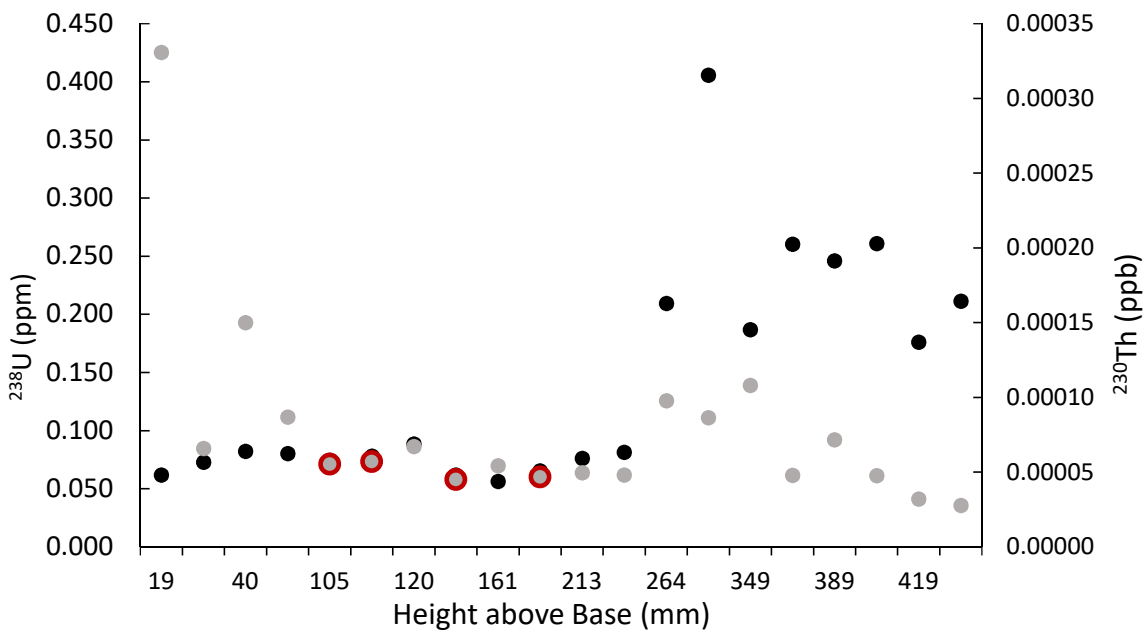
Figure 4.33: Changes in concentrations of ^{238}U (black) and ^{230}Th (grey) by sample depth in HY-8. Samples discussed in this section are highlighted in red. ^{238}U values are located directly underneath ^{230}Th.

HY8 213 **3937 ± 55**

HY8 174 **4665 ± 60**
HY8 161 **6383 ± 75**

HY8 147 **4328 ± 85**

HY8 120 **4958 ± 57**

HY8 110 **4765 ± 51**
HY8 105 **4352 ± 64**
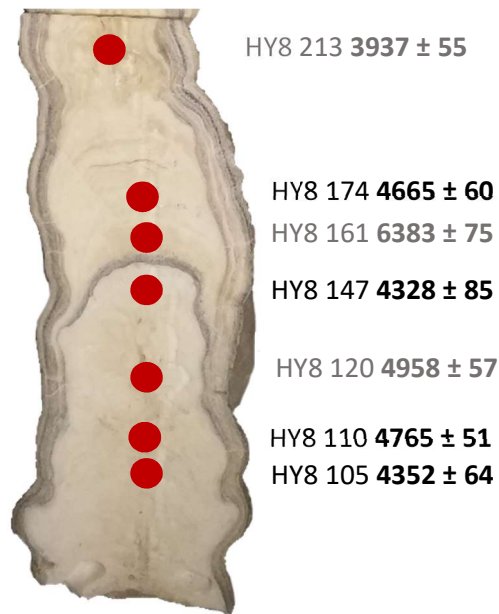
Figure 4.34: Samples discussed in this section highlighted in black compared to neighbouring dates (grey) indicating dates are not stratigraphically coherent.

20 mm

4.3.3.5 Age Model

Samples and dates used in the final age model are listed in Table 4.8. Initially, samples with both apparent anomalies in U-series data and association with evidence for micro-dissolution were removed from the dataset; this included samples HY8 161, HY8 349, HY8 389 and HY8 419.

Data from the base (0-67 mm) of HY-8 is difficult to assess, because all dates could be stratigraphically compatible with younger dates further up the stalagmite. Of the four basal dates, the much older date from sample HY8 19 (23,821 yr BP) is excluded from further consideration as it is clearly pre-Holocene. The relatively low ^{230}Th/^{232}Th ratios (7.0 – 29.0) of the other three samples (HY8 27, HY8 40 and HY8 52) indicates they contain significant detrital contamination. The isotopic composition of the detritus may well differ from the bulk earth isotopic ratios used in the age correction and consequently the corrected ages may not reflect the true age of a sample. Sample HY8 27 (5820 yr BP) is obviously stratigraphically too young, but it is not possible to infer nuclide migration in the data. The ^{230}Th concentration in HY8 40 could be anomalously high, suggesting addition of Th, but again it is not clear in the data. As all three samples show evidence of micro-dissolution (associated with disrupted U-series ages), the lack of evidence in the U-series data as to which dates are likely to be in error gives three options: to either reject HY8 27, reject

both HY8 40 (8188 yr BP) and HY8 52 (6398 yr BP) or to reject all three. Due to the levels of uncertainty, rejecting all three is the only viable option.

Samples located between 105 and 174 mm (with the exception of the clearly anomalous HY8 161 which may have experienced U loss) are problematic. As age inversions are only a few centuries there is limited evidence to separate these dates using U-series data. Only sample HY8 120 shows insecure evidence of microdissolution; it relies on the assumption that dissolution associated with a 6 mm vug was pervasive enough laterally to affect the opposite side of the 180 mm thick slab. Possible vugs seen in the trench following drilling offer some weak support for this and on this basis it was removed from the final age model.

After removing HY8 120, stratigraphic coherency can be achieved by using either HY8 105 and 147 or HY8 110 and 174 in conjunction with each other. Interestingly, the use of either coupled dates produces growth rates which are unusually fast for most speleothems (upper limit 320 µm/yr according to Fairchild et al., (2006a)). The growth rate between HY8 105 and 147 is 1.75 mm/yr, while between HY8 110 and 174 it is 0.64 mm/yr, which is still high but not as far from rates observed in most speleothems. It is not possible to separate these four samples on the basis of nuclide concentration. HY8 105 and HY8 147 are discounted because, despite both growth rates being very rapid for stalagmite growth, these two samples yield less realistic rates.

HY8 213 and HY8 399 are included in the finalised data set despite the presence of micro-dissolution, as their ages are stratigraphically coherent and there are no discrepancies in the U-series data. The evidence for dissolution in these samples is much less than in samples which can be linked to U-series disruption. There are only a few micro-dissolution surfaces and they are discontinuous and prevail for less than 1 mm. It is perhaps possible there is an upper threshold to the amount of dissolution that can take place before nuclides are mobilized enough to affect U-series dates.

Sample Name	Height above base (mm)	Date corr (yr BP)
HY8 484	484	627 ± 12
HY8 399	399	904 ± 12
HY8 364	364	1124 ± 23
HY8 293	293	1296 ± 37
HY8 264	264	2964 ± 39
HY8 250	250	3810 ± 46
HY8 213	213	3937 ± 55
HY8 174	174	4665 ± 60
HY8 110	110	4765 ± 51

Table 4.8: Ages which will be used to create an age model in Chapter 5. Ages included do not show micro-dissolution above a hypothetical threshold which appears to control the amount of removal of nuclides. Samples do not show discrepancies within U-series.

4.3.4 Dim-1: Factors contributing to discordant age patterns

4.3.4.1 Samples containing micro-dissolution

As in HY-8, there is a link in Dim-1 between samples that produce discordant ages and micro-dissolution. Again a small number of problematic dates did not contain micro-dissolution. At least 40 % of Dim-1 samples incorporate calcite or aragonite which has been affected by micro-dissolution. A further 3 samples occur in regions of undulating inclusion horizons without altered the calcite extinction where micro-dissolution is implied (Table 4.8). Samples highlighted in red boxes in Table 4.8 show samples where micro-dissolution occurs in samples with clear age disparities (discussed in the following section). Questionable dates occur in calcite and mixed aragonite-calcite samples.

Sample Name	Calcite/ aragonite	Depth from base (mm)	Date corr (yr BP)	Micro-dissolution
Dim 52-3	aragonite	above top	127,816 ± 688	
Dim 29-10	calcite	568	117,454 ± 588	Micro-dissolution. Linear inclusion horizon with altered extinction zone.
Dim 52-2	aragonite	566	128,759 ± 687	
Dim 41-8	calcite	564	117,201 ± 597	Micro-dissolution. Inclusion horizon just missed by sample trench but remnant aragonite needles and bundles present.
Dim 52-4	aragonite	558	128,477 ± 689	
Dim 37-5	Aragonite and calcite	502	129,199 ± 682	Micro-dissolution. Attempted drilling within aragonitic layer but also incorporates inclusion horizon projecting into the central axis.
Dim 52-1	calcite	493	127,825 ± 741	Micro-dissolution. Inclusion horizon above upper boundary to hiatus (main) layer. Inclusion horizon is associated with aragonite away from the central axis.
Dim 29-9	calcite	485	136,092 ± 809	Dissolution. Larger scale dissolution at time of hiatus showing corrosion of aragonite needles.
Dim 41-6	aragonite and calcite	478	119,698 ± 610	Micro-dissolution. Main layer. Inclusion horizons with remnant aragonite needles.
Dim 52-5	aragonite	478	128,198 ± 688	
Dim 29-7	Aragonite possible calcite	472	120,695 ± 1,025	Micro-dissolution. Main layer. Inclusion horizons with remnant aragonite needles.
Dim 41-5	calcite	463	122,704 ± 659	Micro-dissolution. Inclusion horizons with altered extinction zone.
Dim 41-4	calcite	425	126,377 ± 729	Micro-dissolution. Inclusion horizons and altered extinction.
Dim 37-3	calcite	357	130,422 ± 831	Micro-dissolution. Inclusion horizons but no altered extinction
Dim 33-6	calcite	354	125,439 ± 729	Likely micro-dissolution (not covered by thin section)
Dim 41-2	calcite	304	120,606 ± 642	Micro-dissolution. Inclusion horizons with altered extinction.
Dim 102-2	calcite	257	128,986 ± 663	
Dim 102-1	calcite	215	128,072 ± 670	
Dim 41-1	calcite	166	126,234 ± 672	Micro-dissolution. Singular undulating inclusion horizon.
Dim 33-4	calcite	132	128,590 ± 696	

Dim 37-1	calcite	120	129,439 ± 791	
Dim 37-4	calcite	92	130,650 ± 682	
Dim 33-5	calcite	85	119,973 ± 681	Micro-dissolution. Inclusion horizons with possible detritus
Dim 29-6	calcite	17	132,642 ± 1,363	Micro-dissolution. Inclusion horizons no altered extinction
Dim 37-2	calcite	5	131,412 ± 829	

Table 4.9: Overleaf and this page. Dim-1 U-series results with observations for micro-dissolution including appearance, if extinction is altered or not. Samples highlighted in red boxes show samples that are possible to identify as problematic.

4.3.4.2 Samples with known age discrepancies

Samples in Dim-1 which are obviously stratigraphically incoherent are Dim 37-5 (502 mm), Dim 29-9 (485 mm), Dim 37-3 (357 mm) and Dim 33-5 (85 mm) (Table 4.9, Figure 4.37). There are a number of reasons for highlighting these particular samples. Dim 29-9 yielded a date several thousand years older (136,092 yr BP) than the stratigraphically lowest date 5 mm from the base (131,412 yr BP). Dim 33-5 produced a date several thousand years younger (119, 973 yr BP) than all but 2 dates stratigraphically above it. Dim 37-3 (130,422 yr BP) is positioned higher than a number of dates which do not contain micro-dissolution and are around 2000 years younger. Identifying an age discrepancy in Dim 37-3 then demands that Dim 37-5 (129,199 yr BP) must also be too old.

Dim 29-9 (485 mm) was partially drilled through the hiatus surface present at 480 mm, petrography shows this boundary is strongly corroded providing clear evidence for the most significant removal of $CaCO_3$ observed in Dim-1. Measured $^{234}U/^{238}U$ ratios are > 0.1 lower than surrounding values, but the $^{230}Th/^{238}U$ ratio is consistent implying that there has been some preferential leaching of ^{234}U (Figure 4.35). The concentration of ^{238}U is much higher than other calcite samples, but much lower than aragonite samples. This might be expected if some U has been retained from the dissolved aragonite but also suggests that significant removal of ^{238}U is likely to have occurred during aragonite corrosion (Figure 4.36). ^{230}Th values show the same trend, being typically higher than pure calcite values and lower than aragonite, which would be expected

because of the higher ^{238}U values and therefore also possibly indicate Th migration. However, given the date is nearly 10,000 years older than might be expected, it could possibly indicate non-uniform migration of species, in this instance more U removed relative to Th.

Dim 37-5 (502 mm) is located in a region directly below a corroded aragonitic layer and petrography shows that the sample is mostly calcite but does incorporate a small amount of aragonite and the micro-dissolution surface that corroded it. There are no obvious discrepancies in U-series ratios (Figure 4.35). However the ^{238}U value (0.384 ppm) is elevated for a pure calcite, so probably implies a component of aragonite was sampled. Whereas ^{230}Th of 0.0156 ppb is closer in composition to those of aragonitic samples, suggesting addition of Th but not U, consistent with an older than expected age, despite age overlap at 2 s.d with two samples above (Figure 4.37). Its position below an aragonitic layer suggests the additional Th could have been incorporated into the calcite during dissolution of the overlying aragonite and presumably slight corrosion of the uppermost calcite.

Both Dim 37-3 and 33-5 show inclusion horizons without altered extinction zones; while there is no direct evidence of dissolution, it can be inferred by the widespread association of inclusion horizons and dissolution elsewhere in the speleothem (see Section 4.3.1.2). As with the samples described above, Dim 37-3 (357 mm) is a likely to be few millennia too old. Concentrations of ^{238}U and ^{230}Th are slightly elevated compared to stratigraphically lower dates, but not dissimilar to Dim 41-4 (Figure 4.36). It is possible (but not demonstrable) that the older date produced by this sample is due to the addition of both radioactive species during dissolution. The dissolution event associated with this sample can be related to preserved aragonite at the flank, showing it was a former layer which extended across the width of the stalagmite cap.

Dim 33-5 is the only sample incorporating a dissolution horizon related to a shift in the growth axis at 105 mm, which has produced a date that is clearly too young. U-series ratios and concentration data do not provide evidence for movement of either nuclide. Concentrations are higher than samples below, but similar to samples above (Figure 4.36). It is possible both U and Th have been added, but this contradicts the interpretation of the Dim 37-3 age, where apparently adding both radioactive species resulted in an older date.

Unlike the clearly anomalous dates in HY-8, which show a consistent trend to increased Th and an older date, anomalous dates in Dim-1 are not consistently related to increased Th. Dim 37-5 agrees with HY-8 samples in that the addition of Th can possibly occur during dissolution events and produce an older date but there is not a comparable increase in organic matter. Dim 29-9 and Dim 37-3 apparently show older dates can be created by the removal and addition of both

radioactive species. Although the removal of CaCO₃ is much larger in Dim 29-9 as it is associated with the main hiatus. It is not possible in either sample to observe one radioactive element being removed/added over the other which might be expected. Furthermore a date which is apparently too young might also be created by the addition of both radioactive isotopes: again this is not demonstrated by the data but it might be expected that more ^{238}U is added relative to ^{230}Th to achieve this.
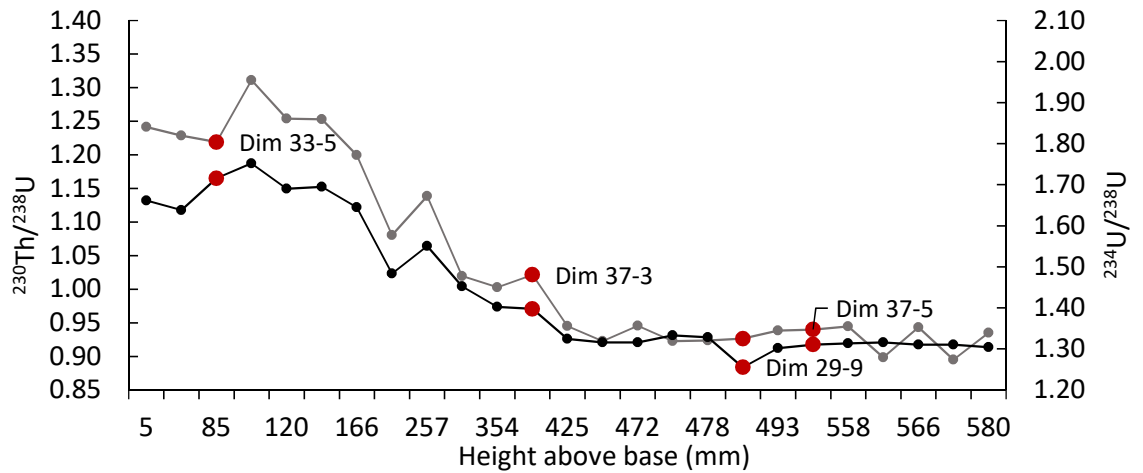
Figure 4.35: $^{234}U/^{238}U$ (black series) and $^{230}Th/^{238}U$ (grey series) relationship and variation against sample depth in Dim-1. Samples discussed in this section are highlighted in red.
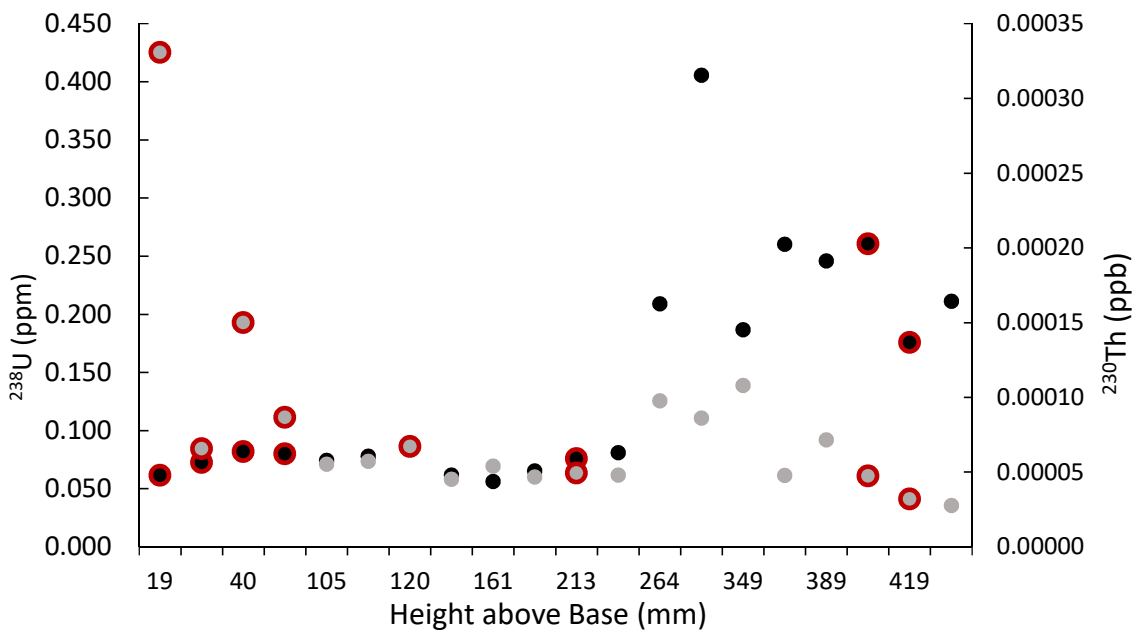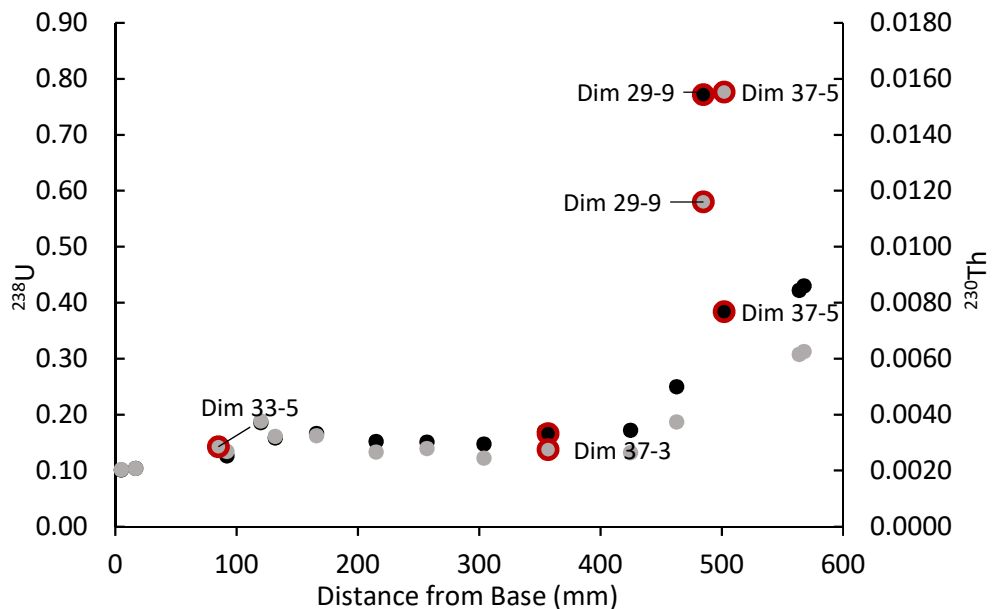

Figure 4.36: Changes in concentrations of ^{238}U (black) and ^{230}Th (grey) by sample depth in calcite samples of Dim-1. Samples discussed in this section are highlighted in red. Samples 29-9 and 37-5 contain a mixture of calcite and aragonite so are placed on the calcite graph. For Dim 33-5 the ^{238}U value is located underneath ^{230}Th value.
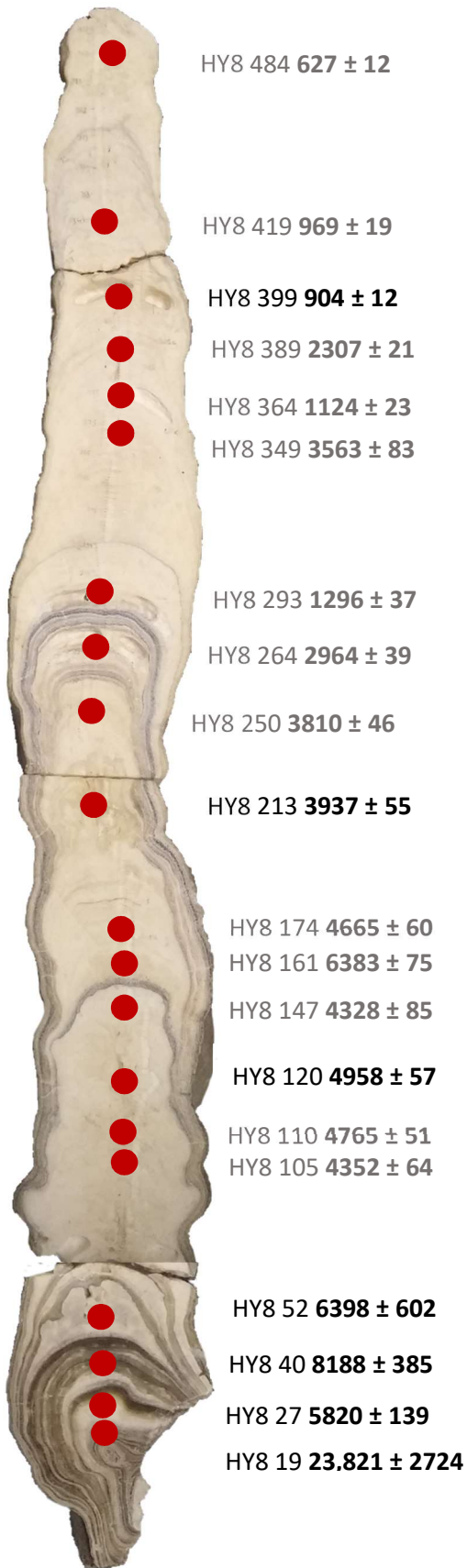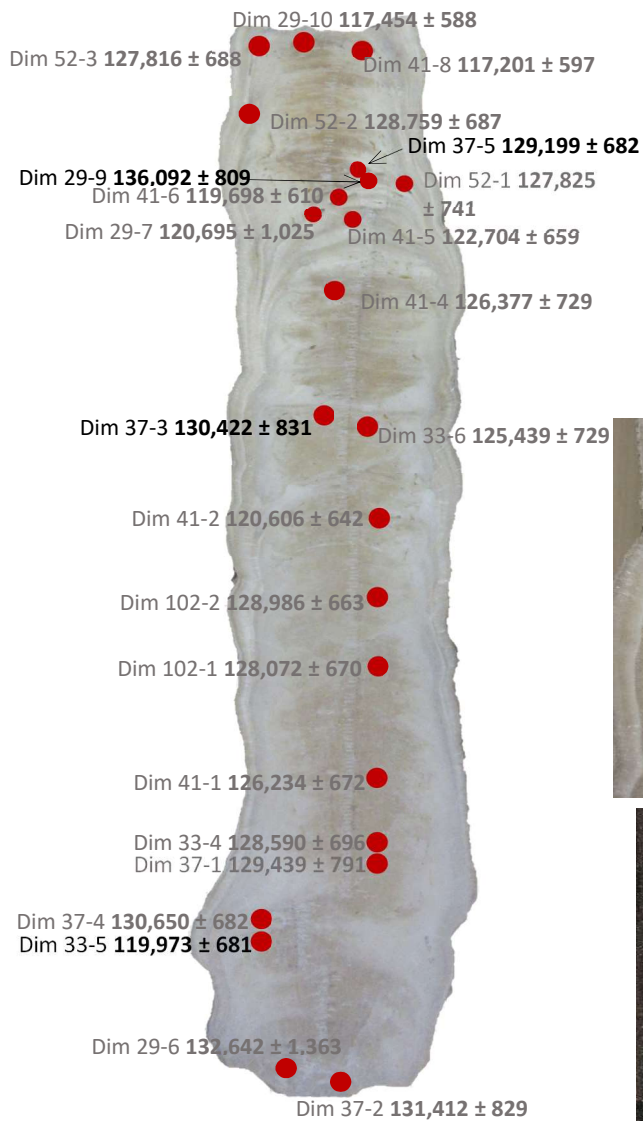
Figure 4.37: Samples discussed in this section highlighted in black compared to neighbouring dates (grey) indicating dates are not stratigraphically coherent. Insets show macromorphology and examples of petrography in more localised areas.

Dim 29-10 **117,454 ± 588**
Dim 52-3 **127,816 ± 688**
Dim 41-8 **117,201 ± 597**
Dim 52-2 **128.759 ± 687**
Dim 37-5 **129,199 ± 682**
Dim 29-9 **136,092 ± 809**
Dim 41-6 **119,698 ± 610**
Dim 52-1 **127,825 ± 741**
Dim 29-7 **120,695 ± 1,025**
Dim 41-5 **122,704 ± 659**
Dim 41-4 **126,377 ± 729**
Dim 37-3 **130,422 ± 831**
Dim 33-6 **125,439 ± 729**
Dim 41-2 **120,606 ± 642**
Dim 102-2 **128,986 ± 663**
Dim 102-1 **128,072 ± 670**
Dim 41-1 **126,234 ± 672**
Dim 33-4 **128,590 ± 696**
Dim 37-1 **129,439 ± 791**
Dim 37-4 **130,650 ± 682**
Dim 33-5 **119,973 ± 681**
Dim 29-6 **132.642 ± 1.363**
Dim 37-2 **131,412 ± 829**

Dim 37-3 **130,422 ± 831**
Stacked undulating inclusion surface no difference in extinction (green box)

500 µm

40 mm

Dim 37-5 **129,199 ± 682** located just below aragonite layer, possible trajectory show by green dashed line. Preserved aragonite highlighted by blue boxes.

Dim 29-9 **136,092 ± 809** sampled over corroded aragonite hiatus surface shown

500 µm

1.480 mm

128

4.3.4.3 Samples containing micro-dissolution associated with former aragonite surfaces

Investigation of dated samples that were clearly out of stratigraphic sequence, and contained evidence of micro-dissolution, did not reveal any consistent trends in the U and Th isotope data. However, it has been shown that there is a link between the dissolution of aragonite and inconsistencies in dates, even if the mechanism differs from case to case. Further samples that are associated with the dissolution of aragonite are displayed in Table 4.10 and discussed in this section.

Sample Name	Calcite/ aragonite	Depth from base (mm)	Date corr (yr BP)	Micro-dissolution
Dim 29-10	calcite	568	117,454 ± 588	Micro-dissolution. Linear inclusion horizon with altered extinction zone.
Dim 41-8	calcite	564	117,201 ± 597	Micro-dissolution. Inclusion horizon just missed by sample trench but remnant aragonite needles and bundles present.
Dim 52-1	calcite	493	127,825 ± 741	Micro-dissolution. Inclusion horizon above upper boundary to hiatus (main) layer. Inclusion horizon is associated with aragonite away from the central axis.
Dim 41-6	aragonite and calcite	478	119,698 ± 610	Micro-dissolution. Main layer. Inclusion horizons with remnant aragonite needles.
Dim 29-7	Aragonite possible calcite	472	120,695 ± 1,025	Micro-dissolution. Main layer. Inclusion horizons with remnant aragonite needles.
Dim 41-5	calcite	463	122,704 ± 659	Micro-dissolution. Inclusion horizons with altered extinction zone.
Dim 41-4	calcite	425	126,377 ± 729	Micro-dissolution. Inclusion horizons and altered extinction.
Dim 41-2	calcite	304	120,606 ± 642	Micro-dissolution. Inclusion horizons with altered extinction.

Table 4.10: Dim-1 samples containing micro-dissolution surfaces associated with the dissolution of former aragonite.

Sample Dim 52-2 is the highest stratigraphically constrained date (566 mm) which does not contain micro-dissolution surfaces and it is therefore deemed reliable. The sample age is 128,760 ± 690 yr BP and thus all the samples discussed in this section produced ages that are too young to relative to Dim 52-2 (Table 4.8).

Dim 29-7 (472 mm) has a $^{234}U/^{238}U$ ratio similar to surrounding samples, but Figure 4.37 highlights a slightly higher $^{230}Th/^{238}U$ ratio, although the difference ~0.02 is not large. Petrographically, Dim 29-7 is predominantly aragonite with a small amount of calcite possible but contained the lowest concentration of both ^{238}U and ^{230}Th of all the aragonite samples (except Dim 52-3, which is not represented on the growth axis) (Figure 4.39). Thus despite no clear difference in U-series ratios concentrations of the nuclides suggest the removal of U associated with a micro-dissolution event removing aragonite.

Dim 41-6 (478 mm) containing calcite but predominantly aragonite, again shows lower ^{238}U and ^{230}Th concentrations compared to other aragonite samples. . The effect of micro-dissolution in Dim 41-6 has resulted in a date ~8000 years younger than Dim 52-5 (located at the same stratigraphic height) (Figure 4.41) which does not contain micro-dissolution surfaces and produced a stratigraphically coherent date (Table 4.4). Concentration data suggests the cause may have been removal of U.

Dim 29-10 (472 mm) and Dim 41-8 (478 mm) were drilled adjacent to one another and both incorporate micro-dissolution from the same surface. These samples produced virtually identical ages and ^{238}U concentrations. It is difficult to compare concentrations of ^{238}U and ^{230}Th in Dim 29-10 and Dim 41-8, which are composed of calcite, to neighbouring samples as they are all at least partially aragonitic in composition (Figures 4.38 and 4.39). Both $^{230}Th/^{238}U$ ratios are clearly lower than neighbouring samples by ~0.05 but show comparable $^{234}U/^{238}U$ ratios (Figure 4.37). This consistency in $^{234}U/^{238}U$ implies that Th has been removed. However, the loss of Th but not U, is highly unlikely and the decay of ^{238}U to ^{230}Th would not be fast enough on short timescales for ^{230}Th to accumulate.

The age obtained from sample 52-1 (127,800 yr BP) is roughly concordant with other reliable ages below it ;however, taking into account ages from overlying samples the age may be 1000 years too young. There is no obvious inconsistency in ratios of the sample, but ^{238}U content is the highest of entire stalagmite, nearly double the nearest aragonite sample (Dim 52-4). By contrast ^{230}Th is more in line with the higher calcite values (Figure 4.40). This could suggest Th loss occurred during the dissolution of the former aragonite layer at this location, but the age error overlaps at 2 s.d. with Dim 52-2 making it impossible to be definitive.

For Dim 41-4 (425 mm) and Dim 41-2 (304 mm) it is not possible to compare $^{234}U/^{238}U$ and $^{230}Th/^{238}U$ ratios because they occur at the end of a long term large decrease in values and Dim 41-5 (463 mm) does not show any discrepancy in U-series ratios (Figure 4.38). The ^{238}U and ^{230}Th concentrations in Dim 41-5 are relatively enriched, but as this sample marks the start of an upward trend in nuclide concentrations in calcite samples (Figure 4.40) it is not obviously anomalous relative to stratigraphically higher samples. Dissolution can be confidently implied here as inclusion horizons are associated with changes in calcite extinction.
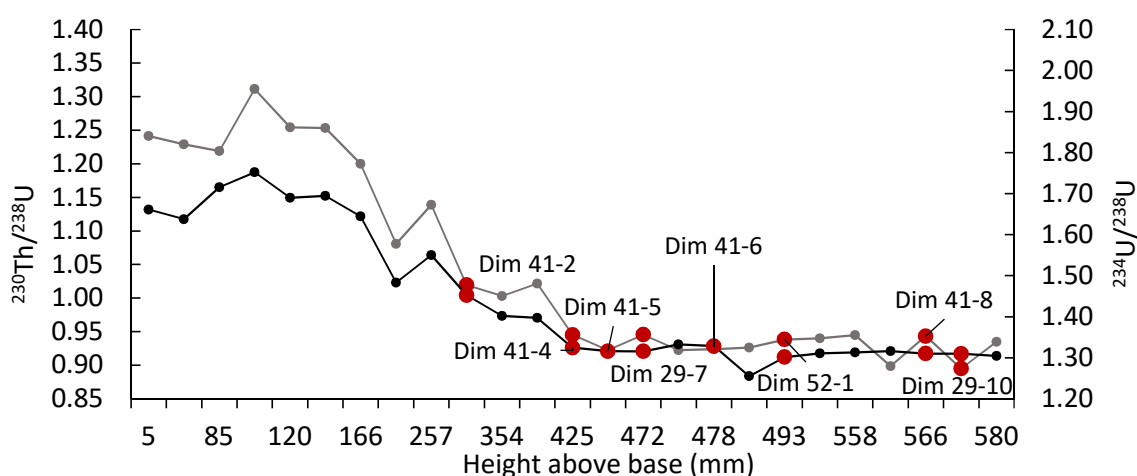
Figure 4.38: $^{234}U/^{238}U$ (black series) and $^{230}Th/^{238}U$ (grey series) relationship and variation against sample depth in Dim-1. Samples discussed in this section are highlighted in red. The $^{230}Th/^{238}U$ values from Dim 41-5 and 41-6 are located underneath the $^{234}U/^{238}U$ ratio.
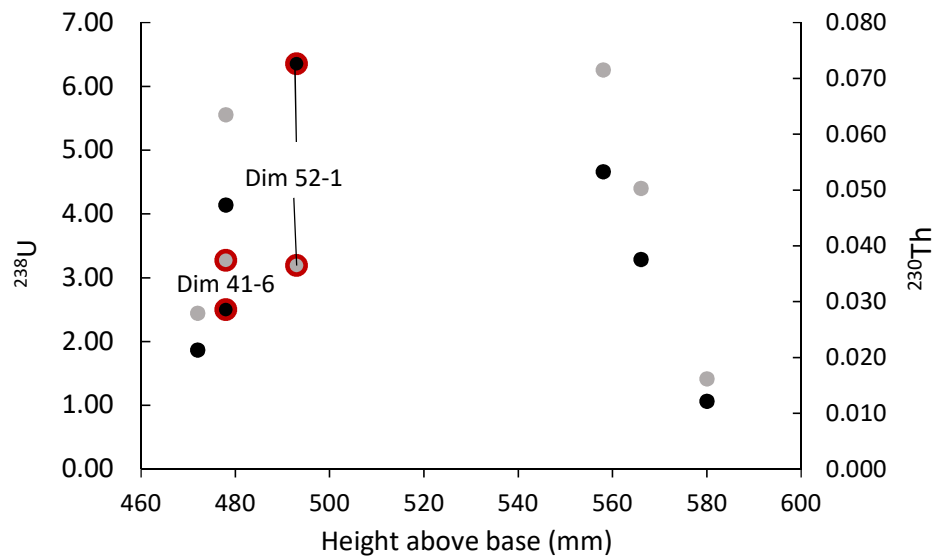
Figure 4.39: Changes in concentrations of ^{238}U (black) and ^{230}Th (grey) by sample depth in aragonite sample of Dim-1. Samples discussed in this section are highlighted in red.
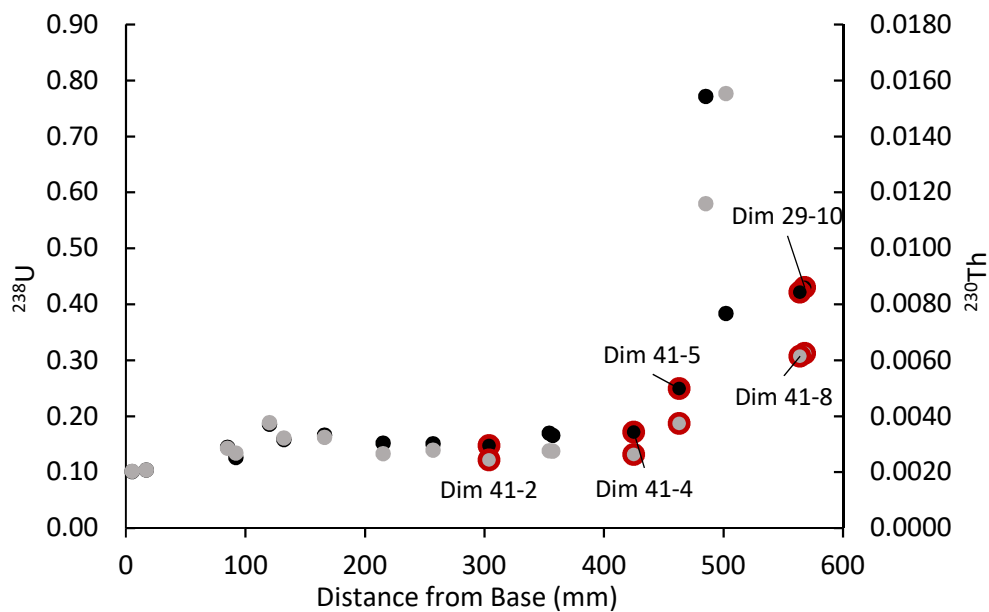
Figure 4.40: Changes in concentrations of ^{238}U (black) and ^{230}Th (grey) by sample depth in calcite samples of Dim-1. Samples discussed in this section are highlighted in red.

Dim 52-3 **127,816 ± 688**
Dim 29-10 **117,454 ± 588**
Dim 41-8 **117,201 ± 597**
Dim 52-2 **128.759 ± 687**
Dim 37-5 **129,199 ± 682**
Dim 29-9 **136,092 ± 809**
Dim 52-1 **127,825 ± 741**
Dim 41-6 **119,698 ± 610**
Dim 29-7 **120,695 ± 1,025**
Dim 41-5 **122,704 ± 659**
Dim 41-4 **126,377 ± 729**
Dim 37-3 **130,422 ± 831**
Dim 33-6 **125,439 ± 729**
Dim 41-2 **120,606 ± 642**
Dim 102-2 **128,986 ± 663**
Dim 102-1 **128,072 ± 670**
Dim 41-1 **126,234 ± 672**
Dim 33-4 **128,590 ± 696**
Dim 37-1 **129,439 ± 791**
Dim 37-4 **130,650 ± 682**
Dim 33-5 **119,973 ± 681**
Dim 29-6 **132.642 ± 1.363**
Dim 37-2 **131,412 ± 829**

40 mm

Representative photomicrograph of the sample region for Dim 29-10 and Dim 41-8. Aragonite from the layer is preserved (blue box) and an inclusion surface present (green box).

Dim 41-2 **120,606 ± 642** located over the trajectory (green line) of a dissolved aragonite layer (preserved in blue box)

Representative photomicrograph of the sample region for Dim 29-7 (upper) and 41-6 (lower). Dim 29-7 is comprised of aragonite with micro-dissolution surfaces (green dashed line). Dim 41-6 is located within alternating calcite and aragonite with dissolution.

Figure 4.41: Samples discussed in this section highlighted in black compared to neighbouring dates (grey) indicating dates are not stratigraphically coherent. Insets show macromorphology and examples of petrography in more localised areas.

4.3.4.4 Dim-1: Other Samples containing Micro-dissolution

Sample Name	Calcite/ aragonite	Depth from base (mm)	Date corr (yr BP)	Micro-dissolution
Dim 33-6	calcite	354	125,439 ± 729	Likely micro-dissolution (not covered by thin section)
Dim 41-1	calcite	166	126,234 ± 672	Micro-dissolution. Singular undulating inclusion horizon.
Dim 29-6	calcite	17	132,642 ± 1,363	Micro-dissolution. Inclusion horizons no altered extinction

Table 4.11: Dim-1 samples containing micro-dissolution surfaces which are not (or are unsure) related to aragonite dissolution.

Dim 33-6 was not covered by a thin section, but the sample trench is stratigraphically similar to Dim 37-3 and is therefore likely affected by dissolution of a former aragonite layer (see discussion of Dim 37-3). Moreover the age is in line with the trend of dates being too young, but there is no clear alteration of U series ratios or nuclide concentrations. The dates from calcitic samples Dim 29-6 and Dim 37-2 are stratigraphically reversed and micro-dissolution is apparent in Dim 29-6, possibly formed during a change in growth axis; again there is no clear disturbance in the U-series data. Dim 29-6 has a large age error that overlaps the basal sample 37-2 at 2 s.d. (Table 4.4).

The final date containing micro-dissolution and an apparent age error (possibly too young) is Dim 41-1 but there is again no clear deviation from the trend in U-series data to link it to disturbances in the system.
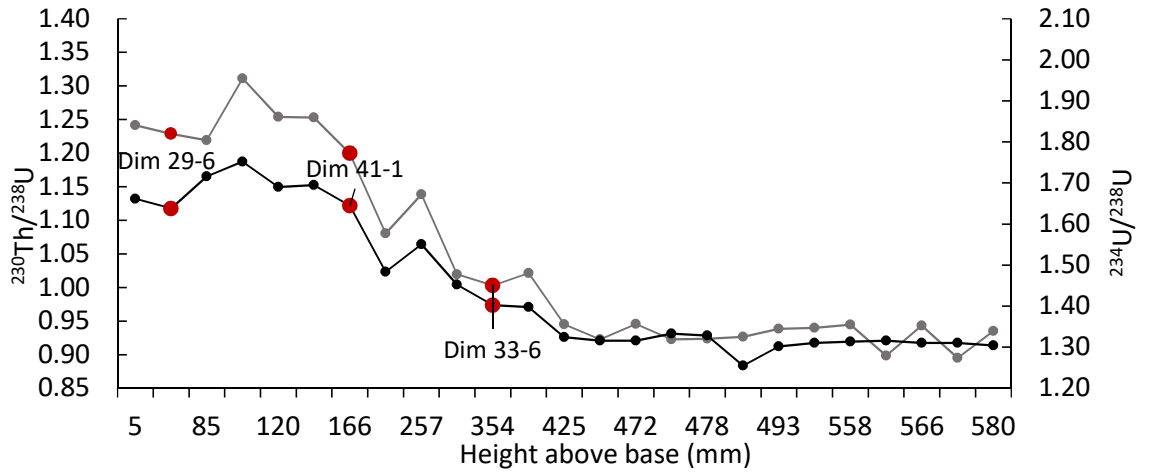
Figure 4.42: $^{234}U/^{238}U$ (black series) and $^{230}Th/^{238}U$ (grey series) relationship and variation against sample depth in Dim-1. Samples discussed in this section are highlighted in red.
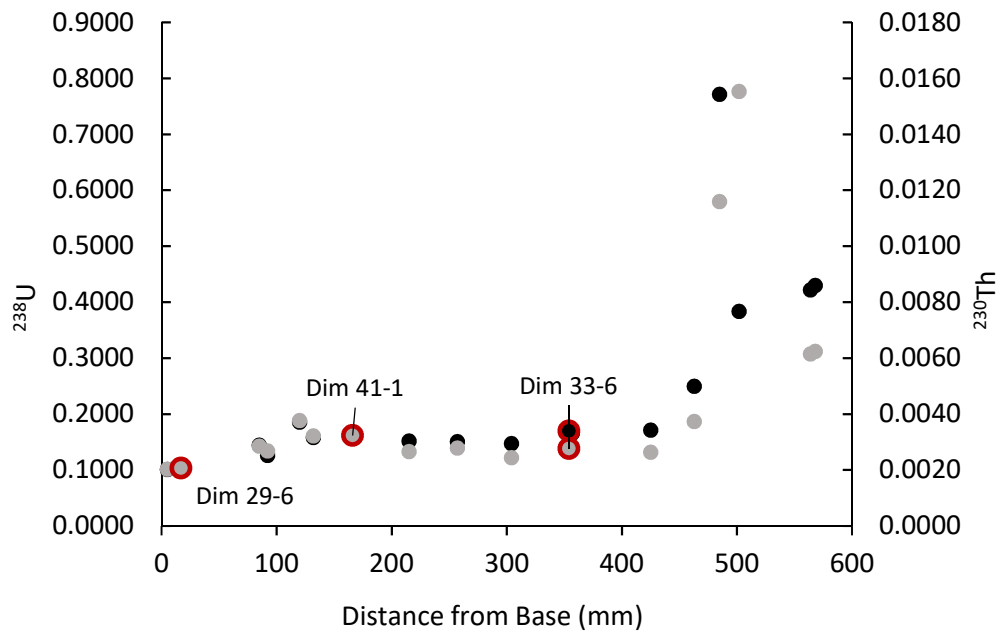
Figure 4.43: Changes in concentrations of ^{238}U (black) and ^{230}Th (grey) by sample depth in calcite samples of Dim-1. Samples discussed in this section are highlighted in red. ^{238}U concentrations of Dim 29-6, Dim 41-1 are located beneath the ^{230}Th value.
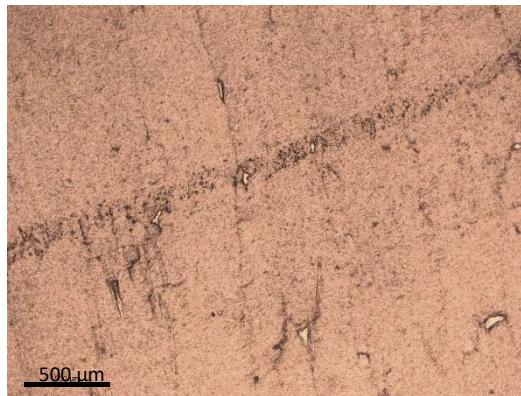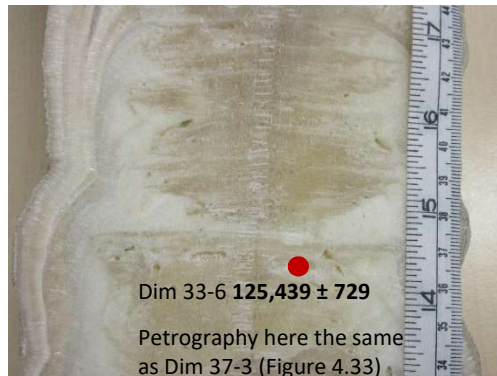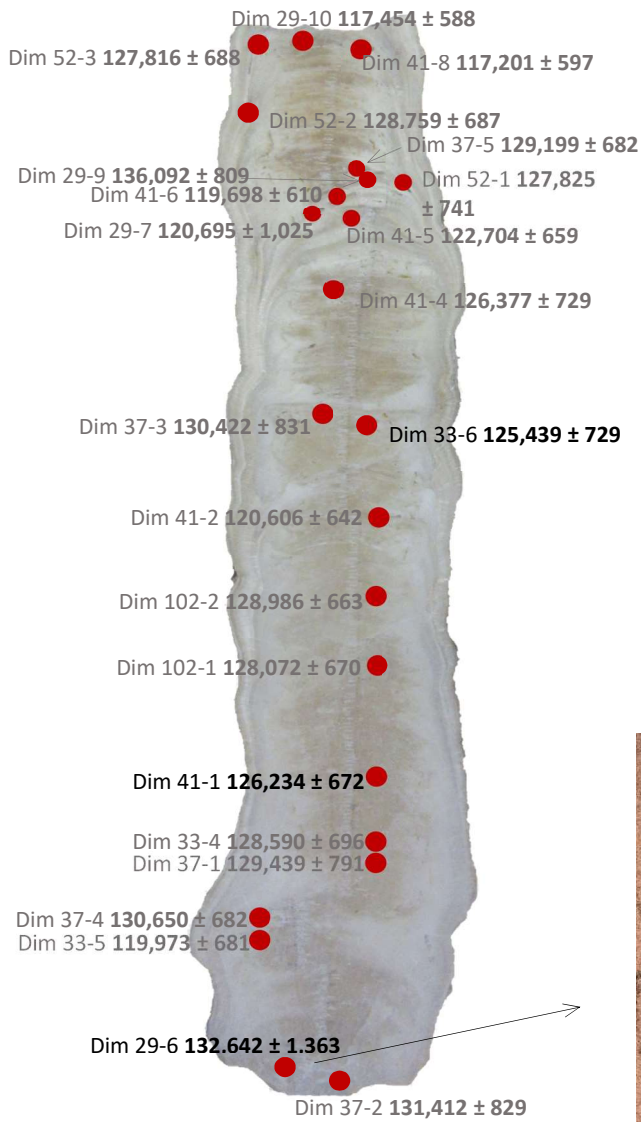
Figure 4.44: Samples discussed in this section highlighted in black compared to neighbouring dates (grey) indicating dates are not stratigraphically coherent. Insets show macromorphology and examples of petrography in more localised areas.

4.3.4.5 Age Model

Wickens (2013) suggested that a Dim-1 age model could only be created using aragonite samples, assuming that calcite present in Dim-1 was diagenetic. However, this research has shown that calcite is mostly of primary origin; therefore, samples from both aragonite and calcite can be used in the finalised dataset. The same approached used for HY-8, i.e., removing dates which showed both micro-dissolution and U-series anomalies, was used for Dim-1. This approach allows removal of both Dim 29-10 and 41-8 which are compromised by the same micro-dissolution surface: both these samples have lower relative ^{230}Th/^{238}U ratios compared to neighbouring samples. The samples both gave ages ~117,000 yr BP, and the removal of these samples means only dates which satisfy a youngest age of ~128,000 yr BP are included in the final age model (see also Section 4.3.4.3). Dim 41-1 does not show clear discrepancies in U-series data, but does not satisfy a youngest age of ~128,000 yr BP and is removed for this reason. The 1300 yr BP reversal in ages in samples Dim 29-6 and Dim 37-2 near the base of the stalagmite cannot be separated by U-series, but Dim 29-6 is associated with microdissolution, allowing its removal. Dim 37-3 does not contain micro-dissolution or an obvious anomaly in U-series, yet yielded a date around 2000 years too old to fit with the overall age model and so cannot be retained. Dim 52-3 is not included as it cannot be located on the central axis. The age model presented here is informed by both petrographic observation and U-series data; even when additional factors are taken into account, in an age model created by Rowe et al., (in prep), the two approaches yield similar outcomes.

Sample Name	Calcite/ aragonite	Depth from base (mm)	Date corr (yr BP)
Dim 52-2	aragonite	566	128,759 ± 687
Dim 52-4	aragonite	558	128,477 ± 689
Dim 52-5	calcite	472	128,198 ± 688
Dim 37-3	calcite	357	130,422 ± 831
Dim 102-2	calcite	257	128,986 ± 663
Dim 102-1	calcite	215	128,072 ± 670
Dim 33-4	calcite	132	128,590 ± 696
Dim 37-1	calcite	120	129,439 ± 791
Dim 37-4	calcite	92	130,650 ± 682
Dim 37-2	calcite	5	131,412 ± 829

Table 4.12: Ages used to create an age model for Dim-1 based on the findings of this study. Samples do not show evidence of micro-dissolution or U-series discrepancies.

4.3.4 Mechanisms for mobility of nuclides

U-series dating of stalagmites HY-8 and Dim-1 has highlighted that the assumptions required to retrieve correct ages from the U-series method may be violated under certain conditions, specifically the presence of micro-dissolution events which bring increased amounts of organic detritus into the stalagmite (HY-8) and micro-dissolution events which remove small amounts of aragonite from a predominantly calcitic stalagmite (Dim-1). However, there is no clear indication in either stalagmite of dates being consistently either too old or too young, suggesting there is not a single mechanism that causes inconsistencies in chronology.

In HY-8 there is a link between either multiple pervasive or large singular dissolution events; these allowed the input of elevated organic detritus and elevated ^{232}Th (and ^{230}Th), resulting in dates which are too old. However 2 dates contained micro-dissolution surfaces but no observable

discrepancies in U-series results and a further 2 dates (HY8 213 and HY8 399) contained micro-dissolution but did not appear to alter U-series or produce a stratigraphically incoherent age. Importantly these latter two dates showed significantly less micro-dissolution than other affected samples and therefore might suggest that singular micro-dissolution events may not have a big enough effect on U-series results.

In Dim-1 micro-dissolution removing aragonite does not have a uniform effect on U-series results. Most ages derived from samples containing micro-dissolution were too young, but these were arguably caused by both the addition and loss of both ^{238}U and ^{230}Th. Older dates were also derived from samples displaying both ^{238}U and ^{230}Th loss and addition. It is not possible to be confident about net nuclide migration as the data are insufficient to allow detailed interpretation. Three younger dates (Dim 52-1, Dim 29-10, Dim 41-8) were apparently caused by ^{230}Th loss alone. It was not possible to observe U-series discrepancies in 6 samples which contained micro-dissolution.

The following section considers plausible mechanisms for nuclide migration but further research is required to be more definitive.

4.3.4.1   Removal of U and Th

The incorporation of U within natural CaCO$_3$ is poorly understood. If U is mostly found in the calcite crystal lattice it should be difficult to remove without a large amount of leaching as natural calcite is stable for hundreds of thousands of years. Under laboratory conditions the majority of U appears to be incorporated directly as the uranyl ion into both polymorphs of CaCO$_3$. However there is no similar study of cave CaCO$_3$ (Reeder et al., 2001). Borsato et al. (2003) proposed that to create the U concentrations in their stalagmite (contributing to a ^{230}Th/^{238}U >1), as much as 89% of calcite needed to be leached if all U was locked in the lattice. It is difficult to estimate how much aragonite or calcite is likely to have been removed from samples which show relative depletion in U concentrations such as Dim-1 29-9 and HY8 161, but as the associated age inversions are not very large for their time periods (~ 9,000 yr BP and ~2,000 yr BP respectively) it seems improbable that it is great. As mentioned in Sections 4.3.4.2 and 4.3.4.3, samples in Dim-1, which can be directly associated with the removal of aragonite layers in the central axis can be used to estimate the former thickness of the layer based on the preserved thickness of aragonite at the flanks. This assumes the true thickness is preserved and that layers are always thicker in the central axis. This does not provide an upper limit which might be considerably more than 2-5 mm.

Although the total input of U associated with organic matter is unknown, U incorporated by association with organic material or adsorbed onto mineral surfaces, would allow easier pathways for the leaching of U from stalagmite $CaCO_3$ compared to within the crystal lattice (Borsato et al., 2003). Stalagmites with high organic material compositions in particular may have a higher amount of total U provided by this pathway than previously thought (e.g. Ivanovich and Harmon 1992 and references therein). This interpretation is potentially corroborated by the HY-8 stalagmite and particularly samples HY8 264 and HY8 293 which are located close to grey layers with known increased levels of organics. All these samples display high ^{238}U values with HY8 293 yielding the highest in the record (located above the grey layer set between 253-279 mm).

A problem arises when some dates in Dim-1, which appear to be too young, only show evidence for the removal of Th. There is no evidence for large influxes in organic material in Dim-1 but different, more easily leached inclusion pathways of ^{238}U and subsequent ^{230}Th could also go towards explaining the depletion in Th in Dim-1 samples. It is not possible to prove in the scope of this study that a larger proportion of U (and therefore decay produced ^{230}Th) than expected is adsorbed onto $CaCO_3$ surfaces rather than residing in the lattice in Dim-1. However, as it does not require significant removal or addition of Th to alter dates yielded by U-series (Borsato et al., 2003), it is possible that accompanying U removal may be too small to appear anomalous. Additionally, this mechanism could explain the disparity in samples of Dim-1 that show both older and younger dates with the removal/addition of ^{238}U and ^{230}Th. However, the amount of authigenic ^{230}Th available to remove would be minute as dissolution occurs very soon after $CaCO_3$ precipitation, which is a particular problem for the nearly 10,000 year differences in some of the Dim-1 dates.

4.3.4.2 Addition of U

As with removal of U, addition of U could be achieved assuming more U is incorporated through association with organics or colloids. This must occur a later date than the original deposition of $CaCO_3$ but the mechanism for this is unclear. Pore spaces may be important in retaining U released by dissolution of aragonite with a higher U content (Dim-1) or trapping U-rich organic matter (HY-8); both processes could increase the U content of the sample. However, if this happens on short timescales (as dissolution in HY-8 at least is likely to be) it is difficult to believe it can change the date of the sample significantly.

4.3.4.4 Addition of Th

In most HY-8 dates considered likely to be too old, there is evidence for addition of Th. The affinity of Th to organic and non-organic colloidal and particulate matter is well known (e.g. Ivanovich and Harmon 1992 and references therein). The solubility of Th can be greatly enhanced at realistic pH's by the presence of common inorganic ligands, including the HPO_4 ion at concentrations below pH 7 and organic ligands such as humic and fulvic acids below pH 8 (Langmuir and Herman 1980). Gaffney et al. (1992) further propose that the association of Th with organic material is more significant than with non-organic detritus. The tendency of Th to form strong complexes can increase its potential for transport by several orders of magnitude (Langmuir and Herman 1980). Elevated concentrations of ^{230}Th in samples HY8 19, 40 and 52, located within organic-rich grey layers and also HY8 264 and 293, occurring between and below grey layers respectively, concur with this behaviour. Samples with visible organic detritus were cleaned using an extra oxidising step which attempted to remove most of the organic material (see Methods Appendix). Additionally, inorganic detritus is accounted for by the ^{232}Th detrital correction applied to all dates. Despite this, elevated Th concentrations are still present and the ages inconsistent. The hypothesized amount of ^{230}Th required to disrupt the U-series system is a few 10^{-4} ppb (Borsato et al., 2003), the same order of magnitude of even the smallest amount of ^{230}Th addition in HY-8 samples. Possibly a more rigorous cleaning step needed was required to remove all organic detritus from samples, or the use of the bulk earth correction for detrital ^{232}Th is incorrect. The detrital correction is possibly inadequate for Th associated with organic matter as it may have a much higher U (and therefore ^{230}Th) content and lower ^{232}Th than rock or mineral detritus accounted for by the bulk earth correction. Alternatively, a process must occur which adds ^{230}Th independently of detrital ^{232}Th. The occurrence of such a process has been proposed as the cause of anomalously old ages in assumed zero age stalactites (Whitehead et al., 1999) and in known open system stalagmites (Borsato et al., 2003); no description of the mechanism was presented in either case.

Unlike ^{232}Th, ^{230}Th groundwater concentrations have two sources, detrital weathering and α-recoil (Porcelli and Swarzenski 2003). In limestone infiltrating groundwaters, ^{230}Th/^{232}Th ratios ranging from 1-1000 have been observed (Ivanovich and Alexander, 1987). Many values in this range are higher than the activity observed in the host rocks and could be related to either α-recoil or differential weathering of minerals bearing ^{238}U (^{230}Th) and ^{232}Th (Porcelli and Swarzenski 2003). To invoke Th anomalies by α-recoil derived ^{230}Th (and not detrital input) requires evidence of cave environmental conditions that increase the solubility of ^{230}Th allowing it to be leached from the host limestone.

Studies of alkaline lakes (pH ~ 10) found Th solubility increases with pH (i.e. Anderson et al., 1982; LaFlamme & Murray 1987; Östhols et al., 1994) leading to Th concentrations >100% higher than in seawater (Anderson et al., 1982). Increasing alkalinity increases Th-carbon complexes (Anderson et al., 1982; LaFlamme & Murray 1987, Östhols et al., 1994) and might also reduce Th adsorption on goethite (and presumably other common resistate compounds) through increased competition for surface sites by HCO_3^-; and CO_3^{-2} (LaFlamme & Murray 1987). It has been suggested that Th carbonate complexes cannot be ignored when determining the distribution of Th in natural waters (Östhols et al., 1994). Carbonate groundwaters are usually slightly alkaline and therefore a small effect could be present (Whitehead et al., 1999). This is an important consideration as an absolute amount of ^{230}Th of only a few 10^{-4} ppb could be enough to alter the U-series results (Borsato et al., 2003). If solubility in groundwater is enhanced enough, ^{230}Th may be easily available but this is not a requirement as typical ^{230}Th values for carbonate groundwaters are sufficient to alter U-series dates (Whitehead et al., 1999). This suggests that the process of dissolution associated with these layers was not synchronous with deposition of organic material, as the former requires slightly acidic waters, undersaturated with respect to $CaCO_3$.

The addition of ^{230}Th as an increased dissolved component affecting U-series dating of carbonate samples has only been applied convincingly to samples of the Pleistocene Lake Lahontan (Lin et al., 1996) and to U-series dating of deep sea coral (Cheng et al., 2000). In both studies the discrepancies are explained as a component of 'hydrogenous' ^{230}Th; the proportion of Th directly dissolved in the water column and not on the surface of continental detritus suspended within the water column (Lin et al., 1996). It must be noted however that the abundance of Th in lakes and seas is much higher than that of groundwater.

Chapter 5: Sirtlanini Cave, SW Turkey: A Record of Middle to Late Holocene Climate

5.1   Introduction

The petrography of HY-8 has been discussed in Chapter 4, in the context of attempting to resolve issues surrounding inconsistences in U/Th dating and to inform on the environment of formation. In this chapter the specifics of climatic information from HY-8 are discussed, with extensive cross-reference to Chapter 4 and introducing the geochemical data.

5.1.1 Sirtlanini Cave

Sirtlanini Cave is located close to the village of Çamarası in south west Turkey (Figure 5.1). The cave entrance is a narrow and tube and located 830 m.a.s.l. The cave comprises of two chambers on two different levels (Mason 2009) within karsified limestone. Epikarst thickness is roughly 25 m and a thin reddish soil above the cave supports sclerophyllous scrub (Mason 2009). In July 2006 the cave temperature was ~17 °C and humidity 100% (Mason 2009).
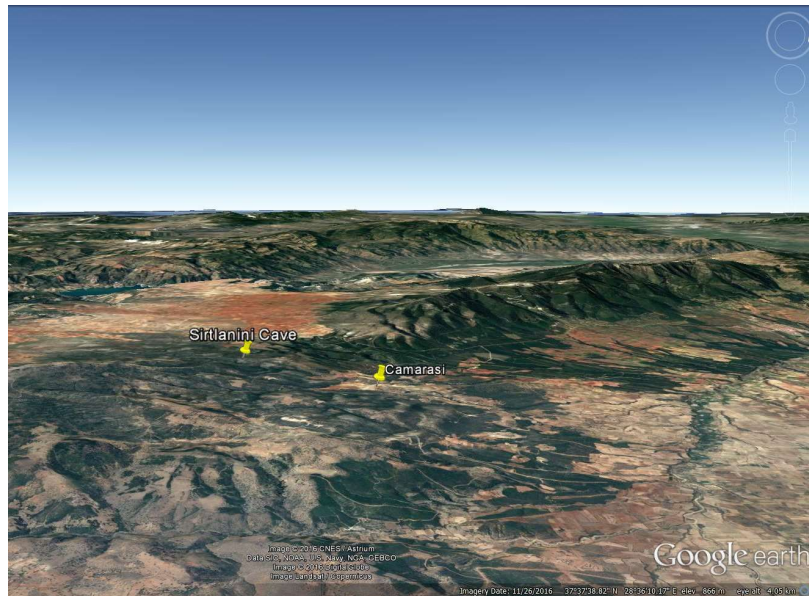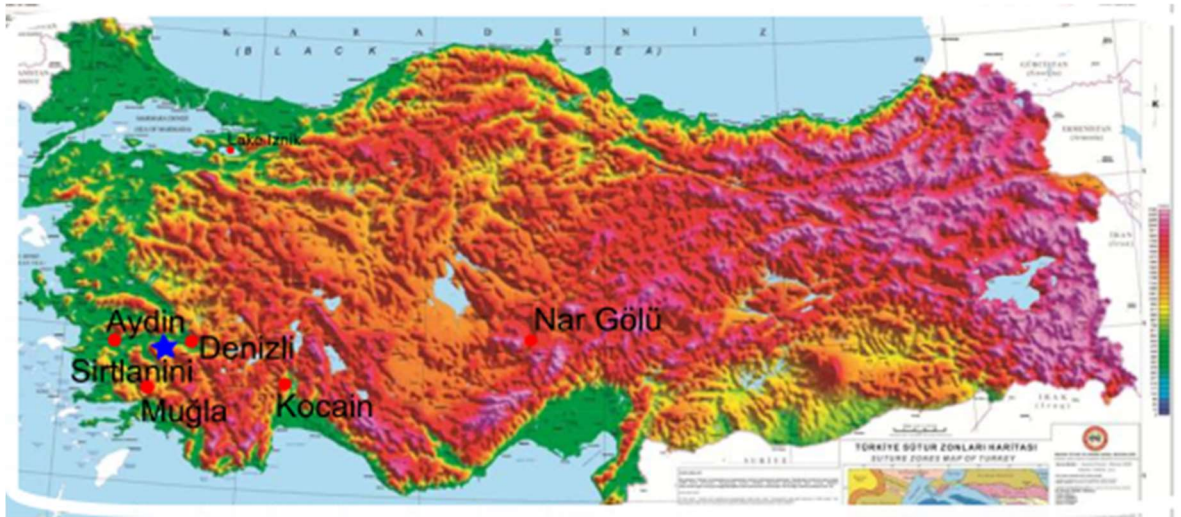
Figure 5.1: Location of Sirtlanini Cave in relation to closest towns and IAEA weather stations. Insets show a Google Earth image for topographic reference, looking west towards Aydin for Sirtlanini and the natural cave entrance.

Topographic map from the Turkish General Directorate Of Mineral Research And Explorations http://www.mta.gov.tr/eng/maps, green represents 0 m elevation, light purple 5000 m.

5.1.2. Stalagmite HY-8

Stalagmite HY-8 (total length 502 mm) was actively forming when collected in July 2006 from the second chamber, 40-45 m from the cave entrance (Mason 2009). Growth probably initiated during the late Pleistocene, but the majority of growth occurred during the Holocene (Chapter 4 Section 4.2.6, Table 4.3). The basal 68 mm of the stalagmite represents a very compressed sequence which has proved very difficult to date and thus most of the data discussed here comes from the mid-late Holocene sequence (Fig. 5.2) which encompasses 437 mm of calcite. Petrographic observation and U-series dating highlighted a major hiatus at 280 mm. Interpolation of ages from the age model date the hiatus to 1700 to 1380 yr BP (Section 5.2.2.3). A distinct period of lamination is present between 287- 403 mm.

Top

Upper

Lower

Base
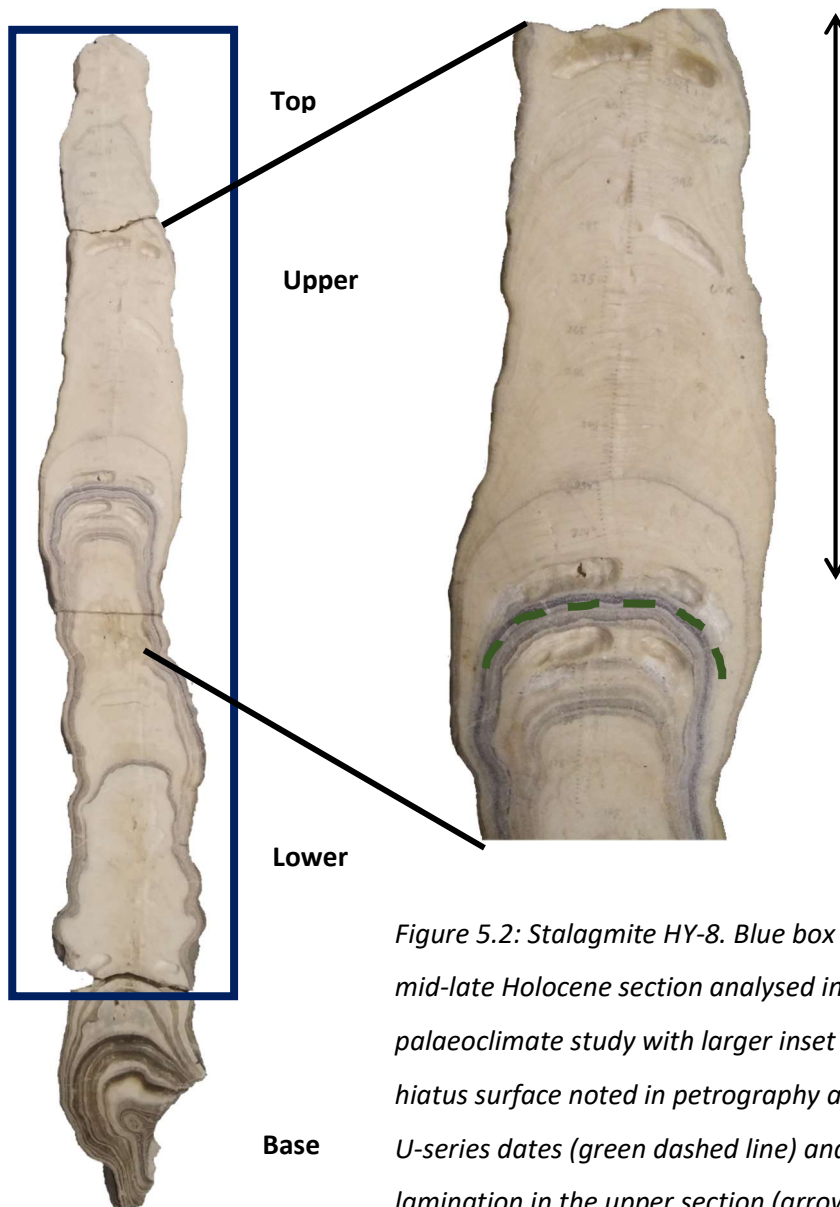
Figure 5.2: Stalagmite HY-8. Blue box highlights the mid-late Holocene section analysed in the palaeoclimate study with larger inset highlighting the hiatus surface noted in petrography and confirmed by U-series dates (green dashed line) and the extent of lamination in the upper section (arrows).

5.1.3 Modern climate and groundwaters

The region of Sirtlanini Cave is within the Mediterranean climate regime of Turkey (Türkeş, 1996) (Figure 5.3), defined by hot, arid summers and mild, wet winters. This is well corroborated by modern precipitation and air temperature averages for nearby weather stations (and from publications) as described in Chapter 4 Section 4.1.4.1. The closest weather stations to Sirtlanini (Muğla and Aydin) record just a few years (1994-1995 and 1987-1993 respectively) of precipitation isotope data (see Appendices). The nearest station with a large dataset of isotopes in precipitation is the Antalya IAEA record. This record is near complete between 1963 and 2015 and is categorised in the same rainfall regime (Türkeş 1996). However, the station is coastal, not within the interior, and at sea-level not high elevation. The average annual precipitation at Antalya (1099 mm) is higher than the average estimated for Sirtlanini (~700 mm, Türkeş 1996). A full discussion of precipitation and air temperature records from Antalya is discussed in Chapter 4, Section 4.1.4.2.
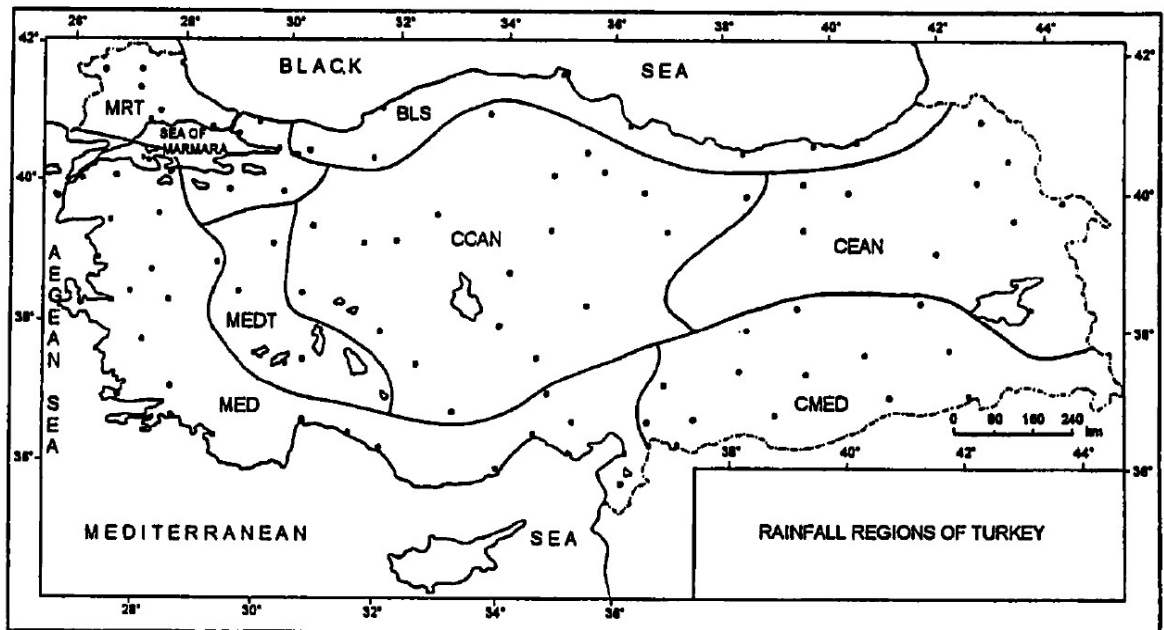
Figure 5.3: Rainfall regions of Turkey from Türkeş (1996).

Antalya precipitation shows a general trend to higher isotopic values in warmer months and lower isotopic values in colder months (Figure 5.4). Peak values in both $\delta^{18}O$ and $\delta^{2}H$ occur in August and September. The rise in isotopes is fairly gradual from March to June but the corresponding autumn decline occurs very rapidly in October from the September peak. A clear negative shift in oxygen and carbon isotopes in observed in July, although this month has a low sample number due to sparse rainfall events that are typically larger than at other times (see Appendices). In Antalya, larger summer precipitation events (>25 mm or greater) have frequency of about 20 years (Çiçek et al., n.d.) and are largely facilitated by its low elevation at the base of the Taurus Mountains and the effect of orographic uplift (Sensoy 2004). Isotope composition in rainfall of this type is controlled by the amount effect with higher precipitation events characterised by more negative values, skewing the July average towards negative values. Figure 5.5 shows a weak positive correlation (R^2= 0.19) between air temperature and $\delta^{18}O$ suggesting that temperature dependence also has some effect on the isotopic fractionation and composition of precipitation ~0.19 ‰/°C (Figure 5.5B) A very weak negative correlation (R^2=0.1) is observed between $\delta^{18}O$ and precipitation amount (Figure 5.5). Figure 5.6 shows the average monthly precipitation amount and its effect on $\delta^{18}O$, highlighting a strong positive correlation (R^2 =0.83) between lower precipitation amounts and heavier $\delta^{18}O$. This suggests that the dominant control on isotopes in the region of Antalya is likely to be the amount effect.

	Antalya Precipitation (%)	Average $\delta^{18}O$ Antalya (‰VSMOW)
Winter	56.5	-6.00
Spring	17.9	-4.14
Summer	2.4	-3.55
Autumn	23.1	-4.14

Table 5.1: Percentage contributions of rainfall per season and average $\delta^{18}O$ values for the Antalya IAEA station during the period 1963-2015.
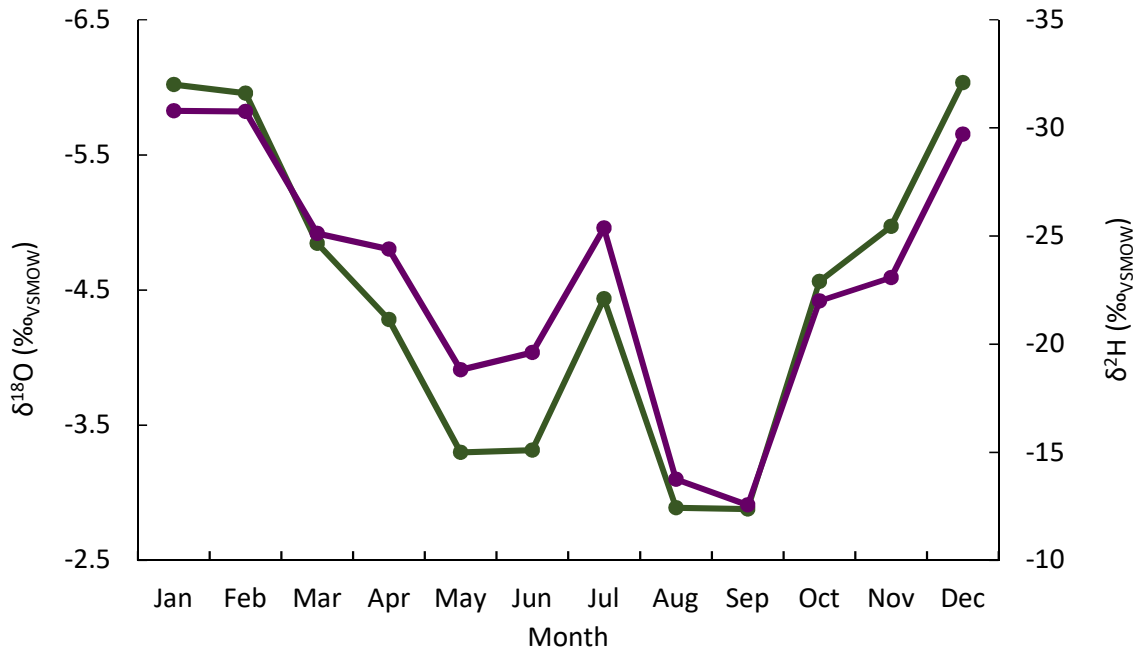
Figure 5.4: Monthly variation in $\delta^2 H$ and $\delta^{18}O$ for the Antalya weather station during the period 1963-2015. Strong seasonal differences are observable in both isotopes, with August and September showing peak values and roughly similar low values during the winter months. Anomalously light isotopes in July are bolstered by extreme rainfall events which are characteristically lighter in composition.
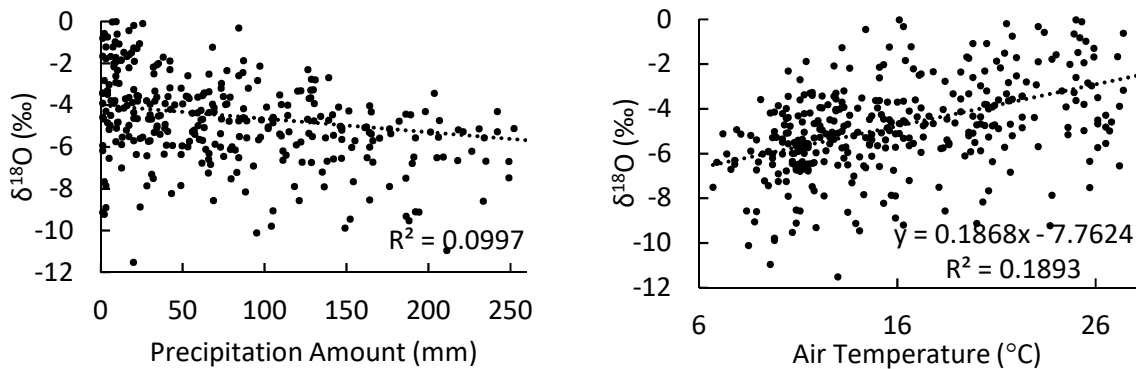
Figure 5.5: $\delta^{18}O$ vs air temperature and $\delta^{18}O$ vs precipitation amount, Antalya for the same period as Figure 5.3. Statistical correlation for precipitation amount and $\delta^{18}O$ is low and slightly negative. Statistical correlation for air temperature and $\delta^{18}O$ is quite low but does show positive correlation.
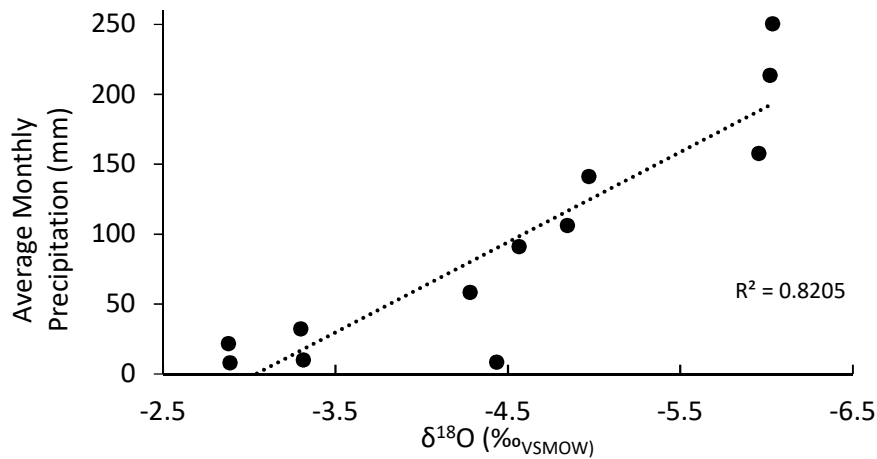
Figure 5.6: δ¹⁸O vs precipitation amount by month at Antalya. A strong positive correlation is observed between wetter months and lighter δ¹⁸O values.

The similarities between IAEA Antalya precipitation values, interpolated precipitation for the Sirtlanini Cave region (Bowen 2016 www.waterisotopes.org, Table 5.2) and cave waters (Mason 2009, Table 5.3) are presented with respect to the Global Meteoric Water Line (Craig 1961, Equation 5.1), Mediterranean Meteoric Water Line (Gat and Carmi 1970, Equation 5.2) and Western Anatolia (including Aydin) local meteoric water line (Simsek 2003, Equation 5.3) in Figure 5.7. The LMWL has the same slope as both the MMWL and GMWL and sits directly between the two. Both the OIPC interpolation and Antalya precipitation plot between the MMWL and GMWL suggesting a mixed source for precipitation, although much of the OIPC data plot closer to the GMWL. Cave waters collected in July 2006 are most similar to the isotopically lighter Sirtlanini precipitation compositions, suggesting that winter recharge is dominant and largely not replaced by summer recharge.

$$\delta^2H = 8\ \delta^{18}O + 10\ (‰_{VSMOW})$$

Equation 5.1: Global Meteoric Water Line (Craig 1961)

$$\delta^2H = 8\ \delta^{18}O + 22\ (‰_{VSMOW})$$

Equation 5.2: Eastern Mediterranean Meteoric Water Line (Gat and Carmi 1970)

$\delta^2H = 8\ \delta^{18}O + 16\ (‰_{VSMOW})$

Equation 5.3: Western Anatolia (including Aydin) local meteoric water line (Simsek 2003)

	Jan	Feb	Mar	Apr	May	Jun	Jul	Aug	Sep	Oct	Nov	Dec
δ^2H (‰$_{V-SMOW}$)	-51	-46	-44	-38	-34	-33	-27	-25	-22	-32	-37	-45
$\delta^{18}O$ (‰$_{V-SMOW}$)	-8.4	-7.7	-7.1	-6.2	-5.7	-5.2	-4.8	-4.1	-4.3	-5.7	-6.9	-7.8

Table 5.2: OIPC isotopic estimates of precipitation for the geographical position and altitude of Sirtlanini Cave

	$\delta^{18}O$ (‰$_{VSMOW}$)	δ^2H (‰$_{VSMOW}$)
Drip 1	−7.1	−42.6
Pool	−7.8	−43.9
Spring 1	−7.2	−43.5
Spring 2	−7.2	−39.7

Table 5.3: Cave water isotopes obtained during the collection of stalagmite HY-8 in July 2006 (Mason 2009).
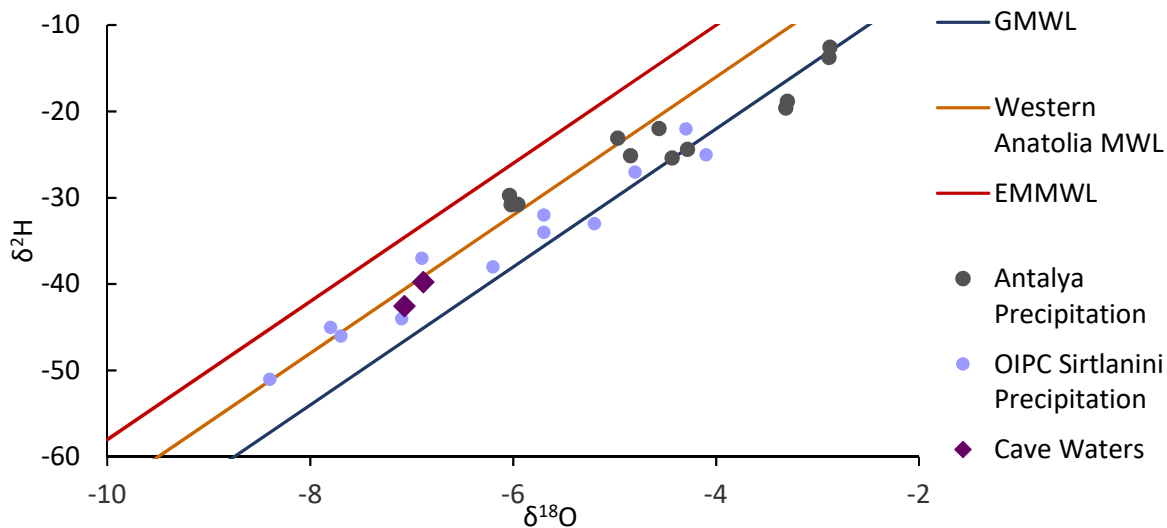
Figure 5.7: Average monthly isotopic compositions of the IAEA Antalya station 1963-2015 (green circles) are plotted with OIPC calculated isotopic composition of precipitation in the region of Sirtlanini Cave (blue circles) (www.wateriso.utah.edu/waterisotopes/pages/data_access/oipc.html) and cave waters sampled in July 2006 (purple diamonds, see Table 5.3) The Global Meteoric Water Line $\delta^2H = 8 \delta^{18}O + 10$ (Craig 1961), Eastern Mediterranean Meteoric Water Line $\delta^2H = 8 \delta^{18}O + 22$ (Gat and Carmi 1970) and Western Anatolian local meteoric water line $\delta^2H = 8 \delta^{18}O + 16$ (Simsek 2003) are also shown. OIPC calculates the isotopic composition at any given latitude, longitude and altitude by interpolating from known IAEA station data.

5.2   Results

5.2.1 Macromorphology and Petrography

The macromorphology and petrography are described in Chapter 4 Sections 4.2.1 and 4.2.2.

5.2.2 U-series dating

5.2.2.1 Sampling strategy

HY-8 had 4 initial dates from Mason (2009), thus the sampling strategy was first aimed at increasing the dating density to improve the robustness of the chronology, and to better constrain the timing of important macromorphological features, such as grey layers. However, as discussed fully in Chapter 4, successive U-series batches produced multiple inconsistencies in the apparent ages, including attempts to replicate the pre-exisiting dates. In total 24 new dates were obtained encompassing the full length of HY-8 (Chapter 4 Section 4.2.6, Table 4.3). Nine dates from this research were used to construct the age model and a date of 5593 +/- 212 yr BP (Mason 2009); which was included as stratigraphically lower dates from this study were not viable.

5.2.2.2 Lamination counting

The development of lamination between 287 and 403 mm was possible to count (method listed in Methods Appendix) and thus was added to the age model as COPRA is able to incorporate lamination counts into its simulations of age models (Breitenbach et al., 2012). From repeat counts an average of 429 laminae were counted.

5.2.2.3 Age model and growth rates

Based on findings in Chapter 4, and following from discussion in Section 4.3.7.1, of the 24 dates obtained from HY-8 only 9 were suitable for use in the construction of an age model. Ages from the basal section of the stalagmite (Figure 5.2) are discussed fully in Chapter 4, but as they were from samples in a portion of compressed stratigraphy they also are not included in the age model. In addition, reversals in ages between 4 samples in the interval ~5000- 4000 yr BP allow two slightly different age models, depending which two samples are selected HY8 110 and HY8 174, or HY8 105 and HY8 147 (Section 4.3.7.1). Ages used in the age model are listed in Table 5.4.

Sample Name	Height above base (mm)	U (ppm)	230Th (ppb)	232Th (ppb)	234U/238U	230Th/238U	230Th/ 232Th	Initial 234U/238U	Date uncorr (yr BP)	Date corr (yr BP)
HY8 484	484	0.211242	0.0000275	0.085670	1.0169 ± 0.002	0.0064 ± 0.0001	48.9	1.0170 ± 0.002	706 ± 9	627 ± 12
HY8 399	399	0.260599	0.0000474	0.112398	1.0168 ± 0.002	0.0090 ± 0.0001	64.2	1.0169 ± 0.002	980 ± 8	904 ± 12
HY8 364	364	0.260229	0.0000478	0.254460	1.0176 ± 0.001	0.0110 ± 0.0002	35.19	1.0177 ± 0.001	1219 ± 10	1124 ± 23
HY8 293	293	0.405539	0.0000861	0.685933	1.0196 ± 0.001	0.0126 ± 0.0004	23.55	1.0197 ± 0.001	1409 ± 11	1296 ± 37
HY8 264	264	0.209079	0.0000976	0.356700	1.0340 ± 0.001	0.0283 ± 0.0004	51.32	1.0342 ± 0.001	3077 ± 18	2964 ± 39
HY8 250	250	0.081028	0.0000479	0.130506	1.0305 ± 0.002	0.0360 ± 0.0004	68.77	1.0308 ± 0.002	3921 ± 32	3810 ± 46
HY8 213	213	0.07593	0.0000494	0.146663	1.0236 ± 0.002	0.0369 ± 0.0005	58.75	1.0238 ± 0.002	4075 ± 38	3937 ± 55
HY8 174	174	0.065252	0.0000467	0.143617	1.0262 ± 0.002	0.0436 ± 0.0005	61.04	1.0265 ± 0.002	4795 ± 39	4665 ± 60
HY8 110	110	0.077948	0.0000571	0.154776	1.0288 ± 0.002	0.0446 ± 0.0005	69.14	1.0292 ± 0.002	4889 ± 30	4765 ± 51
HY8J 75	75	0.067263		0.652133	1.0114 ± 0.004	0.0505 ± 0.0009	50.14	1.0116 ± 0.004		5593 ± 212

Table 5.4: U series data from HY-8 used in the construction of the final age model. All errors are 2 s.d. Age corrections assume a bulk earth composition

for the detrital Th component. This assumes stalagmite calcite is at secular equilibrium with the bulk earth $^{232}Th/^{230}Th$ value (3.8) and that initial

$^{230}Th/^{232}Th$ has an atomic ratio of 4.4 ± 2.2 x10^{-6}. Uncertainty errors are ± 50%.

The age model covers the time period from 5640 yr BP to the present day (2006) and was generated using COPRA (Breitenbatch et al., 2012: see Figure 5.9). A clear hiatus is present at 280 mm, visible in the petrography as a micro-dissolution surface at the end of grey layer deposition (Chapter 4, Section 4.2.2, Figure 4.7 B) and growth at this point was much slower than the rest of the stalagmite. Interpolated ages suggest growth cessation started at 1700 yr BP; growth before the hiatus was generally slower than growth following it. This excludes the period 4765-4665 yr BP which shows the fastest growth rate of 0.64 mm/yr. Growth during formation of laminated section was initially fast (0.41 mm/yr) until 1124 yr BP and then slowed as lamina formation ceased at 904 yr BP (0.16 mm/yr).

HY8 484 **627 ± 12**

HY8 399 **904 ± 12**

HY8 364 **1124 ± 23**

HY8 293 **1296 ± 37**

HY8 264 **2964 ± 39**

HY8 250 **3810 ± 46**

HY8 213 **3937 ± 55**

HY8 174 **4665 ± 60**

HY8 110 **4765 ± 51**

HY8J 75 **5593 ± 212**

15 mm
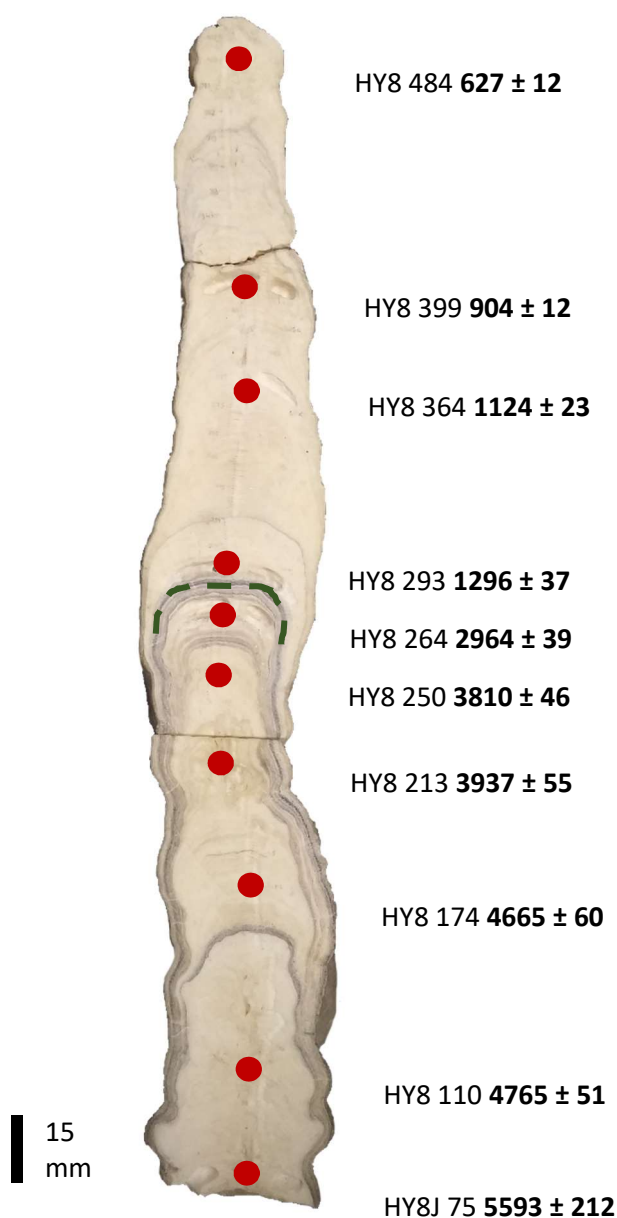
Figure 5.8: Slabbed section of the mid Holocene section of HY-8 with sample locations for U-series dating and dates used to construct the age model. Ages in yr BP.
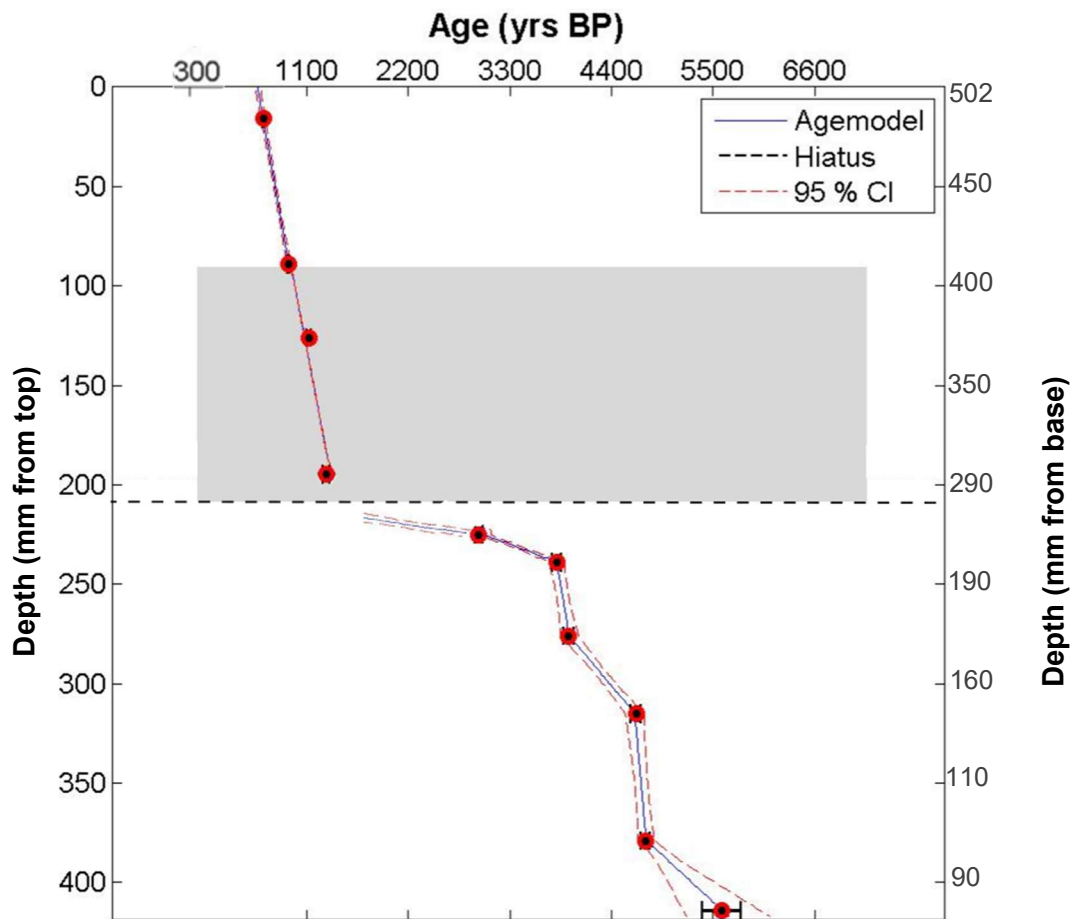
Figure 5.9: Age model for HY-8 generated from COPRA. Dashed horizontal line indicates the hiatus at 280 mm (figure shows the top as 0 mm), grey area shows the section where layer counting was performed and added to increase accuracy.

The StalAge algorithm also struggles to produce a viable age model and the result is difficult to compare to the COPRA model as age errors on palaeoclimatically significant dates vary widely (Table 5.5). One of these is the significantly older date of 2764 yr BP than COPRA (1379 yr BP) at the same depth in the stalagmite as the supposed restart of growth following the hiatus. Although petrographically a hiatus is indicated at 280 mm from the top the ages, above and below (2964 yr BP and 1296 yr BP) are resolved in the StalAge algorithm as a period of very slow growth (Figure 5.10). In an attempt to counteract this a second age model (Figure 5.11) was produced using the upper section of HY-8 taking the hiatus as the base. This age model gave an age of the restart of growth as 1641 yr BP producing an unrealistic growth rate and an age model which was not viable. The final option to attempt to resolve this is to perform a linear regression on the dates in the upper part of the stalagmite following the hiatus. The linear regression gives an age for the restart of growth at about ~1420 yr BP (Figure 5.12), which is closer in age to that given by

COPRA. This finding allows slightly more faith to be placed in the COPRA age model and its continued use within this research.
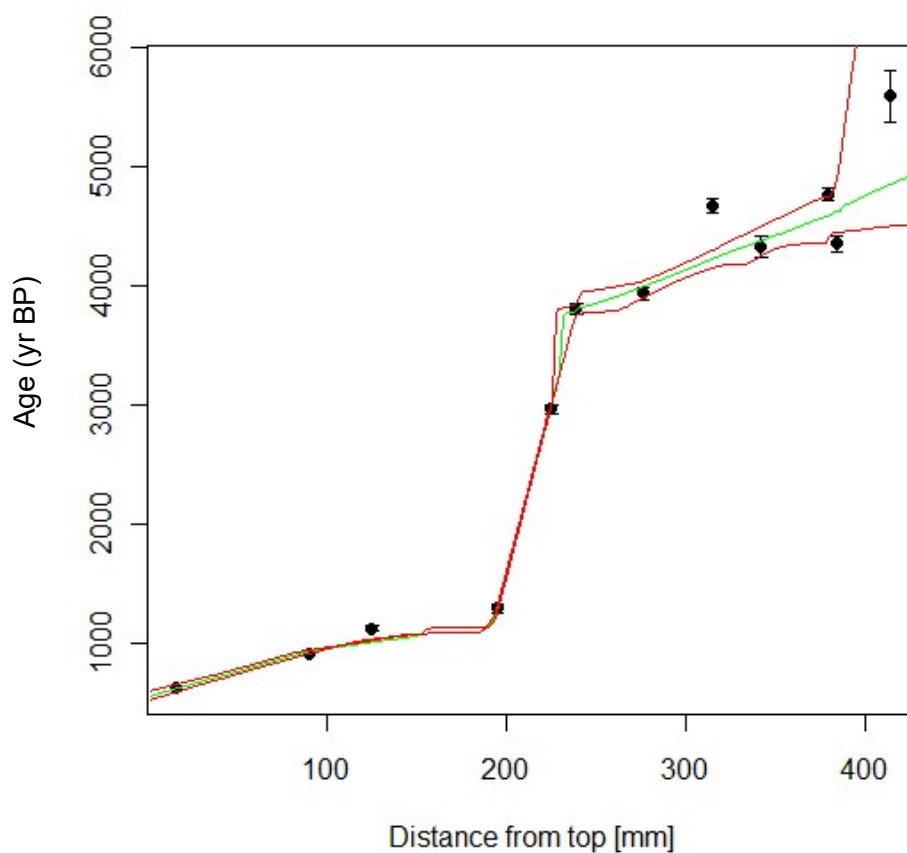
Figure 5.10: Alternative solution for the HY-8 age model presented from StalAge. The StalAge algorithm does not place a hiatus at 280 mm where it appears petrographically there should be. This period is designated as a period of very slow growth. This causes a significant difference within the two age models of well over 1000 years. Red line represents the error at 2 s.d.
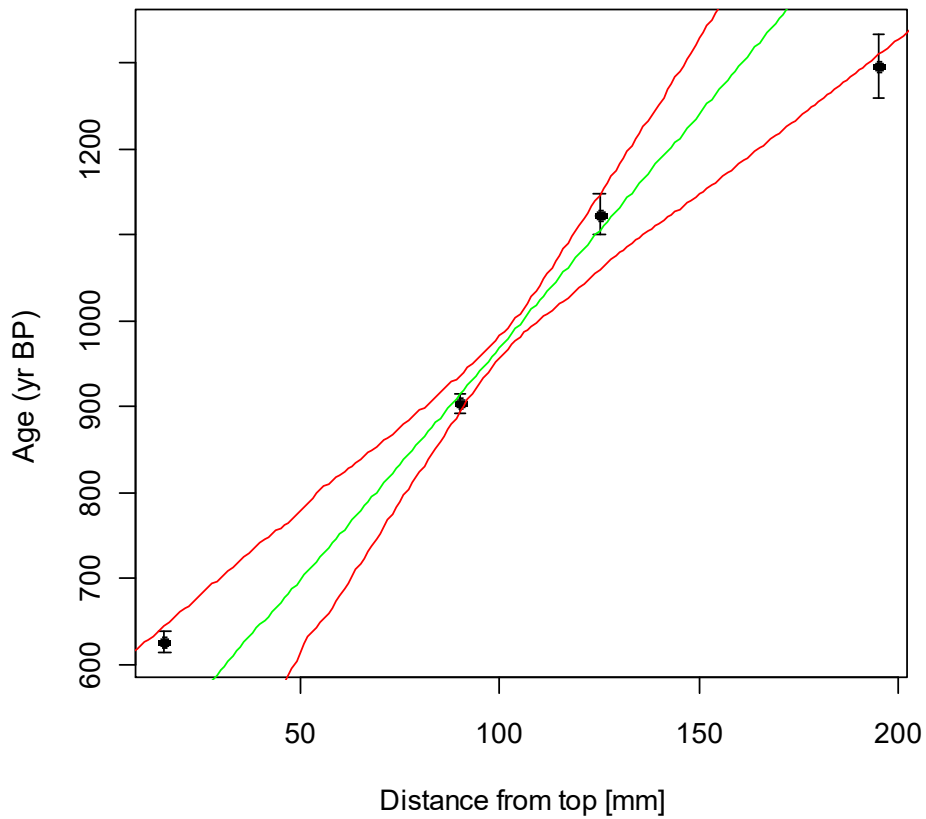
Figure 5.11: Dates from the upper section above the hiatus of HY-8 produce an unrealistic age model from StalAge.
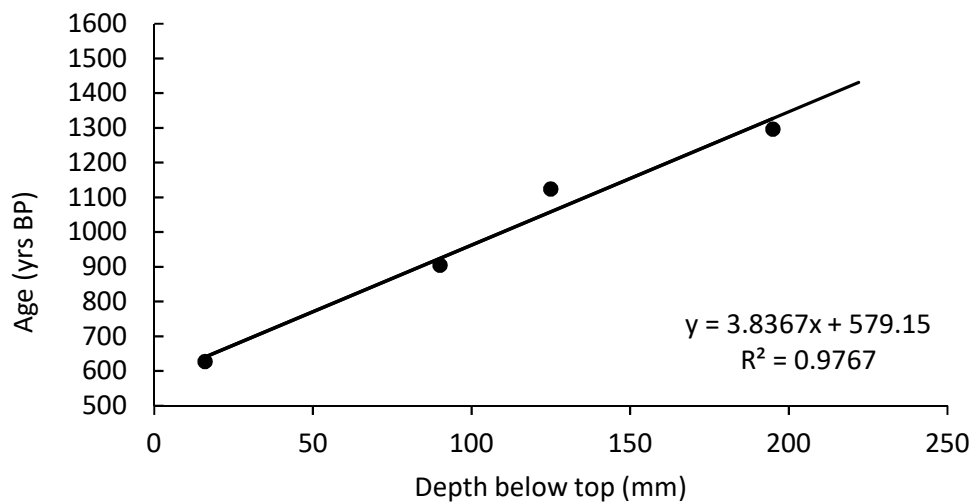
Figure 5.12: Linear regression of the 4 U-series dates located above the hiatus at 280 mm.

Depth (mm from base)	Depth (mm from top)	COPRA (yr BP)	StalAge (yr BP)	StalAge (yr BP) Upper Section	Minimum unknown age error (yr BP)	Minimum unknown age error (yr BP)
156	356	4680	4456		224	
196	316	4197	4233		36	
259	253	3386	3872		486	
291	221	1379	2764	1640	1385	261
481	31	282	681	478	399	196

Table 5:5: Comparison of 5 key ages which are palaeoclimatically or stratigraphically significant in HY-8. Dates which are also present in the age model for the upper section are presented twice with results from both StalAge age models.

5.2.2 Stable Isotopes

5.2.2.1 Sampling strategy

As HY-8 has the potential to record events in the mid-late Holocene, a 1 mm sample spacing was achieved, building on the 5 mm spacing of Mason (2009). Between 197 and 205 mm a large amount of vugs concentrated down the central axis of the stalagmite made sampling difficult. Due to this 8 mm of samples are missing from this region. The frequency of lamination between 1296 and 904 yr BP also indicated an opportunity for a seasonal signal to be obtained. To explore the potential for recovery of a seasonal signal a 6 mm thick sub section of the laminated zone, estimated to have formed during 1160-1120 yr BP, was micromilled. Forty laminae were identified by petrography but of these only 22 alternating light and dark laminae are visible in hand specimen (Figure 5.16); each of these 22 laminae was sampled.

5.2.2.2 Full axial profile

The stable isotope datasets with 5th order polynomials applied to highlight isotopic trends are shown in Figure 5.14. Prior to the hiatus, $\delta^{18}O$ shows high frequency oscillations with an amplitude of up to 1.5 ‰ around a mean of −6.26 ‰. A clear increase is observed leading up to the cessation of growth (1700 yr BP) starting at 2200 yr BP. At the restart of growth ~1380 yr BP

the first $\delta^{18}O$ value is depleted by 1 ‰ relative to those immediately prior to the hiatus but overall $\delta^{18}O$ values are not dissimilar to values before 2200 yr BP. From 1380 yr BP to present a gentle trend to lighter oxygen values is observed with an overall decrease of 0.5‰. Variation about the mean (range in values −4.35 ‰ to −7.53 ‰) is high in $\delta^{18}O$.

From 5600 yr BP to 4890 yr BP, $\delta^{18}O$ values are enriched relative to the mean by ~0.2 to 0.6 ‰ aside from a short period of more negative $\delta^{18}O$ from 4850 yr BP to 4820 yr BP. This interval is also punctuated by a large $\delta^{18}O$ enrichment peaking at −5 ‰ between 4765-4665 yr BP which occurs during a rapid growth period (Section 5.2.2.3). A second rapid growth period occurs between 3940 and 3810 yr BP during which reach peak $\delta^{18}O$ enrichment for the record (−4.35 ‰) at 3850 yr BP.

Similarly to $\delta^{18}O$, $\delta^{13}C$ values prior to the hiatus are stable about a mean of −8.4 ‰. The range in values in $\delta^{13}C$ is also large (−6.12 ‰ to −10.75 ‰) with mostly high variability. Some co-variation is observed in $\delta^{18}O$ and $\delta^{13}C$ but statistical correlation is very low (Figure 5.13). Values of $\delta^{13}C$ are frequently ~1.5 ‰ higher than the mean from the start of growth at 5600 till 3800 yr BP. Following the hiatus $\delta^{13}C$ is depleted by 0.5 ‰ compared to the values before it. A further significant 1.75 ‰ negative shift in $\delta^{13}C$ occurs at 400 yr BP until present.

Two clear positive excursions >2.5 ‰ peak at 3340 yr BP and 2300 yr BP respectively with the former accompanied by a 1 ‰ positive excursion in $\delta^{18}O$.
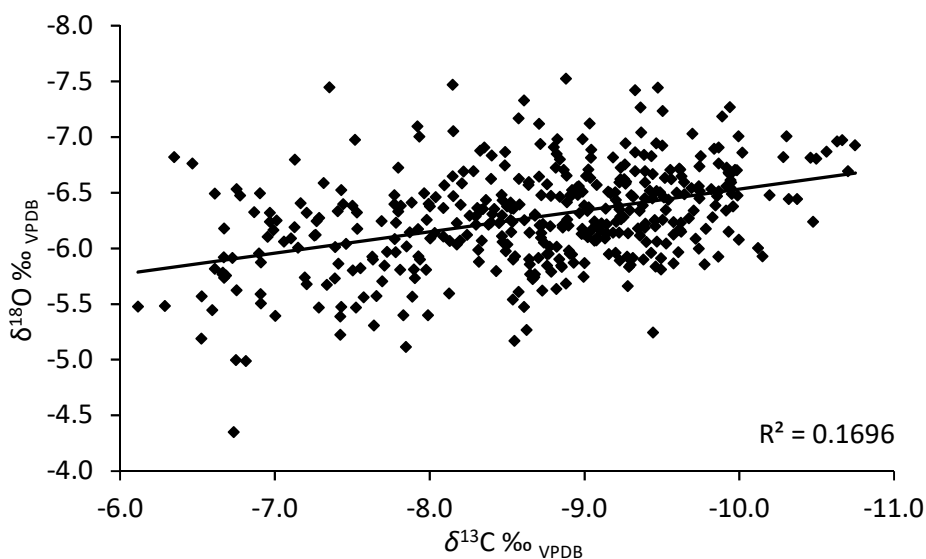
Figure 5.13: Cross plot showing the relationship between $\delta^{13}C$ and $\delta^{18}O$. The correlation (0.17) is very low, showing very weak correlation.
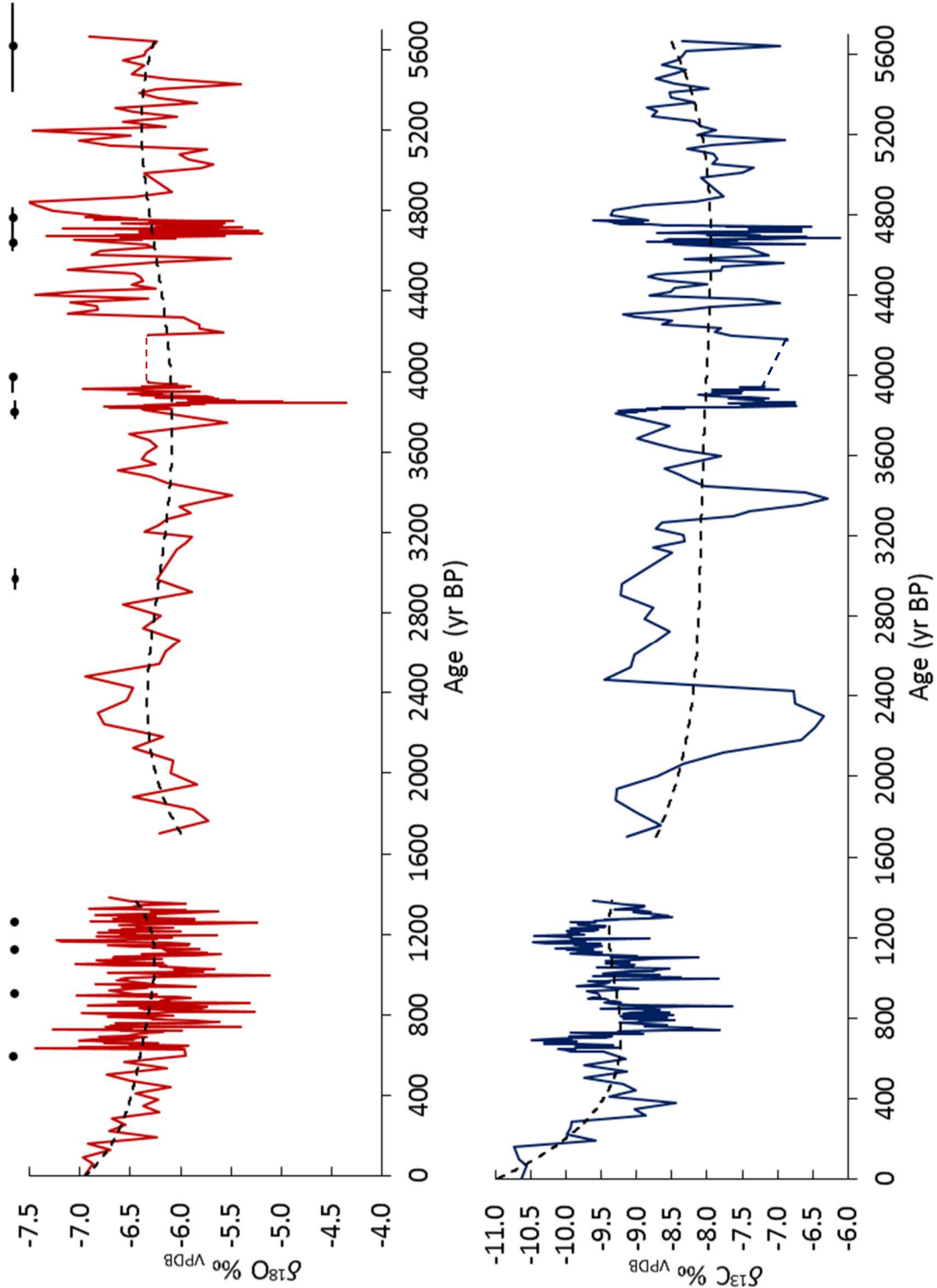
Figure 5.14: Axial stable isotope profiles for the mid Holocene section of HY-8. $\delta^{18}O$ is above in red, $\delta^{13}C$ below in blue. The region of missing samples between 197 and 295 mm from the base is represented by dashed lines in both profiles.

161

5.2.2.3   Laminated sub-section

Both $\delta^{18}O$ and $\delta^{13}C$ in the laminated sub section show a decreasing trend between approximately 1160 yr BP and 1120 yr BP (Figure 5.15). Oxygen and carbon isotopes appear to co-vary although the statistical relationship is not strong (0.38, Figure 5.16). $\delta^{13}C$ shows some negative excursions which are not present in $\delta^{18}O$. The ranges are narrow in both varying from −5.5 ‰ to −6.5 ‰ in $\delta^{18}O$ and −9.15 ‰ to −10.2 ‰ in $\delta^{13}C$.
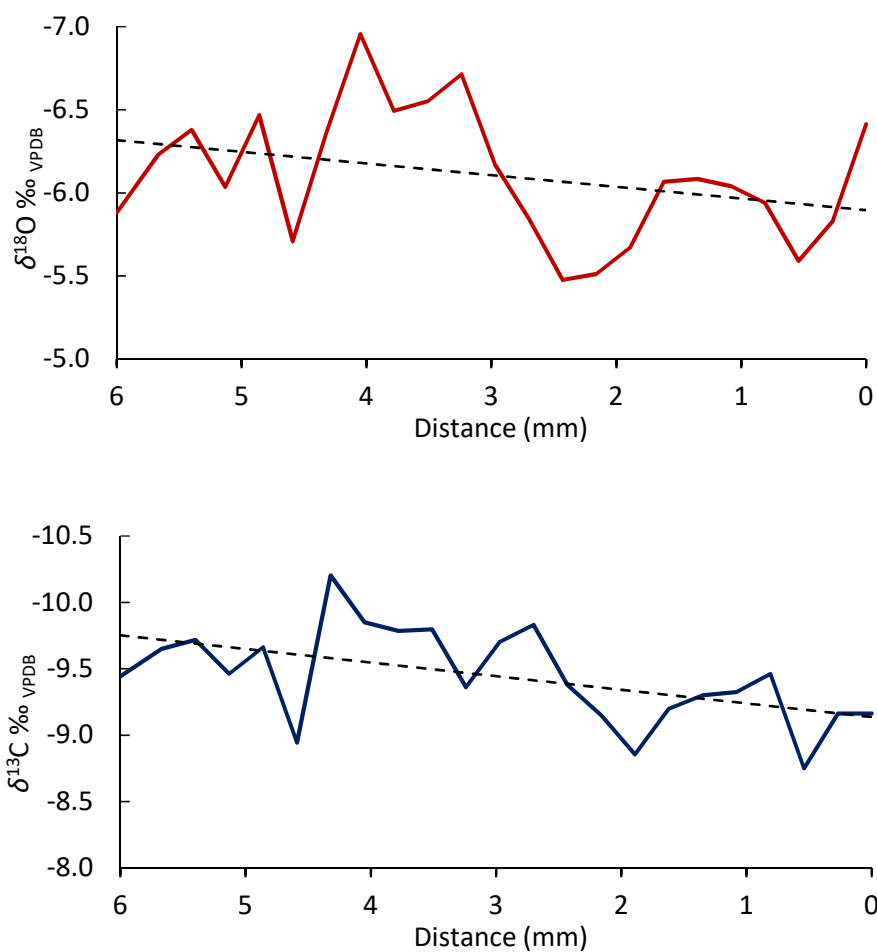
Figure 5.15: Stable isotope profiles for the 6 mm transect, which has the approximate age of 1.16-1.12. 22 samples are presented, roughly half the number counted. $\delta^{18}O$ is above in red, $\delta^{13}C$ below in blue.
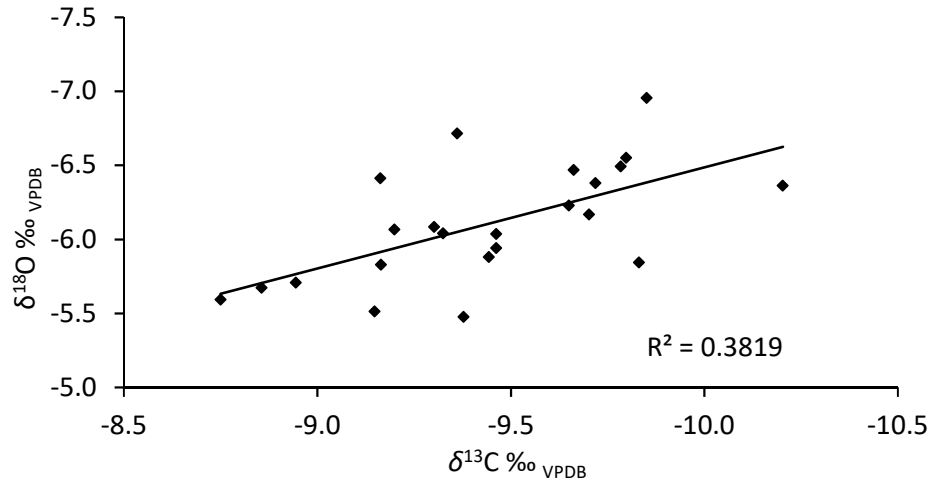
Figure 5.16: Cross plot showing the relationship between δ¹³C and δ¹⁸O. The correlation (0.38) is low, showing weak correlation.

5.2.3 Trace Elements

5.2.3.1 Sampling strategy

Trace elements were utilised for two purposes in HY-8. Firstly, as continuous laser ablation transects across regions of grey layers between 163-164 mm and 260-287 mm in order to identify the composition based on elements highlighted in Hartland et al., (2012) (see also Chapter 4 Section 4.2.3.4). Secondly, following the identification of possible seasonal in laminations between 1296 and 904 yr BP, spot laser ablation ICP-MS was done immediately adjacent to the micromilled transect totalling 7.15 mm (Figure 5.16). As mentioned above, the age of this section is roughly 1160-1120 yr BP. A spot size of 30 μm and increment between spots of 170 μm was used making the sampling frequency roughly double (43 spots) that of the stable isotopes and thus potentially more accurately representing micro-lamination. The increment between the spots was based on the number of laminae as established by thin section light microscopy as the optics of the laser system were not good enough to discern lamina boundaries. Trace elements in this case were selected as possible records of seasonality (see e.g. Mattey et al., 2010; Boch et al., 2011) and as in these papers are presented in ppm units (see also Hartland et al., 2012).

5.2.3.2   Results of the composition of Grey Layers

Grey layer results are presented in Chapter 4 Section 4.2.3.

5.2.3.3   Laminae results

The trace element profiles of Ba, Mg and Sr (Figure 5.17) show broadly similar decreasing concentrations with a marked decrease occurring between 3.6 and 3.0 mm, while Na shows a mainly flat profile. Peaks in concentration for the most part cannot be directly matched between elements although Mg and Ba show co-occurrence of the largest decrease in concentration at 2.55 mm and 2.4 mm respectively. The largest spike in concentration of Mg (756 ppm), Sr (38 ppm) and Na (212 ppm) do however, co-occur at 1.02 mm.

In Figure 5.18, Mg, Sr and Ba are compared to stable isotope data. The overall trend in δ^{13}C and δ^{18}O co-varies and the marked decrease in isotope values corresponds well to concentration decreases in all three trace elements. The largest enrichment in the δ^{18}O (starting at 2.3 mm) trend is similarly timed to the largest broad increase in Mg and Ba.
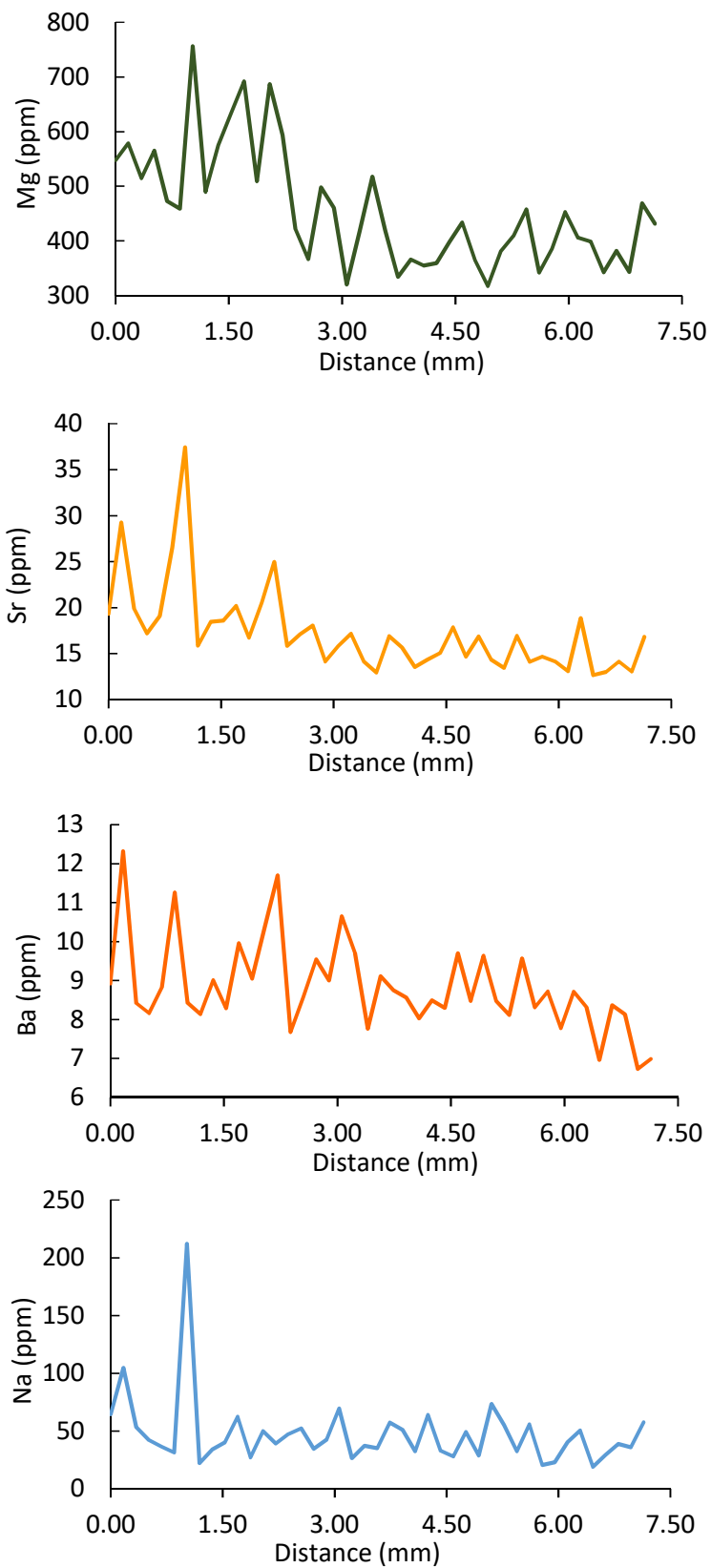
Figure 5.17: Trace element concentration profiles for the 6 mm transect, which has the approximate age of 1160-1120 yr BP. Mg is shown in green, Sr is yellow, Ba in orange and Na in blue. 43 samples are presented, close to the 40 laminations counted in thin section. Distances from the bottom of the 6 mm section.
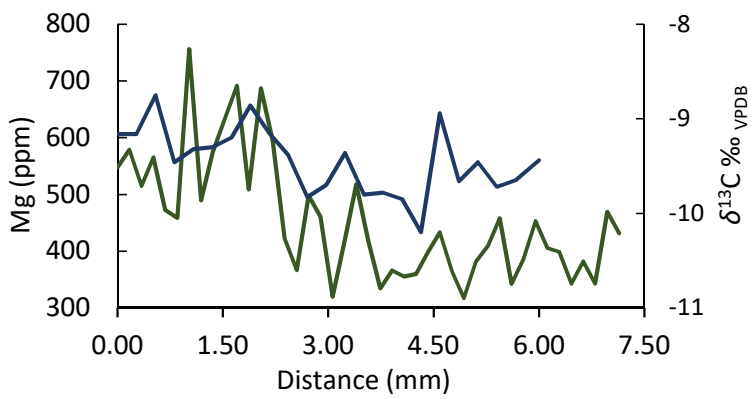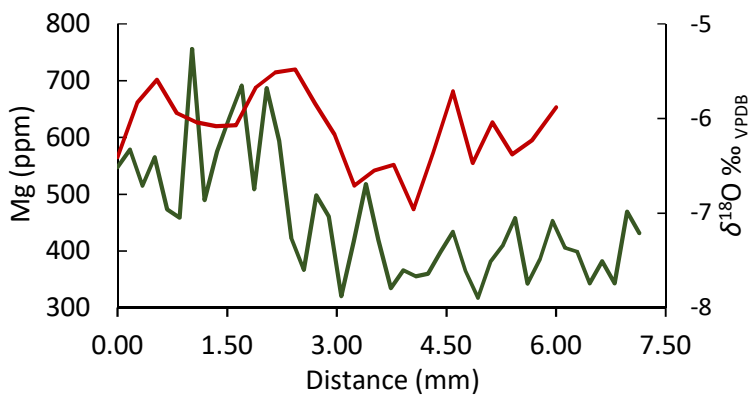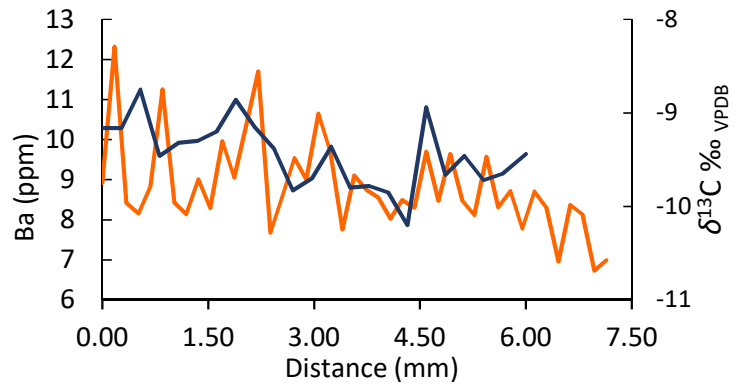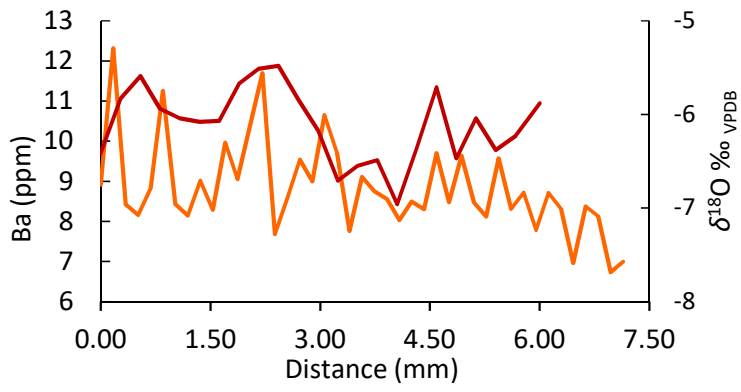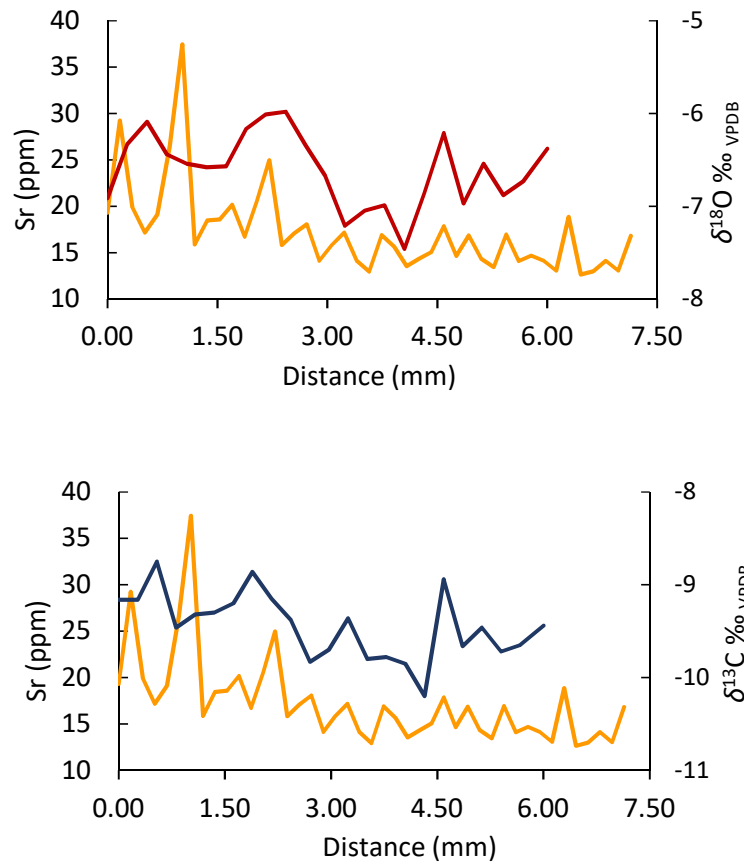
Figure 5.18: This page and overleaf. Trace element concentration profiles for the 6 mm transect compared to δ18O (red) and δ13C (blue), which has the approximate age of 1160-1120 yr BP. 43 samples are presented, close to the 40 laminations counted in thin section. Trace elements are the same colours as in the previous figure.

5.3 Discussion

5.3.1 Petrography and environment of formation

In Chapter 4 Section 4.3.6.1 it was concluded that change in the fabric of HY-8 from dendritic to microcrystalline (and equant) was forced by a change in drip conditions; whereby microcrystalline (and equant) fabrics formed under higher drip volumes than dendritic fabrics. In the growth regime of HY-8, micro-dissolution surfaces are interpreted to represent periods of increased infiltration, reducing calcite supersaturation: moreover their frequent occurrence suggest drip rates were highly variable throughout growth of the stalagmite. The highest infiltration events are likely to be marked by micro-dissolution in grey layers.

Growth of HY-8 appears to have been highly sensitive to drip rate as further indicated by the links between fabric type and growth rate. During the fastest growth rate (4765 yr BP to 4665 yr BP) dendritic calcite precipitated a very open fabric and some spherulitic growth, suggesting drip waters with very high supersaturation with respect to calcite (Frisia et al., 2000). Furthermore, this section of HY-8 is not laminated, suggesting that drip rate was not very variable in comparison to the laminated sections which contain micro-dissolution. Calcite fabrics precipitated during the slowest growth rate (growth ultimately ceased around 1700 yr BP), were mostly microcrystalline with a short period of transitional (microcrystalline-dendritic) fabric. Alternating compact and open dendritic lamination between 1300 and 900 yr BP was probably controlled by variability in drip rate, which could represent annual changes in precipitation/infiltration (see below).

5.3.2 Equilibrium deposition

The average modern calcite and cave water $\delta^{18}O$ values (Tables 5.3 and 5.5) are -6.83 ‰$_{VPDB}$ and -7.45 ‰$_{VSMOW}$ respectively. Using these values and the Kim and O'Neil (1997) and Tremaine et al., (2011) equations as outlined in the Methods Appendix, calculated temperatures are 12 °C and 16.1 °C respectively. A spot temperature taken during the collection of the drip water was 17.2°C (Mason 2009) closest to the temperature calculated by the Tremaine et al., (2011) equation suggesting speleothems in Sirtlanini Cave are precipitating in quasi-equilibrium with their dripwaters. Although Hendy tests are not perfect predictors of equilibrium/disequilibrium (Mickler et al., 2006; Dorale and Lui 2009). Hendy tests were performed along lamina from HY-8 at 84 cm and 103.5 cm (Mason 2009 unpublished) which are dated at 5380 yr BP and 4870 yr BP

and showed both negligible (R^2= 0.005 at 103.5 mm) but also substantial (R^2=0.65 at 84 mm) isotopic co-variation at two positions. (Mason 2009 unpublished). However δ^{13}C and δ^{18}O didn't become progressively enriched across lamination away from the central axis suggesting that HY-8 did not precipitate under disequilibrium conditions (Hendy, 1971; Mickler et al., 2006).

	δ^{18}O (‰$_{VPDB}$)	δ^{13}C (‰$_{VPDB}$)
Active soda straw	−6.7	
Top of HY-8	−6.96	−10.97

Table 5.6: Values for modern calcite precipitation in Sirtlanini Cave.

5.3.3 Potential signal in laminations

In HY-8, lamination is defined by alternating compact and open dendritic calcite. Lamina width varies greatly but usually open dendritic lamina are wider (see Chapter 4 Section 4.2.2 for full description). This variability in lamina width causes only half of the counted laminations to be visible in hand specimen. Many compact laminae are topped by a micro-dissolution surface and it is suggested that here such compact laminae were formed by dissolution events (Chapter 4 Section 4.3.1.1). Micro-dissolution events are likely to affect the recovery of an 'originally full' annual signal.

The lamination count between modelled ages in the 6 mm transect is consistent with annual lamina growth. Across the entire laminated section the number of laminae correspond with the age within error (429 laminations counted in 392 model years with an age error of 37-76 years). Results suggest some co-variation and pattern does occur between Mg, Sr, Ba and δ^{18}O and also co-variation occurs between the stable isotopes. However there is no clear correspondence between the geochemistry and the visible laminae (Figure 5.19 and Figure 5.20) suggesting that the switch between compact or open dendritic calcite is not related to short term fluctuation in geochemistry. Furthermore there is no trend between trace element variability and open or

compact dendritic laminae as seen by others (Mattey et al., 2010; Boch et al., 2011), although there is difference in the resolution, and thus comparability, of these seasonal records. Usually, annual lamination is defined by a change in fabric type or $CaCO_3$ polymorph, forming a couplet that defines a wetter and a drier season (e.g. Railsback et al., 1994; Genty and Quinif 1996; Fleitmann et al., 2004; Tan et al., 2006; Mattey et al., 2008a, 2010; Boch et al., 2011; Muñoz-García et al., 2016). However, in HY-8 the lamination count suggests each individual lamination represents a year not a couplet. This is probably due to the numerous micro-dissolution surfaces present. Although it is not possible to quantify, micro-dissolution could have removed the previous year of calcite growth and its geochemical signal. This is not unprecedented, as annual couplets in a Botswanan speleothem often began with relatively intense fluid flow after a drier spell which sometimes dissolved underlying $CaCO_3$ (Railsback et al., 1994).
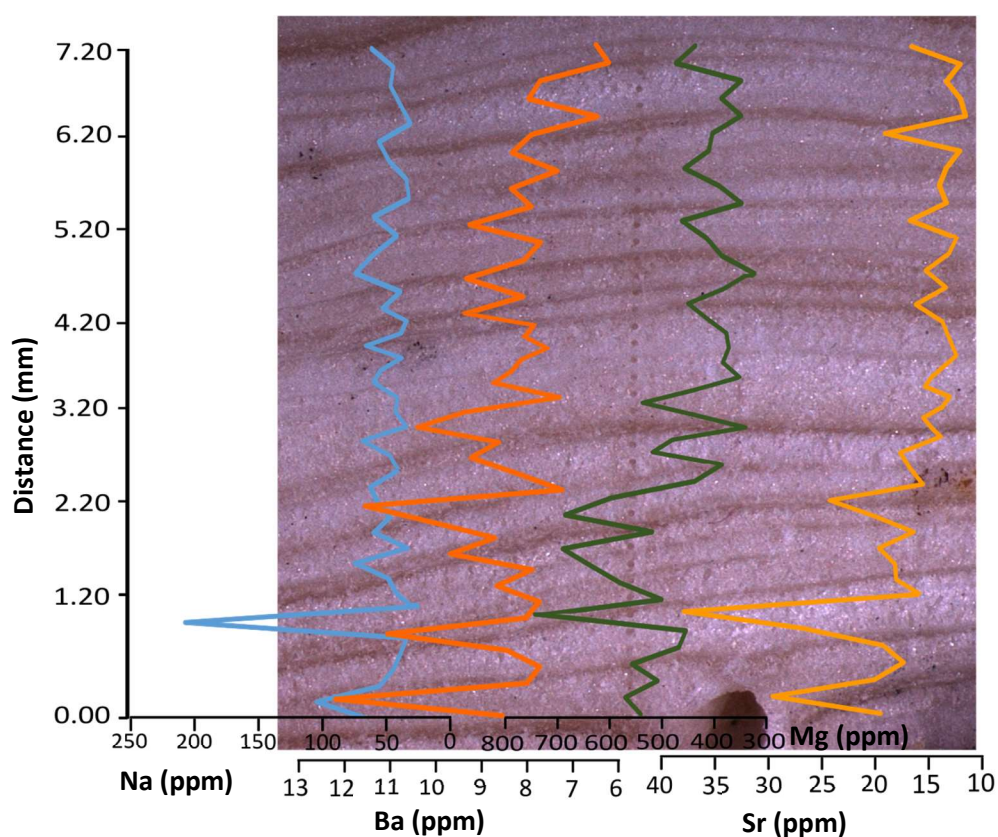
Figure 5.19: Trace element profiles matched with appropriate ablation pit and individual visible layers. Data wiggles are plotted relative to the appropriate ablation pit in the centre of the section not to individual laminae they might visually occupy. Despite some relationships between Mg (green), Ba (orange) and Sr (yellow) these variations are not clearly related to lamina fabric changes from open (light) to compact (dark) dendritic calcite.
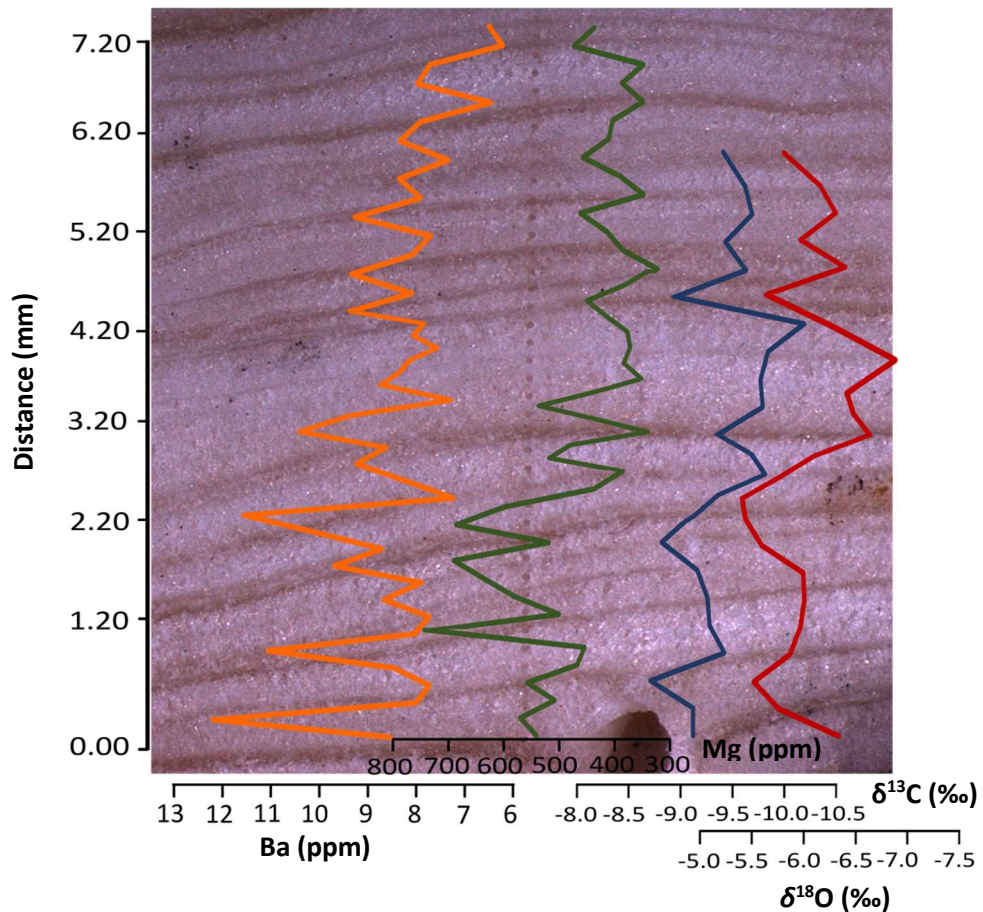
Figure 5.20: Trace elements Ba (orange) and Mg (green) and δ¹³C (blue) and δ¹⁸O (red) matched with appropriate ablation pits and individual visible layers. Despite some relationship between all geochemical proxies these are not clearly related to laminate fabric of open (light) and compact (dark) dendritic calcite.

However, an apparent lack of relationship between open or compact dendritic calcite and geochemistry may be a function of the limitations of the sampling. The number of stable isotope samples were only roughly half of the known number of laminations, which were all that was visible in hand specimen. In this instance resolution was not high enough and the chance of mixing signals of different lamina types was high due to the coarseness of sampling. Similarly instrumental specifications for trace elements may have prevented precise enough sampling from single laminae. The 30 μm spot size, required for adequate signal was, in some instances, wider than the lamina resulting in a mixed signal. Moreover, neither strategy was capable to fully taking into account the variability in width of lamination. Due to the adopted point sampling of both stable isotopes and trace elements the data is also potentially prone to aliasing (Weedon 2003) as variation occurs at a higher frequency than sampling and not at regular sample spacing (Fairchild et al., 2006a).

5.3.4 Controls on Stable Isotopes

Local climate data suggests that seasonally temperature dependent fraction has a strong control on $\delta^{18}O$ of precipitation as there is a large positive offset between winter and summer values (Figure 5.4 and 5.5). However, Figure 5.6 shows a strong relationship between individual monthly precipitation amount and $\delta^{18}O$, which suggests the amount effect also co-controls isotopes of precipitation. The amount effect is a known control on $\delta^{18}O$ in other Turkish stalagmites (e.g. Jex et al., 2010, 2011; Rowe et al., 2012; Wickens 2013). Cave and spring waters plot more consistently with lighter winter $\delta^{18}O$ values of precipitation and the lack of rainfall in the summer months means it is unlikely that a summer signal will be recorded in speleothems forming in Sirtlanini Cave. Furthermore, winter temperatures are unlikely to fluctuate much for sustained periods of time during an interglacial period. This provides a sound basis to assume that $\delta^{18}O$ over the course of the growth of HY-8 is controlled mainly by the amount effect.

An exception to this amount effect control is during the intervals of fastest growth rate (4765 to 4665 yr BP and 3940 to 3810 yr BP) which correspond to periods of enriched $\delta^{18}O$ (Figure 5.14, Figure 5.21); fast growth rate during this time contradicts the interpretation that these periods were drier. Dendritic growth during these periods is open and highly porous, suggesting very fast growth from drip waters highly supersaturated with $CaCO_3$. A degree of enhanced degassing is implied during the formation of dendritic fabric (Frisia et al., 2000) and thus some kinetic fractionation is inferred. Rapid degassing is likely to cause kinetic fractionation and enrichment in $\delta^{18}O$ as documented in other Eastern Mediterranean speleothems (e.g. Bar Matthews et al., 1996). While temporary phases of rapid degassing, as in inferred for HY-8, will promote disequilibrium deposition, they are unlikely to disrupt the general isotopic patterns that reflect broader climatic drivers (see e.g. Spötl and Mangini 2002). In HY-8 the overall control on petrographic fabric types is strongly controlled by drip water (Chapter 4 Section 4.3.6.1), and therefore enhanced degassing can be linked to phases of reduced drip water volume. Correlation between higher Mg/Ca, Sr/Ca and more negative $\delta^{18}O$ along the 6 mm transect provide some evidence that lighter $\delta^{18}O$ can be linked to reduced residence time (higher infiltration events). Thus wetter and drier periods can still be identified via $\delta^{18}O$ in HY-8 but some caution is required when interpreting the fastest growth periods which are likely to have imprinting from kinetic fractionation and less negative $\delta^{18}O$ signals.

$\delta^{13}C$ values of -6.12 ‰ to -10.75 ‰ are within the range for C3 plants (McDermott 2004) and major negative excursions can be associated with increased soil detritus during grey layer deposition (Chapter 4 Section 4.3.6.1 and later in this chapter). $\delta^{13}C$ is thus predominantly responding to the balance between soil carbon input and bedrock dissolution and/or residence

time (PCP). Enriched δ^{13}C correlates somewhat with high Mg and Sr concentrations in the 6 mm transect supporting the interpretation that intervals of enriched δ^{13}C indicate increased epikarst residence time or PCP. There is no statistical correlation between δ^{13}C and δ^{18}O but during phases of rapid growth, enrichment is observed in δ^{13}C as well as δ^{18}O. Periods of aridity are expected to enhance PCP in the epikarst by increasing residence times and would therefore increase δ^{13}C values. It also should be expected that during the periods of rapid growth some effect from kinetic fractionation will contribute to the δ^{13}C signal.

5.3.5 Mid and late Holocene Palaeoclimate recorded in HY-8 and comparison to other records

Mid to late Holocene palaeoclimate data are available in Turkey from lacustrine records (e.g. Leng and Marshall 2004 and references therein; Eastwood et al., 2007; Ocakoğlu et al., 2013; Dean et al., 2015) but these are compromised to some extent by the difficulty in dating lake records at high resolution. Other Pleistocene speleothem records are known from Turkey, e.g. Sofular (Badertscher et al., 2011) and Dim (Wickens 2013; Ünal-İmer et al., 2015; Ünal-Imer et al., 2016) as well as modern (500 years or less) (Jex et al., 2010, 2011). Aside from HY-8, Kocain Cave (Göktürk, 2011) contains the only other speleothem to cover the Holocene in Turkey.

δ^{18}O in HY-8 suggests that there was no significant change in the amount or seasonality of precipitation between the mid and late Holocene, although large excursions in δ^{18}O suggest short periods of relatively enhanced or reduced rainfall were common throughout. Soil productivity, however, was generally higher after 3800 yr BP following a depletion of ~1.5 ‰ ‰ in δ^{13}C relative to values in the earlier record. This change may in part be related to enhanced precipitation amount but may also be related to warmer temperatures. On shorter time-scales, up to a few hundred years, some co-variation between δ^{18}O and δ^{13}C similarly suggests periods of enhanced soil productivity during wetter climatic phases (for example Section 5.3.5.5). Petrology is strongly controlled by drip rate in HY-8 leading to distinct morphologies within the grey layers related to higher drip rates and also two periods of rapid growth related to reduced drip rates and increased degassing. These periods also show strong responses in stable isotopes (Figure 5.22). The stable isotope record of HY-8 can be broadly split into 4 sections highlighted in Figure 5.21 and discussed further below.
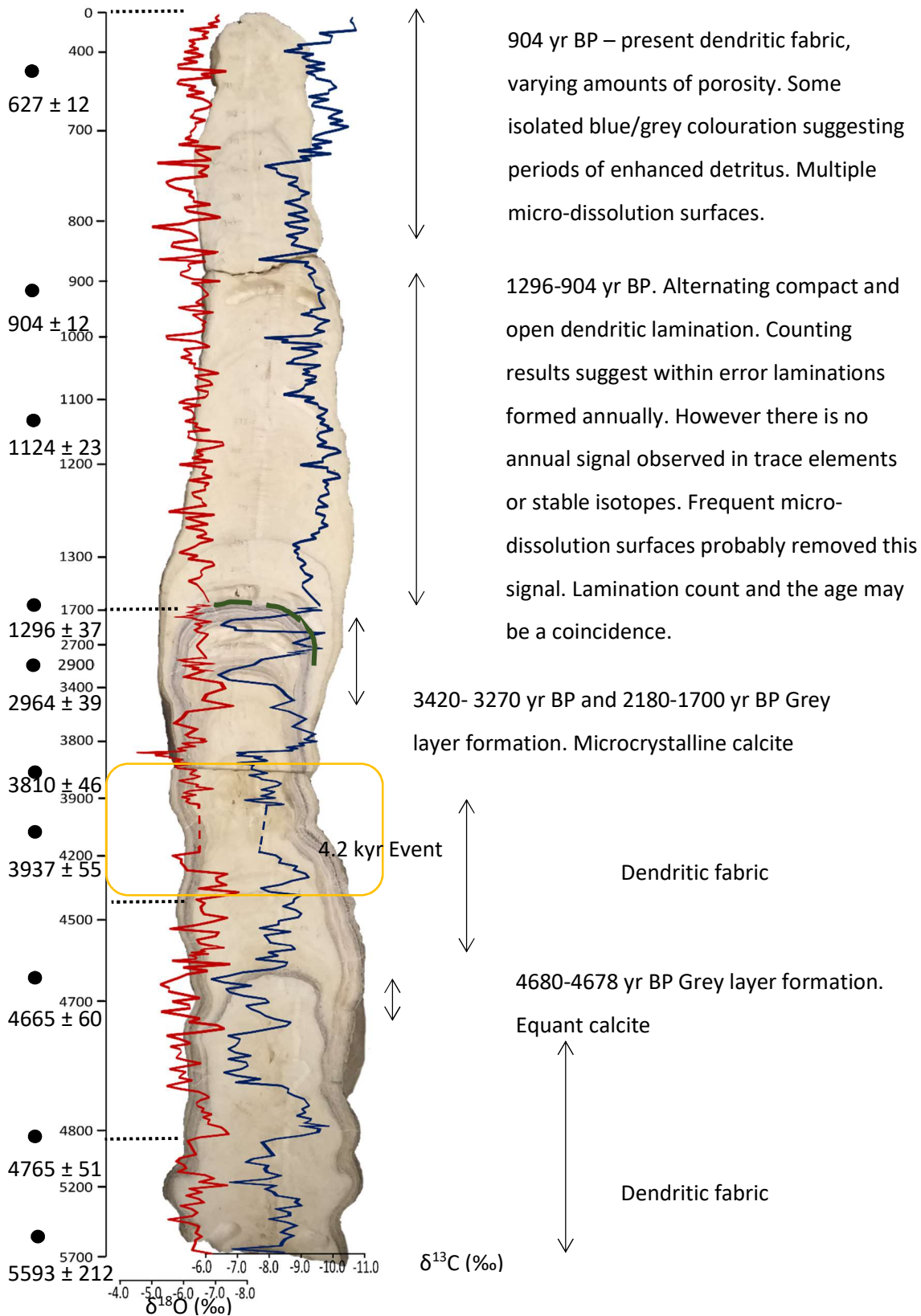
Figure 5.21: Summary of key results of the mid Holocene to present as recorded in HY-8. $\delta^{18}O$ is in red and $\delta^{13}C$ in blue. Black dashed lines highlight the boundaries to major changes in isotopes as discussed in the main text. The post hiatus period from 1380 yr BP to present is shown in more detail in Figure 5.23 and grey layer deposition is shown in more detail in Figure 5.25. The 4.2 kyr event is highlighted in the yellow box and the hiatus as a green dashed line.

5.3.5.1   5660 to 4890 yr BP

Early growth of HY-8 recorded precipitation amounts in $\delta^{18}O$ not dissimilar to most of the rest of the record, but a short lived increase in precipitation is indicated by a negative $\delta^{18}O$ excursion from 5200 to 5150 yr BP. Variation in $\delta^{13}C$ during this period is the lowest of the record before the hiatus. $\delta^{13}C$ values are mainly between -7.5 and -9.0 ‰ suggesting a substantial contribution from soil organic matter, possibly suggesting a well-established biomass above the cave. Although it is not possible to assign an age model to growth before 5660 yr BP, earlier growth of HY-8 shows similar average $\delta^{18}O$ values and thus these conditions had developed before 5660 yr BP. This period ends abruptly at 4890 yr BP as a 1.5 ‰ negative excursion occurs over ~40 years in both isotopes.

5.3.5.2   4890 to 4290 yr BP

Between 4850 and 4290 yr BP $\delta^{18}O$ values are at their most negative of the whole record on average. Values are typically >0.5 ‰ more negative relative to the values following the hiatus, showing a 600 year period of enhanced precipitative relative to the rest of the record. $\delta^{13}C$ is influenced by this increase in precipitation as a strong 2 ‰ depletion is seen at the onset of wetter conditions at 4890 yr BP, possibly showing that increased precipitation has a positive effect on soil productivity. However, unlike $\delta^{18}O$ which returns to values similar to those recorded before the 600 year event, $\delta^{13}C$ values largely remain depleted relative to values from 5660-4890 yr BP. This could indicate that soil productivity remained higher over the rest of the record even though rainfall amounts apparently did not change much over the entire HY-8 record. It is possible that lighter $\delta^{13}C$ also reflects reduced PCP after 4890 yr BP. This could mean that summer temperatures before this time were warmer, i.e. suggesting that PCP between 5660-4890 yr BP was promoted by evaporation.

A large deviation from the trend of wetter conditions occurs during the fastest growth phase of HY-8 between 4765 and 4665 yr BP. During this period $\delta^{18}O$ shows a major positive excursion with values peaking at -5.2 ‰ from values typically lower than -7 ‰. As discussed in Chapter 4 Section 4.3.6.1, the fastest growth phases are likely to be dominantly controlled by degassing during periods of relative aridity. $\delta^{13}C$ shows a similar response to $\delta^{18}O$ with a large positive excursion possibly highlighting a larger bedrock signal due to increased residence time. Additionally grey layer deposition during this interval (4680 to 4678 yr BP) points to a fire event (see Section 5.3.5.7 for discussion). Some caution is required as the large increase in $\delta^{18}O$ and $\delta^{13}C$ values are possibly enhanced by kinetic fractionation due to more rapid degassing. Nevertheless,

the combined proxies indicate a strong 100 year long arid event from 4765 to 4665 yr BP punctuating a longer wet period.

A short term pluvial event recorded in a number of Eastern Mediterranean and Levant climatic proxies lead Robinson et al., (2006) to propose the existence of a 'mid Holocene wet event' beginning around 5000 yr BP. At Soreq, a negative excursion in $\delta^{18}O$ from 4900 yr BP and peaking at 4800-4700 yr BP (Bar-Matthews et al., 2003; Bar-Matthews and Ayalon 2011), shows a very similar timed onset, but shorter duration event than at Sirtlanini (Figure 5.22): however, a $\delta^{13}C$ record from a longer Soreq speleothem indicates the wetter period may have extended to 4500 yr BP (Bar-Matthews et al., 1997) (Figure 5.22). At Lake Van in east Turkey, a distinct wetter phase culminating around 4500 yr BP is superimposed on wetter climatic conditions between 6200-4000 yr BP (Wick et al., 2003). Furthermore, multiple Mediterranean marine core records suggest wetter conditions around this time (Emeis et al., 2000; Kouli et al., 2012; Triantaphyllou et al., 2013) (Figure 5.22) as well as humid phases from 5200 to 4400 yr BP recorded in the Red Sea (Migowski et al., 2006). Marine cores also suggest a strong positive shift in SSTs ~4800 yr BP which continued until 4500 yr BP (Traintaphyllou et al., 2013) and well as a shift towards warmer vegetation types around 4500 yr BP (Kouli et al., 2012).
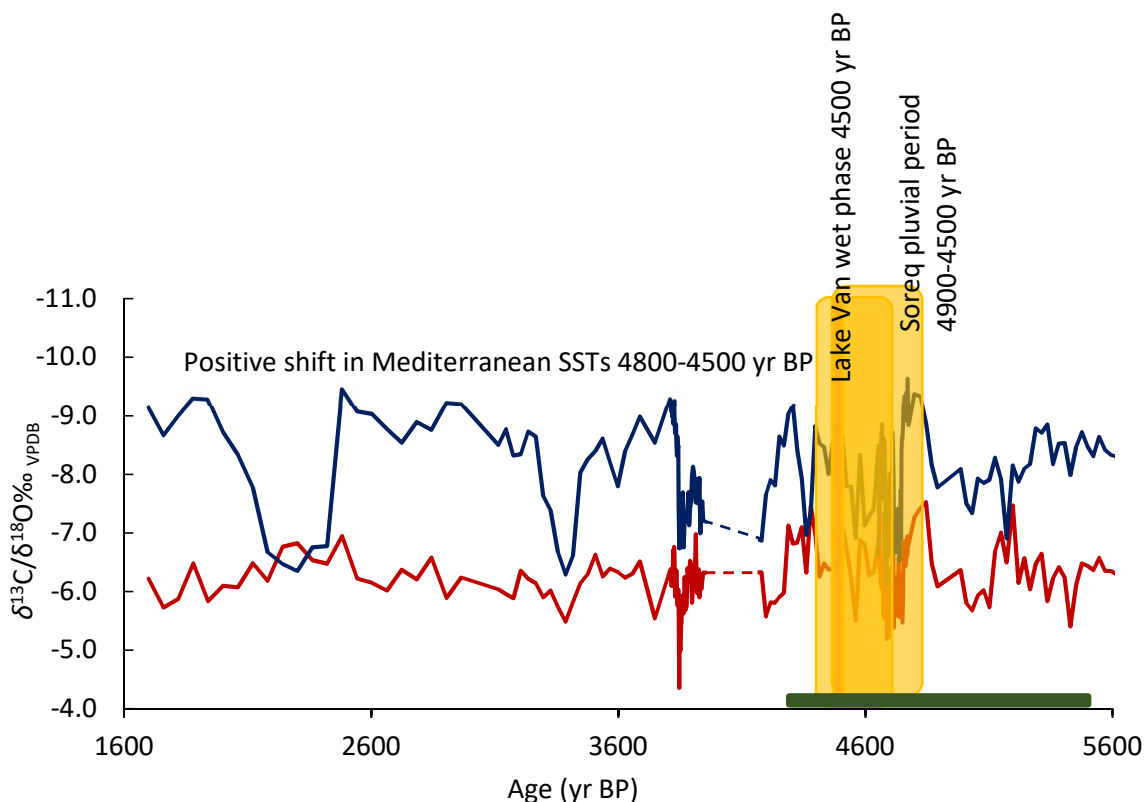
Figure 5.22: Previous page. HY-8 stable isotopes prior to the hiatus (5660-1700 yr BP) compared to regional observations for the period 4890-4290 yr BP. The dashedlines rpresent the section with reduced sample density due to vugs as mentioned in the sampling strategy. A distinct 600 year pluvial event is also seen in various records of the Eastern Mediterranean. At Soreq stable isotope records indicate a wet period spanning from 4900-4500 yr BP (Bar Matthews et al., 1997, Bar Matthews et al., 2003, Bar Matthews and Ayalon 2011). At Lake Van a distinct wet phase is observed ~4500 yr BP superimposed on generally wetter conditions between 6200 and 4000 yr BP (Wick et al., 2003). Positive shifts in Mediterranean SSTs are observed in the Aegean (Traintaphyllou et al., 2013) from 4800-4500 yr BP. The green bar represents the period of wet and humid conditions observed in multiple Mediterranean marine cores (Emeis et al., 2000, Koui et al., 2012, Traintaphyllou et al., 2013).

5.3.5.4   4280-1700 yr BP

A positive δ^{18}O excursion between 4290 and 4200 yr BP marks the end of the wet period with δ^{18}O returning to values not dissimilar to those prior to the wet event. A mean value of ~–6.4 ‰ continues for the next 2000 years indicating that the 600 year wet event discussed above, punctuated longer term drier conditions that began before the dated portion of HY-8 at 5660 yr BP. The second rapid growth phase from 3940 to 3810 yr BP shows a significant positive δ^{18}O shift of 2 ‰ to the most enriched values in the record which likely has some contribution from rapid degassing. From 2200 yr BP to the hiatus at 1700 yr BP, δ^{18}O is enriched by 0.7 ‰ relative to the mean. Such δ^{18}O values are not the highest recorded in the HY-8 and this it is not clear that a decrease in drip rate (caused by lower precipitation amount) was responsible for the growth cessation. Much of this section covers the slowest growth of HY-8 (3810- 1700 yr BP). Deposition of microcrystalline calcite from 2180-1700 yr BP implies drip volume was higher at this time but this is not corroborated by δ^{18}O which does not record a negative shift that might be expected during increased winter recharge.

Initially δ^{13}C is relatively enriched compared to the mean of -8.4 ‰, with a positive excursion at 4280 to 4200 yr BP corresponding with the positive shift in δ^{18}O. Variation is low and values remain at about -6.7 ‰ until after 3810 yr BP, despite the largest positive excursion in δ^{18}O associated with the second rapid growth phase (3940 to 3810 yr BP) (Figure 5.14, Figure 5.21). The lack of a clear positive excursion in δ^{13}C might suggest that rapid degassing did not occur and

that $\delta^{18}O$ is therefore recording an aridity signal. In contrast to $\delta^{18}O$, after 3800 yr BP, $\delta^{13}C$ values are depleted by 1 ‰ relative to values between 5660 and 4900 yr BP. This suggests that although precipitation amounts may not have changed significantly during the growth of HY-8 conditions were on the whole more favorable to vegetation growth between 3800 and 1700 yr BP compared to earlier. The implication of a more developed biomass and increased drip water without a marked increase in precipitation indicates it is possible that effective evaporation was reduced during this time compared to 5660-4890 yr BP. Temperatures were therefore probably cooler between 3800 and 1700 yr BP, possibly linked to the reduction of solar insolation over the course of the Holocene (Berger and Loutre, 1991). Clear deviations to more positive $\delta^{13}C$ values are attributed to reduced vegetation amounts prior to the deposition of grey layers and are discussed in Section 5.3.5.7.

The slowest growth phase of HY-8 between 3810 and 1700 yr BP partially covers the dry rapid climate change event at 3500 to 2500 yr BP identified by Mayewski et al., (2004). However, $\delta^{18}O$ and the lack of persistent open dendritic fabrics during this period do not record overall drier conditions compared to the rest of the record with the possible exception of the fire event associated with grey layer deposition 3416 to 3266 yr BP (Section 5.3.5.6).

5.3.5.5   Post hiatus 1380 to present

$\delta^{18}O$ immediately above the hiatus has values ~1 ‰ more negative than those immediately below, probably indicating that increased groundwater recharge was responsible for the restart of stalagmite growth. $\delta^{18}O$ values during this period are generally similar to those from the earlier HY-8 record, with values centred on -6.5 ‰ but with high variability (-7.64 ‰ to -10.75 ‰). It is possible to observe a gradual decrease in oxygen isotope values of about 0.5 ‰ until the present day (Figure 5.14). Therefore following the hiatus the precipitation regime did not change much except for a small increase over the last 1380 years compared to the record before the hiatus. $\delta^{13}C$ shows a similar structure to $\delta^{18}O$, suggesting that controls on the carbon signal are influenced significantly by rainfall. The restart of HY-8 growth occurred at about the lowest value of solar insolation during the Holocene (Berger and Loutre 1991). Colder temperatures at this time may have facilitated increased effective moisture (less evaporation) providing a mechanism for increased vegetation above the cave (as indicated by $\delta^{13}C$). In the last 300 years a trend towards more negative values in both isotopes implies increasing precipitation and soil productivity to the present day.

Figure 5.23 highlights the detail of $\delta^{18}O$ and $\delta^{13}C$ during this period. It is apparent that short period fluctuations in $\delta^{18}O$ and $\delta^{13}C$ are related, although the statistical relationship (R^2= 0.22) is not much higher than the rest of the record. Nevertheless, this interval can be split into clear periods of relative wet and dry conditions as positive or negative deviations from the mean of $\delta^{18}O$ during this time (−6.34 ‰). $\delta^{13}C$ therefore records the response of vegetation to precipitation increases and decreases. Turkish precipitation is negatively correlated with the NAO index (Türkeş and Erlat 2003), thus during positive NAO phases it should be cooler and drier in Turkey. The onset of growth after the hiatus occurs during a predominantly positive NAO phase (with short intermittent negative NAO phases) (Trouet et al., 2009; Olsen et al., 2012). The positive phase continues until 500 BP as reconstructed from multiple proxies in a lacustrine record from Greenland (Olsen et al., 2012). Fluctuation between wet and dry phases in HY-8 occur more often than switches in the NAO, although some signals present in the record could be linked to events which are interpreted to have been caused by short intermittent changes in the NAO (see below). Moreover the HY-8 record is recording a drier interval during the negative NAO period at 500 BP, it is difficult therefore to relate all changes in precipitation observed in HY-8 to changes in the NAO.

The period 1360 to 1100 yr BP is the only time when $\delta^{18}O$ and $\delta^{13}C$ tend to diverge, and $\delta^{13}C$ is more negative than might be expected for a dry period when compared to the rest of the record (Figure 5.23). A rapid climate change event towards drier conditions between 1200 and 1000 yr BP has similar timing to this HY-8 dry interval (Mayewski et al., 2004). Maxima in Lake Iznik aragonite/calcite deposition and minima in total clay are similarly interpreted as dry indicators between 1350-1150 yr BP (Ülgen et al., 2012). In HY-8, soil productivity and vegetation was apparently enhanced at this time despite the relative dryness. It is possible that while drier, this period was cooler, which helped reduce evaporation and increasing the effective moisture available for vegetation. This observation could be linked to carbonate and diatom $\delta^{18}O$ from Nar Lake, which indicate that from 1371-1170 yr BP there was an interval of enhanced snowfall in the region (Dean et al., 2013), although lack of freezing in the Bosphorus and Black Sea between 1350 BP to 1000 BP, shows that the interval was not extremely cold (Yavuz et al., 2007).

Some regional records suggest that the interval from ~800 to 1200 AD (1200 to 750 BP) was a warm period (Crowley and Lowery 2000; Broecker, 2001; Mann et al., 2009), the so-called Medieval Warm Period or Medieval Climate Anomaly (Figure 5.23). The Medieval Climate Anomaly has been linked to a positive phase of NAO (Mann et al., 2009, Trouet et al., 2009) and La Niná like conditions in the Pacific (Mann et al., 2009). In HY-8, clear structure is present between 1100 and 740 yr BP splitting the timeframe into five wet/dry phases (Figure 5.23). $\delta^{13}C$, however, shows its longest period of relative enrichment from 860-740 yr BP, suggesting either a

reduction in soil productivity or reduced recharge leading to enhanced PCP in the epikarst. The most enriched δ^{13}C occurs at the same time as the most enriched δ^{18}O, thus it is possible that rapid degassing occurred, corroborated by the precipitation of dendritic calcite. It is not, however, clear if a temperature anomaly is present in HY-8 during the Medieval Warm Period. The Medieval Warm period is similarly ambiguous in Kocain Cave, Turkey where warmer periods, but no overall warmer signal, was observed (Göktürk 2011). Warmer conditions are recorded in foraminiferal δ^{18}O from the Eastern Mediterranean, but not significantly warmer in comparison to other events in the last 4000 years (Schilman et al., 2001). Lake records at Lake Iznik, Turkey (Ülgen et al., 2012), Nar Golu, Turkey (Jones et al., 2006; Dean et al., 2013) and Lake Dojran, Macedonia (Francke et al., 2013) are more consistently interpreted to represent warmer and wetter conditions during the Medieval Climate Anomaly.

Following the Medieval Climate Anomaly a period of colder conditions persisted throughout Europe, commonly known as the Little Ice Age (Figure 5.23). There is no consensus on the length of the Little Ice Age although it is thought to be related to changes in El Nino and the NAO and decreased solar radiation (Mann et al., 2009). Mann et al., (2009) identify a coldest period from 1400-1700 C.E (550-250 BP) and Mayewski et al. (2004) identify a rapid climate change event between 600 and 150 yr BP. In Turkey, dry conditions attributed to the Little Ice Age are observed in Nar Golu between ~1400 and 1900 AD (Jones et al., 2006, Dean et al., 2013) and at Lake Iznik between 700-30 yr BP (Ülgen et al., 2012). At Sirtlanini the dry, low productivity period between 630 and 280 yr BP (1290-1600 AD) could be related to the Little Ice Age. Regional proxies indicate this period was cold including δ^{13}C from Kocain Cave (Göktürk 2011) as well as occasional freezing in the Bosphorus (Yavuz et al., 2007). Planktonic foraminiferal δ^{18}O from marine cores off the coast of Israel show a positive excursion which peaks at 250 yr BP (Schilman et al., 2001) and pollen indicators from Lake Iznik also suggest a colder climate (Ülgen et al., 2012).
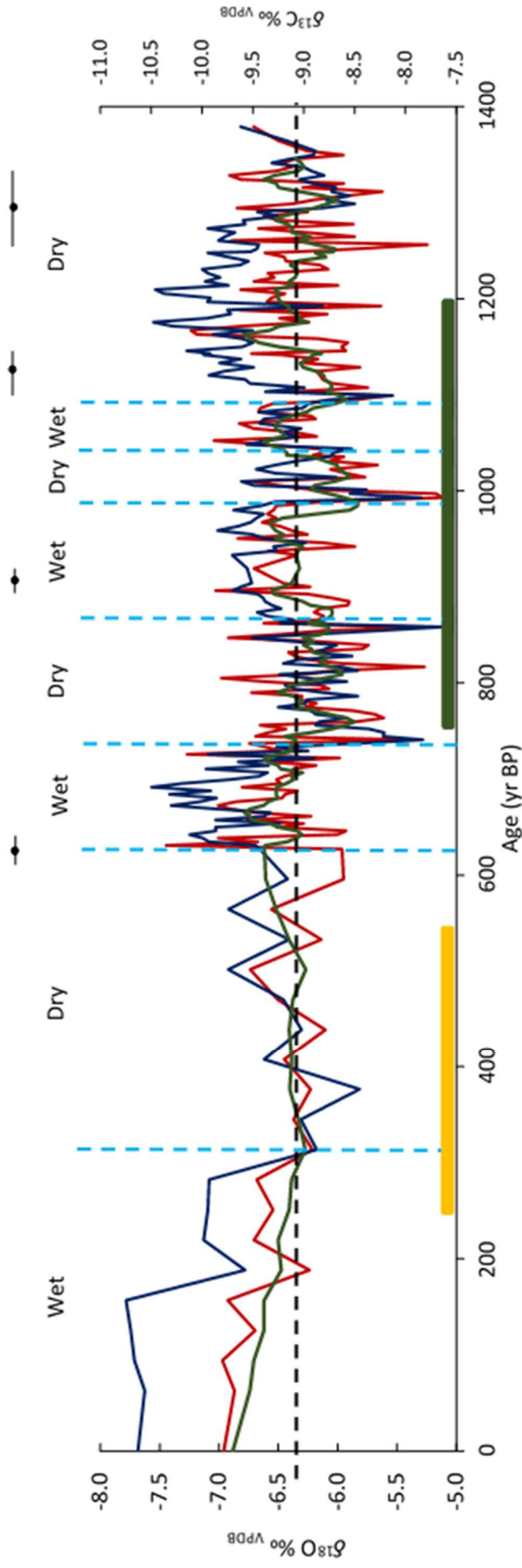
Figure 5.23: Fluctuations between wet and dry events for the post hiatus period 1360 yr BP to present. Assignment of a wet or dry event is based on positive or negative fluctuation about the mean of oxygen for this period (−6.34 ‰, dashed black line). Different relative precipitation periods are separated by bright blue dashed lines. A 5 point running mean is added to $\delta^{18}O$ in green. For the most part $\delta^{13}C$ fluctuates in agreement with $\delta^{18}O$ highlighting the response of soil productivity to relative precipitation amount. The exception occurs between 1300 and 1100 yr BP where $\delta^{13}C$ is more negative than expected for a largely dry period. This may suggest some temperature control, possibly towards colder temperatures which may increase effective moisture. The green bar shows the overall time frame associated with the Medieval Climate Anomaly, the yellow with the Little Ice

181

5.3.5.6 The 4.2 kyr Event

The 4.2 kyr event is considered to have been caused by a short term weakening of North Atlantic westerlies, similar to the 8.2 kyr event (Mayewski et al., 2004). It is associated with the disruption of ancient civilisations across the Mediterranean, the most prominent of which the, Akkadian Empire of Mesopotamia, collapsed (Weiss et al., 1993; de Menocal, 2001; Weiss, 2016). Identification of a possible abrupt climate event was first recognised in archaeological deposits at Tell Leilan (Weiss et al., 1993). Archeologically the 4.2 kyr event is considered to have occurred from 4200 to 3900 yr BP (Weiss 2015). Climatically, changes associated with the 4.2 kyr event span 4400 to 3800 yr BP with most records converging on a period between 4200-4000 yr BP. The evidence is found in a range of different settings across the Mediterranean including lakes (e.g. (Stevens et al., 2001; Stevens et al., 2006; Eastwood et al., 2007; Wagner et al., 2009; Ülgen et al., 2012; Francke et al., 2013), speleothems (e.g. Fleitmann et al., 2003; Drysdale et al., 2006; Bar-Matthews and Ayalon 2011; Railsback et al., 2011; Regattieri et al., 2014; Ruan et al., 2016) and marine cores (e.g. Cullen et al., 2000; Migowski et al., 2006). The event has strong geographic differences (Jung and Weninger 2015), including multiple locations the event is not recorded making the likely signal ambiguous.

In HY-8, evidence for the 4.2 kyr event is most clearly observed in $\delta^{18}O$. $\delta^{18}O$ shows strong fluctuation in precipitation with two clear aridity events between 4290 and 4200 yr BP (1.5 ‰ positive excursion, similar to other excursions in the record) and 3900 to 3850 yr BP (2.5 ‰). The latter excursion peaks at –4.35 ‰ making it the most arid event recorded in HY-8. The anomalous straight line between the two peaks is an unavoidable anomaly of the sudden increase in growth rate and data plotting. As discussed above, some of this heavier $\delta^{18}O$ signal is likely to be contributed to by increased degassing as this event occurs within the second phase of rapid growth (3940 to 3810 yr BP) (Section 5.3.4). Throughout this period $\delta^{13}C$ is relatively enriched by 0.5 ‰ compared to most of the prior record (excluding the first rapid growth phase 4765-4665 yr BP), suggesting that soil productivity during this period was lower than much of the earlier HY-8 record. Enrichment in carbon isotopes could also record an increase in PCP, consistent with an increase in aridity. Furthermore, the proposed end of the event corresponds to a 2.4 ‰ negative excursion in $\delta^{13}C$, and following this, $\delta^{13}C$ is typically 1-2 ‰ lower throughout the rest of the record. Thus after the termination of aridity, soil productivity appears to have increased and/or PCP was reduced due to an increased rate of epikarst recharge.

The aridity event between 4290 and 3850 yr BP in HY-8 clearly fits into the timeframe outlined by a few others (e.g. Figure 5.24) where a period sustained positive $\delta^{18}O$ from ~4500 yr BP to ~3800 yr BP occurs compared to the periods both before and after. This therefore is a short-lived period

of aridity which punctuated the largely wetter climate of the time. The two-phase structure of the event recorded in HY-8 is less common elsewhere, but not dissimilar to some other speleothem datasets (Figure 5.24). Timings vary slightly, for example the first aridity peak occurs ~200 years earlier in Gol-e-Zord, Iran (Carolin et al., in press) and Gueldaman Cave, Algeria (Ruan et al., 2016), but agreement is good for the timing of the second peaks between 3900 and 3850 yr BP in all records (Figure 5.24). The magnitude of the δ^{18}O event varies between caves but is not linked to particular cave settings or modes of stalagmite formation. Corresponding low soil productivity throughout this period fits with archaeological observations of abandonment due to poor growing conditions in Syria (Weiss et al., 1993; Kaniewski et al., 2008; Weiss 2015).
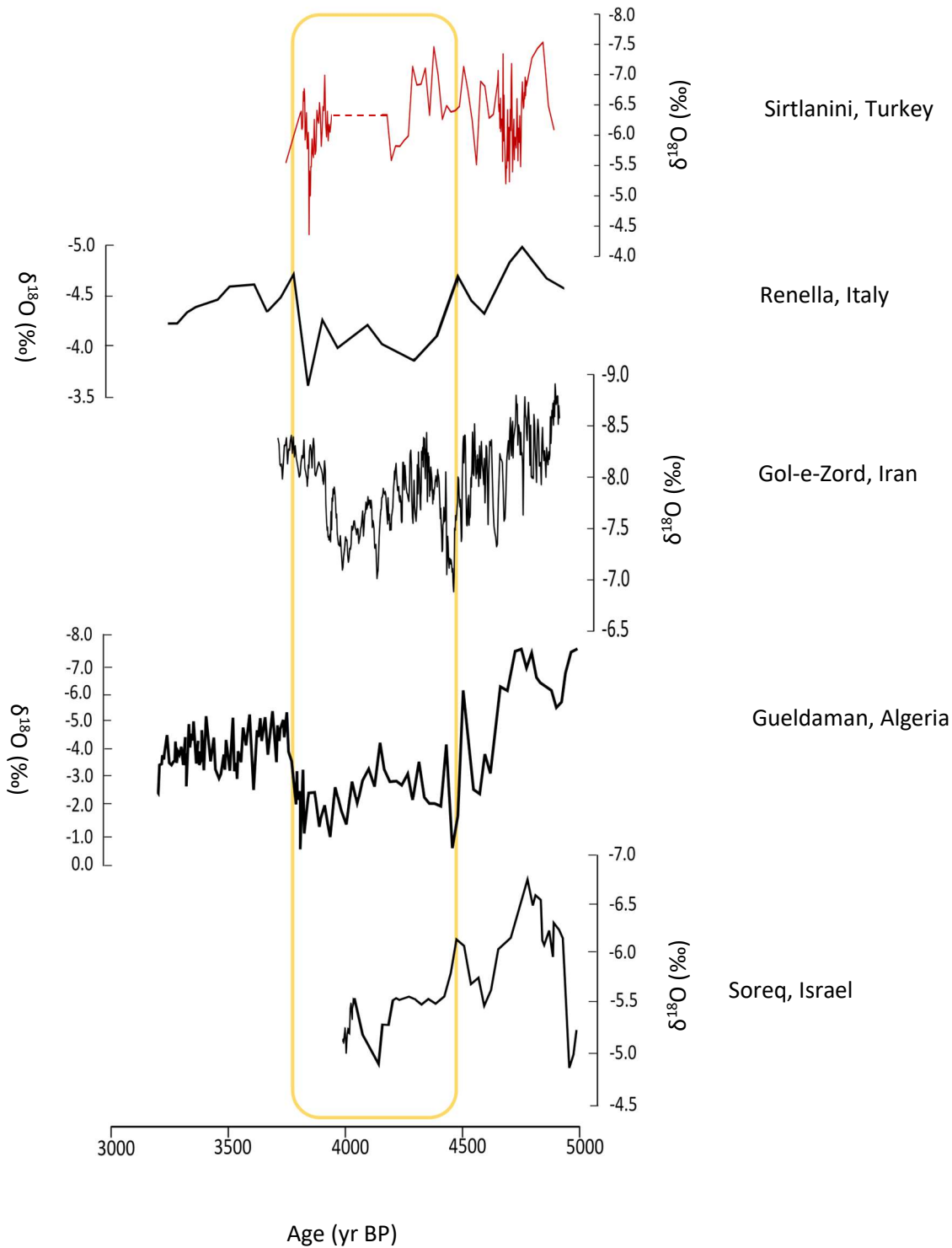
Figure 5.24: δ¹⁸O profiles from caves that display a two-phase aridity pattern, Sirtlanini Cave Turkey (this research), Renella Cave Italy (Drysdale et al 2006), Gol-e-Zord Cave Iran (Carolin et al. in press), Gueldaman Cave Algeria (Ruen et al. 2015) and Soreq Cave Israel (Bar Matthews and Ayalon 2011). The Soreq record ends before 3800 yr BP. The timing of the first peak (4400 to 4200 yr BP) is slightly better constrained than the second (3900-3850 yr BP) although all in good agreement and within error of the age estimates. (continued next page)

Figure 5.24 continued: Magnitudes of the $\delta^{18}O$ excursions between 3850-4400 yrs BP vary between records. The dashed area represents the 8 mm of reduced sampling density as explained previously in this thesis. Note that variability in $\delta^{18}O$ appears to be larger between 5000-4500 yr BP than after that time, a trend that is particularly clear in the Gueldaman record where variability is least marked in the youngest part of the record. As in other figures the dashed line in the HY-8 record represents the 8 mm of lost samples due to vugs down the central axis.

5.3.5.7   Grey Layer deposition

The deposition of grey layers is the most distinct growth phenomena recorded in HY-8. Geochemical and petrographic results, discussed at length in Chapter 4 (Section 4.3.6.1) indicate that these layers represent a distinct shift in petrography and trace element composition in comparison to the rest of the dendritic calcite stalagmite. Grey layers formed between 4680-4678 yr BP, 3420- 3270 yr BP and 2180-1700 yr BP, the latter ending in a hiatus.

The shift from dendritic to microcrystalline fabric during grey layer deposition (Figure 5.25) is a clear indication of an increase in drip volume, although not necessarily a more constant drip rate. The presence of a single layer of equant/euhedral calcite (4680-4678 yr BP) indicates a further increase in drip water, as the euhedral form is associated with a thicker water film (Railsback et al., 1994). Trace metal chemistry from within the grey layers show clear peaks in Mn, Zn, Fe and Al content which directly correlate with the darkest colouration. All these trace metals are preferentially transported as part of colloidal soil, clay and organic particles typically with >100 nm grain size (see e.g. Hartland et al., 2012). Optical microscopy and EDX confirmed the presence of organic detritus within grey layers and structures which appear to be plant cuticle. To concentrate trace metals and organic detritus in such a way into speleothem calcite, a large drip volume is required with fairly rapid flow to flush larger detrital particles through the epikarst (Fairchild et al., 2006a). Frequent micro-dissolution surfaces are evidence that drip waters were often under saturated with respect to calcite, suggesting that residence time in the epikarst is too low to allow equilibration with bedrock carbonate. Raman spectroscopy gave a clear signal of soot (i.e. amorphous carbon) within the layers. It is unlikely that soot originated from human fires within the cave, as the restricted height of the entrance tunnel would have caused the cave to become rapidly filled with smoke; therefore natural fires above the cave were probably the carbon source.

Isotopic data could potentially indicate whether these periods were related to enhanced rainfall, but Figure 5.24 shows that the response is not the same in all 3 depositional phases. Grey layers occurring between 4680 to 4678 yr BP and 3416 to 3266 yr BP begin to deposit on the falling limb of a 1 ‰ positive excursions in $\delta^{18}O$ superimposed on periods of relative aridity. These positive excursions could represent further increases in aridity or an increase in evaporation, which can increase post fire due to the loss of vegetation and reduction in albedo (Nagra et al., 2016). However as the deposition of the detritus begins after the peak of the positive $\delta^{18}O$ excursion, it is possible deposition of grey layers is related to an increase in precipitation, recovering to former precipitation amounts following the event. Grey layers between 2180 and 1700 yr BP are deposited during a smaller positive excursion in $\delta^{18}O$. There is no suggestion that these $\delta^{18}O$ events were more extreme than others within HY-8 not associated with grey layers. Despite this, the presence of larger and more concentrated soil detrital particles, as well as abundant evidence for micro-dissolution suggests that a higher volume of water infiltrated more quickly into the cave system than at any other time during HY-8 growth. As we can infer that a fire occurred above the cave prior to the deposition of the grey layers, it is likely a bare soil was left which provided little stability and made it easier to displace larger amounts of detritus without a significant increase in precipitation. A lack of soil will also reduce translation time into the cave. Micro-dissolution is well-developed at the lower boundary of all grey layers, which may support the notion that they formed as the first response to rapidly infiltrating dripwaters that had not had time to degas.

Before grey layer deposition distinct positive excursions in $\delta^{13}C$ with magnitudes of greater than 2.5 ‰ occur, suggesting significant bedrock input within $\delta^{13}C$. PCP could also be contributing to this heavier $\delta^{13}C$. Where positive excursions in $\delta^{18}O$ coincide with $\delta^{13}C$ the strong bedrock signal is co-genetic with peak aridity. Assuming fire strips a large proportion of the vegetation this would initially increase the relative proportion of the heavy bedrock $\delta^{13}C$ signal. The grey colouration is always related to the falling leg of $\delta^{13}C$ providing evidence that the isotopic signal is partially controlled by the high organic matter content of the layers. Vegetation recovery will also be recorded in this signal as $\delta^{13}C$ returns to pre event values. Recovery is on the scale of 100 years.

Soot deposition within grey layers associated with positive $\delta^{18}O$ excursions may be related to climate induced fire events. At Eski Acigöl, Turkey increases in charcoal flux as a proxy for increased wildfire activity has been directly related to positive shifts in $\delta^{18}O$ of 1.5 ‰ (Turner et al., 2008). From 6000 yr BP climatically induced wildfire was lower than present (Power et al., 2008) but prior to 4000-3500 yr BP the periodicity of regional wildfires still appear to be controlled by aridity (Vanniere et al., 2011). After 3000 yr BP decreasing summer insolation in the Northern Hemisphere reduced climatically controlled fire further (Power et al., 2008). At Lake Gölhişar ~130 km from Sirtlanini increases in wildfire activity due to human occupation began

~3200 yr BP at the start of the Beyşehir Occupation (Eastwood et al., 1998). Aside from the first grey layer deposition phase (4680-4678 yr BP), the events at Sirtlanini occur during the period of increased human occupation at Gölhisar. As the events do not occur during periods of extreme aridity it is possible all three events are human induced although the occupation history of the immediate area is unknown.

Figure 5.24: Next page. Summary of the detail of geochemical and petrographic proxies occurring during grey layer deposition. $\delta^{18}O$ is in red and $\delta^{13}C$ in blue. Distinct positive excursions occur prior to grey layer deposition but do not always in $\delta^{18}O$. Fabric changes to microcrystalline and equant calcite show an increase in drip volume and rate relative to primary dendritic calcite deposition. Increases in concentrations of specific trace elements show an increase in soil detrital input as well as a size increase in the organic colloidal fraction. Soot is present in all layers.

2964 ± 39
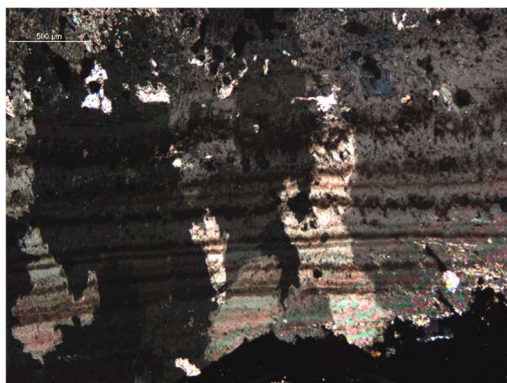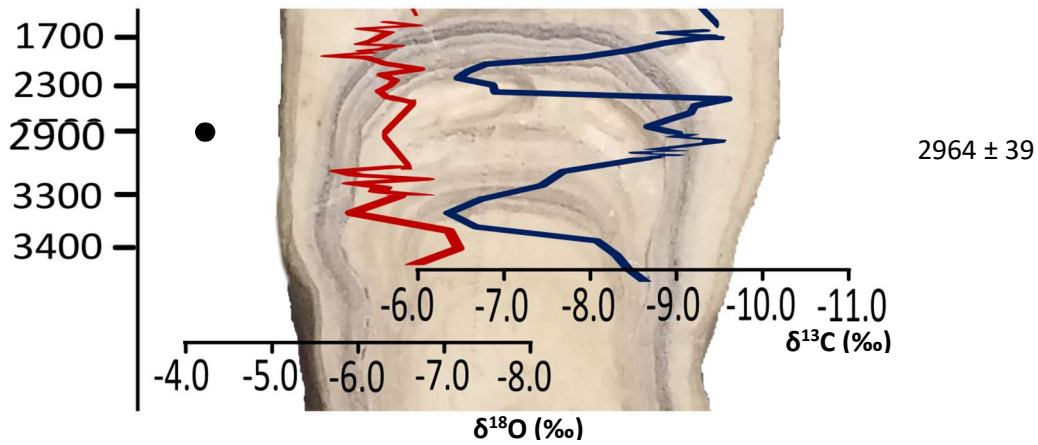
3420- 3270 yr BP and 2180-1700 yr BP. Fabric change to microcrystalline calcite during the formation of grey layers, frequent microdissolution surfaces are present highlighted by detritus. Darkest layers show the highest concentrations of trace elements, Zn, Fe, Mn and Al associated with increased soil detritus and organic colloid size. Soot is also present.
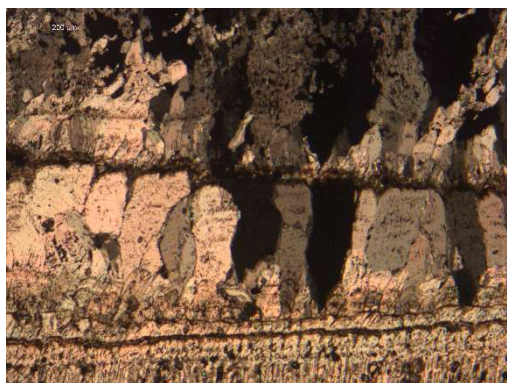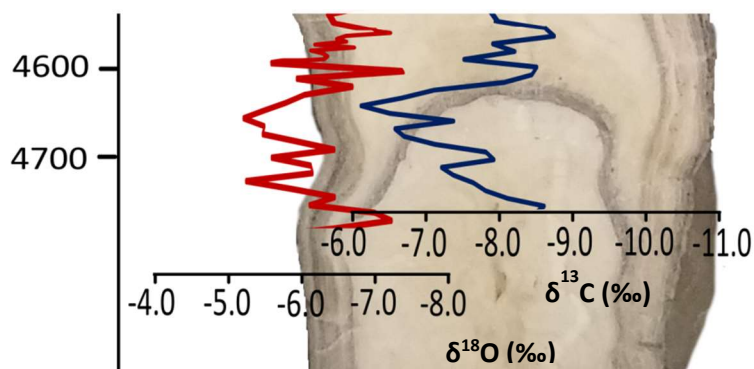
4680-4678 yr BP. Fabric change to equant calcite during the formation of the grey layer, bound by microdissolution surfaces and highlighted by detritus. Higher concentrations of trace elements, Zn, Fe, Mn and Al associated with increased soil detritus and organic colloid size. Soot is also present.

188

Chapter 6. Limnon "The Cave of the Lakes", S. Greece: the early Holocene and the 8.2 Kyr Event.

6.1 Introduction

6.1.1 Limnon Cave

Limnon Cave (37°57' 37.8' N 22°08' 24.9' E) is located in the north of the Peloponnese region of southern Greece, 2 km north of the village of Kastria and 90 km SE of Patras (Figure 6.1). The large natural cave entrance (3.5 m high) is 820 m a.s.l (Mason 2009), below Mount Amolinitsa (Vassilopoulou n.d. www.kastriacave.gr/en). Soil cover above the cave is thin and limited in extent, but supports Mediterranean sclerophyllous scrub (Mason 2009); patches of bedrock outcrop occur in places. The cave developed along a NW trending fault within Late Cretaceous limestones of the Pindos Zone; part of the Tripolis Geotectonic Zone (Vassilopoulou n.d. kastriacave.gr/en). Limnon Cave is of geological and tourist significance due to the presence of 13 successive lakes (Figure 6.2) which are present all year round. The cave is 2 km long and separated into 4 hydrologically distinct sections, which is partly related to faulting (Vassilopoulou n.d. www.kastriacave.gr/en). Despite hydrological compartmentation all parts of the cave are heavily decorated (Vassilopoulou n.d. kastriacave.gr/en) with active calcite precipitation (Mason 2009). There is a range in both cave air temperature (12.33 °C to 17.05 °C) and humidity 71.3 % - 96.3 % (Vassilopoulou n.d. www.kastriacave.gr/en) which is likely caused by enhanced ventilation due to the opening of the tourist entrance. The temperature within the area when sample KTR-2 was collected was 14.6 °C (Mason 2009).

Figure 6.1: Location of Kastria village and Limnon Cave in the northern Peloponnese of southern Greece. The capital Athens and the city of Patras are also highlighted. Inset shows a Google Earth image for topographic reference looking NW towards Patras.
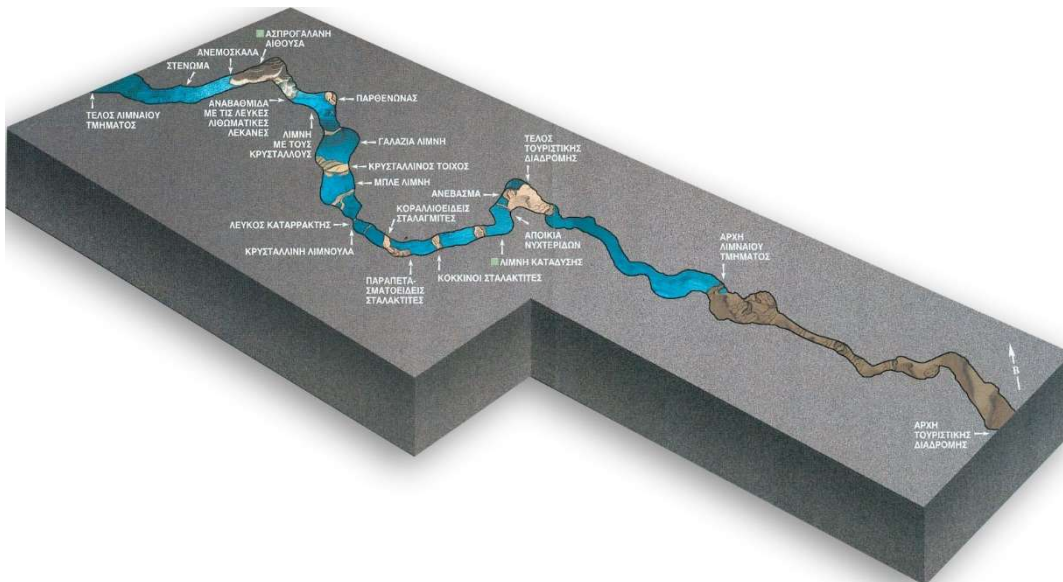
Figure 6.2: Cave schematic floor plan, source http://www.kastriacave.gr/en/το-σπήλαιο-2/cave-maps.html*.*

6.1.2 Stalagmite KTR-2

KTR-2 (Figure 6.3) is a fossil stalagmite, 343 mm in length, collected 400 m from the cave entrance, preceding the lakes. Aside from the earliest growth (not covered in this research) most of the stalagmite grew with two parallel growth axes; results described here are from the left, larger, axis. The basal date obtained by Mason 2009 indicates that growth was probably initiated during Marine Isotope Stage (MIS) 2 (Section 6.2.2.2). A growth hiatus between 26,500 yr BP and 11,900 yr BP indicates there was growth cessation probably around the time of the Last Glacial Maximum (LGM); with growth apparently resuming at the end of Younger Dryas period (Section 6.2.2.2). In this work the focus was on the Holocene record, the last 127 mm of growth; 0 mm is therefore assigned to the hiatus level.
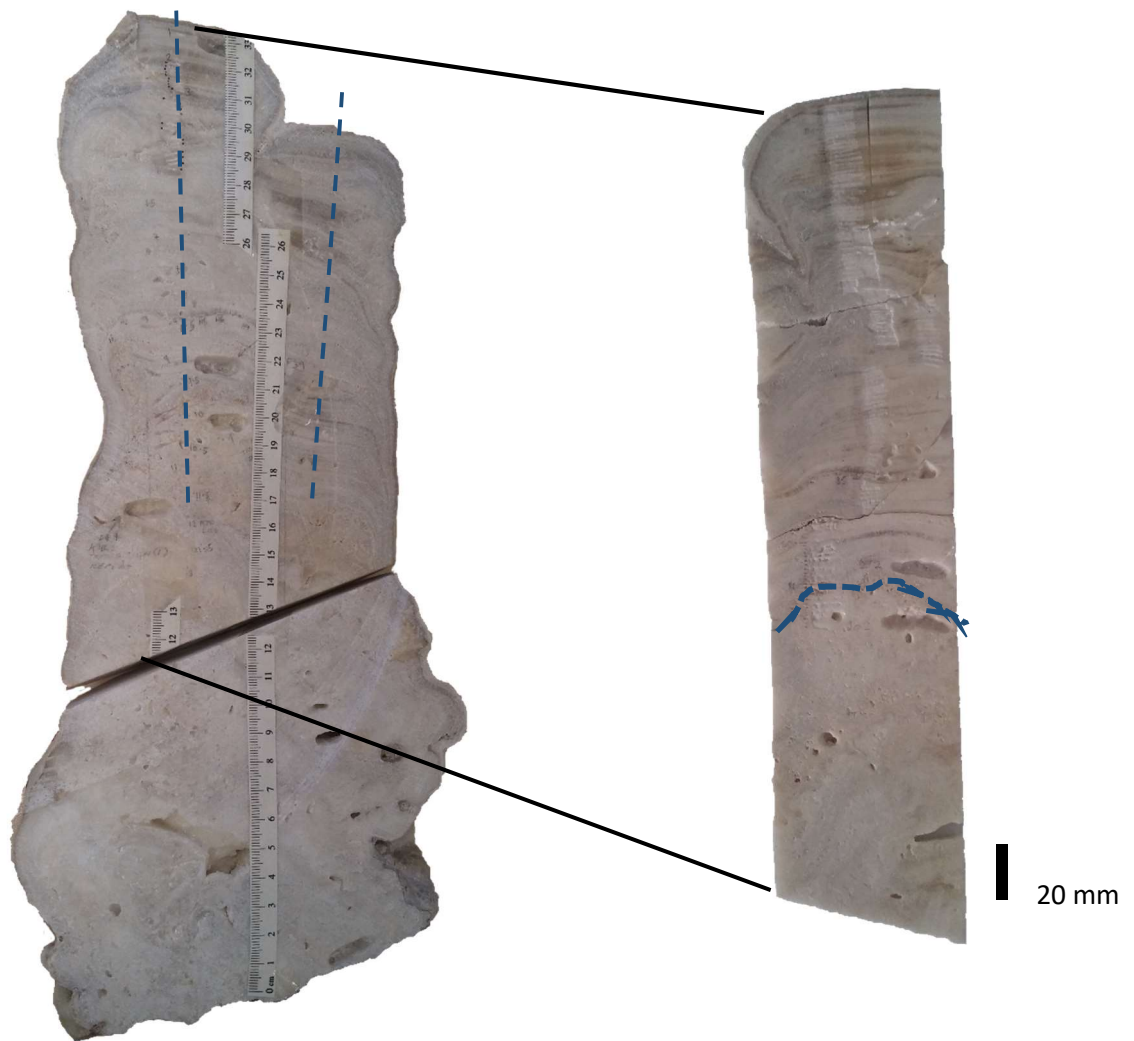
Figure 6.3: Full profile of stalagmite KTR-2 with enhanced view (right) of the section utilised in this research. The hiatus surface (blue pecked line) defines the limit of the section used in this research.

6.1.3 Modern climate and groundwaters

The geographic region of Limnon Cave has a typical Mediterranean climate, modulated to some degree by its montane setting. The closest IAEA and WMO weather stations with available data are at Patras (2000-2014) and Athens - combined Hellinkon Airport (1960-1976) and Pendeli (2001-2014) records. Note that these records are incomplete and are coastal rather than montane.

Data from both Athens and Patras show a strong seasonal precipitation distribution. Over 70% of precipitation falls in the winter and autumn months (Table 6.1) with <20 mm of rainfall in summer months. Some regional differences are apparent, the amount of precipitation being higher in Patras (790 mm total for the recording period) than Athens (612 mm). Seasonality in Patras is more marked with large reductions or increases in precipitation between months defining new seasons (Figure 6.4). In Athens, reduction in precipitation between spring and summer months is more gradual but distinct increases occur between August and September (Figure 6.4).

	Athens Precipitation (%)	Average $\delta^{18}O$ Athens (‰$_{VSMOW}$)	Patras Precipitation (%)	Average $\delta^{18}O$ Patras (‰$_{VSMOW}$)
Winter	44.2	-7.37	43.7	-6.28
Spring	18.3	-5.27	21.2	-4.63
Summer	6.7	-4.56	4.2	-2.29
Autumn	30.8	-5.59	30.8	-5.00

Table 6.1: Percentage of precipitation contribution by season for Athens weather stations for the period 1960-1976 and 2001-2014 in column 1 and for Patras weather station for the period 2000-2014 (column 3). Column 2 shows the average $\delta^{18}O$ value for Athens weather stations between 1960 and 1976 and 2001-2014. Column 4 displays the Patras average $\delta^{18}O$ value 2000-2014.
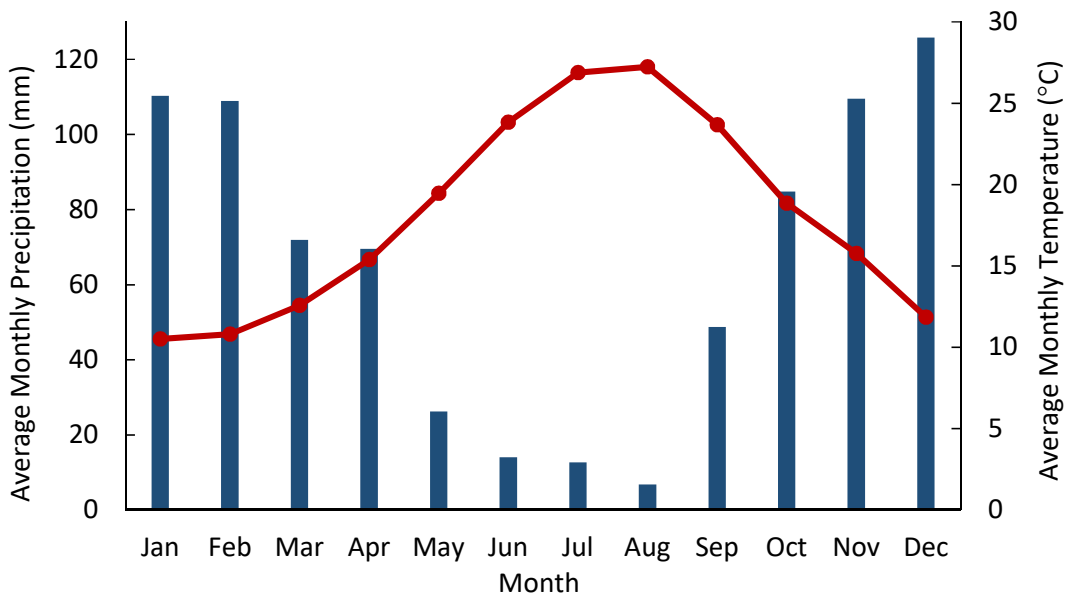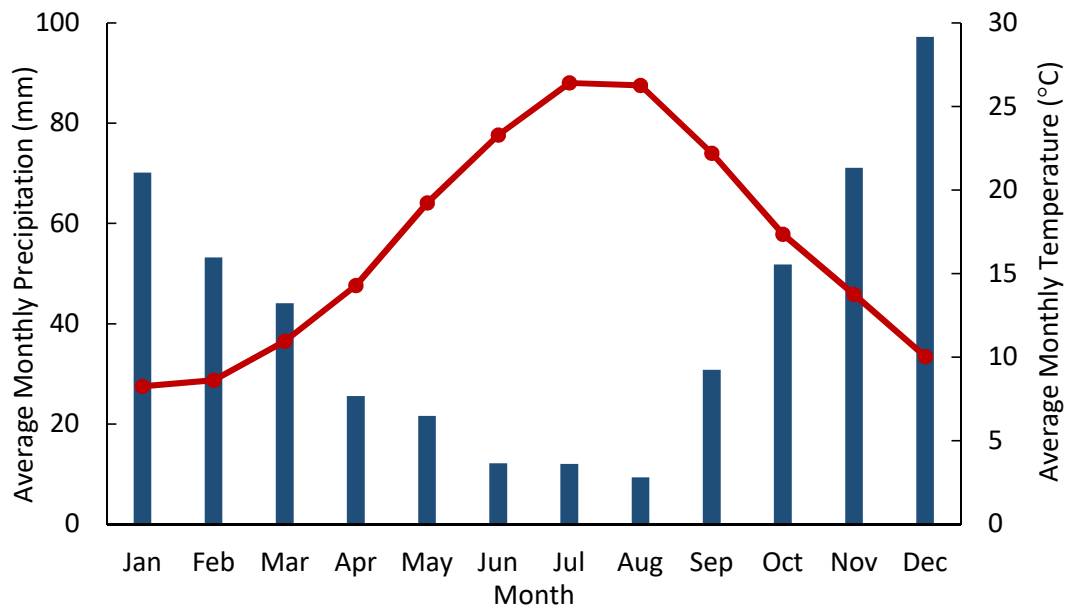
Figure 6.4: Monthly precipitation (blue bars) and temperature averages (red line) for Athens (top) and Patras (below). Timeframes for precipitation are as Table 6.1. Air temperature for Athens was recorded from 1960-1981 and 2001-2014; for Patras between 2000 and 2014.

Clear seasonal differences in precipitation between summer and winter are obvious in both datasets; however seasonality in general is more prominent in Patras where marked increases or decreases in precipitation are clear around seasonal boundaries. Spring to summer shows a gradual decline in precipitation in Athens but an abrupt increase between summer and autumn occurs.

Mean winter temperature at both weather stations does not fall below 10 °C, thus snowfall at the altitude of the weather stations is rare. However snowfall is recorded at nearby Kapsia Cave at an almost identical altitude to Limnon (Finné et al., 2014) and is not uncommon at the Limnon cave site. Average summer temperatures between 23 °C to 27 °C and low rainfall (14 mm to 6.7 mm in Patras) are likely to favour slower drip rates and evaporation in the epikarst during these months by forcing a negative precipitation/evaporation ratio. Therefore speleothem growth rates and isotopic compositions will largely be determined by autumn, winter and early spring rainfall.

In the region of Limnon itself annual rainfall is around 1200 mm per year (Flocas and Giles 1991), much higher than Athens and Patras. Furthermore, the relative intensity of annual rainfall in the region (between 1962 and 2002) was 3.3 mm/h, some of the highest in Greece (Kambezidis et al., 2010). This is related to higher amounts of summer convective thunderstorms created in the central Peloponnese (Kamebezdis et al., 2010) but also to winter depressions which predominantly arrive from the west (Flocas and Giles 1991). As depressions are unstable, precipitation is released by orographic uplift in the region of the Peloponnese (Argiriou and Lykoudis, 2006). Between 65 and 70 % of regional rainfall in the Peloponnese originates from frontal depressions in the winter (Flocas and Giles 1991) meaning a summer convective signal is likely to not be represented in speleothem samples.

For Athens only the Pendeli station isotopic data has been used, the dataset being more complete and the station further from Athens city which creates anomalous summer isotopic compositions. The typically low regional rainfall amounts in July and August mean that intense local convective events driven by the Athens urban heat island (Nastos and Zerefos 2007) have potential to bias the summer data, as the local storms have isotopic compositions controlled by amount effects (Argiriou and Lykoudis 2006) resulting in anomalously negative δ^2H and δ^{18}O compositions.

The Athens Pendeli mean δ^2H and δ^{18}O precipitation data show strong seasonality (Figure 6.5). The lightest compositions occur in January (-49 ‰$_{VSMOW}$ δ^2H and -8.43 ‰$_{VSMOW}$) and from then to August isotopic compositions typically increase (-18 ‰$_{VSMOW}$ δ^2H and -2.59 ‰$_{VSMOW}$ δ^{18}O). The trend from August to December then reverses with compositions decreasing. June shows an isotopic reversal for δ^{18}O the mechanism for which is discussed below (Patras data).

There is no clear relationship between overall precipitation amount and δ^{18}O which shows no statistical correlation (R^2 value of 0.025; Fig. 6.6) but a strong correlation appears between monthly precipitation and δ^{18}O (0.78, Figure 6.7). The relationship between air temperature and δ^{18}O (R^2 value of 0.35; Fig. 6.6) shows a low positive correlation suggesting temperature has a small effect of 0.24 ‰/°C. Heaviest rainfall occurs in the coldest months and so both the temperature and amount effects are likely to affect stable isotopes of precipitation. However

within an interglacial large fluctuations in winter temperatures are not likely and therefore it is more likely that precipitation $\delta^{18}O$ reflects changing rainfall amounts rather than temperatures.
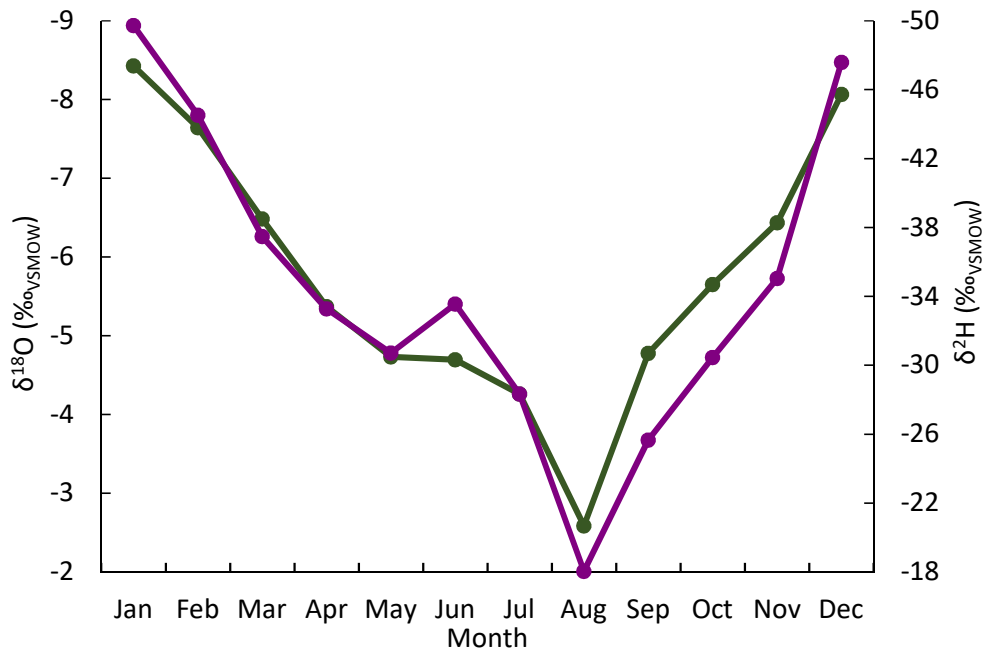
Figure 6.5: Monthly variations for δ^2H (purple) and $\delta^{18}O$ (green) at the Athens Pendeli weather station for the period 2000-2014. Strong seasonal differences can be observed in both isotopes, becoming heaviest in August. Depletion in June presents an anomalous value in terms of the temperature effect.
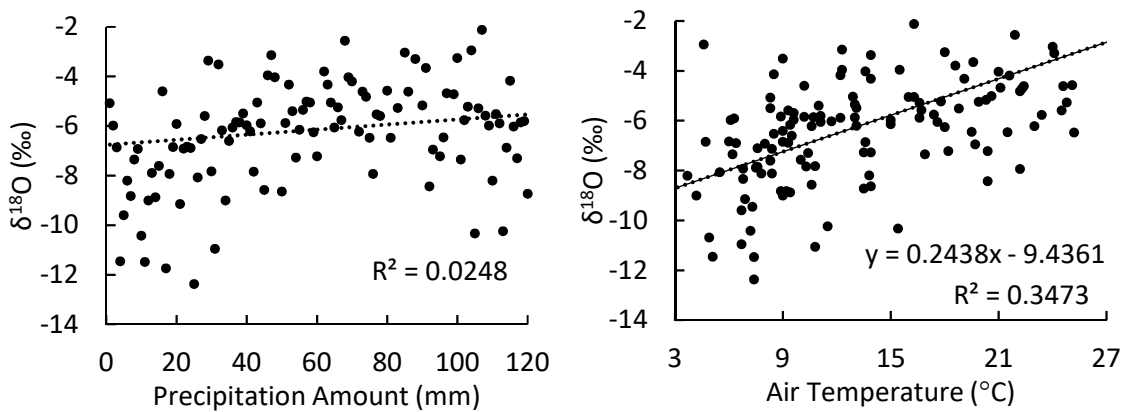
Figure 6.6: $\delta^{18}O$ vs precipitation amount (left) and $\delta^{18}O$ vs air temperature (right), Athens Pendeli. Statistical correlation for precipitation amount and $\delta^{18}O$ is low without correlation. Statistical correlation for air temperature and $\delta^{18}O$ is quite low but does show positive correlation.
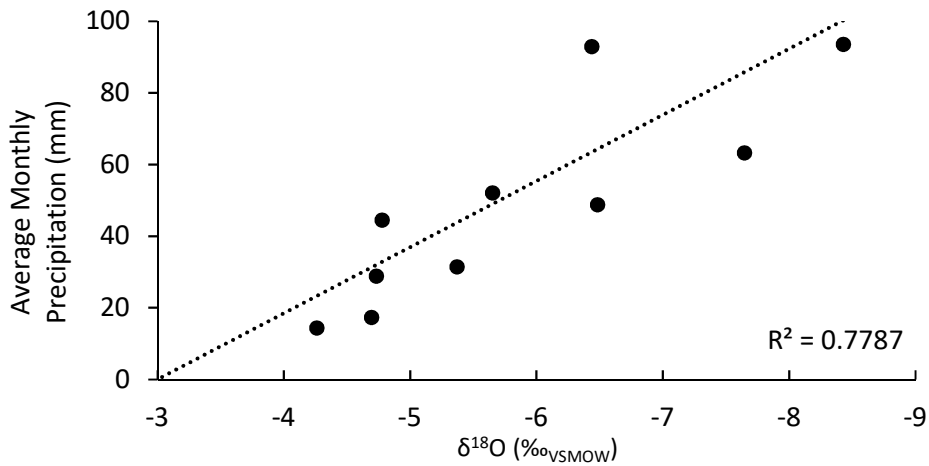
Figure 6.7: $\delta^{18}O$ values vs precipitation amount by month, Athens Pendeli. Data shows a strong positive correlation between wetter months and lighter $\delta^{18}O$ values.

The Patras precipitation isotope data show essentially a similar pattern to Athens Pendelli (Figure 6.7) with increasingly heavier compositions as the months become warmer, peaking in August (0.16 ‰$_{VSMOW}$ δ^2H and -0.39 ‰$_{VSMOW}$ $\delta^{18}O$). Values in both isotopes between November and March are very similar in range (-33 ‰$_{VSMOW}$ to -41 ‰$_{VSMOW}$ δ^2H and -6.4 ‰$_{VSMOW}$ to -5.7 ‰$_{VSMOW}$ $\delta^{18}O$) but rising quickly in April. The Patras data has the same trends as the Athens Pendeli data. A weak positive correlation between $\delta^{18}O$ and air temperature ($R^2 = 0.28$) (Figure 6.9) and a strong correlation between average monthly precipitation amounts and $\delta^{18}O$ (Figure 6.10) implies that both temperature and the amount effects influence stable isotopes of precipitation. However in interglacial times when large variation in winter temperature are unlikely, temperature effects are less likely to dominate isotopic signals. A minor depletion in isotopes is seen in the July mean (see also Athens June data) which includes a heavy (35.6 mm) rainfall year in 2002 and two light rainfall years. As summer precipitation over Greece is mostly convective, these summer events are controlled by the amount affect (Argirou and Lykoudis 2006), i.e. higher precipitation events will generate more negative $\delta^{18}O$ values, skewing the July average. δ^2H and $\delta^{18}O$ for 2002 corroborate this. The same pattern is also observed in the longer Patras weather station data since 1960 (Argirou and Lykoudis 2006) suggesting this is not a short term phenomena.
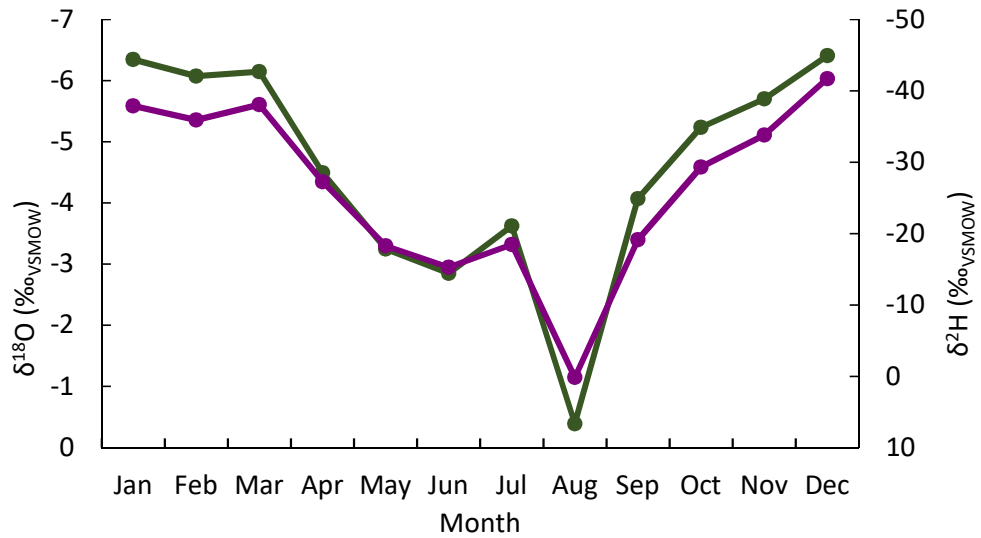
Figure 6.8: Monthly variations for δ²H (purple) and δ¹⁸O (green) at the Patras weather station for the period 2000-2014. Strong seasonal differences can be observed in both isotopes, becoming heaviest in August. Depletion in July presents an anomalous value in terms of the temperature effect.
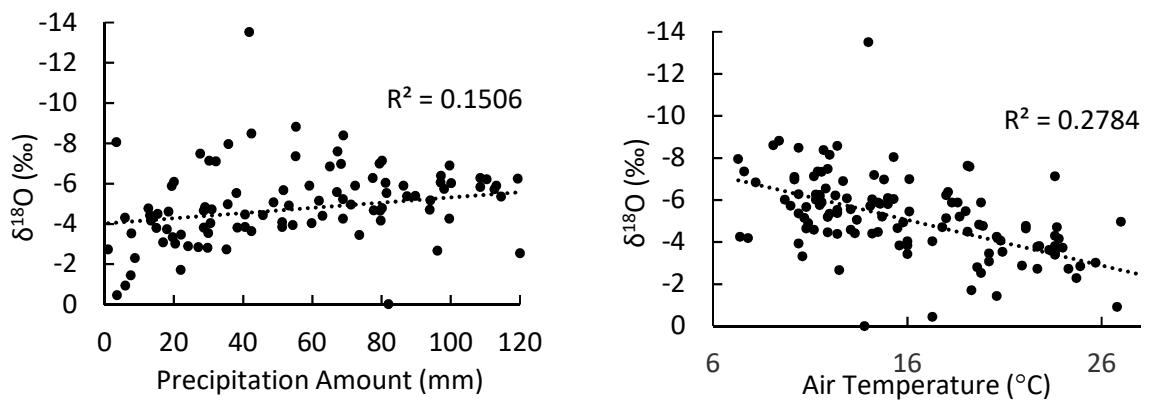
Figure 6.9: δ¹⁸O vs precipitation amount (left) and δ¹⁸O vs air temperature (right), Patras. Statistical correlation for precipitation amount and δ¹⁸O is low but slightly negatively correlated. Statistical correlation for air temperature and δ¹⁸O is quite low but does show positive correlation.
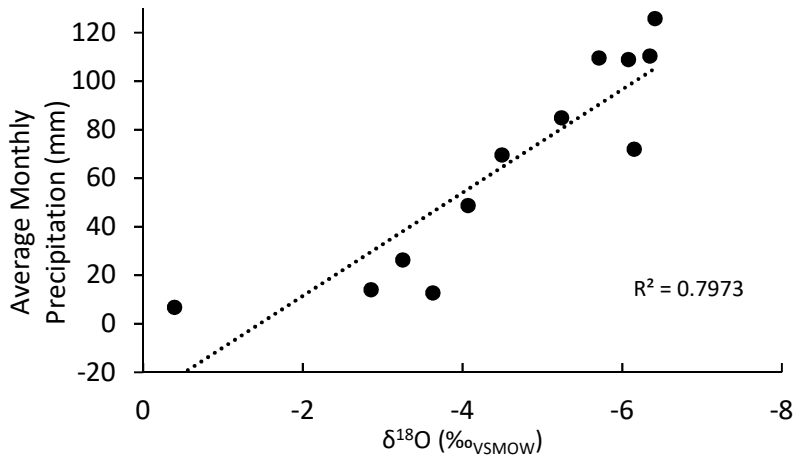
Figure 6.10: δ¹⁸O vs precipitation amount by month Patras. A strong positive statistical correlation is present between months which larger amounts of precipitation and lighter isotopes.

The GMWL (Equation 5.1), EMMWL (Equation 5.2) and Peloponnese LMWL (Dotsika et al., 2010 Equation 6.1) are plotted in Figure 6.11 along with IAEA Patras precipitation values, interpolated precipitation values for the Limnon Cave (Kastria) region (Bowen 2016 www.waterisotopes.org) and cave water values (Mason 2009, Table 6.3). The Peloponnese LMWL plots mainly between the GMWL and the EMMWL and clearly has a steeper gradient than both.

$\delta^2H = 9.20\ \delta^{18}O + 21.6$

Equation 6.1: The LMWL for the Peloponnese (Dotsika et al., 2010)

The Patras and OIPC interpolated Limnon precipitation values for the most part plot closely to the GMWL, aside from the isotopically lighter winter precipitation. The deuterium excess of Patras precipitation is closer to the GMWL (4.2 ‰). Cave drip and pool waters, as well as nearby spring values, form a LMWL halfway between the GMWL and the EMMWL, with a gradient almost parallel (Figure 6.11) suggesting an Atlantic moisture source with some local evaporation. Compositions are similar to more negative winter Limnon precipitation values, consistent with dripwater collection in the winter months but also with predominantly winter-spring recharge.
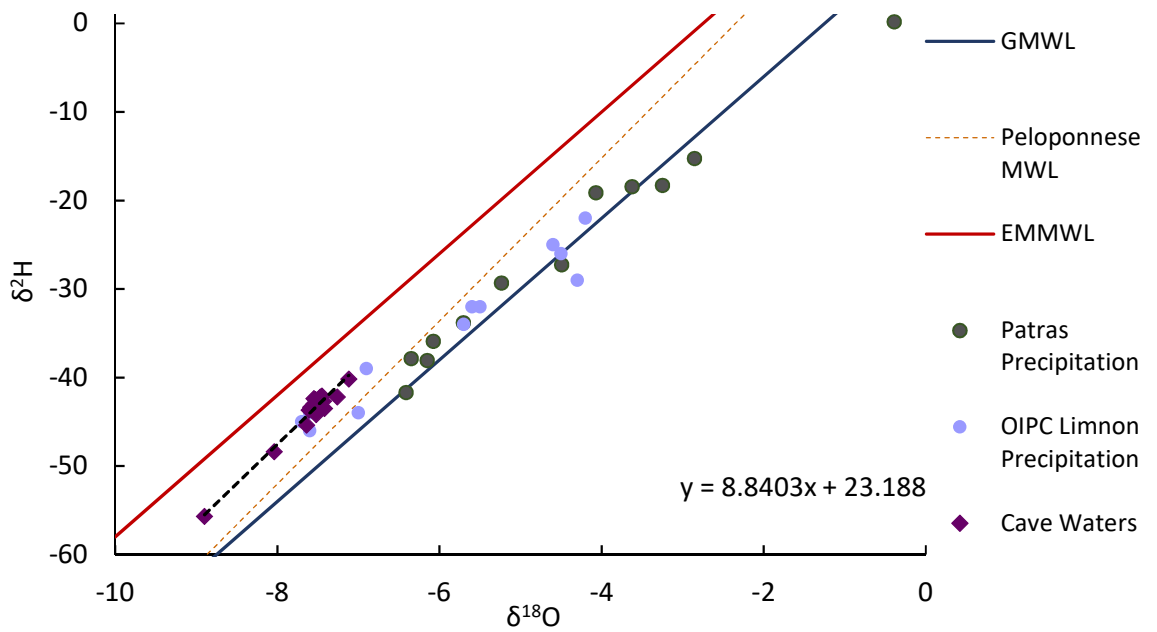
Figure 6.11: Plot of the Global Meteoric Water Line $\delta^2 H = 8 \, \delta^{18}O + 10$ (Craig 1961), Eastern Mediterranean Meteoric Water Line $\delta^2 H = 8 \, \delta^{18}O + 22$ (Gat and Carmi 1970) and Peloponnese local meteoric water line $\delta^2 H = 9.20 \, \delta^{18}O + 21.6$ (Dotsika et al., 2010) in addition to the average monthly isotopic compositions of the IAEA Patras station 2000-2014. The blue circles show the OIPC calculated isotopic composition of precipitation in the region of Limnon Cave (www.wateriso.utah.edu/waterisotopes/pages/data_access/oipc.html). OIPC calculates the isotopic composition at any given latitude, longitude and altitude by interpolating from known IAEA station data. Purple diamonds show cave waters and local spring data (see Table 6.3).

	Jan	Feb	Mar	Apr	May	Jun	Jul	Aug	Sept	Oct	Nov	Dec
$\delta^2 H$ (‰ V-SMOW)	-46	-45	-44	-34	-32	-29	-22	-25	-26	-32	-39	-44
$\delta^{18}O$ (‰ V-SMOW)	-7.6	-7.7	-7.0	-5.7	-5.5	-4.3	-4.2	-4.6	-4.5	-5.6	-6.9	-7.6

Table 6.2: OIPC water isotopic composition estimates by month for the geographical position and altitude of Limnon Cave.

Sample Name	Collection Date	$\delta^{18}O$ (‰$_{VSMOW}$)	δ^2H (‰$_{VSMOW}$)
Drip 1	Nov-06	-7.45	-42.1
	Jan-07	-7.12	-40.2
	Feb-07	-7.58	-43.4
	Feb-09	-7.55	-43.0
	Mar-09	-7.56	-43.4
	Apr-09	-7.64	-45.4
	Feb-10	-7.43	-42.7
	Mar-10	-7.48	-42.4
Drip 2	Nov-06	-7.50	-43.5
	Jan-07	-7.52	-44.2
	Feb-07	-7.55	-43.3
	Feb-09	-7.42	-43.5
	Mar-09	-7.57	-43.5
	Apr-09	-7.61	-43.7
	Feb-10	-7.53	-42.5
	Mar-10	-7.55	-42.4
Pool	Nov-06	-7.47	-42.2
	Average	-7.50	-43.0
Spring 1	Nov-06	-7.26	-42.2
Spring 2	Nov-06	-8.04	-48.4
Spring 3	Nov-06	-8.9	-55.7

Table 6.3: Dripwater isotopic data from Limnon Cave and from regional springs. Spring 1 is ~200m from the cave at 817m, Spring 2 is 3 km north at 972m and Spring 3 is at Kalavrita, 16 km north at 795m. (Mason 2009).

6.2 Results

6.2.1 Macromorphology and Petrography

6.2.1.1 Macromorphology

KTR-2 is a cream calcite stalagmite with fairly consistent diameter throughout its length (~12 cm in total, left hand axis ~7 cm) (Figure 6.3). The main macromorphological feature is the presence of two growth axes, present throughout Late Pleistocene-Holocene growth of KTR-2 but is most obvious at 90-93 mm where it is marked by a distinct cream layer. The diameter of KTR-2 is not largely affected by two growth phases, but the right hand axis, being shorter, appears to have grown at a slower rate than the left. Between 0 and 1 mm a marked, sub-horizontal, orange stained undulating surface 0.7 to <0.1 mm thick is present which can be traced laterally between the two growth phases, occurring stratigraphically lower on the right. Further macro-structure is limited; singular darker grey layers, are present in some places, e.g. at 3, 12 and 31 mm and are associated with flanking calcite that overlaps preceding growth. A section with lamination is defined by alternating cream and denser translucent calcite between 99 mm and 125 mm. Laminae pinch out towards the flank and vary in thickness from 0.2 to 3 mm. The top surface of the stalagmite appears corroded.

6.2.1.2 Petrography

KTR-2 is mostly formed of open columnar calcite (Frisia and Borsato 2010) with patches of microcrystalline calcite (Frisia et al., 2000) in limited but distinct areas. Primary porosity is moderate (~30%) to high (~65%) dependent on the fabric and irregular in form (Figure 6.12) although in some places it is clearly an artefact of thin sectioning (Figure 6.13 A).

Layers and lamination seen in hand specimen are formed of columnar calcite with varying density of inclusions (low density inclusion layers appearing darker in the hand specimen). Inclusions are usually rounded and range from 100 to 480 μm in size. Furthermore, inclusions can be randomly spaced or feature as horizontal inclusion surfaces (Figure 6.13 B-D); inclusion density being highly variable in both instances. Boundaries between these two inclusion types are planar and can occur within the same crystal. Changes in inclusion density may be responsible for discrete changes in colour visible in hand specimen. This is clearly demonstrated by the coloured lamination between 99 and 125 mm as it is defined by alternating inclusion-rich and inclusion-

poor elongate columnar calcite. Phases of inclusion-rich and inclusion-poor growth in this section occur within the same crystals, they do not mark a new phase of crystal growth.

Crystal length of the open columnar calcite typically increases up the stalagmite, accompanied by more planar boundaries and porosity decrease. The best-formed columnar textures occur in a region of lamination near the top of the stalagmite between 99 mm and 125 mm, where crystals are long (typically 2.5 mm) and boundaries are straight (Figure 6.12 D). Porosity in this columnar section is moderate. Where columnar calcites transition into and out of patches of microcrystalline calcite (see below), it is typically less well-formed (Figure 6.12 E-F) with shorter crystals (700 µm to 1.6 mm), and less straight boundaries (Figure 6.12 C). Porosity in these sections is higher than in better formed crystal fabrics.

Calcite growth above the hiatus (1-6 mm) is initially microcrystalline. Crystals are variable in size (0.16 mm to 0.5 mm) but are smallest nearest the hiatus with very irregular boundaries (Figure 6.12 A-B). Microcrystalline calcite is porous to very porous (porosity is ~40-70%), with pores mostly irregular and rounded. This fabric gradually transitions upwards into a poorly formed open columnar fabric. A sharp corroded boundary at the hiatus is not present, but in the immediate vicinity of the orange-stained hiatus layer, highly irregular and highly porous calcite is present, with irregularly curved boundaries (Figure 6.14 A-B). These crystals also contain detritus, accounting for their colour.

Microcrystalline calcite is also found from 19-30.5 mm, directly below the 31 mm dark layer. Here the central axis (of the left side) of growth is microcrystalline with flanking crystals showing some lateral extension. These irregular calcite fabrics are similar to those near the basal hiatus but crystals tend to be larger, up to 2.2 mm. At 30.5 mm a clear horizontal detritus-rich surface is present that truncates lateral crystal growth at the flank. Growth above the surface is vertical, open columnar.

In the region where the two growth axes are best highlighted (87-93mm) columnar calcite shows a period of lateral growth, again within flanking crystals. Toward the left flank the vertical to horizontal boundary is sharp and occurs at 87 mm. Growth more centrally to the growth axis shows columnar crystals gradually curving outwards towards the right. Three curved linear inclusion surfaces cut across both growth directions. These relationships are shown in Figure 6.14 E-F. Angled growth continues until 118 mm gradually returning to vertical.
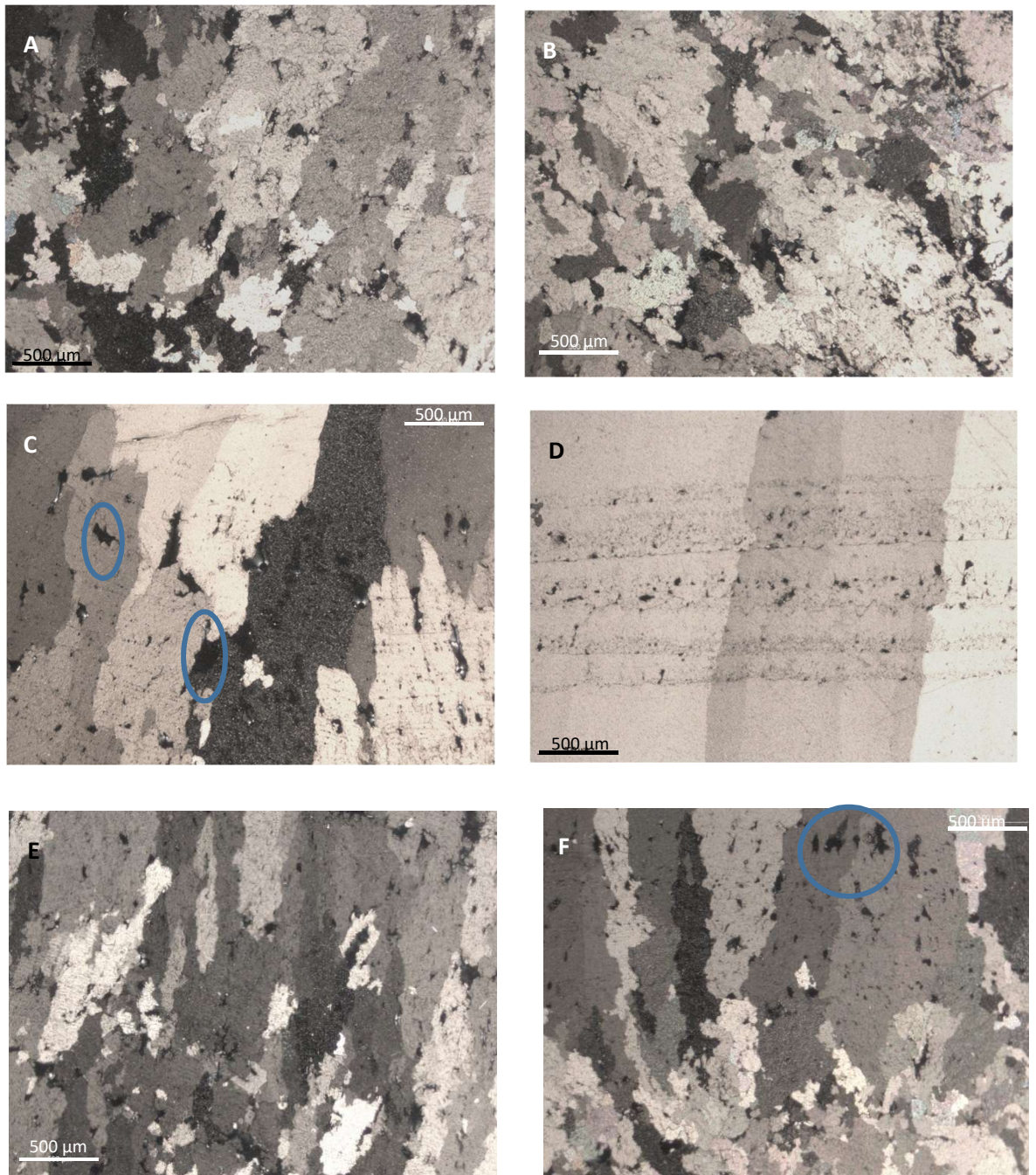
Figure 6.12: Representative fabrics in KTR-2. A and B. Microcrystalline calcite. C and D. Varying forms of columnar calcite. E and F. Gradual transitional boundaries between microcrystalline and columnar. Some examples of porosity are highlighted in blue circles.
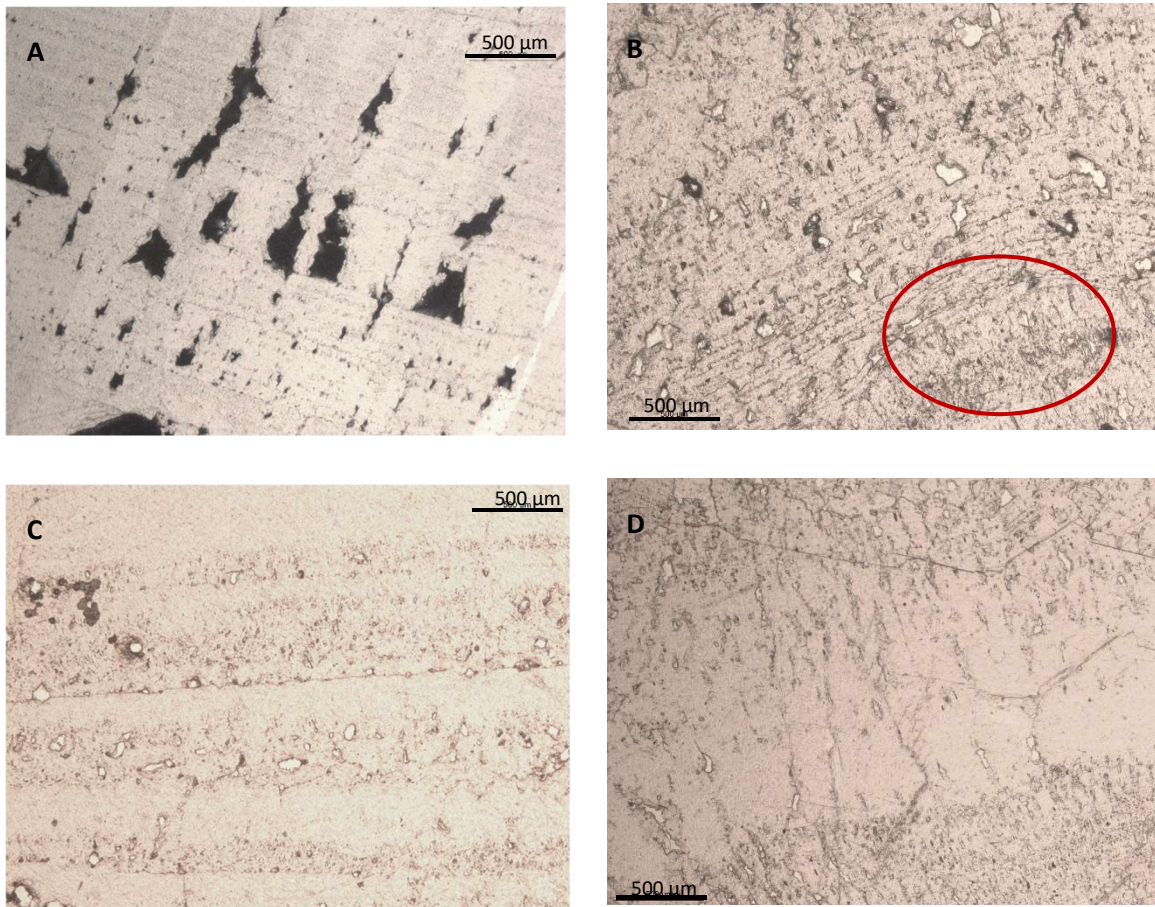
Figure 6.13: Porosity, inclusions and layering in KTR-2. A. Likely secondary porosity. B. High density linear inclusion surfaces with some randomly spaced inclusions (red circle). C and D Layering highlighted by alternating inclusion rich and inclusion poor calcite.
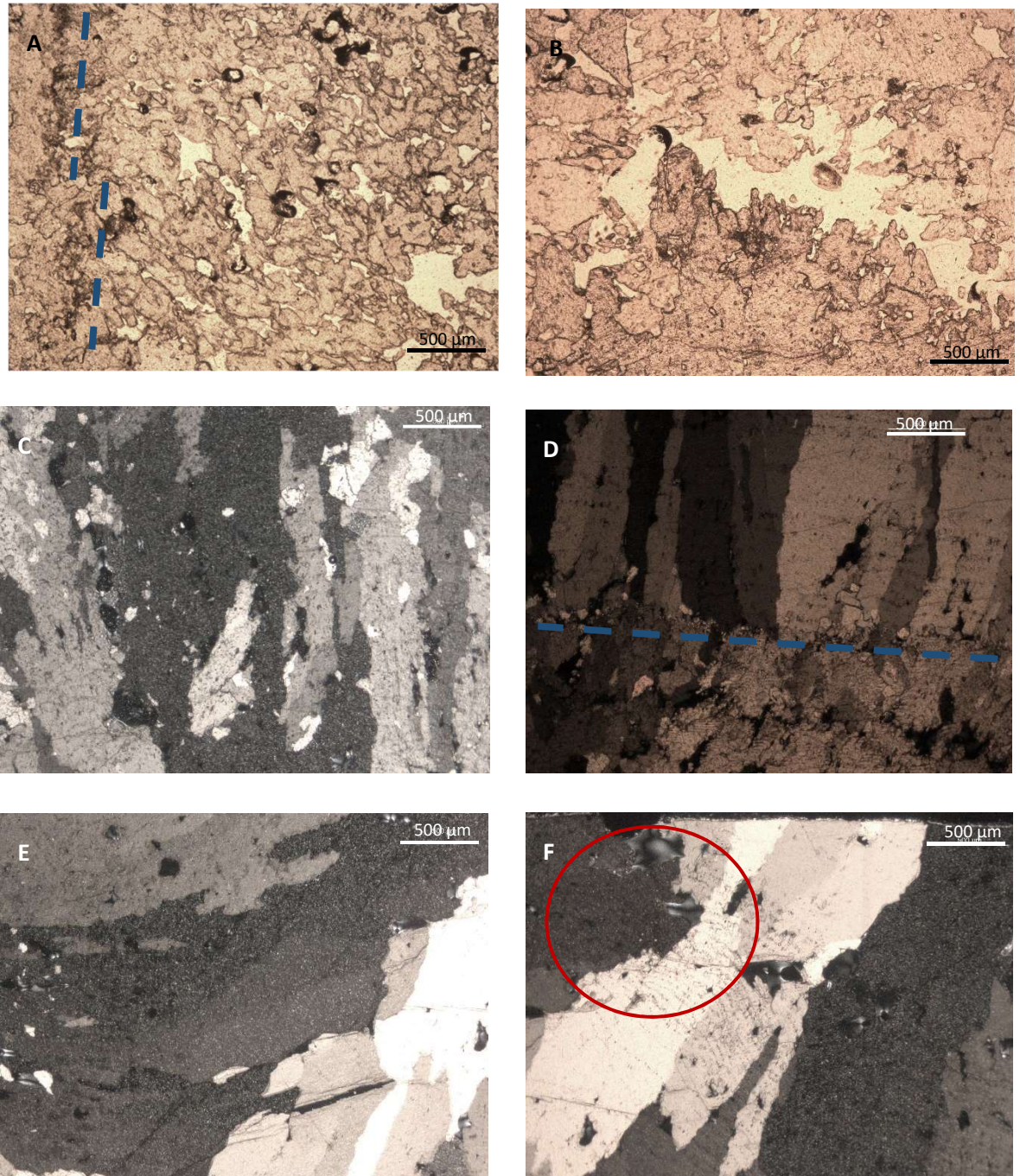
Figure 6.14: A. Hiatus layer marked by detritus (right way up) highlighted by the dashed blue line and showing the small irregular very porous microcrystalline below. B. Porosity and irregular terminations and boundaries suggestive of minor dissolution. C. Poorly formed open columnar calcite located above the transition from microcrystalline after the main hiatus. D. Detrital surface (blue dashed line) at 31 mm representing abrupt transition between microcrystalline and columnar calcites. E. Horizontal growth from left flank of columnar calcite below the surface split at 97 mm. F. Curved growth of columnar calcite below the surface split at 97 mm in a more central region, highlighted is the interaction with a horizontally grown crystal (red circle).

6.2.2 U-series dating

6.2.2.1 Sampling strategy

KTR-2 was first dated by Mason 2009, who also produced a low resolution stable isotope record. As this research investigates the Holocene portion of the stalagmite, the known Holocene growth was sampled, targeting a top age and potentially significant features guided by petrographic and stable isotope results. A total of 9 dates were obtained from this studied section of KTR-2, eight in the Holocene and one below the hiatus to constrain its age (Figure 6.13).

6.2.2.2 Age model and growth rates

Table 6.4 shows the age data. KTR2-1 and KTR2-2 bracket the hiatus that lasted from 26,500 yr BP to 11,500 yr BP close to the base of the Holocene. Extrapolation of ages between the sample trench and the hiatus surface itself gives an age of the restart of growth of 11,920 yr BP. Only KTR2-1 shows evidence of significant detrital thorium contamination (^{230}Th/^{232}Th = 27.5). All ages lie in stratigraphic order except KTR2 5 and 6 (8641 ± 43 yr BP and 8821 ± 50 yr BP respectively). Sample locations were investigated petrographically but no indication of micro-dissolution was seen. KTR2-6 has a lower U content and slightly higher ^{234}U/^{238}U ratio than adjacent samples and may therefore have experienced slight U mobility and consequently this sample was omitted from the age model.

Sample Name	Height above base (mm)	^{238}U (ppm)	^{232}Th (ppb)	$^{234}U/^{238}U$	$^{230}Th/^{238}U$	$^{230}Th/^{230}Th$	Initial $^{234}U/^{238}U$	Date uncorr (yr BP)	Date corr (yr BP)
KTR2 9	120	0.1779	0.1271	1.0209 ± 0.0012	0.0636 ± 0.0032	271.6	1.0213 ± 0.0012	7033 ± 34	6947 ± 37
KTR2 8	92	0.2841	0.1986	1.0094 ± 0.0011	0.0710 ± 0.00029	309.9	1.0096 ± 0.0011	7973 ± 32	7888 ± 35
KTR2 7	84	0.229	0.2618	1.0065 ± 0.0011	0.0745 ± 0.00035	199.1	1.0066 ± 0.0011	8419 ± 34	8321 ± 42
KTR2 6	71	0.1681	0.2714	1.0093 ± 0.0012	0.0790 ± 0.00043	149.7	1.0096 ± 0.0012	8934 ±38	8821 ± 50
KTR2 5	63	0.2174	0.2859	1.0029 ± 0.0012	0.0770 ± 0.00036	178.8	1.0030 ± 0.0011	8746 ± 33	8641 ± 43
KTR2 4	33	0.1797	0.2306	1.0063 ± 0.0012	0.0832 ± 0.0042	197.9	1.0064 ± 0.0012	9442 ± 43	9339 ± 50
KTR2 3	24	0.2575	0.8751	1.0082 ± 0.0012	0.0933 ± 0.00069	84.3	1.0084 ± 0.0012	10,688 ± 41	10,522 ± 82
KTR2 2	9	0.2259	0.7027	1.0105 ± 0.0015	0.1011 ± 0.00064	99.7	1.0088 ± 0.0012	11,585 ± 40	11,428 ± 76
KTR2 1	below	0.2148	5.4331	1.0308 ± 0.0036	0.2232 ± 0.0042	27.5	1.0332 ± 0.0038	27,312 ± 930	26,514 ± 529

Table 6.4: U-series results for KTR-2 including stratigraphically reversed ages at 63 mm and 71 mm. All errors are 2 s.d. Age corrections assume a bulk earth composition for the detrital Th component. This assumes stalagmite calcite is at secular equilibrium with the bulk earth $^{232}Th/^{230}Th$ value (3.8) and that initial $^{230}Th/^{232}Th$ has an atomic ratio of $4.4 \pm 2.2 \times 10^{-6}$. Uncertainty errors are $\pm 50\%$.

Figure 6.16 shows the age model for the Holocene section of KTR-2 derived from COPRA (Breitenbach et al., 2012). The date below the hiatus is not modelled in the plot but an age of 26,500 yr BP suggests the stalagmite began growing during MIS 2 or MIS 3. As shown previously growth restarted near the end of the Younger Dryas. The youngest age of 6947 ± 37 yr BP shows there was an early Holocene growth phase of ~4500 years. Growth was initially slow (0.011 mm/yr) compared to the rest of the stalagmite with a possible hiatus occurring between samples KTR2 3 and 4 (10,522 yr BP and 9339 yr BP respectively). Fastest growth occurred during the interval 8641 yr BP to 8321 yr BP (0.069 mm/yr). KTR2 7 (8321 yr BP) was sampled just prior to the split in growth axis (Figure 6.3) and growth rates between 8321 yr BP and the top are slower but consistent compared to the rest of the previous growth. Growth rates between 8321 yr BP and 6947 yr BP range between 0.021 and 0.029 mm/yr.

KTR2 9 **6947 ± 37**

KTR2 8 **7888 ± 35**

KTR2 7 **8321 ± 42**

KTR2 6 **8821 ± 50**

KTR2 5 **8641 ± 43**

KTR2 4 **9339 ± 50**

KTR2 3 **10,522 ± 82**

KTR2 2 **11,428 ± 76**

KTR2 1 **26,514 ± 529**

20 mm
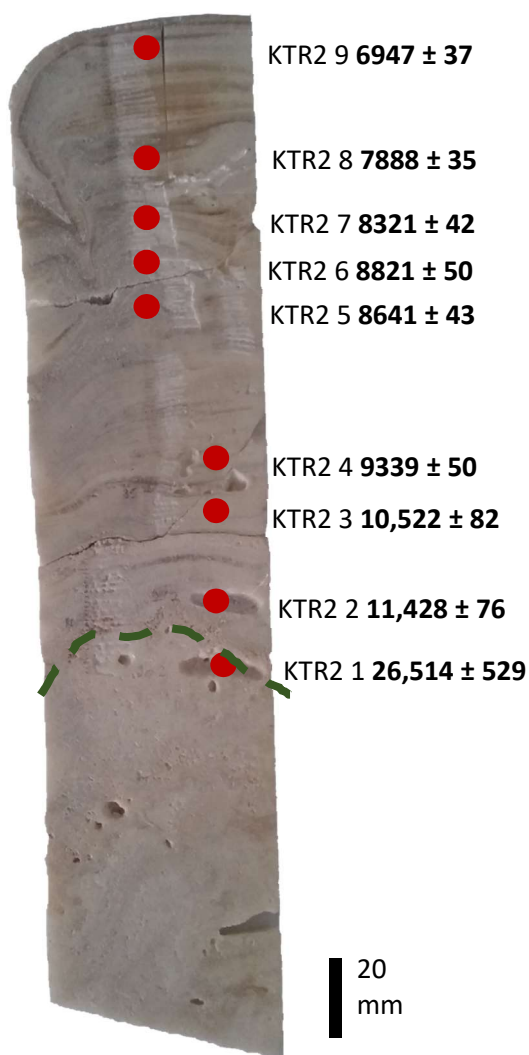
Figure 6.15: Slabbed section of KTR-2 with sample locations for U-series dating and dates. Green dashed line indicates the hiatus surface.
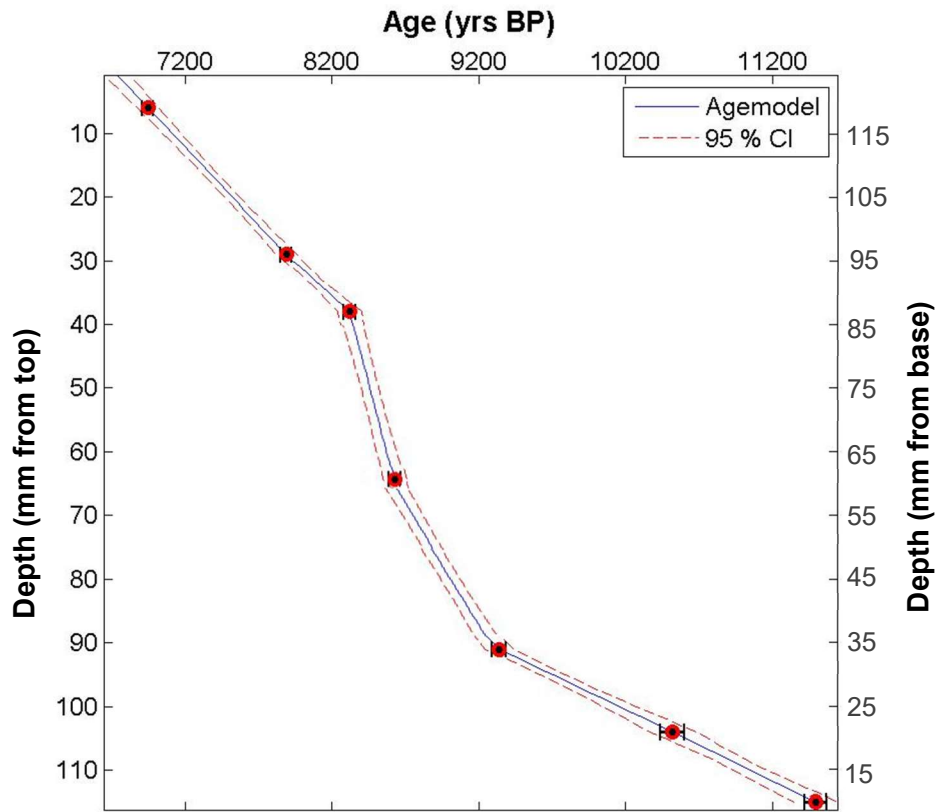
Figure 6.16: COPRA linear age model for the entire Holocene section of the KTR-2 stalagmite. No hiatuses are inferred. Red dashed line represents the error at 2 s.d.

Comparing the results from both statistical methods shows that on the whole uncertainties in ages between the two methods are low. The average unknown age error is 59 years (Table 6.5) but this is heavily influenced by StalAge incorporating 8821 yr BP into the age model rather than it being an outlier. The date of 8641 yr BP was chosen for COPRA for reasons outlined in Section 6.2.2.2. So, for dates between KTR2 5 and KTR2 6 and unknown age error of at least 249 years should be taken into consideration. This is particularly important for changes occurring around the period of the 8.2 kyr event. During the rest of the growth of KTR-2 the error between the two dating methods is negligible and can be ignored.

Depth (mm from base)	Depth (mm from top)	COPRA (yr BP)	StalAge (yr BP)	Minimum unknown age error (yr BP)
31	105	10610	10601	9
35	102	10340	10388	12
85	42	8454	8474	20
98	29	8162	7913	249
118	9	7069	7065	4

Table 6:5: Comparison of 5 key ages which are palaeoclimatically or stratigraphically significant in KTR-2.

6.2.3 Stable isotopes

6.2.3.1 Sampling strategy

Results of the dating show KTR-2 could provide a near continuous early Holocene record in a region which is lacking in palaeoclimate observations from this time period. Thus stable isotope profiles were obtained at 1 mm sample spacing totalling 127 samples. Given its age and continuous growth, KTR-2 could potentially record isotopic changes associated with the 8.2 kyr event if it significantly affected climate, particularly rainfall, in Greece. In light of this, the section of the stalagmite between 8641 yr BP and 7888 yr BP (33 mm) was micromilled at high resolution (see Figure 6.15 for dating locations). Sample resolution in this section is about 5 to 6 years.

6.2.3.2 Full axial profile

Stable isotope data is shown in Figure 6.19 (raw data located in an Appendix) and 5th order polynomials are applied to both oxygen and carbon to highlight isotopic trends. $\delta^{18}O$ shows a range in values of -7.26 ‰ to -4.98 ‰, although upper and lower values occur during short lived excursions. Between 11,900 yr BP and 10,500 yr BP a negative trend with low variation is observed. Relatively negative $\delta^{18}O$ isotopic values are sustained until 8900 yr BP after which the mean becomes progressively enriched up to the cessation of growth. Clear negative excursions of 1 ‰ are present at 8450 and 7900 yr BP. The former is immediately followed by a 1.3 ‰ positive excursion culminating at 8160 yr BP. Further rapid positive shifts occur at 7070 yr BP (1.6 ‰) and 7000 yr BP immediately prior to the termination of growth.

The $\delta^{13}C$ record (Figure 6.19) shows larger variation (range in values -8.72 ‰ to -3.22 ‰) than the $\delta^{18}O$ record. The records show some co-variation at shorter timescales but this is not represented in the statistical relationship (Figure 6.18). Similarly to $\delta^{18}O$, the $\delta^{13}C$ record between 11,900 yr BP and 10,500 yr BP broadly shows decreasing isotopic values. A sustained negative trend occurs until 8900 yr BP, after which isotopes become enriched by 3 ‰, remaining high until 8140 yr BP. From 7900 yr BP to 7200 yr BP relatively negative isotopes similar to values prior to 8900 yr BP are observed before rising by 1 ‰ for the rest of the record. The culmination of decreasing isotopic values in the early Holocene is marked by a major negative excursion (3.46 ‰). This excursion matches a smaller 0.5 ‰ excursion in $\delta^{18}O$. Similarly to $\delta^{18}O$ a large positive excursion is noted at 7000 yr BP.
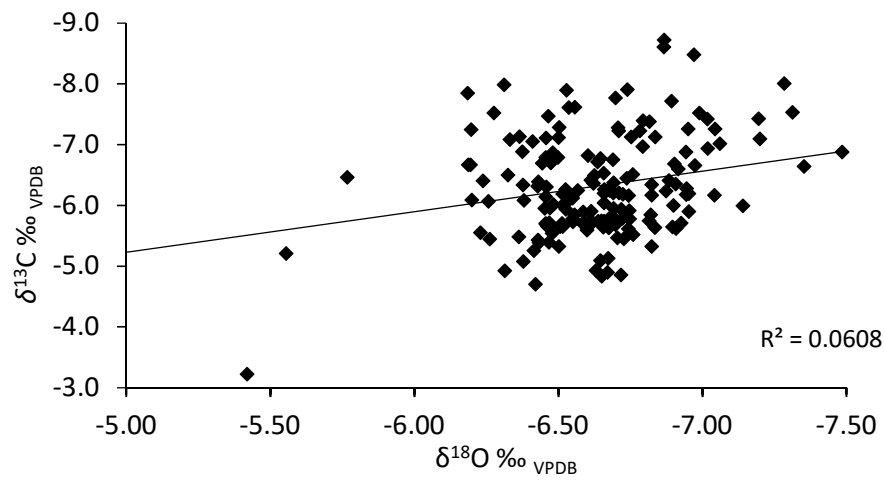
Figure 6.18: cross plot of axial δ¹⁸O and δ¹³C for the KTR-2 stalagmite. There is no correlation but some co-variation exists at shorter time scales.
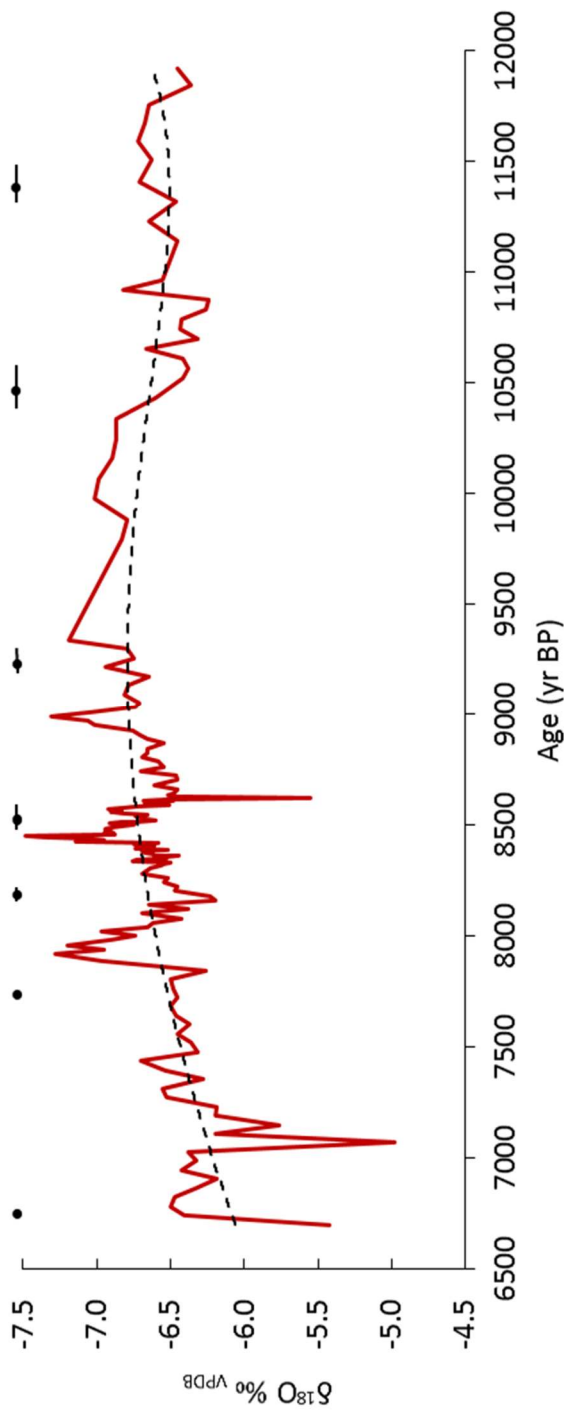
Figure 6.19: Axial stable isotope profiles for the KTR-2 stalagmite. Above (red) $\delta^{18}O$ and below (blue) $\delta^{13}C$.

Absolute ages and error bars, according to the horizontal scale is shown at top of $\delta^{18}O$ record.
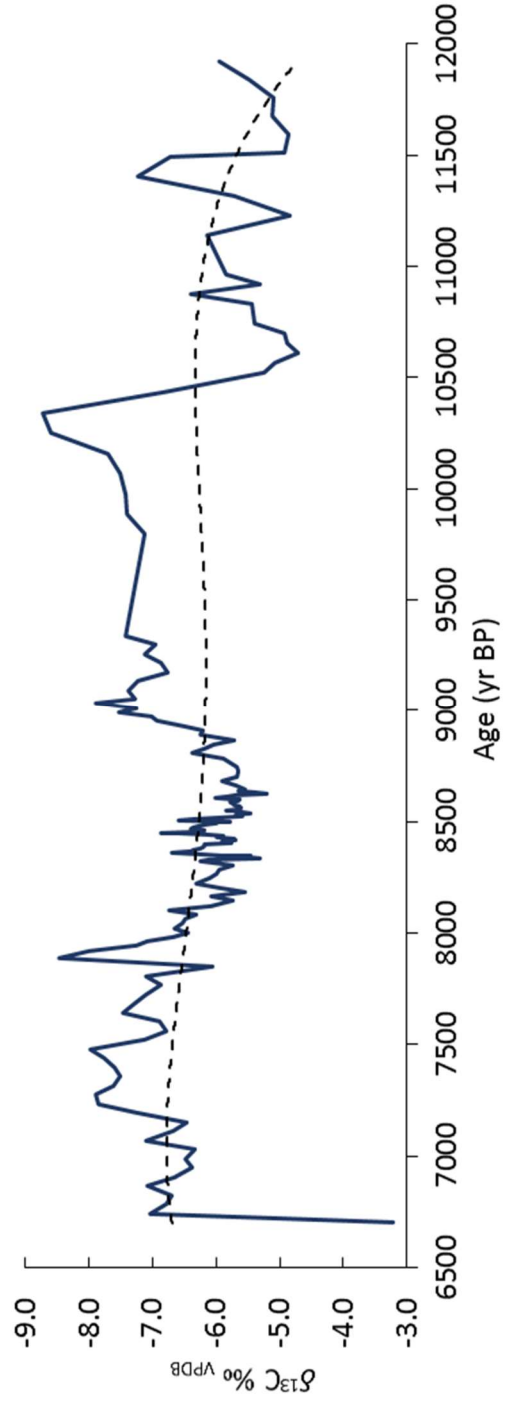
6.2.3.3 Micromilled profile

As with the full stalagmite isotopic profiles, micromilled profiles have 5th order polynomial trendlines fitted (Figure 6.20). The trends observed shows both isotopes co-vary similarly throughout this period. The range in $\delta^{18}O$ is -5.55 ‰ to -7.48 ‰. From the start of the section (8641 yr BP) $\delta^{18}O$ is gradually declining. A significant positive excursion is observed between 8630 yr BP and 8615 yr BP (0.92 ‰). The declining trend abruptly ends with the largest observed negative excursion (0.61 ‰) peaking to the most negative value at 8450 yr BP. Subsequent $\delta^{18}O$ values become more positive and a trend of heavier isotopes persists until 8160 yr BP, where isotopic measurements are the most enriched for this interval (-6.20 ‰). $\delta^{18}O$ shows a declining trend following 8160 yr BP for the rest of the record. Values decrease by over 1 ‰ in this 300 year period.

The overall trend in $\delta^{13}C$ is similar to $\delta^{18}O$ but variation about the mean is higher. The $\delta^{13}C$ range is -5.32 ‰ to -8.48 ‰. The long term trend shows more positive isotopic measurements are prevalent over much of the period 8600 yr BP to 7900 yr BP with a declining trend observed from 8100 yr BP to the end of the record. A small negative excursion occurs at 8450 yr BP as seen in $\delta^{18}O$ but is not significant. Peak increases in $\delta^{13}C$ occur at 8300 yr BP and 8180 yr BP, the latter of which roughly correlates to the highest value in $\delta^{18}O$.
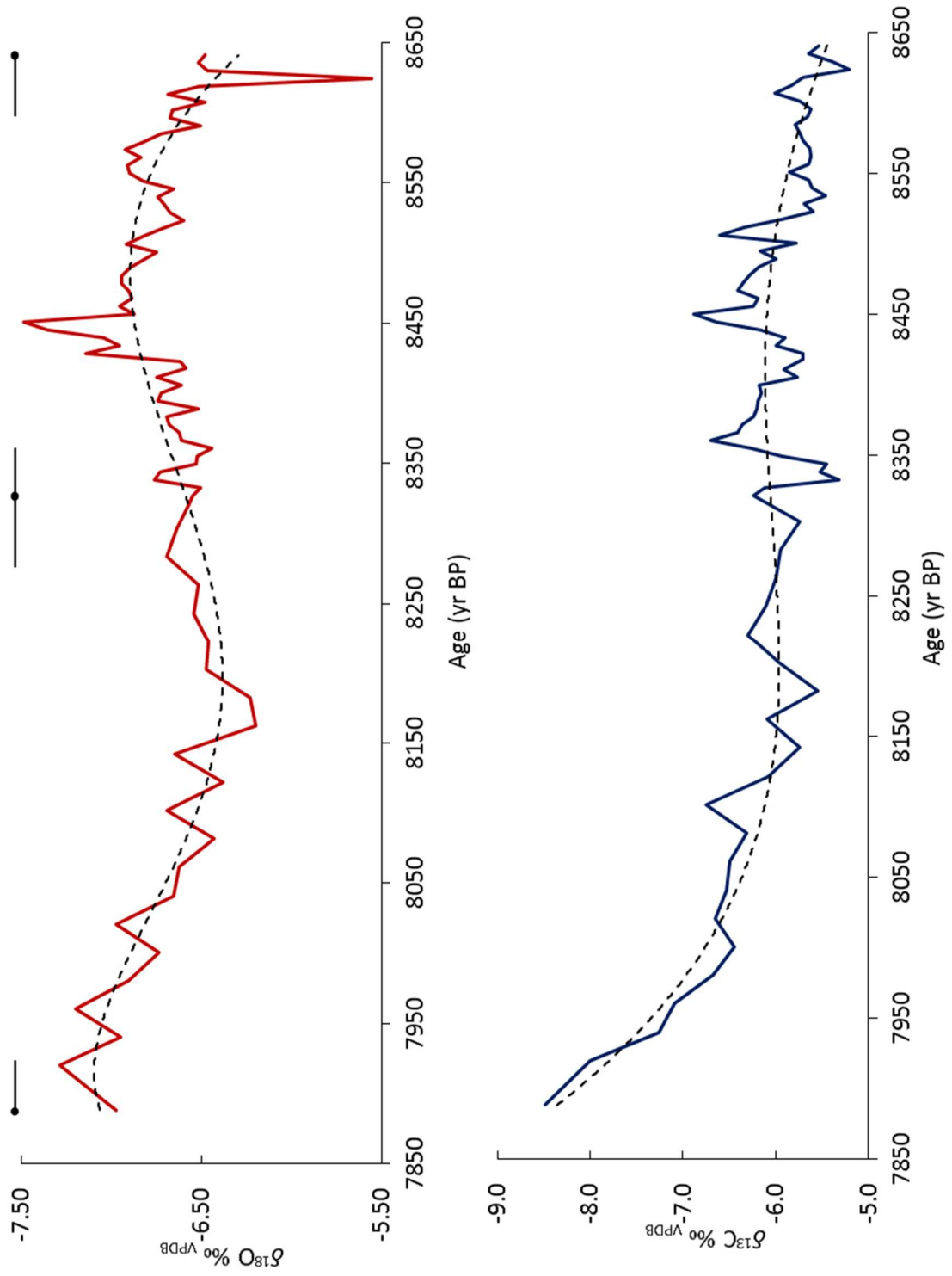
Figure 6.20: Axial stable isotope profiles for the micromilled section of the KTR-2 stalagmite. Above (red) $\delta^{18}O$ and below (blue) $\delta^{13}C$. Absolute ages and error bars shown above $\delta^{18}O$, according to the horizontal scale.

6.2.4 Trace Elements

6.2.4.1 Sampling strategy

A 31.8 mm trace element profile, between 8641 yr BP and 7888 yr BP, was taken to coincide with the micromilled stable isotope profile. The data were generated by laser ablation ICPMS (see Methods Appendix) with a spot size of 30 μm and increment between spots of 200 μm. Ablation was done on a tablet of stalagmite immediately adjacent to the micromilled sample position. Trace elements were chosen to help interpret environmental signals from stable isotopes, particularly Mg and Sr, but also to monitor likely detrital contents (e.g. Ba, K, Na, P); see also Fairchild et al. (2000) and Huang et al. (2001).

6.2.4.2 Profiles and description

The overall shape of the trace element profiles of Mg and Sr are broadly similar (Figure 6.21) but the amount of Sr is smaller (mostly between 100-200 ppm) compared to Mg (mostly between 200-400 ppm). The structure of the profile is clearest in Mg, two small step increases in concentration occur at 8560 yr BP (70 ppm) and 8360 yr BP (90 ppm). The concentration of Mg peaks at 8160 yr BP, 200 ppm higher relative to 'baseline' values, after which, the concentration falls for most of the rest of the record. A large short lived reduction in Mg of 200 ppm is observed between 8445 yr BP and 8430 yr BP. Sr shows less structure than Mg. There is no increase in Sr corresponding with the first step increase in Mg but a small (70 ppm) increase in concentration is observed in Sr at 8360 yr BP. A peak in concentration is observed at 8160 yr BP but the largest peak in Sr follows the short lived reduction in Mg at 8440 yr BP to 8430 yr BP. Unlike Mg, following the 8160 yr BP peak, Sr concentrations remain comparatively high compared to the rest of the record.

The Ba profile is dissimilar to both Mg and Sr but similar to both Na and P. Ba, Na and P are all mostly present at low concentrations (10's of ppm) but distinct, partially correlatable, peaks occur in all elements except Mg in the period 8474 yr BP and 8406 yr BP.
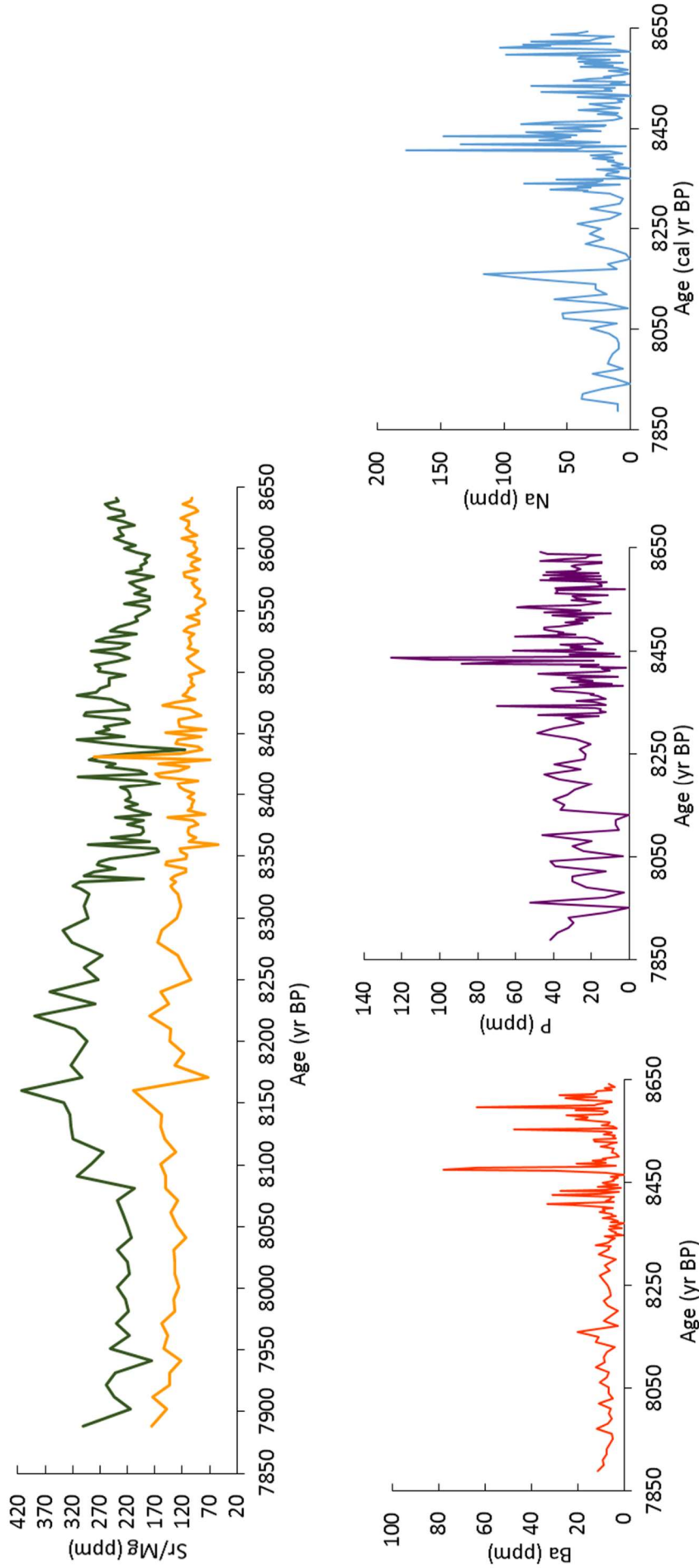
Figure 6.21: Overleaf. Trace element concentration profiles for the micromilled section of KTR-2. Trace element content of each element is recorded in ppm normalised to 100% calcite (i.e. 40 wt% Ca). Sr (yellow) and Mg (green) are plotted together due to similar trends. The concentration of Mg is bigger than Sr but it is clear that they follow the same trend. A large reduction in Mg is seen between 8445 yr BP and 8435 yr BP whilst a large rise is seen in Sr immediately after at 8430 yr BP. Ba (orange), P (purple) and Na (blue) record large peaks in concentration between 8470 yr BP and 8400 yr BP, a similar time to large concentration changes in Mg and Sr.

In addition to concentration data molar ratios of Mg/Ca, Sr/Ca and Mg/Sr are plotted with $\delta^{18}O$ and $\delta^{13}C$ respectively (Figure 6.22 and 6.23). Trace element content is in ppm normalised to 100% calcite (i.e. 40 wt% Ca). Running means are applied to attempt to smooth high frequency variability and account for a reduction in growth rate after 8321 yr BP (Figure 6.15) causing a misleading change in high frequency variability. Smoothed profiles of Mg/Sr, Mg/Ca and Sr/Ca are all essentially similar, although high frequency variability is arguably higher in the Sr record. Increases in Mg/Sr and Mg/Ca are observed at 8550 yr BP with a second increase in all ratios at 8350 yr BP. A decline is observed at 8160 yr BP in Mg/Ca until 7888 yr BP but variation is low.

Variation in $\delta^{13}C$ is not clearly related to any trace element variation; however $\delta^{18}O$ does show some similarity to the smoothed trends in Mg/Sr although changes in Mg/Sr appear to 'lead' those in $\delta^{18}O$ by up to 10 years. There is also some relationship between Mg/Ca and Sr/Ca vs $\delta^{18}O$ particularly the first 100 years of the record and from 8360 yr BP until 8080 yr BP.

The largest negative excursion in $\delta^{18}O$ occurs at 8450 yr BP (-7.48 ‰); a similar magnitude excursion is also present at 7920 yr BP following a 250 year long trend of increasing $\delta^{18}O$ values. The largest decreases in Mg/Ca and Mg/Sr are similarly timed (noting a lag of ~20 years) at 8436 yr BP and 8431 yr BP. Also equivalently timed is the largest rise in the Sr/Ca ratio at 8431 yr BP and peaks in Na, Ba and P. The peak in $\delta^{18}O$ (-6.20 ‰) at 8162 yr BP is closely followed (2 year lag) by significant increases in the ratios of Mg/Ca and Sr/Ca, principally in Mg/Ca which is the largest of the record (1.7). A substantial increase in Mg/Sr is noted slightly prior to the $\delta^{18}O$ excursion at 8170 yr BP.

221
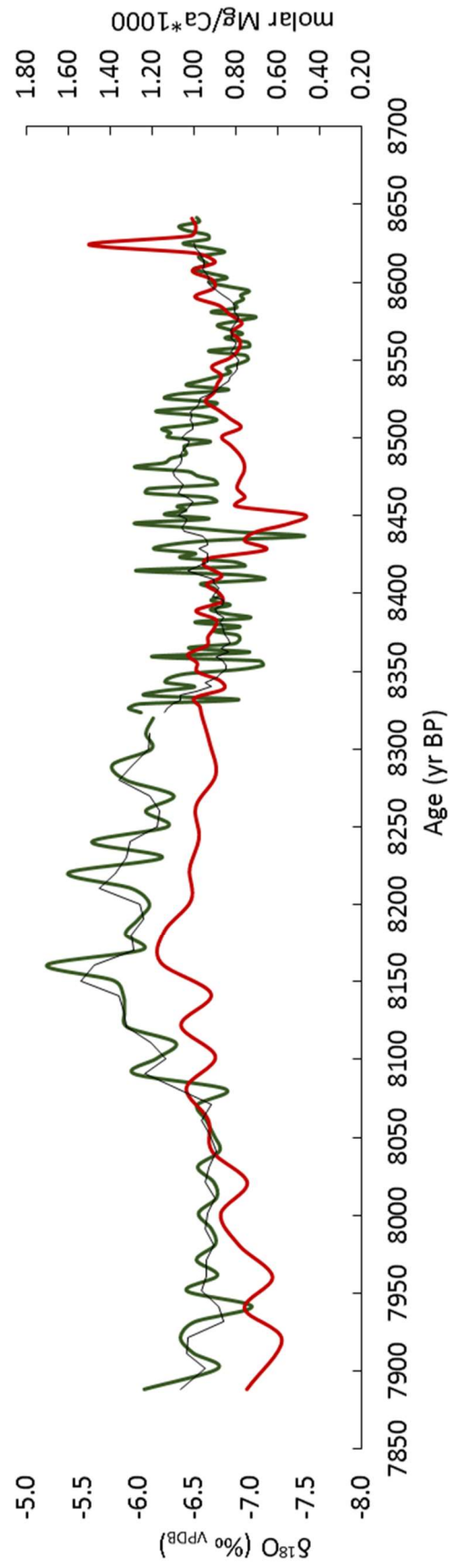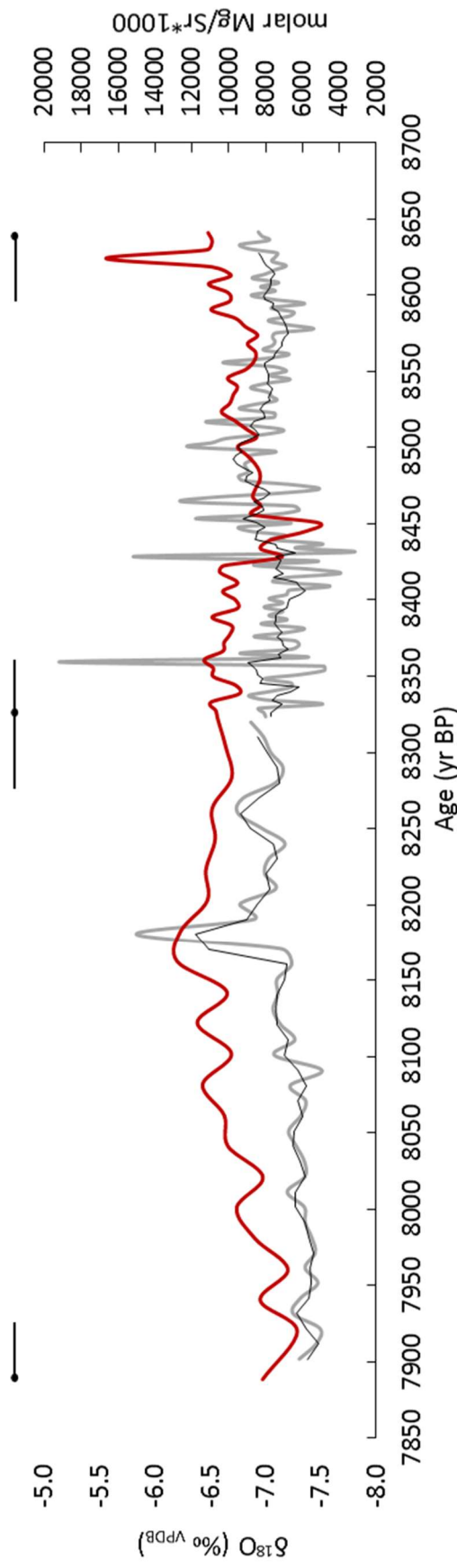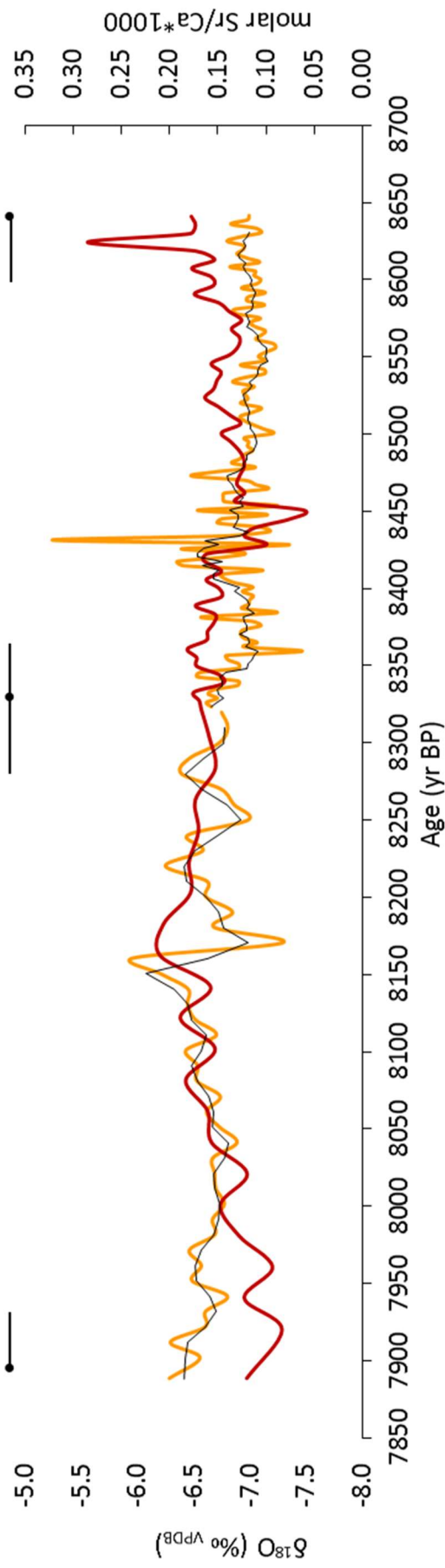
Figure 6.22: This page and overleaf. δ¹⁸O and Mg/Sr (grey), Mg/Ca (green) and Sr/Ca (yellow) ratios. Variation in δ¹⁸O is well correlated with Mg/Sr and partially correlated with Mg/Ca and Sr/Ca. Lag in records is of the order of less than 1 to 2 decades for individual co-varying changes. The periods 8500 yr BP to 8400 yr BP and 8170-8162 yr BP are important in terms of δ¹⁸O excursions and peaks/troughs in trace element ratios.
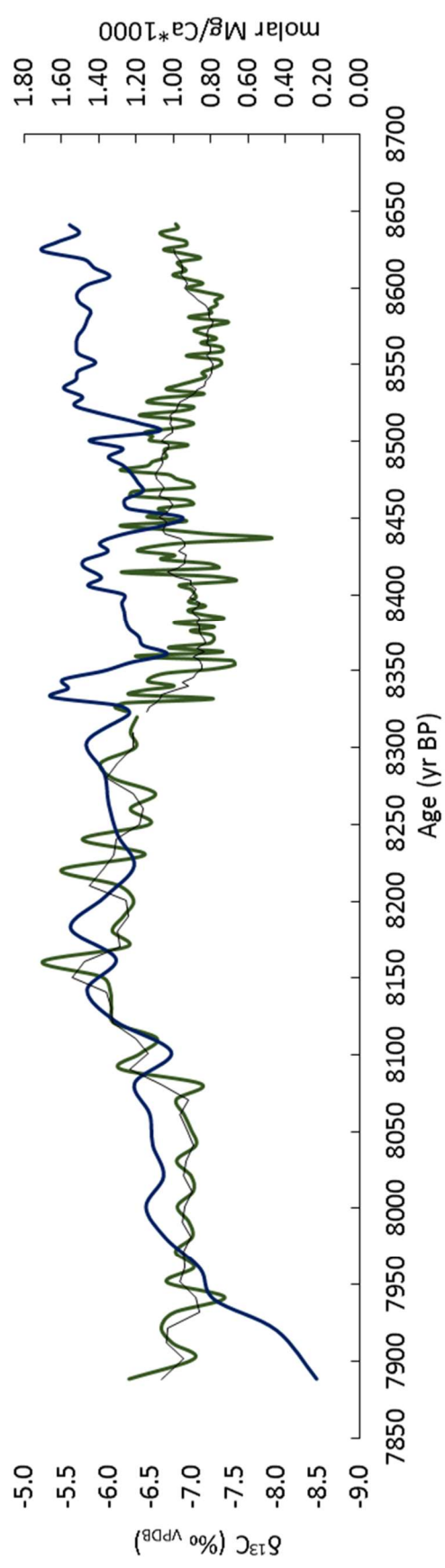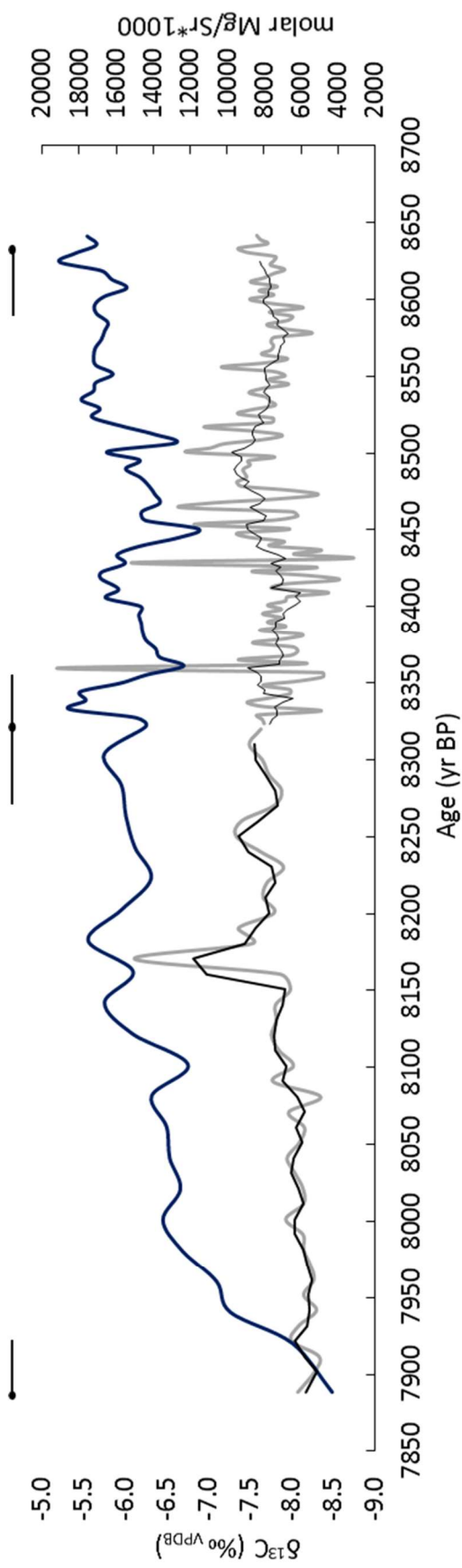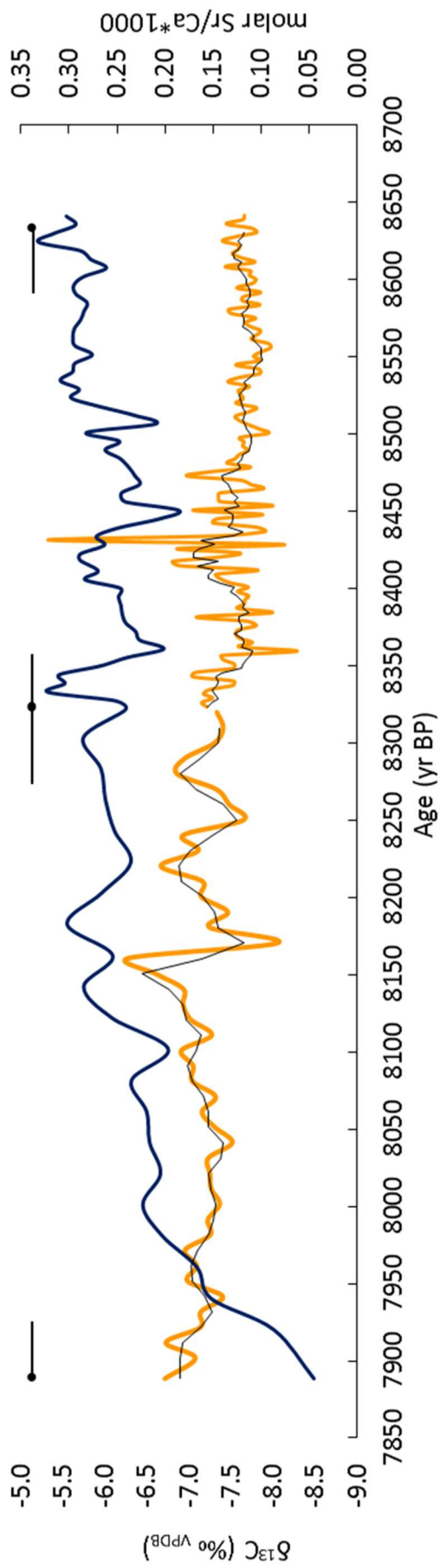
Figure 6.23: This page and overleaf. δ¹³C and Mg/Sr (grey), Mg/Ca (green) and Sr/Ca ratios (yellow). Variation in δ¹³C does not correlate with trace element ratios.

6.3 Discussion and Palaeoclimatic Interpretation

6.3.1 Equilibrium deposition

Dripwater and modern calcite δ^{18}O data from Limnon Cave is shown in Table 6.3 (Section 6.1.3) and in Table 6.6 (Mason unpublished). Dripwater data is from winter months when recharge is at a maximum and most likely to dominate the speleothem isotopic signature.

Modern calcite precipitating in Limnon Cave has an average δ^{18}O value of -6.28 ± 0.13‰$_{PDB}$ (Table 6.5) and average cave water δ^{18}O values are -7.50 ± 0.12‰$_{SMOW}$ (Table 6.5), the scatter in both cases being very low. Using average calcite and cave water values, the calculated temperature from the Kim and O'Neil (1997) equation is 9.4°C and from the Tremaine et al. (2011) equation it is 13.1°C (see Methods Appendix). The range of cave temperatures observed throughout the year is reported as 12.33°C -17.05°C (Vassilopoulou n.d. kastriacave.gr/en) and spot temperatures recorded in the cave in November 2008 were ~14.6°C (Mason 2009). It is likely that temperatures through winter to spring are near the lower end of the annual range and that tourist activity now results in elevated temperatures during the summer and autumn months. The calculated temperature of 13.1°C is compatible with this hypothesis and it therefore seems likely that Limnon calcite is behaving in a similar manner to most other speleothems reported in the literature and is precipitating in quasi-equilibrium with its dripwaters.

	δ^{18}O (‰$_{VPB}$)	δ^{13}C (‰$_{VPB}$)
Active Soda Straw	-6.29	-8.70
Top of active stal 1	-6.16	-8.47
Top of active stal 2	-6.46	-6.95
Active stal drape	-6.22	-7.60
Average	-6.28	-7.93

Table 6.6: Modern calcite stable isotopes for speleothem samples in Limnon Cave (Mason unpublished).

6.3.2 Petrography and environment of formation

Late Pleistocene to Holocene growth of KTR-2 is defined by the development of two growth axes with the left growing more quickly than the right. The hiatus surface at 0-1 mm, which appears to cover most of the time period between 26,500 yr BP and 11,500 yr BP (Table 6.1), clearly defines the split growth phase in the macromorphology, but does not mark the point at which it started, implying that drip positions had changed sometime in the Pleistocene, not necessarily linked to climatic change. While the duration of non-growth at this surface is dated either side, circumstantial evidence from the linear interpolation and the relatively negative isotopic values at the start of the record implies growth restarted during the period of recovery towards the end of the Younger Dryas. The corroded appearance of the hiatus surface along with the orange colouration, indicative of oxidation or ferrous iron during the period of non-deposition, suggests a longer period of non-deposition than anywhere else in the stalagmite. Furthermore microcrystalline calcite immediately below the hiatus is extremely porous and boundaries displayed in Figure 6.12 A and B suggest partial dissolution occurred. The orange colouration may pre-date some of this corrosion, suggesting that some dissolution may have occurred during the post-hiatus resumption of calcite deposition. Microcrystalline calcite also formed above the main hiatus implying conditions at the restart of growth near the start of the Holocene were similar to 26,500 yr BP.

Microcrystalline calcite forms due to the presence of impurities or due to higher crystal growth kinetics when compared to columnar calcite (Frisia et al., 2000) and likely forms from a variable drip rate (in the range 30 ml to <0.1 ml/min; Frisia and Borsato 2010). As detritus is only directly associated with the hiatus it seems unlikely that its presence is the main control on microcrystalline calcite formation. The presence of microcrystalline calcite below a former stalagmite top is thus interpreted mainly as a result of higher crystal growth kinetics forced by low but variable drip rates preceding phases of non-deposition.

Two younger surfaces (at 12 mm and 31 mm) in the macromorphology are here interpreted to define former stalagmite tops associated with short pauses in growth. While dating confirms a growth pause at the main hiatus, long periods of non-deposition are not implied for these younger surfaces (Figure 6.14). Microcrystalline calcite between 19-30.5 mm has much lower porosity than that below the main hiatus. Additionally boundaries do not appear to be dissolutional, consistent with a hiatus of shorter duration. Some lateral crystal growth is also observed in this region which is not the case below the main hiatus. The presence of microcrystalline calcite, in conjunction with irregular, laterally growing calcite crystals toward the flank suggests this section may mark a former slowly-growing stalagmite top. It is possible lateral

growth was forced by the presence of a very thin water film on the stalagmite surface, which prevented substantial vertical growth; a low drip rate is implied by this interpretation. Additionally the surface at 31 mm is a detrital-rich horizon that truncates lateral crystal growth. Dates either side of this surface are 10,522 yr BP and 9339 yr BP suggesting a growth hiatus.

Transitions between microcrystalline and columnar calcite are similarly likely to be drip rate controlled (Frisia and Borsato 2010) with columnar fabrics typically forming under constant drip rates (0.1- 0.3 ml/min; Frisia et al., 2000). Gradual transitions from microcrystalline to open columnar calcite and back again, between 6 and 30.5 mm (11,500 yr BP to 9700 yr BP), therefore suggest an interval of growth defined by marked variation in drip rate. The later shift to open columnar calcite (after 9300 yr BP) perhaps implies more consistent recharge and a steady rate of infiltration through the epikarst.

The black surface present at 95 mm in the macromorphology and bracketed by two ages 8321 yr BP to 7888 yr BP, was not captured in thin section despite efforts to produce overlapping thin section coverage. However, between 87 and 93 mm lateral crystal growth from the left hand flank, and more centrally, crystals gradually curving to the right flank, may again represent morphology restricted by a water film thinner than usual. The 0.8 mm of growth between the bracketing ages implies a growth rate considerably slower than the previous section (see Section 6.2.2.2), although similar to the rate of remaining growth from this point to cessation of deposition. We interpret this section overall to be slow growing without hiatuses.

Microcrystalline calcite is not observed above 67 mm suggesting drip rate was reasonably constant from 8400 yr BP until cessation of growth at 6800 yr BP. This inference is consistent with the petrography of the former stalagmite top surface at 95 mm (between absolute dates of 8321 yr BP to 7888 yr BP) which is here defined by open columnar calcite with lateral and curved growth but without development of microcrystalline calcite. This petrography is consistent with slower growth but without cessation, differing from surfaces below that developed microcrystalline calcite associated with variable and/or low drip rate, and growth pauses.

The final 1000 years of growth (7800 yr BP to 6800 yr BP) displays open columnar fabric with progressively longer crystals and much lower porosity, although not strictly 'compact' as porosity still exists (Frisia 2015). Nevertheless transition toward a more compact columnar fabric is again controlled by drip rate (Frisia and Borsato 2010) resulting in better coalescence achieved under slower drip rate and more effective degassing (Kendall and Broughton, 1978). This period was thus marked by slowing drip rate and stalagmite growth rate. The final 2 mm of the stalagmite shows evidence of later corrosion.

6.3.3 Controls on geochemistry

6.3.3.1 Stable Isotopes

In common with most other Mediterranean rainfall isotopic records, winter precipitation in the Peloponnese is ~6 ‰ more negative than summer (Figure 6.6). This is due partly to temperature dependent fractionation as air temperatures are higher in the summer. However despite the very low correlation between monthly precipitation amounts and $\delta^{18}O$, there is a strong correlation between average monthly amounts and average isotopic values (Figure 6.10) showing depleted isotopic precipitation is at least in part due to the amount effect. The amount effect has been widely reported from the Mediterranean region (Bar-Matthews et al., 2003; Drysdale et al., 2009; Finné 2014; Boyd 2015). Combined with the consistency of $\delta^{18}O$ from waters collected from within the cave and winter $\delta^{18}O$ values there is a good theoretical basis for KTR-2 being a record of winter climate controlled by the amount effect. Any heavy rainfall occurring in summer months will adhere to this as isotopes of convective rains are also controlled by the amount effect (see Section 6.1.3). Early growth of KTR-2 occurs during deglaciation and as sea levels rise the oceans become more isotopically depleted. Sea levels rose at a consistent rate during the early Holocene until ~8200 yr BP but the rate of sea level rise then slowed during the final period of KTR-2 growth (Lambeck et al., 2014). Eastern Mediterranean surface $\delta^{18}O$ was depleted relative to present day by 0.5-3 ‰ after the transition into the Holocene to the end of the deposition of S1 (Emeis et al., 2003). Depletion was ~1.5 ‰ in the Levantine Sea between 10,00 and 8000 yr BP (Almogi-Labin et al., 2009). Most of the growth of KTR-2 occurred after oceanic depletion. The long term $\delta^{18}O$ trend shows that there is no relationship between isotopic trends in KTR-2 and solar insolation. (Figure 6.24).

Long term trends in $\delta^{18}O$ and $\delta^{13}C$ co-vary (except ~8100 yr BP to ~7700 yr BP) suggesting that changes in $\delta^{13}C$ is mainly caused by the relative amount of soil productivity (thus vegetation) vs bed rock input, responding to changes in precipitation amount. However, short term variation in $\delta^{13}C$ appears largely unrelated to $\delta^{18}O$ suggesting that some of the short term variability in $\delta^{13}C$ is related to prior calcite precipitation (PCP) not vegetation changes. This control is likely to be more prevalent during periods of low vegetation cover which may be related to long term changes in climate.
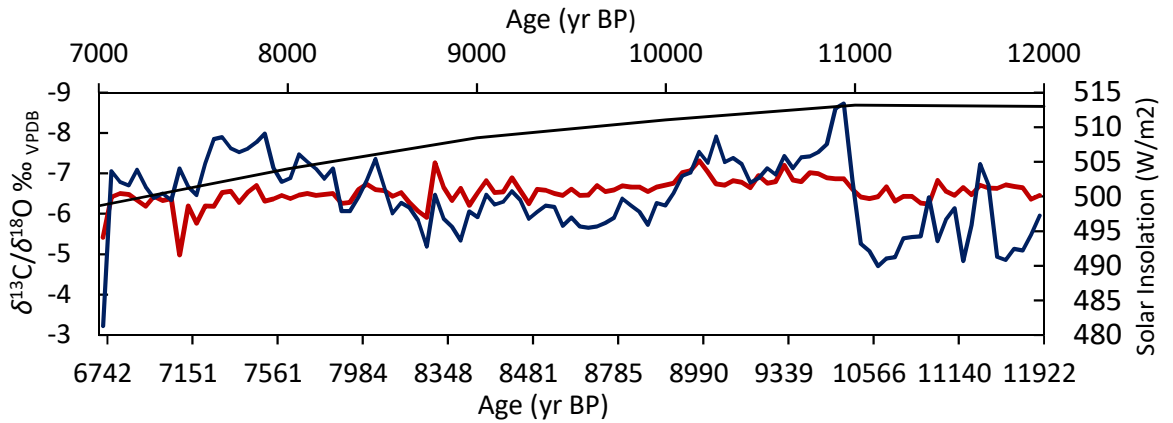
Figure 6.24: Limnon Cave stable isotopes compared to solar insolation at 30 N for June (Berger and Loutre 1991).

6.3.3.2   Controls on Trace Elements

Where records of Mg/Ca and Sr/Ca co-vary over time it is often a clear indicator of karst water residence time. Higher Mg/Ca and Sr/Ca ratios can be indicative of longer water residence times which both enhances selective leaching of the trace elements and also increases PCP (Fairchild et al., 2000). As both trace elements are well correlated with changes in $\delta^{18}O$ it can be suggested that changes in residence time are related to overall precipitation amounts above the cave.

Ba variation in this stalagmite is completely unrelated to Mg and Sr variation. In locations where Ba is unrelated to Mg and Sr it typically indicates incorporation via detrital clay or silicates (Rutlidge et al., 2014). P can be sourced organically or inorganically (Borsato et al., 2007) and considering the likely detrital Ba source it is also likely to be related to deposition with clays. Similarly timed peaks in Na deposition further imply a detrital source for these trace elements.

6.3.4 The early Holocene record from Limnon Cave and comparison to other records

The early Holocene record of Limnon Cave is of wide interest as only a limited number of speleothem studies are currently known from the Peloponnese region (Finné 2014; Finné et al., 2014, 2015; Boyd 2015) and they do not include an early Holocene record. Sedimentological records are more numerous, but again many do not cover the early Holocene (e.g. Jahns 1993; Lazarova et al., 2012; Panagiotaras et al., 2012; Theodorakopoulou et al., 2012; Avramidis et al., 2013; Weiberg et al., 2016). The 8.2 kyr event is a particular enigma within continental Greece and is studied here in high resolution.

Compared to modern calcite values (Table 6.5) the δ^{18}O record of KTR-2 is mostly more negative indicating that the early Holocene at Limnon was wetter than the present day. δ^{13}C, however, is heavier during the early Holocene than present. Enriched δ^{13}C during this period is enigmatic as it might be expected to be lower at this time if vegetation was establishing under relatively wet conditions. If higher δ^{13}C is reflecting low soil productivity, it could suggest that rainfall amount is not the limiting factor on montane vegetation, which may be more strongly controlled by temperature. As insolation is higher during the early Holocene than present day, increased summer temperatures could increase PCP during the summer months via increased evaporation which is then translated into the speleothem calcite during the winter rainfall increase. Broadly the KTR-2 record can be split into four sections (Figure 6.25) as discussed below.
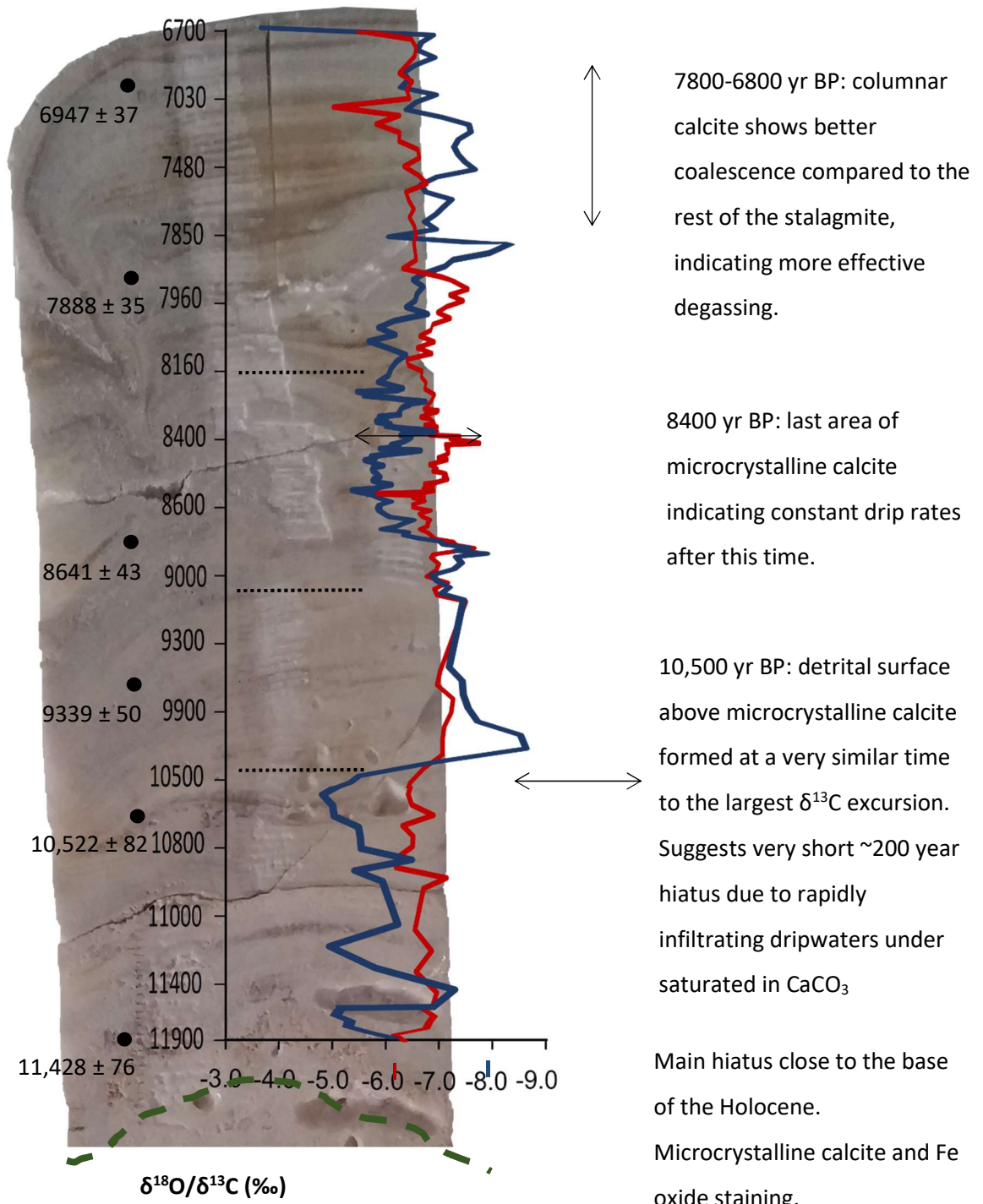
Figure 6.25: Summary of the main isotopic and petrographic features of the KTR-2 stalagmite. δ¹³C is in blue, δ¹⁸O in red. Black dashed lines highlight the boundaries to major changes in isotopes as discussed in the main text. Modern isotopic values are indicated by a red tick (δ¹⁸O) and a blue tick (δ¹³C) on the main isotopic values axis.

6.3.4.1 11,900 to 10,340 yr BP

In the early KTR-2 record (until 10,520 yr BP) δ^{13}C values oscillate around ~-6 ‰ with an amplitude of about 2 ‰; after this a large negative excursion occurs to the lowest value of the record (-8.72 ‰) at 10,340 yr BP. In contrast, δ^{18}O shows little variability around a mean of -6.5 ‰, which is slightly heavy (and therefore due to the amount effect slightly drier) compared to the record before 7800 yr BP (Figure 6.24). δ^{13}C is unusually enriched during this period compared to the rest of the KTR-2 record despite δ^{18}O implying conditions are not unusually arid. The 0.5 ‰ negative excursion in δ^{18}O corresponding to the large excursion in δ^{13}C suggests that δ^{13}C responds to more significant increases in rainfall (Figure 6.25). The response is significantly negative and seems likely to be related to soil productivity, therefore after 10,520 yr BP there was a substantial increase in vegetation above the cave. Prior to this vegetation may have been less developed and δ^{13}C may have been responding largely to changes in PCP.

During this period there is no clear relationship between the stable isotopes and petrography. Petrographic evidence shows an alternation between columnar and microcrystalline calcite suggesting short periods of constant dripwater rate (represented by columnar calcite) regularly giving way to periods of variable drip rate (microcrystalline calcite). However the start of the excursions at 10,520 yr BP can be correlated to microcrystalline calcite deposition which is present just before development of a detrital-rich surface. The presence of detritus suggests a period of increased infiltration that was capable of transporting larger particles through conduits, occurring in conjunction with the increased precipitation implied by δ^{18}O: prior to this event calcite fabrics indicate growth slowing and/or pausing (Section 6.3.2). The end of relatively positive δ^{13}C occurred around 10,560 yr BP, and it is likely that between 10,560 yr BP and the negative excursion at 10,340 yr BP a short ~200 year hiatus occurred (Figure 6.25).

There appears to be no record of the Younger Dryas (dated between 12,850 and 11,650 yr BP (Rasmussen et al., 2006) aridity in KTR-2 stable isotope records. The distinctive lack of variation in δ^{18}O could suggest that the harsh arid conditions attributed to the Younger Dryas do not occur in the region. The event is observed at the closest regional palaeoclimate record from Lake Stymphalia, however the termination is recorded at 12,100 yr BP with transition into a wet climate associated with the Holocene (Heymann et al., 2013). Resolution of dating at Lake Stymphalia is low but if it is close to correct the expected arid δ^{18}O signal may not be observed in KTR-2 due to the hiatus. However, a study by Gogou et al. (2007) suggest cool conditions persisted to as late as ~9,600 yr BP in the Northern Aegean and overall cooling occurred in the Adriatic from 11,000 yr BP to 10,000 yr BP (Rohling et al., 1997). Recovery from the Younger Dryas

may then be represented by the major $\delta^{13}C$ negative excursion (and accompanying 0.5 ‰ $\delta^{18}O$) between 10,520 yr BP and 10,340 yr BP.

6.3.4.2 10,340 to 9000 yr BP

From 10,340 to 9000 yr BP $\delta^{13}C$ remains >1 ‰ above the mean value for the rest of the record (-6.4 ‰). $\delta^{18}O$ is also clearly depleted from 10,300 to 9340 yr BP, the most consistent period of depletion throughout the KTR-2 record (Figure 6.25). This clearly represents longer term wetter conditions compared to the rest of the KTR-2 record and also to isotopically heavier modern values. Prolonged rainfall likely had a positive effect on vegetation growth accounting for the ~1.5 ‰ depletion in $\delta^{13}C$ values. Variation in $\delta^{13}C$ during this period is the lowest in the Holocene section and a lag of 300 years between the decline in $\delta^{13}C$ and $\delta^{18}O$ suggests an established biomass. $\delta^{13}C$ could also be indicating reduced PCP because of increased rainfall. These isotopic results probably mark the Holocene Climate Optimum period in Limnon Cave. $\delta^{18}O$ enrichment following the 9340 yr BP peak marks the end of the wet period.

There is abundant evidence that the entire early Holocene was broadly wetter and warmer than the rest of the Holocene, coinciding with the deposition of S1 in the Eastern Mediterranean from 10,200 yr BP to 6400 yr BP (Mercone et al., 2001). The onset of wetter conditions at Limnon Cave are coincident with this. This period is sometimes termed the Holocene Climatic Optimum but timing of the initiation can vary between records. In Soreq Cave, Israel, it is dated to 8500 yr BP (Bar-Matthews et al., 2000) but in some regional records it immediately follows the end of the Younger Dryas for example at Lake Gölhisar, Turkey (Eastwood et al., 2007) and Lake Prespa, Macedonia (Cvetkoska et al., 2014). Wetter (and possibly warmer) climatic conditions at Limnon Cave are coincident with similar observations from number of regional terrestrial and marine records. A rise in SSTs from ~14 °C to 19 °C from 10,000 to 9000 yr BP is the largest and most rapid observed in the early Holocene Aegean (Triantaphyllou et al., 2016). At the same time frequent pulses of terrestrial organic material (Gogou et al., 2007) and lowering of surface salinity has been linked with higher input from rivers and/or precipitation (Kotthoff et al., 2008a). In the Aegean and Ionian the onset of sapropel formation occurs at ca. 9800 yr BP (Gogou et al., 2007; Geraga et al., 2008; Kotthoff et al., 2008a) during the period of most sustained depleted isotopes at Limnon. Terrestrial records at Tenaghi Phillippon and Nisi Fen (Greece) show increased winter precipitation and stable winter temperatures between 10,400 yr BP and 9500 yr BP (Kotthoff et al., 2008b). Additionally increases in vegetation density surrounding lakes Prespa (Panagiotopoulos et al., 2013), Dojran (Macedonia/Greece border) (Francke et al., 2013) and

Maliq (Bordon et al., 2009) occurred between 11,500 and 10,700 yr BP accounting for reduction in erosion rates despite an increase in run off (Francke et al., 2013).

6.3.3.4   8800 to 8120 yr BP

Between 8800 and 8120 yr BP $\delta^{18}O$ following the 1‰ enrichment event remains relatively unchanged around −6.7 ‰ (discussed fully in Section 6.3.3.6). Values during this period are not dissimilar to those prior to 10,340 yr BP suggesting similar precipitation conditions. A contemporaneous rise in $\delta^{13}C$ of 1.8 ‰ is seen at 8900 yr BP and $\delta^{13}C$ remains heavy during the same time as $\delta^{18}O$ until 8100 yr BP. However, $\delta^{13}C$ is not as heavy as values before 10,340 yr BP. $\delta^{13}C$ could be a partial record of soil productivity as it directly responds to the onset of more arid conditions, similarly to the large increase implied during wetter conditions. However as $\delta^{13}C$ during this period is heavier than present there could also be some contribution by PCP implying aridity was accompanied by summers potentially a bit warmer than present, increasing the amount of surficial evaporation.

While some paleoclimate records show the Holocene Climate Optimum persisted in some regions even after the 8.2 kyr perturbation (discussed below), it is likely that a period of climatic deterioration (aridity) began around 8800 yr BP (Rohling and Pälike 2005) which corresponds quite well with the start of enriched $\delta^{18}O$ and $\delta^{13}C$ isotopes at Limnon from 8900 yr BP (Figure 6.25). Regionally to Greece, increased temperatures are noted in the reduction in abundance of the cool to temperate dinoflagellate species *S. elongatus* in the central Aegean during the same timeframe as suggested by Rohling and Pälike (2005) (Marino et al., 2009). Events around the 8.2 kyr Event discussed in more detail in Section 6.3.3.6.

6.3.3.5   8100 to 6700 yr BP

After 8100 yr BP the KTR-2 record shows declining values in $\delta^{18}O$ until, by around 7900 yr BP, values similar to those recorded prior to 9000 yr BP are attained. Precipitation amounts in this 300 year period were thus as high as precipitation inferred for the early climate optimum between 10,340 and 9000 yr BP. This was however, very short lived as by 7850 yr BP $\delta^{18}O$ had increased again and continues to do so until the end of the record (Figure 6.23) implying increasing aridity up to the cessation of growth. Mean values are only 0.3 ‰ heavier than those recorded at the onset of KTR-2 growth following the hiatus at the base of the Holocene. Aridity is also implied in petrography in the period 7800 yr BP to the cessation of growth as crystal coalescence is higher, suggesting more effective degassing because of a lower drip rate. In

contrast δ^{13}C remains depleted until 7200 yr BP and does not attain values as heavy as those seen during arid phases in KTR-2. In other parts of the KTR-2 record aridity has apparently caused a twofold response in δ^{13}C of both increased PCP and reduced soil productivity. The comparatively lighter isotopes of this arid phase could possibly suggest relatively cooler conditions and reduced PCP (via an increased P/E ratio) as solar insolation has begun to decline at this time. Alternatively rainfall may have increased during the summer and continued to support biomass and soil productivity. If temperatures remained comparatively low growth may have continued due to reduced effective evaporation. By 6700 yr BP δ^{13}C is being strongly affected by aridity as seen in the large positive excursions in both isotopes. The cessation of growth just after the peak of these excursions denotes a pronounced dry period began at the end of the KTR-2 record (Figure 6.23).

Although the beginning of aridity at 7900 yr BP is in good agreement with the end of the Holocene Climate Optimum suggested in Tenaghi Phillippon (Peyron et al., 2011) and Zakynthos (Avramidis et al., 2012), the continuation of low δ^{13}C does not fully support this inference. The continuation of the decrease in δ^{13}C suggest an environment still favourable to growth and possibly the continuation of the Holocene Climatic Optimum following the 8.2 kyr event (Section 6.3.3.6) as observed in multiple Mediterranean records. The increase in δ^{13}C at 7200 yr BP is also possibly associated with the end of S1 deposition at ~7100 yr BP in the north Aegean (Kotthoff et al., 2008a) and around 7000 yr BP in the Ionian (Emeis et al., 2000; Geraga et al., 2008) and Adriatic Seas (Rohling et al., 1997) (Figure 6.26). A large proportion of the overall growth of KTR-2 is therefore coincident with the deposition of S1. Furthermore the end of the Holocene Climate Optimum in the Limnon Cave record defined by δ^{13}C at 7200 yr BP is broadly synchronous with the end of the event as recorded in a speleothem from, Corchia Cave, Italy (Zanchetta et al., 2007) and closer in time to a number of records including Soreq Cave (Bar-Matthews et al., 1999) (Figure 6.26) and Lake Stymphalia (Heymann et al., 2013) where the end occurs at ~7000 yr BP. Aridity is likely to still contribute to the reduction of soil productivity at 7200 yr BP as it corresponds to the beginning of the largest aridity event of the entire KTR-2 record. This event can be correlated regionally to a reduction in precipitation at the Alkyas Lagoon, Zakynthos at 7200 yr BP (Avramidis et al., 2012) as well as in Lake Accesa Italy (Peyron et al., 2011) but the reduction is not as significant in these records.

8400 yr BP: last area of microcrystalline calcite indicating constant drip rate after this time

10,500 yr BP: detrital surface indicating increased infiltration
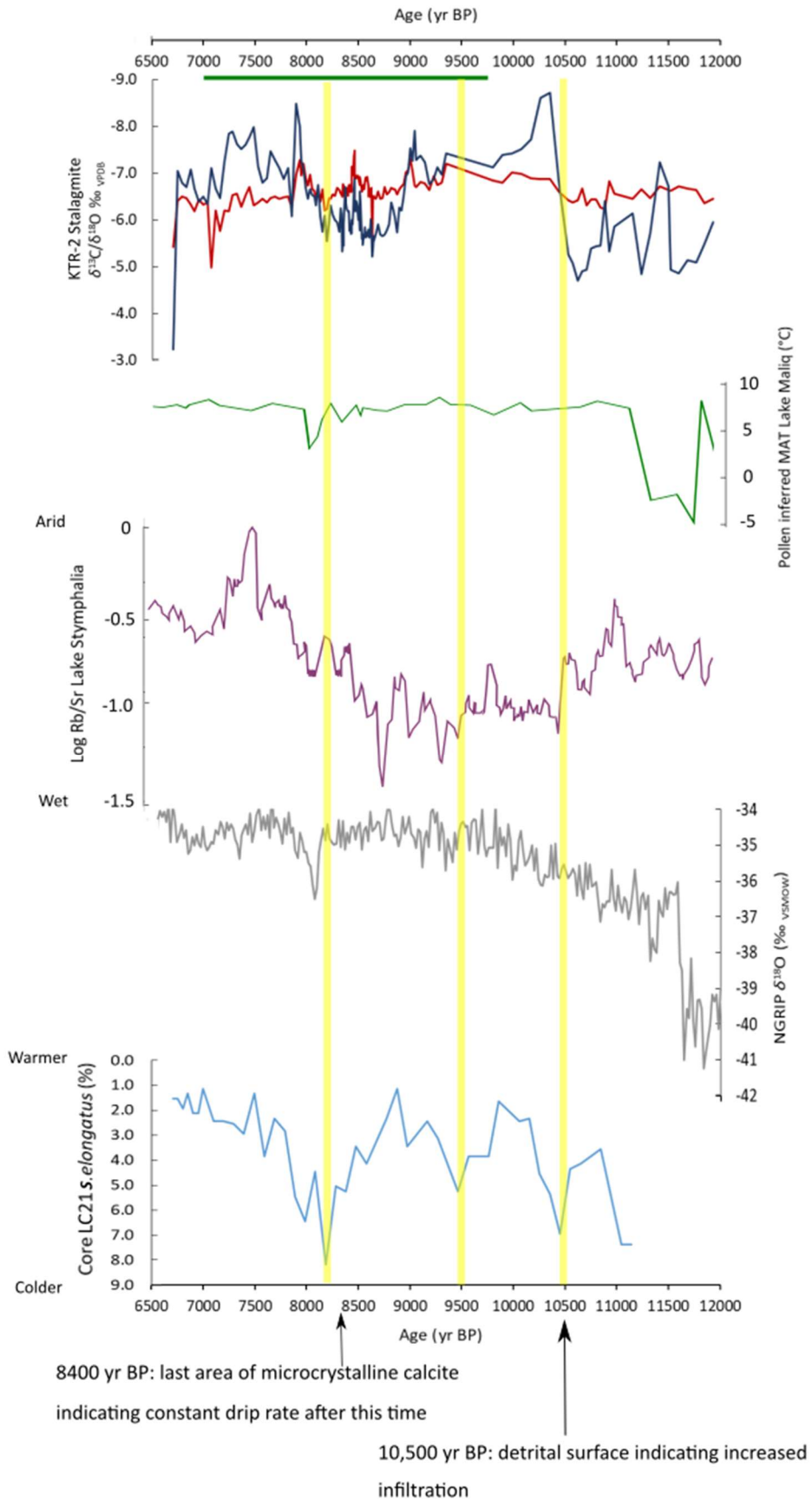
Figure 6.26: Low resolution KTR-2 stable isotope data (δ¹³C blue, δ¹⁸O red) related to regional and global palaeoclimate events. Vertical yellow bars help correlate events, bar width representing a minimum error envelope of ± 60 yrs (from U-series dates). Black arrows indicate timing of key KTR-2 petrographic features. Onset of a warm and wet (climate optimum) conditions in KTR-2 ~10.5 ka, is marked by rapidly declining δ¹³C (increased vegetation), coincident with a cold phase in anotherwise warming SSTs trend in the Aegean as indicated by percentages of the cold-water cyanobacterium S. elongatus (Marino et al. 2009; light blue record). Wetter conditions at nearby Lake Stymphalia (Heymann et al., 2013; purple dataset) also start at this time. The wetter period in KTR-2 was interrupted briefly at 9.34 ka, and decisively at 8.90 ka when δ¹³C and δ¹⁸O indicate periods of dryness and generally cool temperatures until 8.1 ka. This interruption of optimum conditions is close to a period of cold Aegean SST (Marino et al. 2009), centred at 9.5 ka (vertical yellow bar). Both KTR-2 isotopes are relatively high at 8.1 ka (see Fig. 6 for high resolution data) consistent with peak abundance (cool) of S. elongatus (Marino et al. 2009) and within error of the 8.2 ka cold event in NGRIP (grey record) (Andersen et al. 2004) and Lake Maliq (green record, Bordon et al. 2009). Warmer and wetter conditions in KTR-2 re-established after 8.1 ka. However, ~7.2 ka. increasing δ¹³C marks the start of a phase of aridity, and possibly cooling, preceding cessation of speleothem growth, consistent with the end of S1 in seas surrounding Greece (green bar) (Rohling et al., 1997; Emeis et al., 2000; Geraga et al., 2008; Kolthoff et al., 2008a).

6.3.3.6   The 8.2 kyr Event

The KTR-2 high resolution trace element and stable isotopic transect which is designed to detect climate signals indicating the possible presence of the 8.2 kyr event starts at 8641 yr BP and ends at 7888 yr BP (Figure 6.27). As mentioned previously, longer term trends in the full KTR-2 profile (Figure 6.24) do suggest some corroboration to the Rohling and Pälike (2005) study.

δ¹⁸O during the period following the positive excursion marking the end of the wet period at 9000 yr BP is largely unchanged (see above). An interval of negative values between 8600 yr BP to 8450 yr BP in the micromilled section of δ¹⁸O (Figure 6.19, 6.27) suggests a brief period of enhanced precipitation. The lowest δ¹⁸O occurs at the end of this trend as well as peaks in concentrations of Ba, Na and P (8470 yr BP to 8400 yr BP) suggesting that an increase in precipitation reduced the residence time in the karst and was large enough to increase the volume of clay based detritus entering the cave via conduits. δ¹³C on the other hand remains comparatively heavy but does

show a small negative excursion at 8450 yr BP suggesting that only the extreme rainfall events have a marked effect on $\delta^{13}C$. Although the controls on $\delta^{13}C$ are difficult to decipher this observation may suggest that $\delta^{13}C$ is predominantly controlled by PCP and only extreme rainfall events create a significant increase in effective recharge to cause a decrease in PCP. A clear low in Mg/Ca at 8430 yr BP may also point to a reduction in PCP associated with this event.

During this period $\delta^{18}O$ peaks at 8160 yr BP at -6.2 ‰. This point represents the heaviest $\delta^{18}O$ within the micromilled profile aside from a single point excursion at 8620 yr BP, although positive excursions in later growth after 7900 yr BP are larger. In addition to $\delta^{18}O$, Mg/Ca and Sr/Ca values also rise from 8430 yr BP to 8160 yr BP indicating an increase residence time linked to reduced precipitation. The highest $\delta^{13}C$ does not correlate with highest $\delta^{18}O$ and a ~1 ‰ reduction in $\delta^{13}C$ at 8360 yr BP suggests the response is not straightforward. Higher variation in $\delta^{13}C$ may be reflecting variation in PCP controlled by degassing rather than dripwater as dripwaters are likely to be reduced during this period. If $\delta^{13}C$ is controlled by bedrock vs soil changes the broadly implied increase in $\delta^{13}C$ suggests a decline in soil productivity but higher frequency variation is not simply reacting to reduced precipitation.

The layer defined in the macromorphology and partially observed in petrography (95 mm) prior to 7890 yr BP has an age model age of 8160 yr BP to 8000 yr BP. Vertical calcite growth at this point is apparently limited by a thinner film of water (Section 6.3.1) and the age model shows growth at this time was slower than earlier in the Holocene (Figure 6.14). Unlike marked stalagmite top surfaces lower in the stalagmite, this surface is not related to microcrystalline calcite suggesting that drip rate was fairly constant. The start of this growth is well correlated to the peak in aridity implied by $\delta^{18}O$. However, following this, clear decreasing trends are observed in both isotopes and a decline in Mg/Ca and Sr/Ca ratios are observed suggesting an increase in precipitation contributing to reduced residence times (Figure 6.27). There is a lag of less than 10 years before the decline in Mg/Ca and Sr/Ca suggesting that the impact of increased precipitation translated through the karst system fairly quickly. But the persistence of horizontal calcite growth until about 8000 yr BP suggests the effect on growth was longer lasting than the extent of aridity itself. Given the isotopic and trace element evidence, if a hiatus (albeit of very short duration) did occur at the top of the layer it is unlikely to be directly related to a signal of the 8.2 kyr event.
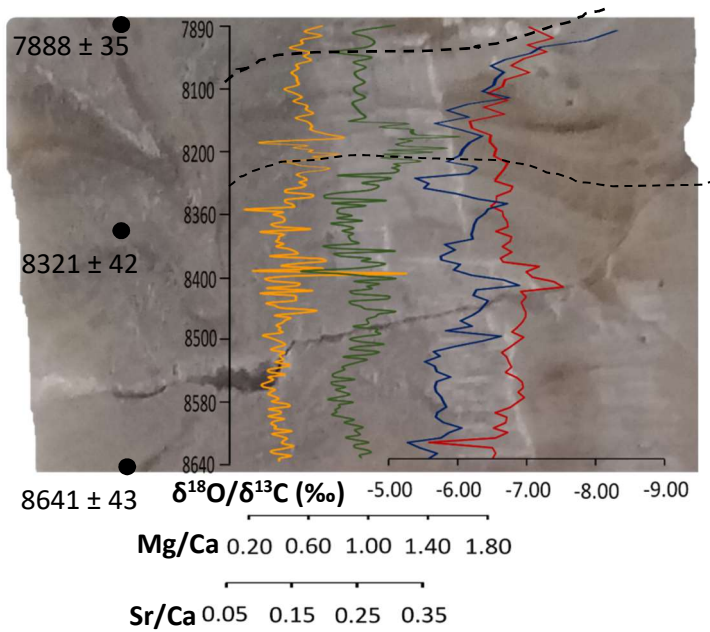
Potential stalagmite top identified by laterally grown columnar calcite. Started forming during period of increasing $\delta^{18}O$ Mg/Ca and Sr/Ca suggesting decreasing precipitation and increasing residence time. However the final surface formed after a reversal to decreasing $\delta^{18}O$ and following peak trace elements (longest residence time). This implies that growth slowed but did not cease as precipitation increased before a hiatus could occur.

Figure 6.27: Summary of the main features of the stable isotope, trace elements and petrography of KTR-2 between 8641 yr BP and 7888 yr BP. Black dashed lines represent zone of laterally grown calcite. Stable isotopes share an axis with $\delta^{13}C$ in blue and $\delta^{18}O$ in red. Trace elements are given separate axis Sr/Ca in yellow with an axis 0.05-0.35 and Mg/Ca is green with an axis 0.20-1.80.

The 8.2 kyr event was a northern hemisphere event centred between 8021 and 8080 yr BP during which cooler and drier conditions prevailed (e.g. Thomas et al., 2007). More recent Greenland ice core data suggests the 8.2 kyr event may be superimposed on Holocene climate deterioration from 8800 yr BP to 7800 yr BP (Rohling and Pälike 2005). Climatic signals related to the 8.2 kyr event are recorded in speleothems from a number of locations including Soreq Cave Israel (Bar-Matthews et al., 1999), Germany (Wurth et al., 2004), Sicily (Frisia et al., 2006), Brazil, China and Oman (Cheng et al., 2009b) as well as from a number of other climate proxies including pollen and lake levels (Robinson et al., 2006). However, a number of speleothem records show either no signal or an unclear record of the 8.2 kyr event (Frumkin et al., 1994; Zanchetta et al., 2007, Verheyden et al., 2008; Boch et al., 2009; Verheyden et al., 2012). A major response to the climatic effect of the 8.2 kyr event in the Eastern Mediterranean is the disruption of S1 formation in the Ionian Sea (De Rijk et al., 1999) and parts of the Aegean Sea (Geraga et al., 2005; Gogou et al., 2007; Kotthoff et al., 2008a; Traintaphyllou 2014) excluding the south east (Triantaphyllou 2014). Timing of the disruption varies between sites, for example two northern Aegean sites suggest similar durations but different timings at 8400 – 8000 yr BP (Kotthoff et al., 2008a) and 8200 – 7800 yr BP (Gogou et al., 2007). All sites agree on a period between 8400 yr BP and 7800 yr BP.

The 8.2 kyr event at Limnon Cave is defined by a period of peak aridity at 8160 yr BP followed by a rapid transition to lighter $\delta^{18}O$ and increased rainfall superimposed on a slightly longer period of increased aridity from 8450 yr BP. The onset of aridity at the cave site begins some 100 years before contemporaneous nearby lake levels begin to reduce including Dojran (Francke et al., 2013), Maliq (Bordon et al., 2009) and Stymphalia (Heymann et al., 2013). This implies that in this region the onset of aridity associated with the 8.2 kyr event occurs earlier than is recorded by lakes, although this may be explained by uncertainties in lake chronologies. A decline in pollen is not observed until 8300 yr BP in Zakynthos (Avramidis et al., 2012). The peak in aridity at Limnon Cave is well correlated to tree pollen percentages at Tenaghi Philippon, Greece which reached a minimum at ~8100 yr BP (Peyron et al., 2011). It is also similarly timed to increased surface salinity in the Ionian Sea ~8000 yr BP (Emeis et al., 2000), with a lake level low stand ~8200 yr BP at Stymphalia (Heymann et al., 2013) and with higher values of K at Lake Prespa, indicating reduced rainfall via enhanced fine clastic sediment supply (Cvetksoka et al., 2014). The amplitude of $\delta^{18}O$ is comparable to Soreq (Bar-Matthews et al., 1999) but the onset is earlier and the duration longer. Timing of the 8.2 kyr event at Limnon Cave is well correlated with the age of the disruption of S1 in the Aegean closest to the Greek coastline between 8400 and 8000 yr BP (Kotthoff et al., 2008a).
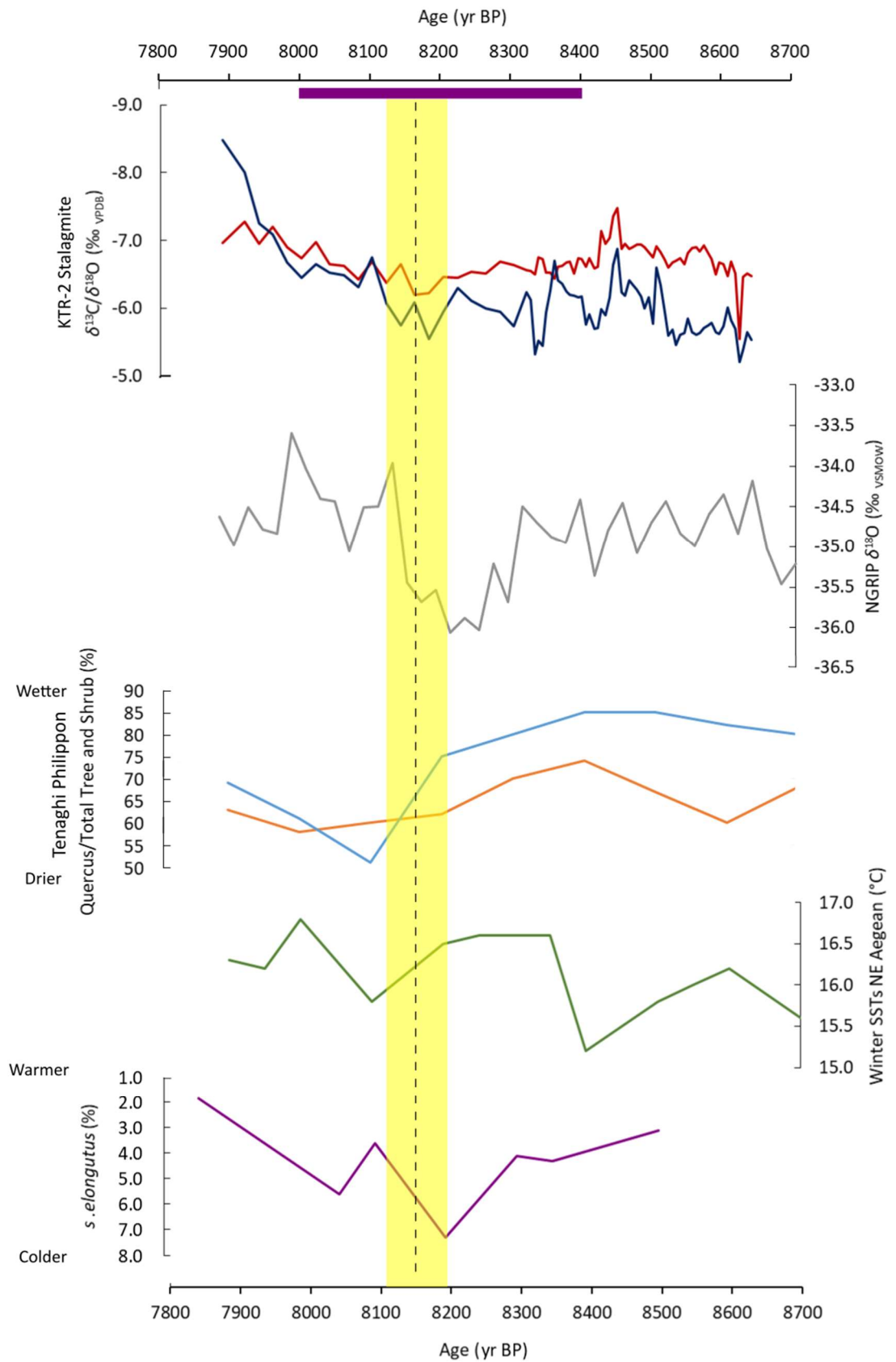
Figure 6.28 previous page: Micro-milled high-resolution stable isotopes for the period around 8.2 ka in context with global and regional observations. Cool ($\delta^{18}O$ in red) and arid ($\delta^{13}C$ in blue) indicators in KTR-2 combine at 8.16 ka indicated by the vertical yellow bar. The bar width is a minimum error envelope (from U-series dates) of ± 60 yrs. This cool and dry period in KTR-2 is within error of the latter part of the NGRIP 8.2 kyr cold event (dataset from Andersen et al. 2004). Regional dryness at his time is consistent with pollen data from Tenaghi Philippon (Peyron et al., 2011) where total tree and shrub pollen percentage (blue dataset) are in rapid decline from 8.4 ka as are the proportion of evergreen oaks (orange dataset). Cooling NE Aegean (Marino et al. 2009; green dataset) winter SSTs between 8.2 and 8.0 ka are indicated both in higher percentages of S. elongatus a cold water cyanobacterium (Rohling et al. 2002). The KTR-2 cool and dry phase also corresponds broadly to the central timing of S1 disruption in the coastal Aegean Sea (purple bar; Kottholf et al. 2008b).

There are examples of regional proxies which suggest the 8.2 kyr event was cold as well as arid, e.g. Lake Dorjan (Francke et al., 2013) and Lake Maliq (Bordon et al., 2009). Independent of timing, a common observation during the interruption of S1 is the reduction of sea surface temperatures (SSTs) (Rohling et al., 2002; Gogou et al., 2007, Geraga et al., 2008, Marino et al., 2009) or air temperature (Kotthoff et al., 2008a). It is possible that disruption in S1 deposition during this time was caused by surface cooling creating convective overturning of bottom waters (De Rijk et al., 1999, Kotthoff et al 2008a). It has been further suggested this cooling was associated with increased duration, intensity or frequency of northerly cold and dry polar/continental air (i.e. the Siberian High) extending further into the Aegean Basin (Rohling et al., 2002) or by dry phases during the Indian Monsoon (Marino et al., 2009). The effects of the 8.2 kyr event are therefore likely predominantly winter phenomena (Rohling and Pälike 2005). Triantaphyllou (2014) suggest that the extension of northerly cold and dry air is further south than the region of Limnon Cave and if this forcing is correct the cave should record cooler temperatures.

Controls on $\delta^{13}C$ may be dependent on long term climate factors and the prevalence of vegetation at the time (Section 6.3.2.1). PCP effects on the $\delta^{13}C$ signal and may have a larger impact during periods of less vegetation, such as this period. A vegetation response similar to that at Tenaghi Philippon (Pross et al., 2009) could have taken place at Limnon Cave where an overall vegetation decline but superimposed seasonal shift is observed. At Tenaghi Philippon it is suggested the

ecosystem response is caused by a change in precipitation regime from winter to summer: the severe decline in evergreen *Quercus* implies low winter temperatures but deciduous *Quercus*, which would be decimated by summer droughts, is less affected (Pross et al., 2009, Peyron et al., 2011). At Limnon Cave, a small amount of vegetation may have been sustained during warmer years if precipitation shifted to coincide with the main growing season (indicated by small negative excursions in $\delta^{13}C$) but still reduced overall. If this assumption is correct the coldest period of the 8.2 kyr event in the Limnon record was from 8340 to 8330 yr.

Chapter Seven. Katalekhor Cave, NW Iran: a Holocene Palaeoclimate Record in the rain shadow region of the Zagros Mountains

7.1   Introduction

7.1.1 Katalekhor Cave

Katalekhor Cave (35°50' 142' N, 048°09' 726' E) is located in Zanjan Province, 5 km from the village of Garmaab and 410 km west of Tehran (Figure 7.1). The cave is situated 1,719 m a.s.l in the forelands of the Zagros Mountains in part of the Central Iranian Tectonic Zone (Laumanns n.d. www.caving-in-Iran.org). The epikarst above the cave entrance is ~100 m thick (Al Omari unpublished) with virtually no soil cover and supporting patchy grass vegetation (Google Earth). The natural cave entrance was a ~1m diameter crawl space which was widened when the cave was designated a show cave in the 1990s (Al Omari unpublished). The cave is hosted in partly dolomitised, karstified limestone of Oligocene/Miocene age positioned in the remnant of an eroded anticline (Laumanns n.d. www.caving-in-Iran.org). The limestone is underlain by Miocene 'Red Beds' of pink sandstones, marls and conglomerates with minor gypsum (Laumanns n.d. www.caving-in-Iran.org). The area is tectonically active: large earthquakes have a return frequency ~8 years (Al Omari unpublished) and at least three major NW-SE-directed faults are present in the mountain range (Laumanns n.d. www.caving-in-Iran.org). The cave has been explored over 12 km at three levels (Laumanns n.d. www.caving-in-Iran.org) and contains a number of galleries with standing pools during the winter months (Al Omari unpublished). Relative humidity at the time of sample collection was 100 % and temperature in the range 15.5 °C - 16.6 °C (Al Omari unpublished). A plan of the cave is shown in Figure 7.2.
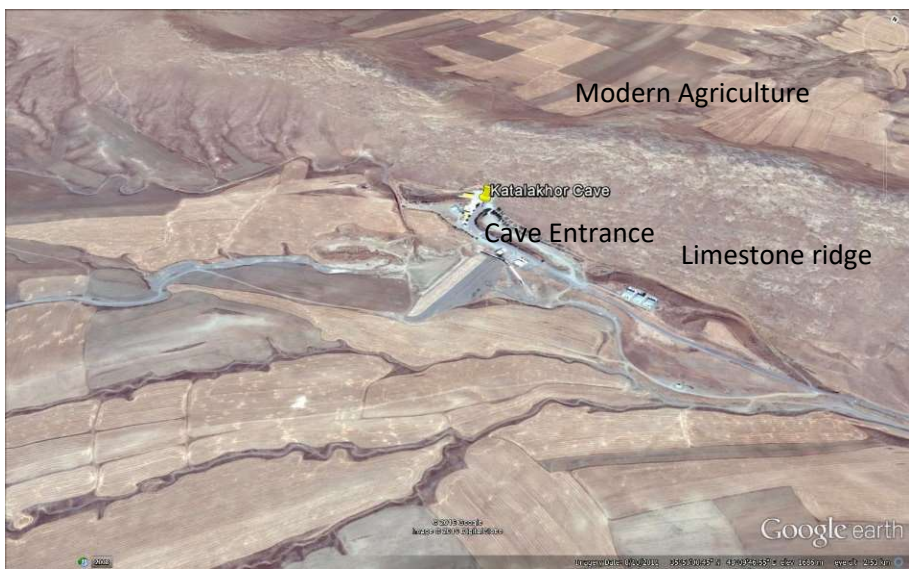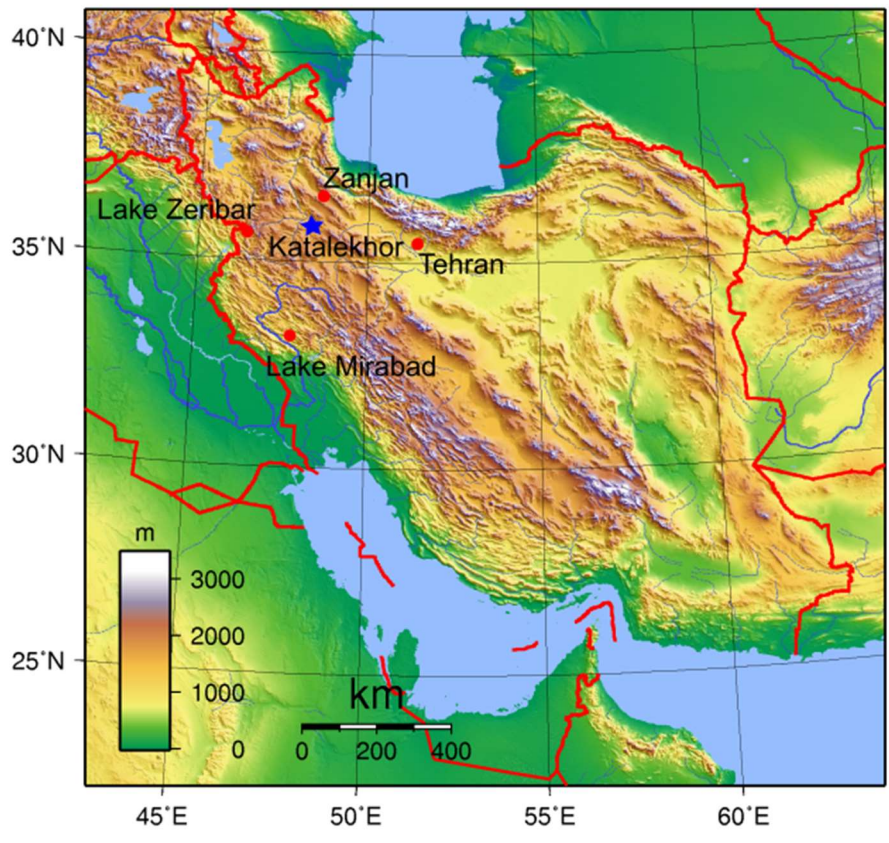
Figure 7.1: Location of the town of Zanjan and Katalekhor Cave in the north west of Iran, in the forelands of the Zagros Mountains. The capital Tehran is highlighted. A Google Earth image shows the cave formed on the slope of a mountain and vegetation is very sparse. Image looks NNE towards Zanjan. Iran topographic map Sadalmelik 2007 www.commons.wikimedia.org.
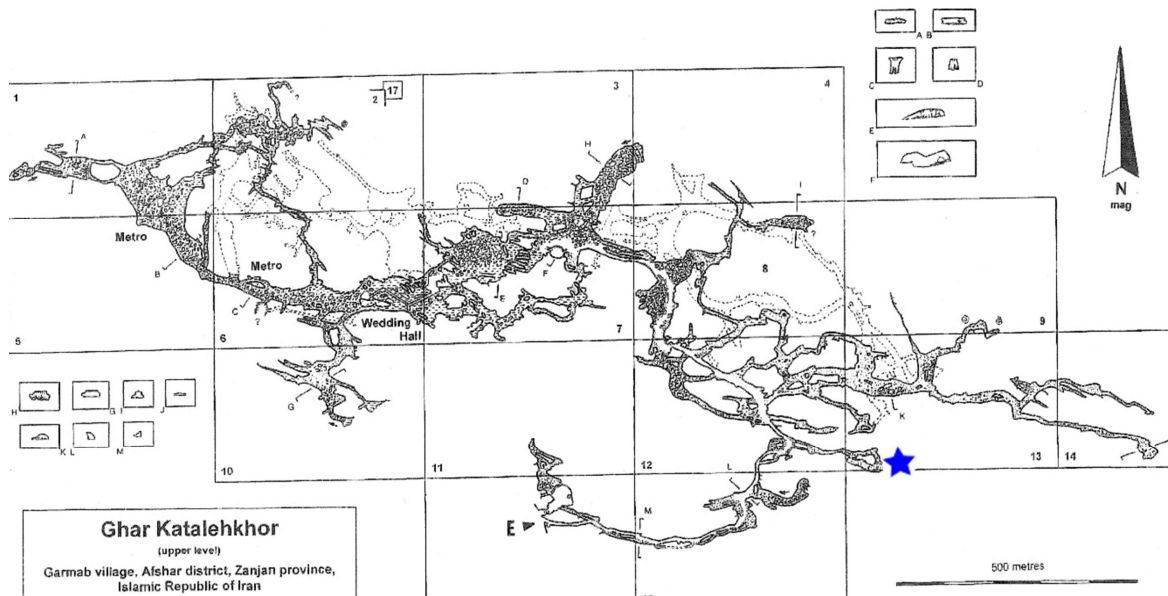
Figure 7.2: Cave Plan of Katalekhor Cave with the location of KT-3 marked by the blue star.

7.1.2 Stalagmite KT-3

Stalagmite KT-3 (Figure 7.3) is 567 mm in length and was active when collected from the highly decorated second gallery approximately 750 m from the cave entrance (Al Omari unpublished). Active dripping occurred above the stalagmite at the time of collection in November 2006 (Al Omari unpublished). Growth initiated during the last interglacial period but the upper 324 mm grew during the Holocene after a long hiatus (see Section 7.2.2.2). This research focussed on the Holocene material so the analytical results in this chapter are presented with 0 mm representing the hiatus surface.
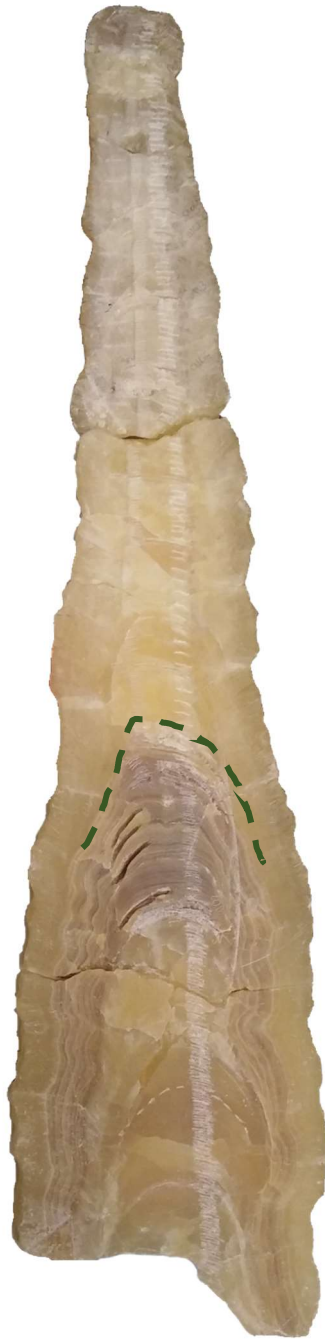
Figure 7.3: Full profile of stalagmite KT-3. The hiatus between the Pleistocene and Holocene is highlighted by the dashed green line. This also marks the base of the measurements and data reported in this chapter.

30 mm

7.1.3 Modern climate and groundwaters

Katalekhor Cave is located on the eastern forelands of the Zagros Mountains. This side of the mountain range has a broadly Mediterranean climate of hot, arid summers and mild wet winters. The closest weather stations to Katalekhor with accessible data are Tehran Airport (Climate Explorer) 1884-2015 and Tehran and Tehran East (IAEA and WMO) combined 1960-1981 and 2000-2004. Both stations are at elevations similar to Katalekhor, but both are incomplete and Tehran is closer to the Caspian Sea which limits its direct comparability (location shown on Figure 7.1).

Precipitation regimes from Tehran (Figure 7.4) show a strong seasonal pattern. Rainfall in the winter and spring months is on average ≥ 30 mm every month typically making up 75% of the total annual rainfall (Table 7.1): there is a sharp reduction in May when values are close to half the values of winter months. Rainfall during the summer months (July - September) is very low, on average less than 5 mm/month (an exception being Tehran East where June rainfall is ~10mm). Groundwater recharge is likely to occur mainly in the winter and spring, with a small contribution in the autumn. However, there is some disparity between the datasets. In the Climate Explorer dataset, precipitation amounts in June are half of those reported in the IAEA station data. Additionally a slight monthly difference occurs with the onset of increased rainfall after the summer (October vs November).

The temperature regimes for the Tehran weather stations show that mean winter temperature do not fall below 3 °C, suggesting that snowfall at these altitudes is likely; despite this it is unlikely that in-cave dripping will cease due to freezing. Average temperatures in July and August rise above 30 °C, which make these months most likely to be affected strongly by evaporation, chiefly as the average precipitation at these times is <3 mm. Modern speleothem growth may therefore exhibit seasonal growth, dependent on the rate of groundwater translation through the epikarst and storage capacity.
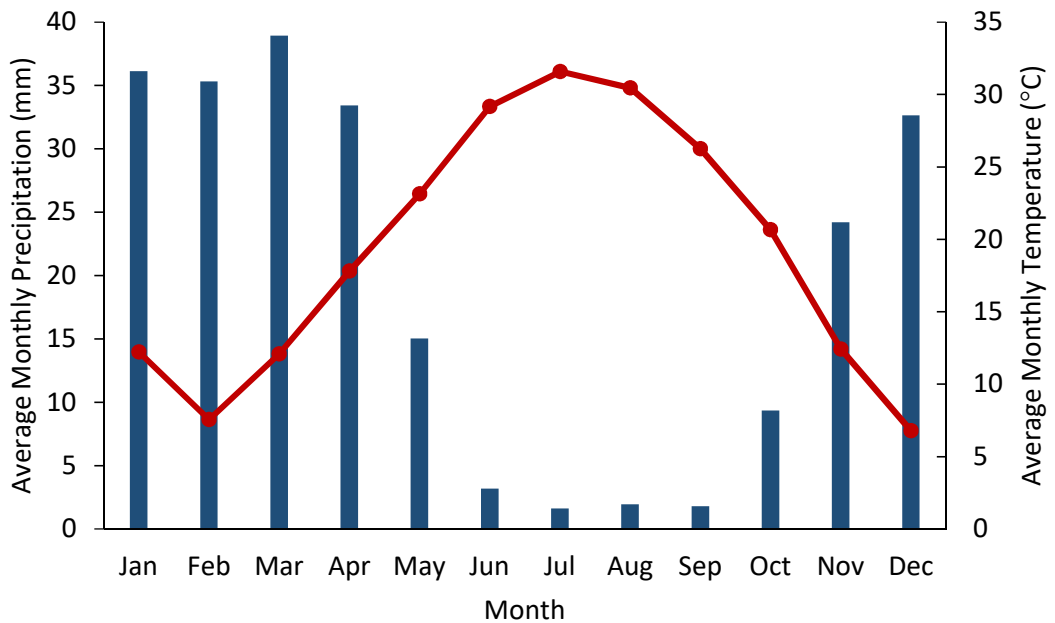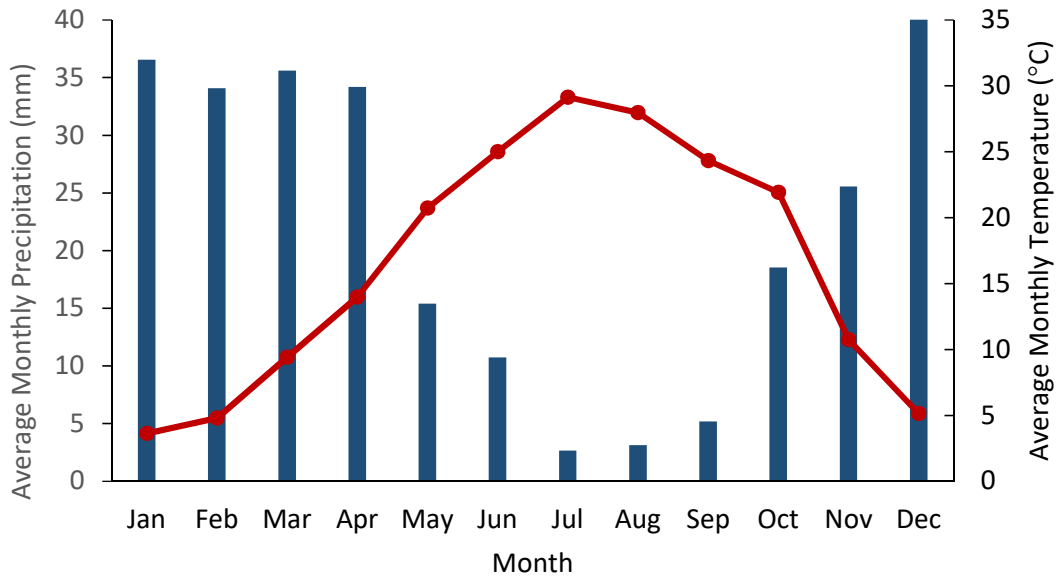
Figure 7.4: Monthly precipitation (blue bars) and temperature (red) averages for Tehran. Top, Climate Explorer precipitation: 1888-2015 and temperature: 1997-2015. Bottom, IAEA and WMO combined averages of both parameters from Tehran and Tehran East for the time frame 1960-1982 and 2000-2004.

Both datasets and parameters show marked seasonality between the winter and summer months, however there is some disparity in both temperature and precipitation during the autumn months with the speed of cooling and increase in precipitation amount.

	IAEA Weather Stations Precipitation (%)	Climate Explorer Weather Station Precipitation (%)	Average $\delta^{18}O$ IAEA Weather Stations (‰_{VSMOW})
Winter	42	44	−8.53
Spring	33	37	−3.86
Summer	6	4	−1.64
Autumn	19	15	−4.42

Table 7.1: Percentage of precipitation contribution by season for Tehran and Tehran East IAEA weather stations for the period 1960-1982 and 2000-2004 in column 1 and Climate Explorer for Tehran Airport for the period 1884-2015 (column 2). Column 3 shows the average $\delta^{18}O$ value from the IAEA weather stations. The disparity between the datasets only affects autumn rainfall amounts by 3%. This could be an artefact due to the Climate Explorer dataset having a much longer record.

The greater Katalekhor area receives about 300 mm annual precipitation (Dinpashoh et al., 2004; Modarres and Sarhadi 2011) originating in large part from the Mediterranean (Modarres and Sarhadi, 2011). However precipitation zones created using data collected between 1951 and 2000 suggest the figure is more like 200 mm in the region of the cave (Fallah et al., 2015). Most precipitation occurs in winter and spring (~60 mm each) with around 40 mm in the autumn and only ~10 mm in the summer months (Fallah et al., 2015). Summer rainfall is deflected along the western foothills by warm winds from the Central Iranian Plateau (Evans et al., 2004; Stevens et al., 2001).

Precipitation data from Tehran shows a strong seasonal difference in both δ^2H and $\delta^{18}O$ which follow similar trends of heavier compositions during the warmer months (Figure 7.5). Lightest isotopic compositions occur in January (average of −63 ‰_{VSMOW} δ^2H, −10.15 ‰_{VSMOW} $\delta^{18}O$) with a sharp increase into February. Heaviest isotopic compositions occur in August (average of 9.05 ‰_{VSMOW} δ^2H, 0.31 ‰_{VSMOW} $\delta^{18}O$). The increase in isotopic compositions is gradual from March-August while the decline into September is faster. It seems likely that these differences are controlled by temperature dependent fractionation driven by large seasonal differences in temperature. However correlation between air temperature and $\delta^{18}O$, whilst positive, has an $R^2=$

0.22 (Figure 7.6) suggesting some effect of temperature dependent fractionation. The relationship at Tehran accounts for 0.26 ‰/°C (Figure 7.6A). There is little clear relationship between precipitation amount and $\delta^{18}O$. A weak (R^2=0.14) negative correlation is likely to be unrepresentative of the relationship as the correlation is bolstered by isotopically light extreme rainfall events (Figure 7.6). This is further demonstrated in Figure 7.7 where monthly precipitation amount has a strong correlation with monthly $\delta^{18}O$ (R^2= 0.67) suggesting that the amount effect is a stronger control than overall values suggest.
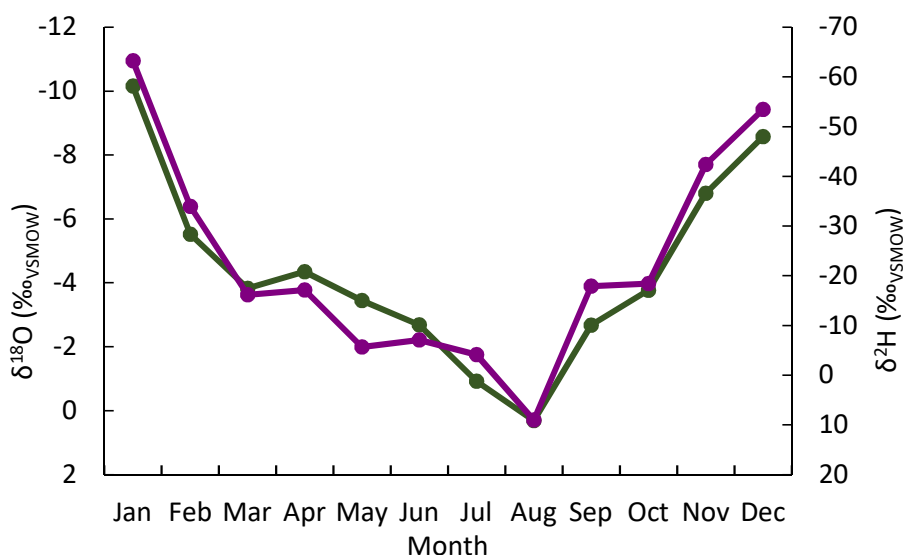
Figure 7.5: $\delta^{18}O$ vs $\delta^{2}H$ monthly variations combined from the Tehran and Tehran East IAEA stations for the period 1960-1982 and 2000-2004 showing strong seasonal differences in both isotopes.
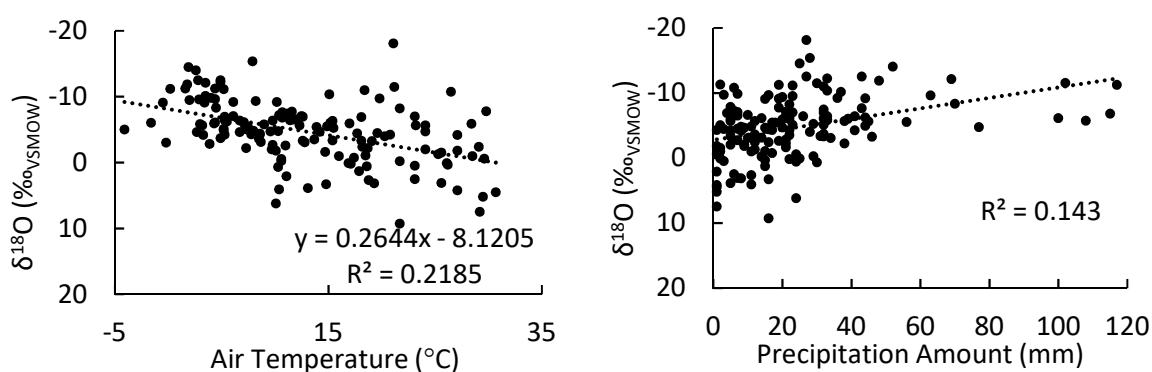
Figure 7.6: $\delta^{18}O$ vs air temperature and $\delta^{18}O$ vs precipitation amount. Both show quite low statistically significant R^2 values but visible positive and negative correlations for air temperature and precipitation amounts respectively.
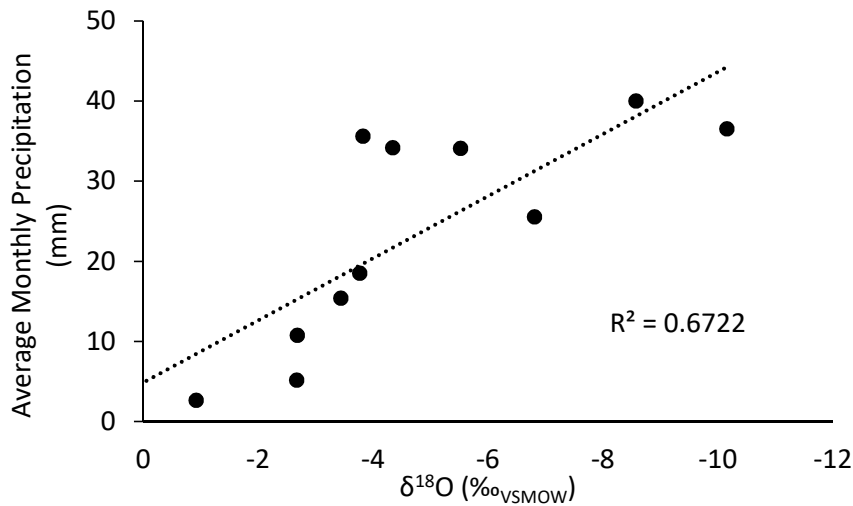
Figure 7.7: δ¹⁸O vs precipitation amount by month. A strong positive statistical correlation is present between months with higher amounts of precipitation and lighter isotopes. August is omitted.

Figure 7.8 displays the average precipitation values from Tehran (IAEA dataset), cave drip and pool waters as well as interpolated isotopic values of precipitation for the region of Katalekhor Cave (Bowen 2016 www.waterisotopes.org). These values are compared to the GMWL (Equation 5.1), the EMMWL (Equation 5.2) and the Tehran LMWL (Shamsi and Kazemi 2014, which should be reasonably representative of the cave region). The LMWL data typically plot below the GMWL in locations where raindrops can be re-evaporated (Stewart 1975), which is the case in this location. Also it is clear that the slope of the Tehran LMWL has a much shallower gradient than both the GMWL and EMMWL. The regression line of the estimates of the isotopes of precipitation in the region of Katalekhor Cave plots very closely to the LMWL, a very similar to identical gradient. Katalekhor precipitation is lighter than most of the Tehran data. The estimates are corroborated by drip water values collected from the cave at the time of stalagmite collection (by Al Omari), which plot at the isotopically lighter end of values but on or close to the Katalekhor/Tehran LMWL (Figure 7.7). The purple diamond highlighted in blue is a sample collected from the drip water supplying KT-3 and has the values of -8.37 ‰$_{VSMOW}$ $\delta^{18}O$ and -55.4 ‰$_{VSMOW}$ δ^2H, slightly depleted in $\delta^{18}O$ in comparison to Katalekhor precipitation.

$\delta^2H = 6.46\ \delta^{18}O + 0.24$ (‰$_{VSMOW}$)

Equation 7.1: Tehran Local Meteoric Water Line (Shamsi and Kazemi 2014)

		$\delta^{18}O$ (‰VSMOW)	δ^2H (‰VSMOW)
KTW061119-3	Drip above KT-3	-8.37	-55.4
KTW061119-1	Pool "Gallery One"	-8.97	-57.0
KTW061119-2	Drip "Wedding Hall"	-8.52	-58.4

Table 7.2: Water samples from Katalekhor Cave from November 2006. Drip water from above KT-3 was too slow to observe drip rate: the sample was collected overnight. The "Wedding Hall" drip rate at 13 drips/sec, was collected in minutes.

	Jan	Feb	Mar	Apr	May	Jun	Jul	Aug	Sep	Oct	Nov	Dec
δ^2H (‰VSMOW)	-74	-68	-67	-47	-36	-32	-27	-17	-33	-46	-54	-67
$\delta^{18}O$ (‰VSMOW)	-11.9	-10.6	-9.6	-7.7	-6.1	-5.7	-4.2	-3.1	-5.3	-7.3	-8.9	-10.7

Table 7.3: OIPC water isotopic composition estimates by month for the geographical position and altitude of Katalekhor Cave.
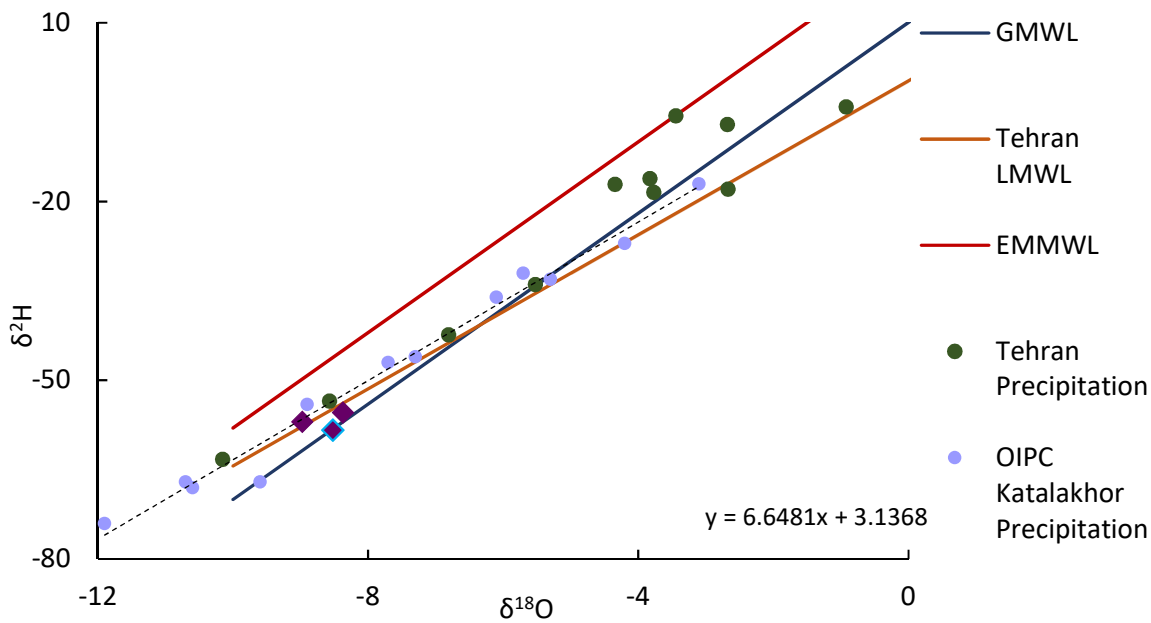
Figure 7.8: Plot of the Global Meteoric Water Line $\delta^2 H = 8\ \delta^{18}O + 10$ (Craig 1961), Eastern Mediterranean Meteoric Water Line $\delta^2 H = 8\ \delta^{18}O + 22$ (Gat and Carmi 1970) and Tehran local meteoric water line $\delta^2 H = 6.46\ \delta^{18}O + 0.24$ (Shamsi and Kazemi 2014) in addition to the average monthly isotopic compositions of the IAEA Tehran station 1960-1981. The blue circles show the OIPC calculated isotopic composition of precipitation in the region of Katalekhor Cave (www.wateriso.utah.edu/waterisotopes/pages/data_access/oipc.html). OIPC calculates the isotopic composition at any given latitude, longitude and altitude by interpolating from known IAEA station data, the equation of the dashed line through this data is displayed on the graph. Purple diamonds show cave waters sampled in November 2006 (see Table 7.2).

7.2   Results

7.2.1 Macromorphology and Petrography

7.2.1.1   Macromorphology

KT-3 is a typical candlestick stalagmite composed of dense, vug-free crystalline calcite (Figure 7.3). The clear hiatus at 324 mm marks the start of the Holocene portion of growth (Section 7.1.2). This part of KT-3 exhibits translucent yellow colouration, lacking obvious macro-structure it contrasts markedly with the pre-Holocene brown laminated crystalline calcite. The diameter of the stalagmite increased significantly following Holocene re-initiation of growth with a maximum diameter of 90 mm; after this the diameter gradually decreased steadily through time with no further significant thickening or thinning, finishing at a diameter of 33 mm.

7.2.1.2   Petrography

The Holocene part of KT-3 is mainly formed from columnar calcite and is generally devoid of internal micro-structure. Porosity is very low (~20 %), as is the presence of fluid inclusions.

The hiatus at 234 mm is not a clear sub-horizontal surface in hand specimen, but is marked in thin section by a zone of angular fragmented calcite crystals (Figure 7.9 A and B). In places these crystals define edges of underlying terminations, also largely angular; it is not clear if the fragmented crystals are located at crystal terminations or within larger crystals. Changes in extinction zones suggest calcite crystals above the surface are smaller than those below but all crystals have similar angles out of extinction so may be showing only a slight difference in optical continuity (Figure 7.9 B).

From the top of the hiatus to 140 mm the calcite is mostly columnar (short and proper of Frisia and Borsato 2010) often with curved and slightly irregular boundaries and rounded terminations (Figure 7.9 C). Calcite crystals are variable in size (from 100 µm to 600 µm), growth direction and degree of elongation. In the central axis of KT-3, elongation of crystal c-axes define upward growth direction, whereas on the flanks growth direction is typically orientated toward the edges. However, some flank regions lack preferred crystal elongation (Figure 7.9 E), forming essentially a calcite mosaic fabric (Frisia and Borsato 2010). Transitions from indisputably columnar calcite to mosaic occur gradually, without sharp boundaries (Figure 7.10 B).

Interestingly the fabrics described above often transition into 'patches' of highly irregular calcite, located at 27 mm, 51-53 mm, 61-79 mm and 101-107 mm (all at furthest extent as boundaries are highly irregular). Here crystals are much larger (up to 1.5 mm and commonly ~ 500 µm in width) and angular (Figure 7.9 F). In the central axis these crystals appear to be mosaic forms, exhibiting no preferred elongation. However, in some areas a local partial pattern of growth orientation has developed that shows some elongation horizontally out towards the stalagmite flank (Figure 7.10 A). In these areas it can be difficult to distinguish from calcite that has gradually lost elongation (mentioned above) and calcite related to irregular growth phases. Although some boundaries between these 'patch' mosaics and other mosaic fabrics appear sharp, the 'patch' calcites typically have high interference colours and apparently higher relief (Figure 7.9 F). It is possible these 'sharp' patch boundaries are an artefact of viewing crystals which themselves have well - defined boundaries, drawing the eye toward transitions that appear sharper than they really are.

Elsewhere, in the central axis 'patch' crystals are associated with more typical columnar calcite, the boundaries to which can be either sharp or gradual (Figure 7.9 C and D). Oddly some columnar crystals appear to terminate against 'patch' crystals but some apparently grew concurrently causing columnar calcite to bend around the mosaic in the competition for space (Figure 7.10 E). Additionally isolated angular crystals can occur close to main boundaries and appear superimposed on top of columnar crystals. The calcite which grows immediately above these is generally unaffected as preferred elongation and orientation returns with growth direction. This top boundary is still irregular as elongation can return gradually or straight from a mosaic terminal surface (Figure 7.10 F).

From 140 mm to the top of the stalagmite, elongated columnar calcite (Frisia and Borsato 2010) is typical (Figure 7.9 D). The transition into this more 'stable fabric' is not preserved as the stalagmite was unfortunately broken after collection. Boundaries between crystals in this section are straight, with angular terminations: the crystals are also longer (1.3 cm or more) with widths from <200 µm to nearly 1 cm. Axial growth is vertical, but at the flanks growth again bends towards the edges of the stalagmite. Minor porosity at crystal terminations and boundaries, was noted, but given the irregular shapes and positioning it is likely that this porosity is an artefact of the thin sectioning process. The only notable petrographic differences in this period of growth is a slight increase in irregularity to some boundaries and shortening of the columnar crystals near the top of the stalagmite. Calcite crystals at the 'tip' of the stalagmite are not eroded or corroded.
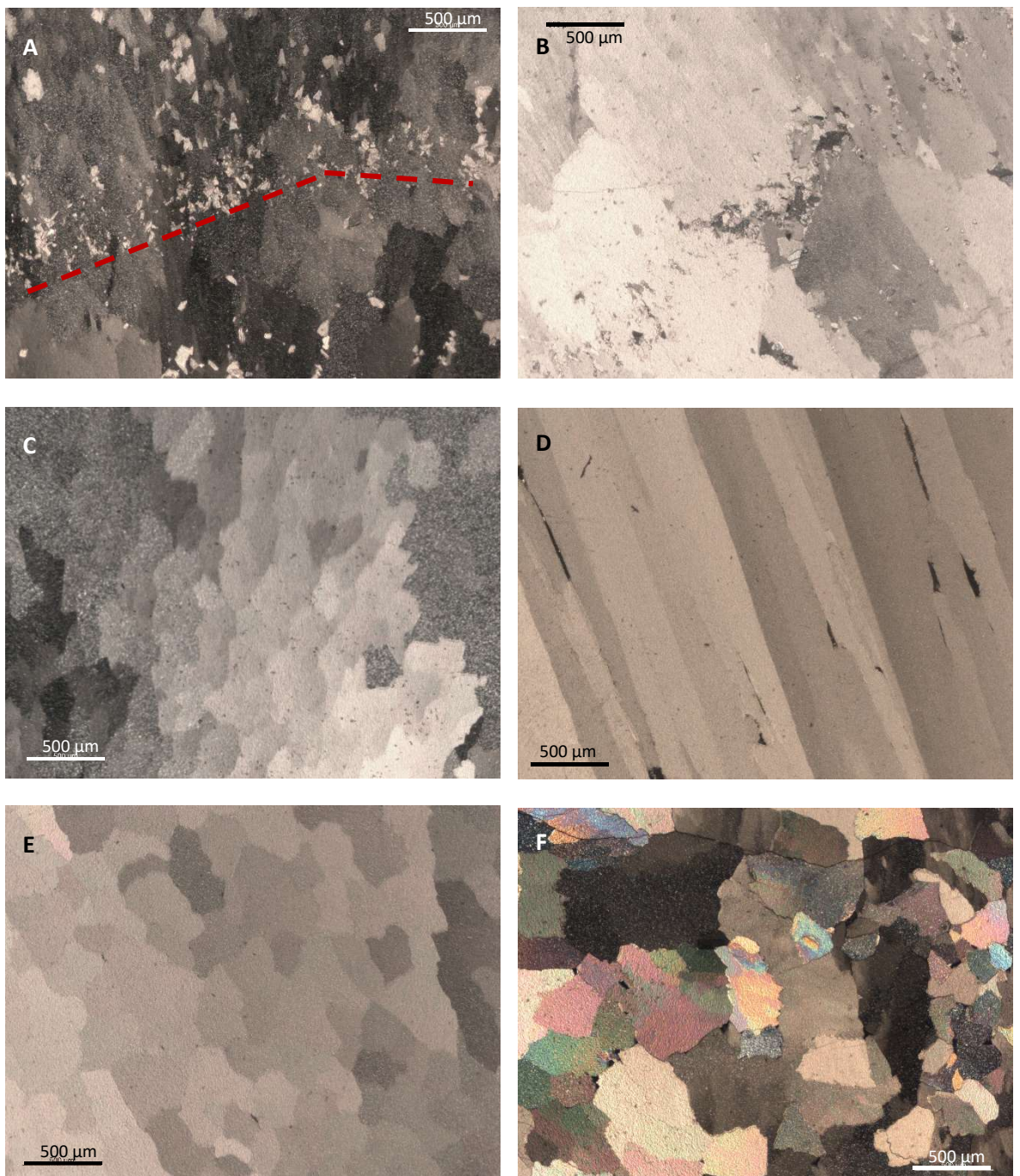
Figure 7.9: KT-3 fabrics. A. Angular crystals associated with the hiatus surface. B. Hiatus surface and slight change in crystal size and optical continuity. C. Short columnar calcite following the hiatus. D. Elongate columnar calcite above 140 mm and secondary porosity. E. 'Mosaic' calcite. F. Typical 'patch' calcites showing angular crystals, some high birefringence and high relief.
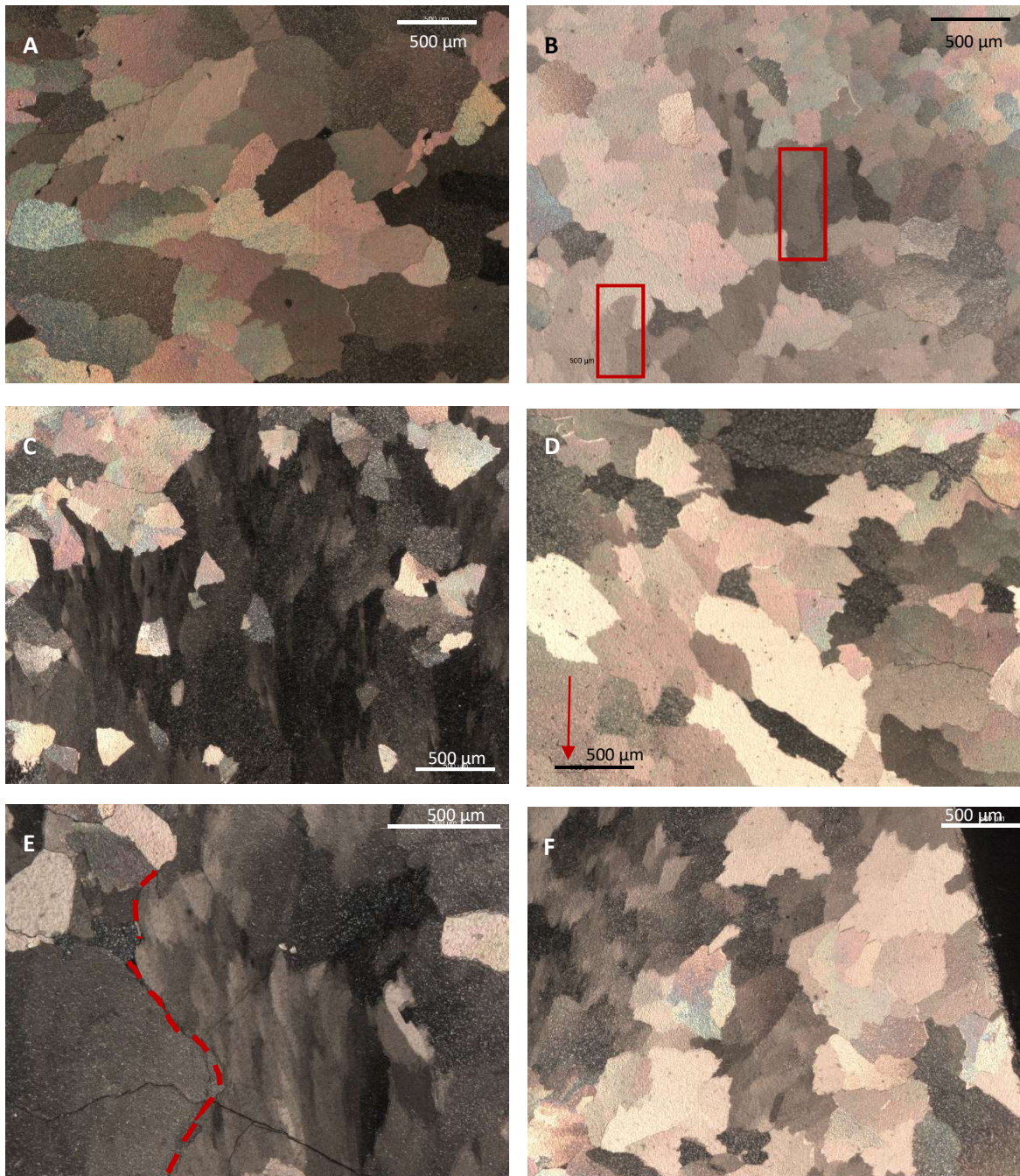
Figure 7.10: Transitions between fabrics. A. Elongation of 'patch' crystals towards the flank. B. Irregular gradual transition between mosaic crystals and short columnar. Short columnar crystals are highlighted in red. C. Sharp boundary between columnar calcite and the 'patch' fabric including isolated angular crystals slightly further from the main boundary. D. Potentially gradual transition between columnar and 'patch' fabrics. The red arrow is placed over a columnar crystal and indicates that below this the fabric is considered columnar. E. Suggested competitive boundaries (highlighted) between 'patch' and columnar crystals. F. Irregular top boundary to a section of 'patch' calcite. Boundaries are likely to be sharp but it is somewhat unclear.

7.2.2 U-series Dating

7.2.2.1 Sampling strategy

Although only the Holocene portion of KT-3 growth is discussed the entire stalagmite was sampled to construct an age model. Initially KT-3 was sampled by Al-Omari in 2006; however discrepancies in the chronology and a low sample density meant it was desirable to improve on the results. Dates used in this thesis are all new analyses from the University of Oxford (courtesy of Stacy Carolin) some of which are re-samples of the Al-Omari locations. The sampling strategy targeted the 324 mm hiatus, top and bottom growth, as well as increasing resolution. To this end a further 7 samples were obtained from the Holocene portion (Table 7.4, Figure 7.11).

7.2.2.2 Age Model and growth rates

Growth of KT-3 began before 125,000 yr BP during the Late Pleistocene and ceased sometime soon after 75,200 yr BP marked by the hiatus at 324 mm. Extrapolation of ages between the sample trench and the hiatus surface itself gives an age of the restart of growth of around 9439 yr BP. The youngest U-series age of 58 yr BP at 2 mm below the top confirms that the stalagmite was active when collected in 2006. Dates were determined in 2016. The linear age model (Figure 7.12) shows that growth was faster in the first 150 mm (up to 6600 yr BP) than the latter 150 mm; the first half of growth occurred in 6000 years, the latter in 4500 years. Growth rate during these two periods is fairly consistent typically 0.063 mm/yr to 0.043 mm/yr in the first period of growth and 0.035 mm/yr - 0.018 mm/yr in the second period. As there are no hiatuses following reinitiation of growth KT-3 provides an essentially continuous and complete record of growth from ~9500 yr BP to present.

Sample Name	Height above hiatus (mm)	^{238}U (ppm)	^{232}Th (ppb)	^{234}U/^{238}U	^{230}Th/^{238}U	^{230}Th/^{232}Th	Initial ^{234}U/^{238}U	Date uncorr (yr BP)	Date corr (yr BP)
ag07	310	0.37349	0.33269	2.2780 ± 0.007	0.0028 ± 0.0004	9.8	2.2783 ± 0.007	72 ± 19	58 ± 23
al01	277	0.30922	0.255719	2.4457 ± 0.008	0.0295 ± 0.0005	191.6	2.4511 ± 0.007	1255 ± 25	1248 ± 25
ag06	226	0.2693	0.141756	2.3611 ± 0.007	0.0897 ± 0.0009	174.6	2.3771 ± 0.008	4210 ± 38	4121 ± 45
al02	211	0.24783	0.119418	2.3419 ± 0.008	0.0952 ± 0.0008	282.2	2.3592 ± 0.007	4511 ± 37	4431 ± 41
al03	185	0.30129	0.104835	2.2554 ± 0.007	0.1119 ± 0.0009	726.3	2.2751 ± 0.007	5522 ± 43	5451 ± 44
al04	156	0.34787	0.131288	2.2561 ± 0.007	0.1346 ± 0.0009	1198	2.2797 ± 0.007	6672 ± 46	6602 ± 48
ag05	115	0.44988	0.104835	2.1905 ± 0.007	0.1446 ± 0.0008	1895.9	2.2155 ± 0.007	7401 ± 42	7334 ± 42
al06	83	0.61115	0.131288	2.2686 ± 0.007	0.1568 ± 0.0008	2230.7	2.2967 ± 0.007	7760 ± 43	7652 ± 42
al07	54	0.59875	0.147195	2.0937 ± 0.007	0.1580 ± 0.0008	1966	2.1202 ± 0.007	8504 ± 46	8435 ± 45
ag04	35	0.57619	0.093435	2.0063 ± 0.007	0.1568 ± 0.0008	2954.4	2.0315 ± 0.007	8816 ± 49	8749 ± 49
an15	10	0.7171	0.0822	2.0023 ± 0.007	0.1659 ± 0.0008	4424.8	2.0290 ± 0.007	9368 ± 67	9262 ± 67

Table 7.4: U-series results for the Holocene section of KT-3, all ages are 2 s.d. Age corrections assume a bulk earth composition for the detrital Th component.

This assumes stalagmite calcite is at secular equilibrium with the bulk earth ^{232}Th/^{230}Th value (3.8) and that initial ^{230}Th/^{232}Th has an atomic ratio of 4.4 ± 2.2

x10^{-6}. Uncertainty errors are ± 50%.

ag07 58 ± 23

al01 1248 ± 25

ag06 4121 ± 45

al02 4431 ± 41

al03 5451 ± 44

al04 6602 ± 48

ag05 7334 ±42

al06 7652 ± 42

al07 8435 ± 45

ag04 8749 ± 49

an15 9262 ± 67

30 mm
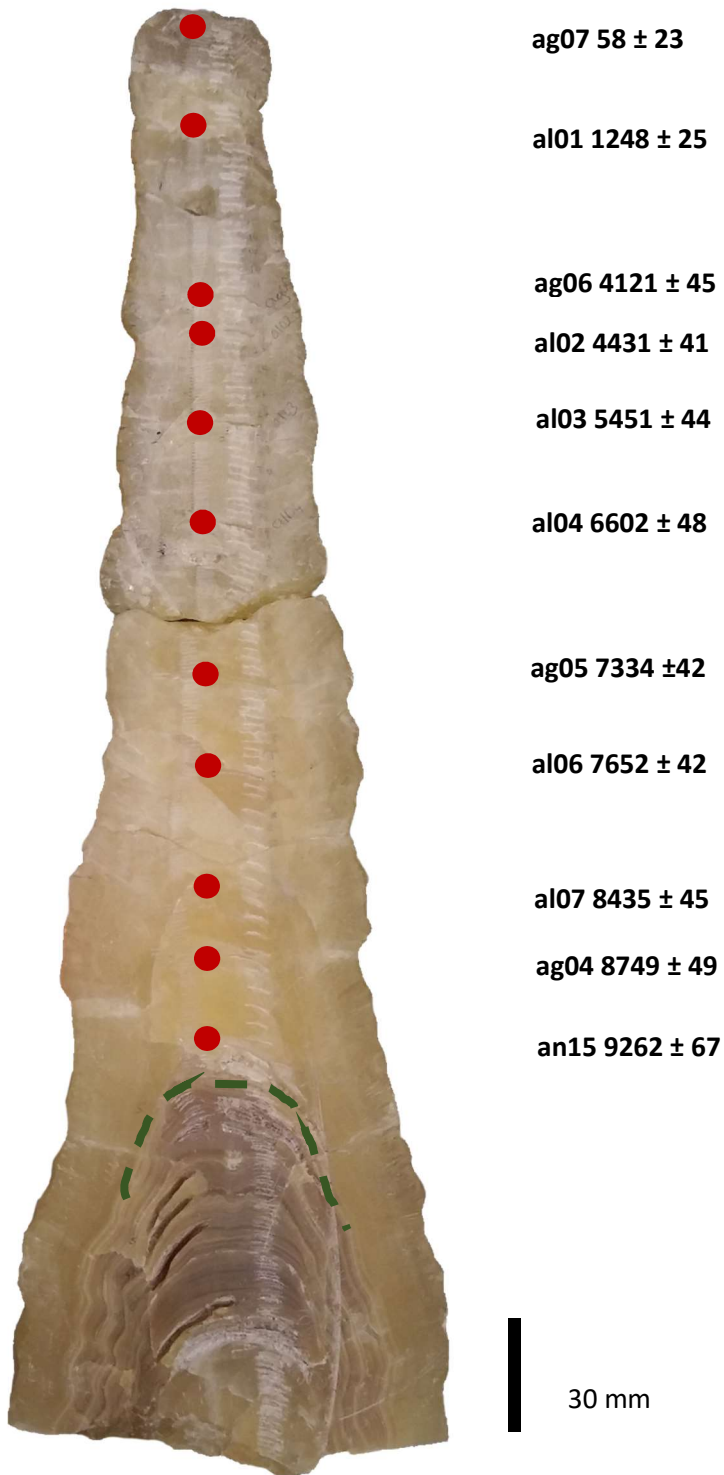
Figure 7.11: KT-3 Holocene section with U-series dates and stratigraphic locations.
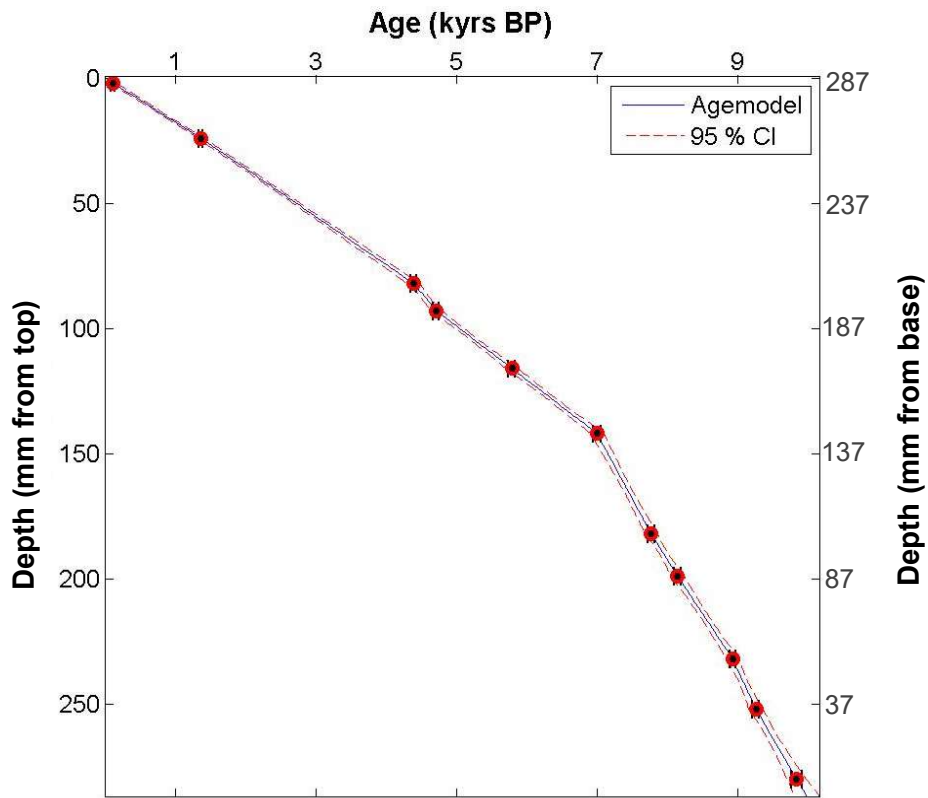
Figure 7.12: COPRA linear age model for the Holocene section of the KT-3. Initial growth up to a depth of 160 mm was faster than later Holocene growth.
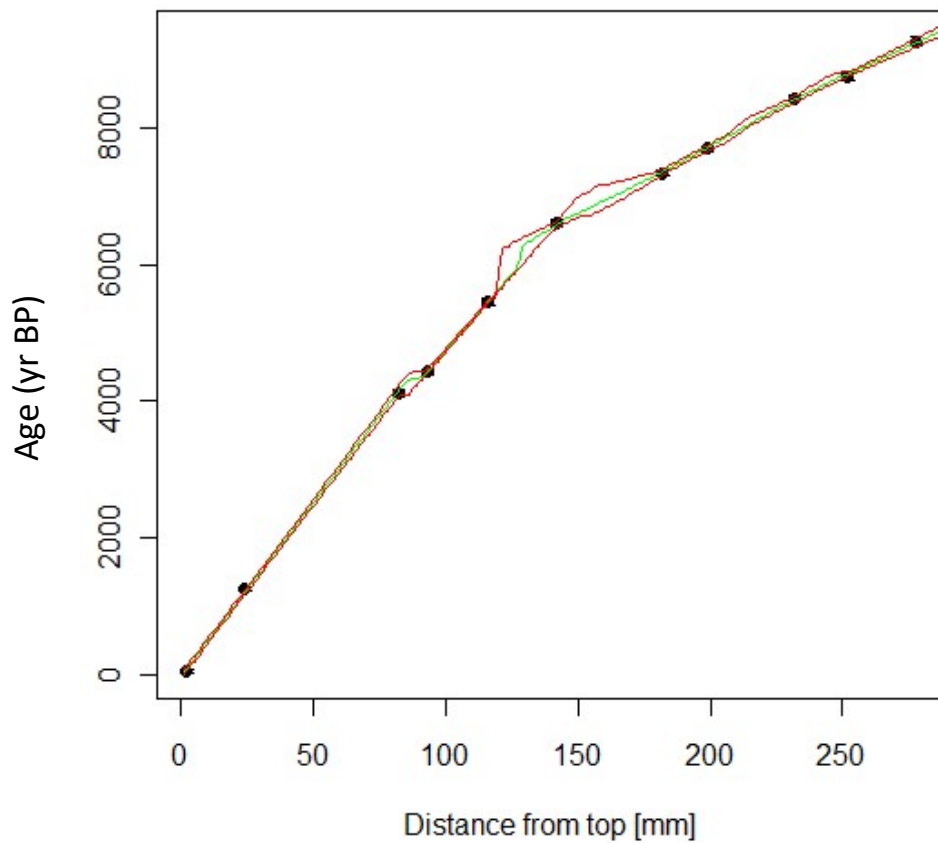
The shape of the profiles created by StalAge and COPRA are comparable. This is confirmed by the sample of 5 depths and ages presented in Table 7.5 which show an average age error of 19 yr BP, well below the errors on the on U-series dates themselves. The highest unknown age error is 35 yr BP. The statistical methods produce age models which are in agreement with each other.

Depth (mm from base)	Depth (mm from top)	COPRA (yr BP)	StalAge (yr BP)	Minimum unknown age error (yr BP)
1	287	9439	9404	35
73	214	8030	8034	4
116	171	7132	7143	11
235	52	2633	2621	12
252	35	1793	1759	34

Table 7:5: Comparison of 5 key ages which are palaeoclimatically or stratigraphically significant in KT-3.

7.2.3 Stable Isotopes

7.2.3.1 Sampling strategy

Previous work by Sa'ad Al-Omari had established a low resolution 5 mm spaced stable isotopic profile for the Holocene portion of KT-3. The 1 mm record produced here covers most of the Holocene and has an average resolution of ~32 years.

7.2.3.2   Oxygen Isotopes

Oxygen isotope data is shown in Figure 7.13. From around 7000 yr BP to 3000 yr BP $\delta^{18}O$ gradually increases from around -10.0 ‰ to -8.0 ‰, remaining ~ -8.0 ‰ until present. Between 9500 and 7000 yr BP $\delta^{18}O$ values oscillate around -9.5 ‰. The overall range in values is -10.59 ‰ to -7.27 ‰ and the average enrichment across the record is ~1.7 ‰.

7.2.3.3   Carbon Isotopes

Carbon isotope data from the Holocene of KT-3 range from -1.69 ‰ to -5.68 ‰ (Figure 7.14), broadly decreasing with time and mirroring the pattern in $\delta^{18}O$. The decline is steady throughout most of the record with the mean falling by 1 ‰ until 2200 yr BP where the remaining record becomes depleted by 1.5 ‰. The $\delta^{13}C$ record has higher variability than $\delta^{18}O$ and is smoothed with a 5 point running mean in Figure 7.14. The range for the profile is -1.69 ‰ to -5.68 ‰ and displays higher variability than the $\delta^{18}O$ record. A significant positive excursion of 1.77 ‰ begins at 8260 yr BP and peaks at 8030 yr BP.

Figure 7.14: Axial isotopic profiles for the KT-3 stalagmite. Above δ¹⁸O (red) and below δ¹³C (blue). Absolute dates and error bars are shown according to the horizontal scale with ages and errors listed in Table 7.1.
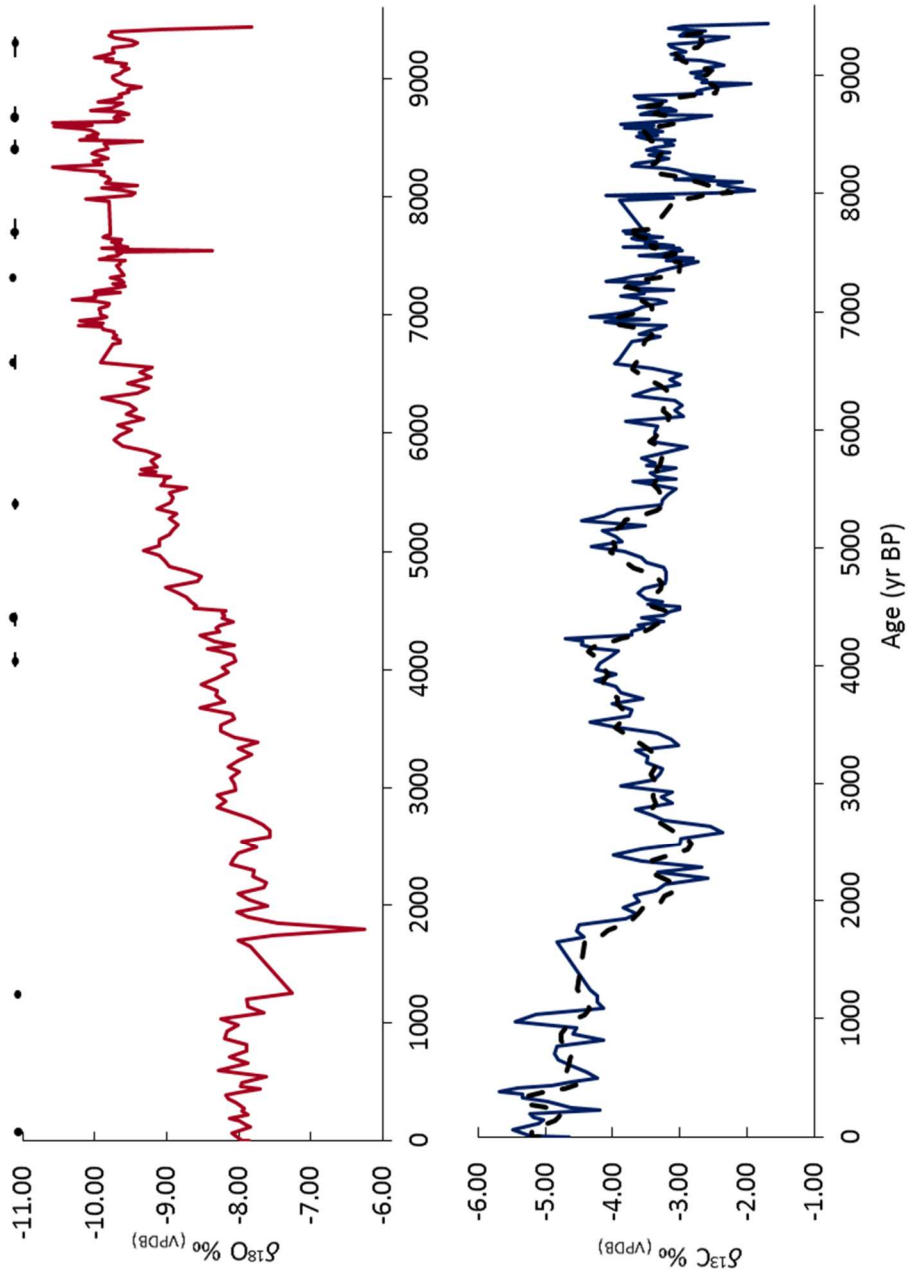
7.2.4 Trace Elements

7.2.4.1 Sampling strategy

The morphological characteristics (thinning upward) and the stable isotopic profile suggested that a trace element profile would aid the climatic interpretation of KT-3, particularly the δ^{13}C record, which is often co-variant (and co-controlled) with trace elements (e.g. Treble et al., 2005; Fairchild and Treble 2009). A 10 mm resolution sample spacing was used initially, allowing the option to increase resolution later if necessary. In the upper part of KT-3, where the stalagmite thins, samples were collected as close to 10 mm separation as practical.

7.2.4.2 Profiles and description

As outlined in previous chapters, trace elements were chosen based on their likely relationship with climatic response (Mg, Sr, Ba) or relationship with organic matter (P) (Fairchild et al., 2000; Huang et al., 2001).

Figure 7.15 shows trace element content in ppm normalised to 100% calcite (i.e. 40 wt% Ca). Mg and Sr have profiles that show decreasing contents over time. Both Sr and Mg decrease into the early Holocene until 8930 yr BP (Mg) and 8620 yr BP (Sr). A sharp decrease in both elements is also noted at 3390 yr BP, though more prominent in Mg. A small increase in both Mg and Sr occurs at the end of the record (710 yr BP). Though the magnitude is smaller, short scale variation is higher in Ba and is not clearly related to Mg but is somewhat similar to Sr. An overall trend of declining concentration can be observed until 2290 yr BP after which it doubles by the end of the record. Prominent peaks in values are found at 8000-7870 yr BP and 7120 yr BP which can be matched to peaks in P. There is no clear trend in P over the course of growth.

Figure 7.15: Next page. Variations in analysed trace elements in ppm. Sr (yellow) and Mg (green) are plotted on the same axis to highlight the similar decreasing trend over time. An inset of Sr better shows the individual variation. Only P (purple) doesn't show an overall decrease in ppm. Ba is orange in colour.

267
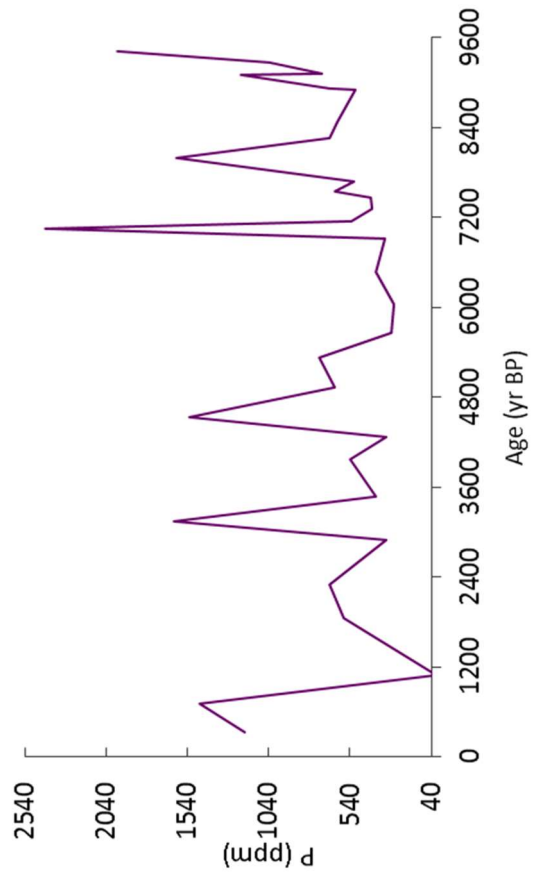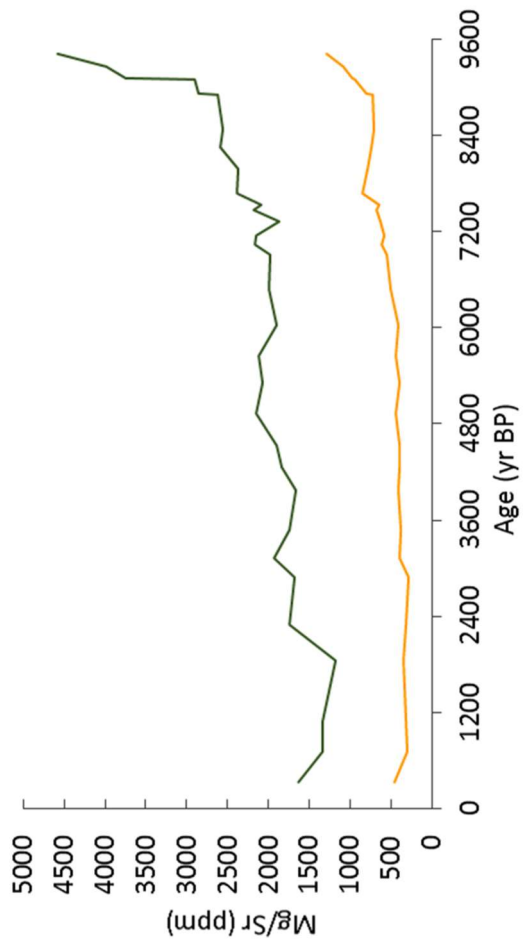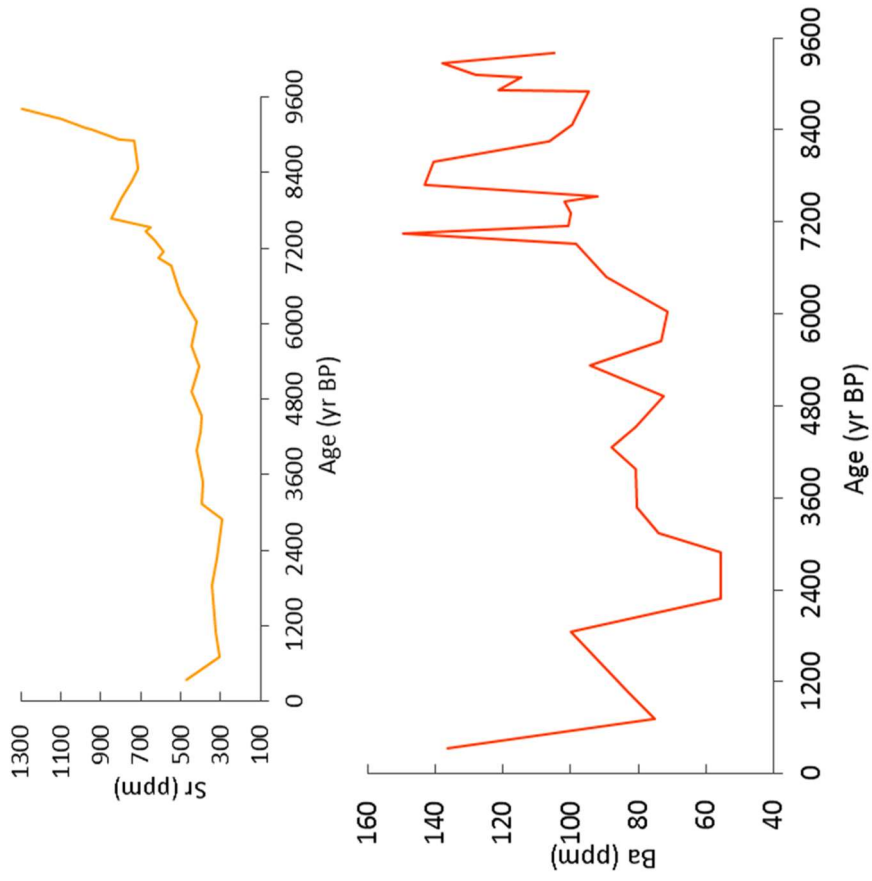
Mg/Ca Sr/Ca and Ba/Ca are also plotted allow comparison to stable isotope profiles (Figures 7.16 for $\delta^{18}O$ and 7.16 for $\delta^{13}C$). Mg/Sr is also plotted in the same manner. Both Sr/Ca and Mg/Ca display overall trends of decreasing concentration over time which is correlated with enrichment in $\delta^{18}O$. The steady plateau in values in Mg/Ca and Sr/Ca is similarly timed to the plateau $\delta^{18}O$ after 3000 yr BP. In Ba/Ca values are higher in the early part of the record and begin to decline at 6900 yr BP, at the same time as enrichment begins in $\delta^{18}O$. Simultaneous increases in Mg/Ca, Sr/Ca and Ba/Ca are observed at 710 yr BP, 500 years after the onset of declining $\delta^{18}O$ at 1250 yr BP and within the continuing trend of lighter isotopes.

Variation in Ba/Ca is surprisingly well correlated to $\delta^{13}C$ after 6880 yr BP, showing an inverse relationship where generally light $\delta^{13}C$ corresponds to higher Ba/Ca ratios, particularly ~2000 yr BP. Mg/C and Sr/Ca are at their highest values at a similar time to the early enriched $\delta^{13}C$ until 8940 yr BP. Mg/Ca in particular shows stable values at the same time as the plateau in the mean of $\delta^{13}C$ (8850-2190 yr BP) and decreases at 2290 yr BP similarly timed to the beginning of the decreasing trend in $\delta^{13}C$. Sr/Ca shows a slightly declining trend overall since the start of the record with observable quicker decreases taking place at 7670 yr BP and 3130 yr BP. Around 2880 yr BP, a slight increasing trend may be seen roughly corresponding to Mg/Ca.

Figure 7.16: Next page till 264. Sr/Ca (yellow), Mg/Ca (green), Ba/Ca (orange) and Mg/Sr (grey) multiplied by 1000 and plotted with $\delta^{18}O$. Graphs show relationships between Sr/Ca, Mg/Ca, Ba/Ca and $\delta^{18}O$ but not Mg/Sr.
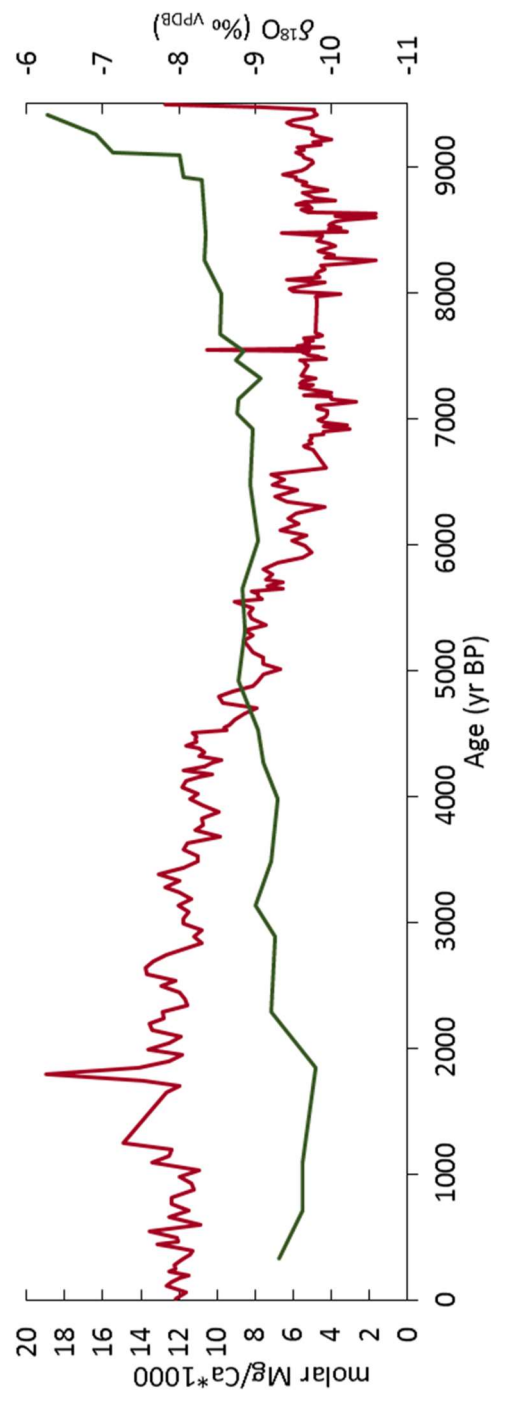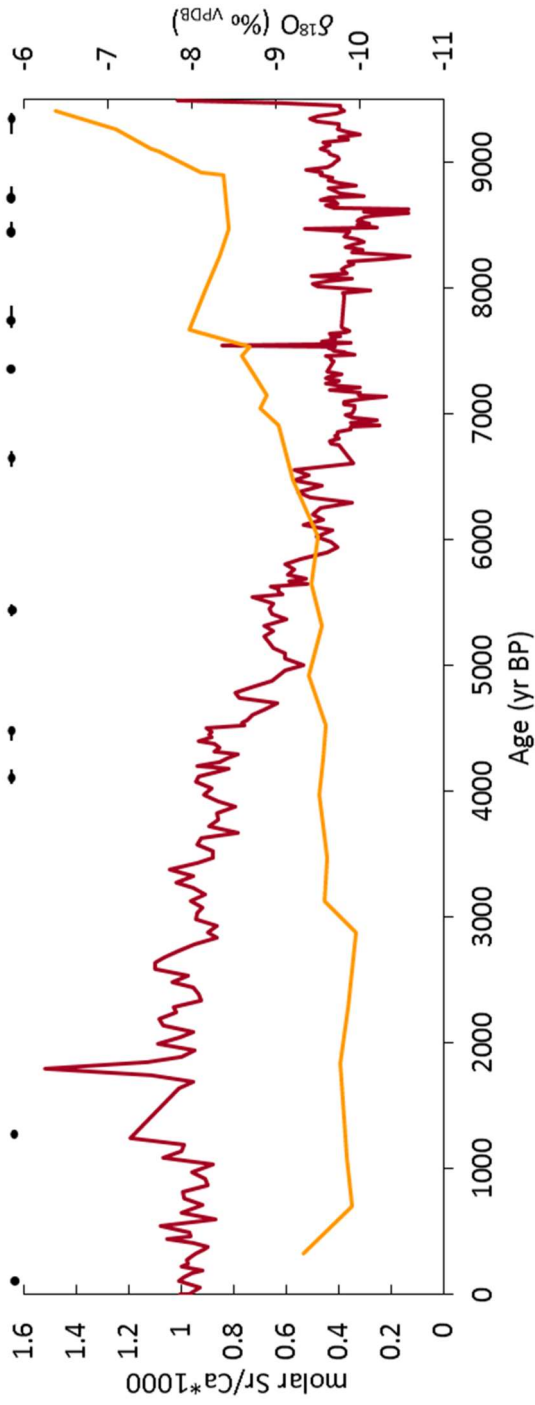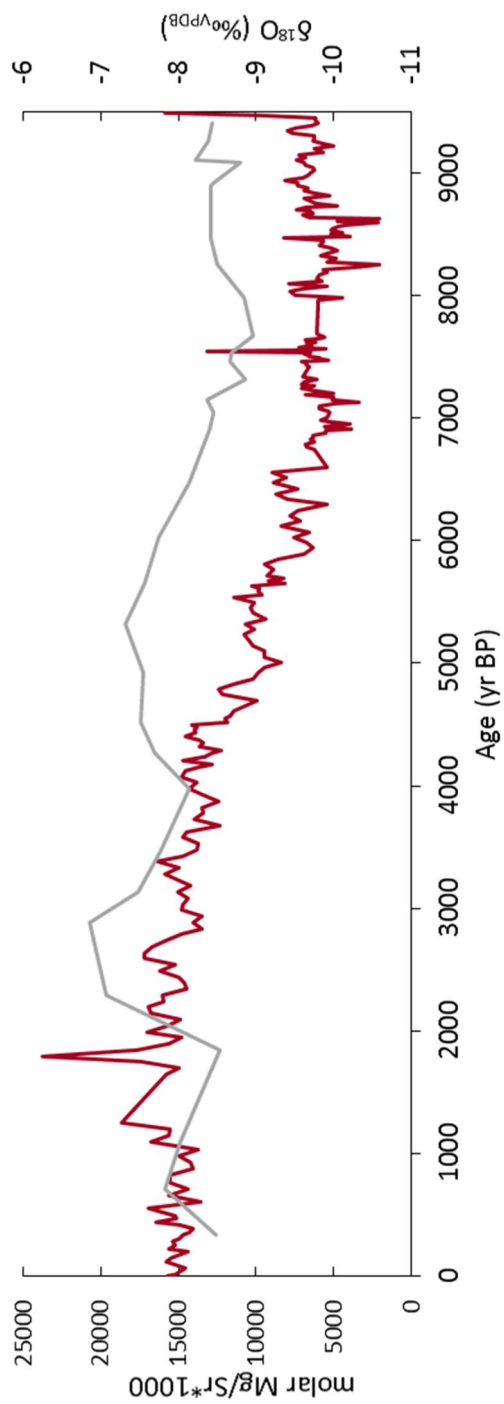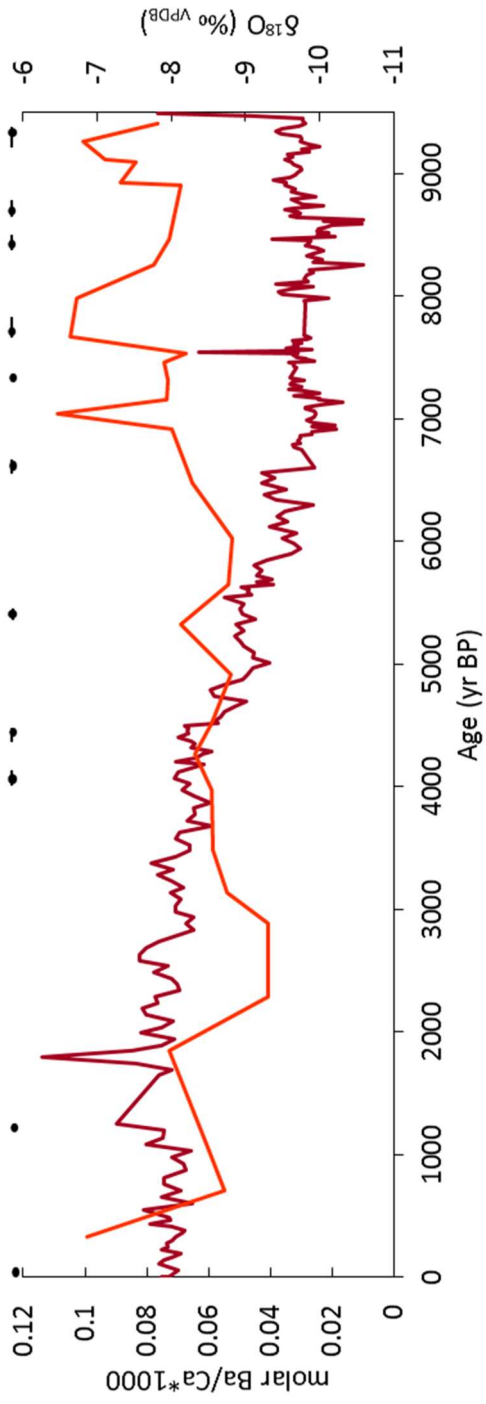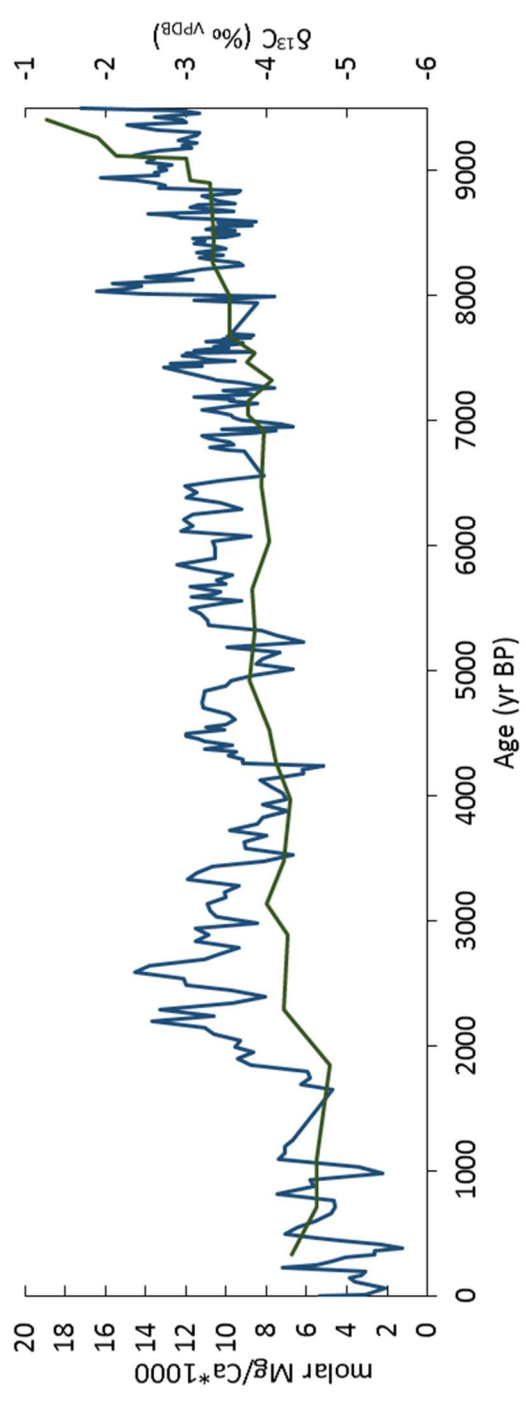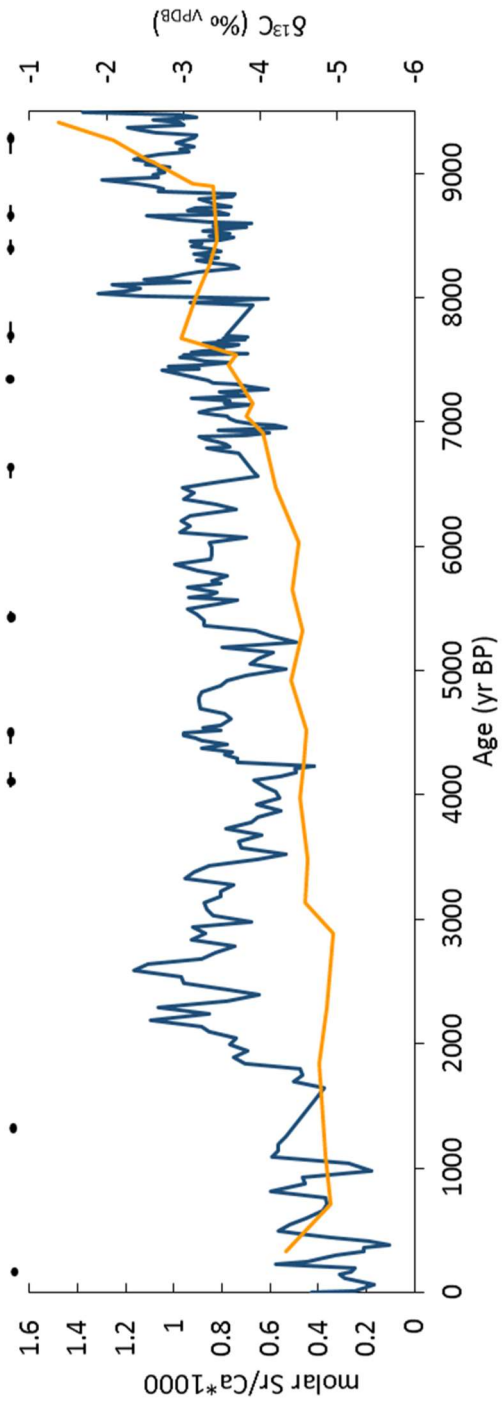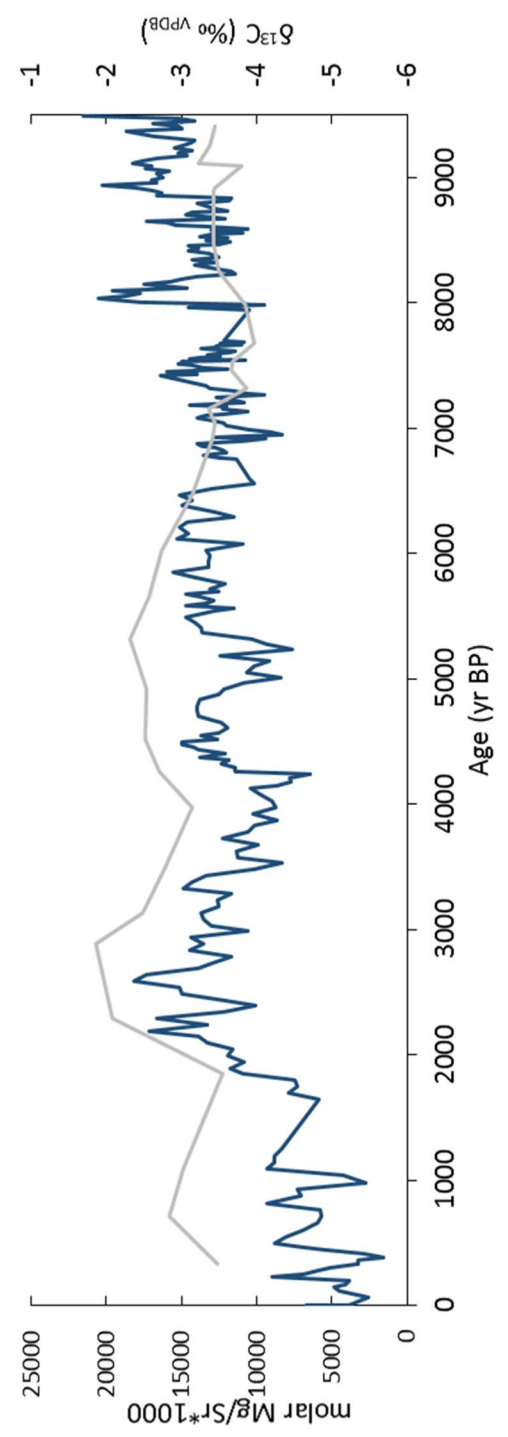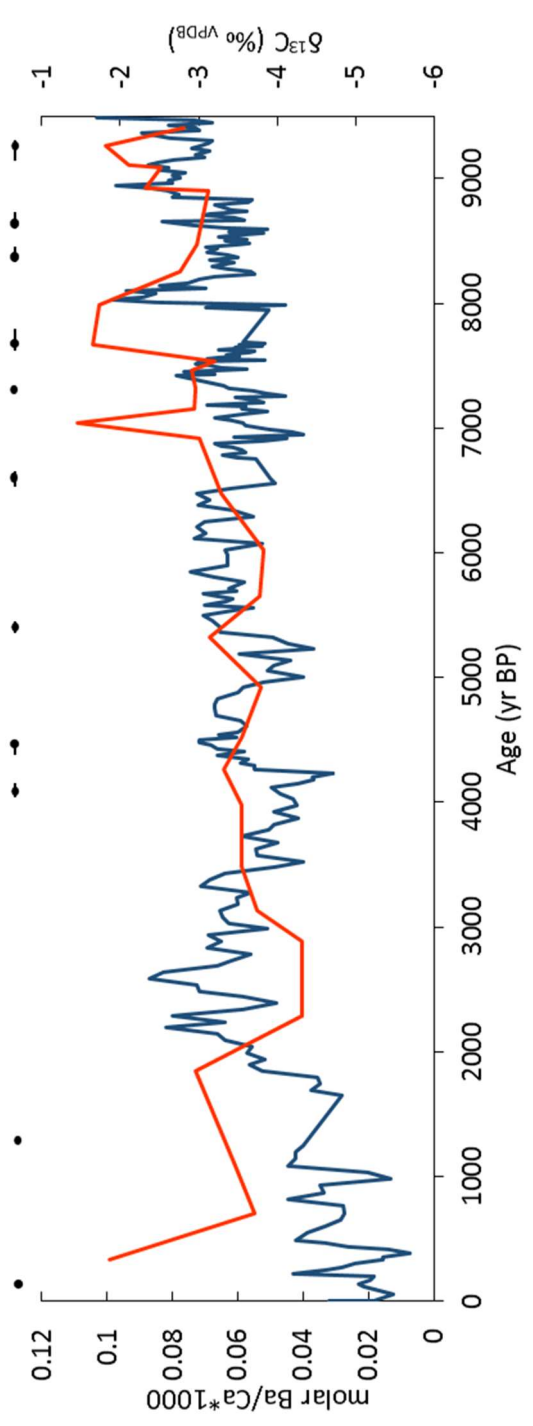
Figure 7.17: Previous pages. Sr/Ca (yellow), Mg/Ca (green), Ba/Ca (orange) and Mg/Sr (grey) multiplied by 1000 and plotted with δ¹³C. Graphs show an inverse relationship between Ba/Ca after 6880 yr BP and δ¹³C and a rough correlation between the decline in Mg/Ca and Sr/Ca values over time with overall progressively lighter δ¹³C.

7.3 Discussion and Palaeoclimatic Interpretation

7.3.1 Equilibrium Deposition

KT-3 was active when collected and gave a $\delta^{18}O$ value from its upper surface of -7.86 ‰vPDB. The composition of its associated drip water was -8.37 ‰vSMOW (Table 7.6). The Kim and O'Neil (1997) equation produces a temperature of 12.5 °C and the Tremaine et al. (2011) equation, a temperature of 16.7°C, close to temperatures measured in November 2006 (15.5- 16.6 °C). The Tremaine relationship thus suggests that active KT-3 precipitate, formed in quasi-equilibrium with its drip waters.

$\delta^{18}O$ (‰vSMOW) drip water	$\delta^{18}O$ (‰vPDB) modern calcite
-8.37	-7.86

Table 7.6: Modern calcite and drip water $\delta^{18}O$ for the KT-3 speleothem.

7.3.2 Petrography and Environment of Formation

The early stage of Holocene growth of KT-3 (9500-6600 yr BP) was faster than the latter growth (6600 yr BP to present). However, thinning of the stalagmite diameter began ~8400 yr BP. The gradual thinning from this time onward can be interpreted to indicate reducing drip rate with time. While a lack of hiatuses suggests no cessation in drips, petrography also shows a change in columnar fabric type at 140 mm (~6700 yr BP) coincident with the switch to lower growth rate.

Characteristics of different columnar calcite fabrics are representative of the conditions of the drip water as crystallites grow in continuity with the substrate producing one composite crystal as viewed by microscope (Kendall and Broughton 1978). Straight, well-defined boundaries and larger crystals are created by regular stacking of crystallites (Frisia et al., 2000). Thus, longer periods of consistent drip rate, promote growth of larger crystals with stable boundaries. This implies that the elongate columnar calcite fabrics above 140 mm (i.e. after ~6700 yr BP) grew under consistent seasonal drip rate. The large size of crystals also suggests these conditions persisted for a number of years, despite the gradually reducing drip water volume inferred from overall thinning in stalagmite diameter. It has been suggested that the formation of elongate columnar fabrics is related to higher Mg/Ca ratios than columnar proper or short fabrics (Frisia et al., 2000); however this relationship is not demonstrated in KT-3 as the Mg/Ca ratio at the time of the formation of elongate columnar calcite is lower than that during the earlier formation of the columnar proper and short columnar calcites (see below).

Below 140 mm, smaller crystals with less straight boundaries are typical of columnar proper and short columnar calcite fabrics. Boundaries which are less straight are indicative of a change in the stacking of crystallites which begin to interfere with the growth of the neighbour (Kendall and Broughton 1978). Changes in stacking are due to defects in crystallites caused by the presence of growth inhibitors such as organic materials or a faster growth rate (Frisia et al., 2000). Flat crystallite faces will, with time, dominate the morphology of calcite crystals thus more defects are present in fabrics which grew more quickly (Frisia and Borsato 2010). A faster drip rate is likely to control the transition between microcrystalline and columnar calcite (Frisia and Borsato 2010) which potentially indicates that the same is true of different columnar calcites which are characterised by the size of the crystal and boundary interactions. Faster growth during the early Holocene period is indicated by both the age model and the wider stalagmite diameter. It is also possible that the higher Ba/Ca (and Sr/Ca) values until 7025 yr BP are indicating a link to the delivery of more organic derived colloidal particles (Borsato et al., 2007), perhaps indicative of larger water volumes and flushing events.

The first ~4000 yr BP of the Holocene is thus characterised by faster stalagmite growth caused by increased drip volume and potentially increased drip rates. The latter half of Holocene KT-3 growth is controlled by consistent but overall decreasing drip waters.

As the 'patch' fabrics are largely lacking in growth direction they are best characterised as mosaics. The term 'mosaic' is often construed to imply a diagenetic origin (Alan C. Kendall pers. comm. 2015), but this should not be assumed. The mosaic patch fabrics in KT-3 show no unequivocal evidence for diagenesis driven by dissolution/reprecipitation reactions. The 'patches' are small and isolated implying dissolution/reprecipitation would be localised and short lived, which is uncommon in stalagmites with no apparent large seasonal variation in water input. Angular jagged boundaries can imply dissolution, but lateral relationships in KT-3 are not ubiquitously sharp. Furthermore there is evidence for competitive growth between mosaic crystals and their neighbours, which have nucleated to define more obvious growth directions. Apparent elongation of mosaic crystals towards the patch flanks matches the growth of columnar crystals and therefore implies some surficial growth control which is unlikely if dissolution/reprecipitation was affecting previously emplaced crystals.

The higher birefringence colours, when compared the rest of the stalagmite crystals, and the apparent higher relief of the patch crystals, suggests simply that the patches grew in a different optical orientation to the rest of the stalagmite.

7.3.3 Controls on Stable Isotopes

Isotopic compositions of modern rainfall are enriched during the summer months (Figure 7.7) and high summer temperatures suggest a strongly negative precipitation/evaporation ratio that precludes extensive summer recharge. Cave water $\delta^{18}O$ compositions are more closely representative of isotopically negative, winter rainfall indicating the strong winter derivation-bias to cave waters.

Long-term trends imply that changes in $\delta^{18}O$ and $\delta^{13}C$ are subject to different controls. Similarly to nearby lake records at Zeribar and Mirabad the $\delta^{18}O$ record in KT-3 could be recording changes in seasonality during the Holocene. Initially low $\delta^{18}O$ in calcite from both lakes has been interpreted to indicate an increase in winter rainfall since the Younger Dryas (Stevens et al., 2001,2006). However following this, in both lake records increasing $\delta^{18}O$ is accompanied by increases in less drought resistant species of pollen (Stevens et al., 2001, 2006) indicating a change in seasonality

to spring-dominated precipitation, thus delivering more moisture at a more favourable time in the growing season. At Lake Zeribar an increase in $\delta^{18}O$ since ~7000 yr BP is combined with the expansion in oak (Stevens et al., 2001). At Lake Mirabad the switch is possibly indicated by the gradual increase in oak pollen at the expense of pistachio since 7700 yr BP, although an increase in $\delta^{18}O$ is not observed until at 5800 yr BP (Stevens et al., 2006). The increase in $\delta^{18}O$ values at Katalekhor ~7000 yr BP is similarly timed to the pollen indicators of a switch in seasonality of rainfall and therefore could also represent increased isotopically heavier spring precipitation over lighter winter precipitation. However, a return to a winter dominated Mediterranean type precipitation regime is observed at Lake Zeribar by 6000 yr BP whereas KT-3 $\delta^{18}O$ continues to increase until ~2000 yr BP and plateaus. There is then no indication of the change in seasonality to modern winter dominated precipitation and thus is unlikely to be the control on $\delta^{18}O$ in KT-3.

Figure 7.18 shows that $\delta^{18}O$ follows a similar trend to the decrease in summer solar insolation during the Holocene. Due to the length of the timescales of Milankovitch cycles, solar insolation is controlled by precession during the Holocene. Sinc~11,000 yr BP the direction of the earth axis has directed the Northern Hemisphere of the Earth away from the sun. This creates lower insolation in the Northern Hemispheric summer and higher insolation in winter decreasing the seasonal contrast (Imbrie et al., 1992). In the Mediterranean, when summer insolation is high, summers are hotter and drier and winters cooler and wetter (Fletcher and Sánchez Goñi 2008). Therefore the gradual increase in $\delta^{18}O$ since ~7000 yr BP reflects the gradual reduction in the amount of winter precipitation due to the reduction in summer solar insolation. In Iran this may be caused by increased intensity of the Siberian High due to enhanced continental warming during the winter. The Siberian High being strongest during winters when summer solar insolation is at a minimum (Miller et al., 2005). Solar insolation controlling $\delta^{18}O$ trends during the Pleistocene has also been observed in a recently published stalagmite from Qal'e Kord cave (Mehterian et al., 2017) in NW Iran 125 km from Katalekhor.
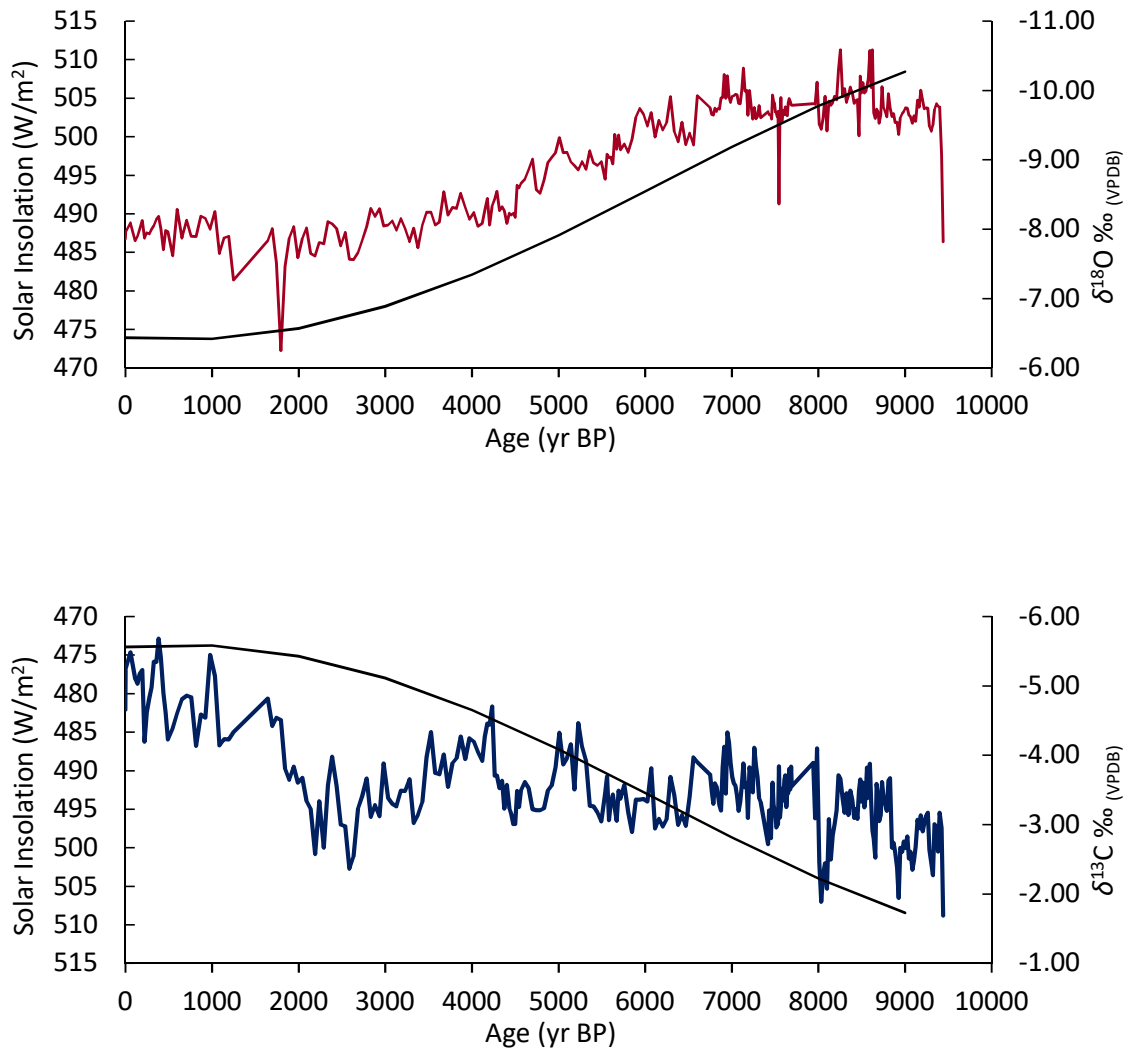
Figure 7.18: KT-3 Holocene $\delta^{18}O$ (top, red) and $\delta^{13}C$ (bottom, blue) profiles compared to solar insolation values during mid-June at 30 °N (Berger and Loutre 1991).

$\delta^{13}C$ shows a trend toward decreasing $\delta^{13}C$ over the same time period when $\delta^{18}O$ is indicating progressive reduction in winter precipitation. $\delta^{13}C$ values in KT-3 are much more enriched relative to other Middle Eastern caves (e.g. Soreq, Jeita) whose values are attributed to variation in soil CO_2 (Verheyden et al., 2008; Bar-Matthews and Ayalon 2011). At the modern cave site bedrock dominates a landscape which is almost devoid of vegetation (Figure 7.1), all of which suggests $\delta^{13}C$ should mainly be recording a bedrock dissolution signal. $\delta^{13}C$ would be expected to get heavier with aridity owing to increased residence times (Bar-Matthews et al., 2003) but long term $\delta^{13}C$ in KT-3 changes very little (arguably slightly depleted) until 2200 yr BP when a significant 1.5 ‰ decrease in isotopic values begins. This suggests that residence time between 9500 yr BP and 2200 yr BP did not change very much. During periods when soil and vegetation degradation was

high in Villars Cave, France, δ^{13}C showed relatively higher values related to a higher atmospheric CO_2 contribution to carbon values (Genty et al., 2003). The lack of soil above Katalekhor Cave suggests equilibration with soil CO_2 is unlikely and therefore drip waters may retain partial signals of atmospheric CO_2 (McDermott 2004). As the composition of modern atmospheric CO_2 is -7.8 ‰ (Keeling et al., 1989), lighter than the δ^{13}C of limestone bedrock (~1 ‰ (McDermott 2004)) shorter scale negative fluctuations in δ^{13}C might then indicate periods of greater atmospheric CO_2 via a smaller bedrock dissolution contribution.

This transition to more negative δ^{13}C coincides broadly with the slowing down of solar insolation reduction to its lowest value (Figure 7.18) which results in cooler temperatures. The reduction of solar insolation could reduce winter temperatures decreasing effective evaporation without an increase in precipitation. This increase in effective moisture would reduce karst water residence time, accounting for the more depleted δ^{13}C signal.

A further speculative suggestion for the decrease in carbon isotopic values after 2200 yr BP is the development of agriculture (visible a few hundred metres north of the cave in Figure 7.1). The effect of the development of agriculture nearby on seepage waters would be to increase the amount of the carbon signal derived from lighter soil CO_2.

7.3.4 Controls on Trace Elements

Overall trends in Mg/Ca and Sr/Ca are weakly statistically correlated to δ^{18}O (R^2= 0.26 and 0.40 respectively) the ratios decreasing with time as δ^{18}O increases. It might be expected that Mg/Ca and Sr/Ca ratios would increase with δ^{18}O if increasing residence time or PCP with increasing aridity were controlling the trace element concentrations (Fairchild et al., 2000). Mg/Ca and Sr/Ca also have weak statistical relationships (R^2= 0.17 and 0.21 respectively) with δ^{13}C showing very little variation but an overall decline in values over the course of speleothem growth. The highest ratios of both trace elements correspond to the heaviest δ^{13}C at the start of the record and the lowest ratios roughly correspond with the largest long term decrease in δ^{13}C value towards the end of the record. Both δ^{13}C, Mg/Ca and Sr/Ca suggest that residence time and PCP in the epikarst does not vary much over time in contrast to δ^{18}O which increases through the Holocene. The decline in carbon isotopes after 2200 yr BP is not reflected in Mg/Ca and Sr/Ca ratios suggesting that the controlling mechanism on δ^{13}C during this period is not changing PCP or residence time of drip water in the karst. Therefore it is not likely to be representing increasing effective moisture due to reducing winter temperatures.

Ba does not show positive covariance with Mg but is partially correlated to Sr implying it is not sourced from the bedrock (McDonald et al., 2007). Statistical relationships between Ba and both $\delta^{18}O$ and $\delta^{13}C$ are low (R^2= 0.15 and 0.0045 respectively). No correlation is observed between Ba and $\delta^{13}C$ although Figure 7.17 shows negative co-variance occurs from at least from ~7000 yr BP. Ba shows a weak negative correlation with $\delta^{18}O$ suggesting that sometimes higher concentrations of Ba occur when $\delta^{18}O$ has more negative periods. Figure 7.16 shows that Ba does not vary similarly to overall trends in $\delta^{18}O$. When Ba is not associated with calcite dissolution it can be related to soil colloids (Borsato et al., 2007; Rutlidge et al., 2014) or dust input (Ayalon et al., 1999). This could demonstrate two periods of increased dust or soil detritus occurred from 9400-7050 yr BP and 2300 yr BP to present.

7.3.5 Holocene palaeoclimate recorded in KT-3

Most Holocene climate records in Iran are from lacustrine records (e.g. van Zeist and Wright Jr, 1963; Bottema, 1986; Griffiths et al., 2001; Stevens et al., 2001, 2006; Jones et al., 2015; Hamzeh et al., 2016; Snyder et al., 2016; Talebi et al., 2016)), which suffer from low resolution and difficulties in dating. To date only one other speleothem record is available from Iran from Qal'e Kord Cave which grew mostly within the Pleistocene (Mehterian et al., 2017).

Orbital forcing is the strongest control on local climate at Katalekhor. The overall trend in $\delta^{18}O$ in Katalekhor indicates a wet early Holocene vs drier mid-late Holocene, with precipitation amount reducing over the record since ~7000 yr BP but plateauing at 2700 yr BP. This is also recorded in the reducing stalagmite diameter and reducing $^{234}U/^{238}U$ values throughout growth. The quick translation time of water through the epikarst due to thin soil cover infers that despite increasing aridity residence time is low, this is corroborated by trace elements.
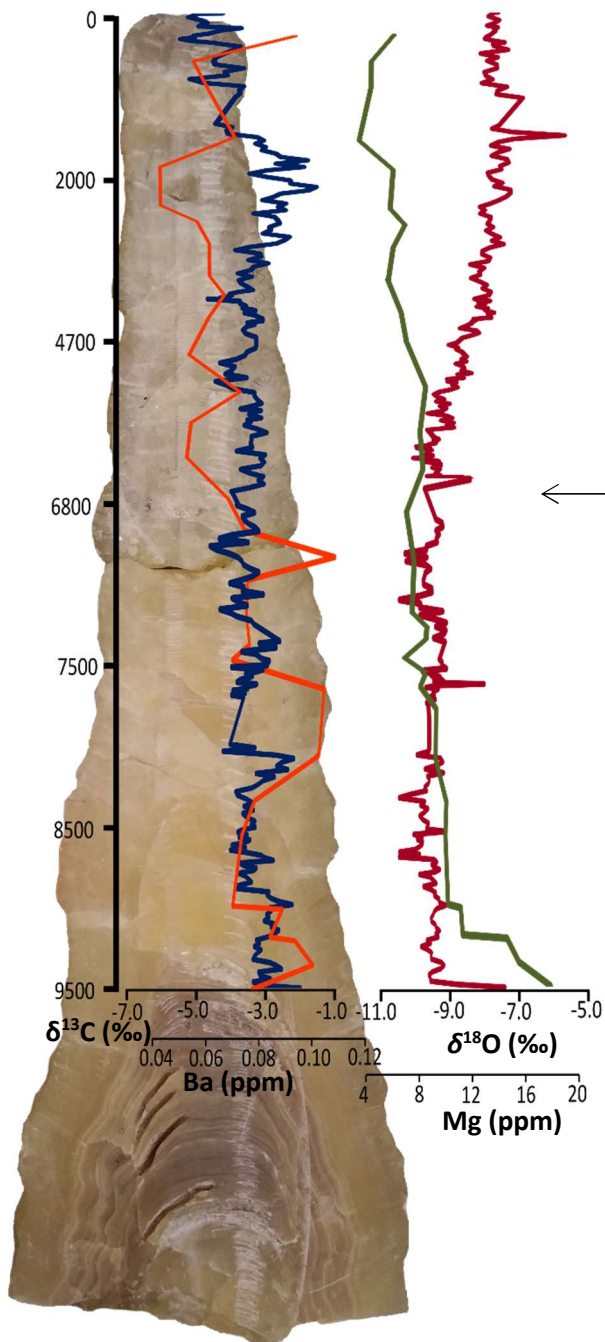
6700 yr BP change in columnar fabric from short and proper forms to elongate columnar calcite. Indicates a continuing constant but slower drip rate than previously.

Figure 7.19: Summary of the isotopic, trace element and main petrographic features of KT-3. Stable isotopes are listed in red (δ^{18}O) and blue (δ^{13}C) on the same axis. Ba/Ca is in orange and directly compared to δ^{13}C with an axis from 0.04 to 0.12. Mg/Ca is in green directly compared to δ^{18}O with an axis 4-20.

δ^{18}O values are enriched by ~2 ‰ at the base of the record compared to the following record, which might indicate that Holocene growth of KT-3 restarted just before a precession-driven

increase in precipitation. A short resumption in growth is also seen in Qal'e Kord Cave NW Iran ~8000 yr BP, another, older stalagmite showing a precession dominated $\delta^{18}O$ record (Meheterian et al., 2017). Initially high Sr/Ca, Mg/Ca and Ba/Ca may similarly indicate flushing of karst water which had had a longer residence time relative to the rest of the record (Figure 7.16, 7.17). $\delta^{13}C$ does not indicate that soils were better developed at this time, thus Ba/Ca might be recoding a higher dust input at this time facilitated by the initially dry conditions and then washed into the cave during subsequent increase in infiltration. $\delta^{18}O$ broadly declines until 8250 yr BP (Figure 7.12) suggesting increasing precipitation until this time. From 7100 yr BP until 2700 yr BP $\delta^{18}O$ displays a significant (1.7 ‰) long term increase in isotopes suggesting a reduction in precipitation, controlled by the reduction in solar insolation (Section 7.3.3) (Figure 7.18).

Throughout the growth of KT-3 the diameter of the stalagmite steadily decreases from 90 to 33 mm. It is known that increases in the interval between drips leads to a thinner diameter stalagmite (Kaufmann 2003). Thus, as precipitation amount decreases indicated by the increasing enrichment in $\delta^{18}O$ the diameter of the stalagmite reduces (Figure 7.20). The initial growth of KT-3 shows the widest diameter of the Holocene portion in agreement with $\delta^{18}O$ that the earliest years were the wettest. The diameter begins to thin around 7600 yr BP more or less at the time of increase in $\delta^{18}O$. $^{234}U/^{238}U$ has also been suggested as a climatic indicator, where periods of aridity are related to higher $^{234}U/^{238}U$ ratios (Kaufman et al., 1998). In KT-3 initial $^{234}U/^{238}U$ ratios begin low and increase steadily through time (Table 7.4) following the same aridity trend indicated in $\delta^{18}O$ (Figure 7.21). The increase in ^{232}Th content since 4400 yr BP (Figure 7.22) and increase in Ba/Ca from 2300 yr BP (Figure 7.23) could both record an increase in windblown dust from increasing aridity.
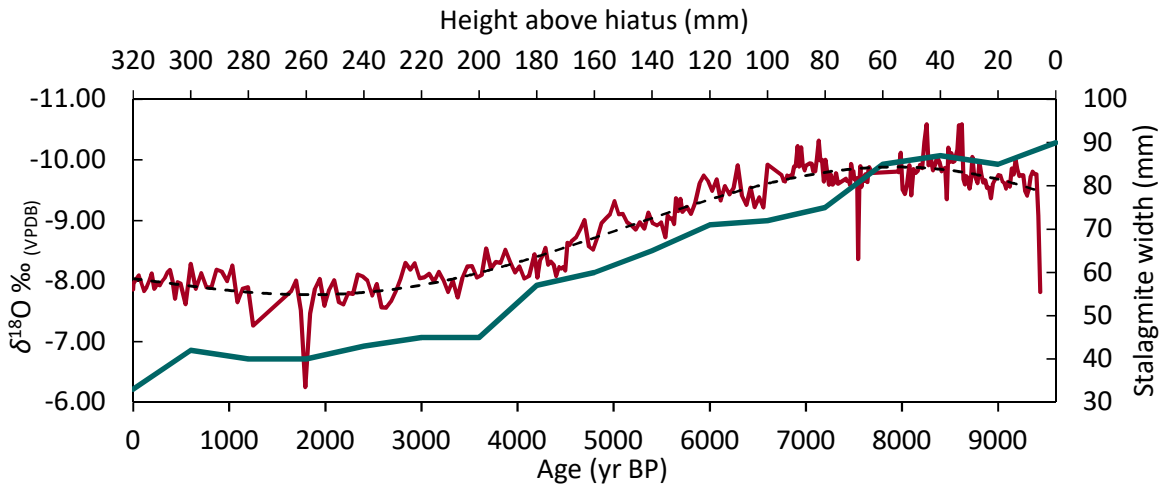
Figure 7.20: Stalagmite diameter (blue) measured at 20 mm intervals compared to the reduction in δ¹⁸O over the course of the Holocene. The widest diameter occurs in good agreement with the most negative δ¹⁸O at Katalekhor and the onset of the reduction in diameter has a similar timing to the increase in δ¹⁸O values ~7200 yr BP.
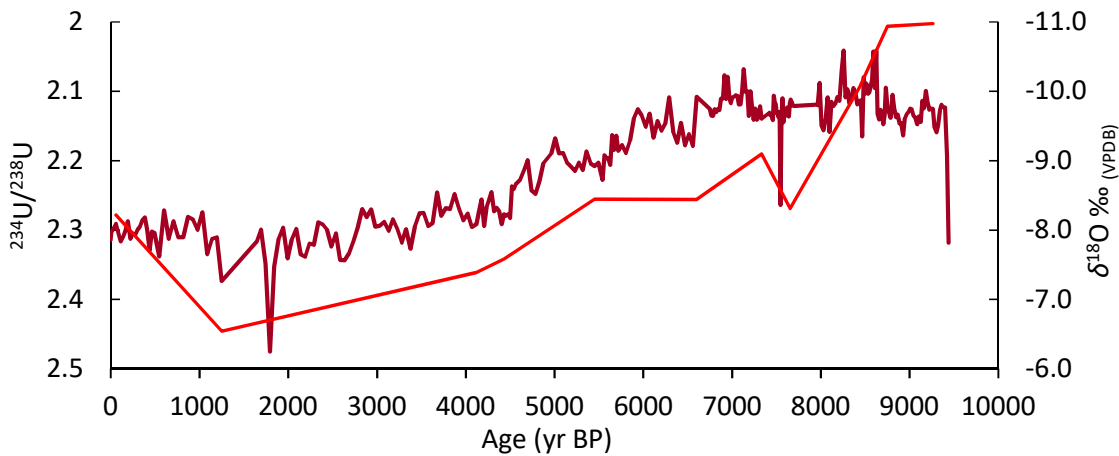
Figure 7.21: The relationship between $^{234}U/^{238}U$ (light red) and δ¹⁸O (dark red). $^{234}U/^{238}U$ increases over the growth of KT-3 as δ¹⁸O values do as well. δ¹⁸O indicates a reduction in precipitation from ~7200 yr BP onwards while higher $^{234}U/^{238}U$ ratios have been used as an aridity indicator (Kaufmann et al. 1998).

Over this time period δ¹³C, Mg/Ca and Sr/Ca suggest that despite a reduction in rainfall, residence time in the epikarst does not vary much between 8900 to 2200 yr BP (Figure 7.17, Figure 7.19). Despite the decrease in precipitation, interactions in the karst apparently did not change much:

the lack of soil suggests a short transit time into the karst, and the path of water feeding the drip may also be short, such that sourcing of trace elements was limited. This is further supported by a 1.5 ‰ decrease in δ^{13}C which is not reflected by change in Mg/Ca or Sr/Ca. Therefore, the mechanism responsible for the δ^{13}C depletion is not linked to residence time, which removes the possibility that this period experienced reduced winter temperatures as a result of reducing solar insolation and an increase in effective moisture (Section 7.3.5).

It is, however, possible that depletion in δ^{13}C since 2200 yr BP was related to the development of agriculture in the immediate region. Ba/Ca is a good indicator of soil derived inorganic detritus (McDonald et al., 2007, Rutlidge et al., 2014) and its increase at the same time as the decrease in δ^{13}C could feasibly show an increase in soil carbon from agricultural practice. Additionally between 1000 and 500 yr BP the diameter of KT-3 increased by about 2 mm Figure 7.3, Figure 7.19) which might indicate an increase in vegetation that produced more soil-CO_2 leading to increased acidity of infiltration water and increased bedrock dissolution. This would increase the supply of $CaCO_3$ available to precipitate in the cave.
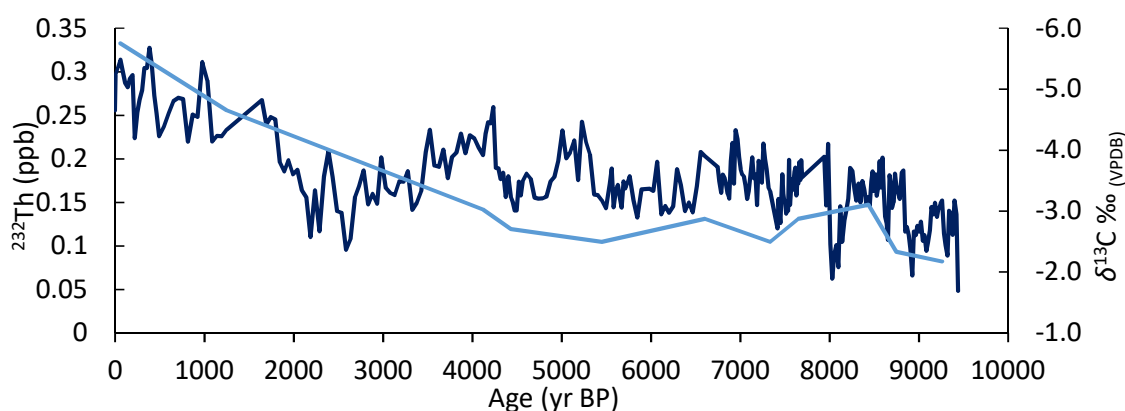
Figure 7.22: The relationship between ^{232}Th (light blue) and δ^{13}C (dark blue). ^{232}Th represents a proxy for inorganic detritus. ^{232}Th levels show an increase from 4400 yr BP to present day indicating an increase in detritus. Lighter δ^{13}C does not begin until 2200 yr BP suggesting the two are not linked by an increase in moisture (reduction in residence time). ^{232}Th could indicate aridity by representing an increased input of windblown dust.
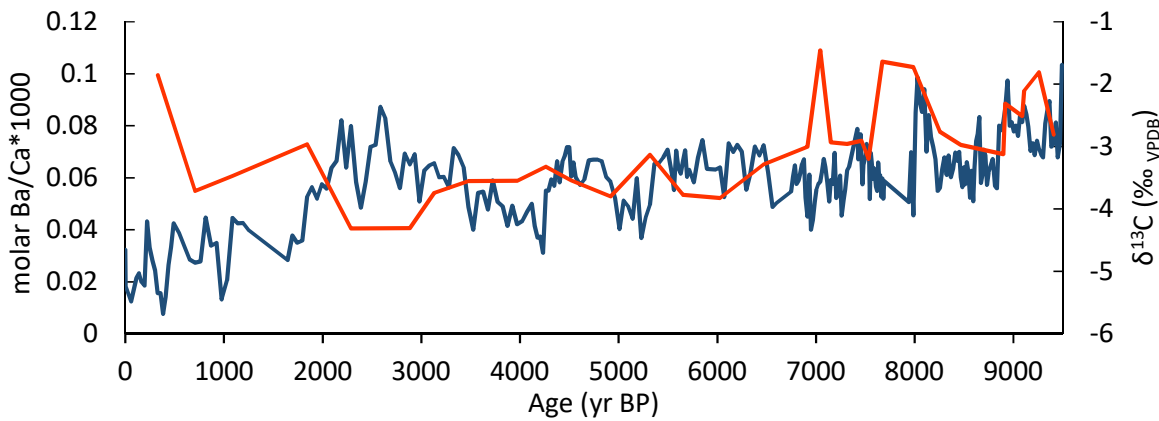
Figure 7.23: Ba/Ca (orange) and δ¹³C (blue) changes over the growth of KT-3. Initially higher Ba/Ca values correspond to higher precipitation amounts as indicated in δ¹⁸O bringing increased detritus and dust into the cave. After 6800 yr BP fluctuations in Ba/Ca can be related to δ¹³C as higher ratios of Ba/Ca occur at a similar time to intervals of reduced δ¹³C. Periods of lower bedrock dissolution (thus comparatively quicker translation through the karst) can be related to increases in detrital or dust content suggesting this is caused by an increase in moisture.

Shorter term fluctuations in $\delta^{13}C$ appear completely unrelated to $\delta^{18}O$. The most prominent of these occurs between 8260 yr BP and 7900 yr BP (Section 7.3.5.1). Despite a lack of statistical correlation ($R^2 = 0.0045$) Figure 7.22 shows that following the reduction of Ba/Ca related to the reduction in rainfall ~7000 yr BP, fluctuations in Ba/Ca correspond to changes in $\delta^{13}C$. Typically higher Ba/Ca ratios correspond to reduced $\delta^{13}C$ periods and vice versa. As discussed above, because of the dominance of the bedrock dissolution signal in KT-3 $\delta^{13}C$, shifts to more negative $\delta^{13}C$ may indicate intervals of greater atmospheric CO_2 influence during periods of lower bedrock dissolution. The shifts towards higher Ba/Ca values corroborate this, as they indicates higher inputs of soil minerals or dust (Ayalon et al., 1999) and thus more rapid translation through the epikarst related to increased moisture. The lack of corresponding fluctuations in $\delta^{18}O$ might indicate a seasonal aspect to these events. Storms that occur in summer have heavier $\delta^{18}O$ than winter rainfall due to the effect of temperature dependent fractionation (see Section 7.3) and this wouldn't show a negative $\delta^{18}O$ shift at the same time as $\delta^{13}C$.

It is therefore possible that $\delta^{13}C$ is a much more sensitive indicator to shorter term precipitation/moisture increases than $\delta^{18}O$. Events linked to a slightly wetter climate may be recorded in $\delta^{13}C$ and Ba/Ca at 5300-5000 yr BP and a longer event at 4200-2590 yr BP.

Furthermore, a decrease in growth rate at 6600 yr BP (Figure 7.12) and also a change in calcite fabric from columnar proper to elongate columnar at ~6700 yr BP (Section 7.2.1.2), related to a shift to slower but constant drip rates, could suggest a more significant reduction in precipitation at this time than indicated by the $\delta^{18}O$ signal.

The change between wetter conditions in the early Holocene and drier conditions in the mid and late Holocene is typical of many transitional Eastern Mediterranean/Middle Eastern records e.g. (Bar-Matthews et al., 1997; Frumkin et al., 1999; Arz et al., 2003; Eastwood et al., 2007; Verheyden et al., 2008) and also some Iranian records (Walker & Fattahi 2011; Jones et al., 2014; Sharifi et al., 2015). $\delta^{18}O$ indicates that wetter conditions began at Katalekhor around 9500 yr BP, and it seems likely that renewal of growth in KT-3 was coincident with a significant increase in rainfall. Wetter conditions in the early Holocene also caused the onset of S1, but this occurred earlier, ~9800 yr BP, in the Aegean and Ionian (Gogou et al., 2007; Kotthoff et al., 2008b; Geraga et al., 2008) than the onset of growth of KT-3. However, the increase in moisture at Katalekhor shows a similar timeframe for the increase observed in geographically closer records in Iranian lakes Mirabad (Stevens et al., 2006) and Neor (Sharifi et al., 2015) (Figure 7.23). Additionally a sharp decrease in $\delta^{13}C$ of Israeli speleothems (more soil productivity) (Bar-Matthews et al., 2003) occurs at the same time as the onset of KT-3 growth. More negative $\delta^{18}O$ in planktonic foraminifera indicate maximum moisture also occurs later the Levantine Sea (Emeis et al., 2000) and at Lake Van (Wick et al., 2003). Importantly the delay in increasing moisture in these regionally close records all correspond to the onset of S1 formation in the Levantine Sea at 9500 yr BP (Almogi-Labin et al., 2009) (Figure 7.24). This could be evidence for a localised increase in precipitation and freshwater input in addition to freshwater from the Nile (Rossignol-Strick, 1985) causing a delay in onset of 300 years compared to sapropel formation further west in the Eastern Mediterranean.

The transition to drier conditions indicated by $\delta^{18}O$ at 7200 yr BP, the reducing stalagmite diameter and to a certain extent reduction in growth rate and the fabric change at ~6700 yr BP are likely related to the end of the Holocene Climate Optimum (Figure 7.24). Timing is consistent with a number of Levantine and Eastern Mediterranean records of the Early Holocene (9500-7000 yr BP) (Robinson et al., 2006). Specifically, the proxies described above in KT-3 define a time comparable to in particular, Soreq Cave (7400 yr BP) (Bar-Matthews et al., 2003) and accounting for the fabric change to Jeita Cave, which sees an increase in $\delta^{18}O$ from 6500 yr BP (Verheyden et al., 2008) (Figure 7.24). The termination of a period of reduced salinity in the Northern Red Sea is also in good agreement at 7250 yr BP (Arz et al., 2003).

A further significant reduction in rainfall is recorded in Oman (Fleitmann et al., 2003), Lake Van Turkey (Wick et al., 2003) and Soreq Cave (Bar-Matthews and Ayalon 2011) at ~4000 yr BP but earlier in Lebanon at 5800 yr BP (Verheyden et al., 2008). This significant reduction is not recorded in the Katalekhor δ¹⁸O data, but a marked reduction in growth diameter is observed at ~4000 yr BP. $\delta^{13}C$ and corresponding Ba/Ca fluctuations may however, indicate wetter conditions at Katalekhor between 5300-5000 yr BP and 4200-2590 yr BP. These are apparently regional events, as contemporaneous records suggest that most of this period was relatively dry. In Soreq short dry events occur within these parameters at 5250-5170 yr BP and 4200-4050 yr BP (Bar-Matthews and Ayalon 2011) and evidence of dry climate from the Gulf of Persia corresponds to the collapse of the Akkadian Empire ~4.1 ka (Cullen et al., 2000).

Iranian pollen records from Lake Zeribar and Lake Mirabad indicate that climate on the western side of the Zagros Mountains differs to that on the east as recorded at Katalekhor. In these lake records the early Holocene was not particularly wet and in fact the Mid Holocene is considered the wettest period of the Holocene (Stevens et al., 2001, 2006). The pollen records show an increase in oak ~5500 yr BP at Lake Mirabad (Stevens et al., 2006) and ~6000 yr BP at Zeribar (Griffiths et al., 2001). Moreover, a study within the Zagros Mountains ~215 km east of Katalekhor shows a dominance of drought resistant pistachio until ~7200 yr BP and an increase in oak in the Mid Holocene (Schmidt et al., 2011), the opposite of events recorded at Katalekhor. A recent speleothem stable isotope record from the western side of the Zagros in Iran, ~350 km west of Katalekhor does not extend as far back in time as KT-3, but modern δ¹⁸O is about −4.75 ‰ (Flohr et al., 2017) significantly heavier than KT-3 (−8.37 ‰), which could indicate a continental orographic rainout effect due to the Zagros Mountains.

Figure 7.24 next page: KT-3 stable isotope profiles compared to regional observations. Numerous records show an increase in moisture at a similar time as the onset of Holocene growth in KT-3. This includes a large negative $\delta^{13}C$ excursion in Soreq Cave (Bar-Matthews et al., 2003) (green line) and a moisture increase in Lake Neor (Sharifi et al., 2015) (teal dataset). The onset of S1 deposition in the Levantine Sea began at 9.5 ka (green bar). A possible signal of the 8.2 kyr event is seen in $\delta^{13}C$ (yellow bar) but this is not a comparable length to that observed in Soreq $\delta^{13}C$. The end of the Holocene Climate Optimum at Katalekhor occurred at 7200 yr BP (first yellow bar, width delineated by the average age error of 40 years), which is very well timed to the end at Soreq cave at 7400 yr BP. Deposition of S1 is highlighted by the green bar ending around 7000 yr BP (Rohling et al., 1997; Emeis et al., 2000; Geraga et al., 2008).

287
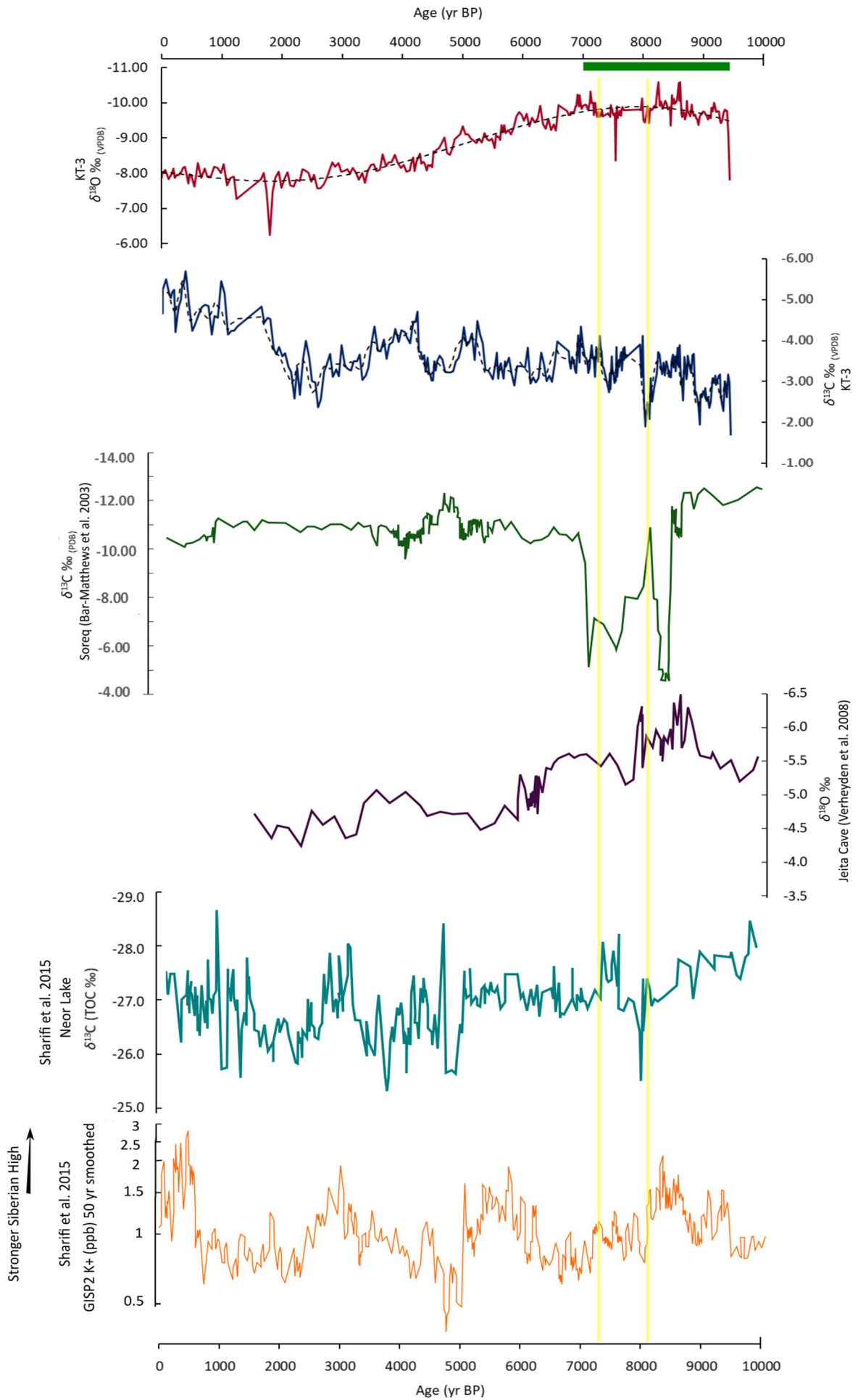
7.3.5.1 The 8.2 kyr Event?

In KT-3 there is no apparent 8.2 kyr event recorded in $\delta^{18}O$. However, between 8260 yr BP and 7900 yr BP (peaking at 8030 yr BP) a 1.77 ‰ increase in $\delta^{13}C$ is observed (Figure 7.24). The magnitude of this $\delta^{13}C$ excursion is only matched once before at the beginning of the record, suggesting it is a significant feature. Unfortunately the trace element data are not at high enough resolution to register the excursion. Identifying the parameters that control $\delta^{13}C$ is difficult. Traditionally the 8.2 kyr event is viewed as a dry cooling event (see Chapter 6 Section 6.3.3.4 for a summary). The enrichment in $\delta^{13}C$ at this time suggests an increase in the bedrock component and residence time in the epikarst. $\delta^{18}O$ does not indicate a reduction in winter precipitation as no positive excursion is seen at this time. Enrichment in $\delta^{13}C$ could, however, indicate colder conditions if a larger temperature differential between the cave and outside increased ventilation and therefore increased degassing.

The timing of the $\delta^{13}C$ excursion is very similar to the $\delta^{13}C$ event observed in Soreq Cave from 8200 yr BP - 8000 yr BP (Bar-Matthews et al., 1999) and to the $\delta^{18}O$ event in Oman between 8200 and 8100 yr BP (Fleitmann et al., 2003). It is not comparable to the event observed in Greek speleothem described in in Chapter 6, which indicated a longer period of aridity from 8450 to 8160 yr BP.
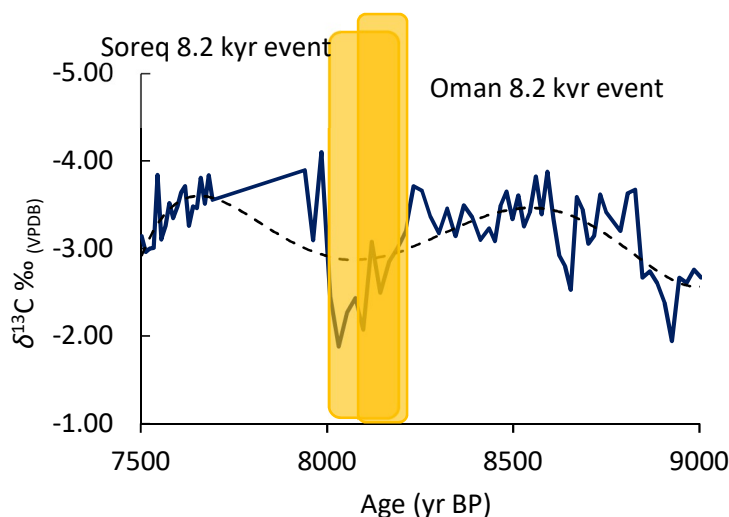
Figure 7.24: KT-3 $\delta^{13}C$ anomaly during the timeframe of the 8.2 kyr event compared to timings of the event in Soreq (also identified by $\delta^{13}C$) (Bar-Matthews et al., 1999) and Oman (Fleitmann et al., 2003).

Climate anomalies for the 8.2 kyr event in Near East proxies are not common and many are contentious. Indeed, it has been noted that before identification of an 8.2 kyr anomaly in stable isotopes, Middle East pollen records had not been interpreted to show climate change at this time and periods of human disturbance were not recognised in archaeological records around 8200 yr BP (van der Horn et al., 2015). In Soreq Cave, the most convincing signal for the 8.2 kyr event is a 200 year decrease in δ^{13}C to -11 ‰ and a simultaneous 1 ‰ increase in δ^{18}O (Bar-Matthews et al., 1999). But excursions of this size are not uncommon in the wider Soreq δ^{18}O record and Frumkin et al., (2000) later suggested that the δ^{13}C excursion might have been a localised soil denudation event. Furthermore the 8.2 kyr event has not yet been recorded in Lebanon (Verheyden et al., 2008) or Jerusalem (Frumkin et al., 2000). Thus, if the 8.2 kyr event exists in Israel it probably indicates colder, but not unusually dry conditions - not dissimilar to the Katalekhor record. A high input of dust compared to the rest of the early Holocene is seen around 8.0 ka in Lake Neor (Sharifi et al., 2015) suggesting a possible dry signal around the time of the 8.2 kyr event in Iran.

7.3.5.2 The KT-3 record and archaeological findings

The wider area of the fertile crescent in general is rich in archaeology with a long history including a number of culturally significant civilisations such as the Mesopotamians. The region is also believed to be the locations where agriculture was first developed including the first evidence of crop domestication in the southern Levant (Bar-Yosef and Meadow 1995) around 11,000 yr BP and the origins of farmed animals initially with goats and sheep ~10,000 yr BP (Zeder 2008). The initiation of these practices occurs before the restart of growth of KT-3 but could be linked to an improving climate following the end of the Younger Dryas. This phase is indicated by the comparatively negative δ^{18}O record immediately following growth initiation. Prior to this as evidenced in the Levant, human settlers appeared to respond to changes in climate via adapting foraging habits (Rosen et al., 2012).

The following humid period which ended ~7200 yr BP according to the Katalakhor record is contemporaneous with further development of agriculture in Mesopotamia but also with frequent resettling of coastal regions due to changes in sea level (Hole 1994). This may have prevented the development of large urban centres in southern Mesopotamia (Hole 1994) but allowed the development of small towns and villages based around fishing (Clarke et al., 2015). It is likely that the relatively stable and unchanging climate of this period is favourable to the

progression of society as there is a lack of environmental challenges and upheaval (Brooks 2006). In the Levant during this period societies became more static and developed intensive food production systems (Rosen et al., 2012).

Throughout the period 4550-2800 yr BP prolonged droughts and associated periods of famine are widespread throughout Iran, Mesopotamia and the fringes of the Eastern Mediterranean (Sharifi et al., 2015). The period broadly coincides with the gradual 2 ‰ increase in oxygen isotopes ending at a similar time to the plateau in the KT-3 record. These droughts had a profound impact on the Assyrian Dynasty. Generally however, throughout the Early Bronze Age to Iron Age many communities appear to be coping with the gradual environmental change by cultivating more drought resistant crops and moving from flax to woollen clothing (Riehl 2009). The KT-3 stalagmite does not suggest any significant changes in climate around the 4.2 kyr event, which is said to have contributed to the decline and subsequent loss of the Akkadian Empire (Weiss 1993, Cullen et al., 2000). Furthermore, the KT-3 record does not indicate a climatically induced famine as hypothesised in Syria and Cyprus (e.g. Kaniewski et al., 2013) to be one of the root causes of social and economic decline associated with the Late Bronze Age Collapse ~3200 yr BP.

Chapter 8: Conclusions

The overarching aim of this research was to investigate multi-proxy Holocene palaeoclimate records from in a transect from the western fringes of the Eastern Mediterranean to the western Middle East, a region where such records are sparse. Throughout this area the large-scale controls on atmospheric circulation, and its influences on climate, are broadly similar, making it possible to analyse continuity of proxy response where records overlap temporally. The research described in this thesis contributes the first Holocene speleothem palaeoclimate records from the eastern forelands of the Zagros Mountains (KT-3) and the first mid-late Holocene record from south west Turkey (HY-8). KTR-2 provides the first early Holocene speleothem record of palaeoclimate in the Peloponnese.

While conducting this research it became clear that detailed petrography (outlined in Chapter 4 but also integral in other chapters) was of critical importance both as an environmental indicator, but also to help achieve a robust and coherent chronology.

8.1   General Remarks

- All three speleothem records confirm established atmospheric circulation and rainfall patterns.
- Variation in $\delta^{18}O$ in all three records is controlled by winter precipitation amount, an interpretation that is now well-established in many Eastern Mediterranean records.
- Early Holocene records in KT-3 and KTR-2 indicate that the early Holocene was wetter than the present day.
- According to the data presented here, following a wetter early Holocene, precipitation amount has not varied much on longer timescales. In KT-3 an enrichment of 1 ‰ in $\delta^{18}O$ is observed from ~7000 yr BP to ~2000 yr BP indicating a progressive drying trend, after which there is little change in amount of precipitation. The HY-8 record (~5600 yr BP to present) oscillates round a steady mean value, suggesting that there is no trend towards increasing or decreasing precipitation amount.
- Neither KT-3 nor HY-8, both of which were active when collected, indicate a prominent drying trend in more modern values despite pronounced regional droughts being observed in the last 900 years (Cook et al., 2016).

- The 8.2 kyr event is recorded in KT-3 and KTR-2 and the 4.2 kyr event in HY-8. Despite the prominence of these events recorded elsewhere in other climate proxies they are not the largest climatic events in any record within this study.

8.2   Specific Remarks

8.2.1   Chapter 4

Dim-1 and HY-8, have micro-dissolution as a common feature occurring very soon after deposition. The petrographic approach employed is novel in that it relates micro-dissolution to inconsistencies in the results of U-series data. Both stalagmites grew in regimes where growth was discontinuous, at times affected by aggressive, or at least, $CaCO_3$ under saturated dripwaters, creating horizons of micro-dissolution forming over short timescales, possibly in one season. Interpretations from both HY-8 and Dim-1 suggest that episodes of dissolution more minor than previously considered are likely able to effect U and Th concentrations, albeit without a consistent predictable effect on U-series dates. This finding, combined with different individual growth mechanisms of each stalagmite, causes disruption in the U-series isotope chain leading to stratigraphically insecure calculated ages unique to each stalagmite. This result highlights the need for detailed petrographic investigation prior to geochemical analyses to build a framework for understanding the growth history of stalagmites. This approach could lead to the re-evaluation of other speleothems with uncertain age models and may help establish new chronologies by highlighting dating inconsistencies from stalagmites that grew discontinuously and thus are difficult to date accurately.

HY-8 specifically presents a possible link between the inclusion of soil-associated organic detritus during micro-dissolution events and potential nuclide mobility. The largest deviations from assumed (correct) ages in HY-8 occur in samples with the largest organic component. A number of these samples indicate Th addition. Th could be more soluble in groundwater than the evidence has so far suggested, particularly in groundwaters with high levels of organics or in more alkaline groundwaters. This may increase the chances of a larger dissolved ^{230}Th source unrelated to non-organic detrital ^{232}Th, thus rendering the bulk earth correction for detrital Th inadequate. Addition of ^{230}Th in sub-ppb amounts may be enough to alter a U-series date in Holocene aged stalagmites. Such amounts could feasibly be present in many speleothem systems with little chance of detection

Most of the micro-dissolution events in Dim-1 involved the dissolution of an aragonite layer during an increase in drip water amount after a period of aridity. Samples which are mostly aragonitic show reduced nuclide concentrations, implying removal during the dissolution event. Other, post-aragonite (predominantly calcite) samples, located within these regions, appear to incorporate nuclides (for example high U content) from the previous aragonite growth unevenly.

Samples in both stalagmites show evidence for the removal of U in locations which are not considered major dissolution events. This requires U location outside the $CaCO_3$ lattice, where it is easier to leach. In HY-8 there is strong evidence that an organic source of U could be larger than anticipated. The incorporation of U in Dim-1 from a previous phase of growth into currently precipitating calcite suggests U could be commonly incorporated into samples via pore spaces or adsorbing to the surface of $CaCO_3$ crystals. HY-8 is particularly instructive as it demonstrates that removal of U can occur on a timescale short enough (potentially a few days) to be a regular growth feature. Small, but repeated successive removal may be sufficient, over the distance of a sample trench, to alter dates. Furthermore any [230]Th formed by radioactive decay of this organically sourced U would also be more easily leached from samples.

8.2.2 The early Holocene in the Peloponnese, Greece

The early Holocene growth of KTR-2 is largely coincident with the deposition of sapropel S1, occurring during more humid conditions. Cessation of growth at 6700 yr BP also occurs at a similar time to the end of sapropel deposition. The KTR-2 stable isotope records indicate that aridity began around 7200 yr BP broadly coincident with the timing of the end of the Holocene Climate Optimum in other records. The 1 ‰ increase in $\delta^{18}O$ values immediately prior to cessation of growth suggests that reduced precipitation may have been the cause.

Despite the timing of the restart of growth in KTR-2, there is apparently no record of the Younger Dryas in the stable isotope record. A large increase in vegetation above the cave is implied from the $\delta^{13}C$ record and an increase in infiltration is marked by a detrital rich surface at 10,520 yr BP. These events could be linked to climate recovery following the Younger Dryas as regionally close marine cores suggest that cooler conditions persisted for longer in the Northern Aegean (Gogou et al., 2007) and Adriatic (Rohling et al., 1997).

The KTR-2 stalagmite record suggests that the 8.2 kyr event was not strongly marked in the Peloponnese. The high resolution stable isotope micromilling and trace element transect highlight a period of aridity between 8641-7888 yr BP, but $\delta^{18}O$ suggests longer term aridity probably

began ~9000 yr BP. Aridity was not sustained as a short negative $\delta^{18}O$ excursion took place between 8600-8450 yr BP. Enrichment in $\delta^{18}O$ is not significant during the 8.2 kyr event when compared to the rest of the KTR-2 record. In fact $\delta^{18}O$ was more enriched from 7900 yr BP to the end of growth at 6700 yr BP. Mg/Ca and Sr/Ca ratios do suggest an increase in epikarst residence time from 8430-8160 yr BP.

As with the KT-3 record from Iran (see below), the 8.2 kyr signal is more prominent in $\delta^{13}C$ as values are the second most enriched values of the KTR-2 record. Potentially, seasonal precipitation patterns during the 8.2 kyr event shifted to more summer-dominated convective rainfall as observed in other Greek records; overall annual rainfall amount also decreased. Years when winters were warmer and more precipitation fell during the growing season would better sustain vegetation, leading to larger more negative fluctuations in the $\delta^{13}C$ record superimposed on a period of aridity and increased prior calcite precipitation (PCP).

Heavier $\delta^{13}C$ during the early Holocene relative to modern values implies that currently vegetation above Limnon Cave is better developed than during the early Holocene, despite higher winter precipitation amounts during the growth of KTR-2 than at present. This could be a rudimentary representation of temperature. Insolation (and therefore summer temperatures) were higher during the early Holocene than at present and are likely to decrease the P/E ratio causing heavier $\delta^{13}C$ via increased PCP.

8.2.3 The mid-late Holocene in SW Turkey

In HY-8 there is a strong relationship between inferred drip rate and the petrographic fabric precipitated. The majority of the stalagmite is comprised of dendritic fabric which forms under low drip rates forcing high supersaturation with respect to $CaCO_3$. Some of the stalagmite is comprised of laminated open and compact dendritic fabrics showing small variations in drip rate were common. The precipitation of microcrystalline or equant euhedral calcite during grey layer deposition must be caused by a higher drip rate but this was not necessarily related to increased precipitation (see below). Faster growth periods between 4765-4665 yr BP and 3940-3810 yr BP are due to an increase in degassing, indicative of increases in aridity, which is required to drive supersaturation. These periods are also marked by enriched $\delta^{18}O$ values.

Distinct grey layers in HY-8, hypothesised to represent fire events by Mason (2009), do contain evidence of soot and charcoal. The presence of clay detritus and elevated concentrations of specific trace elements, combined with the formation of microcrystalline fabric, (requiring a

higher drip rate than the primary dendritic fabric), provides enough evidence to state that these fires occurred above the cave and not within it. There is no suggestion in the $\delta^{18}O$ record that extreme aridity events occurred prior to the deposition of grey layers, but two of the layers did initiate following small $\delta^{18}O$ excursions.

In HY-8 the $\delta^{18}O$ record indicates that on a timescale of a few thousand years, precipitation amount does not vary by much, but that century-scale variability is evident. The most significant of these are a pluvial period from 4890 yr BP to 4290 yr BP which can be regionally correlated to pluvial events at Soreq Cave, Israel and Lake Van, Turkey, the 4.2 kyr event and the Little Ice Age.

The structure of the 4.2 kyr event in Sirtlanini has some resemblance to other records displaying a clear two step aridity event, with an initial 1.5 ‰ positive excursion (4290- 4200 yr BP) followed by a second larger 2.5 ‰ excursion (3900-3850 yr BP). $\delta^{13}C$ during this period is relatively enriched compared to most of the previous record probably indicating both a reduction in soil productivity and increase in PCP.

8.2.4   The Holocene in the eastern forelands of the Zagros, Iran

After ~7000 yr BP multiple proxies in KT-3 indicate increasing aridity plateauing around 3000 yr BP. This includes a gradually decreasing stalagmite diameter, increasing $^{234}U/^{238}U$ ratios and $\delta^{18}O$ values. The trend in $\delta^{18}O$ has a very similar profile to the decline of solar insolation in northern hemisphere mid latitudes over the course of the Holocene, indicating that in the eastern forelands of the Zagros the clear decline in winter precipitation amounts is controlled by the reduction in solar insolation creating drier winters. This presents a clear problem for future water resources of the region as this trend will continue through the next 10,000 years or so until the next precessional cycle. Mg/Ca and Sr/Ca do not reflect the trend towards increasing aridity, thus water residence time in the karst probably has not changed much over the course of the Holocene. This particular cave has almost no vegetation and soil development above it at present, so water translation into the cave may always have been relatively quick compared to caves where a thick soil is present above the karst.

The lack of soil and vegetation above Katalekhor Cave indicates that $\delta^{13}C$ records a bedrock signal. The correspondence between periods of lighter $\delta^{13}C$ (reduced bedrock dissolution) and higher Ba/Ca (increased inorganic detritus) values could be a good indicator for short term moisture increases in the absence of short term fluctuations in $\delta^{18}O$. The $\delta^{13}C$ and Ba/Ca record hint at the

possibility of agriculture in the region since 2000 yr BP. During this period δ^{13}C values become markedly lighter at the same time as Ba/Ca values increase. As there is evidence of agriculture nearby at present this appears to be the only source of decreased bedrock input and increased inorganic detritus over a longer period of time without a significant shift in precipitation amount.

The 8.2 kyr event is observed in the δ^{13}C but not in the δ^{18}O record. This suggests an increase in the bedrock signal via an increased residence time in the epikarst and possibly colder conditions if a larger temperature differential existed between the cave and outside (increasing degassing).

8.3 Future Work

Within the scope of Chapter 4 it was not possible to identify specific mechanisms, or even in a number of samples, the nature of the changes in the U-series isotopes which lead to age discrepancies in HY-8 and Dim-1. Further research should be undertaken involving micro-sampling across both major hiatuses and micro-dissolution surfaces to gain a better understanding of nuclide mobility during dissolution events and how this relates to age discrepancies within U-series data.

A second stalagmite (HY-9) was also studied during this project but the data are not included in the thesis. The stalagmite displayed very similar characteristics to HY-8. It is primarily dendritic in petrographic fabric, laminated in areas and contains grey layers of microcrystalline fabric which contain petrographically visible organic detritus, and similar trace element geochemical signatures as described in HY-8. A 1 mm resolution stable isotope profile was generated for HY-9. However, due to time and resource constraints, only a skeleton chronology could be created (3 dates). The presence of micro-dissolution surfaces meant it was not possible to create a viable age model without further sampling, but indicated HY-9 could have grown during the mid-Holocene, around the same time as HY-8. Further work could use the approach from Chapter 4 to attempt to sample locations for U-series where micro-dissolution surfaces are not present and create an age model. This might allow comparison of climate records from two similarly timed stalagmites from the same cave. The palaeoclimate record from HY-8 would be more robust if a trace element record was created for the entire length of the stalagmite.

Possible further study of KT-3 should concentrate on obtaining a higher resolution trace element profile as this may help with the interpretation of the δ^{13}C if the combined records show higher sensitivity to changes in precipitation than δ^{18}O. In particular, higher resolution is required over the 8.2 kyr signal seen in δ^{13}C isotopes. As no signal for the 8.2 kyr event is observed in δ^{18}O at

this resolution, there might be some benefit to sampling by micromill to check whether or not a $\delta^{18}O$ signal can be detected at high resolution.

References

Alijani, B. (2002) "Variations of 500 hPa flow patterns over Iran and surrounding areas and their relationship with the climate of Iran," *Theoretical and Applied Climatology*, 72(1), pp. 41–54. doi: 10.1007/s007040200011.

Alijani, B. (2008) "Effect of the Zagros Mountains on the Spatial Distribution of Precipitation," *Journal of Moutain Science*, 5(3), pp. 218–231. doi: 10.1007/s11629-008-0126-8.

Alley, R., Mayewski, P., Sowers, T., Stuiver, M., Taylor, K. . and Clark, P. . (1997) "Holocene climatic instability: A prominent, widespread event 8200 yr ago," *Geology*, 25(6), pp. 483–486.

Allison, V. C. (1923) "The Growth of Stalagmites and Stalactites", *The Journal of Geology*, 31(2), pp. 106-125.

Almogi-Labin, A., Bar-Matthews, M., Shriki, D., Kolosovsky, E., Paterne, M., Schilman, B., Ayalon, A., Aizenshtat, Z. and Matthews, A. (2009) "Climatic variability during the last ⸮90ka of the southern and northern Levantine Basin as evident from marine records and speleothems," *Quaternary Science Reviews*. Elsevier Ltd, 28(25-26), pp. 2882–2896. doi: 10.1016/j.quascirev.2009.07.017.

Alpert, P., Baldi, M., Ilani, R., Krichak, S. O., Price, C., Rodó, X., Saaroni, H., Ziv, B., Kishcha, P., Barkan, J., Mariotti, A. and Xoplaki, E. (2006) "Relations between climate variability in the Mediterranean region and the tropics: ENSO, South Asian and African monsoons, hurricanes and Saharan dust," *Mediterranean Climate Variability*, 4(1), pp. 149–177. doi: 10.1016/S1571-9197(06)80005-4.

Alpert, P., Neeman, B. U. and Shay-El, Y. (1990) "Climatological analysis of Mediterranean cyclones using ECMWF data," *Tellus*, 42A, pp. 65–67.

Andersen, K. K. , Azuma, N. , Barnola, J. M. , Bigler, M. , Biscaye, P. , Caillon, N. , Chappellaz, J. , Clausen, H. B. , Dahl-Jensen, D. , Fischer, H. , Flückiger, J. , Fritzsche, D. , Fujii, Y. , Goto-Azuma, K. , Grønvold, K. , Gundestrup, N. S. , Hansson, M. , Huber, C. , Hvidberg, C. S. , Johnsen, S. J. , Jonsell, U. , Jouzel, J. , Kipfstuhl, S. , Landais, A. , Leuenberger, M. , Lorrain, R. , Masson-Delmotte, V. , Miller, H. , Motoyama, H. , Narita, H. , Popp, T. , Rasmussen, S. O. , Raynaud, D. , Röthlisberger, R. , Ruth, U. , Samyn, D. , Schwander, J. , Shoji, H. , Siggard-Andersen, M. L. , Steffensen, J. P. , Stocker, T. , Sveinbjörnsdottir, A. E. , Svensson, A. , Takata, M. , Tison, J. L. , Thorsteinsson, T. , Watanabe, O. , Wilhelms, F. and White, J. (2004). "High-resolution record of the Northern Hemisphere climate extending into the last interglacial period", *Nature*, 431, pp. 147-151.

Anderson, R., Bacon, M. and Brewer, P. (1982) "Elevated concentrations of actinides in Mono Lake," *Science*, 216(4545), pp. 514–516. doi: 10.1126/science.216.4545.514.

Argiriou, A. A. and Lykoudis, S. (2006) "Isotopic composition of precipitation in Greece," *Journal of Hydrology*, 327(3-4), pp. 486–495. doi: 10.1016/j.jhydrol.2005.11.053.

D' Arrigo, R., Jacoby, G., Wilson, R. and Panagiotopoulos, F. (2005) "A reconstructed Siberian High index since A.D. 1599 from Eurasian and North American tree rings," *Geophysical Research Letters*, 32(5), pp. 1–4. doi: 10.1029/2004GL022271.

Arz, H. W., Lamy, F., Pätzold, J., Muller, P. J. and Prins, M. (2003) "Mediterranean moisture source for an early-Holocene humid period in the northern Red Sea.," *Science (New York, N.Y.)*, 300(5616), pp. 118–21. doi: 10.1126/science.1080325.

Asmerom, Y., Polyak, V., Burns, S. and Rassmussen, J. (2007) "Solar forcing of Holocene climate: New insights from a speleothem record, southwestern United States," *Geology*, 35(1), pp. 1–4. doi: 10.1130/G22865A.1.

Avramidis, P., Geraga, M., Lazarova, M. and Kontopoulos, N. (2013) "Holocene record of environmental changes and palaeoclimatic implications in Alykes Lagoon, Zakynthos Island, western Greece, Mediterranean Sea," *Quaternary International*, 293, pp. 184–195. doi: 10.1016/j.quaint.2012.04.026.

Ayalon, A., Bar-Matthews, M. and Kaufman, A. (1999) "Petrography, strontium, barium and uranium concentrations, and strontium and uranium isotope ratios in speleothems as palaeoclimatic proxies: Soreq Cave, Israel," *The Holocene*, 9(6), pp. 715–722. doi: 10.1191/095968399673664163.

Badertscher, S., Fleitmann, D., Cheng, H., Edwards, R. L., Göktürk, O. M. and Zumbühl, A. (2011) "Pleistocene water intrusions from the Mediterranean and Caspian seas into the Black Sea," *Nature Geoscience*. Nature Publishing Group, 4(4), pp. 236–239. doi: 10.1038/ngeo1106.

Baker, A., C Hellstrom, J., Kelly, B. F. J., Mariethoz, G. and Trouet, V. (2015) "A composite annual-resolution stalagmite record of North Atlantic climate over the last three millennia.," *Nature Scientific reports*. Nature Publishing Group, 5, pp. 1–8. doi: 10.1038/srep10307.

Baker, A., Genty, D., Dreybrodt, W., Barnes, W. L., Mockler, Natalie, J. and Grapes, J. (1998) "Testing theoretically predicted stalagmite growth rate with Recent annually laminated samples: Implications for past stalagmite deposition," *Geochemica et Cosmochemica Acta*, 62(3), pp. 393–404. doi: 10.1016/S0016-7037(97)00343-8.

Baker A., Genty D. and Fairchild I. J. (2000) "Hydrological characterisation of stalagmite dripwaters at Grotte de Villars, Dordogne, by the analysis of inorganic species and luminescent organic matter", *Hydrology and Earth System Science,* 4, pp. 439–449. doi: 10.5194/hess-4-439-2000.

Baker, A., Proctor, C. J. and Barnes, W. L. (1999) "Variations in stalagmite luminescence laminae structure at Poole's Cavern, England, AD 1910–1996: calibration of a palaeoprecipitation proxy," *The Holocene*, 9(6), pp. 683–688. doi: 10.1191/095968399676312548.

Baker, A., Smart, P. L. and Ford, D. C. (1993) "Northwest European palaeoclimate as indicated by growth frequency variations of secondary calcite deposits," *Palaeogeography, Palaeoclimatology, Palaeoecology*, 100(3), pp. 291–301. doi: 10.1016/0031-0182(93)90059-R.

Baker, A., Smith, C. L., Jex, C. N., Fairchild, I. J., Genty, D. and Fuller, L. (2008) "Annually laminated speleothems: a review," *International Journal of Speleology*, 37(3), pp. 193–206. Available at: http://scholarcommons.usf.edu/ijs/vol37/iss3/4/ (Accessed: June 16, 2016).

Baldini, J., Mcdermott, F. and Fairchild, I. (2006) "Spatial variability in cave drip water hydrochemistry: Implications for stalagmite paleoclimate records," *Chemical Geology*, 235(3-4), pp. 390–404. doi: 10.1016/j.chemgeo.2006.08.005.

Baldini, J. U. L. (2010) "The geochemistry of cave calcite deposits as a record of past climate," *The Sedimentary Record*, 8, pp. 4–9.

Baldini, J. U. L., McDermott, F., Baker, A., Baldini, L. M., Mattey, D. P. and Railsback, L. (2005) "Biomass effects on stalagmite growth and isotope ratios: A 20th century analogue from Wiltshire, England," *Earth and Planetary Science Letters*, 240(2), pp. 486–494. doi: 10.1016/j.epsl.2005.09.022.

Baldini, J. U. L., McDermott, F., Hoffmann, D. L., Richards, D. A. and Clipson, N. (2008) "Very high-frequency and seasonal cave atmosphere PCO_2 variability: Implications for stalagmite growth and oxygen isotope-based paleoclimate records," *Earth and Planetary Science Letters*, 272(1-2), pp. 118–129. doi: 10.1016/j.epsl.2008.04.031.

Bar-Matthews, M. and Ayalon, A. (2011) "Mid-Holocene climate variations revealed by high-resolution speleothem records from Soreq Cave, Israel and their correlation with cultural changes," *The Holocene*, 21(1), pp. 163–171. doi: 10.1177/0959683610384165.

Bar-Matthews, M., Ayalon, A., Gilmour, M., Matthews, A. and Hawkesworth, C. J. (2003) "Sea–land oxygen isotopic relationships from planktonic foraminifera and speleothems in the Eastern Mediterranean region and their implication for paleorainfall during interglacial intervals," *Geochimica et Cosmochimica Acta*, 67(17), pp. 3181–3199. doi: 10.1016/S0016-7037(02)01031-1.

Bar-Matthews, M., Ayalon, A. and Kaufman, A. (1997) "Late Quaternary paleoclimate in the eastern Mediterranean region from stable isotope analysis of speleothems at Soreq Cave, Israel," *Quaternary Research*, 168(47), pp. 155–168. doi: 10.1006/qres.1997.1883.

Bar-Matthews, M., Ayalon, A. and Kaufman, A. (2000) "Timing and hydrological conditions of Sapropel events in the Eastern Mediterranean, as evident from speleothems, Soreq cave, Israel," *Chemical Geology*, 169(1-2), pp. 145–156. doi: 10.1016/S0009-2541(99)00232-6.

Bar-Matthews, M., Ayalon, A., Kaufman, A. and Wasserburg, G. J. (1999) "The Eastern Mediterranean paleoclimate as a reflection of regional events: Soreq cave, Israel," *Earth and Planetary Science Letters*, 166(1-2), pp. 85–95. doi: 10.1016/S0012-821X(98)00275-1.

Bar-Matthews, M., Ayalon, A., Matthews, A., Sass, E. and Halicz, L. (1996) "Carbon and oxygen isotope study of the active water-carbonate system in a karstic Mediterranean cave: Implications for paleoclimate research in semiarid regions," *Geochimica et Cosmochimica Acta*, 60(2), pp. 337–347. doi: 10.1016/0016-7037(95)00395-9.

Barnston, A. G. and Livezey, R. E. (1987) "Classification, Seasonality and Persistence of Low-frequency Atmospheric Circulation Patterns," *Monthly Weather Review*, 115, pp. 1083–1126. doi: 10.1175/1520-0493(1987)115<1083:CSAPOL>2.0.CO;2.

Bar-Yosef, O., Meadow, R.H. (1995) "The origins of agriculture in the Near East. Last Hunters, First Farmers" eds Price, T.D., Gebauer, A.B. (School of American Research Press, Santa Fe, NM), pp 39–94.

Berger, A. and Loutre, M. F. (1991) "Insolation values for the climate of the last 10 million years," *Quaternary Science Reviews*, 10(1988), pp. 297–317.

Berger, J.-F. and Guilaine, J. (2009) "The 8200 calBP abrupt environmental change and the Neolithic transition: A Mediterranean perspective," *Quaternary International*, 200(1-2), pp. 31–49. doi: 10.1016/j.quaint.2008.05.013.

Van Beynen, P., Bourbonniere, R., Ford, D. and Schwarcz, H. (2001) "Causes of colour and fluorescence in speleothems," *Chemical Geology*, 175(3), pp. 319–341. doi: 10.1016/S0009-2541(00)00343-0.

Biten, A. and Sa' Aroni, H. (1992) "The horizontal and vertical extension of the Persian Gulf pressure trough," *International Journal of Climatology*, 12(7), pp. 733–747. doi: 10.1002/joc.3370120706.

Boch, R., Spötl, C. and Frisia, S. (2011) "Origin and palaeoenvironmental significance of lamination in stalagmites from Katerloch Cave, Austria," *Sedimentology*, 58(2), pp. 508–531. doi: 10.1111/j.1365-3091.2010.01173.x.

Bodnar, R. (2003) "Introduction to Fluid Inclusions," in Samson, A., Anderson, A., and Marshall, D. (eds) *Fluid Inclusions Analysis and Interpretation*. Mineral Association of Canada, Short Course 32, pp. 1–8.

Bordon, A., Peyron, O., Lézine, A., Brewer, S. and Fouache, E. (2009) "Pollen-inferred Late-Glacial and Holocene climate in southern Balkans (Lake Maliq)," *Quaternary International*, 200(1), pp. 19–30. doi: 10.1016/j.quaint.2008.05.014.

Borsato, A., Frisia, S., Fairchild, I. J., Somogyi, A. and Susini, J. (2007) "Trace element distribution in annual stalagmite laminae mapped by micrometer-resolution X-ray fluorescence: Implications for incorporation of environmentally significant species," *Geochimica et Cosmochimica Acta*, 71(1), pp. 1494–1512. doi: 10.1016/j.gca.2006.12.016.

Borsato, A., Frisia, S. and Miorandi, R. (2015) "Carbon dioxide concentration in temperate climate caves and parent soils over an altitudinal gradient and its influence on speleothem growth and fabrics," *Earth Surface Processes and Landforms*, 40(9), pp. 1158–1170. doi: 10.1002/esp.3706.

Borsato, A., Quinif, Y., Bini, A. and Dublyansky, Y. (2003) "Open-system alpine speleothems: implications for U-series dating and paleoclimate," *Studi trentini di scienze naturali - Acta geologica*, 80, pp. 71–83.

Bottema, S. (1986) "A Late Quaternary Pollen Diagram from Lake Urmia (Northwestern Iran)," *Review of Palaeobotany and Palynology*, 47(3-4), pp. 241–261. doi: 10.1016/0034-6667(86)90039-4.

Bourdon, B., Turner, S., Henderson, G.M., Lundstrom, C.C. (2003) "Introduction to U-series Geochemistry", in Bourdon, B., Henderson, G.M., Lundstrom, C.C., and Turner S.P. (eds) Uranium Series Geochemistry, *Reviews in Mineralogy and Geochemistry*, 52, pp. 1-23.

Bowen, G. J. (2016) "The Online Isotopes in Precipitation Calculator", version 3.1. http://www.waterisotopes.org.

Boyd, M. (2015) *Speleothems from Warm Climates – Holocene Records from the Caribbean and Mediterranean Regions*. Stockholm University.

Breitenbach, S. F. M., Rehfeld, K., Goswami, B., Baldini, J. U. L., Ridley, H. E., Kennett, D. J., Prufer, K. M., Aquino, V. V., Asmerom, Y., Polyak, V. J., Cheng, H., Kurths, J. and Marwan, N. (2012) "COnstructing Proxy Records from Age models (COPRA)," *Climate of the Past*, 8(5), pp. 1765–1779. doi: 10.5194/cp-8-1765-2012.

Broecker, W. S. (2001) "Was the Medieval Warm Period Global," *Science*, 291(5508), pp. 1497–1499. doi: 10.1126/science.291.5508.1497.

Brooks N. (2006) "Cultural responses to aridity in the Middle Holocene and increased social

complexity", *Quaternary International,* 151, pp. 29–49. doi:10.1016/j.quaint.2006.01.013

Brunetti, M. and Kutiel, H. (2011) "The relevance of the North-Sea Caspian Pattern (NCP) in explaining temperature variability in Europe and the Mediterranean," *Natural Hazards and Earth System Sciences*, 11, pp. 2881–2888. doi: 10.5194/nhess-11-2881-2011.

Brzović, N. (1999) "Factors affecting the Adriatic cyclone and associated windstorms," *Contributions to Atmospheric Physics*, 72(1), pp. 51–65.

Buhmann, D. and Dreybrodt, W. (1985) "The kinetics of calcite dissolution and precipitation in geologically relevent situations of karst areas 1. Open System," *Chemical Geology*, 48, pp. 189–211.

Burns, S. J., Fleitmann, D., Mudelsee, M., Neff, U., Matter, A. and Mangini, A. (2002) "A 780-year annually resolved record of Indian Ocean monsoon precipitation from a speleothem from south Oman," *Journal of Geophysical Research*, 107(D20), p. 4434. doi: 10.1029/2001JD001281.

Cheng, H., Adkins, J., Edwards, R. and Boyle, E. (2000) "U-Th dating of deep-sea corals," *Geochimica et Cosmochimica Acta*, 64(14), pp. 2401–2416.

Cheng, H., Edwards, R. L., Broecker, W. S., Denton, G. H., Kong, X., Wang, Y., Zhang, R. and Wang, X. (2009) "Ice age terminations.," *Science*, 326(5950), pp. 248–52. doi: 10.1126/science.1177840.

Cheng, H., Edwards, R. L., Wang, Y., Kong, X., Ming, Y., Kelly, M. J., Wang, X., Gallup, C. D. and Liu, W. (2006) "A penultimate glacial monsoon record from Hulu Cave and two-phase glacial terminations," *Geology*, 34(3), p. 217. doi: 10.1130/G22289.1.

Cheng, H., Fleitmann, D., Edwards, R. L., Wang, X., Cruz, F. W., Auler, A. S., Mangini, A., Wang, Y., Kong, X., Burns, S. J. and Matter, A. (2009) "Timing and structure of the 8.2 kyr B.P. event inferred from δ^{18}O records of stalagmites from China, Oman, and Brazil," *Geology*, 37(11), pp. 1007–1010. doi: 10.1130/G30126A.1.

Cheng, H., Lawrence Edwards, R., Shen, C.-C., Polyak, V. J., Asmerom, Y., Woodhead, J., Hellstrom, J., Wang, Y., Kong, X., Spötl, C., Wang, X. and Calvin Alexander Jr, E. (2013) "Improvements in ^{230}Th dating, ^{230}Th and ^{234}U half-life values, and U–Th isotopic measurements by multi-collector inductively coupled plasma mass spectrometry," *Earth and Planetary Science Letters*, 371-372, pp. 82–91. doi: 10.1016/j.epsl.2013.04.006.

Christensen, J., Hewitson, B., Busuioc, A., Chen, A., Gao, X., Held, I., Jones, R., Kolli, R. ., Kwon, W.-T., Laprise, R., Magaña Rueda, V., Mearns, L., Menéndez, C. ., Räisänen, J., Rinke, A., Sarr, A. and Whetton, P. (2007) "Regional climate projections," in Solomon, S., Qin, D., Manning, M., Chen, Z., Marquis, M., Averyt, K. ., Tignor, M., and Miller, H. (eds) *Climate Change, 2007: The Physical Science Basis. Contribution of Working Group I to the Fourth Assessment Report of the Intergovernmental Panel on Climate Change*. Cambridge University Press, pp. 848–940.

Christensen, J.H., K. Krishna Kumar, Aldrian E., An S.-I., Cavalcanti I.F.A., de Castro M., Dong W., Goswami P., Hall A., Kanyanga J.K., Kitoh A., Kossin J., Lau N.-C., Renwick J., Stephenson D.B., Xie S.-P. and Zhou T. (2013) "Climate Phenomena and their Relevance for Future Regional Climate

Change Supplementary Material. In: Climate Change 2013: The Physical Science Basis. Contribution of Working Group I to the Fifth Assessment Report of the Intergovernmental Panel on Climate Change"

Çiçek, I., Türkoğlu, N., Ceylan, A. and Korkmaz, N. (no date) "Seasonal Rainfall Intensity and Frequency in Turkey," pp. 1–11.

Clarke, J., Brooks, N., Banning, E. B., Bar-Matthews, M., Campbell, S., Clare, L., Cremaschi, M., Drake, N., Gallinaro, M., Manning, S., Nicoll, K., Philip, G., Rosen, S., Schoop, U., Tafuri, M. A., Weninger, B. and Zerboni, A. (2016) "Climatic changes and social transformations in the Near East and North Africa during the 'long' 4th millennium BC : A comparative study of environmental and archaeological evidence," *Quaternary Science Reviews*. Elsevier Ltd, 136, pp. 96–121. doi: 10.1016/j.quascirev.2015.10.003.

Cook, B. I., Anchukaitis, K. J., Touchan, R., Meko, D. M. and Cook, E. R. (2016) "Spatiotemporal drought variability in the Mediterranean over the last 900 years," *Journal of Geophysical Research: Atmospheres*, 121, pp. 2060–2074. doi: 10.1002/2015JD023929.

Conte, M., Giuffrida, A., and Tedesco, S. (1989) "The Mediterranean Oscillation. Impact on precipitation and hydrology in Italy", *Conference on Climate Water*, pp. 121–137, Publications of the Academy of Finland, Helsinki.

Craig, H. (1961) "Isotopic Variations in Meteoric Waters," *Science*, 133(3465), pp. 1702–1703. doi: 10.1126/science.133.3465.1702.

Crowley, T. J. and Lowery, T. S. (2013) "Warm Was the Medieval Warm Period ?," 29(1), pp. 51–54.

Crowley, T. and Lowery, T. (2000) "How warm was the medieval warm period?," *AMBIO: A Journal of the Human Environment*, 29(1), pp. 51–54. doi: 10.1579/0044-7447-29.1.51

Cullen, H., DeMenocal, P., Hemming, S., Hemming, G., Brown, F., Guilderson, T. and Sirocko, F. (2000) "Climate change and the collapse of the Akkadian empire: Evidence from the deep sea," *Geology*, 28, pp. 379–382. doi: 10.1130/0091-7613(2000)28<379.

Curl, R. L. (1972) "Minimum diameter stalagmites", *National Speleological Society Bulletin*, 34, pp. 129-136

Cvetkoska, A., Levkov, Z., Reed, J. M. and Wagner, B. (2014) "Late Glacial to Holocene climate change and human impact in the Mediterranean : The last ca . 17 ka diatom record of Lake Prespa (Macedonia/Albania/Greece)," *Palaeogeography, Palaeoclimatology, Palaeoecology*, 406, pp. 22–32. doi: 10.1016/j.palaeo.2014.04.010.

Dansgaard, W. (1964) "Stable isotopes in precipitation," *Tellus*, 16(4), pp. 436–468. doi: 10.1111/j.2153-3490.1964.tb00181.x.

Day, C. C. and Henderson, G. M. (2011) "Oxygen isotopes in calcite grown under cave-analogue conditions," *Geochimica et Cosmochimica Acta*. Elsevier Ltd, 75(14), pp. 3956–3972. doi: 10.1016/j.gca.2011.04.026.

Day, C. C. and Henderson, G. M. (2013) "Controls on trace-element partitioning in cave-analogue calcite," *Geochimica et Cosmochimica Acta*. Elsevier Ltd, 120, pp. 612–627. doi: 10.1016/j.gca.2013.05.044.

Dean, J. R., Jones, M. D., Leng, M. J., Noble, S. R., Metcalfe, S. E., Sloane, H. J., Sahy, D., Eastwood, W. J. and Roberts, C. N. (2015) "Eastern Mediterranean hydroclimate over the late glacial and Holocene , reconstructed from the sediments of Nar lake , central Turkey , using stable isotopes and carbonate mineralogy," *Quaternary Science Reviews*. Elsevier Ltd, 124, pp. 162–174. doi: 10.1016/j.quascirev.2015.07.023.

Dean, J. R., Jones, M. D., Leng, M. J., Sloane, H. J., Roberts, C. N., Woodbridge, J., Swann, G. E. A., Metcalfe, S. E., Eastwood, W. J. and Yiğitbaşıoğlu, H. (2013) "Palaeo-seasonality of the last two millennia reconstructed from the oxygen isotope composition of carbonates and diatom silica from Nar Gölü, central Turkey," *Quaternary Science Reviews*, 66, pp. 35–44. doi: 10.1016/j.quascirev.2012.07.014.

Denniston, R. F., González, L. a., Asmerom, Y., Sharma, R. H. and Reagan, M. K. (2000) "Speleothem Evidence for Changes in Indian Summer Monsoon Precipitation over the Last ~2300 Years," *Quaternary Research*, 53(2), pp. 196–202. doi: 10.1006/qres.1999.2111.

Dinpashoh, Y., Fakheri-Fard, A, Moghaddam, M., Jahanbakhsh, S. and Mirnia, M. (2004) "Selection of variables for the purpose of regionalization of Iran's precipitation climate using multivariate methods," *Journal of Hydrology*, 297(1-4), pp. 109–123. doi: 10.1016/j.jhydrol.2004.04.009.

Domínguez-Villar, D., Baker, A., Fairchild, I. J. and Edwards, R. L. (2012) "A method to anchor floating chronologies in annually laminated speleothems with U–Th dates," *Quaternary Geochronology*. Elsevier B.V, 14, pp. 57–66. doi: 10.1016/j.quageo.2012.04.019.

Dorale, J. A. and Lui, Z. (2009) "Limitations of Hendy Test criteria in judging the palaeoclimatic suitability of speleothems and the need for replication," *Journal of Cave and Karst Studies*, 71(1), pp. 73–80.

Dotsika, E., Lykoudis, S. and Poutoukis, D. (2010) "Spatial distribution of the isotopic composition of precipitation and spring water in Greece," *Global and Planetary Change*. Elsevier B.V., 71(3-4), pp. 141–149. doi: 10.1016/j.gloplacha.2009.10.007.

Drake, B. L. (2012) "The influence of climatic change on the Late Bronze Age Collapse and the Greek Dark Ages," *Journal of Archaeological Science*. Elsevier Ltd, 39(6), pp. 1862–1870. doi: 10.1016/j.jas.2012.01.029.

Dreybrodt, W. (1980) "Deposition of calcite from thin films of natural calcareous solutions and the growth of speleothems," *Chemical Geology*, 29, pp. 89–105.

Dreybrodt, W. (1981) "The kinetics of calcite precipitation from thin films of calcareous solutions and the growth of speleothems: Revisited," *Chemical Geology*, 32(1-4), pp. 237–245. doi: 10.1016/0009-2541(81)90146-7.

Dreybrodt, W. and Scholz, D. (2011) "Climatic dependence of stable carbon and oxygen isotope signals recorded in speleothems : From soil water to speleothem calcite," *Geochimica et Cosmochimica Acta*. Elsevier Ltd, 75(3), pp. 734–752. doi: 10.1016/j.gca.2010.11.002.

Drysdale, R., Hellstrom, J., Zanchetta, G., Fallick, A., Sánchez Goñi, M., Couchoud, I., McDonald, J., Mass, R., Lohmann, G. and Isola, I. (2009) "Evidence for obliquity forcing of glacial termination II," *Science*, 325, pp. 1527–1531. doi: 10.1126/science.1170371.

Drysdale, R. N., Hellstrom, J. C., Zanchetta, G., Fallick, A. E., Sánchez Goñi, M. F., Couchoud, I., McDonald, J., Maas, R., Lohmann, G. and Isola, I. (2009) "Evidence for obliquity forcing of glacial Termination II," *Science (New York, N.Y.)*, 325(5947), pp. 1527–31. doi: 10.1126/science.1170371.

Drysdale, R., Zanchetta, G., Hellstrom, J., Maas, R., Fallick, A., Pickett, M., Cartwright, I. and Piccini, L. (2006) "Late Holocene drought responsible for the collapse of Old World civilizations is recorded in an Italian cave flowstone," *Geology*, 34(2), p. 101. doi: 10.1130/G22103.1.

Dünkeloh, A. and Jacobeit, J. (2003) "Circulation dynamics of Mediterranean precipitation variability 1948-98," *International Journal of Climatology*, 23, pp. 1843–1866. doi: 10.1002/joc.973.

Eastwood, A. W. J., Roberts, N. and Lamb, H. F. (1998) "Palaeoecological and Archaeological Evidence for Human Occupance in Southwest Turkey : The Beyşehir Occupation Phase," *Anatolian Studies*, 48, pp. 69–86.

Eastwood, W., Leng, M., Roberts, N. and Davis, B. (2007) "Holocene climate change in the eastern Mediterranean region: a comparison of stable isotope and pollen data from Lake Gölhisar, southwest Turkey," *Journal of Quaternary Research*, 22(4), pp. 327–341. doi: 10.1002/jqs.

Edwards, R., Chen, J. and Wasserburg, G. (1986) "238 U 234 U 230 Th 232 Th systematics and the precise measurement of time over the past 500,000 years," *Earth and Planetary Science Letters*, 81, pp. 175–192.

Emeis, K., Schulz, H., Struck, U., Rossignol-Strick, M., Erlenkeuser, H., Howell, M. W., Kroon, D., Mackensen, A., Ishizuka, S., Oba, T., Sakamoto, T. and Koizumi, I. (2003) "Eastern Mediterranean surface water temperatures and $\delta^{18}O$ composition during deposition of sapropels in the late Quaternary," *Paleoceanography*, 18(1), pp. 1–18. doi: 10.1029/2000PA000617.

Emeis, K.-C., Struck, U., Schulz, H.-M., Rosenberg, R., Bernasconi, S., Erlenkeuser, H., Sakamoto, T. and Martinez-Ruiz, F. (2000) "Temperature and salinity variations of Mediterranean Sea surface waters over the last 16 , 000 years from records of planktonic stable oxygen isotopes and alkenone unsaturation ratios," *Palaeogeography, Palaeoclimatology Palaeoecology*, 158(3), pp. 259–280. doi: 10.1016/S0031-0182(00)00053-5.

Emrich, K., Ehhalt, D. H. and Vogel, J. C. (1970) "Carbon isotope fractionation during the precipitation of calcium carbonate," *Earth and Planetary Science Letters*, 8(5), pp. 363–371. doi: 10.1016/0012-821X(70)90109-3.

Epstein, S., Buchsbaum, R., Lowenstam, H. A. and Urey, H. C. (1953) "Revised Carbonate-Water Isotopic Temperature Scale," *Bulletin of the Geological Society of America*, 64, pp. 1315–1325.

Evans, J. P., Smith, R. B. and Oglesby, R. J. (2004) "Middle East climate simulation and dominant precipitation processes," *International Journal of Climatology*, 24(13), pp. 1671–1694. doi: 10.1002/joc.1084.

Fairchild, I.J and Baker, A. (2012) "Speleothem Science From Process to Past Environments", *Wiley-Blackwell,* 432 pp.

Fairchild, I. J., Borsato, A., Tooth, A. F., Frisia, S., Hawkesworth, C. J., Huang, Y., McDermott, F. and Spiro, B. (2000) "Controls on trace element (Sr – Mg) compositions of carbonate cave waters : implications for speleothem climatic records," *Chemical Geology: Isotope Geoscience section*, 166(3), pp. 255–269. doi: 10.1016/S0009-2541(99)00216-8.

Fairchild, I. J., Smith, C. L., Baker, A., Fuller, L., Spötl, C., Mattey, D. and McDermott, F. (2006a) "Modification and preservation of environmental signals in speleothems," *Earth-Science Reviews*, 75(1-4), pp. 105–153. doi: 10.1016/j.earscirev.2005.08.003.

Fairchild, I. J., Frisia, S., Borsato, A. and Tooth, A. F. (2006b) "Chapter 7 Speleothems," in *Geochemical Sediments and Landscapes*, pp. 1–21.

Fairchild, I. J., Tuckwell, G. W., Baker, A. and Tooth, A. F. (2006c) "Modelling of dripwater hydrology and hydrogeochemistry in a weakly karstified aquifer (Bath, UK): Implications for climate change studies," *Journal of Hydrology*, 321(1-4), pp. 213–231. doi: 10.1016/j.jhydrol.2005.08.002.

Fairchild, I. J. and Treble, P. C. (2009) "Trace elements in speleothems as recorders of environmental change," *Quaternary Science Reviews*. Elsevier Ltd, 28(5-6), pp. 449–468. doi: 10.1016/j.quascirev.2008.11.007.

Fallah, B., Sodoudi, S., Russo, E., Kirchner, I. and Cubasch, U. (2015) "Towards modeling the regional rainfall changes over Iran due to the climate forcing of the past 6000 years," *Quaternary International*. Elsevier Ltd, pp. 1–10. doi: 10.1016/j.quaint.2015.09.061.

Fensterer, C., Scholz, D., Hoffmann, D. L., Spötl, C., Schröder-Ritzrau, A., Horn, C., Pajón, J. M. and Mangini, A. (2013) "Millennial-scale climate variability during the last 12.5ka recorded in a Caribbean speleothem," *Earth and Planetary Science Letters*, 361, pp. 143–151. doi: 10.1016/j.epsl.2012.11.019.

Finné, M. (2014) *Climate in the eastern Mediterranean during the Holocene and beyond – a Peloponnesian perspective*.

Finné, M., Bar-Matthews, M., Holmgren, K., Sundqvist, H. S., Liakopoulos, I. and Zhang, Q. (2014) "Speleothem evidence for late Holocene climate variability and floods in Southern Greece," *Quaternary Research*, 81(2), pp. 213–227. doi: 10.1016/j.yqres.2013.12.009.

Finné, M., Kylander, M., Boyd, M., Sundqvist, H. S. and Löwemark, L. (2015) "Can XRF scanning of speleothems be used as a non-destructive method to identify paleoflood events in caves?," *International Journal of Speleology*, 44(1), pp. 17–23.

Fleitmann, D., Burns, S. J., Mangini, A., Mudelsee, M., Kramers, J., Villa, I., Neff, U., Al-Subbary, A. A., Buettner, A., Hippler, D. and Matter, A. (2007) "Holocene ITCZ and Indian monsoon dynamics recorded in stalagmites from Oman and Yemen (Socotra)," *Quaternary Science Reviews*, 26(1-2), pp. 170–188. doi: 10.1016/j.quascirev.2006.04.012.

Fleitmann, D., Burns, S. J., Mudelsee, M., Neff, U., Kramers, J., Mangini, A. and Matter, A. (2003) "Holocene forcing of the Indian monsoon recorded in a stalagmite from southern Oman.," *Science*, 300(5626), pp. 1737–9. doi: 10.1126/science.1083130.

Fleitmann, D., Burns, S. J., Neff, U., Mudelsee, M., Mangini, A. and Matter, A. (2004) "Palaeoclimatic interpretation of high-resolution oxygen isotope profiles derived from annually laminated speleothems from Southern Oman," *Quaternary Science Reviews*, 23(7-8), pp. 935–945. doi: 10.1016/j.quascirev.2003.06.019.

Fleitmann, D., Cheng, H., Badertscher, S., Edwards, R. L., Mudelsee, M., Göktürk, O. M., Fankhauser, A., Pickering, R., Raible, C. C., Matter, A., Kramers, J. and Tüysüz, O. (2009) "Timing and climatic impact of Greenland interstadials recorded in stalagmites from northern Turkey," *Geophysical Research Letters*, 36(19), pp. 1–5. doi: 10.1029/2009GL040050.

Fleitmann, D., Treble, P., Cruz Jr, F., Cole, J. and Cobb, K. (2008a) "White Paper on Speleothem based research," in *NOAA Trieste Workshop*, pp. 1–7.

Fleitmann, D., Spötl, C., Newman, L. and Kiefer, T. (2008b) "Advances in speleothem research," *Pages*, 16(3), pp. 1–40.

Fletcher, W. J. and Sánchez Goñi, M. F. (2008) "Orbital- and sub-orbital-scale climate impacts on vegetation of the western Mediterranean basin over the last 48,000 yr," *Quaternary Research*. University of Washington, 70(3), pp. 451–464. doi: 10.1016/j.yqres.2008.07.002.

Flocas, A. A. and Giles, B. D. (1991) "Distribution and intensity of frontal rainfall over greece," *International Journal of Climatology*, 11(4), pp. 429–442. doi: doi:10.1002/joc.3370110407.

Flocas, H., Simmonds, I., Kouroutzoglou, J., Keay, K., Hatzaki, M., Bricolas, V. and Asimakopoulous, D. (2010) "On Cyclonic Tracks over the Eastern Mediterranean," *Journal of Climate*, 23, pp. 5243–5257. doi: 10.1175/2010JCLI3426.1.

Flohr, P., Fleitmann, D., Zorita, E., Sadekov, A., Cheng, H., Bosomworth, M., Edwards, L., Matthews, W. and Matthews, R. (2017) "Late Holocene droughts in the Fertile Crescent recorded in a speleothem from northern Iraq," *Geophysical Research Letters*, 44, pp. 1–9. doi: 10.1002/2016GL071786.

Folk, R. L. (1977) "Reply calcite and aragonite fabrics, Carlsbad Caverns," *Journal of Sedimentary Research*, 47(3), pp. 1400–1401.

Folk, R. L. and Assereto, R. (1976) "Comparative Fabrics of Length-Slow and Length-Fast Calcite and Calcitized Aragonite in a Holocene Speleothem, Carlsbad Caverns, New Mexico," *Journal of Sedimentary Petrography*, Vol. 46(3), pp. 486–496. doi: 10.1306/212F6FCD-2B24-11D7-8648000102C1865D.

Franke, H. W. (1965) "The theory behind stalagmite shapes", *Studies in Speleology,* 1, pp. 89–95.

Francke, A., Wagner, B., Leng, M. J. and Rethemeyer, J. (2013) "A Late Glacial to Holocene record of environmental change from Lake Dojran (Macedonia, Greece)," *Climate of the Past Discussions*, 8(6), pp. 5743–5785. doi: 10.5194/cpd-8-5743-2012.

Frappier, A., Sahagian, D., González, L. A. and Carpenter, S. J. (2002) "El Niño Events Recorded by Stalagmite Carbon Isotopes," *Science*, 298(5593), p. 565. doi: 10.1126/science.1076446.

Frisia S., (1996) "Petrographic evidences of diagenesis in speleothems: some examples", *Speleochronos*, 7, pp. 21-30.

Frisia, S. (2015) "Microstratigraphic logging of calcite fabrics in speleothems as tool for palaeoclimate studies," *International Journal of Speleology*, 44(January), pp. 1–16. doi: 10.5038/1827-806X.44.1.1.

Frisia, S. and Borsato, A. (2010) "Carbonates in Continental Settings: Facies, Environments, and Processes. Chapter 6 Karst.," *Developments in Sedimentology*. Elsevier (Developments in Sedimentology), 61, pp. 269–318. doi: 10.1016/S0070-4571(09)06106-8.

Frisia, S., Borsato, A. and Fairchild, I. (2002) "Aragonite-calcite relationships in speleothems (Grotte de Clamouse, France): environment, fabrics, and carbonate geochemistry," *Journal of Sedimentary Research*, 72(5), pp. 687–699. doi: 10.1306/020702720687.

Frisia, S., Borsato, A., Fairchild, I. J. and Dermott, F. M. C. (2000) "Calcite fabrics, growth mechanisms, and environments of formation in speleothems from the Italian Alps and

Southwestern Ireland," *Journal of Sedimentary Research*, 70(5), pp. 1183–1196. doi: 10.1306/022900701183.

Frisia, S., Borsato, A., Mangini, A., Spötl, C., Madonia, G. and Sauro, U. (2006) "Holocene climate variability in Sicily from a discontinuous stalagmite record and the Mesolithic to Neolithic transition," *Quaternary Research*, 66(3), pp. 388–400. doi: 10.1016/j.yqres.2006.05.003.

Frisia, S., Borsato, A., Preto, N. and McDermott, F. (2003) "Late Holocene annual growth in three Alpine stalagmites records the influence of solar activity and the North Atlantic Oscillation on winter climate," *Earth and Planetary Science Letters*, 216(3), pp. 411–424. doi: 10.1016/S0012-821X(03)00515-6.

Frumkin, A., Ford, D. C. and Schwarcz, H. P. (2000) "Paleoclimate and vegetation of the Last Glacial Cycles in Jerusalem from a Speleothem Record," *Global Biogeochemical Cycles*, 14(3), pp. 863–870. doi: 10.1029/1999GB001245.

Frumkin, A., Ford, D. and Schwarcz, H. (1999) "Continental oxygen isotopic record of the last 170,000 years in Jerusalem," *Quaternary Research*, 327, pp. 317–327. doi: 10.1006/qres.1998.2031.

Frumkin, A., Schwarcz, H. P. and Ford, D. C. (1994), "Evidence for Isotopic equilibrium in stalagmites from caves in a dry region: Jerusalem, Israel", *Israel Journal of Earth Sciences* 43, pp. 221–230.

Gaffney, J., Marley, N. and Orlandini, K. (1992) "Evidence for Thorium Isotopic Disequilibria due to Organic Complexation in Natural Waters," *Environmental Science & Technology*, 26(6), pp. 1248–1250. doi: 10.1021/es50002a615.

Gams, I. (1981). "Contributions to morphometrics of stalagmites", *Proceedings of the International Congress of Speleology*, 8, pp. 276–278.

Gascoyne, M. (1982) "Geochemistry of actinides and their daughters", in Uranium Series Disequilibrium Applications to Environmental Problems, 1st Edition, *Oxford University Press*, pp. 33-56.

Gascoyne, M. (1992) "Geochemistry of actinides and their daughters" in Ivanovich, M. and Harmon R.S. (eds) Uranium-series Disequilibrium Applications to Earth, Marine and Environmental Sciences, 2nd Edition, *Oxford Science Publications*, pp. 34-62.

Gat, J. R. (1996) "Oxygen and Hydrogen Isotopes in the Hydrologic Cycle," *Annual Review of Earth and Planetary Sciences*, 24(1), pp. 225–262. doi: 10.1146/annurev.earth.24.1.225.

Gat, J. R. and Carmi, I. (1970) "Evolution, of the Isotopic Composition of Atmospheric Waters in the Mediterranean Sea Area," *Journal of Geophysical Research*, 75(15), pp. 3039–3048.

Gázquez, F., Calaforra, J. M. and Forti, P. (2011) "Black Mn-Fe Crusts as Markers of Abrupt Palaeoenvironmental Changes in El Soplao Cave (Cantabria, Spain)," *International Journal of Speleology*, 40(2), pp. 163–169. doi: 10.5038/1827-806X.40.2.8.

Gázquez, F., Calaforra, J.-M., Rull, F., Forti, P. and Garcia-Casco, A. (2012) "Organic matter of fossil origin in the amberine speleothems from El Soplao Cave (Cantabria, Northern Spain)," *International Journal of Speleology*, 41(1), pp. 113–123. doi: 10.5038/1827-806X.41.1.12.

Genty, D. (2008) "Palaeoclimate Research in Villars Cave (Dordgone, SW France)," *International Journal of Speleology*, 37(3), pp. 173–191.

Genty, D., Baker, A. and Vokal, B. (2001a) "Intra- and inter-annual growth rate of modern stalagmites," *Chemical Geology*, 176(1-4), pp. 191–212.

Genty, D., Baker, A., Massault, M., Proctor, C., Gilmour, M., Pons-Branchu, E. and Hamelin, B. (2001b) "Dead carbon in stalagmites: Carbonate bedrock paleodissolution vs. ageing of soil organic matter. Implications for $\delta^{13}C$ variations in speleothems," *Geochemica et Cosmochemica Acta*, 65(20), pp. 3443–3457. doi: 10.1016/S0016-7037(01)00697-4.

Genty, D., Blamart, D., Ouahdi, R., Gilmour, M., Baker, a, Jouzel, J. and Van-Exter, S. (2003) "Precise dating of Dansgaard-Oeschger climate oscillations in western Europe from stalagmite data.," *Nature*, 421(6925), pp. 833–7. doi: 10.1038/nature01391.

Genty, D. and Deflandre, G. (1998) "Drip flow variations under a stalactite of the Père Noël cave (Belgium). Evidence of seasonal variations and air pressure constraints," *Journal of Hydrology*, 211(1-4), pp. 208–232. doi: 10.1016/S0022-1694(98)00235-2.

Genty, D. and Quinif, Y. (1996) "Annually laminated sequences in the internal structure of some Belgian stalagmites--importance for paleoclimatology," *Journal of Sedimentary Research*, 66(1), pp. 275–288. doi: 10.1306/D426831A-2B26-11D7-8648000102C1865D.

Geraga, M., Mylona, G., Tsaila-Monopolis, S., Papatheodorou, G. and Ferentinos, G. (2008) "Northeastern Ionian Sea: Palaeoceanographic variability over the last 22 ka," *Journal of Marine Systems*. Elsevier B.V., 74(1-2), pp. 623–638. doi: 10.1016/j.jmarsys.2008.05.019.

Geraga, M., Tsaila-Monopolis, S., Ioakim, C., Papatheodorou, G. and Ferentinos, G. (2005) "Short-term climate changes in the southern Aegean Sea over the last 48,000 years," *Palaeogeography, Palaeoclimatology, Palaeoecology*, 220(3-4), pp. 311–332. doi: 10.1016/j.palaeo.2005.01.010.

Ghasemi, A. R. and Khalili, D. (2008) "The effect of the North Sea-Caspian pattern (NCP) on winter temperatures in Iran," *Theoretical and Applied Climatology*, 92(1-2), pp. 59–74. doi: 10.1007/s00704-007-0309-1.

Gogou, A., Bouloubassi, I., Lykousis, V. and Arnaboldi, M. (2007) "Organic geochemical evidence of Late Glacial – Holocene climate instability in the North Aegean Sea," *Palaeogeography, Palaeoclimatology Palaeoecology*, 256, pp. 1–20. doi: 10.1016/j.palaeo.2007.08.002.

Gokten, E., Havzoğlu, T. and Şan, Ö. (2001) "Tertiary evolution of the central Menderes Massif based on structural investigations of metamorphics and sedimentary cover rocks between Salihli and Kiraz (western Turkey)," *International Journal of Earth Sciences*, 89(4), pp. 745–756. doi: 10.1007/s005310000099.

Göktürk, O. M. (2011) *Climate in the Eastern Mediterranean through the Holocene inferred from Turkish stalagmites*.

Gradziński, M., Górny, A., Pazdur, A. and Pazdur, M. F. (2003) "Origin of black coloured laminae in speleothems from the Kraków-Wieluń Upland, Poland," *Boreas*, 32(3), pp. 532–542. doi: 10.1080/03009480310003414.

Gradziński, M., Hercman, H., Nowak, M. and Pavel, B. (2007) "Age of Black Coloured Laminae Within Speleothems from Domica Cave and Its Significance for Dating of Prehistoric Human Settlement," *Geochronometria*, 28(1), pp. 39–45. doi: 10.2478/v10003-007-0029-7.

Griffiths, H. I., Schwalb, a. and Stevens, L. R. (2001) "Environmental change in southwestern Iran: the Holocene ostracod fauna of Lake Mirabad," *The Holocene*, 11(6), pp. 757–764. doi: 10.1191/09596830195771.

Grove, A. (2001) "The 'Little Ice Age' and its geomorphological consequences in Mediterranean Europe," *Climatic Chnage*, 48, pp. 121–136.

Hamzeh, M. A., Gharaie, M. H. M., Lahijani, K. A. H., Djamali, M., Harami, M. R. and Beni, A. N. (2016) "Holocene hydrological changes in SE Iran, a key region between Indian Summer Monsoon and Mediterranean winter precipitation zones, as revealed from a lacustrine sequence from Lake Hamoun," *Quaternary International*. Elsevier Ltd, 408, pp. 25–39. doi: 10.1016/j.quaint.2015.11.011.

Hartland, A., Fairchild, I. J., Lead, J. R., Borsato, A., Baker, A., Frisia, S. and Baalousha, M. (2012) "From soil to cave: Transport of trace metals by natural organic matter in karst dripwaters," *Chemical Geology*. Elsevier B.V., 304-305, pp. 68–82. doi: 10.1016/j.chemgeo.2012.01.032.

Hiess, J., Condon, D. J., McLean, N., and Noble, S. R., 2012. $^{238}U/^{235}U$ systematics in terrestrial uranium-bearing minerals. *Science*, 335 (6076), pp. 1610–1614

Hellstrom, J. (2006) "U–Th dating of speleothems with high initial ^{230}Th using stratigraphical constraint," *Quaternary Geochronology*, 1(4), pp. 289–295. doi: 10.1016/j.quageo.2007.01.004.

Hendy, C. (1971) "The isotopic geochemistry of speleothems—I. The calculation of the effects of different modes of formation on the isotopic composition of speleothems and," *Geochimica et cosmochimica Acta*, 35, pp. 801–824.

Heymann, C., Nelle, O., Dörfler, W., Zagana, H., Nowaczyk, N., Xue, J. and Unkel, I. (2013) "Late Glacial to mid-Holocene palaeoclimate development of Southern Greece inferred from the sediment sequence of Lake Stymphalia (NE-Peloponnese)," *Quaternary International*, 302, pp. 42–60. doi: 10.1016/j.quaint.2013.02.014.

Hill, C. and Forti, P. (1997) "Cave minerals of the world", 2nd edition, *Huntsville, ALA: National Speleological Society*, 463 pp.

Hole, F. (1994) "Environmental instabilities and urban origins. Chiefdoms and Early States in the Near East: The Organizational Dynamics of Complexity", *Monographs in World Archaeology,* 18. Prehistory Press

Hori, M., Ishikawa, T., Nagaishi, K., Lin, K., Wang, B.-S., You, C.-F., Shen, C.-C. and Kano, A. (2013) "Prior calcite precipitation and source mixing process influence Sr/Ca, Ba/Ca and ^{87}Sr/^{86}Sr of a stalagmite developed in southwestern Japan during 18.0–4.5ka," *Chemical Geology*. Elsevier B.V., 347, pp. 190–198. doi: 10.1016/j.chemgeo.2013.03.005.

Van der Horn, S. A., van Kolfschoten, T., van der Plicht, J. and Hoek, W. Z. (2015) "The effects of the 8.2 ka event on the natural environment of Tell Sabi Abyad, Syria: Implications for ecosystem

resilience studies," *Quaternary International*. Elsevier Ltd, 378, pp. 111–118. doi: 10.1016/j.quaint.2015.04.005.

Huang, Y., Fairchild, I. J., Borsato, A., Frisia, S., Cassidy, N. J., Mcdermott, F. and Hawkesworth, C. J. (2001) "Seasonal variations in Sr , Mg and P in modern speleothems," pp. 429–448.

Hurrell, J. W. (1995) "Decadal Trends in the North Atlantic Oscillation : Regional Temperatures and Precipitation," *Science*, 269(5224), pp. 676–679. doi: 10.1126/science.269.5224.676.

Imbrie, J., Boyle, E. A., Clemens, S. C., Duffy, A., Howard, W. R., Kukla, G., Kutzbach, J., Martinson, D. G., McIntyre, A., Mix, A. C., Molfino, B., Morley, J. J., Peterson, L. C., Pisias, N. G., Prell, W. L., Raymo, M. E., Shackleton, N. J. and Toggweiler, J. R. (1992) "On the structure and origin of major glaciation cycles 1. linear responses to Milankovitch forcing," *Paleoceanography*, 7(6), pp. 701–738.

Indermühle, A., Stocker, T. F., Joos, F., Fischer, H., Smith, H. J., Wahlen, M., Deck, B., Mastroianni, D., Tschumi, J., Blunier, T., Meyer, R. and Stauffer, B. (1999) "Holocene carbon-cycle dynamics based on CO_2 trapped in ice at Taylor Dome , Antarctica," *Nature*, 398, pp. 121–126. doi: doi:10.1038/18158.

Ivanovich, M. and Alexander, J. (1987) "Application of uranium-series disequilibrium to studies of groundwater mixing in the Harwell region, UK," *Chemical Geology: Isotope Geoscience section*, 66, pp. 279–291. doi: 10.1016/0168-9622(87)90047-9.

Ivanovich, M. and Harmon, R.S. (1982) "Uranium Series Disequilibrium Applications to Environmental Problems", 1st Edition, *Oxford University Press*, pp. 571

Ivanovich, M. and Harmon, R.S. (1992) "Uranium Series Disequilibrium Applications to Environmental Problems", 2nd Edition, *Oxford University Press*.

Ivanovich, M. (1982) "Uranium series disequilibria applications in geochronology", in Ivanovich, M. and Harmon R.S. (eds) Uranium Series Disequilibrium Applications to Environmental Problems, 1st Edition, *Oxford University Press*, pp. 56-79.

Jahns, S. (1993) "On the Holocene vegetation history of the Argive Plain (Peloponnese, southern Greece)," *Vegetation History and Archaeobotany*, 2(4), pp. 187–203. doi: 10.1007/BF00198161.

Jensen, K., Lynch, E. A., Calcote, R. and Hotchkiss, S. C. (2007) "Interpretation of charcoal morphotypes in sediments from Ferry Lake, Wisconsin, USA: do different plant fuel sources produce distinctive charcoal morphotypes?," *The Holocene*, 17(7), pp. 907–915. doi: 10.1177/0959683607082405.

Jex, C. N., Baker, A., Eden, J. M., Eastwood, W. J., Fairchild, I. J., Leng, M. J., Thomas, L. and Sloane, H. J. (2011) "A 500yr speleothem-derived reconstruction of late autumn–winter precipitation, northeast Turkey," *Quaternary Research*. University of Washington, 75(3), pp. 399–405. doi: 10.1016/j.yqres.2011.01.005.

Jex, C. N., Baker, A., Fairchild, I. J., Eastwood, W. J., Leng, M. J., Sloane, H. J., Thomas, L. and Bekaroğlu, E. (2010) "Calibration of speleothem $\delta^{18}O$ with instrumental climate records from Turkey," *Global and Planetary Change*, 71(3-4), pp. 207–217. doi: 10.1016/j.gloplacha.2009.08.004.

Johnson, K., Hu, C., Belshaw, N. and Henderson, G. (2006) "Seasonal trace-element and stable-isotope variations in a Chinese speleothem: The potential for high-resolution paleomonsoon reconstruction," *Earth and Planetary Science Letters*, 244(1-2), pp. 394–407. doi: 10.1016/j.epsl.2006.01.064.

Jones, M. D., Djamali, M., Holmes, J., Weeks, L., Leng, M. J., Lashkari, A., Alamdari, K., Noorollahi, D., Thomas, L. and Metcalfe, S. E. (2015) "Human impact on the hydroenvironment of Lake Parishan, SW Iran, through the late-Holocene," *The Holocene Special Issue*, 25(10), pp. 1651–1661. doi: 10.1177/0959683615594242.

Jones, M. D., Roberts, C. N., Leng, M. J. and Türkeş, M. (2006) "A high-resolution late Holocene lake isotope record from Turkey and links to North Atlantic and monsoon climate," *Geology*, 34(5), p. 361. doi: 10.1130/G22407.1.

Jones, S. J., Arzani, N. and Allen, M. B. (2014) "Tectonic and climatic controls on fan systems: The Kohrud mountain belt, Central Iran," *Sedimentary Geology*. Elsevier B.V., 302, pp. 29–43. doi: 10.1016/j.sedgeo.2013.12.008.

Jung, R. and Weninger, B. P. (2015) "Archeological and environmental impact of the 4.2 ka calBP event in the central and eastern Mediterranean," in *2200 BC – A climatic breakdown as a cause for the collapse of the old world?*, pp. 205–234.

Kadioğlu, M. (2000) "Regional variability of seasonal precipitation over Turkey," *International Journal of Climatology*, 1760, pp. 1743–1760.

Kambezidis, H. D., Larissi, I. K., Nastos, P. T. and Paliatsos, A. G. (2010) "Spatial variability and trends of the rain intensity over Greece," *Advances in Geosciences*, 26, pp. 65–69. doi: 10.5194/adgeo-26-65-2010.

Kaniewski, D., Van Campo, E., Paulissen, E., Weiss, H., Bakker, J., Rossignol, I. and Van Lerberghe, K. (2011) "The medieval climate anomaly and the little Ice Age in coastal Syria inferred from pollen-derived palaeoclimatic patterns," *Global and Planetary Change*. Elsevier B.V., 78(3-4), pp. 178–187. doi: 10.1016/j.gloplacha.2011.06.010.

Kaniewski, D., Paulissen, E., Van Campo, E., Al-Maqdissi, M., Bretschneider, J. and Van Lerberghe, K. (2008) "Middle East coastal ecosystem response to middle-to-late Holocene abrupt climate changes," *PNAS*, 105(37), pp. 13941–13946. doi: 10.1073/pnas.0803533105.

Kaniewski, D., Paulissen, E., Van Campo, E., Weiss, H., Otto, T., Bretschneider, J. and Van Lerberghe, K. (2010) "Late second–early first millennium BC abrupt climate changes in coastal Syria and their possible significance for the history of the Eastern Mediterranean," *Quaternary Research*. University of Washington, 74(2), pp. 207–215. doi: 10.1016/j.yqres.2010.07.010.

Karaca, M., Deniz, A. and Tayanç, M. (2000) "Cyclone track variability over Turkey in association with regional climate," *International Journal of Climatology*, 1236, pp. 1225–1236.

Kaufman, A., Wasserburg, G., Porcelli, D., Bar-Matthews, M., Ayalon, A. and Halicz, L. (1998) "U-Th isotope systematics from the Soreq cave, Israel and climatic correlations," *Earth and Planetary Science Letters*, 156(3-4), pp. 141–155. doi: 10.1016/S0012-821X(98)00002-8.

Kaufmann, G. (2003) "Stalagmite growth and palaeo-climate: the numerical perspective," *Earth and Planetary Science Letters*, 214(1-2), pp. 251–266. doi: 10.1016/S0012-821X(03)00369-8.

Keeling, C. D., Bacastow, R. B., Carter, A. F., Piper, S. C., Whorf, T. P., Heimann, M., Mook, W. G. and Roeloffzen, H. (1989) "A three-dimensional model of atmospheric CO_2 transport based on observed winds: 1. Analysis of observational data", in Aspects of Climate Variability in the Pacific and the Western Americas, *American Geophysical Union, Washington, D. C.*, pp. 165-237. doi: 10.1029/GM055p0165

Kehl, M. (2009) "Quaternary climate change in Iran – the state of knowledge," *Erdkunde*, 63(1), pp. 1–17. doi: 10.3112/erdkunde.2009.01.01.

Kendall, A. and Broughton, P. (1978) "Origin of fabrics in speleothems composed of columnar calcite crystals," *Journal of Sedimentary Petrography*, 48(2), pp. 519–538. doi: 10.1306/212F74C3-2B24-11D7-8648000102C1865D.

Kendall, A. C. and Broughton, P. L. (1977) "Disscusion Calcite and Aragonite fabrics, Carlsbad Caverns: by R.L. Folk and Riccardo Assereto.," *Journal of Sedimentary Research*, 47(3), pp. 1397–1400.

Kim, S.-T. and O'Neil, J. R. (1997) "Equilibrium and nonequilibrium oxygen isotope effects in synthetic carbonates," *Geochimica et Cosmochimica Acta*, 61(16), pp. 3461–3475. doi: 10.1016/S0016-7037(97)00169-5.

Kotthoff, U., Pross, J., Müller, U. C., Peyron, O., Schmiedl, G., Schulz, H. and Bordon, A. (2008a) "Climate dynamics in the borderlands of the Aegean Sea during formation of sapropel S1 deduced from a marine pollen record," *Quaternary Science Reviews*, 27(7-8), pp. 832–845. doi: 10.1016/j.quascirev.2007.12.001.

Kotthoff, U., Müller, U. C., Pross, J., Schmiedl, G., Lawson, I. T., van de Schootbrugge, B. and Schulz, H. (2008b) "Lateglacial and Holocene vegetation dynamics in the Aegean region: an integrated view based on pollen data from marine and terrestrial archives," 18(7), pp. 1019–1032.

Kouli, K., Gogou, A., Bouloubassi, I., Triantaphyllou, M. V, Ioakim, C., Katsouras, G., Roussakis, G. and Lykousis, V. (2012) "Late postglacial paleoenvironmental change in the northeastern Mediterranean region: Combined palynological and molecular biomarker evidence," *Quaternary International*. Elsevier Ltd, 261, pp. 118–127. doi: 10.1016/j.quaint.2011.10.036.

Krichak, S. O. and Alpert, P. (2005) "Signatures of the NAO in the atmospheric circulation during wet winter months over the Mediterranean region," *Theoretical and Applied Climatology*, 82(1-2), pp. 27–39. doi: 10.1007/s00704-004-0119-7.

Kuniholm, P. I. (1990) "Archaeological Evidence and Non-Evidence for Climatic Change," *Philosophical Transactions of the Royal Society A: Mathematical, Physical and Engineering Sciences*, 330(1615), pp. 645–655. doi: 10.1098/rsta.1990.0045.

Kunt, K., Yağmur, E. and Elverici, M. (2008) "The cave dwelling arthropods of Dim cave (Turkey: Antalya: Alanya)," *Munis Entomology & Zoology*, 3(2), pp. 682–690.

Kutiel, H. and Benaroch, Y. (2002) "North Sea-Caspian Pattern (NCP) - an upper level atmospheric teleconnection affecting the Eastern Mediterranean: Identification and definition," *Theoretical and Applied Climatology*, 71(1), pp. 17–28. doi: 10.1007/s704-002-8205-x.

Kutiel, H., Maheras, P., Türkeş, M. and Paz, S. (2002) "North Sea - Caspian Pattern (NCP) an upper level atmospheric teleconnection affecting the eastern Mediterranean - implications on the regional climate," *Theoretical and Applied Climatology*, 72(3-4), pp. 173–192. doi: 10.1007/s00704-002-0674-8.

Lachniet, M. S. (2009) "Climatic and environmental controls on speleothem oxygen-isotope values," *Quaternary Science Reviews*. Elsevier Ltd, 28(5-6), pp. 412–432. doi: 10.1016/j.quascirev.2008.10.021.

Lachniet, M. S., Bernal, J. P., Asmerom, Y. and Polyak, V. (2012) "Uranium loss and aragonite–calcite age discordance in a calcitized aragonite stalagmite," *Quaternary Geochronology*. Elsevier B.V, 14, pp. 26–37. doi: 10.1016/j.quageo.2012.08.003.

LaFlamme, B. and Murray, J. (1987) "Solid/solution interaction: The effect of carbonate alkalinity on adsorbed thorium," *Geochimica et Cosmochimica Acta*, 5(2), pp. 243–250. doi: 10.1016/0016-7037(87)90235-3.

Lamb, P. J. and Peppler, R. A. (1987) "North Atlantic Oscillation: Concept and Application," *Bulletin of the American Meteorological Society*, 68, pp. 1218–1225. doi: 10.1175/1520-0477.

Lambeck, K., Rouby, H., Purcell, A., Sun, Y. and Sambridge, M. (2014) "Sea level and global ice volumes from the Last Glacial Maximum to the Holocene," *Preceedings of the National Acedemy of Sciences*, 111(43), pp. 15296–15303. doi: 10.1073/pnas.1411762111.

Langmuir, D. and Herman, J. (1980) "The mobility of thorium in natural waters at low temperatures," *Geochimica et Cosmochimica Acta*, 44(11), pp. 1753–1766. doi: 10.1016/0016-7037(80)90226-4.

Laserna, J. (2006) "Raman Spectroscopy: Introduction", *Encyclopedia of Analytical Chemistry,* Supplementary vol 3. doi:10.1002/9780470027318.a6401

Laumanns no date, www.caving-in-iran.org

Lauritzen, S.-E. and Lundberg, J. (1999) "Speleothems and climate: a special issue of The Holocene," *The Holocene*, 9(6), pp. 643–647. doi: 10.1191/095968399666229065.

Lazarova, M., Koutsios, A. and Kontopoulos, N. (2012) "Holocene vegetation history of the Kotihi lagoon (northwest Peloponnesus, Greece)," *Quaternary International*. Elsevier Ltd, 261, pp. 138–145. doi: 10.1016/j.quaint.2009.10.036.

Leng, M. J. and Marshall, J. D. (2004) "Palaeoclimate interpretation of stable isotope data from lake sediment archives," *Quaternary Science Reviews*, 23(7-8), pp. 811–831. doi: 10.1016/j.quascirev.2003.06.012.

Lin, J., Broecker, W., Anderson, R., Hemming, S., Rubenstone, J. L. and Bonani, G. (1996) "New [230]Th/U and ^{14}C ages from Lake Lahontan carbonates, Nevada, USA, and a discussion of the origin of initial thorium," *Geochimica et Cosmochimica Acta*, 60(15), pp. 2817–2832. doi: 10.1016/0016-7037(96)00136-6.

Lionello, P., Boscolo, R., Alpert, P., Artale, V., Li, L., Luterbacher, J., May, W., Trigo, R., Tsimplis, M., Ulbrich, U. and Xoplaki, E. (2006) "The Mediterranean Climate : An Overview of the Main Characteristics and Issues," *Developments in Earth and Environmental Sciences*, 4(1), pp. 1–26.

Van Loon, H. and Rogers, J. C. (1978) "The seesaw in winter temperatures between Greenland and Northern Europe Part I: General description," *Monthly Weather Review*, 106, pp. 296–310.

Ludwig, K. R. (2003) "Mathematical–Statistical Treatment of Data and Error for 230Th/U Geochronology," *Reviews in Mineralogy and Geochemistry*, 52, pp. 631–656.

Ludwig, K. R. (2012) "User's Manual for Isoplot 3.75 A Geochronological Toolkit for Microsoft Excel Berkeley Geochronology Center," *Berkeley Geochronological Center Special Publication*, 5, pp. 1–75.

Maheras, P., Tolika, K., Anagnostopoulou, C., Vafiadis, M., Patrikas, I. and Flocas, H. (2004) "On the relationships between circulation types and changes in rainfall variability in Greece," *International Journal of Climatology*, 24(13), pp. 1695–1712. doi: 10.1002/joc.1088.

Maheras, P., Xoplaki, E. and Kutiel, H. (1999) "Wet and Dry Monthly Anomalies Across the Mediterranean Basin and their Relationship with Circulation, 1860 - 1990," *Theoretical and Applied Climatology*, 64(3/4), pp. 189–199. doi: 10.1007/s007040050122.

Mann, M., Zhang, Z., Rutherford, S., Bradley, R. S., Hughes, M. K., Shindell, D., Ammann, C., Faluvegi, G. and Ni, F. (2009) "Global signatures and dynamical origins of the Little Ice Age and Medieval Climate Anomaly," *Science*, 326(November), pp. 1256–1260.

Marino, G., Rohling, E. J., Sangiorgi, F., Hayes, A., Casford, J. L., Lotter, A. F., Kucera, M. and Brinkhuis, H. (2009) "Early and middle Holocene in the Aegean Sea: interplay between high and low latitude climate variability," *Quaternary Science Reviews*. Elsevier Ltd, 28(27-28), pp. 3246–3262. doi: 10.1016/j.quascirev.2009.08.011.

Martín-García, R., Martín-Pérez, A. and Alonso-Zarza, A. M. (2011) "Weathering of host rock and corrosion over speleothems in Castañar cave, Spain: an example of a complex meteoric environment," *Carbonates and Evaporites*, 26(1), pp. 83–94. doi: 10.1007/s13146-010-0039-9.

Mason, J. E. (2009) "Palaeoclimatic Records from Speleothems in the Eastern Mediterranean," *Thesis*, pp. 1–234.

Mattey, D., Lowry, D., Duffet, J., Fisher, R., Hodge, E. and Frisia, S. (2008a) "A 53 year seasonally resolved oxygen and carbon isotope record from a modern Gibraltar speleothem: Reconstructed drip water and relationship to local precipitation," *Earth and Planetary Science Letters*, 269(1-2), pp. 80–95. doi: 10.1016/j.epsl.2008.01.051.

Mattey, D., Latin, J. P. and Ainsworth, M. (2008b) "Cave monitoring and calibration of a δ 18 O – climate transfer function for a Gibraltar speleothem," *PAGES*, 16(3), pp. 3–5.

Mattey, D. P., Fairchild, I. J., Atkinson, T. C., Latin, J.-P., Ainsworth, M. and Durell, R. (2010) "Seasonal microclimate control of calcite fabrics, stable isotopes and trace elements in modern speleothem from St Michaels Cave, Gibraltar," *Geological Society, London, Special Publications*, 336(1), pp. 323–344. doi: 10.1144/SP336.17.

Mayewski, P. A., Rohling, E. E., Curt Stager, J., Karlén, W., Maasch, K. A., David Meeker, L., Meyerson, E. A., Gasse, F., van Kreveld, S., Holmgren, K., Lee-Thorp, J., Rosqvist, G., Rack, F., Staubwasser, M., Schneider, R. R. and Steig, E. J. (2004) "Holocene climate variability," *Quaternary Research*, 62(3), pp. 243–255. doi: 10.1016/j.yqres.2004.07.001.

McDermott, F. (2004) "Palaeo-climate reconstruction from stable isotope variations in speleothems: a review," *Quaternary Science Reviews*, 23(7-8), pp. 901–918. doi: 10.1016/j.quascirev.2003.06.021.

McDermott, F., Frisia, S., Huang, Y., Longinelli, A., Spiro, B., Heaton, T. H. E., Hawkesworth, C. J., Borsato, A., Keppens, E., Fairchild, I. J., van der Borg, K., Verheyden, S. and Selmo, E. (1999) "Holocene climate variability in Europe: Evidence from δ18O, textural and extension-rate

variations in three speleothems," *Quaternary Science Reviews*, 18(8-9), pp. 1021–1038. doi: 10.1016/S0277-3791(98)00107-3.

McDermott, F., Schwarcz, H. P. and Rowe, P. J. (2006) "Isotopes in Speleothems," in Leng, M. J. (ed.) *Isotopes in Palaeoenvironmental Research*, pp. 185–226.

McDonald, J., Drysdale, R., Hill, D., Chisari, R. and Wong, H. (2007) "The hydrochemical response of cave drip waters to sub-annual and inter-annual climate variability, Wombeyan Caves, SE Australia," *Chemical Geology*, 244, pp. 605–623. doi: 10.1016/j.chemgeo.2007.07.007.

McMillan, E. A., Fairchild, I. J., Frisia, S., Borsato, A. and McDermott, F. (2005) "Annual trace element cycles in calcite-aragonite speleothems: evidence of drought in the western Mediterranean 1200-1100 yr BP," *Journal of Quaternary Science*, 20(5), pp. 423–433. doi: 10.1002/jqs.943.

Mehterian, S., Pourmand, A., Shari, A., Lahijani, H. A. K., Naderi, M. and Swart, P. K. (2017) "Speleothem records of glacial/ interglacial climate from Iran forewarn of future Water Availability in the interior of the Middle East," *Quaternary Science Reviews*, 164, pp. 187–198. doi: 10.1016/j.quascirev.2017.03.028.

De Menocal, P. . (2001) "Cultural Responses to Climate Change During the Late Holocene," *Science*, 667(5517). doi: 10.1126/science.1059287.

Mercone, D., Thomson, J., Abu-Zied, R. H., Croudace, I. W. and Rohling, E. J. (2001) "High-resolution geochemical and micropalaeontological profiling of the most recent eastern Mediterranean sapropel," *Marine Geology*, 177(1), pp. 25–44.

Mickler, P. J., Banner, J. L., Stern, L., Asmerom, Y., Edwards, R. L. and Ito, E. (2004) "Stable isotope variations in modern tropical speleothems: Evaluating equilibrium vs. kinetic isotope effects," *Geochimica et Cosmochimica Acta*, 68(21), pp. 4381–4393. doi: 10.1016/j.gca.2004.02.012.

Mickler, P. J., Stern, L. A. and Banner, J. L. (2006) "Large kinetic isotope effects in modern speleothems," *Geological Society of America Bulletin*, 118(1-2), pp. 65–81. doi: 10.1130/B25698.1.

Migowski, C., Stein, M., Prasad, S., Negendank, J. F. W. and Agnon, A. (2006) "Holocene climate variability and cultural evolution in the Near East from the Dead Sea sedimentary record," *Quaternary Research*, 66(3), pp. 421–431. doi: 10.1016/j.yqres.2006.06.010.

Miller, G., Mangan, J., Pollard, D., Thompson, S., Felzer, B. and Magee, J. (2005) "Sensitivity of the Australian Monsoon to insolation and vegetation: Implications for human impact on continental moisture balance," *Geology*, 33(1), p. 65. doi: 10.1130/G21033.1.

Modarres, R. and Sarhadi, A. (2011) "Statistically-based regionalization of rainfall climates of Iran," *Global and Planetary Change*. Elsevier B.V., 75(1-2), pp. 67–75. doi: 10.1016/j.gloplacha.2010.10.009.

Morse, J. W. and Bender, M. L. (1990) "Partition coefficients in calcite: Examination of factors influencing the validity of experimental results and their application to natural systems," *Chemical Geology*, 82, pp. 265–277.

Muñoz, A., Bartolomé, M., Muñoz, A., Sancho, C., Moreno, A., Hellstrom, J. C., Osácar, M. C. and Cacho, I. (2015) "Solar influence and hydrological variability during the Holocene from a

speleothem annual record (Molinos Cave , NE Spain)," *Terra Nova*, 27(4), pp. 300–311. doi: 10.1111/ter.12160.

Muñoz-García, M. B., Cruz, J., Martín-Chivelet, J., Ortega, A. I. and Turrero, M. J. (2016) "Comparison of speleothem fabrics and microstratigraphic stacking patterns in calcite stalagmites as indicators of paleoenvironmental change," *Quaternary International*, 407, pp. 74–85. doi: 10.1016/j.quaint.2016.02.036.

Muñoz-García, M. B., López-Arce, P., Fernández-Valle, M. E., Martín-Chivelet, J. and Fort, R. (2012) "Porosity and hydric behavior of typical calcite microfabrics in stalagmites," *Sedimentary Geology*. Elsevier B.V., 265-266, pp. 72–86. doi: 10.1016/j.sedgeo.2012.03.016.

Musgrove, M. and Banner, J. L. (2004) "Controls on the spatial and temporal variability of vadose dripwater geochemistry : Edwards Aquifer, central Texas," *Geochemica et Cosmochemica Acta*, 68(5), pp. 1007–1020. doi: 10.1016/j.gca.2003.08.014.

Nagra, G., Treble, P. C., Andersen, M. S., Fairchild, I. J., Coleborn, K. and Baker, A. (2016) "A post-wildfire response in cave dripwater chemistry," *Hydrology and Earth System Science*, 20, pp. 2745–2758. doi: 10.5194/hess-20-2745-2016.

Nastos, P. T. and Zerefos, C. S. (2007) "On extreme daily precipitation totals at Athens, Greece," *Advances in Geosciences*, 10, pp. 59–66.

Neff, U., Burns, S. J., Mangini, A, Mudelsee, M., Fleitmann, D. and Matter, A (2001) "Strong coherence between solar variability and the monsoon in Oman between 9 and 6 kyr ago," *Nature*, 411(6835), pp. 290–3. doi: 10.1038/35077048.

Ocakoğlu, F., Osman, K., Ömer Yilmaz, İ., Açikalin, S., Eray, C., Tunoğlu, C. and Leroy, S. A. G. (2013) "Early to Mid-Holocene Lake level and temperature records from the terraces of Lake Sünnet in NW Turkey," *Palaeogeography, Palaeoclimatology Palaeoecology*, 369, pp. 175–184. doi: 10.1016/j.palaeo.2012.10.017.

Olsen, J., Anderson, N. J. and Knudsen, M. F. (2012) "Variability of the North Atlantic Oscillation over the past 5,200 years," *Nature Geoscience*. Nature Publishing Group, 5(11), pp. 808–812. doi: 10.1038/ngeo1589.

Orland, I. J., Bar-Matthews, M., Ayalon, A., Matthews, A., Kozdon, R., Ushikubo, T. and Valley, J. W. (2012) "Seasonal resolution of Eastern Mediterranean climate change since 34ka from a Soreq Cave speleothem," *Geochimica et Cosmochimica Acta*. Elsevier Ltd, 89, pp. 240–255. doi: 10.1016/j.gca.2012.04.035.

Ortega, R., Maire, R., Devès, G. and Quinif, Y. (2005) "High-resolution mapping of uranium and other trace elements in recrystallized aragonite–calcite speleothems from caves in the Pyrenees (France): Implication for U-series dating," *Earth and Planetary Science Letters*, 237(3-4), pp. 911–923. doi: 10.1016/j.epsl.2005.06.045.

Östhols, E., Bruno, J. and Grenthe, I. (1994) "On the influence of carbonate on mineral dissolution: III. The solubility of microcrystalline $ThO2$ in CO_2-H_2O media," *Geochimica et Cosmochimica Acta*, 58(2), pp. 613–623. doi: 10.1016/0016-7037(94)90492-8.

Panagiotaras, D., Papoulis, D., Kontopoulos, N. and Avramidis, P. (2012) "Geochemical processes and sedimentological characteristics of Holocene lagoon deposits, Alikes Lagoon, Zakynthos Island, western Greece," *Geological Journal*, 47(4), pp. 372–387. doi: 10.1002/gj.1339.

Panagiotopoulos, F., Shahgedanova, M., Hannachi, A. and Stephenson, D. B. (2005) "Observed Trends and Teleconnections of the Siberian High: A Recently Declining Center of Action," *Journal of Climate*, 18, pp. 1411–1422. doi: 10.1175/JCLI3352.1.

Panagiotopoulos, K., Aufgebauer, A., Schäbitz, F. and Wagner, B. (2013) "Vegetation and climate history of the Lake Prespa region since the Lateglacial," *Quaternary International*. Elsevier Ltd, 293, pp. 157–169. doi: 10.1016/j.quaint.2012.05.048.

Perrin, C., Prestimonaco, L., Servelle, G., Tilhac, R., Maury, M. and Cabrol, P. (2014) "Aragonite-Calcite Speleothems: Identifying Original and Diagenetic Features," *Journal of Sedimentary Research*, 84(4), pp. 245–269. doi: 10.2110/jsr.2014.17.

Peyron, O., Goring, S., Dormoy, I., Kotthoff, U., Pross, J., de Beaulieu, J.-L., Drescher-Schneider, R., Vannière, B. and Magny, M. (2011) "Holocene seasonality changes in the central Mediterranean region reconstructed from the pollen sequences of Lake Accesa (Italy) and Tenaghi Philippon (Greece)," *The Holocene Special Issue*, 21(1), pp. 131–146. doi: 10.1177/0959683610384162.

Porcelli, D. and Swarzenski, P.W. (2003) "The Behaviour of U- and Th-series Nuclides in Groundwater", in Bourdon, B., Henderson, G.M., Lundstrom, C.C., and Turner S.P. (eds) Uranium Series Geochemistry, *Reviews in Mineralogy and Geochemistry*, 52, pp. 317-363.

Power, M. J., Marlon, J., Ortiz, N., Bartlein, P. J., Harrison, S. P., Mayle, F. E., Ballouche, A., Bradshaw, R. H. W., Carcaillet, C., Cordova, C., Mooney, S., Moreno, P. I., Prentice, I. C., Thonicke, K., Tinner, W., Whitlock, C., Zhang, Y., Zhao, Y., Ali, A. A., Anderson, R. S., Beer, R., Behling, H., Briles, C., Brown, K. J., Brunelle, A., Bush, M., Camill, P., Chu, G. Q., Clark, J., Colombaroli, D., Connor, S., Daniau, A.-L., Daniels, M., Dodson, J., Doughty, E., Edwards, M. E., Finsinger, W., Foster, D., Frechette, J., Gaillard, M.-J., Gavin, D. G., Gobet, E., Haberle, S., Hallett, D. J., Higuera, P., Hope, G., Horn, S., Inoue, J., Kaltenrieder, P., Kennedy, L., Kong, Z. C., Larsen, C., Long, C. J., Lynch, J., Lynch, E. A., McGlone, M., Meeks, S., Mensing, S., Meyer, G., Minckley, T., Mohr, J., Nelson, D. M., New, J., Newnham, R., Noti, R., Oswald, W., Pierce, J., Richard, P. J. H., Rowe, C., Sanchez Goñi, M. F., Shuman, B. N., Takahara, H., Toney, J., Turney, C., Urrego-Sanchez, D. H., Umbanhowar, C., Vandergoes, M., Vanniere, B., Vescovi, E., Walsh, M., Wang, X., Williams, N., Wilmshurst, J. and Zhang, J. H. (2008) "Changes in fire regimes since the Last Glacial Maximum: an assessment based on a global synthesis and analysis of charcoal data," *Climate Dynamics*, 30(7-8), pp. 887–907. doi: 10.1007/s00382-007-0334-x.

Proctor, C. J., Baker, A., Barnes, W. L. and Gilmour, M. A. (2000) "A thousand year speleothem proxy record of North Atlantic climate from Scotland," *Climate Dynamics*, 16(10-11), pp. 815–820. doi: 10.1007/s003820000077.

Pross, J., Kotthoff, U., Müller, U. C., Peyron, O., Dormoy, I., Schmiedl, G., Kalaitzidis, S. and Smith, A. M. (2009) "Massive perturbation in terrestrial ecosystems of the Eastern Mediterranean region associated with the 8.2 kyr B.P. climatic event," *Geology*, 37(10), pp. 887–890. doi: 10.1130/G25739A.1.

Rader, L. F., and Grimaldi, F. S. (1961) "Methods of chemical analysis for selected minor elements in Pierre shale", *U.S. Geological Survey Professional Paper,* 391-A.

Raicich, F., Pinardi, N. and Navarra, A. (2003) "Teleconnections between Indian monsoon and Sahel rainfall and the Mediterranean," *International Journal of Climatology*, 23(2), pp. 173–186. doi: 10.1002/joc.862.

Railsback, L. B., Akers, P. D., Wang, L., Holdridge, G. A. and Voarintsoa, N. R. (2013) "Layer-bounding surfaces in stalagmites as keys to better paleoclimatological histories and chronologies," 42(September), pp. 167–180.

Railsback, L. B., Liang, F., Vidal Romaní, J. R., Grandal-d'Anglade, A., Vaqueiro Rodríguez, M., Santos Fidalgo, L., Fernández Mosquera, D., Cheng, H. and Edwards, R. L. (2011) "Petrographic and isotopic evidence for Holocene long-term climate change and shorter-term environmental shifts from a stalagmite from the Serra do Courel of northwestern Spain, and implications for climatic history across Europe and the Mediterranean," *Palaeogeography, Palaeoclimatology, Palaeoecology*, 305(1-4), pp. 172–184. doi: 10.1016/j.palaeo.2011.02.030.

Railsback, L. B., Xiao, H., Liang, F., Akers, P. D., Brook, G. A., Dennis, W. M., Lanier, T. E., Tan, M., Cheng, H. and Edwards, R. L. (2014) "A stalagmite record of abrupt climate change and possible Westerlies-derived atmospheric precipitation during the Penultimate Glacial Maximum in northern China," *Palaeogeography, Palaeoclimatology, Palaeoecology*. Elsevier B.V., 393, pp. 30–44. doi: 10.1016/j.palaeo.2013.10.013.

Railsback, L., Brook, G., Chen, J., Kalin, R. and Fleisher, C. (1994) "Environmental controls on the petrology of a late Holocene speleothem from Botswana with annual layers of aragonite and calcite," *Journal of Sedimentary Research*, A64(l), pp. 147–155. doi: 10.1306/D4267D39-2B26-11D7-8648000102C1865D.

Railsback, L., Dabous, A. A., Osmond, J. K. and Fleisher, C. (2002) "Petrographic and geochemical screening of speleothems for U-series dating: an example from recrystallized speleothems from Wadi Sannur Cavern, Egypt," *Journal of Cave and Karst Studies*, 64, pp. 108–116.

Rasmussen, S. O., Andersen, K. K., Svensson, A. M., Steffensen, J. P., Vinther, B. M., Clausen, H. B., Siggard-Anderson, M. L., Johnsen, S. J., Larsen, L. B., Dahl-Jenson, D., Bigler, M., Röthlisberger, R., Fischer, H., Goto-Azuma, K., Hansson, M. E. and Ruth, U. (2006) "A new Greenland ice core chronology for the last glacial termination," *Journal of Geophysical Research*, 111(D6), pp. 1–16. doi: 10.1029/2005JD006079.

Reeder, R., Nugent, M., Tait, C., Morris, D., Heald, S., Beck, K., Hess, W. and Lanzirotti, A. (2001) "Coprecipitation of uranium (VI) with calcite: XAFS, micro-XAS, and luminescence characterization," *Geochimica et Cosmochimica Acta*, 65(20), pp. 3491–3503.

Regattieri, E., Zanchetta, G., Drysdale, R. N., Isola, I., Hellstrom, J. C. and Dallai, L. (2014) "Lateglacial to Holocene trace element record (Ba, Mg, Sr) from Corchia Cave (Apuan Alps, central Italy): paleoenvironmental implications," *Journal of Quaternary Science*, 29(4), pp. 381–392. doi: 10.1002/jqs.2712.

Richards, D.A. and Dorale, J.A (2003) "Uranium –series Chronology and Environmental Applications of Speleothems", in Bourdon, B., Henderson, G.M., Lundstrom, C.C., and Turner S.P. (eds) Uranium Series Geochemistry, *Reviews in Mineralogy and Geochemistry*, 52, pp. 407-461.

Riechelmann, D. F. C., Deininger, M., Scholz, D., Riechelmann, S., Schröder-Ritzrau, A., Spötl, C., Richter, D. K., Mangini, A. and Immenhauser, A. (2013) "Disequilibrium carbon and oxygen isotope fractionation in recent cave calcite: Comparison of cave precipitates and model data," *Geochimica et Cosmochimica Acta*, 103, pp. 232–244. doi: 10.1016/j.gca.2012.11.002.

Riechelmann, S., Schröder-Ritzrau, A., Wassenburg, J. A., Schreuer, J., Richter, D. K., Riechelmann, D. F. C., Terente, M., Constantin, S., Mangini, A. and Immenhauser, A. (2014) "Physicochemical characteristics of drip waters: Influence on mineralogy and crystal morphology of recent cave

carbonate precipitates," *Geochimica et Cosmochimica Acta*, 145, pp. 13–29. doi: 10.1016/j.gca.2014.09.019.

Riehl, S. (2009) "Archaeobotanical evidence for the inter relationship of agricultural decision-making and climate change in the ancient Near East", *Quaternary International,* 197, pp. 93–114

De Rijk, S., Hayes, A. and Rohling, E. J. (1999) "Eastern Mediterranean sapropel S1 interruption : an expression of the onset of climatic deterioration around 7 ka BP," *Marine Geology*, 153(1-4), pp. 337–343.

Roberts, M. S., Smart, P. L. and Baker, A. (1998) "Annual trace element variations in a Holocene speleothem," *Earth and Planetary Science Letters*, 154(1-4), pp. 237–246. doi: 10.1016/S0012-821X(97)00116-7.

Robinson, S. A., Black, S., Sellwood, B. W. and Valdes, P. J. (2006) "A review of palaeoclimates and palaeoenvironments in the Levant and Eastern Mediterranean from 25,000 to 5000 years BP: setting the environmental background for the evolution of human civilisation," *Quaternary Science Reviews*, 25(13-14), pp. 1517–1541. doi: 10.1016/j.quascirev.2006.02.006.

Rodwell, M. J. and Hoskins, B. J. (1996) "Monsoons and the dynamics of deserts," *Quarterly Journal of the Royal Meteorological Society*, 122(534 B), pp. 1385–1404.

Rogers, J. C. (1984) "The association between the North Atlantic Oscillation and the Southern Oscillation in the Northern Hemisphere," *Monthly Weather Review*, 112, pp. 1999–2015.

Rohling, E. J., Jorissen, F. J. and De Stigter, H. C. (1997) "200 Year interruption of Holocene sapropel formation in the Adriatic Sea," *Journal of Micropalaeontology*, 16, pp. 97–108. doi: 10.1144/jm.16.2.97.

Rohling, E. J., Marino, G. and Grant, K. M. (2015) "Mediterranean climate and oceanography, and the periodic development of anoxic events (sapropels)," *Earth-Science Reviews*. Elsevier B.V., 143, pp. 62–97. doi: 10.1016/j.earscirev.2015.01.008.

Rohling, E. J., Mayewski, P. A., Abu-Zied, R. H., Casfor, J. S. L. and Hayes, A. (2002) "Holocene atmosphere-ocean interactions: records from Greenland and the Aegean Sea," *Climate Dynamics*, 18(7), pp. 587–593. doi: 10.1007/s00382-001-0194-8.

Rohling, E. J. and Pälike, H. (2005) "Centennial-scale climate cooling with a sudden cold event around 8,200 years ago," *Nature*, 434(975-979). doi: 10.1038/nature03421.

Romanov, D., Kaufmann, G. and Dreybrodt, W. (2008) "Modeling stalagmite growth by first principles of chemistry and physics of calcite precipitation," *Geochimica et Cosmochimica Acta*, 72(2), pp. 423–437. doi: 10.1016/j.gca.2007.09.038.

Rossi, C. and Lozano, R. P. (2016) "Hydrochemical controls on aragonite versus calcite precipitation in cave dripwaters," *Geochimica et Cosmochimica Acta*. Elsevier Ltd, 192, pp. 70–96. doi: 10.1016/j.gca.2016.07.021.

Rossignol-Strick, M. (1985) "Mediterranean Quaternary Sapropels, an immediate response of the African Monsoon to variation of insolation," *Palaeogeography, Palaeoclimatology Palaeoecology*, 49(3), pp. 237–263. doi: 10.1016/0031-0182(85)90056-2.

Rowe, P. J., Mason, J. E., Andrews, J. E., Marca, A. D., Thomas, L., van Calsteren, P., Jex, C. N., Vonhof, H. B. and Al-Omari, S. (2012) "Speleothem isotopic evidence of winter rainfall variability in northeast Turkey between 77 and 6 ka," *Quaternary Science Reviews*. Elsevier Ltd, 45, pp. 60–72. doi: 10.1016/j.quascirev.2012.04.013.

Ruan, J., Kherbouche, F., Genty, D., Blamart, D., Cheng, H., Dewilde, F., Hachi, S., Edwards, R. L., Régnier, E. and Michelot, J.-L. (2016) "Evidence of a prolonged drought ca. 4200 yr BP correlated with prehistoric settlement abandonment from the Gueldaman GLD1 Cave, Northern Algeria," *Climate of the Past*, 12, pp. 1–14. doi: 10.5194/cp-12-1-2016.

Rutlidge, H., Baker, A., Marjo, C. E., Andersen, M. S., Graham, P. W., Cuthbert, M. O., Rau, G. C., Roshan, H., Markowska, M., Mariethoz, G. and Jex, C. N. (2014) "Dripwater organic matter and trace element geochemistry in a semi-arid karst environment: Implications for speleothem paleoclimatology," *Geochimica et Cosmochimica Acta*. Elsevier Ltd, 135(1), pp. 217–230. doi: 10.1016/j.gca.2014.03.036.

Sadezky, A., Muckenhuber, H., Grothe, H., Niessner, R. and Pöschl, U. (2005) "Raman microspectroscopy of soot and related carbonaceous materials: Spectral analysis and structural information," *Carbon*, 43(8), pp. 1731–1742. doi: 10.1016/j.carbon.2005.02.018.

Santamaria, A., Falco, G. De, Commodo, M., Minutolo, P. and D'Anna, A. (2013) "Raman features between two clases of carbon nanoparticles generated in ethylene flames," in *XXXVI Meeting of the Italian Section of the Combustion Institute*, pp. 2–7. Available at: http://www.combustion-institute.it/proceedings/XXXVI-ASICI/papers/36proci2013.II3.pdf.

Sariş, F., Hannah, D. M. and Eastwood, W. J. (2010) "Spatial variability of precipitation regimes over Turkey," *Hydrological Sciences Journal*, 55(2), pp. 234–249. doi: 10.1080/02626660903546142.

Schilman, B., Bar-Matthews, M., Almogi-Labin, A. and Boaz, L. (2001) "Global climate instability reflected by Eastern Mediterranean marine records during the late Holocene," *Palaeogeography, Palaeoclimatology, Palaeoecology*, 176(1-4), pp. 157–176. doi: 10.1016/S0031-0182(01)00336-4.

Schmidt, A., Quigley, M., Fattahi, M., Azizi, G., Maghsoudi, M. and Fazeli, H. (2011) "Holocene settlement shifts and palaeoenvironments on the Central Iranian Plateau: Investigating linked systems," *The Holocene*, 21(4), pp. 583–595. doi: 10.1177/0959683610385961.

Scholz, D. and Hoffmann, D. L. (2011) "StalAge – An algorithm designed for construction of speleothem age models," *Quaternary Geochronology*, 6(3-4), pp. 369–382. doi: 10.1016/j.quageo.2011.02.002.

Schwarcz, H. (1978) "Dating Methods of Pleistocene Deposits and Their Problems II," *Geoscience Canada*, 5(4), pp. 184–188.

Schwarcz, H. (2007) "Carbonate Stable Isotopes: Speleothems," in *Encyclopedia of Quaternary Science*, pp. 290–300. doi: 10.1016/B0-44-452747-8/00352-5.

SENSOY, S. (2004), "The mountains influence on Turkey climate", *BALWOIS conference on water observation and information system for decision support*. Available at http://balwois.com/balwois/administration/ppt/fp-239.ppt

Shamsi, A. and Kazemi, G. A. (2014) "A review of research dealing with isotope hydrology in Iran and the first Iranian meteoric water line," *Geopersia*, 4(1), pp. 73–86.

Sharifi, A., Pourmand, A., Canuel, E. A., Ferer-Tyler, E., Peterson, L. C., Aichner, B., Feakins, S. J., Daryaee, T., Djamali, M., Beni, A. N., Lahijani, H. A. K. and Swart, P. K. (2015) "Abrupt climate variability since the last deglaciation based on a high-resolution, multi-proxy peat record from NW Iran: The hand that rocked the Cradle of Civilization?," *Quaternary Science Reviews*, 123, pp. 215–230. doi: 10.1016/j.quascirev.2015.07.006.

Shen, C.-C., Wu, C.-C., Cheng, H., Lawrence Edwards, R., Hsieh, Y.-T., Gallet, S., Chang, C.-C., Li, T.-Y., Lam, D. D., Kano, A., Hori, M. and Spötl, C. (2012) "High-precision and high-resolution carbonate ^{230}Th dating by MC-ICP-MS with SEM protocols," *Geochimica et Cosmochimica Acta*, 99, pp. 71–86. doi: 10.1016/j.gca.2012.09.018.

Shopov, Y. Y., Ford, D. C. and Schwarcz, H. (1994) "Luminescent microbanding in speleothems: High-resolution chronology and paleoclimate," *Geology*, 22(5), pp. 407–410. doi: 10.1130/0091-7613(1994)022<0407:LMISHR>2.3.CO;2.

Simsek, S. (2003) "Hydrogeological and isotopic survey of geothermal fields in the Buyuk Menderes graben, Turkey," *Geothermics*, 32, pp. 669–678. doi: 10.1016/S0375-6505(03)00072-5.

Slack, C. R. and Hatch, M. D. (1967) "Comparative Studies on the Activity of Carboxylases and Other Enzymes in Relation to the New Pathway of Photosynthetic Carbon Dioxide Fixation in Tropical Grasses," *Biochemical Journal*, 1003(3), pp. 660–665. doi: 10.1042/bj1030660.

Snyder, J. A., Wasylik, K., Fritz, S. C. and Wright Jr, H. E. (2016) "Diatom-based conductivity reconstruction and palaeoclimatic interpretation of a 40-ka record from Lake Zeribar, Iran," *The Holocene*, 11(6), pp. 737–745. doi: 10.1191/09596830195753.

Spanos, S., Maheras, P., Karacostas, T. and Pennas, P. (2003) "Objective climatology of 500-hPa cyclones in central and east mediterranean region during warm-dry period of the year," *Theoretical and Applied Climatology*, 75(3-4), pp. 167–178. doi: 10.1007/s00704-003-0726-8.

Spötl, C., Fairchild, I. J. and Tooth, A. F. (2005) "Cave air control on dripwater geochemistry, Obir Caves (Austria): Implications for speleothem deposition in dynamically ventilated caves," *Geochimica et Cosmochimica Acta*, 69(10), pp. 2451–2468. doi: 10.1016/j.gca.2004.12.009.

Spötl, C. and Mangini, A. (2002) "Stalagmite from the Austrian Alps reveals Dansgaard ^ Oeschger events during isotope stage 3 : Implications for the absolute chronology of Greenland ice cores," *Earth and Planetary Science Letters*, 203(1), pp. 507–518.

Spötl, C., Unterwurzacher, M., Mangini, A. and Longstaffe, F. J. (2002) "Carbonate speleothems in the dry, inneralpine Vinschgau valley, northernmost Italy: witnesses of changes in climate and hydrology since the last glacial maximum," *Journal of Sedimentary Research*, 72(6), pp. 793–808. doi: 10.1306/041102720793.

Stevens, L. R., Ito, E., Schwalb, A. and Wright, H. E. (2006) "Timing of atmospheric precipitation in the Zagros Mountains inferred from a multi-proxy record from Lake Mirabad, Iran," *Quaternary Research*, 66(3), pp. 494–500. doi: 10.1016/j.yqres.2006.06.008.

Stevens, L., Wright, H. and Ito, E. (2001) "Proposed changes in seasonality of climate during the Lateglacial and Holocene at Lake Zeribar, Iran," *The Holocene*, 11, pp. 747–755. doi: 10.1191/09596830195762.

Stewart, M. K. (1975) "Stable Isotope Fractionation Due to Evaporation and Isotopic Exchange of Falling Waterdrops: Applications to Atmospheric Processes and Evaporation of Lakes," *Journal of Geophysical Research*, 80(9), pp. 1133–1146. doi: 10.1029/JC080i009p01133.

Stuiver, M., Grootes, P. M. and Brazunias, T. F. (1995) "The GISP2 δ^{18}O Climate Record of the Past 16,500 Years and the Role of the Sun, Ocean, and Volcanoes," *Quaternary Research*, 44(3), pp. 341–354.

Talebi, T., Ramezani, E., Djamali, M., Lahijani, H. A. K., Naqinezhad, A., Alizadeh, K. and Andrieu-Ponel, V. (2016) "The Late-Holocene climate change, vegetation dynamics, lake-level changes and anthropogenic impacts in the Lake Urmia region, NW Iran," *Quaternary International*, 408(A), pp. 1–12. doi: 10.1016/j.quaint.2015.11.070.

Tan, M., Baker, A., Genty, D., Smith, C., Esper, J. and Cai, B. (2006) "Applications of stalagmite laminae to paleoclimate reconstructions: Comparison with dendrochronology/climatology," *Quaternary Science Reviews*, 25(17-18), pp. 2103–2117. doi: 10.1016/j.quascirev.2006.01.034.

Tatli, H. (2007) "Synchronization between the North Sea – Caspian pattern (NCP) and surface air temperatures in NCEP," *International Journal of Climatology*, 27(9), pp. 1171–1187. doi: 10.1002/joc.1465.

Theodorakopoulou, K., Pavlopoulos, K., Athanassas, C. and Zacharias, N. (2012) "Sedimentological response to Holocene climate events in the Istron area, Gulf of Mirabello, NE Crete," *Quaternary International*, 266, pp. 62–73. doi: 10.1016/j.quaint.2011.05.032.

Thomas, E.R., Wolff, E.W., Mulvaney, R., Steffensen, J.P., Johnsen, S.J., Arrowsmith, C., White, J.W.C., Vaughn, B., Popp, T. 2007 "The 8.2ka event from Greenland ice cores", *Quaternary Science Reviews*, 26(1), pp 70-81. doi:/10.1016/j.quascirev.2006.07.017.

Touchan, R., Akkemik, Ü., Hughes, M. K. and Erkan, N. (2007) "May–June precipitation reconstruction of southwestern Anatolia, Turkey during the last 900 years from tree rings," *Quaternary Research*, 68(2), pp. 196–202. doi: 10.1016/j.yqres.2007.07.001.

Treble, P. C., Chappell, J. and Shelley, J. M. G. (2005) "Complex speleothem growth processes revealed by trace element mapping and scanning electron microscopy of annual layers," *Geochimica et Cosmochimica Acta*, 69(20), pp. 4855–4863. doi: 10.1016/j.gca.2005.06.008.

Tremaine, D. M. and Froelich, P. N. (2013) "Speleothem trace element signatures: A hydrologic geochemical study of modern cave dripwaters and farmed calcite," *Geochimica et Cosmochimica Acta*. Elsevier Ltd, 121, pp. 522–545. doi: 10.1016/j.gca.2013.07.026.

Tremaine, D. M., Froelich, P. N. and Wang, Y. (2011) "Speleothem calcite farmed in situ: Modern calibration of δ18O and δ13C paleoclimate proxies in a continuously-monitored natural cave system," *Geochimica et Cosmochimica Acta*. Elsevier Ltd, 75(17), pp. 4929–4950. doi: 10.1016/j.gca.2011.06.005.

Triantaphyllou, M. V (2014) "Coccolithophore assemblages during the Holocene Climatic Optimum in the NE Mediterranean (Aegean and northern Levantine Seas, Greece): Paleoceanographic and paleoclimatic implications," *Quaternary International*. Elsevier Ltd and INQUA, 345, pp. 56–67. doi: 10.1016/j.quaint.2014.01.033.

Triantaphyllou, M. V, Gogou, A., Dimiza, M. D., Kostopoulou, S., Parinos, C., Roussakis, G., Geraga, M., Bouloubassi, I., Fleitmann, D., Zervakis, V., Velaoras, D., Diamantopoulou, A., Sampatakaki, A. and Lykousis, V. (2016) "Holocene Climatic Optimum centennial-scale paleoceanography in the NE Aegean (Mediterranean Sea)," *Geo-Marine Letters*, 36(1), pp. 51–66. doi: 10.1007/s00367-015-0426-2.

Triantaphyllou, M. V., Gogou, A., Bouloubassi, I., Dimiza, M., Kouli, K., Rousakis, G., Kotthoff, U., Emeis, K.-C., Papanikolaou, M., Athanasiou, M., Parinos, C., Ioakim, C. and Lykousis, V. (2013) "Evidence for a warm and humid Mid-Holocene episode in the Aegean and northern Levantine Seas (Greece, NE Mediterranean)," *Regional Environmental Change*, 14(5), pp. 1697–1712. doi: 10.1007/s10113-013-0495-6.

Trouet, V., Esper, J., Graham, N. E., Baker, A., Scourse, J. D. and Frank, D. C. (2009) "Persistent positive North Atlantic oscillation mode dominated the Medieval Climate Anomaly.," *Science*, 324(5923), pp. 78–80. doi: 10.1126/science.1166349.

Turgeon, S. and Lundberg, J. (2001) "Chronology of discontinuities and petrology of speleothems as paleoclimatic indicators of the Klamath Mountains, southwest Oregon, USA," *Carbonates and Evaporites*, 16(2), pp. 153–167. doi: 10.1007/BF03175833.

Türkeş, M. (1996) "Spatial and temporal analysis of annual rainfall variations in Turkey," *International Journal of Climatology*, 16(9), pp. 1057–1076. doi: 10.1002/(SICI)1097-0088(199609)16:9<1057::AID-JOC75>3.0.CO;2-D.

Türkeş, M. (1998) "Influence of geopotential heights, cyclone frequency and Southern Oscillation on rainfall variations in Turkey," *International Journal of Climatology*, 680(6), pp. 649–680. doi: 10.1002/(SICI)1097-0088(199805)18:6<649::AID-JOC269>3.0.CO;2-3.

Türkeş, M. and Erlat, E. (2003) "Precipitation changes and variability in Turkey linked to the North Atlantic oscillation during the period 1930-2000," *International Journal of Climatology*, 23(14), pp. 1771–1796. doi: 10.1002/joc.962.

Turner, R., Roberts, N. and Jones, M. D. (2008) "Climatic pacing of Mediterranean fire histories from lake sedimentary microcharcoal," *Global and Planetary Change*, 63(4), pp. 317–324. doi: 10.1016/j.gloplacha.2008.07.002.

Tyrlis, E., Lelieveld, J. and Steil, B. (2013) "The summer circulation over the eastern Mediterranean and the Middle East: influence of the South Asian monsoon," *Climate Dynamics*, 40(5), pp. 1103–1123. doi: 10.1007/s00382-012-1528-4.

Ülgen, U. B., Franz, S. O., Biltekin, D., Çagatay, M. N., Roeser, P. A., Doner, L. and Thein, J. (2012) "Climatic and environmental evolution of Lake Iznik (NW Turkey) over the last ~4700 years," *Quaternary International*, 274, pp. 88–101. doi: 10.1016/j.quaint.2012.06.016.

Unal, Y. S., Deniz, A., Toros, H. and Incecik, S. (2010) "Temporal and spatial patterns of precipitation variability for annual, wet, and dry seasons in Turkey," *International Journal of Climatology*, 32(3), pp. 392–405. doi: 10.1002/joc.2274.

Ünal-İmer, E., Shulmeister, J., Zhao, J.-X., Uysal, I. T., Feng, Y.-X., Nguyen, A. D. and Yüce, G. (2015) "An 80 kyr-long continuous speleothem record from Dim Cave, SW Turkey with paleoclimatic implications for the Eastern Mediterranean.," Nature *Scientific Reports*, 5, pp. 1–9. doi: 10.1038/srep13560.

Ünal-Imer, E., Shulmeister, J., Zhao, J.-X., Uysal Tonguç, I. and Feng, Y.-X. (2016) "High-resolution trace element and stable/radiogenic isotope profiles of late Pleistocene to Holocene speleothems from Dim Cave , SW Turkey," *Palaeogeography, Palaeoclimatology, Palaeoecology*, 452, pp. 68–79. doi: 10.1016/j.palaeo.2016.04.015.

Urey, H. C. (1947) "The Thermodynamic Properties of Isotopic Substances," *Journal of The Chemical Society*, pp. 562–581. doi: 10.1039/JR9470000562.

Vaks, A., Gutareva, O. S., Breitenbach, S. F. M., Avirmed, E., Mason, A. J., Thomas, A. L., Osinzev, A. V, Kononov, A. M. and Henderson, G. M. (2013) "Supplementary Materials for Speleothems Reveal 500,000-Year History of Siberian Permafrost," *Science*, 340(6129), pp. 0–26. doi: 10.1126/science.1228729.

Vanniere, B., Power, M. J., Roberts, N., Tinner, W., Carrion, J., Magny, M., Bartlein, P., Colombaroli, D., Daniau, a. L., Finsinger, W., Gil-Romera, G., Kaltenrieder, P., Pini, R., Sadori, L., Turner, R., Valsecchi, V. and Vescovi, E. (2011) "Circum-Mediterranean fire activity and climate changes during the mid-Holocene environmental transition (8500-2500 cal. BP)," *The Holocene*, 21(1), pp. 53–73. doi: 10.1177/0959683610384164.

Vassilopoulou no date, www.kastriacave.gr/en all site content derived from the Hellenic Ministry of Culture and Sports, Ephorate for Paleoanthropology and Speleology September 2002 "The Cave of the Lakes".

Verheyden, S., Keppens, E., Fairchild, I. J., Mcdermott, F. and Weis, D. (2000) "Mg, Sr and Sr isotope geochemistry of a Belgian Holocene speleothem: implications for paleoclimate reconstructions," *Chemical Geology*, 169(1-2), pp. 131–144. doi: 10.1016/S0009-2541(00)00299-0.

Verheyden, S., Keppens, E., Van Strydonck, M. and Quinif, Y. (2012) "The 8.2 kyr event: is it registered in Belgian speleothems?," *Speleogenesis and the Evolution of Karst Aquifers*, (12), pp. 3–8.

Verheyden, S., Nader, F. H., Cheng, H. J., Edwards, L. R. and Swennen, R. (2008) "Paleoclimate reconstruction in the Levant region from the geochemistry of a Holocene stalagmite from the Jeita cave, Lebanon," *Quaternary Research*. University of Washington, 70(3), pp. 368–381. doi: 10.1016/j.yqres.2008.05.004.

Wagner, B., Lotter, A. F., Nowaczyk, N., Reed, J. M., Schwalb, A., Sulpizio, R., Valsecchi, V., Wessels, M. and Zanchetta, G. (2009) "A 40,000-year record of environmental change from ancient Lake Ohrid (Albania and Macedonia)," *Journal of Paleolimnology*, 41, pp. 407–430. doi: 10.1007/s10933-008-9234-2.

Walker, M., Johnsen, S., Rasmussen, S. O., Popp, T., Steffensen, J., Cwynar, L. E. S. C., Hughen, K., Gibbard, P., Hoek, W. I. M., Lowe, J., Andrews, J., Björck, S., Cwynar, L., Hughen, K., Kershaw, P., Kromer, B., Litt, T., Lowe, D., Nakagawa, T., Newnham, R. and Schwander, J. (2009) "Formal definition and dating of the GSSP (Global Stratotype Section and Point) for the base of the Holocene using the Greenland NGRIP ice core, and selected auxiliary records," *Journal of Quaternary Science*, 24(1), pp. 3–17. doi: 10.1002/jqs.

Walker, R. T. and Fattahi, M. (2011) "A framework of Holocene and Late Pleistocene environmental change in eastern Iran inferred from the dating of periods of alluvial fan abandonment, river terracing, and lake deposition," *Quaternary Science Reviews*, 30(9-10), pp. 1256–1271. doi: 10.1016/j.quascirev.2011.03.004.

Wassenburg, J. A., Immenhauser, A., Richter, D. K., Jochum, K. P., Fietzke, J., Deininger, M., Goos, M., Scholz, D. and Sabaoui, A. (2012) "Climate and cave control on Pleistocene/Holocene calcite-to-aragonite transitions in speleothems from Morocco: Elemental and isotopic evidence," *Geochimica et Cosmochimica Acta*. Elsevier Ltd, 92, pp. 23–47. doi: 10.1016/j.gca.2012.06.002.

Wassenburg, J. A., Immenhauser, A., Richter, D. K., Niedermayr, A., Riechelmann, S., Fietzke, J., Scholz, D., Jochum, K. P., Fohlmeister, J., Schröder-Ritzrau, A., Sabaoui, A., Riechelmann, D. F. C., Schneider, L. and Esper, J. (2013) "Moroccan speleothem and tree ring records suggest a variable

positive state of the North Atlantic Oscillation during the Medieval Warm Period," *Earth and Planetary Science Letters*. Elsevier, 375, pp. 291–302. doi: 10.1016/j.epsl.2013.05.048.

Weedon, G. P. (2003) "Time-Series Analysis and Cyclostratigraphy Examining stratigraphic records of environmental cycles". 1st edn, *Cambridge University Press*. 1st edn. Cambridge University Press, pp. vii–20.

Weiberg, E., Unkel, I., Kouli, K., Holmgren, K., Avramidis, P., Bonnier, A., Dibble, F., Finné, M., Izdebski, A., Katrantsiotis, C., Stocker, S. R., Andwinge, M., Baika, K., Boyd, M. and Heymann, C. (2016) "The socio-environmental history of the Peloponnese during the Holocene: Towards an integrated understanding of the past," *Quaternary Science Reviews*, 136, pp. 40–65. doi: 10.1016/j.quascirev.2015.10.042.

Weiss, B. (1982) "The decline of Late Bronze Age civilization as a possible response to climatic change," *Climatic Change*, 4, pp. 173–198.

Weiss, H. (2016) "Global megadrought, societal collapse and resilience at 4.2-3.9 ka BP across the Mediterranean and west Asia," *Pages*, 24(2), pp. 62–63. doi: 10.22498/pages.24.2.62.

Weiss, H., Courty, M. A., Wetterstrom, W., Guichard, F., Senior, L., Meadow, R. and Curnow, A. (1993) "The genesis and collapse of the third millennium North Mesopotamian Civilization," *Science*, 261(5124), pp. 955–1004. doi: 10.1126/science.261.5124.995.

White, W. (2012) "Speleothem microstructure/speleothem ontogeny: a review of Western contributions," *International Journal of Speleology*, 41, pp. 329–358.

Whitehead, N. E., Ditchburn, R. G., Williams, P. W. and McCabe, W. J. (1999) "^{230}Pa and ^{230}Th contamination at zero age: a possible limitation on U/Th series dating of speleothem material," *Chemical Geology*, 156(1), pp. 359–366. doi: 10.1016/S0009-2541(98)00192-2.

Wick, L., Lemcke, G. and Sturm, M. (2003) "Evidence of Lateglacial and Holocene climatic change and human impact in eastern Anatolia: high-resolution pollen, charcoal, isotopic and geochemical records from the laminated sediments of Lake Van, Turkey," *The Holocene*, 13(5), pp. 665–675. doi: 10.1191/0959683603hl653rp.

Wickens, L. B. (2013) *Geochemistry and Petrography of speleothems from Turkey and Iran: Palaeoclimate and Diagenesis*.

Wurth, G., Niggemann, S., Richter, D. K. and Mangini, A. (2004) "The Younger Dryas and Holocene climate record of a stalagmite from Hölloch Cave (Bavarian Alps, Germany)," *Journal of Quaternary Science*, 19(3), pp. 291–298. doi: 10.1002/jqs.837.

Xoplaki, E., Luterbacher, J., Burkard, R., Patrikas, I. and Maheras, P. (2000) "Connection between the large-scale 500 hPa geopotential height fields and precipitation over Greece during wintertime," *Climate Research*, 14, pp. 129–146. doi:10.3354/cr014129.

Yavuz, V., Akcar, N. and Schlüchter, C. (2007) "The frozen Bosphorus and its paleoclimatic implications based on a summary of the historical data," in *The Black Sea Flood Question: Changes in Coastline, Climate and Human Settlement*, pp. 633–642.

Zanchetta, G., Bar-Matthews, M., Drysdale, R. N., Lionello, P., Ayalon, a., Hellstrom, J. C., Isola, I. and Regattieri, E. (2014) "Coeval dry events in the central and eastern Mediterranean basin at 5.2

and 5.6ka recorded in Corchia (Italy) and Soreq caves (Israel) speleothems," *Global and Planetary Change*. Elsevier B.V., 122, pp. 130–139. doi: 10.1016/j.gloplacha.2014.07.013.

Zanchetta, G., Drysdale, R. N., Hellstrom, J. C., Fallick, A. E., Isola, I., Gagan, M. K. and Pareschi, M. T. (2007) "Enhanced rainfall in the Western Mediterranean during deposition of sapropel S1: stalagmite evidence from Corchia cave (Central Italy)," *Quaternary Science Reviews*, 26(3-4), pp. 279–286. doi: 10.1016/j.quascirev.2006.12.003.

Van Zeist, W. and Wright Jr, H. E. (1963) "Preliminary Pollen Studies at Lake Zeribar, Zagros Mountains, Southwestern Iran," *Science*, 140(3562), pp. 65–67. doi: 10.1126/science.140.3562.65.

Zeder, M.A. (2008) "Domestication and early agriculture in the Mediterranean Basin: Origins, diffusion, and impact", *Procedures of the National Academy of Science USA*, 105(33, pp. 11597–11604. doi: 10.1073/pnas.0801317105.

Zhou, H., Zhao, J., Zhang, P., Shen, C.-C., Chi, B., Feng, Y., Lin, Y., Guan, H. and You, C.-F. (2008) "Decoupling of stalagmite-derived Asian summer monsoon records from North Atlantic temperature change during marine oxygen isotope stage 5d," *Quaternary Research*, 70(2), pp. 315–321. doi: 10.1016/j.yqres.2008.04.007.

Ziv, B., Saaroni, H. and Alpert, P. (2004) "The factors governing the summer regime of the eastern Mediterranean," *International Journal of Climatology*, 24(14), pp. 1859–1871. doi: 10.1002/joc.1113.

Methods Appendix

M.1   Stable Isotope Analysis

Sample powders for overall stable isotope records were collected by myself using a hand held dentist drill with a steel 0.5 mm circular tipped drill bit at 1 mm resolution. Given that the drill bit is half the width of the resolution needed and the tendency for human error, sample resolution is assumed to be 1 mm but discrepancies will occur. Additionally all stalagmites were broken in at least one place erratically and thus sampling on the all sections of slab may not always align perfectly with each other, which may lead to further discrepancy in sample number vs mm height. Samples for the small section of HY-8 laminations and over the region of the 8.2 kyr event in KTR-2 were drilled using a Micromill at UEA. Sample trenches 10 μm wide and 60-150 μm deep were micromilled at as close to continuous resolution as possible allowing for a slight gap to prevent overlap of trenches. Carbonate powder of sample and standard between 60 and 80 μg were weighed into stainless steel capsules except for the period 2/11/15-7/12/15 when 130-150 μg sizes where used due to temporary reduction in mass spectrometer sensitivity.

Stable isotopes were measured at UEA (by Alina Marca and myself) on a Europa SIRA II dual inlet isotope ratio mass spectrometer. The CO_2 was prepared prior to entering the system from carbonate samples and standards by acid digestion with 105% phosphoric acid at 90°C, using an on-line common acid bath system developed in house.

Data is reported as delta values in per mil units, relative to an international reference material, defined by equation M.1:

$$\delta(‰) = \frac{R_{sam} - R_{ref}}{R_{ref}} \, x \, 1000$$

Equation M.1 stable isotopic notation and equation.

Where R_{sam} and R_{ref} represent the ratio of the heaviest isotope to the light isotope (e.g. $^{13}C/^{12}C$ or $^{18}O/^{16}O$) in the sample's gas and international reference. Both the $\delta^{13}C$ and $\delta^{18}O$ reported here are with respect to the VPDB international reference (Vienna Pee Dee Belemnite). Lower ratios in the sample relative to the standard generate negative delta values and vice versa.

Samples were analysed in batches of 47 capsules, of which 7 were the SIL lab standard (UEACMST - UEA Carrara Marble Standard) The standard deviation (1σ) of 7 repeat analyses per batch of the UEACMST carbonate standard shows a measurement precision 0.09 ‰ for δ^{13}C and 0.08 ‰ for δ^{18}O.

Previous stable isotope work in SIL UEA has found that there are memory effects when using a common acid bath (A Marca pers. comm. 2015). These memory effects arise from the fact that a very small proportion of carbon dioxide remains dissolved in the acid, even after the 15 minute reaction time and consequent pumping time between samples, thus if two consecutive carbonate samples are very different in isotopic composition, then the results of a sample are influenced by the sample reacted in the acid bath beforehand. Also in the SIL UEA case, the UEACMST lab standard is a coarser grain material, which takes longer to digest and therefore some of its CO_2 is retained in the acid bath more than compared to powder carbonate material, thus entering the mass spectrometer with the following sample. To account for the potential memory effects the first two samples in every batch (following the UEACMST lab standard) were rerun again away from the start of the batch to compare replicates. Further duplicate measurements were also obtained for results that appeared anomalous and/or displayed a significant excursion over one data point in order to check the validity of the measurement. Replicates within 0.2 ‰ were within experimental error and either could be used and replicates less than or equal to 0.4 ‰ were averaged. Any replicates which were 0.5 ‰ or greater were rerun where possible and the best fit chosen.

M.2 Calcite equilibrium calculations

Modern calcite must be checked to see if it precipitated in isotopic equilibrium with the dripwater, meaning that the temperature calculated based on the isotopic composition of the calcite and the isotopic composition of the dripwater, should be similar to the measured cave temperatures. Traditionally this is calculated using the Kim and O'Neil (1997) equation (Equation M.2):

1000 ln(αCaCO$_3$-H$_2$0) = 2.76(10^{6}T^{-2}) - 3.96

Equation M.2: Kim and O'Neil (1997)

Where α represents the fractionation factor between the carbonate and the water and T represents the temperature of the carbonate precipitation (in degrees Kelvin). The fractionation factor α can be calculated using the known (measured) isotopic composition of the calcite and that of the parent water as follows (Equation M.3):

$$\alpha = \frac{1000 + \delta^{18}O_{carbonate}}{1000 + \delta^{18}O_{water}}$$

Equation M.3: Isotope fractionation factor

Where the $\delta^{18}O_{carbonate}$ and $\delta^{18}O_{water}$ represent the measured isotopic compositions for the carbonate and the parent water, from which the carbonate had precipitated (both expressed in ‰ with respect to the VSMOW international reference material).

Tremaine et al. (2011) found that cave calcite values are offset from the predicted values using the Kim and O'Neil equation (Equation M.2) because ^{18}O contained within inorganic cave calcite is more enriched than predicted by laboratory experiments by Kim and O'Neil. This is due to the very slow precipitation of calcite in caves from slightly supersaturated dripwaters (Tremaine et al. 2011). The temperature dependant fractionation of Tremaine et al. (2011) takes this into account (see Equation M.4):

1000 ln α= 16.1 (10^3 T^{-1}) -24.6

Equation M.4: Tremaine et al. (2011)

Both equations are utilised within this study to compare which is closer to measured values within individual caves.

M.3 Trace Element ICP-MS and Solutions

Trace element contents in speleothem carbonates were made using either sub-sample dissolution (analysis by optical emission ICP) or by laser ablation (LA) of the solid sample tablet. The

instruments were operated by Graham Chilvers (UEA) although solution preparation was carried out by myself.

The trace element transect for KT-3 was obtained by the solution method. Drilled carbonate samples of 2.5 mg were dissolved in 5 ml of 10% acetic acid, and then diluted to 50 ml with MilliQ water. Samples were analysed on a Varian ICPOES with trace element concentrations determined relative to the CRM00028 calcite standard.

Trace Element	Sr 421.552	Ba 233.527	P 213.618	Mg 285.213	Ca 315.887	K 766.491
precision (ug/l) (±)	0.097533	0.201411	17.06991	0.815934	6.93462	3.341051
limit of detection of measurements	0.000293	0.000604	0.05121	0.002448	0.020804	0.010023
LOD corrected for dilution (mg/l)	5.851974	12.08469	1024.195	48.95604	416.0772	200.4631

Table M.1: Precision and limits of detection for trace elements analysed by the solution method from stalagmite KT-3

Laser ablation analysis was carried out on a Thermo-Electron 277 X-Series ICP-MS using a New Wave Research UP-213 Laser Ablation System and argon carrier gas. Grey layer trace element data was obtained using continuous transects of 5 and 7 mm length, 30 µm wide. Trace elements from the region of the 8.2 kyr event in KTR-2, and for annual laminations in HY-8, were obtained by LA spot sampling, using a spot size of 30 µm and sample spacing of 170 and 200 µm respectively. Both the analyses on KTR-2 and HY-8 were carried out using the following settings: laser output at 55%, 4Hz repetition rate and a dwell time of 40 seconds. All sections were pre-ablated to remove surface contamination to a depth of 10 µm. Samples were calibrated using NIST glass standards 610 and 612 using values published from http:nist.gov/srm, as well as mixed calcite standards due to the fact the laser coupled better with carbonate than with silicate.

Trace Element	^{23}Na	^{24}Mg	^{43}Ca	^{88}Sr	^{137}Ba	^{31}P
precision (mg/kg) (±)	52.41	186.47	3282.74	14.09	12.78	47.28
% precision	2.720	3.840	2.317	2.847	3.019	14.230
Limit of detection (mg/kg)	157.22			49.66	0.76	47.13
Limit of detection (%)		1.870	0.985			

Table M.2: Precision and limits of detection for trace elements analysed by laser ablation spot analysis from stalagmites KTR-2 and HY-8. Mn, Zn, Al and Fe are not included as transect signals will be qualitative.

In this study trace element data are presented as follows: all data is normalised to a Ca internal standard and presented in ppm units. Data is normalised to calcite by dividing the assumed 40 wt% value for Ca (in $CaCO_3$) by the measured wt% of Ca, then multiplying the raw concentration value of the trace element by that divided value. Mg, Sr and Ba are expressed as molar ratios relative to Ca which is achieved by first dividing the concentration in ppm by the atomic weight of the element and then dividing this value for the trace element by the value for Ca. This ratio is multiplied by 1000 to allow for easier comparison to stable isotopes. Mg/Sr molar ratios are also presented.

M.4 U-Series Dating

Analytical work on HY-8, Dim-1 and KTR-2 were undertaken at the NERC Isotope Geosciences Laboratory at the British Geological Survey site in Keyworth. Analytical work on KT-3 was undertaken at the University of Oxford Earth Sciences Department. All dates are presented in yr BP relative to 1950 with present being the date of analysis.

Method provided by Steve Noble, NIGL, BGS. Some samples prepared by myself, all samples prepared and run by Steve Noble and Diana Sahy.

Chemical preparation was carried out in a HEPA-filtered class 100 workstation. Reagents were prepared by sub-boiling in either quartz or Teflon, both in house and purchased from Romil UK (UpA grade) and all vessels used for sample processing were Savillex PFA.

Powdered samples (sizes between 95 and 218 mg) were dissolved in water diluted 15 M HNO_3, dispensed in drops to avoid overly vigorous reaction. Dissolved samples were spiked with a mixed ^{229}Th-^{236}U tracer calibrated against gravimetric solutions prepared from CRM 112a U metal and Ames Laboratory high purity Th metal. Equilibration of the new solution was achieved by refluxing samples overnight in sealed vials, drying down and finally taking up and refluxing again this time in 7M HNO_3.

Following this samples were dried down and reacted in 15 M HNO_3 and 30% H_2O_2 (oxidation maximized via a 10:1 ratio) to consume organic materials which can negatively impact further chemistry. Additionally any samples containing detritus insoluble in nitric acid were separated by the differing solubility and the insoluble fraction was completely dissolved using an HF-HNO_3-$HClO_4$ acid mixture. This whole step was conducted in an Evapoclean device in PFA vessels. The sample was recombined once total dissolution had been achieved. Two oxidation steps were required before column chemistry proper- pre-concentration by coprecipitation of Fe using an FeCl solution prepared from Puratronic Fe nitrate and initial separation of U and Th using AG-1 x 8 anion resin on homemade polypropylene 0.6 ml columns with hydrophilic polyethylene frits (procedures established by Edwards et al. (1988)). Samples were taken up in 1 M HCl before co-precipitation then 4-8 mg of Fe was added as FeCl allowing U and Pb to precipitate with the Fe once 22 M ammonia solution was added. The samples were transferred to tightly sealed precleaned PP tubes and centrifuged at 2500 rpm for 5 minutes. Then the supernatant liquid was pipetted off and discarded. The precipitates were washed and centrifuged 3 times with Milli Q water to remove unneeded sample matrix prior to dissolution in acid.

For column chemistry samples were loaded and washed on cleaned and equilibrated columns in 7 M HNO_3, Th was then eluted in 8 M HCl and the solution was passed through the column again to elute U using 0.2 M HCl. Elements were initially separated on AG- 1 x 8 but Th aliquots undergo a second purification through the AG-1 x 8 columns. Immediately after chemistry samples are filtered through Teflon 0.22 micron syringe filters (Millipore) to remove colloidal material and any

left-over resin beads as this radically lessened the organic load on the mass spectrometer. The final chemical step involved oxidation using 15 M HNO_3 and 30% H_2O_2.

Analysis was performed on a Thermo Neptune Plus MC-ICP-MS (sensitivity ca. 350-500 V/ppm U) with sample introduction through an Aridus II desolvating nebulizer at an uptake rate of ~50 microlitres/minute. U mass bias and SEM/Faraday gain correction of unknowns was based on standard-sample bracketing. Measurements of CRM 112a spiked with a $^{233}U/^{236}U$ tracer (IRMM 3636) were used for the exponential correction for U mass bias, while SEM gain was checked using measured $^{234}U/^{235}U$ of mass bias-corrected unspiked CRM 112a, the mass-bias and spike-corrected $^{234}U/^{238}U$ values of the spiked CRM 112a runs were used as a check on the SEM gain. Hydride and tailing corrections on the measurements followed Hiess et al. (2012). Both hydride and down-mass tailing were on the order of 2 ppm of adjacent peaks and over a timescale of a number of days was very consistent on the Neptune.

SEM gain and mass bias for Th measurements were corrected using an in house ^{229}Th-^{230}Th-^{232}Th reference solution. This solution is calibrated by ICP-MS against the CRM 112a standard. Th isotopes were measured in static multicollection mode utilising Neptune Jet cones collecting 900-1100 V/ppm Th, at an uptake rate of 50 microlitres/minute. ^{238}U and ^{232}Th blanks were negligible relative to samples in this study totalling generally <10 pg and <4 pg respectfully. Standard accuracy and reproducibility of $^{234}U/^{238}U$ was monitored by repeat analyses of Harwell uraninite HU-1 to ensure they remained with 0.1% (accuracy) and 0.2% (reproducibility). Replicate of the ^{229}Th-^{230}Th-^{232}Th reference solution indicate that accuracy and reproducibility for $^{229}Th/^{230}Th$ is on the order of ± 0.2-0.3% for ^{230}Th ion beams with greater than 5000 cps. Data was reduced using an Excel spreadsheet created in –house with the Isoplot version 3 add in (Ludwig 2012) to calculate ages following Ludwig (2003) and decay constants listed in Cheng et al., (2013). Samples are all corrected for detrital Th assuming a bulk earth composition for the detrital Th component. This assumes stalagmite calcite is at secular equilibrium with the bulk earth $^{232}Th/^{230}Th$ value (3.8) and that initial $^{230}Th/^{232}Th$ has an atomic ratio of 4.4 ± 2.2 x10^{-6}. Uncertainty errors are ± 50%.

M.4.2 Early Dim-1 dates

Some early dates obtained from Dim-1 were ran before the Thermo Neptune Plus MC-ICP-MS was acquired at the BGS. Sample preparation and column chemistry was the same but U data was obtained from an Axiom MC-ICP-MS with ^{234}U measured on an SEM. Samples were introduced using an Aridus 1 desolvating nebulizer with an introduction rate of ~50 microlitres/minute and the Axiom performed the data collection in static mode. U sensitivity was ca. 100 V/ppm and the

data again calibrated by replicates analyses of the CRM 112a standard. Th data was collected on another MC-ICP-MS, a Nu instruments Nu HR. The Nu HR is fitted with a DSN desolvating nebulizer and equipment sensitivity was ca. 200 V/ppm U.

M.4.3   KT-3

Method provided by Stacy Carolin, University of Oxford and adapted from Vaks et al., (2013) supplementary material. All samples drilled, prepared and run by Stacy at the University of Oxford.

Powdered stalagmite samples were drilled using a hand held dentist drill and a 0.8 or 1.0 mm tungsten carbide round top bur. All chemical procedures are undertaken under a fume hood using Savillex PFA vessels.

Samples dissolved in 400 µl of 16M HNO_3 are spiked with mixed ^{229}Th-^{236}U spike and shook for 10-15 minutes. If bubbles or detrital material is present after this step an extra 100 µl of 16M HNO_3 is added and the step repeated. Vials are refluxed overnight on a hot plate to equilibrate sample and spike. Before column chemistry samples are converted to nitrate form. This involves evaporating the sample/spike mix on a hot plate then adding 300 µl of 16 M HNO_3, if bubbles or suspended material is still present at this stage the sample is refluxed. All samples are then dried down on a hot plate and once cooled 4ml of 7.5 M HNO_3 is added.

Column chemistry for chemical separation is adapted from procedures in Edwards et al. 1986. Columns are conditioned using 7.5M HNO_3 and some U is eluted from the added sample during this phase. Th is eluted using 6M HCL and the rest of the U is eluted using milliQ water after Th.

Measurements of U and Th were undertaken on a Nu Instrument Multicollector Inductively Coupled Plasma Mass Spectrometer (MC-ICP-MS). U measurements were performed using the Faraday cups for all species except ^{234}U which was measured via ion counter. During initial U measurement abundance sensitivity was corrected for using the half-mass dynamic measurements at 236.5, 235.5, 234.5 and 233.5 on the ion-counter. Dynamic Th measurements were performed. During this step ^{238}U, ^{235}U and ^{232}Th were measured the Faraday cups and ^{230}Th and ^{229}Th on ion-counter. Measurements were performed in two steps firstly ^{235}U-^{232}Th-^{230}Th then ^{238}U-^{235}U-^{229}Th. Signal noise between the two steps was corrected for by normalising to the respective ^{235}U measurement in each step. Instrumental memory has been corrected for. Th abundance sensitivity was corrected for during the final part of measurements on the ion counter using the half-mass dynamic measurements at 230.5, 229.5 and 228.5. Mass fractionation and ion

counter gains were corrected using sample-standard bracketing with CRM-145 for U, and two in house ^{229}Th-^{230}Th-^{232}Th standards for Th. The correction for initial Th and the final dating results were calculated using Isoplot 4.15.

M.5 Lamination counting

Laminations were counted using continuous thin sections from a continuous series of photomicrographs marked at both ends of the count section on each individual photomicrograph so laminations could not be duplicated. Initially laminations were counted manually, with pencil and ruler using the original photomicrographs. A second count was performed using Image J on photomicrographs with contrast altered in an attempt to highlight more subtle differences in the fabric of lamination if it existed. The count was performed manually but within the Image J software. Two more lamination counts were performed one on paper and one again with contrast enhanced on Image J after going back to thin sections to assess which laminae were discontinuous.

M.6 Justification for using COPRA and linear interpolation

M.6.1 Using COPRA over StalAge

The basic premise behind both programmes is the same: both run Monte Carlo simulations in order to determine the best fit for the most likely age model. The differences lie in the functionality. StalAge uses just a linear extrapolation (arguing that simple is best and avoids over interpretation), COPRA allows the choice of linear, cubic or spline dependant on preference. COPRA also allows the addition of incremental counting data. COPRA provides the maximum and minimum possible ages based on all Monte Carlo runs as well as the chosen median age. The main difference however, is that StalAge automatically detects and treats outliers, reversal, hiatuses ect. COPRA does not. Due to the nature of Chapter 4 of this thesis using petrography to rule out dates rather than statistics and the facility to add layer counting data COPRA is preferred over StalAge.

M.6.2 Using linear over spline interpolation

Spline interpolation often ignores absolute dating points. Furthermore Scholz and Hoffmann (2011) argue that any interpolation aside from linear can cause over interpretation of the data.

Though age models used in this thesis are all created using linear extrapolation, ages from KT-3 and KTR-2 were run in COPRA using spline interpolations. Using this interpolation method most of the absolute dates were not at the measured distance they should be (in some cases not present at all with different years favoured. A spline interpolation does not adequately account for differences in growth rate between dating locations to make it worth using over a basic linear interpolation.

M.7 Petrographic Thin Sections

Thin sections were produced both in house (HY-8) by John Brindle and at the BGS (Dim-1, KTR-2, KT-3 and some further HY-8 samples) by John Fletcher. All thin sections utilised were cover slipped. Most are standard size but 3 larger cover slipped thin sections (2 at 110 x 75 mm and 1 75 x 50 mm) were produced by the BGS. Larger sections covered areas of prominent continuous lamination in the HY-8 stalagmite providing more ease in counting and were vacuum resin impregnated to help bonding. Thin sections were observed and photographed using a Leica petrographic microscope (model DM2500 M) with an attached digital camera.

M.8 Raman Spectroscopy

Method provided by John Brindle (UEA)

Raman spectroscopy is not a commonly used method in speleothem studies and was specifically utilised to attempt to locate soot particles (carbon) within stalagmite HY-8 from SW Turkey (Chapter 5). Raman spectroscopy is the measurement of wavelength scattering of monochromatic light (Laserna 2006). This requires the use of lasers to change a photon's energy state (which can be higher or lower than the incident proton) where the change is created by a shift in either the vibrational or rotational energy of a molecule (Laserna 2006). The degree of change in vibrational or rotational energy is a fixed value known for numerous molecules and can be related to specific bonding and other structural details using wavelength spectra (Laserna 2006).

The Raman instrument consists of a modified Olympus metallurgical microscope operating in infinity mode, using an 80X plan objective. The laser is a Quantum Gem working at 532 nm and linked to the illumination optics of the microscope by a 50 μm fibre-optic lead. The Aseq HR1-T spectrometer is again connected fibre optically and is configured for Stokes operation with a focal length of 10 cm and using a 25mm 1200 lpmm grating in the Czerny-Turner configuration. It has a

TE cooled CCD linear array detector. Raman-shifted signals can be distinguished down to 60cm^{-1} from the laser line and a 15mW 10 μm spot is produced. Integration time was 30 sec throughout, and correction was made for the instrument's background signal. Curve corrections on spectra are applied following the method in Santamaria et al. (2013).

M.9   HY-8 Filtered residues

Three filtered residues were created from a chip of the base of HY-8, dissolved in 10% hydrochloric acid (HCL) and filtered via a syringe attachment through polycarbonate Millipore filters of 1 μm and 0.4 μm pore sizes and a cellulose filter of 1 μm pore size. A further residue of a much larger section of the base of the stalagmite was dissolved in 30% nitric acid and filtered through a 0.4 μm Millipore filter. The residue left on the Millipore filters was investigated through SEM and the chemical composition was investigated using EDX (uncoated under low vacuum). Sections of the filters were gold coated to gain better visual definition using high vacuum. The cellulose filter was also investigated using a standard transmitted light microscope.
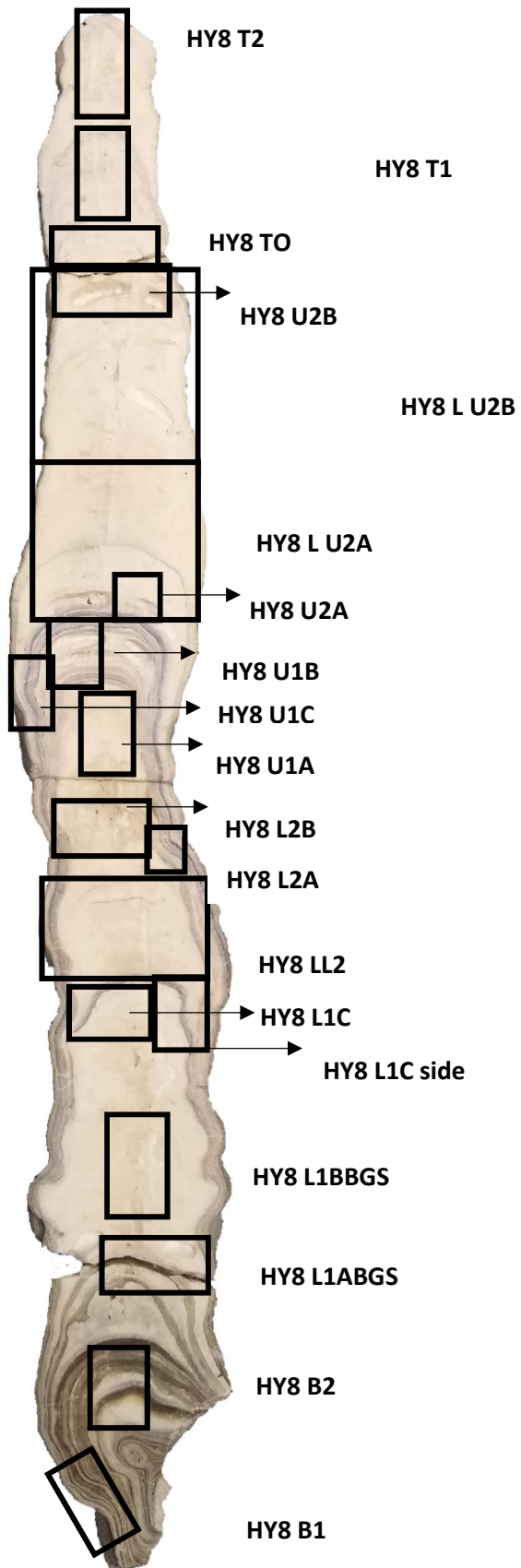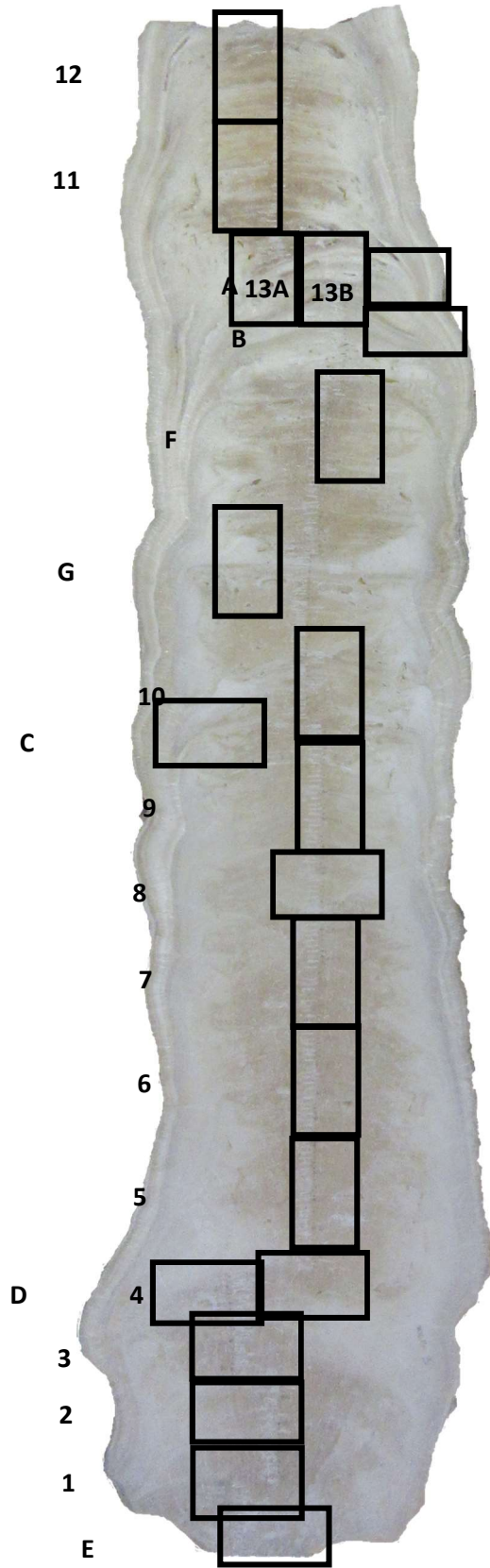
Appendix

A.1   Thin Section Locations

A.1.1   KTR-2

KTR2-4

KTR2-3

KTR2-2

KTR2-1

A.1.1.2   HY-8

HY8 T2

HY8 T1

HY8 TO

HY8 U2B

HY8 L U2B

HY8 L U2A

HY8 U2A

HY8 U1B

HY8 U1C

HY8 U1A

HY8 L2B

HY8 L2A

HY8 LL2

HY8 L1C

HY8 L1C side

HY8 L1BBGS

HY8 L1ABGS

HY8 B2

HY8 B1

A.1.1.4 KT-3

KT3-8

KT3-7

KT3-6

KT3-5

KT3-4

KT3-3

KT3-2

KT3-1